



**This electronic thesis or dissertation has been downloaded from Explore Bristol Research, <http://research-information.bristol.ac.uk>**

*Author:*  
**Dietz, Matthew**

*Title:*  
**Developing an holistic understanding of interface friction using sand with direct shear apparatus.**

**General rights**

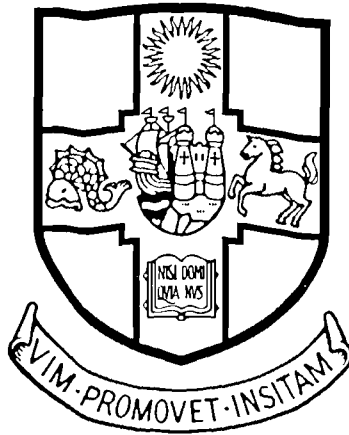
The copyright of this thesis rests with the author, unless otherwise identified in the body of the thesis, and no quotation from it or information derived from it may be published without proper acknowledgement. It is permitted to use and duplicate this work only for personal and non-commercial research, study or criticism/review. You must obtain prior written consent from the author for any other use. It is not permitted to supply the whole or part of this thesis to any other person or to post the same on any website or other online location without the prior written consent of the author.

**Take down policy**

Some pages of this thesis may have been removed for copyright restrictions prior to it having been deposited in Explore Bristol Research. However, if you have discovered material within the thesis that you believe is unlawful e.g. breaches copyright, (either yours or that of a third party) or any other law, including but not limited to those relating to patent, trademark, confidentiality, data protection, obscenity, defamation, libel, then please contact: [open-access@bristol.ac.uk](mailto:open-access@bristol.ac.uk) and include the following information in your message:

- Your contact details
- Bibliographic details for the item, including a URL
- An outline of the nature of the complaint

On receipt of your message the Open Access team will immediately investigate your claim, make an initial judgement of the validity of the claim, and withdraw the item in question from public view.



**Developing an holistic understanding of interface friction  
using sand within the direct shear apparatus**

by

Matthew S Dietz

A dissertation submitted to the University of Bristol in accordance with the requirements of the degree of Doctor of Philosophy in the Faculty of Engineering, Department of Civil Engineering

December 2000

## Abstract

A new direct shear apparatus has been devised which removes many of the defects inherent in the archetype whilst retaining its simplicity, thereby providing a cost-effective alternative to the more sophisticated examples of the apparatus found in the literature. The salient features of the device, known as the Winged Direct Shear Apparatus (WDSA), include a free-floating upper half, which permits the reliable estimation of stress on the central plane, and an articulation that minimises secondary forces and moments otherwise generated during testing. Performance has been optimised producing a test configuration unlike that stipulated by the Standards; substantial increases in the opening between the shearbox's frames requires rubber shielding to limit sample extrusion, dentated plates are discarded, and the shearbox's upper components are secured together prior to testing creating a symmetrical arrangement. Fine, medium and coarse sands have been tested in the optimised WDSA, resulting in data of quality comparable to the Cambridge simple shear apparatus. Measured direct shear angles of friction are found to be very insensitive to test conditions, which has led to a simple method of estimating the plane strain angles of friction. Data traits indicative of progressive failure are highlighted, which can cause erroneous results if the sample to grain size ratio is too large. An experimental procedure able to generate data equivalent to the direct shear test but unencumbered by the prospect of progressive failure is proposed.

A fundamental study of interface behaviour was undertaken using the WDSA with attention paid to the mechanics of interaction as indicated by the tribology literature. A range of sands, at various densities and stress levels, were tested on mild steel surfaces prepared to a wide range of roughness. Three interfacial states are discussed: peak, large displacement, and run-in. Surface topography, quantified using numerous conventional roughness descriptors and a newer fractal roughness parameter, correlate well with peak behaviour. Considerations of stress-dilatancy lead to a classification of interfaces as either non-dilatant, where the preferred particle movement is sliding; or dilatant, where particle rolling predominates. The large displacement interface response, elsewhere incorrectly linked to a critical state, shows stress-level and shear-displacement dependency. Run-in behaviour, observed in reversal tests, results from degradation of surface topography, visualised through fractal analysis, and particle crushing. For coarse sand on mild steel, the run-in angle of interface friction is unique, being independent of initial stress level, density and surface roughness. It represents the appropriate value to use for driven steel piles.



## Acknowledgements

During this work I was supported by the Engineering and Physical Research Council for which I am grateful.

Many members of the University of Bristol's Faculty of Engineering and particularly within the Department of Civil Engineering have been of assistance to me during my work. Only few are mentioned here.

First and foremost, I would like to express my appreciation to my supervisor Mr M L Lings for his invaluable guidance, encouragement and support throughout all stages of this work and particularly during the preparation of this manuscript. Thanks also go to the other members of the Geomechanics Research Group, both past and present, who have provided much inspiration.

For laboratory assistance and expert craftsmanship many thanks go to Mr M Pope who was always on hand to provide words of practical advice. The computer support team also deserves a mention, and especially Mr D Clay.

My thanks also go to the Staff at the Institute of Grinding Technology, and in particular Dr T Pearce and Mr A Speight, for their patience and flexibility.

On a more personal note, I am always grateful to my friends and family who have provided indispensable support and encouragement throughout. This work is dedicated to my mother and father.

.



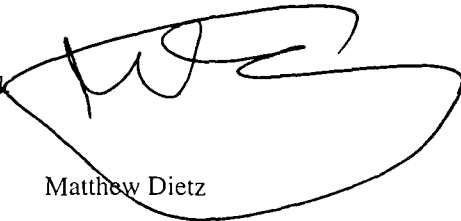
## Declaration

I declare that the work in this dissertation was carried out in accordance with the regulations of the University of Bristol. The work is original except where indicated by special reference in the text and no part of the dissertation has been submitted for any other degree.

Any views expressed in the dissertation are those of the author and in no way represent those of the University of Bristol.

The dissertation has not been presented to any other university for examination either in the United Kingdom or overseas.

Signed

A handwritten signature in black ink, appearing to be 'M. Dietz', enclosed within a large, hand-drawn oval shape.

Matthew Dietz

Date:

11 / 1 / 1





# Contents

Abstract.....	i
Acknowledgements.....	iii
Declaration.....	v
Contents.....	vii
List of symbols and abbreviations.....	xi
List of tables.....	xiii
List of figures.....	xv

<b>1. INTRODUCTION.....</b>	<b>1</b>
-----------------------------	----------

## **PART I**

---

<b>2. DIRECT SHEAR TESTING OF SOILS.....</b>	<b>5</b>
--	----------

2.1 THE DIRECT SHEAR APPARATUS.....	5
2.2 DSA PROCEDURE.....	9
2.3 COMMON INTERPRETATIONS OF DIRECT SHEAR DATA .....	11
2.4 CRITIQUE OF THE DSA.....	13
2.4.1 <i>Stress and strain fields within the DSA</i> .....	14
2.4.2 <i>Stress and strain fields within modified DSA</i> .....	17
2.5 MODIFICATION OF THE ARCHETYPAL DSA.....	18
2.5.1 <i>Enforced rotational restraint</i> .....	19
2.5.2 <i>Induced rotational restraint</i> .....	23
2.6 SUMMARY.....	25

<b>3. THE NEW WINGED DIRECT SHEAR APPARATUS.....</b>	<b>27</b>
--	-----------

3.1 HISTORICAL DEVELOPMENT.....	27
3.2 DESCRIPTION OF THE APPARATUS.....	29
3.2.1 <i>The Winged Direct Shear Apparatus (WDSA)</i> .....	29
3.2.2 <i>The WDSA's shearbox</i> .....	31
3.3 TEST MATERIALS.....	32
3.3.1 <i>Coarse test material</i> .....	32
3.3.2 <i>Medium test material</i> .....	33
3.3.3 <i>Fine test material</i> .....	33

3.4	SAMPLE PREPARATION VIA PLUVIATION .....	34
3.4.1	<i>Checking the Pluviator's efficacy</i> .....	35
3.4.2	<i>Summary of the pluvial deposition investigation</i> .....	37
3.4.3	<i>Preparation of loose deposits</i> .....	37
3.4.4	<i>Levelling the uppermost sand surface</i> .....	37
3.5	INSTRUMENTATION.....	38
3.6	MANIPULATION OF TEST DATA.....	41
3.6.1	<i>The reducing plan area of the central plane</i> .....	41
3.6.2	<i>The estimation of <math>\sigma'_v</math></i> .....	43
3.7	VALIDATION OF DATA.....	45
3.7.1	<i>Comparisons with other's test data</i> .....	46
3.7.2	<i>Comparison with data obtained distant from the WDSA</i> .....	47
3.7.3	<i>Correlation with formulated relations</i> .....	49
3.8	SUMMARY .....	55
<b>4.</b>	<b>OPTIMISATION OF THE NEW WDSA.....</b>	<b>57</b>
4.1	TRANSMISSION OF THE SHEAR LOAD TO THE SAMPLE.....	58
4.2	THE WF-25300 AND THE WDSA COMPARED.....	60
4.2.1	<i>Force and moment equilibrium</i> .....	61
4.2.2	<i>The symmetrical WDSA</i> .....	62
4.2.3	<i>The unsymmetrical WDSA</i> .....	63
4.2.4	<i>The WF-25300</i> .....	65
4.2.5	<i>Comparison of WDSA and WF-25300 data</i> .....	66
4.2.6	<i>The adopted test configuration</i> .....	67
4.3	THE OPENING BETWEEN THE SHEARBOX FRAMES.....	68
4.3.1	<i>Sample extrusion</i> .....	69
4.3.2	<i>Shielding</i> .....	71
4.3.3	<i>The size of the opening between frames</i> .....	73
4.4	THE EFFECT OF APPLIED MOMENTS ON WDSA DATA.....	75
4.5	SAMPLE DIMENSIONS .....	76
4.5.1	<i>Background</i> .....	76
4.5.2	<i>VLB samples of different dimension</i> .....	78
4.5.3	<i>SFS samples of different dimension</i> .....	82
4.5.4	<i>Discussion</i> .....	84
4.6	OPTIMUM CONFIGURATION .....	86

4.7	WDSA TEST PROCEDURE.....	87
4.8	SUMMARY.....	88
<b>5.</b>	<b>BEHAVIOUR OF SANDS WITHIN THE OPTIMUM WDSA .....</b>	<b>91</b>
5.1	GENERAL DISCUSSION OF EXHIBITED BEHAVIOUR.....	91
5.2	PRE-PEAK TRENDS.....	93
5.3	PEAK STATE TRENDS .....	95
5.3.1	<i>Stress level dependency.....</i>	95
5.3.2	<i>Estimates of <math>(\phi'_{ps})_{peak}</math>.....</i>	96
5.3.3	<i>Correlation of converted parameters.....</i>	96
5.3.4	<i>The verification and interpretation of direct shear data.....</i>	97
5.4	STRAIN SOFTENING TRENDS .....	99
5.5	LARGE DISPLACEMENT TRENDS.....	100
5.5.1	<i>Comparison with other's test data.....</i>	103
5.5.2	<i>Comparison with the angle of repose.....</i>	104
5.6	SUMMARY.....	105
 <b>PART II</b> <hr/>		
<b>6.</b>	<b>INTERFACE FRICTION: THE STATE OF THE ART .....</b>	<b>107</b>
6.1	THE TERMINOLOGY OF TRIBOLOGY.....	107
6.2	CONVENTIONAL TOPOGRAPHY QUANTIFICATION.....	108
6.3	PREPARATION AND QUANTIFICATION OF INTERFACE BLOCKS.....	110
6.4	THE FRACTAL DIMENSION .....	112
6.5	FRACTAL ANALYSIS OF SURFACE ROUGHNESS.....	116
6.6	FRICTION AND WEAR .....	119
6.7	ASPERITY-SURFACE INDENTATION.....	122
6.8	ASPERITY-SURFACE SCRATCHING .....	124
6.9	THE MOVEMENT OF PARTICLES RELATIVE TO SURFACES.....	127
6.10	INTERFACE FRICTION IN THE SOIL MECHANICS LITERATURE .....	128
6.11	SUMMARY.....	136
<b>7.</b>	<b>INTERFACE TESTING.....</b>	<b>139</b>
7.1	METHODOLOGY .....	139
7.2	IDEAL INTERFACE TESTING.....	141
7.3	UNIDIRECTIONAL INTERFACE TESTING .....	143

7.3.1	<i>Correlating peak state interface data with surface roughness</i> .....	145
7.3.2	<i>The effect of particle size on peak interface response</i> .....	147
7.3.3	<i>The effect of density on interface response</i> .....	148
7.3.4	<i>The effect of confining stress on interface response</i> .....	149
7.3.5	<i>Peak stress-dilatancy response of interfaces</i> .....	150
7.3.6	<i>A large-displacement critical state for interfaces?</i> .....	151
7.4	REVERSE INTERFACE TESTING.....	154
7.4.1	<i>Signs of interfacial wear</i> .....	154
7.4.2	<i>Interfacial wear and test data</i> .....	156
7.4.3	<i>Discussion</i> .....	158
7.5	SUMMARY .....	160
<b>8.</b>	<b>CONCLUDING REMARKS</b> .....	<b>165</b>
8.1	DIRECT SHEAR TESTING .....	165
8.2	INTERFACE TESTING.....	169
8.3	RECOMMENDATIONS FOR FURTHER WORK .....	172
	<b>REFERENCES</b> .....	<b>175</b>
	<b>FIGURES</b> .....	<b>185</b>

## List of symbols and abbreviations

The following list does not present the entire catalogue of abbreviations used in this manuscript.

Abbreviations used only locally are not included as their definition can be found on the page of reference.

$A(l)$	apparent length
$a$	area of contact
$C$	constant
$C_r$	cross-over length roughness parameter
$D_c$	compass dimension
$D_r$	relative density
$D_s$	self-similarity dimension
$D_{10}$	particle diameter of which 10% of particles are smaller
$D_{50}$	mean particle diameter
$DSA$	direct shear apparatus
$E$	Young's modulus
$e$	void ratio
$f$	misalignment between line of thrust and central plane
$g$	initial vertical separation between frames
$H$	sample height, hardness
$i$	angle of repose
$I_r$	Bolton's (1986) relative dilatancy index
$k$	wear coefficient
$l$	step-length
$L$	sample length
$m_{10}$	mass of particles finer than the $D_{10}$ of the original sand
$n$	number
$N$	normal force
$P(l)$	projected length
$p'$	mean stress
$R_{a, q, p, v, t, sk, ku, n}$	amplitude roughness parameters
$R(l)$	relative length
$r$	radius
$S$	shear force
$S, S_m, \Lambda_q$	wavelength roughness parameters
$SSA$	simple shear apparatus
$s'$	mean stress in plane strain
$S_r$	degree of strain softening from force measurements

$T$	thickness of shear zone
$t$	maximum shear stress in plane strain
$v_x$	cumulative shear displacement
	displacement, Poisson's ratio
$W$	sample width
$W$	work
$W$	work done by shear force
$W_n$	work done by normal force
$Y$	uniaxial flow stress
$Y$	degree of strain softening from displacement measurements
$\alpha$	cumulative shear strain
$\Delta_a, \Delta_q$	absolute surface slope roughness parameters
$\delta$	angle of wall friction
$\sigma$	normal stress
$\sigma_1, \sigma_2, \sigma_3$	principle stresses
$\tau$	shear stress
$\psi$	angle of dilation
$\omega$	rotation

### Superscripts

'	effective stress quantity
---	---------------------------

### Subscripts

<i>ax</i>	axisymmetric
<i>crit</i>	critical state value
<i>ds</i>	direct shear
<i>front</i>	at front of shearbox
<i>ps</i>	plane strain
<i>ld</i>	large displacement
<i>lp</i>	load pad
<i>max</i>	maximum
<i>min</i>	minimum
<i>min vol</i>	minimum volume
<i>peak</i>	peak
<i>r</i>	Part 1: relative, Part 2: run-in
<i>rear</i>	at rear of shearbox
<i>uf</i>	upper frame

## List of tables

Table 1.1: Summary of interface testing apparatus (modified from Kishida & Uesugi, 1987, and Paikowsky et al, 1995) .....	4
Table 2.1: The three types of DSA identified by Shibuya et al (1997) .....	19
Table 3.1: Physical properties of the test materials .....	33
Table 3.2: The transducers used in this project .....	38
Table 3.3: Calibration and regression characteristics of the WDSA's transducers .....	40
Table 3.4: The angles of repose obtained using two procedures on three different sands .....	49
Table 3.5: A summary of the cardinal parameters encountered in discussion relating to the WDSA .....	50
Table 3.6: Flow rule summary with the conversion between published $\phi'_{ds}$ and $\phi'_{ps}$ occurring through Davis' (1968) relation .....	54
Table 4.1: Cardinal parameters from direct shear tests employing the WF-25300 modified by differing degrees .....	66
Table 4.2: The effect that thinning a dense VLB sample confined under 25kPa has on test data .....	79
Table 4.3: The effect that shortening a dense SFS sample confined under 252kPa has on test parameters .....	82
Table 5.1: The estimation of $(\phi'_{ps})_{peak}$ from direct shear test data .....	96
Table 5.2: Comparison between different measured angles of repose $i$ and the large-displacement angle of friction averaged over a wide variety of tests for different sands .....	104
Table 6.1: Some often used conventional roughness parameters (figures modified from Dagnall, 1980, and Thomas, 1982) .....	109
Table 6.2: Typical conventional roughness parameters for the surfaces here investigated .....	112





## List of figures

### CHAPTER 2

---

Figure 2.2: Schematic diagram showing Collin's direct shear apparatus.....	185
Figure 2.3: Principle of early type of controlled stress shearbox (from Head, 1982) .....	185
Figure 2.4: The direct shearbox while testing .....	185
Figure 2.5: The Direct Shearbox (modified from Head, 1982).....	186
Figure 2.6: Long section of the DSA illustrating its general configuration .....	187
Figure 2.7: The WF-25300's arrangement for transmitting the shear force to the upper frame .....	187
Figure 2.8: The frictional force inherent in the WF-25300's arm and sleeve arrangement .....	188
Figure 2.9: Long section of the WF-25300 (adapted from Wykeham Farrance's WF-25300 literature)	188
Figure 2.10: Stresses acting on an element taken from the central region of a direct shear sample whilst testing .....	189
Figure 2.11: Principal stresses acting during direct shear testing (a) after consolidation and (b) after an increment of shear displacement .....	189
Figure 2.12: Mohr's circle of stress assuming the central plane aligns with planes of maximum stress ratio .....	189
Figure 2.13: Mohr's circles of (a) strain and (b) stress for an element of soil taken from a zero-extension, horizontal rupture band of the DSA .....	190
Figure 2.14: Deformations of a plasticine sample subjected (a) 12.4kPa and (b) 494.4kPa confining stress in the DSA (after Roscoe, 1953) .....	190
Figure 2.15: Sequence of ruptures forming within a kaolin DSA sample (after Morgenstern & Tchalenko, 1967) .....	191
Figure 2.16: Contours of stress level $S$ within the DSA obtained as the finite element simulation progresses (after Potts et al, 1987) .....	191
Figure 2.17: Measured incremental strains at peak shearing resistance within the DSA: (a) principle strains; (b) directions of zero incremental linear strain (after Jewell & Wroth, 1987).....	192
Figure 2.18: Long section of Wernick's (1977) direct shearbox .....	192
Figure 2.19: Long section of Mikasa's direct shear apparatus (modified from JGS 0561-2000).....	192

Figure 2.20: The influence of front wall roughness on the pull-out resistance of a length of reinforcement (after Palmeira & Milligan, 1989b) .....	193
Figure 2.23: Force diagrams illustrating the couples applied when employing the conventional arrangement (Jewell, 1989).....	194
Figure 2.24 The Japanese Standard Direct Shearbox with Fixing Screw (adapted from Matsuoka & Liu, 1998) ... ..	194
Figure 2.25: Force diagrams illustrating the force distribution during symmetrical direct shear tests (Jewell, 1989) .....	194

### CHAPTER 3

---

Figure 3.1: Force and moment consideration of the shearbox's upper half when the line of thrust is (a) distant from and (b) coincides with the central plane .....	195
Figure 3.2: Equilibrium of the WF-25300's upper half considering the loading applied by the button and housing arrangement.....	195
Figure 3.5: Essential modifications that comprise the WDSA .....	198
Figure 3.6: (a) Schematic diagram of a ball race bearing on a wing's hardened steel plate after substantial upper ensemble rotation $\omega$ and (b) the forces acting on the plate.....	198
Figure 3.7: The Winged Apparatus' Shearbox .....	199
Figure 3.8: Particle size distribution charts for the test materials: (a) ALB, (b) VLB, (c) MGS and (d) SFS .....	200
Figure 3.9: The configuration of the MSP .....	201
Figure 3.10: The effect the Pluviator's control parameters have on average $D_r$ .....	202
Figure 3.11: The effect of the lower pipe on the Pluviator's horizontal density distribution .....	202
Figure 3.12: Pluvial deposition using different nozzles and different heights of drop into moulds of varying depth d .....	203
Figure 3.13: (a) Shear force and (b) moment sensitivity of the load cell.....	203
Figure 3.14: The effect of area-correction assumptions on large displacement test data .....	203
Figure 3.15: Large-displacement stress data obtained with different $g$ values (a) after employing a correction to account for the transition in shear area and (b) with no such correction .....	204
Figure 3.16: The gradient of the large-displacement stress ratio plot for tests with $g$ circa $5D_{50}$ for two	

sands deposited at various densities and confined under different stresses (a) after employing the area correction and (b) with no area correction.....	204
Figure 3.17: The linking of parameters (circles), both measured (dashed) and derived (dotted), using flow rules (diamonds) and other relationships (rectangles).....	205
Figure 3.18: Comparison of Taylor's (1948), Rowe's (1962) and Bolton's (1986) flow rules on axes relating to (a) plane strain and (b) direct shear.....	205
<b>CHAPTER 4</b>	
Figure 4.1: The influence of dentated plates on WDSA test data (VLB, $D_r = 95\%$ , $\sigma'_{yy} = 25$ kPa, $f = 0$ mm, $g = 5D_{50}$ ).....	206
Figure 4.2: Reductions of $\psi_{peak}$ brought about by including dentated plates during WDSA tests with various initial openings between frames (VLB, $D_r = 95\%$ , $\sigma'_{yy} = 25$ kPa, $f = 0$ mm).....	206
Figure 4.3: The force and moment equilibrium of the upper half of a WDSA sample with different separations between the central plane and the line of thrust for (a) the symmetrical arrangement and (b) the unsymmetrical arrangement.....	207
Figure 4.4: Data for three identical symmetrical WDSA tests featuring dense VLB confined under 25kPa ( $g = 0.5$ mm, $f = 10$ mm, no shielding).....	208
Figure 4.5: Data for three identical unsymmetrical WDSA tests featuring dense VLB confined under 25kPa ( $g = 0.5$ mm, $f = 10$ mm, no shielding) compared to the representative symmetrical WDSA test.....	209
Figure 4.6: The shear stresses imposed on the sample's boundaries by the clockwise rotation of the load pad within the upper frame.....	209
Figure 4.7: The relative displacements of the unsymmetrical WDSA's load pad within the upper frame for three tests featuring dense VLB confined under 25kPa ( $g = 0.5$ mm, $f = 10$ mm, no shielding).....	210
Figure 4.8: Data for three WF-25300 tests featuring dense VLB confined under 25kPa ( $g = 0.5$ mm, $f = 10$ mm, no shielding) compared to the representative symmetrical WDSA test.....	210
Figure 4.9: The relative displacements of the WF-25300's load pad within the upper frame for three tests featuring dense VLB confined under 25kPa ( $g = 0.5$ mm, $f = 10$ mm, no shielding).....	211
Figure 4.10: (a) The x ordinate, relative to the sample centre, about which the upper frame rotates during testing and (b) the relationship between vertical displacement and rotation of the upper frame when using the WF-25300 and dense VLB confined under 25kPa.....	211

Figure 4.11: The incremental rotations of (a) the symmetrical WDSA's upper ensemble, (b) the unsymmetrical WDSA's load pad and upper frame and (c) the WF-25300's load pad and upper frame (dense VLB, $\sigma'_{yy} = 25\text{kPa}$ , $g = 0.5$ , no shielding, $f = 10\text{mm}$ ) .....	212
Figure 4.12: The stress dilatancy relation recorded using different apparatus (dense VLB, $\sigma'_{yy} = 25\text{kPa}$ , $g = 0.5$ , no shielding, $f = 10\text{mm}$ ).....	213
Figure 4.13: The effect of $g$ on test data featuring a number of sands with various densities and at various stress levels within the JGS's standard DSA.....	213
Figure 4.14: The generation and effect of the additional volume created during the shear of a non-dilative sample .....	213
Figure 4.15: Unshielded WDSA data (VLB, $\sigma'_{yy} = 25\text{kPa}$ , $90\% D_r$ , $f = 0\text{mm}$ , $g = 5D_{50}$ ) .....	214
Figure 4.16: Unshielded WDSA displacement data corrected to account for the additional volume created during shear (VLB, $\sigma'_{yy} = 25\text{kPa}$ , $90\% D_r$ , $f = 0\text{mm}$ , $g = 5D_{50}$ ).....	214
Figure 4.17: The effect of shielding configuration on the direct shear test data of dense Toyoura sand ( $\sigma'_{yy} = 49\text{kPa}$ , $D_{50} = 0.16$ , $g = 3\text{mm}$ ) (after Shibuya et al, 1997) .....	215
Figure 4.18: Effect of shielding on test data on test data (VLB, $\sigma'_{yy} = 25\text{kPa}$ , $90\% D_r$ , $f = 0\text{mm}$ , $g = 5D_{50}$ ) .....	215
Figure 4.19: Deformations of (a) continuous and (b) split shielding after considerable $v_x$ .....	216
Figure 4.20: The effect of increasing $g$ on WDSA test data (VLB, $95\% D_r$ , $\sigma'_{yy} = 25\text{kPa}$ , $f = 0\text{mm}$ ).....	216
Figure 4.21: The effect of increasing $g$ on (a) peak stress dilatancy response and (b) direct shear angles of friction (VLB, $95\% D_r$ , $\sigma'_{yy} = 25\text{kPa}$ , $f = 0\text{mm}$ ) .....	217
Figure 4.22: The stress-dilatancy response of dense VLB confined under $25\text{kPa}$ in the symmetrical WDSA with $g$ values as indicated (VLB, $95\% D_r$ , $\sigma'_{yy} = 25\text{kPa}$ , $f = 0\text{mm}$ ) .....	217
Figure 4.23: The system of forces acting on (a) the portion of the sample contained within the upper ensemble and (b) the upper ensemble .....	218
Figure 4.24: The effect on test data of limiting the rotation undergone by the upper ensemble by increasing the anticlockwise moment applied to the sample .....	218
Figure 4.25: The effect on cardinal parameters of increasing the separation between the line of thrust and the central plane.....	219
Figure 4.26: Palmeira & Milligan's (1989) DSA data obtained in shearboxes of different sizes .....	219

Figure 4.27: The relationship between $t/H$ and $H/D_{50}$ found by different authors for the same sand in shearboxes of different sizes .....	220
Figure 4.28: The effect of sample dimensions on dense VLB data ( $\sigma'_{yy} = 25\text{kPa}$ , $g = 5D_{50}$ , $f = 0\text{mm}$ ) ...	220
Figure 4.29: Vertical displacements recorded at the front and rear of dense VLB samples of different dimension ( $\sigma'_{yy} = 25\text{kPa}$ , $g = 5D_{50}$ , $f = 0\text{mm}$ ).....	221
Figure 4.30: The effect of sample dimensions on the stress-dilatancy relationship of VLB ( $\sigma'_{yy} = 25\text{kPa}$ , $g = 5D_{50}$ , $f = 0\text{mm}$ ) .....	221
Figure 4.31: The effect of reducing the length $L$ of a dense SFS sample ( $\sigma'_{yy} = 252\text{kPa}$ , $g = 5D_{50}$ , $f = 0\text{mm}$ ) .....	222
Figure 4.32: The relationship between stress ratio and dilation rate for dense SFS samples of different length $L$ ( $\sigma'_{yy} = 252\text{kPa}$ , $g = 5D_{50}$ , $f = 0\text{mm}$ ).....	222
Figure 4.33: The effect of normalising dense (a) SFS and (b) VLB data with by specimen length $L$ .....	223
Figure 4.34: The effect of reducing the height $H$ of a dense SFS sample ( $\sigma'_{yy} = 252\text{kPa}$ , $g = 5D_{50}$ , $f = 0\text{mm}$ ) .....	224
Figure 4.35: The relationship between stress ratio and dilation rate for dense SFS samples of different heights $H$ ( $\sigma'_{yy} = 252\text{kPa}$ , $g = 5D_{50}$ , $f = 0\text{mm}$ ).....	224
Figure 4.36: The effects found in the literature and during experimentation of increasing the length $L$ of sands with different gradings .....	225

## CHAPTER 5

---

Figure 5.1: VLB test data .....	226
Figure 5.2: MGS test data .....	227
Figure 5.3: Contours of stress ratio $\tau_{yx}/\sigma'_{yy}$ in $(\sigma'_{yy}, \nu_x)$ space for dense VLB ( $D_r$ circa 90%) in the WDSA .....	228
Figure 5.4: Contours of stress ratio $\tau_{yx}/\sigma'_{yy}$ in $(\sigma'_{yy}, \alpha)$ space for dense VLB in Stroud's (1971) SSA .....	228
Figure 5.5: Contours of stress ratio $\tau_{yx}/\sigma'_{yy}$ in $(\sigma'_{yy}, \nu_x)$ space for (a) medium VLB and (b) loose VLB in the WDSA .....	229
Figure 5.6: The rate at which the upper ensemble rotates during WDSA testing using (a) VLB and (b) MGS deposited at various densities and at different stress levels.....	230
Figure 5.9: The variation of $(\nu_y)_{min}$ with (a) stress level and (b) stiffness for VLB and MGS .....	231

Figure 5.10: ( $\tau_{xy}/\sigma'_{yy}$ ) at maximum contraction (a) VLB and (b) MGS at various $D_r$ and $\sigma'_{yy}$ .....	231
Figure 5.11: Pre-peak relationships between $\tau_{xy}/\sigma'_{yy}$ and $dv_y/dv_x$ for (a) dense, (b) medium and (c) loose VLB at various stress levels.....	232
Figure 5.12: Pre-peak relationships between $\tau_{xy}/\sigma'_{yy}$ and $dv_y/dv_x$ for (a, b & c) dense, (d, e & f) medium and (g, h & i) loose MGS at various stress levels .....	233
Figure 5.13: The variation of peak state data with stress level and initial sample density .....	234
Figure 5.14: Contrasting the peak state stress ratio recorded in Stroud's (1971) SSA with WDSA data for VLB .....	234
Figure 5.15: Different batches of LB tested under identical conditions in the WDSA ( $\sigma'_{yy} = 25\text{kPa}$ , 90% $D_r$ , $g = 5\text{mm}$ ).....	235
Figure 5.16: The relationship between sample strength and sample stiffness as measured in the WDSA .....	235
Figure 5.17: Peak stress ratio and rate of dilation values for (a) VLB and (b) MGS compared with Taylor's (1948) energy correction with $\phi'_{crit} = 35^\circ$ and $38^\circ$ .....	236
Figure 5.18: Different estimates of $\phi'_{ps}$ for (a) VLB and (b) MGS tested under wide ranging conditions .....	236
Figure 5.19: Comparison of peak, plane-strain experimental data with three flow rules .....	237
Figure 5.20: The reduction of $(t/s)_{peak}$ and $\psi_{peak}$ with increasing stress level $s'$ .....	237
Figure 5.21: Comparison of peak state data with Bolton's (1986, 1987) relative dilatancy index .....	237
Figure 5.22: The deviations of $\phi'_{ps}$ for a sample with $(\phi'_{ds})_{peak} = 45^\circ$ , $\psi_{peak} = 25^\circ$ and $\phi'_{crit} = 35^\circ$ derived using various relationships when (a) $\psi_{peak}$ is underestimated by $\Delta\psi$ and (b) $\phi'_{crit}$ is overestimated by $\Delta\phi'_{crit}$ .....	238
Figure 5.23: The reduction in $\tau_{yx}/\sigma'_{yy}$ and $\psi$ from peak for (a) dense, (b) medium and (c) loose MGS..	238
Figure 5.24: The definition of strain softening parameters $S_r$ and $Y_r$ .....	239
Figure 5.25: The variation of strain softening parameters $S_r$ and $Y_r$ with the displacement from peak shear resistance for (a) dense, (b) medium, and (c) loose MGS.....	239
Figure 5.26: Averaged strain softening data for (a) MGS and (b) VLB.....	240
Figure 5.27: The equal transition between softening parameters $S_r$ and $Y_r$ for (a) MGS and (b) VLB ...	240
Figure 5.28: The relationship between $\tau_{yx}/\sigma'_{yy}$ and $dv_y/dv_x$ during the strain softening of VLB samples	241

Figure 5.29: The relationship between $\tau_{yx}/\sigma'_{yy}$ and $dv_y/dv_x$ during the strain softening of MGS samples	242
Figure 5.30: Negative values of $\psi_{ld}$ for (a) VLB and (b) MGS .....	243
Figure 5.31: Taylor's (1948) energy correction applied to WDSA data .....	243
Figure 5.32: The value of $\sin\phi'_{crit}$ ( $= \tan\phi'_{ds} - \tan\psi$ ) obtained using Taylor's (1948) flow rule for different sands deposited at different densities and at different stress levels.....	244
Figure 5.33: Comparison between $(\tau_{yx}/\sigma'_{yy})_{ld}$ and $(\tau_{yx}/\sigma'_{yy})_{int}$ to illustrate the small gradients of the large displacement stress data .....	244
Figure 5.34: The relationship between $\tau_{yx}/\sigma'_{yy}$ and $W$ for all VLB tests .....	245
Figure 5.35: The relationship between $\tau_{yx}/\sigma'_{yy}$ and $W$ for VLB tests at different stress levels.....	245
Figure 5.36: The relationship between $\tau_{yx}/\sigma'_{yy}$ and $W$ for MGS tests at different stress levels .....	245
Figure 5.37: Large displacement shear resistance compared to that reported for Leighton Buzzard 14-25 by Cole (1967).....	246
Figure 5.38: Large displacement shear resistance of MGS at various initial densities and stress levels .	246

## CHAPTER 6

---

Figure 6.1: Profiles of the steel surfaces used during interface testing .....	247
Figure 6.2: ALO surface profile with equivalent vertical and horizontal scales .....	248
Figure 6.3: Fractal analysis of the ALO surface .....	248
Figure 6.4: Comparison of average fractal plots of the metal surfaces .....	248
Figure 6.5: Comparison of the magnitudes of various roughness parameters in relation to that recorded for the roughest metal surface .....	249
Figure 6.6: The effect of decreasing the data point spacing on the structured walk plot.....	249
Figure 6.7: Comparison of (a) the fractal plots and (b) roughness parameters of granular surfaces.....	249
Figure 6.8: Isocromatics beneath the contact between a cylinder and a plane due to (a) normal load and (b) normal and tangential load (after Arnell et al, 1991).....	250
Figure 6.9: Pictures of wear scars left by conical asperities of different internal apex angle (Childs, 1988) .....	250
Figure 6.10: The effect of abrasive particle size during the two-body, three-body and erosion wear of copper (Misra & Finnie, 1981).....	250

Figure 6.11: Applying a shear stress to a crystal lattice containing a dislocation (modified from Askeland, 1996).....	251
Figure 6.12: Silhouettes of (a) a sliding particle and (b) a rolling particle (Fang et al, 1993).....	251
Figure 6.13: Tracks left by (a) a sliding particle and (b) a rolling particle (Fang et al, 1993).....	251
Figure 6.14: Micrographs of a phosphor-bronze surface after abrasive wear featuring primarily (a) sliding and (b) tumbling particles (Williams & Hyncica, 1992) .....	252
Figure 6.15: Friction coefficients of (a) a sliding particle and (b) a rolling particle (from Fang et al, 1993) .....	252
Figure 6.16: The force equilibrium of Fang et al's (1993) abrasive particle.....	252
Figure 6.17: Contact between a single VLB particle and two surfaces of different roughness .....	253
Figure 6.18: Contact between a single SFS particle and two surfaces of different roughness .....	253
Figure 6.19: Yoshimi & Kishida's (1981b) ring shear interface data for Tonegawa ( $D_{50} = 0.27$ ), Niigata ( $D_{50} = 0.27$ ), and Toyoura ( $D_{50} = 0.27$ ) sand confined under 105kPa.....	254
Figure 6.20: Uesugi & Kishida's (1986a) simple shear data featuring Toyoura sand under 78.4kPa on surfaces of different roughness .....	254
Figure 6.21: Functional filtering of surface texture on surface (a) with and (b) without large wavelength irregularities (after Kishida & Uesugi, 1987) .....	255
Figure 6.22: Effect of (a) surface roughness and (b) confining stress on peak interfacial resistance after Uesugi & Kishida (1986a) .....	255
Figure 6.23: (a) The classification of interfaces using Uesugi & Kishida's (1986b) normalised roughness (after Paikowsky, 1995) (b) Correlation of peak resistance considering particle shape (after Uesugi & Kishida, 1986b) .....	255
Figure 6.24: (a) Schematic diagram of the transition of deformation during SSA interface tests (modified from Uesugi & Kishida, 1986a) and (b) contrast between SSA and DSA interface data (from Kishida & Uesugi, 1987) .....	256
Figure 6.25: Uesugi et al's (1989) (a) influence of cycle number on interface resistance and (b) resistance after repeated loading for dense Seto sand under 98kPa .....	256
Figure 6.26: Jardine et al's (1993) (a) summary of $\delta'$ values on interfaces featuring various sands confined under 100kPa on surfaces with $R_t \approx 10\mu\text{m}$ and (b) effect of particle size on $\delta'_{crit}$ .....	256
Figure 6.28: The pre-peak stress distribution within a collection of photo-elastic disks subjected	



to direct shear against a rough surface (Paikowsky et al, 1996) .....	257
Figure 6.29: Paikowsky et al's (1995) apparatus: isometric view and detail of the instrumented friction bar .....	257
Figure 6.30: Distribution of friction angles and vertical displacements along interfaces featuring dense Ottawa sand and various surfaces (after Paikowsky, 1995).....	258
Figure 6.31: Peak interfacial resistance of interfaces comprising a smooth HDPE Geomembrane and (a) Ottawa sand and (b) glass beads and an angular blasting sand (after Dove & Frost, 1999) .....	258

## CHAPTER 7

---

Figure 7.1(a): Equivalent ideal interface and shear tests for dense VLB at various stress levels .....	259
Figure 7.2: Ideal interface resistance of dense VLB confined under different stresses when work is used as the reference axis .....	261
Figure 7.3: The effect of $g$ while ideal interface testing using dense VLB under 25kPa.....	261
Figure 7.4: The effect of increasing $f$ and hence the anticlockwise moment on ideal interface behaviour of dense VLB confined under 25kPa.....	262
Figure 7.5(a): Comparison between ideal interface and equivalent shear tests for MGS at different density under 25kPa.....	263
Figure 7.6: Comparison between ideal interface and shear tests using dense SFS and 25kPa confining stress.....	265
Figure 7.7: Interfacial behaviour of dense sands on surfaces of different roughness under 25kPa .....	266
Figure 7.8: The variation of peak interface resistance dilatancy rate with (a) $R_a$ and (b) $R_a/D_{50}$ for different sands, deposited at densities close to their maximum and tested under confining stress of 25kPa.....	267
Figure 7.9: The variation of (i) $\tan(\delta'_{peak})$ and (ii) $\psi_{peak}$ with (a) $C_r$ , the smooth-rough crossover length derived from structured walk analysis, and (b) $C_r/D_{50}$ for different dense sands under 25kPa confining stress.....	268
Figure 7.10: Peak-state interface data featuring various dense sands confined under 25kPa on surfaces of various roughness quantified using $\Delta_a$ .....	269
Figure 7.11: The peak response of interfaces featuring various sands and various surfaces plotted with reference to $D_{50}$ .....	269
Figure 7.12: Response of interfaces featuring MGS deposited at different densities confined	

under 25kPa on surfaces with roughness (a) GND, (b) SIC, (c) MGS.....	270
Figure 7.13: The effect of density on MGS's peak response during interface and direct shear testing when confined under 25kPa.....	271
Figure 7.14: The influence of density on the interfacial resistance of MGS under 25kPa on surfaces of different roughness.....	271
Figure 7.15: Confining stress dependency of interfaces featuring dense VLB and (a) POL, (b) ALO and (c) SIC.....	272
Figure 7.16 The effect of $\sigma'_{yy}$ on the peak states of interfaces of different roughness as indicated.....	273
Figure 7.17: The strength-dilatancy relationship for interfaces featuring surfaces of various roughness, as indicated, and (a) three different dense sands confined under 25kPa, (b) MGS at different densities confined under 25kPa, (c) dense VLB confined under various $\sigma'_{yy}$ .....	273
Figure 7.18: Taylor's (1948) flow rule applied to tests that experience dilation from the outset.....	273
Figure 7.19: Consideration of Paikowsky et al's (1995) model of interface friction in the light of stress-dilatancy interface analysis.....	274
Figure 7.20: Large displacement resistance of VLB and MGS on surfaces of different roughness.....	274
Figure 7.21: The influence of roughness on the $(\tau_x/\sigma'_{yy})_{ld}$ featuring various densely deposited sands ..	274
Figure 7.22: The increase in worn fragments brought about by interface testing on various surfaces.....	275
Figure 7.23: Results of structured walk analysis of an initially smooth surface (POL) taken (a) parallel and (b) perpendicular to $v_x$ before (empty figures) and after (solid figures) interface tests at increasing $\sigma'_{yy}$ .....	275
Figure 7.24: Structured walks taken (a) parallel and (b) perpendicular to $v_x$ over an initially rough surface (SIC) before (empty figures) and after (solid figures) testing at the confining stresses indicated...	276
Figure 7.25: The effect of subjecting worn surfaces to further testing-POL.....	276
Figure 7.26: The effect of subjecting worn surfaces to further testing- SIC.....	277
Figure 7.27: Repeated shear of a dense VLB-SIC interface under 128kPa confining stress.....	277
Figure 7.28: Repeated shear of a dense VLB-POL interface under 252kPa confining stress.....	278
Figure 7.29: The evolution of response of a dense VLB-SIC interface ( $\sigma'_{yy} = 252\text{kPa}$ ).....	279
Figure 7.30: The evolution of response of a dense VLB-POL interface ( $\sigma'_{yy} = 252\text{kPa}$ ).....	279
Figure 7.31: The effect of initial roughness on multi-reverse interface behaviour featuring dense VLB	

confined under 252kPa.....	280
Figure 7.32: The final traverse of interfaces featuring dense VLB and surfaces of different initial roughness, each confined under 252kPa .....	280
Figure 7.33: The effect of confining stress during the reverse shearing of an interface comprising dense VLB and (a) SIC and (b) ALO.....	281
Figure 7.34: The relationship between $\delta'_r$ and $\sigma'_{yy}$ for dense VLB interfaces .....	281
Figure 7.35: Reverse ideal interface test featuring dense VLB confined under 252kPa.....	282

# 1. INTRODUCTION

Systems in which discrete particles interact with solid surfaces are commonplace and the shear forces such systems are able to withstand are of practical importance in many fields. Within the machinist's workshop, for example, particles are scraped over surfaces to generate a desired surface finish during grinding and polishing. Worn fragments of material may then themselves become the discrete particles interacting with the sliding surfaces of the machine. Buried or submerged pipelines perhaps carrying sand/water slurries for mining operations, tools used for cultivating soils, the transportation and storage of grains and other granular media, liners used to contain municipal or hazardous waste, and silos are just a few more of many possible examples. In the field of geotechnical engineering, what with soil reinforcement, earth retaining structures, piles, soil sampling and testing apparatus, examples of systems where granular material come into contact with solid surfaces are even more prevalent. Consequently, such systems have received a great deal of multidisciplinary attention.

The region of interaction between the bulk of a granular mass and the bulk of a solid material is here called the interface. A multitude of system characteristics have been reported to influence an interface's response to applied stress and strain. When subjected to a shear load, a granular mass alone exhibits behaviour dependent on a number of inherent and imposed factors. The constituent particle's mechanical and geometrical characteristics, their positioning with respect to their neighbours and the environment in which they are found all play a part in determining behaviour. Additionally, interface response is influenced by the physical and mechanical characteristics of the constituent solid surface, further increasing system complexity.

The consequences of interface complexity are threefold. Firstly behaviour is often examined from a particular viewpoint. Soil mechanics has concentrated primarily on the behaviour exhibited by the granular portion of the interface, whereas tribology has concerned itself predominantly with solid surface phenomena. Studies have rarely given equal weight to each of an interface's constituent parts. Secondly, the mechanisms of interaction and the processes at work are often ignored in favour of performing broad-based correlations of experimental data. Thirdly, the literature abounds with disparate conclusions.

What is required is a fundamental reassessment, integrating the findings of soil mechanics and tribology, and resulting in an holistic understanding of interface response. It is the primary objective of this work to obtain a better understanding of the governing principles and mechanics of sand-steel interface friction and in so doing clear up some of the discrepancies apparent in the literature. The spine of the study is to be an experimental investigation.

Potyondy's (1961) seminal work on interface friction set a precedent much followed when half of a direct shearbox was substituted by a solid block across which sand was displaced under load. A number of other devices have also been used to investigate interface friction and are summarised in a manner similar to Kishida & Uesugi (1987) in Table 1.1. Some of these testing rigs, like Potyondy's (1961), were adaptations of more conventional testing apparatus and some were specially devised for interface friction research

The longstanding prevalence of the Direct Shear Apparatus when investigating the shear strength of granular materials arises from the relative simplicity of its testing procedure and its capability at testing a wide range of geomaterials. However, the literature abounds with criticisms of the apparatus generating much scepticism of its reliability. Internal investigations have revealed internal stresses and strains can be extremely non-uniform making uncertain the appropriate interpretation of acquired data (Saada & Townsend, 1981). Elsewhere, however, it is reported that appropriate modification can bring with it a dramatic improvement in the apparatus' performance and generate strength parameters which correspond closely to those recorded in far more sophisticated pieces of equipment (Wernick, 1979, Jewell, 1989, Shibuya, 1996). The devices that have proved reliable are significantly dissimilar in size and configuration to those commonly available and the features necessary for conventional apparatus to be viable thus remain obscured. In addition, investigations have tended to proceed only over the small displacements necessary to mobilise the sample's peak strength. The strain softening and critical state response have rarely been remarked upon and, until now, it has remained uncertain whether even modified DSA are capable of providing reliable large displacement data.

Regardless of the DSA's suitability for investigation of the response of a soil to a shear load, its pervasion suggests its suitability for interface testing. It has been reported that interface activity is intensely localised within a narrow band of deforming soil adjacent to the surface. Nedderman & Laohakul (1980) found that powder flowing down a parallel-sided bin had a constant velocity profile when the internal walls were smooth. The shear zone produced when a layer of adhered powder roughened the walls was a mere 6 particle diameters in width. Other estimates of the width of an interface obtained by direct observation include 5-8 (Yoshimi & Kishida, 1981a) and 2-5 (Gudehus & Tejchman, 1988) times the mean particle diameter of the sand. The DSA is therefore a good candidate for interface investigation since these failure characteristics concur with the apparatus' kinematics. However, to the Author's best knowledge, investigation of interface behaviour has not before been attempted using a direct shear device modified to improve its performance.

The weighting of this thesis is not as initially intended. The archetypal Direct Shear Apparatus was found

to require a fairly radical redesign to generate reliable data. Thus, the interface-testing programme was curtailed and the resulting database not as comprehensive as originally hoped. However, because the DSA is the most commonly used device for obtaining the shear strength parameters of soils, enhancing its performance was a worthwhile objective in its own right. Approximately two-thirds of this work is focussed towards the successful development of a working apparatus. The remainder details the results of the reduced interface-testing programme which nevertheless results in a fundamentally different characterisation of behaviour that, were it not for the redesigned apparatus, would have remained hidden.

The thesis naturally falls into two parts. The first considers the DSA, its modification and optimisation. Chapter 2 introduces the archetypal DSA and notes the objections raised by its critics in the literature. The modifications made by others in the hope of improving the DSA's reliability are also discussed and those thought necessary to produce a viable apparatus determined. The resources of this work are detailed in Chapter 3; the redesigned apparatus is described along with its instrumentation, the test materials, and sample preparation techniques employed. Data manipulation and verification methods are also highlighted. Test data are first encountered in Chapter 4, which details the optimisation of the new apparatus' performance by considering aspects of testing often overlooked but actually influential in determining the quality of resulting test data. The first part of this dissertation ends with Chapter 5, which contains a detailed examination of data obtained using the optimised apparatus in conjunction with a variety of test parameters. The reliability of shearbox data is revealed through comparison with various theoretical and experimentally derived relations and correlation with applicable experimental data either obtained outside of the shearbox or presented within the literature.

Part two commences with Chapter 6 and an examination of the contact phenomena between sand particles and a steel surface. The emphasis is placed on issues more usually found within the tribology literature and aims to develop an understanding of the fundamental processes at work within an interface. Included is a detailed exploration of the science of surface topography. The chapter ends with a review of the soil mechanics literature. Chapter 7 discusses the details and findings of the fundamental experimental investigation of interface behaviour featuring a wide variety of test parameters. Attention is focussed on aspects of response often overlooked, casting interface behaviour in a new light. Finally, in Chapter 8, the major findings of this work are summarised and suggestions made for future research.

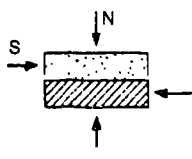
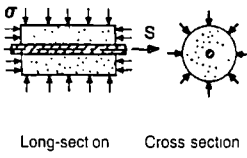
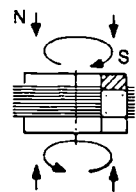
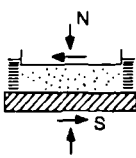
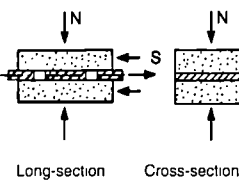
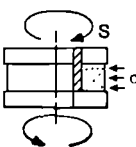
Type	Reference	Advantages	Complications
<p>Direct shear</p> 	<p>Potyondy (1961), Rowe (1962), Acar et al (1982), Tatsuoka &amp; Hiabara (1985), Bosscher &amp; Ortiz (1986), Boulon (1989), O'Rourke et al (1990), Everton (1991), Al-Douri &amp; Poulos (1992), Athanasopoulos (1993), Tabucanon et al (1995), Dove et al (1997), Subba Rao et al (1998), Frost &amp; Han (1999)</p>	<p>Simple system</p> <p>Failure characteristics thought to comply with apparatus' kinematics</p> <p>Can be adapted from standard apparatus</p>	<p>Doubts concerning the uniformity of stress and strain</p> <p>Loss of material during testing through opening between surface and apparatus</p>
<p>Axisymmetric loading</p>  <p>Long-section    Cross section</p>	<p>Coyle &amp; Sulaiman (1963), Brumand &amp; Leonards (1973, 1987)</p>	<p>Geometrically similar to skin friction of piles</p> <p>Can be adapted from standard apparatus</p>	<p>Normal stress on interface unknown</p> <p>Stress concentration at ends</p>
<p>Ring shear</p> 	<p>Yoshimi &amp; Kishida (1981b), Nigussey et al (1988), Tika-Vassilikos (1991), Lehane (1992), Evans &amp; Fennick (1995)</p>	<p>Endless interface</p> <p>Can be adapted from standard apparatus</p>	<p>Gradient of displacement across the interface</p> <p>Friction between side walls of the anulus and soil complicates results</p> <p>Complicated system</p>
<p>Simple shear</p> 	<p>Uesugi &amp; Kishida (1986a, b), Kishida &amp; Uesugi (1987), Uesugi et al (1988), Uesugi et al (1989), Uesugi et al (1990), Evgin &amp; Fakharian (1996)</p>	<p>Soil deformation measured separately from interfacial surface slip</p> <p>Can be adapted from standard apparatus</p>	<p>End effects complicating data</p> <p>Boundary conditions promote the globalisation of sample strains</p>
<p>Dual shear</p>  <p>Long-section    Cross-section</p>	<p>Paikowsky et al (1995)</p>	<p>Interface friction is measured on central third of interface away from sample boundaries</p>	<p>Instrumentation of the apparatus is necessarily complicated</p> <p>Data complicated by sand-over-steel and steel-over-sand behaviour being investigated simultaneously</p>
<p>Ring simple shear</p> 	<p>Gennaro &amp; Lerat (1999)</p>	<p>No end effects</p> <p>Endless interface</p> <p>No material loss</p>	<p>Interaction between particles and horizontal boundaries</p>

Table 1.1: Summary of interface testing apparatus (modified from Kishida & Uesugi, 1987, and Paikowsky et al, 1995)

## PART I

---



## 2. DIRECT SHEAR TESTING OF SOILS

Direct shear is induced when shear stresses are created from a direct action of forces trying to cut through a material, as opposed to those shear stresses established when members are subjected to compression, torsion or bending. A practical example of direct shear stresses are those induced along planes a-b and c-d in the bolt connecting the flat bar and the clevis of Figure 2.1.

Strictly, within the field of soil mechanics, the term “direct shear” can be used to describe a number of tests where the applied forces directly act to induce shear stresses (i.e. the vane test, the ring shear test, and the simple shear test). However, it has become customary for the term to be applied when considering one test arrangement in particular. The direct shear test is one where a shear stress is generated on a mechanically-induced horizontal plane within a laterally restrained soil mass by the application of a constant rate of translatory displacement of one portion of the soil mass relative to the other.

### 2.1 The Direct Shear Apparatus

#### Historical background of the DSA

A primitive direct shear device was used in 1846 by the French engineer Alexandre Collin during the first known tests investigating the shear strength of soil (Skempton, 1949). His apparatus, illustrated in Figure 2.2, bears a close resemblance to the bolted connection shown in Figure 2.1. In his device three horizontal, coaxial box sections were filled with cohesive soil. The outer two were supported while an increasing vertical load was applied to the central member, inducing failure on two vertical planes. A device that more closely resembles today's direct shear box was devised by Leygue, another Frenchman, in 1885. He tilted a hollow box, split at mid-height and filled with cohesionless soil until the top half slid relative to the bottom (Saada & Townsend, 1981).

While working at Harvard in 1932, Casagrande developed a device similar to Leygue's but employed an alternative load application system (Matthews, 1988). The upper half of a similar metal box, square in plan and split at mid height, was forced to slide relative to the lower half under an increasing applied shear load. A schematic diagram of a device developed soon afterwards by the Building Research Station (Cooling and Smith, 1935) also using the stress control method was presented by Head (1982) and is reproduced here as Figure 2.3.

Although the stress-control method employed by Collin, Leygue and Casagrande may have some advantages when investigating the creep of soils or during very long-term stress tests, it does not allow the investigation into the post-peak strength behaviour of soils. To overcome this, Gilboy developed the first displacement controlled apparatus using a fixed speed drive motor while working at MIT in 1936, improved upon by Fidler in 1938. Similar direct shear devices were devised in the UK by Golder (1942) at the Building Research Station and Bishop at Imperial College in 1948. The simplicity of the constant rate of displacement shearbox proved popular and it was enthusiastically accepted by industry. Its use in an unmodified form remains commonplace today.

### **The Archetypal DSA**

At the heart of the DSA is the shearbox: a rigid metal box split at mid-height to produce an upper frame and a lower frame. The horizontal plane dividing the upper and lower frames will be called the central plane. It is customary in the UK for the split box to be square in plan and hence the apparatus discussed is that pictured mid-test in Figure 2.4 and exploded in Figure 2.5.

The lower frame is fitted with lifting lugs to enable its easy transportation, and four lug pins protruding from its internal side-walls. In plan, two vertical tapped holes exist in opposite corners enabling clamping screws, which pass through the upper frame, to lock the frames together and thereby prevent the shear of the sample prior to the test's initiation. Aside from the clearance holes aligning with the lower-frame's tapped holes, the upper frame has a tapped hole in both of its remaining corners. Threaded through these are the separating screws, whose clockwise rotation lifts the upper frame off of the lower prior to the start of the test to prevent the inclusion of a metal-on-metal friction force in the shear strength of the soil.

The shearbox's floor comprises a removable retaining plate which has a close fit inside the lower frame and has four recesses cut into its lowermost surface which catch on the lug pins of the lower frame when the shearbox is lifted. The lower-frame's lug pins are not designed to be in contact with the retaining plate when the shearbox is placed on a level surface as they would be damaged if made to transmit the confining stress applied to the sample. Consequently, when the shearbox is lifted using the lifting lugs, the retaining plate falls relative to the shearbox frames until the uppermost faces of the recesses make contact with the pins, a vertical displacement of as much as 2mm. The shearbox's lid is known as the load pad and is fitted with a central ball seating through which a confining force  $N$  is applied to the specimen. The load pad has a plan area less than that of the shearbox sample. In this way, a measure of a specimen's dilatational capabilities can be obtained by monitoring the average vertical displacement  $v_y$  of the load pad. Within the shearbox's frames, between the retaining plate and load pad, the soil sample to be tested

is confined between two dentated plates, designed to transmit the shear load to the sample via shear stresses at the upper and lower boundaries.

The test is initiated on the application of a constant rate of displacement to the lower frame using the arrangement illustrated in Figure 2.6. The rigid base on which the shearbox sits is known as the carriage. The side and end walls of the carriage extend above the shearbox to provide a watertight container enabling saturated tests to be performed. The carriage is free to move longitudinally on an arrangement of linear bearings and can be displaced by the action of a worm drive connected to an electric motor by way of a gearbox. The lower frame sits between two centring kerbs that run longitudinally along each side of the carriage. It is prevented from sliding longitudinally within the carriage by a shelf protruding from carriage's rear wall. The relative displacement of the carriage, here called the shear displacement  $v_x$ , is monitored by way of a displacement transducer attached to the machine body.

A tailstock unit anchored to the machine bed provides the reaction force  $S$ , transmitted to the upper frame through a load measuring device and swan-neck yoke. The ram of the load-measuring device, which bears against the swan-neck, is aligned with the horizontal using a low friction support. The swan neck permits the transmission of  $S$  around the watertight container that is the carriage. In addition, and perhaps more importantly, it allows the shear-load's line of action to coincide with the central plane and be coaxial with the drive spindle, ensuring the lines of action of the forces induced on the central plane coincide with the external forces  $S$  and  $N$ . Here, the coaxis of the drive spindle and the load-measuring device will be called the "line of thrust".

Discussion is made easier by adopting a classification system to enable the specific parts of the shearbox to be referenced. The swan neck is attached to what will be called the front of the shearbox (irrespective of the direction of travel of the shearbox) which automatically results in the opposite end of the shearbox being called the rear. The shearbox's front and rear walls are joined by its side walls, shown running parallel to the direction of the applied shear displacement in Figure 2.4.

### **Peculiarities of the WF-25300**

Details of any particular DSA are often unique to its specific make and model number. The apparatus employed during testing was purchased from Wykeham Farrance, the first commercial producer of shearbox machines, in 1987. It will be henceforth referred to as the WF-25300 after its model number. The WF-25300 has a number of features that distinguishes it from the archetypal DSA as discussed

above. These atypical details, and their reasons for being, are discussed here.

Within the archetypal DSA, the transmission of the shear load to the shearbox's upper frame occurs through a swan-neck, a feature present in earlier incarnations of Wykeham Farrance shearboxes that has, in their latest model (WF-25400), been reverted to. Instead of the swan-neck design, the WF-25300 utilises the arrangement depicted in Figure 2.7 which features two novel components: the button and housing, and the ram and sleeve.

The minimal self-weight of the housing relative to a swan-neck yoke increases the uniformity of loading on a sample and also allows the performance of "reverse" shear tests during which the carriage is repeatedly moved back and forth between its limiting positions. Such testing methods were devised primarily to enable the large shear displacements necessary to investigate the residual shear strength of cohesive soil samples. Within the WF-25300 reversals of the worm drive are automated using micro-switches attached to the carriage and triggered when the maximum shear displacement is reached, providing a desirable safeguard against damage due to over-running. Wykeham Farrance's experience of designing shearboxes determined in what direction the initial shear displacement would occur. The WF-25300 manual states that "the first direction of shear is by a pulling action which reduces the possibility of a judder effect sometimes found with the archetypal shearbox pushing action." Consequently, Figure 2.4 and Figure 2.6 are inappropriate to the WF-25300 as they illustrate an initial pushing action, subjecting the load measuring device to a compressive force, opposite of that imposed initially by the WF-25300. From here on, all discussion is directed towards the operating action of the WF-25300 and an initial shear displacement that subjects the load-measuring device to a tensile force. The lower frame is prevented from sliding longitudinally by a pair of thumbscrews threaded through the carriage's front wall which bear on the lower frame, as seen in Figure 2.7(a).

Although the button and housing arrangement does not have the eccentric loading effect apparent when using a bulky swan neck, the benefits of using a swan neck are lost. Firstly, the shear load is not transmitted around the carriage's front wall. The WF-25300 overcomes this by incorporating the ram support conventionally remote from the carriage within the carriage's front wall using a "sleeve". The sleeve has internal O-rings fitted to prevent the escape of water when testing saturated soils and is hence associated with frictional force dissipation that should be accounted for during data manipulation. A plot charting the development of the frictional force inherent in the ram and sleeve as the carriage is displaced back and forth is presented in Figure 2.8 alongside the idealisation used when manipulating WF-25300 data. Secondly, the button and housing arrangement prevents the aligning of the central plane with the

line of thrust, which are in fact separated by 10mm, as seen in Figure 2.7(a).

Turning attention away from the shear-load application system, the normal load is applied by way of a counter-balanced loading yoke. The loading yoke is attached to a load hanger by way of a lever-arm loading system of ratio 10:1, as seen in the WF-25300's long section of Figure 2.9. The lever-arm's counter balance is adjusted to provide minimal normal force when free from load.

## 2.2 DSA procedure

Considering the long history of the DSA, it is surprising that the most recent British Standard, BS 1377 (1990), was the first to consider its methodology. The test procedure employed in years prior to 1990 was probably based on that described by Head (Vol. 2, 1982) which in turn was based on the US standard ASTM 3080 (1979), more recently updated as ASTM D 3080-90 (1995). The following procedure for direct shear tests on dry, coarse-grained granular materials is compiled from each of these three sources.

To avoid unnecessary detail, the test procedure presented is that for a "quick" test on dry sand, the procedure that is applicable to the testing programme performed later. In addition, procedural details irrelevant to the specific apparatus later used, the WF-25300, have been omitted. For example, the sub-procedure to determine the settlement of the sample under the weight of the loading yoke is not discussed since the WF-25300 has a counter-balanced loading yoke, causing negligible settlement. The terms "displacement transducer" and "load cell" are used in place of "micrometer dial gauge" and "load measurement device" as it was an electronic instrumentation system employed during testing.

The direct shear test procedure begins with the preparation of the shearbox assembly. Firstly, a thin coating of silicone grease is applied to the shearbox frame's internal walls and the mating surfaces before being fastened together with the clamping screws. The separating screws are threaded into the upper frame so as they just encounter the lower frame and the retaining plate and lower dentated plate are lowered into position. The shearbox is positioned, using the lifting lugs, within the carriage and secured between the carriage's shelf and thumbscrews. The shear displacement transducer is secured in position and it is ensured that all of the adjacent components from the worm drive to the apparatus' tailstock are properly in contact yet transmitting negligible horizontal force. The assembly is then ready for specimen preparation.

To obtain a loose sample, a quantity of sand is poured rapidly from a small height into the shearbox. A dense specimen is prepared by slow pouring from a high drop, vibration using a small vibrating hammer,

or compaction by using a square ended tamper. A medium dense sample is achieved by the pouring of the sample in thirds and tamping by a pre-determined amount, ensuring the centre of the middle third is aligned with the plane of separation between the upper and lower frames. The uppermost sand surface is then levelled some distance below the upper-frame's top using a suitable template while avoiding disturbance of the main body of the placed soil. The upper dentated plate is then placed and gently bedded down followed by the load pad, ensuring uniform clearance all round. The distance between the top of the upper frame and load pad is then measured to enable the determination of the height of the sample.

The normal loading yoke is lowered gently onto the load-pad's spherical seating and the vertical displacement transducer is positioned so that its stem rests against the yoke's centre. Weights are added to the load hanger to achieve the desired normal stress and the settlement of the sample under this normal load noted. The clamping screws are removed freeing the shearbox's upper and lower frames from each other. The separating screws are rotated clockwise in tandem by an amount sufficient to prevent the upper and lower frames coming together during the course of the test. BS1377 notes that the size of the opening  $g$  should be limited to 1mm to prevent excessive sample extrusion. Head (1982), however, recommends  $g$  be slightly larger than the specimen's mean particle diameter in order to prevent particles crushing between the frames during testing, but nevertheless limited to 2mm.

The constant rate-of-displacement drive unit is next started and at regular intervals of time the shear displacement  $v_x$ , shear force  $S$ , and vertical displacement  $v_y$  are recorded. During single cycle tests, shear displacement continues until a peak strength has clearly been defined or until the travel of the apparatus has been reached. The carriage is then returned to its original position, disassembled, and the sample weighed to allow the derivation of the average sample density.

The normal load and the shear force mobilised on the central plane constitute all of the force measurements made when using the DSA. Clearly, this limited information is insufficient to describe the stress state within the soil. Likewise, because of the unknown thickness of deforming soil, strains within a direct shear sample cannot be determined. Hence deformations are left in terms of relative displacement between the frames and vertical displacement of the load pad. Consequently, the direct shear test is commonly used to display qualitative differences in the deformation behaviour of soil at various initial densities, and to determine the relationship between the measured shear stress at failure, being the maximum shear resistance provided by the soil, and the confining stress.

## 2.3 Common interpretations of direct shear data

The stresses assumed acting on an element of soil taken from within the central region of a direct shear sample after an increment of  $v_x$  are shown in Figure 2.10. Adopting the ordinate axes shown in the figure defines the normal stress acting on the central plane as  $\sigma'_{yy}$ , and the shear stress on the central plane as  $\tau_{yx}$ . The ratio between these stresses is the tangent of what is known as the direct shear angle of friction,  $\phi'_{ds}$ :

$$\tan \phi'_{ds} = \frac{\tau_{yx}}{\sigma'_{yy}} \quad 2.1$$

Knowledge of  $\sigma'_{yy}$  and  $\tau_{yx}$  is insufficient to describe the stress state within the sample. The discussion that follows relates to how this sparse experimental data is often manipulated to provide a measure of the sample's shear strength.

The major, minor and intermediate principal stresses,  $\sigma'_1$ ,  $\sigma'_3$  and  $\sigma'_2$  respectively, imposed on a direct shear sample prior to the application of  $v_x$  are those shown in Figure 2.11(a). The application of  $v_x$  brings about rotations of  $\sigma'_1$  and  $\sigma'_3$ , as shown in Figure 2.11(b), but  $\sigma'_2$  is assumed to remain acting orthogonal to the shearbox's side-walls, although strictly this is only true if the shearbox's internal walls are frictionless. Consequently, zero deformation is applied in  $\sigma'_2$  direction implying that the direct shear test strives for a plane strain condition.

The strength of sand in plane strain is expressed as an angle of shearing resistance based on the Mohr-Coulomb criterion. This criterion states that in the absence of cohesion, the maximum possible ratio of shear stress to normal stress is equal to  $\tan \phi'_{ps}$  where  $\phi'_{ps}$  is the soil's plane-strain angle of friction, often expressed in terms of  $\sigma'_1$  and  $\sigma'_3$ :

$$\sin \phi'_{ps} = \frac{\sigma'_1 - \sigma'_3}{\sigma'_1 + \sigma'_3} \quad 2.2$$

When direct shear testing, simple boundary measurements do not reveal the magnitude and direction of the principal stresses and to determine  $\phi'_{ps}$  an assumption is needed.

The test interpretation suggested by both the American and British standards assumes that rupture planes align with planes on which are mobilised the maximum ratio of stress components. Thus, since the direct shear apparatus forces a rupture across the central plane, the stress ratio on this plane would assume its

maximum value and hence define the Mohr-Coulomb failure envelope, as seen in Figure 2.12. The upshot of this conventional interpretation is that  $\phi'_{ds}$  is equivalent to  $\phi'_{ps}$ .

Another test interpretation apparent within the literature relies on the strain constraint suggested by the apparatus' fixed end-walls that the horizontal plane within the DSA is one of zero linear extension. First, however, it must be assumed the elastic stiffness is sufficiently high that the elastic strains are much smaller than the plastic strains. This has been found true for most soils under most test conditions (Houlsby, 1992), and is anyway true at peak state and large displacements when the stresses are unchanging and the elastic strain rates consequently zero. Then, if  $t$  is the undefined thickness of the DSA's rupture, the current angle of dilation  $\psi$  defined by the ratio of incremental volume change  $d\varepsilon_v$ , and incremental shear strain  $d\gamma_{yx}$  can be derived from the ratio of the DSA's incremental boundary displacements:

$$\tan \psi = \frac{-d\varepsilon_{vv}}{d\gamma_{yx}} = \frac{dv_v}{dv} \frac{t}{t} = \frac{dv_v}{dv_t} \quad 2.3$$

A Mohr's circle of incremental strain illustrating the plastic strains observed as a direct shear sample is shearing with peak resistance is plotted in Figure 2.13(a) illustrating this relation. From this figure, it is clear that the directions along which the sand does not elongate make an angle of  $\pm(45 - \psi/2)$  with the direction of the major principle strain increment.

For this finding to be useful when interpreting direct shear test results an assumption next needs to be made relating the orientation of the ruptures with the direction of the principal axes of stress. In a perfectly plastic isotropic material the incremental plastic strain depends on the current state of stress, and the principal axes of stress and plastic incremental strain coincide (Hill, 1950). Coincidence of the principal axes of stress and strain rate has been measured by Roscoe et al (1967), Cole (1967) and Stroud (1971) when investigating the behaviour of Leighton Buzzard sand within the Cambridge SSA, and by Arthur & Menzies (1972) for Leighton Buzzard in the true triaxial device. Jewell & Wroth (1987) reported on a series of tests on a light sensitive artificial crushed glass granular material in which the directions of principal stresses could be observed as light stripes. Measuring strains using the changing positions of opaque markers led to the conclusion that within the accuracy of experimental measurements, the principal axes of stress and strain rate coincided.

Assuming coaxiality between axes of principal stress and axes of incremental strain for sand deforming within the DSA allows the angle of dilation to be incorporated into Mohr's circle of stress, as seen in



Figure 2.13(b). The geometry of this figure allows the plane strain friction angle to be defined as:

$$\sin \phi'_{ps} = \frac{\tan \phi'_{ds}}{\cos \psi + \sin \psi \tan \phi'_{ds}} \quad 2.4$$

where  $\tan \phi'_{ds}$  is given by the ratio of boundary forces and  $\tan \psi$  is given by the ratio of boundary displacements. This formula was first published by Davis (1968) and is henceforth referred to as Davis' (1968) relation. Since Equation 2.4 makes reference to the angle of dilation it strictly holds only when the elastic strain rates are zero. At peak state, when the stresses are instantaneously unchanging, this condition holds and Equation 2.4 becomes:

$$\sin(\phi'_{ps})_{peak} = \frac{\tan(\phi'_{ds})_{peak}}{\cos \psi_{peak} + \sin \psi_{peak} \tan(\phi'_{ds})_{peak}} \quad 2.5$$

The stresses are similarly unchanging at large displacement once the sample's dilatancy potential has been overcome and deformation proceeds without changes in volume ( $\psi = 0$ ). This condition has been termed the critical state and often indicated with subscript *crit*. Equation 2.4 then reduces to:

$$\sin(\phi'_{ps})_{crit} = \tan(\phi'_{ds})_{ld} \quad 2.6$$

where the term  $(\phi'_{ds})_{ld}$  represents the angle of friction mobilised on the central plane of a direct shearbox at large displacement. The subscripts *ps* and *ds* of Equation 2.6 are not necessary and are henceforth neglected. Hence, Equation 2.6 is written:

$$\sin \phi'_{crit} = \tan \phi'_{ld} \quad 2.7$$

## 2.4 Critique of the DSA

Perhaps the severest criticism of the DSA was put forward by Saada and Townsend (1981) after a general consideration of the test's operating mechanism. Their primary concern was the uniformity of stress in the specimen, noting that a test specimen should ideally represent a single point in a soil medium. Thus, any cuboidal element from within a specimen is intended to have the same stress vectors acting on its faces as all others. This requirement, they said, can not be satisfied for elements within a direct shear sample. The application of  $v_x$  generates a non-uniform vertical-stress distribution across the central plane by the mechanical inducement of a plane of shearing failure with given orientation within a sample.

Saada & Townsend (1981) termed such obligatory failure a “strain restraint”; the suggested consequence being a line of thrust from the upper frame’s rear to the lower frame’s front obliquely across the sample.

As shear displacement progresses, the advancing upper and lower frames cut a direct shear sample. The consequential stress and strain concentrations envisaged adjacent to the apparatus' end walls were said to induce the ‘progressive failure’ of a sample advancing from the shearbox’s front and rear internal walls towards the sample centre. Any simple interpretation of data based on uniformity along the central plane would thus be made inappropriate by the non-uniform mobilisation of strength across the central plane. At every point in the sample, a different state of stress was envisaged with principal values varying in both magnitude and direction. Saada & Townsend concluded that the only viable use for the test would therefore be in comparative studies between various samples tested under similar conditions.

To decide whether this condemnation of the DSA can be substantiated, the following discussion conveys the evidence available within the literature relating to the uniformity and distribution of stresses and strains within a direct shear sample. Such information is often obtained using sophisticated measuring techniques performed in different laboratories using DSA differing from the archetypal in many respects. The main differences between these apparatus are discussed. However, since Saada and Townsend’s (1981) critique concerns itself primarily with the stress and strain distributions, it is here where discussion commences.

### **2.4.1 Stress and strain fields within the DSA**

Whereas a direct shear sample’s internal strains or strain field can be directly measured through sample deformations, the internal stress field usually remains invisible. Consequently, literature addressing the distribution of stress within the DSA is scarce. However, indications of the stress field are sometimes provided by strain investigations.

Early studies addressing the adequacy of the DSA featured mainly cohesive specimens. Deformed sample shapes could then be used to gauge the uniformity of strain with the premise that uniform straining indicates the true mechanical response of the soil. Roscoe (1953), for example, performed a series of direct shear tests using 60mm square and 20mm tall striped plasticine samples primarily to compare the strain field within the DSA with that in the then-new simple shear apparatus. After testing, the sample could be carefully removed from the apparatus whilst retaining its deformed shape. Although this technique primarily indicated the strain field, indications of the stress field ensued.

Figure 2.14 contrasts the long sections of initially identical samples subjected to 7mm of shear displacement under both low (12.4kPa) and high (494.4 kPa) confining stress. Severe strain non-uniformity is evident in the differential gradients of the curves described by the striped bands. This nonuniformity was contrasted with the uniform tilting of the stripes of an identical sample subjected to shear within the then new simple shear apparatus. In addition, the sample subjected to a low confining stress (Figure 2.14a) became separated from the shearbox's ceiling and upper-wall at the front, and floor and lower-wall at the rear. Such a pattern of deformation can only arise from the occurrence of tensile forces within the sample and is therefore indicative of stress non-uniformity. An identical test but under a higher confining stress (Figure 2.14b) seemed to indicate less separation, suggesting that a decrease in the sample's freedom for displacement aids uniformity.

Morgenstern & Tchalenko (1967) made use of the optical properties of kaolin crystals to study the shear-induced fabric of a direct shear sample. The test specimens were cut from a kaolin block whose original fabric was induced by consolidation under a vertical effective pressure of 430kPa. On release of the consolidation pressure, and viewed through the crossed nicols of a polarising microscope, the bi-refracting properties of kaolin crystals enforced the original fabric to manifest itself as a series of near-parallel stripes, perpendicular to the direction in which the consolidating pressure acted. A number of 60 by 60 by 25mm direct shear samples were cut from this block to have these bedding planes vertical.

On testing, the first indication of shear was the non-uniform rotation of the average crystal orientation with respect to the original vertical banding and in the direction of the applied shear displacement. Rotation was not seen to be homogenous over the whole section but more intense near the shearbox's end walls and away from its horizontal boundaries. In addition to this non-uniform deformation, steeply inclined ruptures at the sample's front and rear originating from the opening between the frames developed during the early stages of the test. As shear displacement progressed, each rupture's development became arrested and another formed at a lower angle, as can be seen in Figure 2.15. At or immediately after peak resistance a pair of ruptures appeared within the sample each of which spanned more than half of the sample's length. Their inclination, however, prevented their meeting. Further shear displacement developed these ruptures until, ultimately, when residual strength was approached, a wavy horizontal rupture had progressed right across the central plane.

Both Roscoe's (1953) and Morgenstern & Tchalenko's (1967) experimental observations bear similarities to an investigation into the DSA using the finite element method by Potts et al (1987). A 60 by 60 by 20mm direct shear sample was idealised as a fully drained, isotropic, linear elastic-perfectly plastic material whose properties were defined by a Young's Modulus, Poisson's ratio, angle of shearing

resistance, cohesion and angle of dilation. Defining stress level  $S$  as “the mobilised proportion of the strength that is currently available at the normal stresses operating” allowed the stress distribution within the sample to be plotted. Contours of  $S$  within the idealised soil were presented for the case where  $\psi$  equalled zero, which are reproduced here in Figure 2.16. They illustrated that highly stressed zones propagate obliquely from the apparatus’ cutting edges during the early stages of loading before growing and rotating and ultimately aligning closely with the central plane.

Although verifying the nonuniformities predicted by Saada & Townsend (1981) and Morgenstern & Tchalenko (1967), Potts et al (1987) demonstrated an absence of progressive failure within the direct shear box. Despite the stress nonuniformities, a failure zone was seen to appear suddenly across the centre of the box at peak resistance in which shear strains were uniform over 80% of its length. Consequently, the peak shear resistance was seen to agree remarkably well with that recorded in an equivalent simple shear analysis.

Turning attention to samples comprising particles greater in size, the progressive failure of a 330 by 50 by 25mm direct shear sample comprising an agglomeration of cohesionless particles with  $D_{50}$  between 0.3 and 0.5mm was observed directly by Scarpelli (1981) and Scarpelli & Wood (1982). A radiographic technique capitalising on the observation that X-rays are absorbed to a lesser extent by a less dense material was employed. Radiographs taken of a DSA sample during testing showed areas with significantly reduced density, the highly dilated ruptures, as light stripes within the darker mass of the sample. Experimental results displayed similar traits to those of Morgenstern and Tchalenko (1967). Rupture zones were seen to progress obliquely from the cutting edges of the apparatus before the occurrence of a near-horizontal rupture that advanced across the central plane. Scarpelli (1981) monitored the progress of this rupture zone by measuring the changing positions of a close mesh of lead markers positioned throughout the sample. It was found that the horizontal rupture consisted of a length of dilatant sand, at the front of which the sand was mobilising its peak angle of dilation, followed by a fully developed rupture in which  $\psi = 0$ .

Hartley (1982) modified Scarpelli’s (1981) apparatus to investigate the ruptures forming when three sands with differing  $D_{50}$  (0.12, 0.4 and 0.9mm) were tested within shearboxes of height 26mm, width 51mm but differing lengths (65.5, 134, and 231.5mm). The longer shearboxes were both seen to contain oblique ruptures during testing with either of the sands, akin to those observed by Scarpelli (1981). The 65.5mm long apparatus, however, was associated solely with near-horizontal ruptures, regardless of the mean size of the sand particles tested. It was reasoned that the boundary constraint that firstly impeded

and then arrested the oblique ruptures in longer shearboxes was sufficient in the shorter box to prevent their formation. That is, the kinematic constraint offered by a small shearbox to the sample was sufficient to enforce the rupture to coincide with the central plane. Wood & Budhu (1980) drew similar conclusions when investigating the simple shear behaviour of coarse sand ( $D_{50}$  circa 1mm) which was seen to develop a single near-horizontal zone of preferential dilation, and fine sand ( $D_{50}$  circa 0.2mm) where the zones aligned with several different directions across the sample. The different behaviour within the two tests was said to be due to a change in the sample's internal degree of freedom, which is higher the smaller the grain size, so that the external kinematic constraints when shearing fine sand are more easily overcome.

## 2.4.2 Stress and strain fields within modified DSA

The literature presents a number of direct shear devices that provide a sample with a higher degree of kinematic constraint than that offered by the archetypal apparatus. The modifications necessary to impose this additional constraint are discussed in Section 2.5. First, however, the outcome of internal investigations into these devices are reported which suggests a somewhat limited but more attainable requirement for test viability than that envisaged by Saada & Townsend (1981).

Arthur et al (1988) report on a series of direct shear tests conducted in 1975 using a modified shearbox. Measurements using a radiography technique showed that for over 75% of the central plane, strains within the apparatus were uniform up to peak shearing resistance after which a horizontal rupture developed suddenly right across the sample.

Radiography of lead shot markers positioned in a 254 by 152 by 152mm DSA sample consisting of a coarse sand ( $D_{50}$  approximately 1mm) allowed Jewell & Wroth (1987) to derive the deforming sample's incremental strain field. The magnitude and directions of the principal incremental strains occurring at peak shear resistance were displayed in a figure that is here reproduced as Figure 2.17. At peak shearing resistance, no evidence of any oblique ruptures or progressive failure was observed, with good uniformity of strain occurring right across the central plane. In addition, as one might suppose considering the fixed end walls of the shearbox, the horizontal was seen to be a direction of zero linear incremental strain. (This observation had been made previously by Arthur et al, 1977, and Scarpelli and Wood, 1982.) Thus, within this narrow deforming band, the soil was approximating simple shear.

Shibuya et al (1997) reinforced Jewell & Wroth's (1987) findings whilst using a fine sand ( $D_{50}$  0.16mm) in a differently modified apparatus and an alternative technique to determine the deforming sample's strains. One side-wall of the shearbox was constructed from Perspex plates between which and the 150

by 150 by 120mm sample was positioned a latex sheet, split along the central plane. Onto this latex sheet and facing the Perspex was marked a grid made of extensible rubber strips. Photographs taken during testing allowed the displacements of the grid's nodes to be tracked and the normal and shear boundary strains determined. The photography technique revealed no evidence of oblique ruptures. From the small shear displacement necessary to mobilise peak shearing resistance, to much larger shear displacements of up to 12mm, volumetric and shear boundary strains were recorded within a 20mm thick band straddling the central plane

Both Je vell & Wroth's (1987) and Shibuya et al's (1997) findings led them to construe a direct shear sample as a relatively thin zone of material bounded vertically by two rigid blocks of non-deforming soil. On the application of a shear displacement, all deformations occurred within the thin "operational" layer. Therefore, reasonable uniformity need be achieved only within this operational layer, rather than throughout the full depth of the specimen. Their devices, each with additional kinematic restraint, were found able to provide this somewhat abridged requirement.

To summarise, the evidence relating to uniformity within a deforming direct shear sample is diverse. Various investigators have found the operating action of the DSA to induce severe stress and strain nonuniformity and to bring about the progressive failure of the sample. Simple test interpretations based on uniformity are then invalidated and any benefits that could be envisaged from the DSA's simplicity are done away with. However, it appears that with adequate kinematic constraint uniformity can be improved. At best, simple shear of a thin horizontal layer aligning with the zero-extension central plane can be induced in which stresses and strains are uniform over a good deal of the shearbox's length.

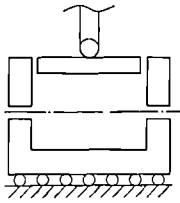
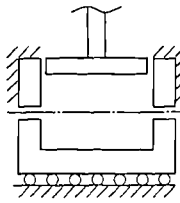
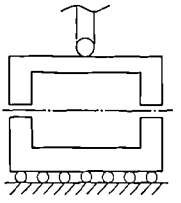
## 2.5 Modification of the archetypal DSA

As discussed (Section 2.3) the boundary measurements taken during the course of a conventional direct shear test are somewhat limited when wanting to describe the actual soil behaviour occurring within the shearbox, even when sufficient uniformity of stress and strain is achieved. Without sophisticated measuring equipment, however, this limitation of test data cannot be overcome. Therefore, it is beneficial to maximise the degree to which boundary measurements reflect the behaviour of the soil. Modifications of the DSA have often been imposed in order to optimise test data in precisely this way.

By far the most prevalent modifications to the archetypal apparatus have been introduced to combat the non-uniform displacement of the load pad and upper frame, seemingly endemic during conventional direct shear testing. Hvorslev (1939) noted that under light normal loads the DSA's upper frame

had a tendency to “ride” over the sample and hence be subject to rotations along with the expected vertical displacements. Other investigators have recorded rotations of the load pad and even counter rotation between the load pad and upper frame (Wernick, 1979). It is generally accepted that such behaviour is indicative of non-uniformity and makes test results unreliable since neither the shear displacement nor average vertical displacement of the load pad would directly indicate the strains within the soil. Shibuya et al (1997) identified two modifications of the archetypal DSA which aim to provide additional kinematic constraint and thereby impose a more uniform deformation to the sample. The nomenclature devised here to describe these apparatus indicates the philosophy behind the rotation preventative adaptation. An apparatus providing “enforced” rotational restraint physically prevents its components from rotating. One that “induces” rotational restraint aims to prevent rotations but does not restrict the free displacement of the apparatus’ components.

A diagrammatic comparison between the archetypal apparatus and those inducing and enforcing rotational restraint is shown in Table 2.1 and below, each is discussed with reference to examples found within the literature.

Rotational restraint:	None	Enforced	Induced
Schematic representation:			
Examples:	Archetype	Mikasa (Takada, 1993) Wernick (1979) Shibuya et al (1997)	Jewell & Wroth (1987) Jewell (1989) Bica & Clayton (1998)

**Table 2.1: The three types of DSA identified by Shibuya et al (1997)**

### 2.5.1 Enforced rotational restraint

Perhaps the most palpable means for eliminating rotations is the physical restraint of the apparatus’ components to permit deformations only in the sense required. Examples of apparatus’ employing this technique are those developed by Wernick (1979), Mikasa (Takada, 1993), and Shibuya et al (1997) whose apparatus resembles a hybrid of the previous two. Each device achieves the objective of zero rotation but succeed as workable devices to differing degrees.

A detail of Wernick’s (1977) apparatus showing its essential components, is illustrated in Figure 2.18. The apparatus closely resembles the archetypal DSA, and the modification is hence simple.

However, arrangements are not made to implement an opening between the frames and hence  $S$  will be affected by the friction force developed between the rubbing surfaces of the upper and lower frames. Mikasa's device overcomes this problem by the imposition of an opening between the frames that remains constant throughout the course of the test. However, as seen in Figure 2.19, his device requires a drastic overhaul of the archetypal apparatus' configuration, akin to turning Wernick's (1979) device upside-down. Mikasa's upper frame is attached the roof of the shearbox creating an ensemble to which  $v_x$  is applied, necessitating a load-measuring device free to translate horizontally. The upper ensemble is restrained from moving vertically or rotating using a system of ball-races also designed to prevent the upper and lower frame coming into contact during a test. The normal load is applied through a lever system to the floor of the shearbox that is not permitted to rotate but may displace vertically within the lower frame, whose position is fixed. The sample volume change is hence measured on the underside of the shearbox. Although Mikasa's device was adopted as the standard by the Japanese Society of Soil Mechanics and Foundation Engineering (JSSMFE), it loses the simplicity that makes the archetypal DSA so attractive.

Both Wernick's (1977) and Mikasa's devices may be successful in providing samples with the required additional degree of kinematic constraint but it is probable that test data obtained by their use will be erroneous. The reason why can be discovered by the consideration of the forces mobilised between the shearbox's vertical walls and the included sand grains; a similar situation as found at the front vertical wall of a pull-out test box, investigated by Palmeira & Milligan (1989b).

Changing only the roughness of the front wall of their apparatus, Palmeira & Milligan (1989b) measured remarkable increases in the pull-out resistance of a length of reinforcement, best elucidated by consideration of Figure 2.20 where a diagram of the apparatus is presented along with the relevant results. By way of explanation, Palmeira & Milligan (1989b) noted that because the sample's uppermost vertical boundary was stress controlled, a band of dilating sand adjacent to the reinforcement was able to bring about the heave of the overlying sample. The sand above the reinforcement and adjacent to the end wall was thus subjected to an additional down-drag, the magnitude of which was dependent on the frictional characteristics between the sand and the end wall. This down-drag increased the normal stress on the reinforcement above that applied at the sample's top boundary. Thus, if significant wall friction forces develop, then the stress ratio derived from the overburden pressure and the pullout force would greatly overestimate that mobilised along the reinforcement, as seen in Figure 2.20.

Similar phenomena may be envisage when direct shear testing. Considering, for simplicity, Wernick's (1977) apparatus, on application of a shear displacement a dilatant sample's particles would rise relative



to the fixed upper frame thereby increasing the thickness of the sample. In doing so, the particles adjacent to the internal walls would be subject to a frictional force that acts in a direction to increase the average normal stress on the central plane. Consequently, if the normal load were assumed constant in an apparatus where significant wall friction was allowed to develop, then a dilatant sample would lead to an overestimation of the shear strength. A contractant sample, on the other hand, would be associated with the overestimation of the normal stress on the central plane and hence have its shear strength underestimated.

Evidence corroborating this effect of wall friction on DSA results can be found within the literature. Wernick (1977) found the peak stress ratio recorded for a dense sand within his modified apparatus to significantly exceed that obtained in the archetypal DSA. Arthur & Dunstan (1988) reported on a series of direct shear tests in which the end walls of the shearbox were made “non-slip” to aid the mobilisation of complementary shear stresses on the shearbox’s vertical end walls.  $\phi'_{ds}$  was recorded for a dense sand as  $48.2^\circ$  in this modified apparatus, but only  $41.0^\circ$  in a device which didn’t suffer from excessive frictional forces on the end walls. Likewise, Jewell (1989) comments on an investigation made by Assadi (1975) who found that by increasing the roughness of the end walls the peak resistance of a dense sand could be increased by as much as  $4.2^\circ$ .

The wall friction between the sand grains and the shearbox’s walls cannot be easily quantified. Therefore it is expedient to exploit palliative measures which reduce the wall friction’s magnitude. Two approaches can be used. Firstly, following from Palmeira & Milligan (1989b), the shearbox’s internal walls may be lubricated. Secondly, slip between the sand grains comprising the sample and the shearbox’s walls may be prevented.

#### **Lubrication of the shearbox’s internal walls**

Tatsuoka & Haibara (1985) used a modified DSA to investigate the frictional resistance occurring between dense Toyoura sand (comprising of angular particles with  $D_{50}$  circa  $160\mu\text{m}$ , uniformity coefficient 1.46 and specific gravity 2.64) and nine types of surfaces lubricated to different degrees. Within their apparatus, the lower frame was replaced with a solid block of material whose uppermost surface was lubricated. Methods of lubrication featured various combinations and configurations of  $200\mu\text{m}$  thick latex membrane,  $50\mu\text{m}$  thick Teflon sheets, and two different types of silicone grease (standard and high vacuum).

It was demonstrated that a sheet of latex, separated from the solid surface with standard silicone grease,

provided frictional resistances close to that of far more complicated lubrication systems, and far below that between sand and a polished steel surface, as seen in Figure 2.21.

### Prevention of displacement between sand grains and walls

When investigating the frictional resistance mobilised between sand and steel in the simple shear apparatus, Kishida & Uesugi (1987) managed to differentiate the total shear displacement into that accounted for by the shear distortion of the sand mass, and that arising from the slip of sand grains along the interface. They found that on smooth steel surfaces, peak shear resistance was mobilised as the grains adjacent to the solid surface were in a state of incipient slip. Therefore, if no displacement between the grains and a surface is permitted, the mobilised wall friction must be below its peak value. If the internal walls are also lubricated, one can be confident that the wall friction will not significantly affect the normal stress on the central plane. Shibuya et al's (1997) apparatus enabled the investigation of this theory.

By developing a device akin to Wernick's (1979) but installing a high-rigidity load cell beneath the apparatus' retaining plate, Shibuya et al (1997) managed to overcome the shortcomings of other apparatus offering enforced rotational restraint. Since the load cell's rigidity disallowed any significant vertical displacement between sample and the lower frame, the displacement required to mobilise significant wall friction forces within the lower frame was not permitted. Shibuya et al's (1997) apparatus allowed the "upper" average normal stress derived from the vertical force measured above the load pad, beneath which displacement between the sample and the upper frame was permitted, to be compared with the "lower" derived from the vertical force measured below the retaining plate, above which no such displacement between sand and frame was permitted. The comparison took place on axes of  $\tau_{yx}$  against  $\sigma'_{yy}$  and is presented here as Figure 2.22. The large wall friction mobilised when the frame's walls were unlubricated was seen to significantly increase  $(\sigma'_{yy})_{lower}$ , resulting in a large overestimation of  $(\phi'_{ds})_{peak}$  ( $14.6^\circ$ ) when derived using  $(\sigma'_{yy})_{upper}$ . When the shearbox's walls were lubricated, the difference between  $(\phi'_{ds})_{peak}$  derived from  $(\sigma'_{yy})_{lower}$  and  $(\sigma'_{yy})_{upper}$  was much smaller ( $1.6^\circ$ ). In addition, the influence of lubrication on  $(\phi'_{ds})_{peak}$  derived from  $(\sigma'_{yy})_{lower}$  was small ( $2.3^\circ$ ).

It was concluded that the measured vertical force on the underside of the sample was a more accurate representation of that acting on the central plane because relative displacement between the sample's particles and the lower frame could not occur. Lubrication of the shearbox's internal walls helped overcome the wall friction and thus made the normal stress acting on the top of the sample a closer representation of that on the central plane. The Japanese Geotechnical Society, have paid heed to these

findings. The standard DSA recommended by JGS-0561 (2000) is a simple adaptation of Mikasa's (1960) design, identical in configuration to that previously illustrated in Figure 2.19 other than the provision of a low-strain load cell between the roller-guide and the upper frame. Thus the force used to estimate the normal stress is measured on the "load-receiving" side of the shearbox, which does not permit displacement between the frame's internal walls and the sample.

In summary, it is a necessity to reduce by as much as possible the frictional force between the sample and the shearbox's internal vertical walls if the confining stress applied to the top of the sample is to be used to derive the average normal stress on the central plane. This can be achieved by preventing the displacement of the sand particles adjacent to the shearbox's lubricated walls.

### 2.5.2 Induced rotational restraint

Enforcing rotational restraint on the DSA's components provides a means of addressing the problem of non-uniformity without having to consider its underlying causes. Jewell & Wroth (1987) and Jewell (1989) confronted the problem by first considering the cause of the rotation. They postulated that the often-recorded rotations of the shearbox's upper components were a consequence of the mechanism of load transfer to the sample.

Observation of the stress pattern within a shearbox sample comprising both light-sensitive crushed-glass granular materials and photo-elastic discs has revealed that little stress is transferred to the test material by way of shear stress at the upper and lower boundary (Dyer, 1985, Paikowsky et al, 1996, Allersma, 1999). This observation agrees with investigations into the frictional resistance developed between sand and dentated plates where it was found that significant displacement was necessary to mobilise appreciable forces (Hryciw & Irsyam, 1993). Clearly, this displacement is not consistent with the fixed end walls of the shearbox. Instead, load cells installed within a shearbox have shown the load to be transferred to the sample by way of normal stresses on the apparatus' vertical internal walls (Palmeira & Milligan, 1989a, Paikowsky et al, 1996, Shibuya et al, 1997). Such a mechanism of load transfer within the archetypal DSA results in an equal but opposite couple acting on the upper frame and the included sample, as illustrated in Figure 2.23. An equal and opposite moment,  $M_{Req}$ , is hence required to maintain equilibrium. If no provision is made to generate  $M_{Req}$ , anticlockwise rotation of the upper frame and the associated clockwise rotation of the sample is inevitable. Extra kinematic constraint, indicated by the elimination of rotation, can hence be imparted to a sample by the provision of  $M_{Req}$ .

The modifications to the archetypal DSA already discussed can be seen as making provision for  $M_{Req}$ ; be

it either by the forces transmitted through ball races in Wernick's (1977) and Mikasa's (Takada, 1993) devices or by the mobilisation of significant shear stresses on the apparatus' end-walls in Arthur et al's (1977, 1988) device. The Japanese Geotechnical Society's (JGS) standard apparatus prevents the riding up of the upper frame using a "fixing screw", as seen in Figure 2.24, thereby generating  $M_{Req}$  by the application of an extraneous vertical load. Such an extraneous force aids the mobilisation of wall friction within the shearbox and hence has adverse consequences relating to the assumed normal stress acting on the central plane. Also, since the load pad of this device was free to rotate, Matsuoka & Liu (1998) reported it to become trapped within the upper frame imposing, albeit temporarily, constant volume shearing conditions.

Jewell (1989) found that by securing the load pad to the upper frame prior to the test's initiation, rotation of the apparatus could be eliminated. This modification, depicted in Figure 2.25, was termed the "symmetrical arrangement" as symmetry about the central plane was achieved. By enabling significant shear stress transmission from the upper frame to the load pad, securing these components together was alleged to generate a non-uniform distribution of vertical stress across the top of the sample, inducing  $M_{Req}$  and balancing applied couples. Essentially, Jewell's (1989) symmetrical arrangement applies a bending stress to the top of the sample that disappears as one moves towards the horizontal split plane just as the bending moment at a cantilever's fixed end can be zero despite a uniformly distributed load if a bending moment of appropriate magnitude is applied at its free end.

For the symmetrical arrangement to be successful, and to enable the correct estimation of the normal stress acting on the central plane, the upper ensemble must be free to rise and fall with the deforming sample. Vertical restraint of either the upper frame or load pad would result in changes of the normal stress acting on the central plane and its incorrect estimation using the applied normal load. A "free floating" upper ensemble, however, able to rise and fall unimpeded with the contained sand, allows the average normal stress acting on the central plane to be correctly estimated from the applied normal load. In addition, with the load pad and upper frame secured together throughout a test's duration, unwanted temporary interactions like those experienced when using the JGS standard apparatus would not arise.

In summary, the kinematic restraint that is offered by Jewell's (1989) symmetrical arrangement may be sufficient to promote uniform strain within a single thin operational layer aligned with the central plane. In accord with traditional direct shear testing, the simplicity of the modification is appealing. In addition, the disadvantages associated with other's modifications are not in evidence and one can be confident that the stresses assumed to be acting on the central plane are a close estimation of those actually occurring.

## 2.6 Summary

The preceding discussion has introduced the DSA, standard test procedures and the test interpretations commonly employed. The test's long history and world-wide popularity can be concluded to stem from its simplicity. However, its crudeness leaves test results open to interpretation and concern has been expressed over the non-uniformity of the stress and strain distribution induced within a sample. The latter is said to produce rotations of the shearbox's upper components and many modifications have been proposed to rectify this aspect of testing. Devices employed to prevent rotation provide one of two types of rotational restraint: induced, which allows the free displacement of the apparatus components, and enforced, which doesn't. The latter does away with the simplicity that makes the DSA so attractive, requiring additional instrumentation to provide reliable estimates of the stresses induced on the central plane. Thus, an apparatus able to induce rotational restraint yet retain the archetype's simplicity is considered desirable.

The modification devised by Jewell (1989) is purported to eliminate rotations and can be achieved by simply securing the load pad to the upper frame prior to the application of any shear displacement to create a symmetrical test arrangement. The apparatus Jewell (1989) employed to test his adaptation was of dissimilar dimension (254 by 152 by 152mm) to the archetype and it is unclear whether the symmetrical arrangement would have any benefit for more conventionally sized apparatus.

The WF-25300 has a number of features that set it aside from the archetypal DSA. To remove the need for a swan neck yoke and its associated eccentric loading the WF-25300 features a novel arrangement for transmitting the shear load  $S$  to the upper frame. A frictional connector is employed which requires the line of thrust to be separated from the central plane. It was this wayward apparatus which was available for investigation and its use and modification is next discussed.

### 3. THE NEW WINGED DIRECT SHEAR APPARATUS

This chapter introduces a new DSA designed to limit the inadequacies of the archetype indicated in the previous chapter. Discussion starts with a note on the development of the apparatus before a general description is given. Following this, details of the equipment (test materials and instrumentation), procedures (sample preparation and data manipulation) and tools (data validation methods) employed later are given. In short, this chapter indicates the resources that are made use of in the following chapters.

#### 3.1 Historical development

It seems logical that talk of a modified apparatus should begin with criticism of that from which it was built. From the considerations of the preceding chapter, two criticisms of the WF-25300 are apparent. The first relates to the in-built separation between the loading system's line of thrust and the shearbox's central plane. If one assumes no other sources of loading other than the normal and shear force,  $N$  and  $S$  respectively, then in such an apparatus force and moment equilibrium are provided by a non-uniform distribution of normal stress across the central plane. This is illustrated in Figure 3.1(a) after making the assumptions of the weightlessness of shearbox's components and a trapezoidal distribution of normal stress across the central plane. It can be seen that the moment applied about the sample centre by the normal stress distribution across the central plane is numerically equal to the product of  $S$  and  $f$ . Moment equilibrium about the sample centre  $m$  reveals expressions for the intensity of vertical stress on the central plane at the sample's front and rear:

$$\frac{(\sigma'_{yy})_{front}}{\sigma'_{yy}} = 1 + 6 \frac{\tau_{yx}}{\sigma'_{yy}} \frac{f}{L} \quad 3.1$$

$$\frac{(\sigma'_{yy})_{rear}}{\sigma'_{yy}} = 1 - 6 \frac{\tau_{yx}}{\sigma'_{yy}} \frac{f}{L} \quad 3.2$$

from which:

$$\frac{(\sigma'_{yy})_{front}}{(\sigma'_{yy})_{rear}} = \frac{\sigma'_{yy} L + 6 \frac{\tau_{yx}}{\sigma'_{yy}} \frac{f}{L}}{\sigma'_{yy} L - 6 \frac{\tau_{yx}}{\sigma'_{yy}} \frac{f}{L}} \quad 3.3$$

Substituting approximate values into Equation 3.3 ( $f = 10\text{mm}$ ,  $L = 100\text{mm}$ ,  $\tau_v/\sigma'_{vy} = 1$ ) it is revealed that the nonuniformity of the induced stress distribution worsens as  $\sigma'_{vy}$  reduces. If a confining stress of 25kPa is used, the normal stress at the front of the central plane is a factor of 1.63 times that at the rear. For a confining stress of say 250kPa, however, the factor is a mere 1.05. Clearly such a non-uniform stress distribution will not promote the uniform behaviour of the sample across the central plane, especially at low stress levels. As seen in Figure 3.1(b), such considerations are not relevant to the global equilibrium when the central plane coincides with the line of thrust and hence it was thought necessary to raise the WF-25300's central plane to coincide with the line of thrust.

In actual fact, the system used to transmit the shear force to the WF-25300's upper frame ensures that an assumption made in the preceding discussion is invalid. During testing, sample dilation will cause the heave of the soil contained within the apparatus' upper frame. Shear stresses mobilised on its internal walls are reacted against by the frictional forces induced between the mated surfaces of the button and housing arrangement, which thus provides an additional source of loading, the second criticism of the WF-25300. A force and moment equilibrium diagram more applicable to the upper half of the WF-25300 is presented in Figure 3.2 that illustrates the condition for a dilating soil. The direction of  $P$ , the extraneous vertical force imposed by the button and housing arrangement, is variable and depends on the sample's deformation properties. Thus, the normal load acting on the central plane can be added to or subtracted from by an unknown amount depending on whether the soil is dilating or contracting. The situation is further complicated if non-uniform deformation of the sample results where portions of the sample appear contractile while others appear dilatant, i.e. by rotation of the load pad. All in all, one can say that the presence of such an extraneous vertical force increases the uncertainty associated with the estimation of  $\sigma'_{yy}$  and it is thus detrimental to the apparatus' performance.

Two adaptations bring significant improvements to the WF-25300's performance: aligning the line of thrust with the central plane, and removing the extraneous vertical force applied by the button and housing arrangement. The first of these requirements was initially satisfied using a swan-neck loading yoke like that of the archetypal DSA and a spacer plate positioned between the shearbox and the carriage. To balance the bulky swan-neck's self-weight, a dead weight was attached to the rear of the shearbox inducing considerable and regrettable increases in the inherent load of the upper-frame's self-weight.

The second requirement could then be satisfied using a system of bearings through which the shear load was applied to the swan-neck yoke. However, without the point of transmission of the shear load to the swan neck being a point of fixity (as it was when using the button and housing arrangement), rotation of the upper frame bought with it translation of the point of transmission away from the central plane. The

shear force  $S$  then generated a considerable moment about the sample centre. The magnitude of such moments can be limited by translating the point at which the shear force is transmitted to the upper frame from out in front of the sample to coincide with point  $m$  in Figure 3.1. Thus the new Winged Direct Shear Apparatus (WDSA) was born.

## 3.2 Description of the apparatus

### 3.2.1 The Winged Direct Shear Apparatus (WDSA)

A long section and plan of the WDSA prior to test initiation are presented in Figure 3.3 and 3.4 respectively. An isometric drawing focussing on the key modifications is displayed in Figure 3.5. A description of the essential features follows.

To avoid the out of balance force often applied to the shearbox's front by way of a bulky swan neck and bring the point of shear load transmission to the sample centre, the WDSA features a pair of swan-neck type yokes attached to the mid points of the upper frame's side-walls, which are consequently named "wings". In much the same way as a conventional swan neck spans the front wall of the carriage allowing the line of thrust to lie within the central plane, the wings are designed to span the carriage's side walls.

The shear load is applied in equal measure to each wing through an arm with a horizontal axis extending from the wing out in front of the carriage. Transmission of the shear load from each arm to each wing occurs through a ball-race that is subject to low rolling resistance. The ball races slot into a recess cut into the overhanging portion of each wing, and a vertical plane coincident with the ball races' axes divides the sample in two. To prevent indentation of the wings, which would hinder the free movement of the upper ensemble, the ball races bear on hardened steel plates attached to the front and rear faces of the wings. The benefits of this arrangement over more conventional systems lie in its well-defined geometry and good knowledge of the forces that act on the upper ensemble.

Within the radial-load range investigated (0.02 - 0.5kN), the rolling resistance offered by a single ball race,  $r$ , was measured as 0.5N. Thus, if the upper frame does not rotate during shear, a 1N limit ( $= 2r$ ) is placed on the extraneous vertical force provided by the shear loading system  $R_N$ . This force could act to increase or decrease  $\sigma'_{yy}$  by a maximum of 0.1kPa depending on whether the sample exhibits dilatant or contractile behaviour respectively. It will be seen that this accounts for a mere 0.4% of the lowest stress level investigated.



Rotation of the upper frame during testing causes the ball races to bear on no-longer vertical hardened steel plates of the apparatus' wings. Figure 3.6(a) illustrates a detail of a single ball race as it transmits a shear force  $S$  to a plate that has previously undergone a much-exaggerated clockwise rotation  $\omega$  from the vertical. The forces being imposed on the inclined plate are pictured in Figure 3.6(b). Thus:

$$\begin{aligned}\sigma'_{yy} &= \frac{N + R_N}{A} \\ &= \frac{N + S \tan \omega + 2r \cos \omega}{A}\end{aligned}\tag{3.4}$$

and also:

$$\tau_{xy} = \frac{S - 2r \sin \omega}{A}\tag{3.5}$$

In actual fact, because  $r$  is so small in relation to  $N$  and rotations of the upper frame, especially when symmetrical testing, rarely exceed  $2^\circ$ , the effect on derived stress parameters of these considerations is small. However, the assertion is that unlike within the archetypal DSA, no undefined loading is incurred by a WDSA sample and the estimation of average stresses is thus reliable.

It should be noted that along with influencing forces, clockwise rotation of the upper frame is associated with two other effects depicted in Figure 3.6(a). Firstly, the carriage displacement becomes an overestimate of the shear displacement applied to the sample and secondly the point of contact between the ball races and the steel plate falls below the central plane. However, the typically small rotations and the 26mm diameter of the ball races combine to produce insignificant values of  $\Delta f$  and  $\Delta v_r$ .

The alignment of the 26mm diameter ball-race axis with the sample centre, combined with the small magnitudes of  $\Delta f$ ,  $\omega$ , and  $r$ , ensures that any moments applied to the sample about its centre are kept to a minimum. However, an inclined hardened steel plate induces a bending moment in the arms to which the ball-races are attached.

The opposite ends of the arms are attached to a bar which spans the front of the carriage so that, in plan, the arm and bar arrangement is seen to straddle the carriage. The bar is cradled by a support block using a system of ball bushings and hardened steel shafts. This assembly is designed to satisfy a number of requirements, as highlighted below:

- Coaxiality between the line of thrust and the arm and bar arrangement
- Provision that the arm and bar arrangement remains in the horizontal plane
- Be subject to a low resistance to horizontal displacement
- Provision of a degree of horizontal freedom equivalent to tailstock thereby aiding test preparation procedures
- Remove any moment induced in the arms before transmission to the (moment-sensitive) load cell

### 3.2.2 The WDSA's shearbox

Conventional methods of imposing an opening between the upper and lower frames prior to the imposition of shear displacement are judged neither sound nor precise. Raising the upper frame relative to the lower after sample deposition is likely to have an adverse effect on the uniformity of a carefully prepared sample's fabric. There is no guarantee that the imposed opening is uniform and its magnitude,  $g$  (mm), cannot be measured since it is hidden within the carriage's walls. Consequently, conventional procedures result in an approximation of  $g$ . The WDSA's shearbox makes use of a system of screws to overcome this insufficiency, as illustrated in Figure 3.7. Four grub screws installed vertically within the upper frame's side-walls can have their protrusion from its underside determined before the upper and lower frames are clamped together. After clamping,  $g$  can be measured using vernier calipers, thereby obtaining a reliable estimate of its magnitude. Only after the clamping of the upper and lower frames is the sample prepared, removing the need for any substantial displacement between the upper frame and the sample prior to the start of a test.

The test can be made symmetrical by the clamping of the load pad to the upper frame prior to the application of any shear displacement thereby preventing their relative movement. This is done using a pair of restraining screws installed horizontally through the front wall of the upper frame in much the same way as the shearbox itself is clamped within the carriage using thumbscrews positioned through the carriage's front wall. The frame's restraining screws bear on stub rams designed to transform the screw's rotary motion to translatory. Although not a requirement of the symmetrical arrangement, the retaining plate is clamped within the lower frame in the same way that the load pad is clamped within the upper frame. Unlike in the archetypal DSA relative movement between the retaining plate and lower frame cannot occur and the sample may thus be prepared remote from the carriage, allowing the utilisation of more sophisticated sample preparation techniques than those suggested by convention.

### 3.3 Test materials

Soils are commonly categorised in relation to their dominating particle size. Within the UK, following the work of Glossop and Skempton (1945), sands are classified as having particles ranging between 0.06 and 2mm (BS 1377), bounded on the over-side by gravel and the underside by silt. Sands are further classified as fine, medium or coarse depending on whether their particles lie in the range 0.06-0.2mm, 0.2-0.6mm or 0.6-2mm respectively.

Here, to aid a comprehensive study, a sand representing each category is chosen for the research. Beginning with the coarse sand, this section describes each of these test materials. Each of the sands was sieved, washed and oven dried before testing and discarded after testing. No sand particles were tested more than once. The grading curves and physical properties of each sand after this preparation procedure are those displayed in Figure 3.8 and Table 3.1. The grading curves of Figure 3.8 are those of three individual samples taken from the test material. Only slight variations are in evidence between the curves. The quantities expressed in Table 3.1 are those determined by accepted British practice as laid out by BS 1377.

#### 3.3.1 Coarse test material

Leighton Buzzard Sand is a rounded quartz sand used throughout the years in numerous laboratories and by various researchers to investigate the stress-strain relationship of granular media. It originates as an aeolian deposit, geologically classified as Lower Greensand, and is extracted from gravel pits in Leighton Buzzard, Bedfordshire, UK. Leighton Buzzard Sand is supplied as a graded product and, in its most ubiquitous form, is graded between BS sieves number 14 and 25 to produce a uniform sand with mean particle size,  $D_{50}$ , circa 0.8mm. Consequently, it is often referred to as LB 14-25.

Two batches of Leighton Buzzard Sand are available for use within the University of Bristol's Department of Civil Engineering. The first, purchased in 1988, has been used extensively, primarily within the Earthquake Engineering Research Centre's Shear Stack: a 4.8m long by 1.0m wide by 1.2m deep hollow box with flexible walls which can be filled with soil and subjected to dynamic loading on the Research Centre's Shaking Table (Crewe et al, 1995). The sand was found to contain an appreciable portion of fines that displayed themselves as clouds of dust when a mass of the sand was poured. It was thought that this material must be comprised of fragments of abraded particles. Consequently this batch was named abraded Leighton Buzzard, ALB.

The second batch was acquired for this research work from Garside Industrial Sands in Leighton

Buzzard and had hence never before been subjected to experimental investigation. To allow distinction to be made between these two batches of sand, the second batch was named virgin Leighton Buzzard, VLB.

The particle distribution curves of both ALB and VLB are displayed in Figure 3.8(a) and (b), and their physical properties are listed in Table 3.1. Microscopic examination of ALB and VLB reveals that both sands have rounded particles. However, examination of their grading curves reveals that ALB has a smaller proportion of large particles, possibly a result of the wear and tear previously experienced by the sand.

	G	$e_{min}$	$e_{max}$	$D_{10}$ (mm)	$D_{50}$ (mm)	$D_{60}$ (mm)	$U_c$	Shape
ALB	2.647	0.486	0.780	0.63	0.76	0.80	1.27	Rounded
VLB	2.651	0.506	0.802	0.64	0.78	0.81	1.27	Rounded
MGS	2.657	0.494	0.806	0.34	0.44	0.45	1.32	Sub-rounded
SFS	2.654	0.684	1.017	0.09	0.13	0.14	1.56	Sub-rounded

**Table 3.1: Physical properties of the test materials**

### 3.3.2 Medium test material

A supply of material was found within the University of Bristol's Department of Civil Engineering uniformly graded between 500 and 212 $\mu$ m, which was therefore judged appropriate to represent a medium sand. The material had sub-rounded particles, orange or golden in colour. Unfortunately, however, the source of the material is unknown. Because of its grading and colour, it became known as medium golden sand, MGS. The particle distribution curve of MGS is displayed in Figure 3.8(c), and its physical properties are listed alongside those of the other test materials in Table 3.1.

### 3.3.3 Fine test material

The fine test material is a silver-grey quartz silica sand extracted from Lower Greensand deposits with sub-rounded particles. It was acquired from David Ball Group PLC, Cambridge, UK. The selected grading, between 212 and 63 $\mu$ m (BS 72-240), was chosen to represent a predominantly fine sand, with a maximum of 3% of included particles being classified as medium (>200 $\mu$ m). The sand's grading and colour led to the material being called silver fine sand, SFS. The particle distribution curve of SFS can be seen in Figure 3.8(d), and Table 3.1 lists its physical properties.

### 3.4 Sample preparation via pluviation

The attributes built in to a granular medium during any reconstitution procedure are void ratio and granular fabric, both of which profoundly influence a resulting sample's stress-strain behaviour. Bearing this in mind, the requirements for a viable sample reconstitution technique can be said to be uniformity, flexibility, and replication.

The uniformity of a reconstituted granular material is, within the literature, rarely measured. However, direct measurements of density at different locations within test samples have questioned the uniformity within those prepared by both tamping (Vaid & Negussey, 1988) and vibration (Mulilis et al, 1977). That these techniques are recommended by the standards is thus unsettling.

Even with density uniformity, a complete study cannot be attained without investigating behaviour at a variety of initial void ratios and it is unlikely that fabric uniformity between such samples can be attained if they are prepared using a variety of techniques. Vaid et al (1999) showed the undrained simple shear behaviour of sands prepared to similar average densities by different techniques depended strongly on the sample preparation method indicating the significance of fabric. Ideally a single reconstitution technique flexible enough to prepare samples with void ratios spanning between the sand's limiting values would be used, thereby preventing fabric variation between samples.

In addition, it is necessary for this flexible reconstitution technique to replicate the uniform samples it produces and thus aid a comprehensive testing program. A technique reportedly able to satisfy these requirements is pluvial deposition.

The word pluviation comes from pluvia, the Latin word for rain, and the concept of a Pluviator is a device that "rains" sand into the specimen mould. It has been suggested that pluviation "is the most promising technique for obtaining uniform samples within the laboratory" (Vaid & Negussey, 1984) and its has become increasingly used during the preparation of small scale, reconstituted samples of a granular medium. Here, it is not the task to undertake a comprehensive investigation of sample preparation by pluvial deposition, but only to develop the technique to be efficacious for this particular study.

The details for a number of differently designed Pluviators are presented within the literature, perhaps the most common being based on Miura & Toki's (1982) Multiple Sieve Pluviator (MSP). The MSP consists of a hopper that discharges sand through several layers of sieves before depositing it into a sample mould. The particular MSP described is that developed by Garner & Dietz (1995) and adapted for this work,

illustrated in Figure 3.9. This apparatus differs from Miura & Toki's (1982) apparatus in several respects in order to provide several benefits, as highlighted.

Garner and Dietz's (1995) hopper consists of a  $0.002\text{m}^3$  capacity funnel. Limiting the hopper's outlet aperture by the installation of one of a selection of interchangeable nozzles that sits within the funnel's snout controls the rate of discharge from the hopper. Miura & Toki (1982) found the hopper's outlet aperture to have the primary influence over the density of a resulting sample.

On exiting the hopper through the nozzle, pluviated sand falls through a vertical height of 300mm,  $v_1$ , before coming into contact with the uppermost sieve of the stack. Coaxiality between the hopper and sieve stack is achieved using a vertical portion of pipe and a thick Perspex disc. This upper section of pipe has a cutaway to enable access to the nozzle providing a means, with the use of a bung, to prevent sand deposition before the time required. The sieve stack comprises six 200mm diameter, mesh number 5 (3.35mm aperture) sieves (BS 410: 1969). They are arranged so as each consecutive sieve has its mesh at  $45^\circ$  to the previous. The sieves are supported by clamp stands 800mm tall, which thereby impose a maximum limit for the vertical drop of sand particles from the lowest sieve,  $v_2$  (mm). Miura & Toki (1982) found  $v_2$  to have little influence within the range investigated (300-700mm). Vaid & Negussey (1984) found the height of drop to become significant only when its magnitude fell below approximately 300mm, after which decreases in density were apparent.

Beneath the sieve stack, a second section of Perspex pipe extends from the base of the sieve stack to approximately 100mm above the receiver. The receiver consists of a 300mm diameter, 5.6mm mesh aperture sieve, on which sits the sample mould, nested in a sieve tray that collects the sand deposited outside of the mould.

### 3.4.1 Checking the Pluviator's efficacy

The Pluviator can be judged efficacious only if shown to produce uniform deposits with a range of densities repeatedly. The uniformity of a deposit may be investigated by pluviation into moulds of differing dimensions located in different positions under the sieve stack. The reproducibility and range of the Pluviator can be verified by the deposition of a multitude of samples varying the parameters found within the literature to be influential in determining a deposits density, namely nozzle aperture and height of fall,  $v_2$ .

The effect on the average density of two sands deposited within a cylindrical mould of internal diameter

75mm and height 75mm positioned to be coaxial with the Pluviator is seen in Figure 3.10(a). By increasing the nozzle aperture from 8 to 32mm deposits from dense to medium could be produced. Densities obtained by altering the nozzle aperture were found to be reproducible to within 3%, a value which agrees well with that found for Pluviators elsewhere in the literature (Vaid & Negussey, 1988) yet the replication of dense samples was much more consistent. Miura & Toki (1982) found a 32mm hopper outlet aperture, a stack of six 3.66mm mesh sieves, and a 700mm height of fall to produce deposits with  $D$  as low as 25%. It is thought such low density could be achieved because fine Toyoura sand ( $D_{50}$  circa 0.2mm) was used as the test material. The higher ratio of  $D_{50}$  to sieve mesh size in this work is thought to remove the control capability of the nozzle aperture. This is best seen when use of a 50mm nozzle produced a sample of LB 14-25 with relative density of 51%, only marginally below that obtained using the 32mm nozzle, the sand coming to rest in a pile on the uppermost sieve after exiting the hopper. Lo Presti et al (1993) found that an increase in the mesh size to  $D_{50}$  ratio brought about a decrease in deposit density.

Lessening the height of fall,  $v_2$ , is found to reduce the resulting sample density, as can be seen in Figure 3.10(b). The effect of height of fall on test data is significantly less than that reported by Vaid & Negussey (1984) where, on reducing  $v_2$  from 1000 to 100mm, a decrease in the relative density of an Ottawa Sand deposit ( $D_{50}$  circa 0.4mm) from 100% to 81% was measured. The lesser influence of  $v_2$  observed in experimental results is thought to be due to differences between each investigation's Pluviators. Vaid & Negussey's (1984) device was configured for  $v_1$  to equal zero, the nozzle itself being screened by a single 1.17mm mesh sieve. Consequently the total drop height  $v$  ( $= v_1 + v_2$ ) of their apparatus was far smaller than that imposed by this study's Pluviator, where  $v_1$  was fixed at 300mm. During tests where  $v_2$  was varied, the consistency of sample density again worsened as the deposit density reduced, but nevertheless remained within 4%.

The horizontal density distribution can be investigated by pluvial deposition into a cylindrical mould of internal diameter 75mm and height 75mm whose axis is separated from that of the Pluviator's by an amount  $h$  (mm), equalling zero when the mould is coaxial with the Pluviator. If the Pluviator is made to more closely mimic Miura and Toki's (1982) by the exclusion of the lower Perspex pipe, the resulting horizontal density distribution is non-uniform, an increase in  $h$  causing the loosening of dense samples and the reverse for loose samples as seen in Figure 3.11(a). With the lower Perspex pipe attached, however, a much more uniform deposit is produced over the Pluviator's entire cross section, as seen in Figure 3.11(b), since the spread of sand grains is restricted.

The vertical density distribution is investigated by comparing the density of samples deposited in moulds

of different heights. As can be seen from Figure 3.12, varying the deposit depth between 25 and 200mm had no effect on density outside of the envelope of results for the 75mm tall mould, shown in Figure 3.12 as vertical bars, regardless of the nozzle aperture or drop height  $v_2$ .

### 3.4.2 Summary of the pluvial deposition investigation

In summary, a preliminary investigation has shown that a modified version of Miura & Toki's (1982) MSP allows a deposit's density to be varied between medium and dense by the considered selection of a nozzle aperture and height of drop  $v_2$ , with loose deposits being prevented by a high  $D_{50}$  to sieve mesh aperture ratio. Uniformity of the average density within a deposit has been improved by using a Perspex pipe to reduce the spread of the sand grains exiting the sieve stack resulting in uniform horizontal density distributions across the sieve stack's diameter. A deposit's density has also been shown to be independent of its mould's depth, indicating a high degree of vertical density distribution uniformity.

### 3.4.3 Preparation of loose deposits

The technique used to prepare loose samples is that based on the method of obtaining the minimum density of a granular material recommended by the Japanese Geotechnical Society (JGS, 1990) described by Miura et al (1997). Here, a funnel is positioned so its snout is in against the sample mould's floor. The funnel is filled with sand before being lifted vertically thereby forming a sand pile within the mould. If the funnel is lifted slowly, so as its snout is kept in contact with the peak of the sand pile, sand exiting from the funnel intermittently slides down the pile's surface in thin layers. The high shear distortion within these sliding layers activates fully the dilational capabilities of the sand, the sand pile hence being left in an extremely loose state. Deposits of both LB 14-25 and MGS produced in this manner were found to have densities very close to those recorded using the method for determining  $(\rho_d)_{min}$  by BS 1377.

### 3.4.4 Levelling the uppermost sand surface

After sample deposition it is unlikely the height of sand within the shearbox is that required or the uppermost surface is level. It is also unlikely that the methods proposed by either the BS 1377 or Head (1982) for levelling the sample at a uniform distance below the top of the shearbox, which involves the scraping away of excess sand using a "suitable template", will leave the remaining sand undisturbed. Consequently, the method of surface preparation employed is based on that developed by Stroud (1971) and involves the sucking off of excess sand using a vacuum device. This device consists of a bar long enough to span between opposite walls of the shearbox. Pointing vertically downwards through this bar is



the vacuum device's inlet whose protrusion from the underside of the bar is adjustable. Thus, by methodically sweeping the bar to-and-fro across the shearbox, the uppermost sand surface can be levelled at any desired distance below the shearbox's top.

This is further improved by removing any remaining mounds on the uppermost sand surface by lowering in a (99.8 by 99.8mm) platen smeared with silicone grease. The platen was gently lowered onto the sand surface and carefully removed, taking the highest grains with it, then wiped clean and the process repeated. The surface was considered level when on extraction the platen had a uniform covering of sand grains.

### 3.5 Instrumentation

Testing was carried out within a temperature controlled laboratory and, as individual tests were of short duration, it was presumed that that laboratory conditions were unchanging. A list of the transducers used for this study is displayed in Table 3.2. The calibration of each was performed with all others energised to ensure a constant load on the power supply, and the system was left running to ensure a stable operating temperature was maintained. Transducers were monitored every three months throughout the two-year testing period. No significant variations in calibration and regression characteristics were found during this time.

Manufacturer	Model	Serial no.	Measures	Rated limit	Units	Physical overload limit	Nominal excitation (Vdc)	Nominal output (Vdc)	Accuracy (NLHR % fsd)
IC		102	Force	4500	N	100%	10	0.04	0.05
MPE	HS25	3335	Displ.	25	mm	n/a	10	0.07	0.1
MPE	HS10	4473	Displ.	10	mm	n/a	10	0.05	0.15
MPE	HS10	4503	Displ.	10	mm	n/a	10	0.05	0.15
MPE	HS10	4508	Displ.	10	mm	n/a	10	0.05	0.15
MPE	HS10	4511	Displ.	10	mm	n/a	10	0.05	0.15
MPE	HS5	3312	Displ.	5	mm	n/a	10	0.04	0.15

**Table 3.2: The transducers used in this project**

#### Transducer for force measurement

The type of load cell employed to measure the shear force,  $S$ , is more commonly found within the cell of a triaxial apparatus. The load cell is able to measure axial load by the deformation of three triangular webs spanning between the ram and a slot in the load cell's casing. The arrangement of strain gauges on

these webs is designed to provide a high output. Such a load cell was thought suitable for the current application for several reasons:

- The full scale deflection of the transducer is 0.02mm and so the carriage's horizontal displacement closely approximates the actual shear displacement
- The load cell is dimensionally appropriate and has reported low hysteresis and non-linearity characteristics

Typical load cell calibration and linear regression characteristics obtained after calibration against the reference masses of a Budenberg Dead Weight Calibrator (S/N 21096/380), which applies load to the transducer through rotating hydraulic piston cylinders, are displayed in Table 3.3. At extremely light loads under approximately 30N an increasing sensitivity highlighted a particularly non-linear response. The rate of increase is small and since when direct shear testing under even the lowest confining stress this magnitude of force is exceeded during the very early stages of testing the increased non-linearity is for practical reasons ignored. Calibration took place over load ranges corresponding to those incurred whilst testing (0 - 0.2, 0 - 0.75, 0 - 1.2, 0 - 1.5, 0 - 1.75 and 0 - 2.5 kN). Aside from the accuracy over the smallest load range being slightly lower due to an increased hysteresis, calibration statistics from each of the load ranges agreed sufficiently for the response to be described in terms of a single sensitivity.

An investigation into the load cell's shear-load and moment sensitivity was carried out. Using simple hanger and pulley systems, the load cell was subjected to a known axial force  $F_a$  using dead weights whilst increments of either radial load  $F_r$  or moment  $M$  were added, the output of the load cell  $F$  each time being recorded. To prevent any bias caused by unintentional inclined loading of the cell, the loading system was reassembled prior to each axial force investigated. The limitations of the loading system allowed the investigation of behaviour at only low magnitudes of  $F$ , the results of which are seen in Figure 3.13.

The influence of radial load  $F_r$  on the measured axial force  $F_a$  is small, agreeing with the manufacturer's literature that states the load cell to "reject the influence of the transverse load component in the plane of the transducing element." The susceptibility of the output to bending moment is, however, appreciable with  $F_a$  increasing with  $M$  at an approximate rate of 0.001kN/Nm irrespective of  $F$  over the range investigated.

The structure of the load cell is such that there is a "dead spot" as the load changes from tensile to

compressive and the triangular webs are momentarily unrestrained. It is thus expected that during multi-ersal tests and on stress reversal, the carriage's displacement will not represent the shear displacement applied to the soil as the triangular webs displace relative to the load cell's casing.

		With 95% confidence				
Load cell		Approximate sensitivity	Coeff. of correlation	Resolution (N)	Max error $\pm$ units	Accuracy $\pm$ % fsd
	Tension	200 N/mv	0.99986	0.41	20N	0.7
	Compression	192 N/mv	0.99980	0.33	32kN	1.1
LSC	5	0.34 mm/mv	1.00000	Infinite	0.008mm	0.16
	10	0.52 mm/mv	1.00000	Infinite	0.007mm	0.07
	25	0.90 mm/mv	1.00000	Infinite	0.005mm	0.02

**Table 3.3: Calibration and regression characteristics of the WDSA's transducers**

### Transducers for displacement measurement

6 linear displacement transducers were used during the course of this work: 5 monitoring the displacement of the load pad and the remaining monitoring the carriage's horizontal displacement. The five transducers monitoring the vertical displacement of the load pad were arranged to record its average vertical displacement, by the positioning of a transducer on the midpoint of the apparatus' normal load hanger, and any rotations, by positioning a transducer over each of the load pad's corners. Transducers with three spindle displacements were employed: 25mm (for the carriage displacement), 10mm (monitoring the vertical displacement of the load pad's corners) and 5mm (for the vertical displacement at the load pad's centre).

The displacement transducers were of the Linear Strain Conversion (LSC) type, which produce a voltage output in proportion to spindle displacement via the four active arms of a strain gauge bridge arrangement. Typical calibration and regression characteristics obtained from calibration against a 10 $\mu$ m micrometer mounted in a gauge block are displayed in Table 3.3.

### Data logging

A 700 series Autonomous Data Acquisition Unit (ADU) manufactured by Mowlem Microsystems was used to log test data.

Each of the 7 transducers had its output read continuously, the values being recorded when triggered by a defined incremental change of the control transducer's output, here the transducer used to monitor the carriage displacement. Since a constant rate of displacement was applied to the carriage, the

increment of displacement necessary to initiate data capture can be approximately expressed as a frequency. Two rates of data retrieval were used during a test. The first, employed during the early stages of the test as the shear resistance increases rapidly, at frequency of approximately 0.4hz and the second at the lower frequency of approximately 0.05hz during the later stages of a test.

Recorded test data was exported to a personal computer at the end of the test and from where it could be imported into a data processing software package.

## 3.6 Manipulation of test data

Different data manipulation techniques are suggested by American (ASTM 3080) and British (BS 1377) standards. Here a discussion on data handling methods and the assumptions contained therein is presented with the specific techniques employed being explicitly identified.

### 3.6.1 The reducing plan area of the central plane

During any direct shear test the plan area of soil resisting each increment of shear displacement progressively reduces as the shear displacement increases. An increasing area of soil-metal contact accompanies the reducing plan area of the central plane as the horizontal surfaces of the shearbox's walls are progressively revealed. Whereas both the American and British standards agree that this transition has no effect on the normal stress acting on the central plane, its effect on the measured shear force is in dispute with a different technique for the treatment of data suggested by each.

In effect, the British Standard ignores the ever-decreasing area of the central plane stipulating the resistive shear stress mobilised on the central plane to be derived using the following expression:

$$\tau_{yx} = \frac{S}{L^2} \quad 3.6$$

where  $\tau_{yx}$  is the mobilised shear stress

S is the measured shear force

L is the sample length

By treating data in this manner the assumption is made that the friction angle mobilised on the progressively revealed horizontal surfaces is equivalent to that mobilised on the central plane within the soil mass. Following the American Standards, the soil-metal frictional forces are assumed negligible in

relation to those mobilised within the soil itself. Thus the shear stress mobilised on the central plane is given by:

$$\tau_{yx} = \frac{S}{L(L-v_x)} \quad 3.7$$

where  $v_x$  is the shear displacement

Alternatively, an estimated angle of interface friction can be assumed on the progressively revealed metal surfaces. An appropriate correction would involve only the uncovered horizontal face of the lower frame at the shearbox's front since dilation and clockwise rotation of the upper ensemble is usually found to separate it from the portion of the sample contained within the rear of the lower frame. Thus, a suitable expression is given by:

$$\tau_{yx} = \frac{S - v_x L \sigma'_{yy} \tan \delta'}{L(L-v_x)} \quad 3.8$$

where  $\sigma'_{yy}$  is the normal stress on the central plane

$\delta'$  is an assumed angle of interface friction

This assumption has its basis firmly grounded in reality, but is complicated by uncertainty over the magnitude of  $\delta'$ .

### **When the opening between frames ( $g$ mm) is small**

Since the effect of each data handling technique increases with  $v_x$  their efficacy is judged using large-displacement data where it is commonly thought the sample shears at constant volume and with constant resistance. An example of such large displacement data after manipulation using each of the proposed techniques is presented in Figure 3.14 wherein the assumption of a  $12^\circ$  angle of friction on the uncovered horizontal face of the lower frame is seen to produce a more nearly constant large displacement stress ratio. The assumption of a  $12^\circ$  angle of wall friction has been found to have a similar levelling effect on the majority of large-displacement test data considered here and hence it has been employed for all tests featuring small openings.

### **When the opening between frames ( $g$ mm) is large**

The definition of the central plane specifies that it bisects a sample. Thus, when employing larger magnitudes of  $g$ , the progressively revealed horizontal face of lower frame is located at a distance of  $g/2$

below the central plane. A correction to test data equivalent to that applied when employing small  $g$  may therefore be inappropriate. To assess whether this is so large displacement stress data obtained during tests with a variety of  $g$  values is presented both with and without the area correction in Figure 3.15. On the data are superimposed the linear approximation to the final 10 data points and the results of corresponding linear regression analysis.

The levelling effect of the area correction on large displacement stress data apparent when employing small magnitudes of  $g$  is not evident when  $g$  is large. Instead, the linear approximations are more horizontal when the correction is not applied. Figure 3.16 presents the gradients of stress ratio plot over the final 10 data points (approximately equivalent to the final 2mm of shear displacement) for a wider variety of test data than that presented in Figure 3.15. All presented data were obtained with  $g$  circa  $5D_{50}$  but using different sands, confined under various stresses, and deposited at various densities (for the "dense sand"  $90\% < D_r < 100\%$ , the "medium"  $66\% < D_r < 82\%$  and the loose  $4\% < D_r < 17\%$ ). Figure 3.16(a) illustrates the gradients after the application of the area correction whereas Figure 3.16(b) is not associated with any area correction.

The appropriateness of the area correction for test data obtained with substantial  $g$  values can be ascertained by considering the data's weighting about the abscissa. The predominantly positive gradient of the stress plots after the application of the area correction indicates the sample's unprecedented large-displacement strain hardening. Uncorrected data, however, at both low and medium stress levels, is distributed more equally about the abscissa. At high stress levels, however, uncorrected stress data has a negative gradient, perhaps indicating that the shear displacement applied has been insufficient to mobilise a highly stressed sample's critical state. Thus the area correction is deemed inappropriate when handling test data obtained employing substantial  $g$  values.

### 3.6.2 The estimation of $\sigma'_{yy}$

Since the measured shear force corresponds to that mobilised on the central plane it is the normal force bearing down on this plane that is of interest. Providing an opening is maintained between the upper and lower frame throughout the course of a test, this force is made up of the vertical force imposed on the load pad  $N$  in addition to the "inherent" load imposed by the self weight of the upper half of the shearbox. Calculation of  $\sigma'_{yy}$  as stipulated by the Standards without reference to this inherent load will result in overestimation of  $\tau_{yv}/\sigma'_{yy}$  through the underestimation of  $\sigma'_{yy}$ . The inherent load associated with the WDSA generates a normal stress on the central plane of close to 5kPa, sufficient in magnitude to cause

appreciable underestimate of  $\sigma'_{yy}$ , if left unaccounted for, especially when testing at low stress levels.

The estimate of  $\sigma'_{yy}$  will be made unreliable if the horizontal faces of the upper and lower frame come into contact during testing. When employing a free-floating upper frame, retraction of the separating screws pre-test will lead to subsidence of the upper frame if the shear forces on its internal walls are of insufficient magnitude to balance its self-weight. Derivation of the magnitude of wall friction depends on an estimate of the angle of wall friction,  $\delta'$ , and knowledge of the horizontal stress acting normal to each of the internal walls. Before the application of shear displacement, the maximum vertical force able to be sustained through wall friction alone,  $P_{max}$ , can be estimated using:

$$P_{max} = (K\sigma'_y) a \tan \delta' \quad 3.9$$

where  $K (= \sigma'_{xx}/\sigma'_{yy})$  is assumed to be 0.4

$\sigma'_{yy}$  is the applied confining stress (inclusive of self-weights of the components above the sample)

$\delta'$  is the angle of wall friction and assumed to be  $12^\circ$

$a$  is the area of the internal vertical face of the specimen in the upper frame, and is equivalent to  $4hL$  where  $h$  is the height of sand contained within the upper frame (approximately 17mm) and  $L$  is the specimen length

At the lowest stress level investigated here ( $\sigma'_{yy} = 25\text{kPa}$ ), it is estimated that approximately 14N of the upper-frame assembly's 24.5N self-weight can be supported by wall friction. Consequently, as the upper-frame's separating screws are retracted, a free-floating upper frame is expected to, and indeed does, fall relative to the sample until it comes to rest against the lower frame.

Without an opening between the frame's, uncertainties as to how best to handle data are introduced. Whereas a contractant sample would experience a wall friction induced uplift lessening  $\sigma'_{yy}$  below its assumed value, a dilatant sample would experience a down-drag whose magnitude could assume any value up to the self-weight of the upper frame. Thus,  $\sigma'_{yy}$  would be liable to fluctuate during the course of a test.

Fortunately, however, once the test is initiated an opening is soon introduced between the frames. To demonstrate that the inability of wall friction to sustain the self-weight of the upper-frame assemblage is short-lived, two assumptions are made. Firstly, the shear force  $S$  is assumed to be transmitted to the

sample entirely through normal forces on the upper-frame's rear wall and secondly, the other internal walls of the upper frame are assumed frictionless. Assuming a  $\delta'$  of  $12^\circ$ , the minimum shear force necessary to generate a vertical component on the end wall sufficient to balance the self-weight of the upper-frame assembly is a mere 120N, 20% lower than that necessary to maintain the large-displacement shear of the sample at the lowest stress level to be investigated (25kPa). Thus, although the self-weight of the WDSA's upper frame assembly cannot be supported by wall friction initially, soon after test initiation the vertical component of the shear force on the upper frame's rear wall alone becomes sufficient to support the assembly's self-weight. Vertical friction forces occurring on the other internal walls would further decrease the shear force necessary for uplift of the upper frame. Hence, sample dilation results in the upward vertical displacement of the upper frame assembly soon after test initiation. Thus an opening between the frames is reinserted and the average  $\sigma'_{yy}$  can be as reliably estimated as in symmetrical WDSA tests.

The WF-25300's upper frame assembly has a self-weight of 18N, 6.5N less than that of the WDSA due to the absence of the wing yokes, and equivalent to the maximum force able to be withstood by wall friction forces under the confining stress investigated. However, unlike during unsymmetrical WDSA tests where retraction of the separating screws brought about subsidence of the upper frame prior to the application of any shear displacement, the WF-25300's upper frame generally remains in its intended position as the separating screws are retracted. Once shear displacement is initiated, sample dilation and contraction will endeavour to raise or lower the upper frame. However, within the WF-25300 a resistance to displacement is provided by the frictional forces developed between the mated surfaces of the button and housing arrangement. Thus, the normal force on the central plane will either be added to or subtracted from depending on the sample's deformation behaviour and a good deal of uncertainty is associated with the correct estimation of  $\sigma'_{yy}$ .

### 3.7 Validation of data

The optimum direct shear apparatus will reveal itself through the relative merit of the resulting test data. Here the tools at the disposal of the experimenter to assess the quality of his or her direct shear test data are identified. They can be split into three camps: comparisons with other investigator's test data obtained using similar sands and apparatus, comparisons with data obtained for the test materials outside of the WDSA, and comparison with theoretically derived strength-dilatancy relationships.



### 3.7.1 Comparisons with other's test data

A limitation to the integrity of comparison with other's test data is that the consistency of strength and strain parameters between different batches of specific sands should not be assumed. Within a DSA, Arthur and Dunstan (1988), found variations in  $(\phi'_{ds})_{peak}$  of up to 3° between different batches of the same type of dense Leighton Buzzard sand. Between different gradings of Leighton Buzzard sand, Palmeira (1988) found differences in  $(\phi'_{ds})_{peak}$  of as much as 12°. Other plane strain apparatus have revealed similar variations. Yasin et al (1999) found consistent variations in the strength and deformation characteristics of different batches of Leighton Buzzard sand with no clear distinction of physical properties (gradation, specific gravity, minimum and maximum void ratios, particle shape and crushability) irrespective of the plane strain device in which they were tested. Similar variations were recorded when investigating the behaviour of different batches of Toyoura sand. Experimental results thus suggest that the strength and deformation characteristics of a granular medium going by any particular name need not necessarily correspond precisely to another's with the same name.

Consequently, the quest for exact consistency between different author's test results, even when obtained in identical apparatus, should be abandoned. Without ensuring consistent sand characteristics using batch control, established data for a named sand should be seen as an estimate of what will be recorded when investigating the shear behaviour of that named sand.

Aside from the behavioural differences between different batches of a named sand, other difficulties arise when trying to relate recorded test data with that obtained elsewhere. The amount of viable data available within the literature is limited by the presentation of stress data without corresponding strain data, uncertainty over the data quality, ambiguity over how results have been interpreted and a predilection for peak state data over that obtained at other stages of testing. Also, considering Leighton Buzzard sand in particular, confusion seems to have developed between the Silver and the Standard (yellow/orange in colour) sands, both having the same abbreviation and available with similar grain size distributions. In summary, great care needs to be taken to ensure veracious comparison.

Here, several authors' test data are judged applicable for comparison. At Cambridge University, a number of authors have compiled a database of the behaviour of Leighton Buzzard 14-25 within the Simple Shear Apparatus (Cole, 1967, Stroud, 1971, and Budhu, 1979). Stroud (1971) in particular carried out a detailed investigation of mainly dense Leighton Buzzard 14-25 at low stress levels. When developing the symmetrical direct shear test Jewell & Wroth (1987) and Jewell (1989) used an identically named test material densified and confined to similar degrees presumably with the aim of using Stroud's (1971) data

as a reference. Other authors to use this test material within DSA include Palmeira (1988) and Palmeira & Milligan (1989).

### 3.7.2 Comparison with data obtained distant from the WDSA

As has been mentioned, the direct comparison of a given sand's strength and deformation behaviour as measured in different apparatus reveals, in general, disparate conclusions. However, a laboratory technique able to determine an independent measure of a test material's strength comparable to recorded test data would help to verify an apparatus' behaviour.

The oldest and simplest method for obtaining the friction angle of a dry, cohesionless soil is to measure the angle that the free surface of a pile of the material makes with the horizontal. This angle is known as the angle of repose,  $i$ . Taylor (1948) interpreted  $i$  as the angle of internal friction under a pressure of practically zero, but went on to say it tends to differ from the angle of internal friction for the following reasons:

- The surface of a sand heap is likely to be in a looser condition than its interior and it is understood that the angle of internal friction reduces with density
- $i$  includes little or no strength due to interlocking which is known to increase the angle of internal friction
- $i$  is determined by the stability of the least stable grains on a sand heap's surface whereas the angle of internal friction depends on the average condition of all of the grains

Consequently, Taylor (1948) concluded that  $i$  would be appreciably smaller than the angle of internal friction. Although generally true, Taylor's arguments indicate that  $i$  may bear a close resemblance to  $\phi'_{crit}$ , the angle of friction mobilised when the interlocking component of strength has been overcome and the sand loosened by way of dilatancy. Referencing Cornforth's (1973) studies, Bolton (1986) remarks that  $i$  can approximate  $\phi'_{crit}$  to about 1°. If this is so, then the angle of repose could provide a means to verify that the WDSA can reliably measure a test material's strength parameters.

Unfortunately, however, and inconsistent with the fundamental nature of  $i$ , there exists no standard method for obtaining its estimation. Within the literature, often only cursory references to  $i$ 's determination are made. For example, Bolton (1986) remarks that  $i$  can be estimated by measuring the slope of a heap of sand loosely tipped and subjected to excavation at the toe. However, where more detail

is presented, it becomes clear that  $i$  is influenced by the experimental parameters involved in its determination. Miura et al (1997) found  $i$  to be influenced by the size of the tipped sand pile, the rate at which the sand pile was formed, and the roughness of the floor on which the pile sat. A device and associated experimental technique was thus developed by Miura et al (1997) which aimed to overcome these experimental variables

Here both Bolton's (1986) and Miura et al's (1997) methodologies are employed to investigate  $i$  for each of the test materials details of the apparatus and technique being described below:

- A 'scree' of material is formed against the internal end wall of a glass fish tank by the slow lifting of a sand-filled hopper whose outlet is initially in contact with the fish tank's floor. This procedure is akin to pluviation with a zero height of fall, and therefore produces a loose deposit. To aid the establishment of a uniform slope the scree sits away from the fish tank's side walls, thereby eliminating boundary wall friction effects, and its width is large compared to its height. The toe of the scree is then excavated until its slope is in a state of incipient collapse. The maximum uniform slope is then measured using a height gauge and rule. The arctangent of this slope will be called the "plane strain" angle of repose,  $i_{ps}$ .
- Miura et al's (1997) indented pedestal and annulus apparatus is employed to determine the *axisymmetric angle of repose*. Here a heap of sand is deposited by the slow lifting of a sand-filled hopper as above, but on a 75mm diameter pedestal that has a lip protruding 10mm above the base of the sand heap. Level with the uppermost edge of this lip, encircling the pedestal is a 20mm wide annulus. The sand heap is deposited to cover both the pedestal and annulus before the annulus is gently lowered relative to the pedestal. The "axisymmetric" angle of repose,  $i_{ax}$ , is then determined by using a height gauge to measure the height of the sand heap left sitting on the pedestal.

To aid comparison between the two procedures, the height of the scree of procedure 1 is made to approximately equal the height of the heap of procedure 2.

The average of 5 measurements of  $i_{ps}$  and  $i_{ax}$  and their standard deviations for three different sands are presented in Table 3.4.

	$i_{ps}$ : °	±% error with 95% confidence	$i_{ax}$ : °	±% error with 95% confidence
VLB	35.0	2.3%	35.7	0.7%
MGS	34.2	2.0%	34.3	0.8%
SFS	32.2	4.0%	33.5	2.2%

**Table 3.4: The angles of repose obtained using two procedures on three different sands**

Noteworthy observations include:

- There is good agreement between the angles of repose measured using both procedures although the magnitudes of  $i_{ax}$  are slightly higher than their plane strain counterparts. This result may seem surprising since plane strain strength parameters are often found to be in excess of axisymmetric. However, the smaller magnitude of  $i_{ps}$  when compared to  $i_{ax}$  probably arises from the smoothness of the fish tank's floor. Miura et al (1997) showed that the angle of repose of a heap of sand can increase with the roughness of the surface on which the heap sits by as much as 3 or 4°. When using a smooth pedestal without a raised lip to obtain the  $i_{ax}$  value for VLB, Miura et al's (1997) apparatus gave 33.7° (with a 95% confidence maximum error of  $\pm 0.53^\circ$ ), 2° less than the value presented in Table 3.4. It is reasonable to assume that  $i_{ps}$  would be affected by base surface roughness in the same way, and hence resemble more closely or even exceed  $i_{ax}$  if the fish-tank's internal surfaces were roughened.
- $i_{ax}$  appears more consistent than  $i_{ps}$ , probably arising from an improved experimental method.
- The angles of repose for VLB lie very close to the critical state angle of friction quoted for the same sand by Stroud (1971), a value of 35°.
- The variability of  $i$  for SFS is comparatively high. The SFS heap was found more sensitive to small disturbances or vibrations, the slope often exhibiting slips and partial slips during measurement.

### 3.7.3 Correlation with formulated relations

Validation of direct shear results has also made use of theoretically and empirically derived relations between friction, dilation, density and pressure. Relationships between the stress ratio and the plastic strain increment, known as flow rules, are fairly well established both theoretically and experimentally, with broadly similar conclusions being reached by different authors. The relations between density,

pressure and dilation are less well established although a practicable rule is in existence.

Before commencing, and to provide a reference, the cardinal parameters involved in the following discussion are tabulated and described in Table 3.5. The included parameters were first introduced in Chapter 2

	Description	Derived using:
$\phi'_{ds}$	The angle of friction mobilised on the DSA's central plane	$\phi'_{ds} = a \tan(\tau_{vx} / \sigma'_{yy})$
$\phi'_{ld}$	The angle of friction mobilised on the central plane of the DSA at large displacement	$\phi'_{ld} = a \tan(\tau_{yx} / \sigma'_{yy})_{ld}$
$\psi$	The ratio between volumetric shear strain rate	$\psi = a \tan(dv_v / dv_s)$
$\phi'_{ps}$	The maximum stress obliquity within a WDSA sample	$\phi'_{ps} = a \sin[\tan \phi'_{ds} / (\cos \psi + \sin \psi \tan \phi'_{ds})]$
$\phi'_{crit}$	The critical state angle of friction	$\phi'_{crit} = a \sin(\tau_{vx} / \sigma'_{yy})_{ld}$

**Table 3.5: A summary of the cardinal parameters encountered in discussion relating to the WDSA**

### Flow rules

Many attempts have been made to describe the relationship between the plastic strain increment and stress ratio. A detailed review of these flow rules has been given by Stroud (1971) and here, the ones previously found best in correlating the behaviour of a sand are highlighted. Approaches used have treated the soil as a continuum (Taylor, 1948), a collection of discrete particles (Rowe, 1962), or been based around an empirical correlation of the experimental data presented in the literature (Bolton, 1986). Even with these very different approaches, the three flow rules result in broadly similar conclusions.

Consideration of the dissipation of energy during a direct shear test led Taylor (1948) to distinguish between that expended in overcoming internal friction and that required to cause the sample to dilate against  $N$ . The separation of energy components in this manner allowed the increase in strength with sample density to be seen as being due primarily to the increased tendency for the sample to dilate (Bishop, 1950). Hence the total energy input could be “corrected” to establish only that needed to overcome the internal friction. Taylor’s (1948) flow rule therefore became known as an “energy correction” when in fact it is more accurately described, as Rowe et al (1964) noted, as an energy separation.

Following the derivation of Houlsby (1991) by defining the rate of input work as  $\dot{W}$ , then:

$$\dot{W} = \tau_{yx} \dot{\gamma}_{yx} + \sigma'_{yy} \dot{\epsilon}_{yy} \quad 3.10$$

Assuming that this work input is dissipated internally within the soil at a rate proportional to  $\sigma'_{yy}$  and  $\dot{\gamma}_{yx}$  then:

$$\dot{W} = C \sigma'_{yy} \dot{\gamma}_{yx} \quad 3.11$$

Combining Equations 3.10 and 3.11 gives:

$$\frac{\tau_{yx}}{\sigma'_{yy}} + \frac{\dot{\epsilon}_{yy}}{\dot{\gamma}_{yx}} = C \quad 3.12$$

Noting that Wroth (1958) found  $C$  constant for all constant  $\sigma'_{yy}$  direct shear tests using steel balls, Housby (1991) concluded that the constant of proportionality was the stress ratio at the critical state. Thus:

$$\frac{\tau_{vx}}{\sigma'_{vy}} + \frac{\dot{\epsilon}_{vy}}{\dot{\gamma}_{vx}} = \tan \phi'_{crit} \quad 3.13$$

However, this is not necessarily true. Bishop (1950) found that once direct shear data had been accordingly treated, the constant  $C$  in Equation 3.12 was equivalent to the stress ratio mobilised at large displacement once the dilatancy potential of the sample had been overcome. Thus, Equation 3.13 only holds if the central plane is one of maximum stress obliquity. Internal investigations detailed in Chapter 2 have revealed this not to be true, the central plane of the DSA instead being one of zero extension. Thus, Equation 3.13 should instead be written:

$$\frac{\tau_{vx}}{\sigma'_{vy}} + \frac{\dot{\epsilon}_{vx}}{\dot{\gamma}_{vx}} = \tan \phi'_{ld} = \sin \phi'_{crit} \quad 3.14$$

Which is equivalent to:

$$\begin{aligned} \tan \phi'_{ds} &= \tan \phi'_{ld} + \tan \psi \\ &= \sin \phi'_{crit} + \tan \psi \end{aligned} \quad 3.15$$

Stroud (1971) found Taylor's (1948) flow rule to successfully correlate the behaviour of Leighton Buzzard 14-25 when subjected to constant confining stress within the Cambridge Simple Shear

Apparatus. More recently, Jewell (1989) and Shibuya et al (1997) have found good agreement between their direct shear data and Taylor's (1948) flow rule. It can be seen that each parameter of Taylor's (1948) flow rule is measured during a direct shear test which accounts for this particular flow rule's predominance in this work.

The approach taken by Rowe (1962) when developing his stress-dilatancy theory is conceptually quite different from that used by Taylor (1948) but leads to a similar result. By examining the properties of first regular packings of spheres, he was able to obtain expressions for both the stress ratio  $\sigma'_1 / \sigma'_3$  and the strain rate ratio  $-\dot{\epsilon}_3 / \dot{\epsilon}_1$  in terms of the geometry of the packing. Drawing analogies between this idealised system and irregular packings of real soil particles, and using a minimum energy ratio principle, led Rowe to express his stress-dilatancy formula for plane strain as:

$$\frac{\sigma'_1}{\sigma'_3} = \tan^2 \left( 45 + \frac{\phi'_f}{2} \right) \left( \frac{-\dot{\epsilon}_3}{\dot{\epsilon}_1} \right) \quad 3.16$$

or more commonly:

$$R = KD \quad 3.17$$

where  $R$  is the principal stress ratio,  $D$  the principal strain rate ratio, and  $K$  is a coefficient representing the internal friction and may be expressed as:

$$K = \tan^2 \left( 45 + \frac{\phi'_\mu}{2} \right) \quad \text{where } \phi'_\mu \leq \phi'_f \leq \phi'_{crit} \quad 3.18$$

$\phi'_\mu$  is the angle of friction existing between individual soil particles, which remains a difficult parameter to obtain. Budhu (1979) found an excellent correlation between Rowe's flow rule and his simple shear data when  $\phi'_f$  was taken to be  $\phi'_{crit}$ .

In terms of more familiar parameters, and assuming  $\phi'_f = \phi'_{crit}$ :

$$R = \frac{\sigma'_1}{\sigma'_3} = \frac{1 + \sin \phi'_{ps}}{1 - \sin \phi'_{ps}} \quad 3.19$$

$$D = \frac{-\dot{\epsilon}_1}{\dot{\epsilon}_3} = \frac{1 - \sin \psi}{1 + \sin \psi} \quad 3.20$$

$$K = \frac{1 + \sin \phi'_{crit}}{1 - \sin \phi'_{crit}} \quad 3.21$$

Substitution of which into Equation 3.17 results in:

$$\sin \phi'_{ps} = \frac{\sin \psi + \sin \phi'_{crit}}{1 + \sin \psi \sin \phi'_{crit}} \quad 3.22$$

In addition, a consideration of Mohr's circles of stress and strain increment, after assuming the coincidence of principal axes, in conjunction with his stress-dilatancy formula led Rowe (1969) to publish a theoretical relationship between the plane strain and direct shear angles of friction:

$$\tan \phi'_{ds} = \tan \phi'_{ps} \cos \phi'_{crit} \quad 3.23$$

Quite different from the theoretical approach employed by Rowe (1962), Bolton (1986) found a simple relation based on a "saw tooth" model,  $\phi'_{ps} - \phi'_{crit} = \psi$ , to overestimate the  $\phi'_{ps} - \phi'_{crit}$  predicted by Rowe's stress dilatancy relation by approximately 20%. Hence, an "operationally indistinguishable" expression to Rowe's was presented as:

$$\phi'_{ps} = \phi'_{crit} + 0.8\psi \quad 3.24$$

Flow rules can be used in two distinct senses. The mobilised angle of friction can be plotted against the current dilation rate to correlate data throughout the course of an entire single test. Or, alternatively, peak state data from a variety of individual tests can be assessed together. Employing this second technique, Bolton (1986) found the plane-strain peak-strength test data obtained for 4 different sands by as many researchers to agree well with his expression, the widest departure in the prediction of  $\phi'_{ps} - \phi'_{crit}$  being 2°.

So, in summary, three flow rules have been described which are derived using very different considerations able to estimate an angle of friction, either direct shear or plane strain, from the dilation rate and the critical state angle of friction. These flow rules should not be confused with the theoretical relationships proposed by Davis (1968) and Rowe (1969) which link subsets of these same parameters. To help clarify, a diagram illustrating the relationships which link  $\phi'_{ps}$ ,  $\phi'_{ds}$ ,  $\phi'_{crit}$  and  $\psi$  is presented in Figure 3.17. In this figure, the pre-described flow rules are enclosed within diamonds in contrast to the



theoretical relationships that are enclosed within rectangles. Circles enclose the parameters and have dashed outline if directly obtainable from test data and dotted if not. The interconnecting lines reveal the parameters involved in each equation and direction of the arrows reveals the direction of flow of measured test data. For example, estimates of  $\phi'_{ps}$  can be obtained directly from measured test data using either Davis' (1968) relationship if  $\phi'_{ds}$  is combined with  $\psi$ , or Rowe's (1969) relationship, if  $\phi'_d$  is combined with  $\phi'_d$ . The resulting estimates can then be compared to measures of  $\phi'_{ps}$  obtained by substituting  $\psi$  and  $\phi'_{id}$  into either Rowe's (1962) or Bolton's (1986) flow rule.

Complicating the picture, either Davis (1968) or Rowe's (1969) relationship can be used in conjunction with the published flow rules to widen their scope. Hence Taylor's (1948) flow rule can be used to relate  $\phi'_{ps}$  as opposed to  $\phi'_{ds}$  to  $\psi$  and  $\phi'_{crit}$ , and likewise Rowe's (1962) and Bolton's (1986) flow rules can be used to relate the same parameters to  $\phi'_{ds}$  as opposed to  $\phi'_{ps}$ . The results of such manipulation using Davis' (1968) relation (as introduced in Section 2.3) are given in Table 3.6.

	$\phi'_{ds} = f(\phi'_{crit}, \psi)$	$\phi'_{ps} = f(\phi'_{crit}, \psi)$
Taylor (1948)	$\tan \phi'_{ds} = \sin \phi'_{crit} + \tan \psi$	$\sin \phi'_{ps} = \frac{\sin \psi + \cos \psi \sin \phi'_{crit}}{1 + \sin \psi \cos \psi \sin \phi'_{crit}}$
Rowe (1962)	$\tan \phi'_{ds} = \frac{\sin \phi'_{crit} + \sin \psi}{\cos \psi}$	$\sin \phi'_{ps} = \frac{\sin \psi + \sin \phi'_{crit}}{1 + \sin \psi \sin \phi'_{crit}}$
Bolton (1986)	$\tan \phi'_{ds} = \frac{\cos \psi \sin(\phi'_{crit} + 0.8\psi)}{1 - \sin \psi \sin(\phi'_{crit} + 0.8\psi)}$	$\phi'_{ps} = \phi'_{crit} + 0.8\psi$

**Table 3.6: Flow rule summary with the conversion between published  $\phi'_{ds}$  and  $\phi'_{ps}$  occurring through Davis' (1968) relation**

By way of comparison, plotting Taylor's (1948), Rowe's (1962) and Bolton's (1986) flow rules as summarised in Table 3.6 on axes of (a)  $\phi'_{ps}$  against  $\psi$  and (b)  $\tau_{yx}/\sigma'_{yy}$  against  $dv_v/dv_v$  produces Figure 3.18. Taylor's (1948) and Bolton's (1986) flow rules are seen to closely bound Rowe's (1962), with their deviancy widening at high rates of dilation. As one would expect, each flow rule intersects the abscissa at  $\phi'_{crit}$  in the first part of the figure and  $\tau_{yx}/\sigma'_{yy} = \sin \phi'_{crit}$  (equivalent to  $\tan \phi'_{id}$ ) in the second.

### Density-dilation and pressure-dilation relations

Both Bolton's and Taylor's flow rules explicitly express the notion that the current angle of friction is equal to the to the sum of a critical state angle of friction and a term which depends on the angle of dilatancy. For a sand with known  $\phi'_{crit}$ , the prediction of its shear strength thus centres on the prediction of its angle of dilatancy. Realising that dilatancy would occur within a granular media only when it is

dense enough and subjected to a low enough confining stress, Bolton (1986) suggested that a successful predictor of  $\psi$  would need to involve a stress parameter multiplied by a density parameter. Consideration of peak state data of 17 sands found within the literature led Bolton (1986) to define a relative dilatancy index,  $I_R$ . The original formulation  $I_R$  was soon-after modified in the original paper's closure to account for the negligible particle crushing in lowly stressed sands (Bolton, 1987) and it is this modified version which is presented here:

$$I_R = I_D [5 - \ln(p'/150)] - 1 \quad 3.25$$

for  $p' > 150\text{kPa}$  and

$$I_R = 5I_D - 1 \quad 3.26$$

for  $p' < 150\text{kPa}$ . Within these relations,  $I_D$  is the relative density index ( $D_r/100$ ), and  $p'$  is the mean effective stress in the sand. The expressions ensures that zero dilatancy is achieved at a critical effective stress and also reduces strongly when the relative density assumes small values, the two conditions critical to meaningful relations. For plane strain conditions, within the range  $0 < I_R < 4$ , Bolton (1986) found the following relation to correlate well with experimental data:

$$\phi'_{peak} - \phi'_{crit} = 0.8\psi = 5I_R \quad 3.27$$

Houlsby (1991) found a close correlation between this relation and a similar expression derived by Wroth (1958) which, instead of empirical correlation, has its basis in critical state soil mechanics and whose parameters therefore relate to well defined and measurable quantities. However, because of the unknown thickness of the rupture within the DSA, the void ratio within is incalculable. Thus Bolton's (1986, 1987) relation is more straightforward to apply.

### 3.8 Summary

Taking on board the criticism found within the literature, a DSA resembling the archetype has been modified. Compared to the device from which it was built, the modified device, called the Winged Direct Shear Apparatus (WDSA), has the following main advantages:

- When using the WDSA, a reliable estimate of  $\sigma'_{yy}$  can be obtained from the consideration of applied

forces and inherent self-weights due to the removal of any undefined source of loading and the application of the shear load through a system of bearings.

- Any rotations or displacements of the WDSA's upper components which may occur during testing will not impart undesirable moments onto a sample due to its novel articulation.
- The apparatus' line of thrust may be aligned with its central plane and thus the normal stress bearing down on this plane can be made more uniform.
- Disturbance to the sample post-deposition is minimised by establishing an opening between the shearbox's frames prior to deposition.

Sample preparation by pluviation has been shown able to provide reproducible and highly homogenous deposits over areas in excess of the plan area of the shearbox. It is recommended that the somewhat archaic techniques suggested by the Standards are ignored in preference for this quick and straightforward reconstitution method requiring the use of standard laboratory equipment.

A review of the data manipulation methods proposed by the Standards reveals high levels of imprecision and approximation. Recommendations for improved data manipulation methods include:

- Taking account of the self-weight of the upper half of the shearbox when calculating  $\sigma'_{v,}$ .
- When the opening between the shearbox's frames is small, the assumption of a realistic angle of interface friction acting on the progressively revealed horizontal face of the lower frame has a levelling effect on large displacement stress data when treated appropriately. Here, an angle of 12° has been found effectual.
- When the opening between the frames assumes large values, the central plane is appreciably above the progressively revealed horizontal face of the lower frame and the appropriate data manipulation method is that proposed by the British Standard (BS 1377) ignoring the reduction of the sample's plan area.

## 4. OPTIMISATION OF THE NEW WDSA

The effects of modifying the WF-25300 to the WDSA and influence of the WDSA's configuration on test data are addressed in this chapter. The aim is to optimise the apparatus' performance. The optimisation process involved the adoption of numerous devices intended to improve the apparatus' performance. Sometimes the adaptations were found beneficial and kept, but sometimes not and discarded. Certain modifications proved appropriate to particular test configurations and yet unsuitable to others. Also, in order to provide appropriate data for comparison, conditions known to be detrimental were often imposed. The result of this is a large body of data sets, numbering in excess of two hundred, ordered somewhat non-sequentially.

To limit the complexity of the modification and optimisation process, experimentation primarily involved the use of VLB pluviated to achieve a relative density close to its maximum ( $D_r$ , circa 90%) and confined and tested under a confining stress circa 25kPa. This stress level was chosen to promote non-uniformity and thereby focus investigation on the worst-case scenario (as indicated in Section 3.1), and provide appropriate comparison with Stroud's (1971) SSA data. The shearbox's drive unit was configured to apply a carriage displacement rate of 1.2mm/min, thereby minimising test duration. These test parameters can be assumed unless otherwise indicated. In addition, and because of the incremental nature of WDSA improvements, the test data first presented are obtained with constituents the nature and implications of which are described in detail only later. Thus, it is first necessary to define some terms.

As previously discussed, the shearbox's upper and lower frames are separated by an opening of magnitude  $g$ , installed prior to sample deposition. Unless otherwise indicated,  $g$  can be assumed to have an initial magnitude of  $5D_{50}$ , the effects of which are discussed in Section 4.3.3. To prevent excessive sample extrusion via this opening, sheets of flexible material called "shielding" can be attached to the shearbox's internal walls, spanning the divide. Unless stated otherwise, the optimum configuration of this shielding (as determined in Section 4.3.2) should be assumed. In addition, in all but Section 4.4, the WDSA's line of trust is coincident with the central plane.

A length  $L$ , height  $H$  and width  $W$  defines the sample dimensions. The sample width during all tests is of magnitude 100mm less the thickness of the shielding material used on the apparatus' side walls. The height of the sample comprises the depth of sand in the upper and lower frames and the magnitude of  $g$ . If  $H$  is large, the sample is said to be thick, if small then thin. Like the sample width, the sample length is marginally reduced by the use of shielding. A sample is said to be long when  $L$  assumes high values and short when low.

## 4.1 Transmission of the shear load to the sample

Golder (1942) presented a design of the DSA that bears close resemblance to the archetype. His test procedure makes reference to the inclusion of dentated plates positioned immediately above and below the sample employed in an attempt to unify sample behaviour. If the shear load  $S$  is transmitted to the sample through the end wall of the shear box, Golder reasoned, then the shear strain occurring at the edges of the box would be greater than that in its middle. Thus, the full strength would not be mobilised at all points on the central plane simultaneously resulting in the underestimation of the sample's strength and dilatancy characteristics. However, if the shear load could be transmitted to the sample by shear stresses at the upper and lower boundaries, the degree to which progressive failure occurs would be limited. It was argued that by confining the sample between dentated plates, the shear load could be spread across the entire sample length and a more realistic estimate of the sample strength result. The use of dentated plates when direct shear testing has since become commonplace and is recommended by both BS-1377 and Head (1982).

Hryciw & Irsyam (1993) observed the displacements of sand particles around ridged ribbed inclusions of various geometry by using a direct shear device constructed of transparent plexiglass. Instead of a lower frame, however, the apparatus featured a dentated plate whose inclusions penetrated upwards into the sample. Thus the application of shear displacement between the upper frame and the dentated plate allowed the visual observation of the mechanisms of load transfer to be identified.

It was discovered that although relatively high shear stiffness was mobilised over the first 0.25mm of shear displacement, frictional resistance was built up gradually as normal stresses were established between individual grains, their neighbours and the ribbed inclusions. Consequently, an appreciable magnitude of relative displacement between the upper frame and the dentated plate was required to mobilise significant shear resistance. Peak shear resistances were mobilised only after about 2mm of relative displacement. If a direct shear sample is confined between two dentated plates, the fixed and rigid walls of the shearbox's frames do not allow any such relative displacement and therefore load transfer by shear stresses at the top and bottom boundaries cannot occur.

Further evidence of the dentated plates inefficacy is provided by the literature. Pressure cells mounted within Palmeira & Milligan's (1989a), Paikowsky et al's (1996) and Shibuya et al's (1997) shearboxes indicated that the shear load was transmitted to a sample primarily by normal stresses across the internal end walls. Allersma (1999) and Dyer (1985) examined the pattern of stress within the DSA using photoelasticity and a crushed glass granular medium. Again, the shear load was seen to be transmitted

through the apparatus' end walls. Thus, it seems likely that the dentated plates commonly used within the DSA are ineffectual at applying the shear load to the sample.

WDSA data obtained both with and without dentated plates are compared in Figure 4.1. Figure 4.1(a) reveals the dentated plate's insignificant effect on stress data. Displacement data, however, reveal that the dentated plates' exclusion gives rise to increases in both the magnitude (Figure 4.1b) and rate (Figure 4.1c) of dilation. The differences in test data are small, equalling  $1.5^\circ$  in  $\psi_{peak}$  and 0.15mm in the ultimate magnitude of dilatancy, and could thus be put down to the natural variability of test samples. However, the differences were found to be consistent for tests performed using various configurations. Figure 4.2, for example, displays the  $\psi_{peak}$  values recorded during tests with various initial openings between the frames, both with and without dentated plates. Those tests employing dentated plates are associated with  $\psi_{peak}$  values on average  $1.3^\circ$  lower than those without.

The lowering of the rate of and magnitude of dilation without alteration of the shear resistance appears contradictory but can be explained with reference to the imperfect bedding between the sand mass and the dentated plates. As the first pluviated sand particles land within the lower frame, it is feasible that spurious voids are created adjacent to the dentated plates that are uncharacteristic of those created later, higher in the sample. In addition, the penetration of the upper dentated plate into the carefully levelled sand surface will bring about the loosening of the uppermost sand layer and may not be complete, the areas between ribs being impregnable to the sand particles. Although the shear stresses and strains are thought to be small within the sample's extreme layers, the vibrations caused by the apparatus' operation and the rearrangement of grains further within the sample could bring about the collapse of any spurious voids and increases in the upper ensemble's subsidence. Thus, the sample's dilatancy characteristics would be underestimated and any test interpretation based on the correct derivation of  $\psi_{peak}$  would be inappropriate.

Thus it appears that dentated plates are not only ineffectual in transmitting the shear load to the sample but also detrimental to the correct estimation of a sample's shear strength parameters. Their use is not recommended. Thus, presented test data were obtained without the use of dentated plates, the sample instead being confined between smooth aluminium plates.

## 4.2 The WF-25300 and the WDSA compared

Within the literature, and as highlighted in Chapter 2, reports of modifications to the DSA which are purported to improve data quality are common (for example: Jewell, 1989, Wernick, 1977, Shibuya 1997, Arthur et al, 1977). However, suggested modifications often comprise a medley of alterations whose individual effects are left undocumented. Jewell (1989), for example, dramatically increased the sample size from convention, secured the load pad to the upper frame prior to testing, and allowed the upper frame to displace unimpeded, and went on to report a good agreement between experimental test data and strength parameters reported elsewhere. Thus, uncertainty as to which of these modifications are necessary to achieve such correlation remains.

To avoid uncertainty as to the effects of the conversion to the WDSA, three series of tests were undertaken using the WF-25300 modified to differing degrees. The test series were performed in order of increasing complexity of the necessary modifications: the first test series featured the WF-25300 as provided by the manufacturer, the second featured the WDSA in its unsymmetrical arrangement and the third, the WDSA in its symmetrical arrangement. To enable the consistency of test data to be assessed, each series featured three identical tests. The term “identical” is here used to convey that the test material, procedure, experimental variables, and apparatus configuration (outside of the modifications being investigated) were consistent between each of the tests.

To provide the appropriate comparison between WDSA and WF-25300 data, the test configuration adopted in this section is dissimilar to that highlighted in this chapter's introduction. Namely, the central plane of the WDSA was positioned 10mm below the apparatus' line of thrust, the implications of which are discussed in Section 4.4. Also the initial opening between the frames  $g$  is set at a conventionally recognisable 0.5mm. Thus, shielding was not required to limit sample extrusion and was therefore not employed (although exploratory tests showed shielding to have negligible effect on test data when  $g$  assumed small values), and data interpretation took account of a  $12^\circ$  angle of friction on the revealed horizontal face of the lower frame (as discussed in Section 3.6.1). This configuration is adopted throughout Section 4.2.

To avoid over-complication when performing inter-series comparisons it is prudent to focus on the data recorded during a single test chosen as being typical and thus representative of data obtained under those conditions. This representative test was selected to avoid extraordinary events and identified when close agreement between data of two identical tests was recorded.

It will be seen that as the complexity of the modification increases, so does the confidence in

test interpretation and performance. For this reason discussion will begin by examining the WDSA's symmetrical arrangement test results, and to these the results of the other test series will be compared. First however, force and moment equilibrium considerations are applied to each configuration in the hope of providing an indication of how test configuration may affect data.

### 4.2.1 Force and moment equilibrium

Considering the upper half of the WDSA in isolation, the normal stress distribution on the central plane is established to resist any moment applied about the sample centre due to the separation of the line of thrust and the central plane, as briefly discussed at the outset of Chapter 3. Thus, the distribution of  $\sigma'_{yy}$  across the central plane is independent of the configuration of the upper half of the apparatus yet varies with  $f$ , the moment arm between the line of thrust and central plane. With this as the starting point, the force and moment equilibrium of the portion of the sample contained within the upper frame is here discussed.

A number of assumptions are needed. Firstly, shear stresses will only be mobilised on the internal walls of the apparatus if sufficient displacement between the sample and the internal walls is permitted. Thus, by disallowing the relative displacement of the load pad within the upper frame the symmetrical arrangement is not associated with any such wall friction. Secondly, as discussed in Section 4.1, it is assumed that  $S$  is transmitted to the sample entirely through the upper frame's rear wall and has a line of action separated from the central plane by vertical distance  $h_s$ . Thirdly, the upper portion of the sample is here for simplicity considered weightless. Lastly, trapezoidal distributions of normal stress are induced on the sample's faces.

Figure 4.3(a) and (b) features free body diagrams of the portion of the sample contained within the WDSA's upper frame in its symmetrical and unsymmetrical arrangements respectively. As one progresses down through the figure the line of thrust falls relative to the central plane, as indicated on the figure's right hand side, inducing different normal stress distributions across the central plane. It is reiterated that this distribution is independent of the apparatus configuration (the distributions across the central plane in parts (a) and (b) of Figure 4.3 are identical) and results in a moment about the sample centre numerically equal to the product of  $f$  and  $S$ .

Considering first the symmetrical arrangement, as the line of thrust falls and to provide force and moment equilibrium, the distribution of normal stress across the sample top accommodates the changes in the normal stress distribution across the central plane. If  $f$  is greater than  $h_s$ , for example, as in row one of the



figure, the anticlockwise moment resulting from the centroid of the normal stress distribution on the central plane lying to the right of the sample centre will exceed the clockwise moment caused by the shear force  $S$  acting across the sample's rear wall. Hence an additional clockwise moment about the sample centre is required for equilibrium which is provided by the normal stress distribution across the sample's top. If the line of thrust coincides with the central plane, however, and as in row three of the figure, an anticlockwise moment is required and the centroid of the normal stress distribution across the sample's top lies left of centre.

When testing the unsymmetrical arrangement, because the normal stress distribution across the sample top must be uniform the equilibrating moment must instead be provided by shear stresses on the sample's sides. Within the figure the shear stress on the side walls are shown as solid arrows. No stress is mobilised on the sample's front wall because the experimental evidence suggests the normal force acting on this wall soon drops to nearly zero at the outset of a direct shear test (e.g. Shibuya et al , 1995 Paikowsky et al, 1996). The directions of the shear stresses indicate that necessary to provide moment equilibrium. Force equilibrium can only be provided if the net effect of the wall friction is zero.

It is arguments similar to these that Jewell (1989) relied on when explaining the kinematics of the direct shear apparatus. He presented diagrams similar to row three of Figure 4.3 and noted that the directions of the necessary shear stresses were consistent with the rotation of the load pad within the upper frame, concluding that the rotations were a product of the force and moment equilibrium requirement.

## 4.2.2 The symmetrical WDSA

Three data sets obtained using the WDSA in its symmetrical arrangement are presented in Figure 4.4. A cursory examination reveals expected trends typical of those usually found when a dense sand is subjected to direct shear under constant normal stress conditions. The resistive shear force increases at a decreasing rate until a peak value is mobilised coinciding with the sample's peak rate of volume change. The sand then strain softens whilst undergoing large increases in volume. As dilatancy ceases and the sand begins shearing with a near constant volume, a relatively constant shear resistance is mobilised. The vertical displacements recorded above the rear of the apparatus dwarf those at the front and clockwise rotation of the upper ensemble proceeds at a near constant rate throughout each test.

The cause of the rotation is difficult to ascertain. Pressure cell measurements on the rear wall of their large shearbox (1m<sup>3</sup>) revealed to Palmeira & Milligan (1989) a non-linear stress distribution on the apparatus' rear wall with a considerable increase in the total stress as one approaches the central plane.

Using pressure sensors Paikowsky et al (1996) found a near triangular distribution of horizontal stresses on the 70mm tall rear wall of a direct shear apparatus' upper frame at both peak state and larger displacements. If similar horizontal stress distributions are generated on the rear face of the 17mm of sand contained within the WDSA's upper frame, then it is likely that an  $f$  of magnitude 10mm will exceed the magnitude of  $h_s$ . Thus, as in row one of Figure 4.3, the front of the sample's upper half will be compressed between higher stresses than the rear and it is reasonable to expect the portion of sample at the shearbox's rear to be more dilatant than that at the front. If this were the sole cause one would expect rotations during the sample's dilatant period that cease at higher shear displacements as a sample commences shearing with constant volume when in fact, as revealed in Figure 4.4(d), the rotation rate is nearly constant throughout testing.

Returning to Figure 4.4, the consistency of both stress and displacement data is generally excellent. However, opposed to the trends exhibited by the other two tests, Figure 4.4(a) reveals the large displacement data of one test is seen to reduce with increasing  $v_x$ . In addition, Figure 4.4(f) reveals this same test to suffer from large displacement levelling of its  $(v_y)_{front}$  plot. Thus, it is plausible that interaction between the near horizontal faces of the upper ensemble and lower frame, either directly or by way of stray sand grains, has occurred at the sample front. The consequence of this during a symmetrical test is to provide a reaction to  $N$  and thus reduce the normal stress on the central plane below its assumed value. The stress ratio derived assuming a too high normal stress would hence be an underestimation of that actually mobilised on the central plane.

### 4.2.3 The unsymmetrical WDSA

The test data of three unsymmetrical WDSA tests with configurations directly comparable to those symmetrical tests discussed in Section 4.2.2 are presented in Figure 4.5 wherein trends similar to those symmetrical tests are recorded. To illustrate this, the figure depicts the symmetrical WDSA test data chosen as representative. Also shown are the upper frame's displacements.  $(v_y)_{uf}$  is seen to closely follow  $(v_y)_{ip}$  and  $\omega_{uf}$  remains relatively small throughout testing.

The kinematics of the apparatus suggest shear stresses will be mobilised on the internal walls of the upper frame. With the load pad rotating clockwise within the upper frame, and assuming a weightless sample, the necessary displacements of sand grains over the internal walls will generate a system of shear stresses as illustrated in Figure 4.6. That no shear stress is pictured on the sample's front wall relates to the experimental observations that the horizontal stress acting normally on this face drops to negligible values at the initiation of a direct shear test (Shibuya et al, 1997, Paikowsky et al, 1996). Such a system

of shear stresses produces an anticlockwise moment about the sample centre.

If as when considering the symmetrical WDSA, the magnitude of  $h$ , is reasoned to be less than  $f$ , then these boundary stresses are inconsistent with the force and moment equilibrium considerations of Section 4.2.1. Thus, either the distribution of horizontal stress on the sample's rear face is unlike that occurring in larger shearboxes and  $h$  is greater than  $f$ , or it can be concluded that such simple equilibrium considerations are of limited use when considering the complex behaviour within the DSA.

Returning to Figure 4.5, the foremost differences between data of the symmetrical and unsymmetrical arrangements are the lower rate of strain softening and greater magnitude of dilatancy of the latter. The relative displacement and rotation between the load pad and upper frame are presented in Figure 4.7, herein the relative angle between the components is seen to change by  $2^\circ$ . Such deformation can be understood to apply a simple shear deformation to the portion of the sample contained within the upper frame. Cole (1967) defined the progress of his simple shear tests in terms of the cumulative horizontal shear distortion,  $\alpha$

$$\alpha = \sum \dot{\gamma}_x = \sum \frac{\dot{v}_x}{h} \quad 4.1$$

where  $\dot{v}_x$  is the incremental horizontal displacement  
 $h$  is the sample height

Drawing an analogy between the portion of the sample contained within the upper frame and a 17mm tall sample subjected to simple shear, a  $2^\circ$  rotation of the upper frame relative to the load pad can be interpreted as a shear distortion of  $\tan 2$  or 0.035. When investigating the behaviour of dense LB under equivalent confining stresses, Stroud (1971) found equivalent values of  $\alpha$  to produce increases in void ratio of approximately 0.015. An equivalent increase in void ratio within the portion of the sample contained within the upper frame of the WDSA would produce an increase in the recorded magnitude of dilation over and above that recorded during a test where no such shear deformation is applied,  $\Delta v$ , of:

$$\begin{aligned} \Delta v_v &= \frac{\Delta V_u}{L^2} \\ &= \frac{h \Delta e}{1 + e_{\text{initial}}} \end{aligned} \quad 4.2$$

where  $\Delta V_u$  is the change in volume of the portion of the sample within the upper frame  
 $h$  is the height of the portion of the sample within the upper frame

$e_{initial}$  is the void ratio to which the sample is prepared

$\Delta e$  is the estimated increase in void ratio of the sample brought about by the relative rotation of the upper frame and load pad

With a VLB sample 17mm deep in the upper frame and deposited at 95%  $D_r$  ( $e_{initial} = 0.5211$ ), the estimate of  $\Delta v_y$  equals 0.20mm. Figure 4.5(b) illustrates that in relation to the unsymmetrical WDSA tests, the shortfall of the magnitude of dilation recorded during the representative symmetrical test wherein no such simple shear deformation of the sand contained within the upper frame can occur is 0.26mm. Thus the additional dilation recorded during unsymmetrical tests is of the correct magnitude to be explained by the shear distortion of the sample portion contained within the upper frame.

Aside from the increased magnitude of dilation and reduced rate of strain softening brought about by the increased degree of kinematic freedom of unsymmetrical tests, when compared to the more constrained symmetrical tests, effects on test data are small, and certainly less than that reported by Jewell (1989). Reasons for this probably relate to the different scales of the apparatus, as discussed in Section 4.5.4.

#### 4.2.4 The WF-25300

Test data for three identical WF-25300 tests are illustrated in Figure 4.8 wherein a comparison is again made with representative symmetrical WDSA test. Test data is generally less consistent than that of the WDSA discussed previously. Two of the three individual tests are seen to agree whereas the other experiences appreciably smaller  $(v_y)_{lp}$ , higher  $(v_y)_{uf}$ , a smaller and less certain  $\psi$ , and a larger kink in its rotation curve. These observations are consistent with the load pad having its displacement impeded by becoming temporarily stuck within the upper frame. This can be envisaged by considering the relative displacement of the load pad within the upper frame as illustrated in Figure 4.9. Between shear displacements of 2 and 7mm, the relative displacement and rotation of the load pad within the upper frame for the suspect test all but cease. This is quite unlike the relative movements occurring during the other tests where both the relative rotation and relative vertical displacement between the two components attain higher magnitudes at somewhat more constant rates. Why one test should be subjected to interactions between the upper frame and load pad while another supposedly identical test is not may relate to stray sand grains becoming trapped between load pad and upper frame.

The kinematics of WF-25300 testing are significantly different from those of the WDSA. The upper frame rotates clockwise at a reducing rate throughout testing and achieves a substantial magnitude by the end of the test. The  $x$  co-ordinate relative to the sample centre of the point about which the upper frame rotates over an increment of  $v_x$ ,  $(x_\omega)_{uf}$ , is plotted against  $v_x$  in Figure 4.10(a) where, in all but the early

stages of the testing, rotation is seen to occur about a point approximately 75mm in front of the sample centre. Considering the sample is 100mm long, the front wall of the shearbox 18mm thick, and from this the button and housing arrangement protrudes 10mm, it is about this component that rotation occurs. This accounts for the linear relationship between the rotation and vertical displacement of the upper frame as illustrated in Figure 4 10(b)

Although the gross rotations of the WF-25300's load pad are the largest yet experienced, Figure 4.9 shows that relative to the rotation of the upper frame, they achieve magnitudes similar to those recorded when using the WDSA. Thus, by the end of testing, a global rotation has been applied to the upper half of the apparatus due to the button and housing being a point of fixity. The net rotation between the upper frame and load pad, however, obtains similar magnitudes as that of the load pad or upper ensemble during unsymmetrical or symmetrical WDSA testing.

#### 4.2.5 Comparison of WDSA and WF-25300 data

A comparison of the averaged cardinal parameters obtained using the WF-25300 with those of the symmetrical and unsymmetrical WDSA is presented in Table 4.1. A number of features are of note. Firstly, the shear resistances of all the samples are extremely high with those offered by the WF-25300's samples exceeding those of the WDSA. This is a result of the extraneous vertical load imparted by the button and housing arrangement increasing the magnitude of  $\sigma'_{yy}$  above its estimated value.

	Symmetrical WDSA	Unsymmetrical WDSA	WF-25300
$(\tau_{yx}/\sigma'_{yy})_{peak}$	1.222	1.221	1.238
$(\tau_{yx}/\sigma'_{yy})_{ld}$	0.634	0.664	0.672
$(dv_y/dv_x)_{peak}$	0.486	0.437	0.386
$(\phi'_{ps})_{peak}$	58.5°	60.3°	63.9

**Table 4.1: Cardinal parameters from direct shear tests employing the WF-25300 modified by differing degrees**

Secondly, the peak rate of dilation is more susceptible than the shear resistance to changes in apparatus configuration. The peak rate of dilation is maximised when using the symmetrical WDSA and minimised when using the WF-25300. It will be seen later that if an equivalent reduction in  $(dv_y/dv_x)_{peak}$  were brought about solely by an increase in confining stress,  $\sigma'_{yy}$  would need to be increased to around 170kPa. The small magnitudes of  $\delta'$  (on the shearbox's internal walls) and  $S$  makes it impossible for this increase in  $\sigma'_{yy}$  to be provided by the extraneous loading of the button and housing arrangement. Thus, the decreased measures of dilation rate may indicate poorer strain uniformity within the unsymmetrical

apparatus.

As seen in Table 4.1, a reduced dilation rate produces substantial increases in the already high  $(\phi'_{ps})_{ak}$  when derived using Davis' (1968) relation. Thus, to obtain "safe" shear strength parameters when data is interpreted in this manner, the optimum configuration of the direct shear apparatus may well be one that maximises the peak rate of dilation.

Figure 4.11 presents the incremental rotation of the upper components during testing. The symmetrical WDSA, considered in Figure 4.11(a), requires the monitoring of only a single component and rotation increments assume low values that are nearly constant in all but the early stages of testing. The relationship between the rotation increment and the stress ratio is also presented. As peak state is approached, before the dilatancy is embarked upon, the relationship is approximately linear. Once dilatancy ceases and the stress ratio falls to a constant value, the dilation increment corresponds well with the initial linear relationship. The higher incremental rotations of the unsymmetrical WDSA test configuration pictured in Figure 4.11(b) have a more unique relationship with the stress ratio. The rotation increments of the WF-25300 are considerably more erratic and any rotation increment-stress ratio relationship is less clear.

The stress dilatancy relationship recorded for each configuration is presented in Figure 4.12 on which is also pictured a line of gradient unity intercepting the abscissa at a value 0.575 which corresponds to Taylor's (1948) flow rule with a critical state angle of friction of 35°. Disregarding data from the early stages of shearing, the WF-25300 gives a bi-linear relationship with the gradient on the ascent to peak exceeding that on the descent. Data of the WDSA approximates more closely a unique relationship but nevertheless has gradient in excess of unity.

#### 4.2.6 The adopted test configuration

The WF-25300 is judged inferior to the WDSA for the following reasons:

- WF-25300 test data is infused with uncertainty over the correct assumptions to make during data manipulation.
- $\sigma'_{yy}$  is likely to vary by significant but unknown amounts as a test progresses.

- Consistency of test data is lacking.
- Displacements of the upper frame and load pad do not coincide and may influence the behaviour of each other
- Non-uniformity of strains, indicated by excessive rotations, hamper test data.

Symmetrical WDSA tests are seen as advantageous because:

- The running of the test is most straight forward with the displacements of only a single component needing to be monitored.
- $\psi_{peak}$  is maximised when using this configuration, underestimation of which may result from increased non-uniformity of strain.
- strains are concentrated at the central plane.
- the lowest degree of rotation is recorded.
- a high degree of consistency of test results is recorded.

It is for these reasons that investigation of the symmetrical WDSA only will continue.

### 4.3 The opening between the shearbox frames

The British, American and Japanese Standards recommend an opening to be introduced between the shearbox's frames prior to the start of testing to prevent the development of metal-metal frictional forces and a reaction to  $N$ . They stipulate the opening magnitude, here called  $g$  (mm), be limited to prevent excessive sample extrusion.

Recent commentaries on the DSA have reported  $g$  to have a significant influence on test data. That the origin of these investigations is Japanese can be explained because in Mikasa's (1960) DSA, the Japanese Geotechnical Society's standard,  $g$  is an experimental constant. Nakamaru et al (1995) were reported to find small openings to be associated with  $(\tau_{yx}/\sigma'_{yy})_{peak}$  values 10% higher than those mobilised with larger openings (Kuwano, 1999). The reason for this was said to be that the shear band could not develop

freely during tests with small openings due to the restraint offered by the shearbox itself. Their own investigation led Shibuya et al (1997) to the same conclusion. Their data is presented alongside examples of Nakamaru et al's (1995) in Figure 4.13 where the increases in stress ratio as the opening decreases are apparent for a number of sands with wide ranging  $D_{50}$ , prepared to various  $D$ , and subjected to different  $\sigma'_{yy}$ . In this figure, the abscissa has been normalised with respect to the mean particle diameter revealing that increases in  $(\tau_{yx}/\sigma'_{yy})_{peak}$  occur only if  $g$  is below approximately  $5D_{50}$ .

That the limitation of the range of influence of  $g$  to  $5D_{50}$  is encouraging, suggesting a "true" parameter is revealed when shear band development is unrestrained. However, this value is obtained after investigations using a device dissimilar to the WDSA. The opening's influence within apparatus where the magnitude of  $g$  changes with a sample's volumetric changes and with rotation of the upper frame is unknown. Thus an investigation into the influence of  $g$  on WDSA data is warranted.

The likelihood and degree of sample extrusion from the shearbox is dependent on  $g$ . Thus, for a thorough investigation of the influence of  $g$  exclusive of the detrimental effect of soil extrusion, it is necessary to determine an experimental technique capable of adequately confining the sample.

### 4.3.1 Sample extrusion

Two forms of sample extrusion have been identified when operating direct shear tests employing large magnitudes of  $g$ . The first of these is perhaps what comes to mind when considering the term and relates to individual particles initially adjacent to the sample boundary becoming released from stress and tumbling out between the frames. The more significant second type of extrusion relates to a more systematic process by which every increment of shear displacement is associated with a uniform extrusion volume.

When a substantial opening is implemented between the shearbox's frames prior to testing, an increment of shear displacement brings with it the extrusion of the portion of the sample immediately beneath the upper frame and adjacent to its end wall by the rear wall's cutting action. By way of explanation, a schematic representation of the long section of a shearbox before and after considerable shear displacement is displayed in Figure 4.14. The sample contained therein is non-dilative and hence has constant area in long section. Figure 4.14(b) clearly shows the extruded volume created due to the application of the shear displacement that brings with it the creation of an additional volume at the sample's front, the consequences of which are depicted Figure 4.14(c). To appreciate the effect this has on test data an initial opening of 5mm may be assumed. 1mm of shear displacement creates  $g \times L$  or



500mm<sup>3</sup> of additional volume at the front of the box causing a shortfall in average vertical displacement of 0.05mm. Thus by the end of the test, the shortfall in average vertical displacement would be a substantial 0.60mm. A dilatant sample tested in the symmetrical arrangement would be associated with the creation of further magnitudes of additional volume as the average opening between the frames progressively increases throughout the test's duration, thus producing a higher rate of subsidence.

Test data obtained during an unshielded, symmetrical WDSA test with  $g$  of 5mm is displayed in Figure 4.15. In contrast to  $(v_y)_{rear}$ , which increases to a near constant value,  $(v_y)_{front}$  indicates a dramatic large-displacement subsidence. The large-displacement subsidence at the sample front induces a rate of subsidence at the sample's midpoint of about 0.055, slightly in excess of that predicted by considering the theoretical subsidence of a non-dilatant sample brought about by the creation of additional volume. Thus, it seems likely that the unprecedented traits of the average vertical displacement plots are a consequence of additional created volume. This finding sits well with Qiu et al's (2000) data which indicated large displacement sample contraction when  $g$  assumed large values (6-12mm) and no attempt was made to limit the creation of additional volume. Constant volume conditions were only attained after the opening had been shielded with a layer of sponge.

The well-defined geometry of the symmetrical WDSA allows  $v_y$  to be corrected to account for the additional volume created during shear.

$$(v_y)_{corrected} = (v_y)_{measured} + \sum \frac{g_{front} \dot{v}_x}{L} \quad 4.3$$

where  $(v_y)_{corrected}$  is the average vertical displacement exclusive of the additional volume  
 $(v_y)_{measured}$  is the average vertical displacement measured experimentally  
 $g_{front}$  is the average opening between the upper and lower frames at the sample front over an increment of shear displacement  $\dot{v}_x$   
 $L$  is the sample length

Corrected average vertical displacement data is presented alongside the uncorrected data in Figure 4.16(a) and converted to rates of dilation in Figure 4.16(b). Corrected data exhibits the traits expected when shearing a dense sand, whereas the uncorrected data is associated with peculiarities such as large displacement contraction. In addition, the angles and magnitudes of dilatancy derived from the corrected data correspond closely to those recorded when the creation of additional volume is limited (e.g. when  $g$

is small or shielding used, as discussed below).

### 4.3.2 Shielding

Prior to  $g$  becoming the focus of experimental interest, its magnitude remained small and no thought was given to the restriction of sample extrusion. To disallow the mobilisation of shear stresses and thereby make the side-walls of his DSA plane strain Arthur et al (1977) smeared them with silicone grease onto which was stuck sheets of rubber spanning the entire height of the specimen. The end walls of his apparatus were masked using similar rubber sheets but without the lubricating layer in order to aid the mobilisation of complementary shear stresses. Radiography measurements revealed the horizontal to be a direction of zero linear incremental strain. Such a barrier system could be employed to limit extrusion rather than to affect wall friction as demonstrated by Al-Douri & Poulos (1991) who used a strip of 0.5mm thick rubber membrane to encase the sample, clamped the upper frame's front and rear walls and extending down underneath the sample. It is likely that such a system will be associated with considerable shear stresses on the box's internal walls and consequent uncertainty relating to the magnitude of  $\sigma'_{xy}$  and appreciable membrane forces.

A similar system was employed by Shibuya et al (1997) within a DSA configured to maintain a constant opening between frames. Two types of barrier material were there investigated: paper and latex, but instead of spanning the entire height of the internal walls, that attached to the upper frame was detached from that in the lower. Boundary strain measurements through a transparent side wall again revealed the inclusion of the material to have no effect on the horizontal direction being one of zero linear incremental strain extension. The test data obtained using the different barrier material is contrasted with data obtained without in Figure 4.17. Noting that it was the post peak behaviour that was affected by the different boundary conditions, Shibuya et al went on to conclude that it was advantageous to cover the central gap. Such tests were not associated with the sudden drops in shear resistance attributed to the "partial edge collapse" of the uncovered specimen.

Here, the inclusion of such membrane into the shearbox is said to "shield" the sample. Both Arthur et al's (1977) "continuous" and Shibuya et al's (1997) "split" shielding arrangements were investigated in conjunction with two types of shielding material: 0.3mm thick latex membrane more usually found within a triaxial cell, and 1mm thick rubber sheet. Silicone grease was used to attach the shielding to the internal walls of the shearbox. The shielding's deformed shape was examined both during testing, achieved using a dental mirror, and after the careful excavation of the sample post-test. The former provides a cheap and, providing a well-positioned light source, effective way of visualising shielding

deformations

The shielding configuration employed within the shearbox needs to perform in a manner suitable to its location. Continuous shielding is not appropriate on the shearbox's side walls if tests are to proceed to large shear displacements since  $S$  will then include a component relating to the force induced within the shielding material itself. In addition, when employing latex-membrane side wall shielding in the split configuration, splaying had occurred by the end of even low stress level tests, allowing sand grains to spill out between the frames. Such splaying was not observed when employing split rubber sheet shielding and so this configuration was adopted.

To determine the most appropriate form of shielding for implementation on the shearbox's end walls, where the phenomenon of additional volume creation may be affected, a more rigorous study was undertaken using each shielding material in both configurations. The resulting test data is presented in Figure 4.18. Discussion starts with the vertical displacements recorded at the sample's front and rear, illustrated in Figure 4.18(e) and (f) respectively, with reference to the shielding's deformed shape, as illustrated in Figure 4.19.

$(v_y)_{rear}$  is found independent of whether shielding adopts the continuous or split configuration but is affected by the material from which the shielding is constructed. The reduced stiffness of latex end wall shielding allows it to become moulded to the upper frame's rear wall (Figure 4.19a & b, i) as the test progresses. Thus, when compared to the unshielded test, its presence has little effect on the vertical displacements recorded above (Figure 4.18e). The stiffer rubber shielding, however, prevents the cutting of the sample by the lower corner of the upper frame and instead applies a type of deformation that more closely corresponds to simple shear (Figure 4.19a & b, ii). Sample extrusion is prevented and the vertical displacements recorded above dwarf those recorded above the rear of other samples (Figure 4.18e).

In contrast, at the sample front data is affected by shielding configuration and not material. Regardless of the material from which it is constructed, continuous shielding limits the additional volume created by the application of shear displacement by preventing the collapse of the sample into the newly created volume (Figure 4.19a, i & ii). This is reflected in Figure 4.18(f) where  $(v_y)_{front}$  of the continuously shielded samples dwarf those of the split shielded and unshielded. The presence of split shielding at the shearbox's front has a much reduced effect and perhaps only increases  $(v_y)_{front}$  by preventing the spilling of the grains in front of the advancing front wall of the upper frame (Figure 4.19b, i & ii).

Turning now to the remaining test data, Figure 4.18(a) shows continuous shielding is associated with

increased shear resistance, larger increases becoming apparent earlier on when using the rubber opposed to the less-stiff latex. Higher magnitudes of  $(\tau_{yx}/\sigma'_{yy})_{peak}$  may in part arise from the increase in horizontal stress brought about by the use of continuous shielding. That high resistances are maintained until large displacement, however, suggests that the measured shear force  $S$  includes a factor relating to the indeterminate force induced within the shielding material. Thus, the less stiff latex shielding will be associated with lower shear resistances in comparison to the rubber shielded sample until the shear displacement becomes sufficient to establish as equivalent force within the material, at a displacement of about 7mm. Assuming this to be the case, it is concluded that continuous shielding should be eliminated from further consideration. With no such forces able to become established within the split shielding, the resistances offered tally closely with those of the unshielded sample.

The latex shielded sample is associated with magnitudes and rates of dilation that correspond closely to those of the unshielded sample due to the shielding's lesser ability to constrain the sample. Data obtained employing split latex shielding is therefore not seen as being advantageous to unshielded test data. The benefits of employing split rubber shielding, however, are plentiful. Higher  $\psi_{peak}$  values may indicate improved uniformity, which is what one would expect by considering the shielding's deformation. At large displacement a near constant volume condition is mobilised with recorded angles of dilation being zero. Data associated with split rubber shielding bears a strong resemblance to unshielded data corrected to account for the creation of additional volume. It is thus the split rubber shielding configuration which was employed.

### 4.3.3 The size of the opening between frames

As reported in Chapter 3, data obtained employing different magnitudes of  $g$  is best manipulated in different ways. When small openings are installed prior to testing, appropriate data manipulation techniques account for the reducing area of the central plane and an angle of friction on the progressively revealed horizontal face of the lower frame. With large openings, however, it is appropriate to assume a constant planar area. Difficulties thus arise when comparing test data obtained with wide ranging  $g$  values. To avoid the disparate test data obtained if a limiting value of  $g$  were defined below which an area correction was applied and above which it was not, no correction is applied to the test data presented below, regardless of  $g$ 's magnitude. In general, however, if an area correction was employed peak state stress ratio values would be approximately 2% higher and large displacement (taken as the average of the final 10 measurements) 8% higher than those derived from presented data.

Data obtained implementing openings between 0.5 and 8mm are presented in Figure 4.20. Other than the

magnitude of  $g$ , care was taken to provide consistent experimental configuration. Measures were taken to ensure that the initial sample height was an experimental constant and that the line of thrust was coincident with the central plane.

In general, increases in  $g$  bring reductions in  $(\tau_{yx}/\sigma'_{yy})_{peak}$ , as Shibuya et al (1997) noted, in addition to reductions in a sample's dilation response and larger rotations of the upper ensemble. Since similar  $(v_y)_{rear}$  are recorded regardless of  $g$ , these latter trends are rooted in differences in behaviour exhibited at the sample front.

Similar differences in test data were recorded when shielding was first employed to limit additional volume creation during unshielded tests. Recalling that the magnitude of additional volume created during an unshielded test over an increment of  $v_r$  increases with  $g$ , and noting that shielding deformation ensures limitation of additional volume is not absolute, it may be reasoned that  $g$ 's influence on shielded test data is an additional volume effect. The rear wall shielding extending down from the upper ensemble can be likened to a cantilever whose deflection will increase with its length. Substantial  $g$  values increase shielding deflections and consequential sample extrusion. Thus larger volumes are created at the sample front bringing with them the associated effects of reduced  $v_v$ , reduced  $\psi_{peak}$ , and increased  $\omega$ .

Considering peak state data, the reductions in  $\psi_{peak}$  brought about by an increase in  $g$  are insufficient in explaining the associated reduction in  $(\tau_{yx}/\sigma'_{yy})_{peak}$ . This point is illustrated in Figure 4.21(a), where values of  $(\tau_{yx}/\sigma'_{yy})_{peak}$  are plotted against  $\psi_{peak}$  and a reducing  $(\phi'_{ps})_{peak}$  (obtained using Davis' (1968) relation) recorded. Closer appraisal reveals the reduction in  $(\tau_{yx}/\sigma'_{yy})_{peak}$  is not uniform, data points for both 2mm and 4mm openings being coincident. Mimicking Nakamaru et al's (1995) data, which was presented here in Figure 4.13, Figure 4.21(b) plots  $\phi'_{ds}$  values against  $g/D_{50}$ . Opposed to Shibuya et al's (1997) results, which are also therein presented, a plateau exists during the general trend of reducing  $\phi'_{ds}$  with increasing  $g$ . This plateau is centred around a  $g/D_{50}$  ratio of 5.

The effect of initial opening on the large displacement stress ratio is much reduced. This can be explained by charting the upper frame's course throughout a test's duration. At the displacements necessary to mobilise critical state parameters, vertical displacement of the upper frame has increased the average  $g$  by in excess of 1mm. Rotation of the upper frame has further increased  $g_{rear}$  by between approximately 0.5 and 1.5mm. Therefore, any effect that a small gap has on peak resistances disappears as the opening expands during testing.

The stress-dilatancy response of the aforementioned samples is presented in Figure 4.22 in which

Taylor's (1948) flow rule with  $\phi'_{crit}$  of  $35^\circ$  is also presented. Whereas the data obtained using small openings are associated with a gradient greater than unity, samples with larger openings approximate Taylor's flow rule to a much higher degree.

It is concluded that symmetrical WDSA data are optimised when the opening imposed between the shearbox's frames equals  $5D_{50}$ .

#### 4.4 The effect of applied moments on WDSA data

The novel way in which the shear load is applied to the upper ensemble of the WDSA provides for the first time the opportunity to investigate the effect that rotation has on shearbox data. By positioning a spacer plate of defined thickness underneath the shearbox and thereby raising it relative to the carriage, the central plane can be raised relative to the line of thrust by a chosen amount. Here, the vertical separation between the line of thrust and the central plane,  $f$  (mm), is taken as positive if the line of thrust is above the central plane. The consequence of imposing a negative value of  $f$  prior to test initiation is to increase the lever arm between the line of thrust and the reaction force generated on the rear wall of the upper frame. Thus, all else being equal, the upper frame would be subjected to an increased anticlockwise moment. When employing the symmetrical arrangement the effect of a negative  $f$  value is to increase the non-uniformity of the normal stress distribution across the sample top thereby imposing an anticlockwise moment on the sample counteracting the often observed clockwise rotation, as seen in Section 4.2.1.

To elucidate this further by considering the assumed system of forces acting on the portion of the sample contained within the upper ensemble and those on the upper ensemble as illustrated in Figure 4.23(a) and (b) respectively. Moment equilibrium of the upper ensemble about point  $m$  results in the following expressions for  $(\sigma'_{yy})_{front}$  and  $(\sigma'_{yy})_{rear}$ :

$$\frac{(\sigma'_{top})_{rear}}{\sigma'_{yy}} = 1 + 6 \left( \frac{h_s + f}{L} \right) \left( \frac{\tau_{yx}}{\sigma'_{yy}} \right) \quad 4.4$$

$$\frac{(\sigma'_{top})_{front}}{\sigma'_{yy}} = 1 - 6 \left( \frac{h_s + f}{L} \right) \left( \frac{\tau_{yx}}{\sigma'_{yy}} \right) \quad 4.5$$

where the included parameters are defined in Figure 4.23. Thus:

$$\frac{(\sigma'_{top})_{rear} - (\sigma'_{top})_{front}}{\sigma'_{vy}} = 12 \frac{\tau_{vx}}{\sigma'_{vy}} \left( \frac{h_s + f}{L} \right) \quad 4.6$$

Consequently, the gradient of stress distribution across the sample's top is seen to increase with increasing  $f$  and in this way rotations of the upper ensemble can be reduced whilst leaving  $\sigma'_{yy}$  unaffected.

Figure 4.24 displays the test data obtained during tests identical other than differing degrees of separation imposed between the line of thrust and central plane. In contrast to the large effect on the recorded rotations of the upper ensemble depicted in Figure 4.24(c), the variation in strength and dilatancy data brought about by increasing  $f$  is small. Cardinal parameters obtained from Figure 4.24 are presented in Figure 4.25 and illustrate that decreases in rotation brought about by increasing  $f$  have an insignificant effect on any of the parameters which may be used during data interpretation.

## 4.5 Sample dimensions

### 4.5.1 Background

Wood & Budhu (1980) used radiographic techniques to determine the positions of ruptures developed within two sands after the application of simple shear deformation. Sketches of the rupture patterns revealed that the coarser sand, LB 14-25, developed a single zone of preferential dilation nearly aligning with the direction of zero extension whereas the finer sand ( $D_{50}$  circa 0.2mm) was associated with a network of differently orientated ruptures. Commenting on this finding, Scarpelli & Wood (1982) reasoned that individual particles of the finer sand were less aware of the sample boundaries than those of the coarser sand and thus subjected to a lesser degree of restraint.

Using radiography of exceptionally long direct shear samples Scarpelli (1981) showed that similar networks of shear induced ruptures could develop within the apparatus. Zones of preferential dilation initiating at different times and with different orientations were seen to propagate towards the sample centre from each of the apparatus' end walls. Some of the ruptures were linked to the induced stress state and the sample's governing stress-strain law, while others acted to provide kinematic compatibility.

By testing different grades of LB in direct shearboxes of different lengths, Hartley (1982) showed the complexity of the induced rupture pattern to decrease with a shortening of the sample or increase in the particle size. Thus it was reasoned that for a given sand the external constraints applied by the sample boundaries can be made sufficient to subdue all oblique ruptures by reducing  $L$ , therefore requiring the

formation of a single horizontal zone of dilation across the central plane.

Neither Scarpelli's (1981) nor Hartley's (1982) apparatus permitted the measurement of the shear force induced by the applied shear displacement. In what is perhaps the most comprehensive study of the scale of the direct shear test, however, Palmeira & Milligan (1989a) presented both stress and dilatancy test data obtained using shearboxes of three different sizes. The dimensions of their samples (length by width by height, mm) ranged from the small, 60 by 60 by 32, through the intermediate 252 by 152 by 152, to the large, 1000 by 1000 by 1000. In each of the apparatus the load pad's vertical displacement was restrained and the normal load  $N$  applied by way of a rubber bag filled with pressurised water positioned between the load pad and sample. The outflow of water from the rubber bag was monitored which allowed the average vertical displacement of the sample to be calculated.

The behaviour exhibited by dense LB confined under 30kPa within each of these devices is presented in Figure 4.26(a). This figure also includes test data obtained using the WDSA in its unsymmetrical arrangement and employing  $g$  of 0.5mm, data judged most appropriate for this comparison. The scale of a direct shear test is seen to have a profound effect on stress and dilatancy data. By constructing the shearbox's side-walls from transparent Perspex Palmeira & Milligan (1989a) were able to identify the thickness  $t$  (mm) of the shear zone formed within their apparatus. The magnitude of  $t$  for Leighton Buzzard 14-25 ( $D_{50} = 0.80\text{mm}$ ) was found to be dependent on the test's scale, increasing from  $9\pm 2\text{mm}$  to  $18\pm 2\text{mm}$  to  $100\pm 10\text{mm}$  as the size of the shearbox increased from small to intermediate to large. Palmeira & Milligan (1989) reported that normalising direct shear test data with respect to their observed shear zone thickness had the effect of unifying test data, as illustrated in Figure 4.26(b).

By correlating data obtained using three different grades of Leighton Buzzard (with  $D_{50}$ 's of 0.4, 0.8 and 1.6mm) in addition to results of other investigators, Palmeira & Milligan (1989a) revealed a consistent pattern. The shear zone as a proportion of the sample height ( $t/H$ ) was shown to increase as the sample height decreased relative to the particle size ( $H/D_{50}$ ). If  $t$  were independent of  $H$  then a trend of reducing  $t/H$  with increasing  $H/D_{50}$  would anyway be apparent. Thus, to differentiate between Palmeira & Milligan's (1989a) findings and this inherent trend, Figure 4.27 reproduces Palmeira & Milligan's (1989) diagram but includes lines of constant  $t/D_{50}$  illustrating the trends if the shear zone were a specified multiple of  $D_{50}$  irrespective of sample height. Although Palmeira & Milligan's (1989a) data initially follows the  $t/D_{50} = 10$  line, deviancy becomes large at values of  $H/D_{50}$  of around 80.

In contrast to this, Hartley's (1982) data for various grades of LB in different lengths of shearbox, also presented in Figure 4.27 but not considered by Palmeira & Milligan (1989a), shows a much closer



correspondence with the  $t/D_{50} = 10$  trend-line at all values of  $H/D_{50}$ . The reason for this is thought to relate to differences in what was being measured. Hartley (1982), whilst observing networks of ruptures in the longer of his shearboxes, recorded the thickness of individual ruptures. Palmeira & Milligan (1989a), on the other hand, must have recorded the thickness of the total active zone that, in their larger boxes, would have comprised of a number of oblique ruptures. Only in this way could the shear zone reach the reported 100mm thickness. Thus, Palmeira & Milligan's (1989a) shear zone thickness is actually a measure of the complexity of the rupture pattern within the shearbox, which, if Hartley (1982) is believed, increases with the sample length.

So, in summary, the interpretation of the direct shear test based on the assumption of a single horizontal rupture zone is valid only if the degree of constraint offered by the sample boundaries is sufficient to bring this failure mechanism into being. Data suggests that either a shortening of the sample, or an increase of the mean particle diameter can increase the degree of constraint operating within the shearbox. To determine whether the degree of constraint offered by the WDSA is sufficient, an investigation into the effect of sample dimensions on test data is warranted.

Without major adaptation, the scale of the WDSA's sample is restricted by the geometry of the WF-25300 from which the WDSA was constructed, the machine body providing the limiting dimensions of the carriage which in turn limits those of the shearbox. Thus, the maximum sample size (length  $L$  by width  $W$  by height  $H$ ) is that of the WF-25300: 100 by 100 by 40. However, sample sizes may be reduced by the inclusion of aluminium blocks within the shearbox's frames symmetrically positioned to reduce either  $H$  or  $L$ . The self-weight of such blocks is taken account of when deriving  $\sigma'_{yy}$ .

#### 4.5.2 VLB samples of different dimension

The effect of limiting the length and height of dense VLB samples confined under 25kPa is shown in Figure 4.28 wherein Jewell & Wroth's (1987) data obtained for dense LB under 30kPa within their 152 by 252 symmetrical direct shearbox is also presented. (Jewell & Wroth's (1987) stress ratio trace is obscured due to close similarity with  $H/L = 40/98$  and  $27/98$  traces.) All WDSA data are associated with a rubber-sheet shielded, 5mm opening imposed between the frames prior to sample deposition, and coincidence between the apparatus' line of thrust and the central plane.

Agreement between data obtained with reduced sample dimensions is generally good, with all but the shortest and thinnest samples exhibiting similar trends and near identical strengths, peak rates of dilatancy and large displacement resistances, as illustrated in Table 4.2. Possible explanations for the

smallest dimensioned samples exhibiting such unprecedented behaviour will first be discussed.

	H/L					
	40/98	27/98	19/98	40/60	40/38	Jewell & Wroth's 152/250
$(\phi'_{ds})_{peak}: ^\circ$	48.0	48.7	46.8	47.4	45.0	48.4
$\psi_{peak}: ^\circ$	24.5	20.8	12.7	25.9	21.6	23.1
$(v_x)_{peak}: \text{mm}$	1.584	1.789	3.910	1.317	0.994	1.453
$(\tau_{yx}/\sigma'_{yy})_{kd}$	0.629	0.614	0.725	0.573	0.460	-

**Table 4.2: The effect that thinning a dense VLB sample confined under 25kPa has on test data**

### Limiting minimum dimensions

After a similar build up of shear resistance the shortest sample ( $H/L = 40/38$ ) mobilises a strength significantly lower than that of the longer samples. Thereafter, unsteady strain softening occurs until the test's end, the rate of which reduces with increasing  $v_x$ . Rates of dilatancy correspond with the stress data, the shortest sample exhibiting low  $\psi_{peak}$  and continued reductions in  $\psi$  until the tests end. The unremitting reductions in data may well relate to need for data manipulation methods to account for the shear displacement being a substantial proportion of the sample length, in excess of 30% by the test's end. Prior to the development of substantial  $v_x$ , however, a  $L/D_{50}$  ratio under 50 anyway suggests that a large proportion of the sample will have its behaviour determined by boundary conditions. Thus, VLB data from the shortest box is disqualified from further consideration and a minimum  $L/D_{50}$  ratio of 75 (relating to VLB in the 60mm long shearbox) set in place.

An understanding of behaviour of the thinnest sample ( $H/L = 19/98$ ) can be gained with the realisation that as the sample thins, the likelihood of passive failure of the sand in front of the advancing rear wall of the upper frame increases. Assuming negligible friction on the shearbox's lubricated vertical walls and a rectangular stress distribution across the sample's top, one would expect passive failure of the sample to occur when the horizontal normal stress on the end wall exceeds the passive Rankine pressure given by:

$$\sigma'_{xx} = \sigma'_{yy} \left( \frac{1 + \sin \phi'_{ps}}{1 - \sin \phi'_{ps}} \right) \quad 4.7$$

Under a confining stress of 25kPa, and assuming  $\phi'_{ps} = 54^\circ$ , the value recorded for the 40mm thick sample, the average  $\sigma'_{xx}$  needs to exceed approximately 237kPa for passive failure to occur. The average horizontal stress acting at peak conditions on the 40mm thick sample is approximately 160kPa, almost 80kPa under that required for passive failure, whereas that acting on the 19mm thick sample is nearly

390kPa. Considering the point where the rate of dilation plot for the 19mm thick sample first deviates from that recorded for the 40mm thick sample, at a shear displacement of approximately 0.60mm, the average horizontal stress is calculated as 247kPa, correlating closely to the passive failure stress predicted by theory.

The angles that planes of passive failure make with the horizontal are defined by Mohr's circle as:

$$\theta = 45 - \frac{\phi_{ps}}{2} \quad 4.8$$

Thus, if failure was to occur on a single passive failure plane originating at the opening between the shearbox s frames and subtending at an angle of  $18^\circ$  to the horizontal, one might expect the rear of the upper ensemble to rise by 0.325mm per mm of shear displacement. When shearing the 19mm thick sample, the vertical displacement recorded over the rear of the upper ensemble approximates a straight line with gradient 0.339 as illustrated in Figure 4.29, close to the rate of increase predicted by the consideration of the angles of passive failure planes. Thus, the passive failure of the 19mm thick sample is indicated by the consideration of average horizontal stress on the sample and by recorded displacement data.

It can be concluded that the WDSA's sample height and length need to exceed limiting minimum values to prevent either the passive failure of a sample or test data becoming dominated by boundary effects. Tests using dense VLB at low stress levels reveal data to go obviously awry when reducing between a  $H/D_{50}$  ratio of 33 and 20, and  $L/D_{50}$  ratio of 75 and 48. However, test data remains influenced by increases in either  $H$  or  $L$  above these minimum ratios.

### **Increases in $H$**

An increase in  $H$  from 27 to 40mm increases  $\psi_{peak}$  by  $3.7^\circ$  while changing  $(\phi'_{ds})_{peak}$  by a mere  $0.7^\circ$ . The significance of this disparity comes to light when the relationship between stress ratio and dilatancy rate is compared with Taylor's (1948) energy correction ( $\phi'_{crit} = 35^\circ$ ) in Figure 4.30(a, b & c). Disregarding the initial data points, a reasonable 1:1 relationship is followed by the 40mm thick sample. Thinner samples, however, and especially that thought to be exhibiting passive failure ( $H/L = 19/98$ ), are associated with an approximate dual-linear relationship with the ascent to peak have a gradient in excess of the descent. Concluding that dilation data is significantly more susceptible to changes in  $H$ , it is thought beneficial to maximise the height of a VLB WDSA sample.

### Increases in $L$

Lengthening the sample from 60 to 100mm has an effect on post peak data similar to that observed by Palmeira & Milligan (1989) when comparing data obtained in shearboxes of different dimension (Figure 4.26). The rate of strain softening reduces and larger  $v_y$ 's recorded. In addition, the upper ensemble undergoes lesser rotation. The effect on the stress ratio and rate of dilation relationship is seen in Figure 4.30(d & e). Possible reasons for these trends in WDSA test data follow:

The larger magnitudes of  $v_y$  and a slower rate of strain softening of longer samples could be interpreted as consequences of a thicker rupture layer therein but may have their root in other aspects of testing. It has previously been shown that when substantial initial openings are imposed between the shearbox's frames, the recorded average vertical displacements of an unshielded sample can be corrected to account for the additional volume created during shear using Equation 4.3.

The shortfall of average vertical displacements,  $(v_y)_{corrected} - (v_y)_{measured}$ , brought about by the creation of additional volume is inversely proportional to the sample length. When compared to their longer counterparts, thin unshielded samples will therefore be associated with lower magnitudes of dilation, increased rates of contraction at large shear displacements, and also, since the volume is created at the sample front, larger rotations of the upper ensemble. Although the use of split shielding has been shown to limit such volume creation, its deformation during testing ensures that the limitation is not absolute. Thus one might expect the trends predicted for unshielded tests to be apparent in split shielded data. Figure 4.29 reveals this to be the case, with the main differences in vertical displacements being recorded at the sample front, coinciding with where the additional volume is created.

The system of forces acting on the upper portion of the sample can be likened to those acting on a very short column with the horizontal load  $S$  distributed over its height, an axial load  $N$ , and a moment applied to its free end. Narrowing such a column reduces not only its strength but, by reducing the section's second moment of area, also its flexural rigidity. Thus, for a given system of loads, deflections of the narrow column could be expected to exceed those experienced by the broader. In the same way, a reduction in  $L$  for a shearbox sample rectangular in plan will decrease the "flexural rigidity" of the portion of the sample contained within the upper ensemble in proportion to  $L^3$ . To generate equivalent stresses within the shorter sample the applied loads reduce in proportion to  $L$ , a reduction outweighed by that of the flexural resistance. This analogy thus suggests that larger "deflections" should be expected when testing shorter samples. If the rotation of the upper ensemble is indicative of such deflections, this trend is seen in test results.

Despite the large effect on post-peak data, pre-peak WDSA data remain virtually unaffected by changes in specimen length. This is contrary to the findings of Palmeira & Milligan (1989) whose data show large increases in  $v_x$  were needed to mobilise equivalent pre-peak resistances in longer shearboxes. This may be due to the maximum  $L/D_{50}$  ratio in Palmeira & Milligan's (1989) study (1250) being so much higher than the maximum incurred when testing VLB (125). To extend the range of the present study the behaviour of the finer SFS was investigated within shearboxes of different dimension.

### 4.5 3 SFS samples of different dimension

Figure 4.31 shows that reducing  $L$  has a profound influence on the shear resistance offered and displacements undergone by SFS samples deposited at densities close to their maximum and confined under 25kPa at any given value of shear displacement. However, despite the obvious differences in data, Table 4 3 reveals both  $(\phi'_{ds})_{peak}$  and  $\psi_{peak}$  to be remarkably resilient of changes in  $L$ , with only  $(\tau_{yx}/\sigma'_{yy})_{ld}$  being dramatically affected. In addition, Figure 4.32 reveals approximate dual-linear stress-dilatancy relationships irrespective of specimen length.

	L (mm)		
	98	60	38
$(\phi'_{ds})_{peak}: ^\circ$	41.0	40.3	41.2
$\psi_{peak}: ^\circ$	13.4	12.8	14.8
$(v_x)_{peak}: \text{mm}$	4.068	2.579	1.742
$(\tau_{yx}/\sigma'_{yy})_d$	0.752	0.683	0.563

**Table 4.3:** The effect that shortening a dense SFS sample confined under 252kPa has on test parameters

It is the data corresponding to the shortest sample that sits most comfortably with expected trends. The densely deposited sand shows a distinct peak in mobilised shearing resistance that reduces substantially as shear displacement progresses. Although  $\tau_{yx}/\sigma'_{yy}$  falls until the test's close, its magnitude at large displacement most closely corresponds to the angle of repose recorded for SFS (33.5°). Vertical displacements indicate a short period of dilatancy, the peak rate of which coincides with peak shearing resistance, and a rapid switch to constant volume shearing conditions. The rapid post-peak reduction in  $\psi$  is what is expected when testing such a fine sand. The majority of vertical displacement occurs as the sand strain softens most rapidly. The stress-dilatancy relationship displayed for the shortest SFS sample in Figure 4.32(a) is similar in form to that of the shortest VLB sample (Figure 4.30d) perhaps indicating sample behaviour being dominated by boundary effects.

Longer SFS samples require more shear displacement to mobilise equivalent pre-peak resistances, are associated with larger but less rapid vertical displacements of the upper ensemble, and strain soften to a lesser degree resulting in  $(\tau_{yx}/\sigma'_{yy})_{ld}$  values independent of  $v_x$ , but the arcsine of which are extremely high in relation to the angle of repose. Dilatant behaviour in the longest sample is prolonged.

An understanding of the exhibited behaviour is earned with the realisation that networks of oblique ruptures are likely to be propagating inwards from SFS sample's end walls as shear displacement progresses. Indeed, the ratio between  $L$  and SFS's  $D_{50}$  in the 100 and 60mm long shearboxes (equalling approximately 500 and 300) bound that in Scarpelli's (1981) apparatus (412.5) where such ruptures were directly observed. Assuming similar rupture patterns to exist within the WDSA, differences in data obtained within shearboxes of different lengths can be explained.

The initial shear displacement applied to an SFS sample is absorbed by ruptures propagating obliquely into the sample. Consequentially the average stress ratio and rate of dilation across the central plane takes longer to develop and larger shear displacements are necessary to mobilise equivalent states of longer samples. Figure 4.33(a) illustrates that by normalising both  $v_x$  and  $v_y$  by  $L$ , consistent pre-peak trends are exhibited irrespective of sample length. VLB data obtained with  $L/D_{50}$  ratios too small to promote oblique ruptures (the maximum being 123) is presented after identical treatment in Figure 4.33(b) where the normalisation provides no correlating prowess. Figure 4.33(c) shows Palmeira & Milligan's (1989) data for LB obtained in much larger shearboxes ( $L/D_{50} = 1250$  and  $314$ ) to reveal a unification on normalisation akin to that recorded for SFS and a least as good as when normalised by their recorded shear zone thickness  $t$  (Figure 4.26b).

The behaviour of samples post-failure depends on a combination of shearing along many ruptures, variously orientated and initiating at different times. Longer shearboxes are associated with continued dilation, lower rates of strain softening and high magnitudes of  $(\tau_{yx}/\sigma'_{yy})_{ld}$  in relation to the angle of repose. Scarpelli's (1981) long shearbox data also exhibited dilatancy up until the end of the test (occurring at around 40mm of shear displacement). That the post-peak rate of strain softening of SFS samples reduces as the sample lengthens concurs with the theoretical work of Mroz & Drescher as presented by Scarpelli (1981) which derived the post-failure behaviour within a plane strain test when various geometries of rupture networks were hypothesised. A single rupture gave the steepest post-peak reduction in strength. The slower rates of strain softening of longer SFS samples might therefore be linked to the more complicated rupture patterns within.

It is interesting to note that the 100mm long SFS sample is associated with considerably less rotation of

the upper frame and yet is likely to be associated with the most complex rupture network and thus the highest degree of non-uniformity within the sample. It is therefore suggested that rotations of the upper ensemble are perhaps not a reliable estimator of the degree of internal uniformity.

For completeness, the effect of reducing the height of an SFS sample is seen on conventional test data in Figure 4.34 and on the stress dilatancy relationship in Figure 4.35. Up until a shear displacement of about 2.5mm consistent trends are exhibited by test data irrespective of the sample height. Thereafter, however sample dimensions are seen to have a profound effect on test data with both shear resistances and displacements being affected. Scarpelli (1981) showed that as an oblique rupture approached an upper or lower sample boundary it was required to change direction, triggering further ruptures within the sample. The earliest oblique ruptures initiating at an SFS sample's front and rear adjacent to the opening between frames will be required to change direction at a shear displacement dependent on the sample height. Thus data from the early stages of testing, prior to the first redirecting of ruptures, coincides.

It is the thinnest sample that first absconds from the paths traced by the thicker samples' data. The relationship that the thinnest SFS sample data has with its thicker counterparts corresponds closely to that found when investigating VLB. It may be that the horizontal stress transmitted across the advancing rear wall of the upper ensemble is sufficient to cause passive failure in the SFS sample. This is reinforced by the consideration of the average horizontal stress acting on the upper ensemble's rear wall in relation to  $\sigma'_{yy}$ , the ratio of which exceeds a value of 10.5 during testing. The passive pressure coefficient for sand with  $(\phi'_{ps})_{peak}$  of 50° is 7.548.

#### 4.5.4 Discussion

The WDSA sample height can affect data in several ways. Very thin samples can be associated with the passive failure of the portion of the sample positioned adjacent to the upper ensemble's rear wall. The test data of thicker samples are susceptible to changes in  $H$  if  $L/D_{50}$  is of a sufficient magnitude to generate a network of oblique ruptures. Otherwise, when the constraint offered by the boundaries is sufficient to limit the rupture network, the influence of  $H$  is diminished. An increased susceptibility of dilation data to sample dimension is apparent in the appreciable fall in  $\psi_{peak}$  brought by reducing the height of a VLB sample from 40 to 27mm, a change which has little effect on the more resilient stress data.

WDSA data obtained using specimens of different sands in shearboxes of different lengths is summarised alongside the findings of other investigators in Figure 4.36. From this figure, a number of conclusions can be drawn. The diagram points to the existence of a minimum length below which sample behaviour

will be dominated by boundary effects. Symptoms are low peak state parameters (when compared to results obtained for longer samples) and an ever-reducing large displacement resistance caused by the applied shear displacement reaching a magnitude equivalent to a substantial proportion of the sample length. WDSA data becomes impaired during the transition between sample lengths of 60 and 38mm irrespective of  $D_{50}$ . Thus, samples of different mean particle diameter are affected at different  $L/D_{50}$  ratios (48 for VLB and 190 for SFS).

The propagation of oblique ruptures through a direct shear sample is commonplace and the degree to which test data is affected by their presence differs. At worst, when incurring the high  $L/D_{50}$  ratios usually associated with fine sands, no horizontal rupture forms and data thus relate to a combination of shearing on many ruptures that progress from the sample end walls inwards. Peak strength and dilation rate may then be underestimated, and average vertical displacements may increase throughout testing. Also the large displacement resistance may be a dramatic overestimation of that offered by a single rupture. Since the rupture pattern induced is affected by the sample height, so is test data. Any simple test interpretation is inapplicable. The behaviour of SFS within the WDSA of 60 and 98mm length displays the behavioural traits thought to be associated with the propagation of a complex network of ruptures inwards from the shearbox's end walls. Thus, before a fine sand's sample length shortens sufficiently to promote a single horizontal rupture, boundary effects come to dominate measured data. Therefore, discussion of SFS data will henceforth be sidelined and the conclusion drawn that fine sands are not suitable for WDSA testing at least in its current configuration.

Sample data associated with high  $L/D_{50}$  ratios or very low  $H$  display an approximate dual-linear relationship when the stress ratio is plotted against the dilation rate. Such a relationship may well be indicative of the direct shear test data, for one reason or another, going awry.

The transitional  $L/D_{50}$  ratio marking the onset of more uniform behaviour with the occurrence of a horizontal rupture spanning the sample is unclear. Jewell & Wroth (1987), for example, used radiographic techniques to observe the single rupture developed across the central plane of their 254mm long LB 14/25 sample. Hartley (1982) used similar techniques but observed oblique ruptures in a far shorter sample of the same sand (134mm). The reason for these contradictions may relate to the particular example of DSA in use. Jewell & Wroth (1989) were the proponents of the symmetrical apparatus, designed to apply a more uniform deformation to the soil whereas Hartley (1982) used a far simpler apparatus designed to study the kinematics of deformation. The same argument can be used to explain the inference from test data of oblique ruptures within Palmeira & Milligan's (1989) apparatus, which was



actually that designed by Jewell but applied the normal stress through a pressure bag.

Interestingly, it now becomes clear why the effect of the conversion to the symmetrical arrangement found by Jewell & Wroth (1987) far exceeds the same conversion when applied to the WDSA. Oblique ruptures in Jewell & Wroth's (1987) 251mm long unsymmetrical apparatus would be far more prevalent than those occurring within the shorter unsymmetrical WDSA, and their prevention would thus have a larger effect.

It may be that the prolonged dilation increment and slower strain softening of a longer sample indicates the increased influence of oblique ruptures or a thicker shear zone when testing VLB in the WDSA. However, these effects can also be explained by the idiosyncrasies of direct shear testing (i.e. additional volume creation). That unique pre-peak behaviour, peak strength, peak rate of dilation, and large displacement resistances are measured in VLB WDSA samples of 60 and 100mm, and that the stress ratio and dilation increment are harmonious, is enough to verify that the apparatus is recording significant parameters. The similarities between VLB and MGS test data (not yet discussed) validate the latter's behaviour. In order to minimise the scatter in test data, 100mm long samples will be employed.

## 4.6 Optimum configuration

The optimum configuration can now be identified and, at its heart, features a sample of length 100mm and height around 40mm confined between two flat plates. The sample's vertical sides are bounded by strips of 1.1mm thick rubber membrane attached to the shearbox's internal walls using a thin layer of silicone grease. The shielding contained within the upper half of the apparatus is separated from that in the lower immediately above the lower frame. An opening is installed between the frames prior to sample deposition of magnitude  $5D_{50}$ . The apparatus is configured so the shearbox's central plane is coincident with the line of thrust.

The primary benefits provided by this configuration are:

- Low measured rotations
- Maximised angle of dilation
- No membrane force

- No undesired interactions between components
- High consistency of test data
- Derived strength parameters of appropriate magnitude
- Accordance with Taylor's (1948) flow rule

## 4.7 WDSA test procedure

The WDSA testing procedure consists of the following stages: shearbox assembly, sample preparation, WDSA assembly, and finally test initiation. The test procedures for each stage are described below.

The procedure begins with the thorough cleaning of the WDSA removing stray sand grains and any trace of silicone grease. The shearbox is then assembled. The retaining plate is placed within the lower frame while on a level surface. The lower frame's restraining screws are tightened clamping the retaining plate in place. The upper frame is positioned squarely on the lower frame and its separating grub screws rotated until the desired opening is uniformly imposed between the frames. The clamping screws are then positioned and tightened by an amount sufficient to prevent unwanted displacement between the frames. Each section of the shielding has one of its faces smeared with silicone grease. Beginning with the side walls, the shielding is installed within the shearbox, the silicone grease adhering to the shearbox's internal walls. The sample is deposited and the uppermost surface levelled before an upper spacer plate is lowered on. The load pad is placed onto the spacer plate and the vertical distance between the upper frame and the top of the load pad is measured at the midpoint of each side. Thus the pre-consolidation sample volume is obtainable.

The carriage is configured to accept the shearbox with a minimum of fuss by retracting its thumbscrews and sufficiently loosening the tailstock unit. The shearbox is then placed within the carriage using a spacer plate positioned below the shearbox to ensure that the line of thrust bisects the sample. The carriage's thumbscrews are tightened until the lower frame's rear is hard up against the carriage's shelf. The wings are then attached to the shearbox whilst encasing the ball races. This operation is eased by the adjustment of the carriage's horizontal position by way of the drive unit and the ball races by way of the tailstock unit.

The counterbalanced normal load yoke is positioned on the load-pad's conical seat without applying any

load to the hanger. Five vertical displacement transducers are next positioned, with their axes vertical, onto the load pad: one in each corner and one, as a check, on the normal load yoke. Load sufficient to generate the required stress on the central plane is applied to the normal load yoke's hanger, consolidating the sample. The vertical displacement of the load pad is then recorded making possible the derivation of the post-consolidation volume.

The tailstock unit is then tightened and the transducer to record the shear displacement positioned, ensuring it has sufficient travel. The shearbox's clamping screws are then released and removed before the upper-frame's restraining screws are tightened. The grub screws are retracted and the vertical displacement of the load pad re-recorded. Thus, the fully loaded sample volume and the reduction of the opening between the frames caused by settlement under the upper-frame's weight can be calculated. The difference between the post-consolidation and the fully loaded sample volumes were usually found negligible, even when testing a sample with an initially high void ratio.

The test can then be initiated by activating the drive unit that imparts a constant rate of displacement of 1.2mm/min to the WDSA's carriage. After testing, the shearbox is emptied and the sample weighed to enable the calculation of the initial density.

## 4.8 Summary

The optimum configuration of a DSA has been determined via consideration of the test's operating principles, the kinematics of testing and the merit of resulting data. For a DSA to be viable, it is essential that no undefined sources of loading be imposed. Within the WF-25300, such undefined loading is incurred from the system used to transmit  $S$  to the upper frame. Shear strength data obtained within the apparatus is therefore unreliable.

Given there to be no extraneous loads, the benefits of employing Jewell's (1989) symmetrical arrangement when direct shear testing using a conventionally sized apparatus are plentiful. Firstly, the displacements of a single component only need to be monitored. Secondly, by preventing the relative rotation between the upper frame and the load pad, undesired temporary interactions which otherwise may occur are not permitted and strains are concentrated within the vicinity of the central plane. In addition, rotation of the upper half of the apparatus, although not eliminated, is reduced. It is recommended that the symmetrical arrangement be adopted as the standard test configuration.

A direct shear sample's response is dependent on the size of the opening installed between the apparatus'

frames. Small openings have a reinforcing effect on sample strength. Larger openings give peak and large displacement strength parameters of magnitude more like those expected and produce a stress-dilatancy response in accordance with Taylor's (1948) flow rule. Openings of magnitude  $5D_{50}$  are considered optimum.

When symmetrical testing, shear displacement creates additional volume whose magnitude increases with the size of the opening between the frames and results in subsidence of the upper ensemble's front and indications of large displacement sample contraction. However, if the average vertical displacement and rotation of the upper ensemble are monitored during testing, the well-defined geometry of the symmetrical WDSA allows the additional volume to be calculated and corrected for. Only then will large displacement data indicate constant volume conditions. Alternatively, the implementation of shielding attached to the internal end walls of the sample can limit the additional volume created during shear and result in unmodified test data equivalent to corrected unshielded data. The optimum shielding configuration ensures the measured shear force  $S$  does not include a component relating to the force generated within the shielding itself and thus gives rise to a shear stress which is that mobilised wholly by the sample. The use of such shielding is recommended during direct shear tests that employ large openings between the frames.

To promote the uniformity of normal stress distribution, the apparatus' line of thrust should coincide with the central plane. Rotations of the upper ensemble occur, but for reasons that remain unclear. By imposing a moment across the sample's top, rotations can be practically eliminated, but the effect on other test data is minimal. It is concluded that rotations are not a good indicator of the direct shear test's reliability. This is also suggested by the widely varying rotations that are measured when testing SFS.

Tests featuring WDSA samples of different dimension tell of limiting minimum dimensions necessary for meaningful data. Excessively thin samples are subject to passive failure and consequential large rotations of the upper ensemble. Boundary effects dominate the behaviour of short samples that at large displacement indicate an ever-decreasing shear resistance as the progressively revealed horizontal face of the lower frame becomes a substantial portion of the central plane.

A single horizontal rupture will propagate through a direct shear sample only if its boundaries apply a sufficient degree of kinematic constraint. Otherwise a network of oblique ruptures will be induced and simple test interpretations invalidated. The necessary degree of constraint may be expressed as an  $L/D_{50}$  ratio that is dependent on the apparatus' configuration. For the WDSA, it appears that complex rupture patterns are produced at  $L/D_{50}$  ratios of around 250, although elsewhere  $L/D_{50}$  ratios of much higher

values have been reported as being successful. The traits of data that indicate a complex rupture network include:

- A bi-linear stress-dilatancy response.
- Prolonged dilatancy.
- Low rates of strain softening.
- An unrealistically high magnitude of  $\phi'_{crit}$  when estimated from the arcsine of the large displacement stress ratio.
- Sudden changes in the direction of test data.
- Underestimation of  $\psi_{peak}$ .

The peak shear resistance, however, is remarkably robust irrespective of the induced rupture network. Thus, if it is uncertain whether a DSA has sufficient kinematic constraint to produce a single horizontal rupture, data interpretation should be based solely on this measure and not measured dilation rates or constant-volume resistance data.

## 5. BEHAVIOUR OF SANDS WITHIN THE OPTIMUM WDSA

It is widely accepted that the strength and deformation behaviour exhibited by a given sand is affected by its density and stress level. Thus experimentation will only provide a satisfactory description of the material strength when a sufficiently large range of densities and stress levels are investigated.

Test data for two sands (VLB and MGS) deposited at various densities within the 100 by 100mm shearbox of the WDSA are here presented. The range of stress level investigated concurs with the limitations of the apparatus and spans between 25 and 250kPa. A deposit's density is referred to as either dense ( $90\% < D_r < 100\%$ ), medium ( $66\% < D_r < 82\%$ ) or loose ( $4\% < D_r < 17\%D_r$ ). The WDSA's pre-determined optimised configuration was employed featuring the symmetrical arrangement,  $g$  set at  $5D_{50}$ , coincidence of the central plane with the line of thrust ( $f = 0\text{mm}$ ), and employing split rubber shielding on the shearbox's internal walls. The rate of displacement imparted by the drive unit to the apparatus' carriage was 1.2mm/min. Data obtained is discussed with reference to that obtained by others and various experimentally and theoretically derived relations.

### 5.1 General discussion of exhibited behaviour

Test data recorded for both VLB and MGS deposited at various densities and confined under different stresses is displayed in matrix form in Figure 5.1 and Figure 5.2 respectively. The rows of these figures represent the different data formats:  $\tau_{yx}/\sigma'_{yy}$ ,  $v_y$ ,  $\psi$  and  $\omega$ , all of which are plotted against  $v_x$ . The columns represent different states of packing, the initial deposit density loosening as one progresses through the matrix from left to right. Trends displayed by both sands are very similar and so the following discussion makes no distinction between Figure 5.1 and Figure 5.2.

Considering first the dense deposits, data of which is displayed in column (a) of Figure 5.1 and Figure 5.2, at any particular stress level and from the  $\tau_{yx}/\sigma'_{yy} = 0$  condition,  $\tau_{yx}/\sigma'_{yy}$  increases rapidly with  $v_x$  at a rate that becomes progressively less with further increments of  $v_x$  until a peak value is mobilised. Increases in  $\sigma'_{yy}$  bring about reductions in the magnitude of  $(\tau_{yx}/\sigma'_{yy})_{peak}$  and increases in  $(v_x)_{peak}$ , the displacement required to mobilise peak strength. Thus, more highly stressed samples can be said to exhibit less stiffness and greater ductility. The post-peak reduction in strength occurs at a rate which reduces with increasing  $\sigma'_{yy}$  and precedes the mobilisation of a near-constant resistance, which a cursory examination of the data reveals to be independent of further increases in  $v_x$  and  $\sigma'_{yy}$ .

The above trends can be summarised by a series of contours in  $(\sigma'_{yy}, \nu_x)$  space for which  $\tau_{yx}/\sigma'_{yy}$  is constant. Such contours are displayed in Figure 5.3 and can be compared to those plotted in  $(\sigma'_{yy}, \alpha)$  space by Stroud (1971) for LB 14-25 in the SSA, reproduced in Figure 5.4. Overlooking for now the values ascribed to the different sets of contours, pre-peak contours described by WDSA and SSA data are similar in form despite the abscissa being  $\nu_x$  and  $\alpha$  respectively. The WDSA's failure locus, shown in both Figure 5.3 as a heavy line passing through each contour set's summit, is more linear than that of the SSA in Figure 5.4. Unlike those of the SSA, the WDSA post-failure contours fold back on themselves indicating the more rapid strain softening associated with deformation becoming localised within a single rupture.

Vertical displacement data shown in row two of Figure 5.1 and Figure 5.2 reveals a slight fall in the level of the upper ensemble at test initiation after which rapid upward displacement commences as samples begin dilating. The high sample density, close to the maximum of both VLB and MGS, ensures that the initial subsidence of the upper ensemble is small. The rate of dilation expressed in terms of  $\psi$  indicates a rapid increase to a peak value occurring at a displacement corresponding closely to that required to mobilise  $(\tau_{yx}/\sigma'_{yy})_{peak}$ . At  $\psi_{peak}$  the change in level of the upper ensemble, indicated by the lines which connect individual  $\nu_y$  data sets, is greater the higher  $\sigma'_{yy}$ . As  $\nu_x$  progresses from  $(\nu_x)_{peak}$ , the rate of vertical displacement of the upper ensemble falls attaining a near constant and negative value as the sample commences shearing with constant resistance. Although not present for all test series, dense MGS of Figure 5.2 being the obvious exception, there is a trend for  $(\nu_y)_{max}$  to decrease with increasing  $\sigma'_{yy}$ .

The trends displayed by looser deposits are broadly similar to those of the dense tests with decreases in stress level tending to push the  $\tau_{yx}/\sigma'_{yy}$ ,  $\nu_y$  and  $\psi$  curves upwards and to the left. The peak states of looser samples are appreciably lower than their denser counterparts and yet their large displacement shear resistance is very similar. By way of comparison with dense VLB data, contours of constant  $\tau_{yx}/\sigma'_{yy}$  in  $(\sigma'_{yy}, \nu_x)$  space are displayed for medium and loose VLB in Figure 5.5.

The rotations of the upper ensemble are documented in the final row of Figure 5.1 and Figure 5.2 and taken to be negative when rotating clockwise. As Hvorslev (1939) noted, the rotation decreases with increases in stress level. Although this trend occurs irrespective of the sample density, it appears to affect dense samples to a greater degree for which rotation nearly vanishes at high stress levels. The rates of rotation for the data of Figure 5.1 and Figure 5.2 of are presented in Figure 5.6 and are seen to be dependent on stress level and density. In general, the first part of the test is associated with a decreasing rotation rate before a more constant rate is mobilised during a test's closing stages.

## 5.2 Pre-peak trends

Pre-peak direct shear data are here classified and assessed using parameters that quantify the sample stiffness, the sample's contractile behaviour, the stress ratio at constant volume, and also by the consideration of the relationship between the stress ratio and dilation rate.

Conventional direct shear test procedures do not permit the determination of the shear strains applied to a sample and a sample's stiffness modulus cannot be determined. The desire to describe the pre-peak stress response of a direct shear sample has led to the use of a parameter which expresses the increase in resistance with shear displacement rather than shear strain. The similarity between this parameter and the stiffness modulus obtained during, for example, triaxial compression tests (Maeda & Miura, 1999) has led to it being represented by the symbol  $E$  commonly used to describe moduli. However, a subscript  $ds$  is intended to indicate the parameter's determination with reference to a direct shearbox's horizontal displacement. With reference to Figure 5.7,  $(E'_{50})_{ds}$  is defined as the gradient of the line subtended from the origin to the point on the resistance curve at which the sample mobilises 50% of its peak strength and has units of  $\text{mm}^{-1}$ . It is reiterated that this parameter is not a modulus and is intended to merely provide comparative measure of stiffness for WDSA test results.

Figure 5.8 illustrates that decreases in  $(E'_{50})_{ds}$  for both VLB and MGS are brought about by either increasing the confining stress or decreasing the initial density. Maeda & Miura (1999) found similar trends when increasing the stress level during triaxial compression tests featuring 80 granular materials at relative densities of around 70% where  $(E'_{50})_{ic}$  was defined in terms of the stress ratio and axial strain. The size of the reduction in  $(E'_{50})_{ic}$  with a given increase in stress level of the triaxial compression test showed a positive correlation with what was termed the void ratio extent ( $e_{max} - e_{min}$ ). It was argued that sands with a high propensity for structural change (as suggested by a high value of void ratio extent) would be associated with a higher degree of stress concentration at their necessarily sharper contact points. Thus, the likelihood of fracture or deformation of the contact points is increased relative to a more rounded sand and the associated larger changes in soil structure associated with a given increase in  $\sigma'_{yy}$  triggered. Figure 5.8 illustrates that a given change in  $\sigma'_{yy}$  results in larger reductions of  $(E'_{50})_{ds}$  for MGS than for VLB. That MGS has a larger void ratio extent than VLB holds with Maeda & Miura's (1999) argument.

For a dilatant sample, the maximum fall in position of the upper ensemble marks the point where a sample first shears with constant volume. The magnitude of the fall,  $(v_y)_{min}$ , is a measure of sample deformability and should thus have a negative correlation with sample stiffness. The stress ratio



mobilised at minimum volume,  $(\tau_{yx}/\sigma'_{yy})_{min\ vol}$ , has elsewhere been used, on theoretical grounds, to provide an estimate of  $(\tau_{yx}/\sigma'_{yy})_{crit}$  (Maeda & Miura, 1999). The definitions of both  $(v_y)_{min}$  and  $(\tau_{yx}/\sigma'_{yy})_{min\ vol}$  are illustrated in Figure 5.7.

For deposits of different densities, Figure 5.9 shows the variation of  $(v_y)_{min}$  with (a) stress level and (b) stiffness. To distinguish the comparatively small contractions of the denser samples from those of the loose, the former are plotted on enlarged scales in the right hand portion of Figure 5.9. The general trends are as expected with larger contractions being associated with increasing stress level and decreasing stiffness. Closer examination reveals confused trends, for example that dense deposits may be more contractile than medium, that probably have their grounding in the very small recorded magnitudes of  $(v_y)_{min}$ .

The benefit of employing  $(\tau_{yx}/\sigma'_{yy})_{min\ vol}$  as a measure of  $\phi'_{crit}$  is that the shear displacement necessary to attain this state is less than that necessary to mobilise peak resistance, and thus once peak resistance has been mobilised and the sample begins strain softening the test can be stopped. Values of  $(\tau_{yx}/\sigma'_{yy})_{min\ vol}$  for both VLB and MGS deposited at various densities and confined under different pressures are displayed in Figure 5.10.

Opposed to conventional wisdom concerning the behaviour of sand at large shear displacement within the DSA  $(\tau_{yx}/\sigma'_{yy})_{min\ vol}$  appears to be a function of stress level and initial density of the deposit, loose sample's attaining magnitudes closer to what one might expect for  $(\tau_{yx}/\sigma'_{yy})_{crit}$ . A possible explanation for this is that the shear displacement necessary to mobilise  $(\tau_{yx}/\sigma'_{yy})_{min\ vol}$  increases as the initial sample density decreases. For dense samples, where  $(\tau_{yx}/\sigma'_{yy})_{min\ vol}$  is mobilised soon after the test's outset, data are changing rapidly and measurement is less precise. Thus the looser the deposit the more reliably  $(\tau_{yx}/\sigma'_{yy})_{min\ vol}$  will estimate  $(\tau_{yx}/\sigma'_{yy})_{crit}$ . Clearly, such a variable estimate of  $(\tau_{yx}/\sigma'_{yy})_{crit}$  is undesirable.

The relationships between the stress ratio  $\tau_{yx}/\sigma'_{yy}$  and the rate of dilation  $dv_y/dv_x$  for dense, medium and loose deposits of VLB subjected to the complete range of confining stresses are displayed in Figure 5.11. Also displayed in the figures comprising Figure 5.11 are lines of gradient 1:1 intersecting the abscissa at a value of 0.575, alignment with which would indicate exact agreement with Taylor's (1948) flow rule and Stroud's (1971) measure of  $\phi'_{crit}$ . Similar plots for MGS are displayed in Figure 5.12 where Taylor's (1948) predictor is made to intersect the abscissa at a value of 0.600.

Ignoring the uncertain rise of the initial portion of the plots, once dilatancy is activated, data for dense sand are seen to consistently lie above the indicated expected behaviour. In addition, the linearity of the

plots once dilatancy has been activated decreases with increases in stress level. Loose deposits indicate the poorest agreement with Taylor's (1948) prediction. Similar findings by other investigators (Stroud, 1971, Budhu, 1979) have been explained by the higher degree of stress and strain non-uniformity occurring within loose deposits.

## 5.3 Peak state trends

### 5.3.1 Stress level dependency

The reduction of  $(\tau_{yx}/\sigma'_{yy})_{peak}$  and  $\psi_{peak}$  with increasing stress level is charted for both VLB and MGS deposited at the various densities in Figure 5.13. The general conclusions which may be drawn are that higher values of  $(\tau_{yx}/\sigma'_{yy})_{peak}$  and  $\psi_{peak}$  are mobilised at lower stress levels and higher initial sample densities. The data for VLB is displayed alongside Stroud's (1971) in Figure 5.14 where a similar stress level dependency is apparent. However, WDSA data for VLB at equivalent densities is found to substantially exceed Stroud's (1971) in magnitude. WDSA data should not be rejected on this count, however, since different batches of the same sand are known to have different strengths.

This is demonstrated for WDSA data by comparison of test results featuring two batches of Leighton Buzzard sand: VLB and ALB, each graded 14-25, but obtained from different sources. The small differences in the sands' grading curves seems insufficient to account for the disparate peak-state WDSA data displayed in Figure 5.15. The abraded sample data give a  $(\phi'_{ps})_{peak}$  value of 52.1°, substantially closer to the 50.9° mobilised in Stroud's (1971) SSA than the 54.3° of the VLB sample. Jewell & Wroth (1987) found similar trends when investigating the behaviour of different batches of LB in their modified DSA, one mobilising a  $(\phi'_{ps})_{peak}$  of 54.4° while the other only 51.9°. To enhance the correlation with Stroud's data, the latter sand was concentrated on. Here, because the weaker sand was in short supply, the overwhelming majority of tests featuring Leighton Buzzard 14-25 featured VLB.

The relationship between the shear strength, defined by  $(\tau_{yx}/\sigma'_{yy})_{peak}$ , and shear stiffness, defined by  $(E'_{50})_{ds}$  is displayed in Figure 5.16. Concurring with conventional understanding, those samples with higher shear stiffness also exhibit higher shear strength.

Recorded values of  $(\tau_{yx}/\sigma'_{yy})_{peak}$  for VLB are plotted against peak rates of dilation  $(v_y/v_x)_{peak}$  in Figure 5.17(a) and for MGS in Figure 5.17(b). Taylor's (1948) flow rule employing  $\phi'_{crit}$  values of 35° and 38° is also displayed. Agreement between experimental data and the theoretical relation is good, especially considering the wide range of densities and confining stresses employed. Thus, although the strength of

VLB is above that measured elsewhere for the same sand, it corresponds with an increased dilational capability in accordance with Taylor's (1948) energy considerations.

### 5.3.2 Estimates of $(\phi'_{ps})_{peak}$

The two relationships considered here which permit the derivation of  $(\phi'_{ps})_{peak}$  from  $(\phi'_{ds})_{peak}$  are reiterated in Table 5.1. The relationship published by Davis (1968) includes terms relating to  $\psi_{peak}$  unlike that of Rowe (1969) whose relationship contains a term relating to  $\phi'_{crit}$ .

	Relation	Assumptions
Davis (1968)	$\sin(\phi'_{ps})_{peak} = \frac{\tan(\phi'_{ds})_{peak}}{\cos \psi_{peak} + \sin \psi_{peak} \tan(\phi'_{ds})_{peak}}$	<ul style="list-style-type: none"> <li>• Coaxiality of axes of principal stress and strain increment</li> <li>• Zero extension of horizontal planes</li> </ul>
Rowe (1969)	$\tan(\phi'_{ps})_{peak} = \frac{\tan(\phi'_{ds})_{peak}}{\cos \phi'_{crit}}$	<ul style="list-style-type: none"> <li>• Coaxiality of axes of principal stress and strain increment</li> <li>• Stress-dilatancy relation</li> </ul>

**Table 5.1: The estimation of  $(\phi'_{ps})_{peak}$  from direct shear test data**

The values of  $(\phi'_{ps})_{peak}$  estimated from each of the above equations for VLB and MGS confined under a variety of loads and deposited over a range of densities are displayed in Figure 5.18. Excellent agreement is observed between the different estimates with  $(\phi'_{ps})_{peak}$  for the sands investigated being approximately  $6^\circ$  higher than  $(\phi'_{ds})_{peak}$  irrespective of the stress level or initial density.

The close agreement between the estimates of  $(\phi'_{ps})_{peak}$  based on different sets of test data gives confidence in the measured shearing resistance and dilational properties of the samples. That the agreement exists over such wide-ranging testing conditions illustrates the versatility of the WDSA.

Because estimates of  $(\phi'_{ps})_{peak}$  are in such close agreement it is fruitless to continue discussion of both. For this reason, only Davis' (1968) estimate will continue to be used since its applicability is reinforced by internal investigations of the shearbox performed elsewhere.

### 5.3.3 Correlation of converted parameters

Assuming that at peak-state the horizontal is a direction of zero linear incremental strain and the principal axes of stress and strain rate coincide then the average stress level,  $s'_{peak}$ , and the maximum shear stress,  $t_{peak}$ , can be derived. Irrespective of stress level and density, Stroud (1971) found that the intermediate principle stress within his SSA increased to a value of  $0.74s'$  soon after a test's initiation that was

maintained at least until peak resistance was mobilised. If the same were true for the WDSA then the stress invariant  $p'$  could be derived thus allowing data to be assessed using Bolton's (1986) density-dilatancy relation.

Values of  $(\phi'_{ps})_{peak}$  obtained using Davis' (1968) relation are plotted against  $\psi_{peak}$  and compared against the three flow rules of Table 3.5 in Figure 5.19. Agreement between the flow rules and experimental data is generally good with Bolton's (1986) and Taylor's (1948) relations providing an envelope between which the majority of the data lie. When  $\phi'_f$  is taken to be  $\phi'_{crit}$  Rowe's (1962) stress-dilatancy formula, falling between the others, is found to correlate results most precisely. Data for loose VLB shown in Figure 5.19(a) lie consistently and appreciably above the flow rules.

The reduction in VLB's peak stress ratio expressed as  $(t/s)_{peak}$  and angle of dilatancy  $\psi$  with increasing stress level  $s'$  is displayed in Figure 5.20 where the increased strength of VLB relative to Stroud's test sand is again apparent.

Figure 5.21 compares experimental data with Bolton's (1986, 1987) relative dilatancy index with which WDSA data is found to correlate fairly well. Certainly the correlation is no worse than that found by Bolton (1986) for plane strain data obtained elsewhere.

### 5.3.4 The verification and interpretation of direct shear data

As Jewell (1989) noted, concurrence between the output of flow rules (in terms of  $\phi'_{ps}$ ) and the theoretical relationships between  $\phi'_{ps}$  and  $\phi'_{ds}$  gives confidence that the experimental parameters are being reliably measured. To clarify this, Figure 5.22 illustrates the effect on the derived  $\phi'_{ps}$  when  $\psi$  or  $\phi'_{crit}$  are either underestimated or overestimated respectively. Chapter 4 revealed that when test data goes awry (i.e. when testing SFS), it becomes afflicted with these symptoms (assuming that the sample height is sufficient to prevent the passive failure of a sample and associated underestimates of  $\phi'_{ds}$ ). In addition,  $\psi$  is particularly sensitive to the experimental configuration and is underestimated when, for example, the sample is confined between dentated plates, as also revealed in Chapter 4.

Underestimates of  $\psi$  produce underestimates of  $\phi'_{ps}$  when flow rules are used to interpret data and overestimates of  $\phi'_{ps}$  if Davis' (1968) relation is used (Figure 5.22a). Overestimates of  $\phi'_{crit}$  consistently produce overestimates of  $\phi'_{ps}$  irrespective of interpretation method (Figure 5.22b). Thus, if an underestimation of  $\psi$  alone was to occur, the results of Davis' (1968) relation would exceed those of the flow rules, and vice-versa if  $\phi'_{crit}$  alone was overestimated. If, as with SFS in Chapter 4, the simultaneous

underestimation of  $\psi$  and overestimation of  $\phi'_{crit}$  occur, the effect on the flow rule's output is counteractive and would produce a  $\phi'_{ps}$  value below the overestimate provided by Davis' (1968) relationship. Thus, if good agreement is achieved between all outputs, it is likely that experimental data are reliable. As Jewell (1989) argued, direct shear test data can be verified by employing different test interpretations.

The discussion of the DSA given by Jewell (1989) assumes a reliable estimate of  $\phi'_{crit}$ , obtained by measuring the sand's angle of repose, is available for data interpretation. Here, however, interpretation is discussed on the merits of the test's output alone. As mentioned, defects of direct shear data can include the arcsine of  $(\tau_{yx}/\sigma'_{yy})_{ld}$  overestimating  $\phi'_{cv}$  and an underestimation of  $\psi$ . The measured peak stress ratio, however, appears to be remarkably robust. In Chapter 4, when changing the size of an SFS sample, variations in  $(\phi'_{ds})_{peak}$  of under 2% coincided with variations of  $\psi_{peak}$  of over 16%. Similarly,  $\phi'_{ds}$  recorded for various gradings of Leighton Buzzard in shearboxes of different sizes led Palmeira & Milligan (1989a) to conclude that  $\phi'_{ds}$  was independent of the test's scale. Thus, it seems sensible to base a universal interpretation of direct shear results on the measured peak stress ratio. Reconsidering Figure 2.7, the following equations are available to estimate  $\phi'_{ps}$  from a measure of  $\phi'_{ds}$ :

- Rowe's (1969) relationship which requires an additional input of the perhaps overestimated  $\phi'_{crit}$  resulting in the undesirable overestimate of  $\phi'_{ps}$
- Davis' (1968) relation that requires an additional input of the perhaps underestimated  $\psi$  again resulting in the undesirable overestimate of  $\phi'_{ps}$
- Taylor's (1948) relation which requires an additional input of the perhaps underestimated  $\psi$  to provide an estimate of  $\phi'_{crit}$  to be compared to the measured value of  $\text{asin}(\tau_{yx}/\sigma'_{yy})_{ld}$ . Rowe's (1969) relation can then be employed with the estimated  $\phi'_{crit}$  and the measured  $\phi'_{ds}$  to give  $\phi'_{ps}$ . (This path through Figure 2.7 is judged preferable to others also starting with Taylor's (1948) flow rule which require further use of perhaps incorrectly measured parameters.)

It is perhaps most straightforward to make use of the finding that seemingly, at least for the sands tested here,  $\phi'_{ps}$  is approximately 6° higher than  $\phi'_{ds}$ . Thus, merely by adding 6° to  $\phi'_{ds}$  a reasonable estimate of  $\phi'_{ps}$  is produced. For the SFS samples whose data was presented in Chapter 4, this procedure would result in a value of  $\phi'_{ps}$  of around 46°. It will be shown later that this is a good approximation of  $\phi'_{ps}$  for this sand. In addition, a 6° difference was found between the values of  $\phi'_{ps}$  and  $\phi'_{ds}$  recorded for dense Leighton Buzzard 14-25 confined under 30kPa in the SSA by Stroud (1971). However, before such a

simple interpretation is proposed, further work would be required to establish the universality of the  $6^\circ$  difference between  $\phi'_{ps}$  and  $\phi'_{ds}$  by, for example, investigating the response of sands with wide ranging  $\phi'_{crit}$ .

## 5.4 Strain softening trends

To characterise the strain softening behaviour of sand within the WDSA it is convenient to express the shear displacement as that relative to peak resistance,  $(v_x)_r$ :

$$(v_x)_r = v_x - (v_x)_{peak} \quad 5.1$$

Figure 5.23 charts the reductions of  $\tau_{yx}/\sigma'_{yy}$  and  $\psi$  as  $(v_x)_r$  increases from 0 to 6mm for MGS under different confining stresses and deposited in different states of packing. Within this range the overwhelming majority of strain softening occurs. The higher strengths associated with those tests carried out at lower stress levels are indicated by increased values of  $\tau_{yx}/\sigma'_{yy}$  at  $(v_x)_r = 0$ . The rates at which both  $\tau_{yx}/\sigma'_{yy}$  and  $\psi$  diminish reduce as the stress level increases.

Consistent strain softening trends are exhibited by employing parameters that relate  $\tau_{yx}/\sigma'_{yy}$  and  $\psi$  to their peak and large displacement values:

$$S_r = \frac{(\tau_{yx}/\sigma'_{yy}) - (\tau_{yx}/\sigma'_{yy})_{peak}}{(\tau_{yx}/\sigma'_{yy})_{ld} - (\tau_{yx}/\sigma'_{yy})_{peak}} \quad 5.2$$

$$Y_r = \frac{\psi - \psi_{ld}}{\psi_{peak} - \psi_{ld}} \quad 5.3$$

The meaning of parameter  $S_r$  is best understood with reference to Figure 5.24(a) where the peak-state is seen to be associated with a  $S_r$  value of zero indicating that no strain softening has occurred. Once shear displacement has been sufficient to mobilise a near constant resistance,  $S_r$  assumes a value of unity indicating the sample has fully strain softened. Hence,  $S_r$  is an index parameter expressing the degree to which a sample has strain softened. Similarly, and as seen in Figure 5.24(b),  $Y_r$  is an index parameter expressing the magnitude of  $\psi$  relative to its peak and large displacement value. As  $S_r$  increases with  $(v_x)_r$ ,  $Y_r$  reduces from unity to zero as the dilation rate reduces from  $\psi_{peak}$  to  $\psi_{ld}$ . Thus, from peak conditions, a trade-off is expected to occur between  $Y_r$  and  $S_r$ .

Figure 5.25 plots the evolution of both  $S_r$  and  $Y_r$  with  $(v_x)_r$  for MGS confined under various stresses and deposited at different densities. Where significant strain softening is observed (i.e. for the dense and medium deposits depicted in Figure 5.25a and b) a smooth transition between the limiting values of  $S_r$  and  $Y_r$  is recorded with increasing  $(v_x)_r$  that is independent of stress level. Although the scatter associated with loose sample data (Figure 5.25c) is considerable, that any trend is depicted at all is remarkable considering the negligibly small degree of softening undergone by such deposits (Figure 5.1c and Figure 5.2c).

By averaging the sets of curves depicted in Figure 5.25 and thereby producing a single representation of softening behaviour for a particular initial sample density irrespective of stress level, the effect of density on softening characteristics can be examined. Such averaged curves are displayed in Figure 5.26(a) and (b) for MGS and VLB respectively. Disregarding the data of loose VLB, the least dilative of the samples tested, the general trend is for denser samples to strain soften faster.

The transition of  $S_r$  and  $Y_r$  between their limiting values occurs in step, any increase in  $S_r$  being balanced by an equivalent decrease in  $Y_r$ . This is demonstrated in Figure 5.27 where the sum of the softening parameters are plotted against  $(v_x)_r$ . For all but the loosest of deposits and throughout the duration of strain softening,  $(S_r + Y_r)$  is seen to maintain a value of approximately unity. Despite the negligible degree of strain softening of loose deposits and the consequential scatter in the data, the magnitude of  $(S_r + Y_r)$  does not deviate far from unity.

The close links between post-peak stress and deformation data can also be assessed on axes of  $\tau_{yx}/\sigma'_{yy}$  and  $dv_y/dv_x$  as in Figure 5.28 and Figure 5.29 for VLB and MGS respectively. The broken lines in these figures represent the behaviour up to peak resistance and the continuous 1:1 line Taylor's (1948) energy correction. The clusters of data points centred on the abscissas that comprise loose deposits'  $\tau_{yx}/\sigma'_{yy}$  vs.  $dv_y/dv_x$  plots make their consideration fruitless. Dilatant samples, on the other hand, exhibit very clear trends. Reductions in  $\tau_{yx}/\sigma'_{yy}$  are balanced by equal reductions in  $dv_y/dv_x$  producing post-peak plots that agree very closely with Taylor's (1948) prediction.

## 5.5 Large displacement trends

Large displacement data is taken as the 10 experimental measurements that comprise close to the final 2mm of shear resistance. As seen in Figure 5.1 and Figure 5.2 and relative to the differentials apparent in preceding test sections, the data during this period is stable and far less influenced by either  $\sigma'_{yy}$  or  $D_r$ . Although the displacements of the upper ensemble usually indicate large displacement contraction

this is a product of additional volume creation (as described in Chapter 4) and thus data extracted from the closing stages of testing are indicated with a *ld* subscript to indicate large displacement.

Regardless of the sand type, stress level or initial density, falls in the level of the upper ensemble are recorded during the closing stages of testing giving the impression of large displacement sample contraction directly adverse to conventional wisdom concerning the large shear strain behaviour of granular materials. Such behaviour has in Chapter 4 been related to the inability of deformable shielding to adequately limit the creation of additional volume and sample extrusion from between the upper and lower frames. The rate of fall of the upper ensemble is approximately linear regardless of test parameters and thus reveals itself as a constant and negative large displacement angle of dilation  $\psi_{ld}$ , values of which are displayed in Figure 5.30. Despite the scatter within the data,  $\psi_{ld}$  is seen to decrease further below zero with increases in confining stress apparently indicating more rapid sample contractions at higher stress levels. One might expect higher stress levels to be associated with larger shielding deformations and thus a higher degree of particle extrusion. Different densities of deposit are associated with different rates of contraction but no clear trend is seen within the data.

Although useful for illustrating the relationship between stress and strain increment up to peak and during strain softening, axes of  $\tau_{yx}/\sigma'_{yy}$  against  $dv_y/dv_x$  (Figure 5.28 and Figure 5.29) are not helpful when considering large displacement data when  $dv_y/dv_x$  assumes values close to zero. Following Bishop (1950), large displacement data can better be compared with Taylor's (1948) energy correction on axes of  $(\tau_{yx}/\sigma'_{yy} - dv_y/dv_x)$  against  $v_x$  as in Figure 5.31.  $(\tau_{yx}/\sigma'_{yy} - dv_y/dv_x)$  is then seen to achieve a quasi-constant value irrespective of initial sample density. This value lies somewhat above the average value of  $(\tau_{yx}/\sigma'_{yy})_{ld}$  across all tests, displayed in Figure 5.31 as a dashed line. The overshoot in the magnitude of  $(\tau_{yx}/\sigma'_{yy} - dv_y/dv_x)_{ld}$  is in part due to the negative angles of dilation recorded during the closing stages of testing. However, as seen in Figure 5.32, the general trend is for  $(\tau_{yx}/\sigma'_{yy} - dv_y/dv_x)_{ld}$  to decrease with increasing  $\sigma'_{yy}$  and thus, since  $\psi_{ld}$  becomes increasingly negative with increasing  $\sigma'_{yy}$ , the negative values of  $\psi_{ld}$  cannot provide the entire explanation for the overshoot in  $(\tau_{yx}/\sigma'_{yy} - dv_y/dv_x)_{ld}$  and so attention is turned to stress data.

As noted in Chapter 2 when considering the manipulation of test data, the large displacement rates-of-change of  $\tau_{yx}/\sigma'_{yy}$  with  $v_x$  have a tendency to be negative at high stress levels indicating a reducing shear resistance with  $v_x$ . From this result alone it could be argued that the increased shear displacement required to mobilise equivalent stages of higher stressed tests makes the WDSA's limiting shear displacement insufficient to mobilise the critical resistance in such high stress level tests. Recorded vertical displacements contradict this argument, however, by indicating steady subsidence of the upper ensemble



at the test's close.

Extending the linear approximation to large displacement data back to the ordinate amplifies any differential there may be over the final 2mm of shear displacement. The close agreement between the magnitude of the intercept,  $(\tau_{yx}/\sigma'_{yy})_{int}$ , and the average of the large displacement data,  $(\tau_{yx}/\sigma'_{yy})_{ld}$ , shown in Figure 5.33 reveals just how small the gradients are. Closer consideration of Figure 5.33 reveals that although values of  $(\tau_{yx}/\sigma'_{yy})_{ld}$  seem independent of initial sample density, a reduction with increasing  $\sigma'_{yy}$  is apparent. Two recent investigations that have also found a reducing large displacement stress ratio with increasing stress level when investigating the behaviour of sands within the DSA include Frost & Han (1999) and Kuwano (1999). Both authors suggest the effect indicates the curvature of the critical state envelope and state the underlying reason to be particle crushing, mimicking the recognised explanation for curvature of the peak state envelope.

A consistent picture of the reduction in  $(\tau_{yx}/\sigma'_{yy})_{ld}$  with increasing  $\sigma'_{yy}$  and  $v_x$  can be obtained through the consideration of work expended whilst testing:

$$\begin{aligned} W &= W_s - W_N \\ &= \sum (S\dot{v}_x - N\dot{v}_y) \end{aligned} \quad 5.4$$

where  $W$  is the work done

$W_s$  is the component of work done by the shear force  $S$

$W_N$  is the component of work done by the normal load  $N$  (negative during dilation)

$\dot{v}_x$  is the incremental shear displacement

$\dot{v}_y$  is the incremental average vertical displacement of the upper ensemble

Moving away from convention by charting  $\tau_{yx}/\sigma'_{yy}$  against  $W$  as opposed to  $v_x$  for all tests featuring VLB results in Figure 5.34. Regardless of either initial density or stress level, the large displacement data is seen to have a unique relationship with  $W$ . To elucidate the trend further, data corresponding to each particular stress level are plotted separately in Figure 5.35 beside the best-fit line passing through the final ten data points of every test. The large displacement data for VLB can thus be approximated by:

$$\left( \tau_{yx} / \sigma'_{yy} \right)_{ld} = 0.6094 - 0.0025W \quad 5.5$$

The corresponding plot for MGS is displayed in Figure 5.36 where the linear approximation to large

displacement data is given by:

$$\left( \tau_{yx} / \sigma'_{yy} \right)_{id} = 0.6385 - 0.0030W \quad 5.6$$

In effect, the plotting of shear resistance with reference to work normalises the abscissa in a similar manner as the ordinate when shear stresses are converted to stress ratios. Since the literature suggests that curvature of the  $\phi'_{crit}$  envelope may be a particle crushing phenomena and one might expect the degree of particle crushing to be a function of stress level, the normalising of the abscissa in this way to reveal a consistent trend seems logical. However, it should be noted that the studies indicating such large displacement behaviour have all featured the DSA. Thus, it is entirely possible that this behaviour is generated from particular features of this method of testing. It has already been indicated (Chapter 3), for example, that large-displacement data is sensitive to the manipulation methods used to account for the reducing area of the central plane (although Chapter 7 will dispute that the reducing area is the source of the large displacement curvature). Thus, further investigation is required as to the source of this unusual trend.

### 5.5.1 Comparison with other's test data

Most DSA are stopped soon after peak and hence research into large displacement shear resistances obtained using the DSA is uncommon and no detailed work relating to the effect of experimental parameters on the large displacement shear resistance is known of. It is often assumed that the large strain stress ratio of a granular material attains a constant value as all dilatancy within the material is overcome, the stress ratio being independent of both stress level and density

A direct consequence of Davis' (1968) relationship (Chapter 2) is that at large displacement, when  $\psi$  is approximately zero, the maximum shear stress is mobilised on the central plane. Hence, the critical state angle of friction is estimated by the *arcsine* of the large-displacement stress ratio:

$$\sin \phi'_{crit} = \left( \frac{t}{s'} \right)_{crit} = \tan \phi'_{id} = \left( \frac{\tau_{yx}}{\sigma'_{yy}} \right)_{id} \quad 5.7$$

Clearly from Equation 5.7, the critical state angle of friction is defined via the *arcsine* of the large displacement stress ratio. The *arctangent* of this stress ratio, marking as it does the top of the Mohr's circle for a sample shearing at critical state, is given an alternative denotation  $\phi'_{id}$ . As will be seen in Chapter 7, misleading advice born from a failure to recognise this is apparent within certain sections of

the literature.

Bearing in mind that batch variations often make comparison between different sets of experimental data fruitless and the interpretation of large strain simple shear data when samples invariably contain local ruptures is uncertain, experimental data can be compared with Cole's (1967) large strain (>80% shear strain) data. Such a comparison is made in Figure 5.37.

Remarkable agreement is recorded between the two sets of data, Cole (1967) reporting a  $\phi'_{crit}$  of 35.1° and the experimental data highlighting that  $\phi'_{crit}$  is 35.2°. The scatter of WDSA data is far less than that inherent in Cole's (1967) simple shear data and, from Figure 5.37, it is hard to recognise a reduction of large displacement stress ratio with stress level. In summary, the good agreement between experimental data and Cole's (1967) reinforces the data manipulation and interpretation methods being employed whilst bearing testament to the quality of the WDSA test data.

An equivalent plot showing the large displacement data for MGS at different initial densities and confined under various stresses is presented in Figure 5.38. Again good consistency of data from tests with wide ranging configurations is recorded with  $\phi'_{crit}$  equalling 36.9°.

### 5.5.2 Comparison with the angle of repose

The angles of repose obtained in axisymmetric and plane strain conditions,  $i_{ax}$  and  $i_{ps}$  respectively are compared to the  $\phi'_{crit}$  values presented above in Table 5.2.

	$i_{ax}$	$i_{ps}$	$\phi'_{crit}$
VLB	35.7	35.0	35.2
MGS	34.3	34.2	36.9

**Table 5.2: Comparison between different measured angles of repose  $i$  and the large-displacement angle of friction averaged over a wide variety of tests for different sands**

Whereas the agreement between the recorded  $i$  values and  $\phi'_{crit}$  for VLB is excellent, for MGS the agreement is less good. This may be due to the difficulties associated with measuring the angle of repose, in particular the increased tendency that a scree or pile composed of a finer soil has to slip during measurement of its height, as discussed previously. Nevertheless, it is thought the measured parameters agree sufficiently well to help corroborate the WDSA's performance.

## 5.6 Summary

Data from 19 tests featuring two sands at a wide range of stress levels and densities and obtained in the optimised WDSA have been analysed in detail. In general, the response concurs with conventional wisdom and published test data.

A measure of stiffness of a direct shear sample has been defined to enable the response of direct shear samples subjected to various testing parameters to be compared. Concurring with conventional wisdom, it has been shown that sample stiffness quantified in this way increases with its strength and decreases with sample deformability when defined as the maximum fall in level of the upper ensemble. The stress ratio mobilised at this point of maximum contraction within the WDSA has been shown to provide a poor estimate of  $\phi'_{crit}$ .

Peak state test data interpreted using the theoretical relations of Davis (1968) and Rowe (1969) provide an excellent match with each other and correlate well with Taylor's (1948), Rowe's (1962) and Bolton's (1986) flow rules. Agreement between the output of these relationships gives confidence that the strength and dilational characteristics of the sands investigated here are being accurately measured because each draws on different sets of parameters. Hence, as Jewell (1989) concluded, concurrence between the output of different test interpretations can serve as a validation of test data.

Consideration of WDSA test data for different sands suggests that if erroneous estimates of test data result, they are most likely to influence either  $\phi'_{ld}$  or  $\psi$  (Chapter 4). The peak shear resistance provides the most robust experimental measurement and hence, if a universal test interpretation is required, it should be based solely on this parameter. For the sand's investigated here,  $\phi'_{ps}$  is found to exceed  $\phi'_{ds}$  by around 6°. It is therefore suggested that a straightforward test interpretation involving the addition of a constant to the arctangent of the experimentally measured peak stress ratio could provide a reasonable estimate of  $\phi'_{ps}$ . The benefits of such a simple interpretation include that the required test duration is shortened, needing to only encapsulate the peak state, and only the shear resistance need be measured. However, before such a test interpretation can be more widely adopted, further work is needed to investigate the relationship between  $\phi'_{ps}$  and  $\phi'_{ds}$  for a wider variety of sands.

Although the reasons for rotations of the upper ensemble in symmetrical tests remain hidden, they have been meticulously documented and presented as an aspect of direct shear testing that is often overlooked or ignored. Rotations increase with reducing stress level and with reducing initial density of the sample.

By quantifying the shear displacement relative to that required to mobilise peak states, the strain

softening trends of WDSA sample's have been investigated. Consistent trends are observed when strain softening parameters are defined which quantify the measured shear resistance and the rate of dilatancy relative to their peak values. The reductions in strength are then seen to match precisely the reductions in dilatancy rate, even for loose deposits that undergo extremely small degrees of strain softening.

Although independent of density, the large displacement resistance is seen to reduce with increasing stress level. This is contrary to conventional wisdom but reinforced by recently published studies also featuring the DSA. A consistent trend is displayed when shear resistance data is plotted with respect to the work done rather than shear displacement, perhaps indicating that the reduction in  $(\tau_{yx}/\sigma'_{yy})_{ld}$  with increasing  $\sigma'_{yy}$  is a particle crushing phenomena. However, it should be born in mind that the trend is just as likely to result from the testing method itself. Regardless, the effect on the  $\phi'_{crit}$  envelope is small and test data reveals excellent correlation with those recorded by others and acceptable agreement with the angle of repose.

It is concluded that the adaptation to the symmetrical WDSA provides a viable apparatus for investigating the response of sands to a shear load. Although it has limitations (fine sand displays wayward trends), one can be certain the apparatus provides reliable data, unlike that of the archetype which is also handicapped with similar limitations. Relative to the working DSA reported in the literature, which tend to have sizes and configurations very different from the archetypal DSA, the necessary adaptations are minor and cost-effective. It is recommended that archetypal DSA be adapted in this way for standard testing.

## PART II

---

## 6. INTERFACE FRICTION: THE STATE OF THE ART

Now a reliable means for experimental investigation has been developed in the form of the WDSA, attention is turned to the study of sand-steel interface friction. As mentioned in the introduction to this thesis, the interface is defined as the region of interaction between the bulk of a granular mass and the bulk of the steel. This definition is different from those found elsewhere in the literature where the term interface is used interchangeably with surface. Discussion is split in two. The details and findings of experimental investigation itself are left for Chapter 7. Here in Chapter 6, and to approach the subject, attention is given primarily to the literature. That of soil mechanics is initially overlooked, discussion instead focussing on a science known as tribology.

Tribology is defined as "the science and technology of interacting surfaces in relative motion and of related subjects and practices" (Arnell et al, 1991). It is a multidisciplinary science encompassing friction, wear and lubrication and draws on the expertise of the physicist, the chemist, the mechanical engineer and the materials scientist. Although bearing great relevance to the subject of sand-steel interface friction, *the findings of tribology have only recently started to be assimilated into the soil mechanics literature.*

Discussion begins with enquiry into the attributes of the solid surface thought to be important in determining interface behaviour. Following this, the interaction between opposing surfaces is considered before attention is turned to the behaviour of discrete particles in contact with a surface. The chapter closes with a review of the interface behaviour as described by the soil mechanics literature. First, however, a definition of terms.

### 6.1 The terminology of tribology

A surface is defined as the boundary between two materials, often a solid and air. If one could descend into a nominally-horizontal metal surface from the air above, before the metal itself was encountered a compound layer of contaminants (e.g. dust) and oxidised material that results from the reaction between the metal and its environment would need to be passed through. Next, and before the regular crystalline structure of the bulk material is reached, a heavily deformed layer would be encountered with properties different from that of the bulk due to the processes used to manufacture the surface.

The surfaces found in modern engineering show the marks of a great variety of formative processes. The resulting geometry, what is known as the surface "topography", is often the culmination of a great variety of individual events, each of which affects only one small region of the surface. The result is a great

many local topographical maxima and minima, known as the surface "asperities". Surface topography is perhaps most widely investigated using "contact stylus profilometry". Profilometers employ a stylus with usually a round tip made of a suitably hard material, often diamond, which is dragged across a surface under a very low load. Its vertical movements are amplified electrically to produce a set of  $x$  and  $y$  ordinates, the latter usually relative to a mean line about which they are evenly distributed. The resulting trace is called a "profile".

Typical profiles of engineering surfaces often exhibit irregularities with different wavelengths superimposed on each other. This has led to a distinction between "roughness", "waviness" and "form" (Dagnall, 1980). The roughness comprises the irregularities inherent in the production process or left by the actual machining agent. Waviness is the component of topography on which roughness is superimposed and may result from machine or work-piece deflections, vibrations or chatter. Form is the general shape of the surface neglecting the variations due to roughness and waviness. Although qualitative, such distinctions have proved to have considerable practical value.

The behaviour of engineering surfaces can depend on different aspects of surface topography. In some cases the valleys are important, for example in the leakage of seals, or the ability of a surface to tolerate particulate contaminants or debris. Conversely the contact between solids is controlled primarily by the peaks since when opposing surfaces come into contact, they almost always do so near the summits of their asperities. Consequently, numerous descriptors of surface topography can be derived from a set of profile ordinates, each of which characterises certain topographical aspects. The most prevalent measures of surface topography are introduced in the following section.

## 6.2 Conventional topography quantification

The complexity of typical engineering surfaces has prevented the development of an objective roughness parameter capable of quantifying surface texture in its entirety. Instead, convention specifies a number of parameters that can be categorised with reference to three groups: amplitude parameters, spacing parameters and hybrid parameters.

As one would expect, derivation of the amplitude parameters makes reference only to the  $y$  ordinates of a surface profile, the spacing parameters only the  $x$  ordinates, whereas the hybrid parameters make use of both amplitude and spacing of the profile irregularities. A selection of the most commonly used of these are displayed in Table 6.1 wherein it is not the intention to reveal the strict mathematical definition of



each parameter but to indicate the surface feature that each parameter relates to.

Amplitude roughness parameters			
$R_a$	the roughness average, the most universally recognised roughness measure that relates to the arithmetic-mean absolute deviation of the profile from the centre line	$R_a = \frac{1}{L} \int_0^L  f(x)  dx$	
$R_q$	the root mean square parameter corresponding to $R_a$ . With a Gaussian height distribution, $R_q$ is approximately equal to $0.8R_a$	$R_q = \sqrt{\frac{1}{L} \int_0^L f^2(x) dx}$	
$R_t$	the vertical height between the highest and the lowest points on the profile		
$R_p$	the highest point of the profile above the mean line		
$R_v$	the lowest point on the profile below the mean line		
$R_{sk}$	the skewness of a profile, measures the symmetry of the profile about the mean line, defined with reference to the amplitude distribution curve		Derivation of the amplitude distribution curve: 
$R_{ku}$	the kurtosis of the distribution, measures the sharpness of a profile with spikey surfaces having higher kurtosis values than bumpy surfaces, defined with reference to the amplitude distribution curve		
Spacing roughness parameters			
$S_m$	the mean spacing between profile peaks. A profile peak is the highest part of the profile between adjacent crossings of the mean line	$S_m = \frac{1}{n} \sum_{i=1}^{i=n} S_{mi}$	
$S$	the mean spacing of adjacent local peaks. A local peak is one whose height, measured from the smallest adjacent valley is not less than 1% of $R_t$	$S = \frac{1}{n} \sum_{i=1}^{i=n} S_i$	
$\Lambda_q$	the root mean square average wavelength of a profile obtained through Fourier analysis		$\Lambda_q = 2\pi \frac{R_q}{\Delta_q}$
Hybrid roughness parameters			
$\Delta_a$	the mean slope of the profile, the arithmetical average of the absolute values of the rate of change of the profile		$\Delta_a = \frac{1}{L} \int_0^L \left  \frac{df(x)}{dx} \right  dx$
$\Delta_q$	the root mean square parameter relating to $\Delta_a$		$\Delta_q = \sqrt{\frac{1}{L} \int_0^L \frac{df^2(x)}{dx} dx}$

Table 6.1: Some often used conventional roughness parameters (figures modified from Dagnall, 1980, and Thomas, 1982)

The different surface parameters are successful in correlating different surface performance. For example, a good bearing surface is provided by a surface with strongly negative skew. It is often found that friction is best correlated by slope parameters.

### 6.3 Preparation and quantification of interface blocks

This is a convenient juncture to describe the interfaces' constituent surfaces which, in Chapter 7, will be investigated. Surface profiles were digitised, recorded and the roughness parameters were calculated using a Talysurf profilometer whose stylus (Talysurf 112/2009) is reported by the manufacturer to have a spherical tip with radius  $2\mu\text{m}$  and contact force of between 0.7 and 1mN. The nominal vertical resolution of the digitised points is  $\pm 0.5\text{nm}$  but the resolution of the mechanical elements of the measuring system is probably less. The profilometer was supported on a massive granite block, which itself was supported on air cushions. The background noise resulted in vertical deflections of the stylus tip of around 3nm.

The maximum number of ordinate pairs able to be handled by the profilometer system was 120,000. Thus, for traverses of less than 30mm, the spacing between individual pairs of ordinates was  $0.25\mu\text{m}$ . For the smoother surfaces investigated, traverse lengths of almost 6mm were employed, each providing a 5mm long segment of profile over which roughness parameters were evaluated. A total of ten profile segments were used to characterise a surface, five running parallel to the direction in which the WDSA would apply its shear displacement, and five running perpendicular. Each traverse was taken at a different location on the surface to provide an indication of the topography's uniformity, which was generally found to be high. The topographical descriptors derived from each of the set of five traverses were averaged to produce the nominal roughness parameters discussed below.

To limit the number of ordinate pairs, the data point spacing was automatically increased to  $1\mu\text{m}$  for traverses longer than 30mm. For the rougher surfaces investigated here it was necessary to increase the traverse length to 70mm to acquire sufficient profile data to enable accurate estimate of roughness parameters. Hence the  $1\mu\text{m}$  sampling interval was employed. The profilometer was configured to add a horizontal mean line to profile data using the least-squares method and also produce estimates for the conventional roughness parameters.

For a meaningful study of interface friction, it is essential to have the ability to provide a consistent set of initial conditions. Thus, just as the Pluviator was developed in Chapter 3 to enable the repeatable deposition of uniform samples with various densities, techniques are here developed that enable the repeatable establishment of uniform surface topographies with different roughness magnitudes. It is endeavoured to produce interface surfaces with form comprising a horizontal plane, no waviness and merely a roughness component. This validates the direct comparison of interface data featuring the different surfaces.

Grade 43A mild steel was used to create the interface's constituent surfaces. The raw material

was machined down to be dimensionally equivalent to the WDSA's lower-frame, threaded holes drilled for the apparatus' clamping screws, and opposite surfaces ground parallel to each other. The resulting specimens became known as "interface blocks". The final topography was installed on a block's principal surface using one of the following techniques, presented in order of increasing resulting roughness:

1. Abrasion using progressively finer grades of abrasive paper before polishing with Brasso to a mirror finish. The resulting surface is named POL. A typical profile of POL is pictured in Figure 6.1(a) and the associated roughness parameters tabulated in Table 6.2. The use of abrasive paper erodes the peaks of the initially ground surface and consequently  $R_p$  is around a third of  $R_v$ . Since material is removed from above the mean line, the resulting surface has a strongly negative skew, and a high kurtosis indicating a reflective surface with occasional, relatively deep valleys.
2. The surface was left in its as produced ground state and thus named GND. Unlike the other surfaces, which displayed consistent surface parameters irrespective of traverse orientation, the roughness parameters for GND were directionally dependant, as seen in both Figure 6.1(b), Figure 6.1(c) and Table 6.2. This relates to the action of the grinding wheel that, like a wheel-spinning car tyre, leaves striations in its direction of spin along with a larger wavelength "waviness" relating to the jumping of the wheel over the surface. Thus, parallel to the striations, amplitude parameters and  $\Delta_q$  assumes smaller magnitudes since the stylus runs parallel to the gouges, but  $S_m$  and  $\lambda_q$  assume larger values due to the waviness. When the GND surface is used during testing, it is arranged so that  $v_x$  is perpendicular to the striations left by the grit on the grinding wheel. In this way a surface with roughness significantly greater than POL investigated and direct comparisons between a surface with a waviness component to those without are avoided.
3. Abrasive particles entrained within an air-stream were propelled towards the surface using a technique known as shot blasting. The interfacial block was positioned inside a sealed blast tank. Into the tank were fed two separate lines whose outlets were perpendicular: an airline and a line to a separate container of the abrasive. Activation of a trigger mechanism inside the tank made use of the Venturi principle to entrain the abrasive in the air stream, which was subsequently expelled through a nozzle and propelled towards the interface block. In this way the principal surface of the interface block was eroded. To ensure consistency, the abrasive particles were fired only once from a nozzle kept a constant distance from the interface block. The abrasives employed were either 120 grit aluminium oxide powder ( $D_{50} = 0.2\text{mm}$ ), which produced the ALO surface, or 16 grit silicone carbide ( $D_{50} = 1.8\text{mm}$ ), which produced the SIC. The increased hardness, particle-size and angularity of the silicone carbide grit in relation to aluminium oxide powder resulted in SIC having a roughness

well in excess of ALO. However, the consistent surface formation process made SIC resemble an enlarged version of ALO, each roughness parameter being approximately 3 or 4 times higher in magnitude. Although the profiles of both ALO and SIC pictured in Figure 6.1(d) and (e) appear jagged, this is a product of the larger ordinate scale relative to the abscissa. Figure 6.2 presents a portion of the same profile pictured in Figure 6.1(d) but with the vertical scale closely approximating the horizontal in which the asperities on even this relatively rough surface are seen to be fairly low and blunt.

4. A uniform coating of Araldite was smeared over the blocks onto which particles of either SFS, MGS or VLB were pluviated. Stylus profilometry of such granular surfaces probably led to underestimation of roughness parameters for two reasons. Firstly the full penetration of the stylus into the deepest valleys is unlikely. Secondly "flanking" may occur when the slope of an asperity is steeper than the cone used to hold the stylus' diamond tip and thus the tip loses contact with the surface. As one would expect considering average particle diameters, the resulting surface parameters of the granular surfaces SFS, MGS and VLB, are seen in Table 6.2 to be very much higher than those previously considered.

	POL	GND		ALO	SIC	SFS	MGS	VLB
		Parallel to striations	Perpendicular to striations					
$R_a$ ( $\mu\text{m}$ )	0.147	0.320	0.356	2.487	9.401	33.745	113.958	180.173
$R_q$ ( $\mu\text{m}$ )	0.206	0.393	0.458	3.273	11.843	41.328	145.462	226.406
$R_p$ ( $\mu\text{m}$ )	0.468	0.951	1.713	10.315	32.867	101.818	507.784	660.862
$R_v$ ( $\mu\text{m}$ )	1.512	1.143	2.132	14.277	34.180	100.396	372.297	661.886
$R_t$ ( $\mu\text{m}$ )	1.980	2.095	3.845	24.592	67.046	202.214	880.081	1322.748
$R_{sk}$	-1.662	-0.349	-0.721	-0.363	-0.123	-0.105	0.426	0.069
$R_{ku}$	9.799	2.749	4.103	3.881	3.265	2.793	3.340	3.105
$S$ ( $\mu\text{m}$ )	5.78	5.858	6.354	13.004	35.963	78.227	327.729	591.367
$S_m$ ( $\mu\text{m}$ )	10.294	28.073	19.764	46.644	157.444	387.282	950.200	1421.545
$\Lambda_q$ ( $\mu\text{m}$ )	11.529	22.696	15.755	41.819	133.094	302.910	550.393	761.576
$\Delta_a$ ( $^\circ$ )	5.064	4.689	7.517	20.193	23.063	34.543	37.203	40.400

**Table 6.2: Typical conventional roughness parameters for the surfaces here investigated**

## 6.4 The fractal dimension

The desire to find parameters that characterise a surface's performance has pushed surface science towards considering the fractal dimension. The basic concept of the fractal dimension is one of scale; the

length of a profile is a function of the length of the device with which it is measured. Mandelbrot (1977) introduced the subject of fractals by asking the question: "How long is the coast of Britain?" Setting a pair of dividers to a prescribed opening or step-length  $l$  and walking these dividers along the coastline with each new step starting from where the previous landed will result in an estimate given by:

$$A(l) = nl \quad 6.1$$

from which:

$$\log l = \log A(l) - \log n \quad 6.2$$

where  $A(l)$  is the apparent or measured length

and  $n$  is the number of steps

Shortening the divider opening and repeating the operation a second approximation of  $A(l)$  results which is greater in magnitude than the first. Repetition of this process revealed to Mandelbrot that  $A(l)$  increases with decreases in  $l$  without limit. Clearly, the reason for the observed behaviour is that a bay or peninsular on a 1/100,000 scale map comprises of sub-bays and sub-peninsulas which only become visible when a 1/10,000 map is studied. And these sub-bays themselves are comprised of sub-sub-bays and sub-sub-peninsulas, each of which adds to the measured length. Similarities between portions of the coastline at very different scales are seen.

Performing analogous measurements on a standard curve from Euclid, one finds an altogether different result. For an interval of straight line, the approximate measurements are essentially identical and define the length. For a circle the approximate measurements increase before rapidly converging to a limit, the circle's diameter. Mandelbrot (1977) called such curves where a length is defined "rectifiable".

Mandelbrot (1977) showed that a log-log plot of the measured length  $A(l)$  against the step-length  $l$  to be associated with linear portions for both the rectifiable circle and non-rectifiable coastline. Thus, for these linear portions, a power law was defined:

$$\log A(l) = d \log l + \log c \quad 6.3$$

$$A(l) = cl^d \tag{6.4}$$

where  $d$  is the gradient of the log-log plot

$c$  is a constant

and choosing appropriate length units to produce a constant  $c$  of magnitude unity then:

$$\log A(l) = d \log l \tag{6.5}$$

For rectifiable curves,  $d$  had magnitude zero whereas non-rectifiable curves had gradients in excess of unity. (For the coastline of Britain,  $d$  was found to equal 0.36.) Thus the power law was said to characterise the complexity of a figure by expressing how quickly the length increases if we measure with ever-finer accuracy.

Scaling properties and self-similarity, concepts which have arisen above, are reflected in a structure's "dimension". A line segment might for example consist of three copies of itself scaled by a factor of a third. Thus the segment has a self-similarity dimension:

$$D_s = \frac{-\log 3}{\log 1/3} = 1 \tag{6.6}$$

A square, on the other hand, consists of 9 copies of itself each scaled by a factor of a third. Consequently:

$$D_s = \frac{-\log 9}{\log 1/3} = 2 \tag{6.7}$$

And likewise a cube, being made up of 27 copies of itself scaled by a factor of a third, has self-similarity dimension:

$$D_s = \frac{-\log 27}{\log 1/3} = 3 \tag{6.8}$$

Thus for these Euclidean forms there is a power law relationship between the number of self-similar components and the scaling factor whose exponent corresponds with those numbers familiar as (topographical) dimension:

$$D_s = \frac{-\log n}{\log s} \quad 6.9$$

where  $D_s$  is the self-similarity dimension

$n$  is the number of components

$s$  is the scaling factor

hence:

$$n = \frac{1}{s^{D_s}} \quad 6.10$$

The Koch snowflake, one of the better known fractal shapes, is constructed by taking an equilateral triangle with a side length of unity and attaching to the middle third of each side another identical triangle one third of the size. This transformation repeated ad infinitum results in a finite area enveloped by an infinitely long line. Examining one side of this figure, the curve can be seen to be made up of four copies of itself scaled by a factor of a third resulting in a self-similarity dimension  $D_s$  of 1.2619. The Koch curve has dimension lying somewhere between that of a line and that of a plane, a fraction more than 1. Mandelbrot termed such sets fractal, deriving the term from the Latin verb *frangere*, to break or create irregular fragments.

The Koch curve is truly fractal, exhibiting the same self-similar behaviour at every scale. If like a coastline or a rough surface, however, fractal features disappear if they are viewed at sufficiently small or large scales then one can say that only at certain scales do they appear very much like fractals and at such scales may usefully be regarded as such. Mandelbrot states "to obtain a Koch curve, the cascade of smaller and smaller promontories is pushed to infinity, but in nature every cascade must stop or change character. While endless promontories may exist, the notion that they are self-similar can only be applied between certain limits. Below the lower limit the concept of coastline ceases to belong to geography." In the same way, a metal surface will best be viewed as flat above a certain scale and rough below.

So, given a self-similar structure, there is a relation between the scaling factor and the number of pieces into which the structure can be divided given by Equation 6.10. Realising that the step-length of a structured walk is equivalent to the scaling factor, Equation 6.10 can be rewritten:

$$n = \frac{1}{l^{D_s}} \quad 6.11$$

$$\log n = -D_c \log l \quad 6.12$$

where  $n$  is the number of steps

$l$  is the step-length

and  $D_c$  is the empirical estimate of the self-similarity dimension or "compass" dimension<sup>1</sup>

Substitution of Equations 6.5 and 6.12 into Equation 6.2 reveals:

$$\log l = d \log l + D_c \log l \quad 6.13$$

$$d = 1 - D_c \quad 6.14$$

and thus, by substitution into Equation 6.4:

$$A(l) = cl^{(1-D_c)} \quad 6.15$$

A log-log plot of the apparent length measured using decreasing divider openings will be linear with gradient  $(1 - D_c)$  if the path walked is self-similar.

## 6.5 Fractal analysis of surface roughness

Although of vastly different scale, profilometer data bears a resemblance to Mandelbrot's (1977) coastline of Britain. Asperities that comprise the surface roughness are set on others which relate to the larger scaled waviness just as sub-promontories comprise a coastline's larger scaled promontories. This similarity has led to the description of engineering surfaces using fractal parameters.

Fractal analysis has been used to determine the intricacy or complexity of engineering surfaces from fracture surfaces of steel specimens (Underwood & Banerji, 1986), to rock joints (Huang et al, 1992), geomembranes (Vallejo et al, 1995) and even individual particles of sand (Vallejo, 1995). Although it is

---

<sup>1</sup> A structured walk taken along either a Koch curve or a line segment produces values of  $D_c$  equivalent to  $D_s$ . No such result is possible when considering the plane or cube discussed previously as taking a structured walk over an area or volume is hard to imagine.



universally agreed that most engineering surfaces exhibit fractal characteristics over certain scales, the relation of fractal surface parameters to surface performance or processes has achieved mixed success and rarely proceeds from the comparison of conventional measures to the derived fractal parameters. However, methods of deriving fractal parameters from profilometer data have been documented (e.g. Underwood & Banerji, 1986, Vallejo & Zhou, 1995).

### Fractal analysis of steel surfaces

The method used here is based on the structured walk technique pioneered by Mandelbrot (1977) and bears a close resemblance to that laid out by Brown & Savary (1991). For the surfaces investigated here other than granular, the profile ordinates obtained using the Talysurf profilometer and corresponding to five parallel traverses at different locations across a surface of 5mm length and with sampling interval of 0.25µm were transferred to a personal computer for analysis. A computer programme was written to enable the derivation of compass-method fractal plots by measuring the apparent length of each profile using progressively shorter rulers. The measuring sequence always started with a digitised point on the profile. The straight-line distance to each progressive point was compared to the yardstick until, in general, two adjacent points were identified between which the end of the yardstick fell. The new starting point was found by considering the right-angled triangle whose sides consisted of the line passing through these two points, its perpendicular passing through the previous starting point, and hypotenuse of length equal to that of the yardstick. Because no fractions of yardsticks were allowed, the nominal or single-straight-line projected lengths of the profiles ( $P_L$ ) were in general slightly different for each yardstick length. Hence, following Brown & Savary (1991), the measured or apparent lengths  $A(l)$  were normalised by dividing by  $P_L$  to produce  $R(l)$ , the relative profile length. From Equation 6.15:

$$\frac{A(l)}{P_L} = \frac{cl^{(1-D_s)}}{P_L} \quad 6.16$$

$$R(l) = Cl^{(1-D_s)} \quad 6.17$$

Typical data for five profile segments of the ALO interface block are presented in the form preferred by Brown & Savary (1991) in Figure 6.3(a). The close similarity of the five traces relates to the uniformity of topography produced by the grit-blasting process. The average of the five traverses is displayed in Figure 6.3(b) in which four separate regions are seen, similar to those observed by Brown & Savary (1991):

1. When using large yardstick lengths,  $R(l)$  is close to unity, illustrating scale above which the surface is best described by Euclidean geometry.
2. Shorter yardsticks are associated with a transition region during which  $R(l)$  increases at a rate in excess of the decreasing step length. Within this region is the step length below which the surface can no longer be regarded as planar.
3. The plot then again becomes linear and increases in  $R(l)$  are proportional to the decreases in  $l$ . This region corresponds to the scales at which the surface exhibits self-similarity and fractal characteristics.
4. The gradient of the plot reduces as  $R(l)$  asymptotically approaches a maximum value. Scanning electron microscopy used by Brown and Savary (1991) to obtain a three-dimensional impression of the scar left by their Profilometer's stylus indicated that the uppermost peaks of the highest asperities were flattened by interaction with the stylus. In addition, the full penetration of the deepest valleys was not observed. Recalling that the spacing between the profile points comprising the data set was here  $0.25\mu\text{m}$ , the tendency towards constant  $R(l)$  at short step lengths is probably a consequence of  $R(l)$  becoming close to the data point spacing exacerbated by the contact nature of the measuring device.

These four regions were found to be common for each of the metal surfaces roughened to different degrees as seen in Figure 6.4 where increases in roughness are seen to push the curves upwards and to the right. The inset of Figure 6.4 relates to a detail of the main figure between step-lengths of 1 and  $10\mu\text{m}$ .

Using similar plots, Brown & Savary (1991) derived two parameters that they claimed characterised the surface texture. The first, relating to region 3, was derived from the  $\log R(l)$  against  $\log l$  plot and was equal to the most-negative gradient of the linear regression analysis over ten consecutive step lengths. Alternatively, the regression coefficient over a similar number of step lengths that is closest to 1 could be used, although here the difference between the parameter obtained using both methods is negligible. Recalling Equation 6.17, the surface's fractal dimension  $D_c$  can be obtained by adding a value of 1 to the absolute value of this slope. However, the utility of the measure is not increased by such an operation and so here the measure of roughness complexity or intricacy is left as the absolute value of the minimum slope and called  $d_c$  to distinguish it from the compass dimension  $D_c$ .

The second parameter derived from the structured walks relates to the scale above which the surface is

essentially smooth and best characterised by Euclidean geometry. Termed the roughness threshold or smooth-rough crossover  $C_r$ , it characterises the step length at which  $R(l)$  begins to deviate significantly from its minimum value of unity. Brown & Savary (1991) defined  $C_r$  with reference to the maximum value of  $R(l)$  when  $l$  assumes small values close to the profile's data point spacing.  $C_r$  was then defined to be the step length at which  $R(l)$  first exceeds 10% of its maximum value.

The relative magnitudes of the fractal parameters are compared to those of conventional parameters in Figure 6.5. The pattern of increase in  $C_r$  from POL to SIC is very similar to that of the amplitude parameters. The relationship between values of  $d_c$  recorded for the different surfaces bears a closer relation to the conventional parameters that provide a measure of the average absolute slope of surface texture.

### Fractal analysis of granular surfaces

The longer traverses necessary to acquire sufficient profile information for the reliable estimate of roughness parameters of the granular surfaces are associated with a larger horizontal spacing between the constituent data points. In this way, small-scale profile data of large traverses is lost. The effect on fractal analysis can be seen by increasing the data point spacing of say a SIC profile and comparing the resulting structured walk data with that of the original profile. This is done in Figure 6.6 where increases in data point spacing prematurely reduce the gradient of the fractal plot. However, because  $d_c$  is derived from region 3 soon after the step length that corresponds to  $C_r$ , small increases in data point spacing have little effect on its magnitude. The value of  $C_r$  itself, however, will be overestimated because of the underestimate of the 10% value of the asymptotic  $R(l)$ .

Structured walk plots relating to the granular surfaces are displayed in Figure 6.7(a) and have their relative magnitudes compared to those of conventional parameters in Figure 6.7(b). Again  $C_r$  is seen to most closely correspond to the amplitude parameters, especially if the value presented here is an overestimate and recalling that amplitude parameters of granular surfaces may be associated with underestimation due to stylus flanking and an insufficient stylus penetration. Like for the smoother metallic surfaces,  $d_c$ , exhibits a pattern similar to the slope parameters.

## 6.6 Friction and wear

Attention is now turned from the geometry of solid surfaces to the interaction of surfaces in relative motion. Friction, the resistance acting in the opposite direction to motion when one body slides across

another under load, has been scientifically studied for over three hundred years. Amontons (1699) postulated a model of friction based on experimental observations that is still much in evidence within the literature today. The tangential or frictional force  $S$  between two surfaces in relative motion was found to be directly proportional to the normal force  $N$  acting across them with a constant of proportionality of  $\mu$ , the coefficient of friction. Hence:

$$\mu = \frac{S}{N} \qquad 6.18$$

Many theories have attempted to explain Amontons' (1699) observations, perhaps the most lauded being Bowden and Tabor's (1967) adhesion theory.

The adhesion theory of friction starts with the premise that when typical engineering surfaces are loaded together, actual inter-body contact occurs at the tips of opposing asperities and amounts to an extremely small percentage of the apparent area of contact. The stresses transmitted at the points of inter-body contact are consequently sufficient to cause plastic flow and thus, the true area of contact increases until  $N$  can just be supported elastically. Thus, the area of contact is proportional to the normal load. At the points of actual inter-body contact, strong attractive forces are generated between the neighbouring atoms of opposing asperities and "junctions" are formed as the materials of opposing surfaces cold-weld. Bowden & Tabor's (1967) premise is that the shear strength of these junctions, which continually break and reform as asperities of opposing surfaces interact during sliding, comprises the main source of friction. In this way Amontons' (1699) model is satisfied, since the adhesion term is proportional to the true area of contact and thus to the normal force between surfaces. In addition, the experimental finding that the friction coefficient between very smooth metal surfaces can be equivalent to the bulk shear strength of the metal is explained.

Such adhesive behaviour is not confined to metal surfaces. Freshly cleaved rock salt crystals loaded together by Bowden & Tabor (1967) needed a force to separate them equivalent to the shear strength of an intact crystal. In addition, adhesive behaviour is exhibited between surfaces of very different materials. When Bowden & Tabor (1967) loaded a cone of the soft metal indium onto a clean rock salt surface under 3kg without sliding, a 2kg tensile force was required to separate it, leaving a patch of indium attached to the rock salt surface.

Under normal experimental conditions, Bowden & Tabor (1967) note that surfaces are often covered with a contaminating layer of oxide and contaminants such as grease and dust forming a film which disrupts

the formation of junctions. In addition, as opposing surfaces slide, material becomes deformed and perhaps detached producing work hardened fragments of material trapped between the surfaces, diverting behaviour further from the idealised adhesion model. Such phenomena were used to explain the deviancy of various sliding systems from Amontons' (1699) model.

In addition to the adhesion component, Bowden & Tabor (1967) recognise the existence of a ploughing term in the coefficient of friction. They report that this term becomes significant only when sufficient differences in hardness exist between sliding surfaces and relates to the force required to bring about flow of one surface material around the harder counterface's asperities. The total friction force is then given by the sum of the adhesion and ploughing components. More recently, it has been suggested that even between surfaces optimised to reduce the ploughing term, the mechanical interactions at the sliding interface remain extremely important in determining the friction force (Kim & Suh, 1991).

The removal of material via surface processes is known as wear, a phenomena that has been the focus of scientific investigation for a mere fifty years. When caused by hard particles it is called abrasive wear, two-body abrasive wear being caused by hard protrusions on a counterface, and three-body abrasive wear by discrete particles free to roll and slide between surfaces. The former comprises most of the voluminous literature concerning wear and results are often interpreted using the Archard (1953) wear equation. This much cited equation relates the volume of worn material  $V$  to the normal load  $N$ , the sliding distance  $v_s$ , and the hardness of the worn surface  $H$  via a wear coefficient  $k$ , analogous to the friction coefficient  $\mu$ :

$$V = \frac{kNv_s}{H} \quad 6.19$$

Thus, in much of the wear literature no reference is made to the friction force, only volumes or rates of material removal.

Contact between abrasive particles and a surface occurs at many locations each with different geometry and loading, and each of which contributes to the friction force. The precise local conditions at each point of contact will determine the behaviour there exhibited. The properties of the surface change not only as one moves across the surface, with the peaks and valleys of surface texture, but also as one descends into the surface, with hardness gradients arising from particular surface preparation procedures and the presence of contaminant films covering the surface. In addition, the surface material's properties (hardness and texture) may change during the abrasive process as it is stirred by the abrasive particles.

Abrasive particles may become embedded within the surface material, and removed surface material will become mixed up within the abrasive particles. Fatigue may play a role as both abrasive grains and surface asperities are continually subjected to load cycles.

The complexity of everyday wear processes is tremendous and a great deal of research has been done in the hope of identifying the critical mechanisms at work. To prevent discussion becoming bogged down in details, it is not the intention to give a state-of-the-art review of this body of work. Instead it is intended merely to indicate some of the findings of wear research that bear close resemblance and carry enough weight of experimental evidence to perhaps be influential during sand-steel interface friction. Discussion begins with a theoretical look at the interaction between a single asperity and a plane.

## 6.7 Asperity-surface indentation

The interaction between a single asperity and a softer body falls within the realms of a branch of tribology known as hardness testing. Here a theoretical consideration of the contact between a sphere and a plane surface is given.

Hertz studied the contact between a perfectly-smooth elastic sphere of radius  $R$  is loaded into a perfectly-smooth elastic plane under a force  $N$  (Johnson, 1985). The area of contact  $a$  is given by

$$a = \pi \left( \frac{3NR}{4E} \right)^{\frac{2}{3}} \quad 6.20$$

where  $E$  is an elastic modulus which depends on each materials' Young's moduli,  $E_1$  and  $E_2$ , and Poisson's ratios,  $\nu_1$  and  $\nu_2$ , given by:

$$\frac{1}{E} = \frac{(1-\nu_1^2)}{E_1} + \frac{(1-\nu_2^2)}{E_2} \quad 6.21$$

Thus, if contact remains elastic,  $a$  is proportional to  $N^{2/3}$ , the mean contact stress is given by  $N/a$  and varies as  $N^{1/3}$ . The stress distribution is not constant over the contact area but has a maximum in the centre and falls to zero at the edge. Underneath the contact area's centre the maximum stress is a factor of 1.5 times the mean stress.

Increases in  $N$  eventually bring about the plastic deformation of either the sphere or the plane when the

shear stresses developed within satisfy a yield criterion. The case considered here is one where the sphere is rigid and plastic flow is confined to the plane. Hertz's analysis of the elastic stress field generated underneath a spherical indenter on a flat surface shows that the maximum shear stress beneath the centre of the contact area occurs at a depth of approximately  $0.47a$  and it is at this point where plastic deformation will first commence. This is perhaps best envisaged by the isochromatics of the photo-elastic stress distribution within the plane beneath a cylindrical indenter's footprint reproduced from Arnell et al (1991) in Figure 6.8(a). Increases in  $N$  bring with it expansions of the zone of plastic deformation although until it extends to the surface, the area of contact between the indenter and the surface remains small since the plastic zone is constrained by surrounding elastic material.

Yielding of the surface material marks the onset of significant indentation of the sphere. The mean contact pressure underneath the indenter then becomes nearly constant and any increase in  $N$  is balanced by an increase in  $a$  as the indenter sinks into the surface until the full load can just be supported elastically. The constant of proportionality between  $a$  and  $N$  is known as the hardness  $H$  and can be interpreted as the mean contact pressure when deformation is fully plastic:

$$H = \frac{N}{a} \quad 6.22$$

Hardness values are related to a material's uniaxial plastic flow or yield stress  $Y$  (the mean stress at which a cylindrical specimen loaded between two flat, parallel plates becomes fully plastic) via the constraint factor  $C$  such that:

$$H = CY \quad 6.23$$

The magnitude of  $C$  depends upon the geometry of the indenter among other things but for metals is not found to deviate substantially from 3 (Shaw, 1971).

The Vickers hardness is found by pressing a square based pyramid indenter with an included angle between its sides of  $136^\circ$  into a smooth surface under load  $N$ . The contact area of the footprint remaining after the removal of the indenter is calculated and the hardness quoted with symbol HV replacing the units to which the reading corresponds ( $\text{kg force per mm}^2$ ). Noting that the contact stresses on a hardness tester's indenter are equivalent to those imposed on the test specimen, to ensure plastic deformation is confined to the test specimen the indenter's hardness must substantially exceed that of the surface. Shaw (1971) states an indenter's hardness should be at least two and a half times greater than that of the test

material.

The hardness of silica is quoted by Hutchings (1992) as lying in the range 750 to 1200 HV which envelopes the hardness values for the same material found elsewhere (Lambe & Whitman (1969): 1100 HV, Bowden & Tabor (1964): 1000 HV). The nominal hardness of the Grade 43a steel out of which the interface blocks are machined is 121-149 HV. Thus, taking extreme values, the hardness of the sand particles is likely to be at least a factor of five times greater than that of the interface blocks and sufficient normal load will thus cause indentation.

## 6.8 Asperity-surface scratching

The application of a tangential force to a hard protrusion loaded against a softer surface is to stress a smaller volume of material closer to the plane surface, as indicated by the photo-elastic distribution in Figure 6.8(b). Thus, macroscopic plastic deformation becomes easier in the presence of tangential forces. Increases in the magnitude of the tangential force will eventually bring about the displacement of the protrusion relative to the surface. There is a voluminous body of literature addressing the sliding of both single and multiple protrusions against a softer counterface. This section introduces some of the findings of that work.

Childs (1988) identified three main types of surface flow associated with the scratching of a metal by a harder asperity by investigating the flow around conical asperities of different internal apex angle. Photographs of the resulting wear scars are reproduced in Figure 6.9. Blunt asperities were associated with the flow of material around them in a wave with little material removal. Sharper asperities, on the other hand, removed threads of material from the surface, deflecting them upward over the asperity's cutting face and thereby removing large volumes of material from the surface. Intermediate asperities caused a prow of material to be formed ahead of them at the start of sliding which intermittently became detached and replaced. For a surface to be said to be worn there must be loss of mass. A surface undergoing plastic deformation which although modifying its topography fails to result in material detachment is not, strictly speaking, worn at all. The changes in surface topography by redistribution of material due to plastic flow without net loss has been called "plastic squeezing" (Summers-Smith, 1969). The wear associated with sharp asperities has been called "severe" and linked to the roughening of the surface texture (Hutchings, 1992).

Maan & Broese Van Groenou (1977) carried out low-speed, single-point scratching experiments similar to those of Childs (1988) but on steels of various composition. What makes their work especially



relevant is that the force required to plough the resulting wear scars was measured. The asperity angle, the surface hardness and the normal load were found to be influential in determining the friction and wear response. These will be discussed in turn.

### **Asperity angle**

As one would expect, considering Child's (1988) micrographs (Figure 6.9), Maan & Broese Van Groenou's (1977) friction coefficients and wear volumes increased with the sharpness of the indenter. Many theories of friction based on deformations of surface material have this as a common characteristic: the energy consumed in plastic deformation increases with the sharpness of the asperities (see, for example Edwards & Halling, 1968). This helps explain the widely accepted observation that friction coefficients between macroscopic bodies increase with the mean absolute surface slope (Koura & Omar, 1981, Tabor, 1987, Arnell et al, 1991).

### **Surface hardness**

Many researchers (e.g. Goddard & Wilman, 1962) duplicate Maan & Broese Van Groenou's (1977) finding that the friction coefficient reduces with increasing hardness. Although Bowden & Tabor (1967) conclude hardness has little effect on the adhesion component of friction, they recognise its importance in sliding situations dominated by deformation. By sliding indenters of various geometry along a metal bar one end of which was subjected to suitable heat treatment, thereby introducing a hardness gradient along its length, Bowden & Tabor (1967) showed scratching to increase friction coefficients when the surface became sufficiently soft. It was concluded that an asperity would just scratch a surface when its hardness exceeded 1.2 times the hardness of the surface. It should be recalled from Section 6.7 that the relative hardness of silica and mild steel is greatly in excess of this value.

### **Normal load**

Maan & Broese Van Groenou's (1977) finding that  $\mu$  increases with normal load is contrary to Amontons' (1699) model of friction but is supported by experimental evidence voiced elsewhere in the literature. For example, when investigating three-body abrasive wear, Misra & Finnie (1983) found the friction coefficient between a spinning disk and a 19mm diameter column of particles held within a tube to decrease when the load bearing down on the column fell below 1kgf (equivalent to  $\sigma'_{yy}$  of 35kPa). Low normal stresses necessarily load small volumes of surface material. Within the literature, a "size effect" apparent during surface processes is well documented.

Sin et al (1979) found the friction coefficient between emery paper and a metal pin increased with the size of the paper's abrasive particles when they had diameter below  $100\mu\text{m}$ , yet remain essentially constant above this size. It has been established that the wear rate in two-body abrasion increases rapidly with abrasive particle size to some critical size after which particle size has a lesser or no effect on wear rates (Misra & Finnie, 1981). In three-body abrasion, wear rates are also seen to reduce as the mean diameter of abrasive particles falls below a specific size (Misra & Finnie, 1983). Similar trends are also apparent during "erosion" of metal surfaces, when the abrasive particles carried by a fluid stream strike a surface and are deflected. This size effect is illustrated in Figure 6.10 where a diameter of around  $100\mu\text{m}$  marks the critical particle size after which increases in size have little effect on wear rates.

Researchers have often tried to explain the size effect for individual processes, even though it is apparent during wear processes involving numerous abrasives and abraded materials, single or multi-point contacts and over a wide range of interaction speeds. Consequently, numerous explanatory theories have been suggested as highlighted by Misra & Finnie (1981). Gane & Skinner (1973) suggested an explanation that has applicability for all wear situations and has been replicated on numerous occasions.

Metals are made up of crystals consisting of arrangements of atoms held together by the electromagnetic forces between electrons of neighbouring atoms. The strength of metals is very much lower than the value predicted by the electrostatic attraction between the valence electrons and positively charged atoms because defects disturbing individual crystal lattices are born during crystal growth. The defects that are mainly responsible for metal plasticity are termed dislocations and it is their mobility that is the cause of macroscopic permanent deformations, as illustrated in Figure 6.11. As the scale of abrasive surface interactions diminish, be it by reducing the normal load or decreasing the particle size, so does the volume of surface material affected by the interaction. When the volume becomes very small, it may not contain the concentration of dislocations representative of the metal in bulk making the operation of dislocation processes more difficult.

This postulate has been used to explain why tensile strength of metal whiskers increases rapidly as their diameter reduces and why micro-scratch and indentation hardness tests, which necessarily stress lower volumes of material, produce estimates of hardness many times greater than macro-scale tests (Mott, 1957). In addition, Gane & Skinner (1973) invoked the postulate to explain why scratch hardness was measured to be larger than indentation hardness since indentation tests load the half space below the indenter while scratch tests load only the forward quadrant bounded by the surface and the stylus's axis. Likewise during abrasive processes, small-scale interactions involve harder surface material and are

therefore associated with lower wear rates and friction coefficients.

## 6.9 The movement of particles relative to surfaces

Of course, when discrete particles are made to displace relative to a solid surface under load, they do not necessarily slide but are also free to roll.

Fang et al (1993) investigated the movements of single sand particles sandwiched between two horizontal metal faces when one of the surfaces was displaced at a rate of 0.6mm/s to the other. Photographs taken as the test progressed are shown in Figure 6.12 and reveal that there were indeed two types of movement: sliding and rolling. Examination of the metal faces revealed the tracks left by a sliding particle took the form of a groove whereas rolling particles were associated with a more random pitting as seen in Figure 6.13. Micrographs taken by Williams & Hyncica (1992) of a worn surface during which abrasive particles had primarily rolled or slid are reproduced in Figure 6.14 illustrating similar effects of topography.

The evolution of the friction coefficient from the test's outset for Fang et al's (1993) rolling and sliding particles are shown in Figure 6.15. The rolling particle, being associated with large fluctuations of friction coefficient, mobilised a peak value in excess of but an average value below that of the sliding particle.

Fang et al (1993) attempted to discover the criterion that determined a particle's choice of movement pattern by investigating the system's force and moment equilibrium permitted by the well-defined geometry of their experiment, as indicated in Figure 6.16. Using a series of simple inequalities, it was argued that the critical parameter in determining the movement pattern was the geometric ratio  $el/h$ , as defined in Figure 6.16, and that sliding would occur only when the magnitude of this ratio exceeded the coefficient of friction  $\mu$  of the system. Experimental evidence from 20 different particles did indeed indicate that particles with  $el/h$  ratios in excess of  $\mu$  slid whereas those with lower ratios rolled.

By modelling the particle as a sphere,  $el/h$  was shown to be a function of the tribological system. A rather complicated expression for  $el/h$  was derived in terms of the system parameters assuming the upper and lower surface to have different hardness from which a much simpler expression can be formed if the hardness values are assumed equivalent. For our purposes, this simpler expression contains the necessary explanatory potential:

$$\frac{e}{h} = \frac{1}{1 - N/\pi R^2 H}$$

6.24

From this it can be seen that  $e/h$  increases either with increases in the normal load  $N$  or with decreases in the surface hardness  $H$  or particle radius  $R$ , bringing with it an increased likelihood of sliding. Thus Larsen-Basse & Premaratne (1983), who performed similar experiments but with collections of silica sand particles sandwiched between steel faces of different hardness, found that under a load of 1.6N the abraded surfaces of the steel post-test were covered in pits caused by particle rolling. The abraded surfaces left after testing under a 6N load, however, were covered in scratches brought about by the sliding of particles. In addition, it is a common finding that large particles are more likely to slide on a given surface than smaller particles (e.g. Uesugi & Kishida, 1986(a) and Paikowsky et al, 1995). This may relate to increases in the load per particle when such samples are tested in shear apparatus with constant plan area.

## 6.10 Interface friction in the soil mechanics literature

The overview of the tribology literature illustrates that the mechanisms of interaction between particle and surface are determined by the hardness ratio between the two. Within the soil mechanics literature, it will be seen that hardness differentials between interface constituents have been considered only recently and only in relation to geosynthetics. An upshot of this has been a concentration on the geometry of sand-steel contact. Diagrams theorising the contact geometry have formed the basis of fundamental arguments concerning the mechanisms of interface friction. For example, by considering a circle sitting on a saw-toothed plane, Paikowsky et al (1995) concluded that increases of surface roughness or decreases of particle size bring with them increases in the angle  $\alpha$  between the average plane of contact and the plane of movement and consequential increases in the angle of interface friction.

A representation of this geometry is here provided by contrasting small-scale profile segments of single sand particles and surfaces. Particle segment profiles have been obtained with the judicious use of the Talysurf profilometer to traverse a portion of a particle after its attachment to a massive steel block with Araldite to prevent the particle's relative displacement under the force of the stylus. Segments of a VLB and SFS particle pictured above the GND and ALO surfaces are shown in Figure 6.17 and Figure 6.18 respectively. The geometrical effects apparent in Paikowsky et al's (1995) highly idealised model are again apparent in these more realistic representations of contact geometry. However, it is the premise here that such diagrams give a misleading insight into interface behaviour.

The tribology literature indicates that it is incorrect to regard the constituent steel surface of an interface as an unyielding boundary whose influence is entirely accounted for by characterisation of its topography. Nevertheless, this is the path chosen by the overwhelming majority of interface friction investigations, as highlighted in the following review. The work considered here is by no means a complete catalogue. It is merely intended to highlight the most important findings.

### Early studies

Potyondy's (1961) seminal study featured two soils, a cohesive and non-cohesive, deposited in a direct shearbox of which the lower frame had been replaced by a specimen of a construction material, be it steel, concrete or wood. Four factors were determined as being influential to the resistance each interface was able to offer: the moisture content of the soil, the construction material's topography, the composition of the soil, and the intensity of the normal stress. For the roughest surfaces, the peak angle of wall friction  $\delta'_{peak}$  approached the  $(\phi'_{ds})_{peak}$  value recorded in equivalent soil tests. On smoother surfaces, lower  $\delta'_{peak}$  values were recorded. Interfaces constituting silt also produced higher resistances than those constituting sand. Similarly, Rowe (1962) found the  $\delta'_{peak}$  value between a quartz block and quartz particles to decrease with increasing size of the particles, from  $31^\circ$  for silt to  $22^\circ$  for pebbles.

Skinner (1969) was interested in particle movements during shear. Reporting that the presence of water increased the friction coefficient between sliding glass surfaces by as much as thirty-fold, he demonstrated that the inter-particle friction did not affect the direct shear response of a collection of glass ballotini by performing tests dry and saturated. Flooding markedly affected the response of an interface comprising glass ballotini and a glass plate. Its resistance nearly doubled and dilatancy activated as particles were said to roll rather than slide.

Butterfield & Andrawes (1972) showed great foresight by considering the frictional force developed between a mass of particles and a solid surface to relate to ploughing phenomena. Until very recently, this role of ploughing in interface friction has been forgotten within the soil mechanics literature.

Brummond & Leonards (1973) performed an experimental study to investigate the friction between two sands and rods of different materials: steel, smooth mortar and rough mortar, some of which were coated with graphite or Teflon. The test configuration consisted of a cylinder of sand encased in a rubber membrane with a rod located along its axis. Normal stresses were applied to the rod by evacuating air from the sample. An axial force then caused the relative displacement between the soil and the rod. The coefficient of friction was greatly influenced by the size, angularity and surface texture of the grains with

angular particles consistently producing higher friction coefficients than well-rounded particles.

Heerema (1979) investigated interface friction by applying a vertical shear load to a steel plate pressed against soil contained within a sampling tube stood on its end and split in half length ways. The angle of wall friction was found to be independent of normal (horizontal) load.

Kulhawy & Peterson (1979) performed sand-concrete interface tests using a large (406 by 406mm) DSA and found that for dense sands,  $\delta'_{peak}$  values were typically higher than equivalent  $(\phi'_{ds})_{peak}$  values. Contrarily, Yoshimi & Kishida (1981a) found  $\delta'_{peak}$  values less than  $\phi'_{peak}$  values, even on very rough surfaces ( $R_r = 510\mu\text{m}$ ) where the surface irregularities were of magnitude in excess of  $D_{50}$  (0.2 to 0.3mm).

### The 1980's

Yoshimi & Kishida (1981b) utilised a ring torsion device in which steel rings of wide ranging roughness were lowered onto an annulus of sand and subjected to torsion. The steel rings' roughness was quantified using the  $R_r$  amplitude parameter, defined as the maximum vertical distance between the highest peak and the lowest valley over the traverse length (there called  $R_{max}$ ), the standard measure of roughness in Japan. Radiography of the changing positions of lead markers positioned within the sample during deposition allowed the sand's deformation to be observed. As illustrated in Figure 6.19(a), the mobilisation of interfacial resistance was initially independent of steel topography. The changing positions of the lead markers revealed that early displacement was accounted for by deformation of the sand mass. For the rougher surfaces, as the circumferential displacement increased, the increase in resistance reduced until a surface-roughness dependent maximum was mobilised of limiting magnitude approximating  $\phi'_{crit}$  (Yoshimi & Kishida, 1981a). The resistance of interfaces featuring smooth surfaces exhibited peak behaviour at small displacements and dilatancy was not activated. As shown in Figure 6.19(b & c) a wide range of interfacial resistances, both peak and large displacement or what they called residual, were found to correlate well with surface roughness. Interfacial response was found to be independent of density, the trend lines shown in Figure 6.19(b & c) agglomerated from data for sands with  $D_r$  ranging from 40 to 90%. In addition, the more angular Tonegawa sand tended to mobilise larger resistances.

Contrary to Yoshimi & Kishida (1981a & b), many authors have concluded that density does have significant influence on interface behaviour, with dense sands offering higher interface resistances just as in soil tests. Subba Rao et al (1996a) surveyed the literature and explained the contrary conclusions relating to density as being due to differences in test configuration, and in particular whether the surface was positioned above the sand mass to create a "Type A" configuration, or below to create a "Type B". A

"surface film" of grains was said to exist adjacent to a sand mass's free surface with a structure irrespective of the density to which the sand mass was prepared but resembling the internal structure of a loosely deposited sample. Thus, an interface created when a surface is lowered onto a sand mass will mobilise a resistance independent of sample density and limited by the soil's critical state friction angle. Conversely, if a sand mass is deposited on a surface then the resulting behaviour is density dependent and the maximum limiting interface resistance is equivalent to the peak shear strength of the sand at the same density. Subba Rao et al (1996a) concluded that the sand-over-steel test configuration was the optimum since it was able to provide information concerning the density-dependent resistance, at peak, and the non-density-dependent resistance, at large displacement.

Uesugi & Kishida (1986a) investigated interface friction using a SSA that consisted of a stack of Teflon-coated aluminium plates, each with an internal opening in which the sample was deposited, overlying the steel surface. A constant confining load was applied to the sample and a shear load to the steel. Typical data for dense Toyoura sand ( $D_{50} = 0.19\text{mm}$ ) under 78.4kPa on surfaces of different roughness are reproduced here in Figure 6.20. The concept of functional filtering was applied to the assessment of interface surface roughness. Filtering profilometer data has the effect of smoothing surface irregularities of certain wavelengths in order to exclude their effect on derived roughness parameters. Filters are usually employed when the roughness component of surface texture needs to be separated from the waviness component. Functional filtering involves limiting the range of irregularity wavelengths considered to include only those relevant to the application (Thomas, 1982). Uesugi & Kishida realised that the length of the Profilometer's traverse set the upper limit to the surface wavelengths that can affect the texture measurement. Postulating that long wavelength surface irregularities do not necessarily have a slope great enough to increase the coefficient of friction, they proposed limiting the traverse length to  $D_{50}$ , the mean particle diameter of the interface's constituent sand. Fundamentally, the recognition was that there were specific scales of interaction relevant to the contact phenomena between a granular material and a solid surface, and thus only irregularity wavelengths relevant to that scale should be considered. Uesugi and Kishida's (1986a) functional filtering can be summarised with reference to Figure 6.21 where the desired reductions in  $R_f$  seen when reducing the traverse length for wavy surfaces is contrasted to the small effect the same operation has on surfaces without large wavelength irregularities. However, to obtain sufficient profile information to produce a roughness parameter representative of the surface when employing the necessarily short traverse lengths, Kishida & Uesugi (1987) found it averaged the roughness parameters recorded at 390 individual points across the surface.

The quantification of surface texture in this manner produced reasonable linear relationships when plotted against the peak interface resistance of various granular materials, as seen in Figure

6.22(a). The upper limiting value of the peak resistance was the shear strength of the sand and, as seen in Figure 6.22(b), the normal stress was found to have little influence on peak resistance. The large number of experimental variables requiring control led Uesugi & Kishida to set a precedent for reporting interface results by presenting broad-based correlations featuring data obtained under a variety of circumstances. Consequently, peak strength is the interface parameter most often reported, with attention being turned to strengths at larger displacements only recently, and dilational behaviour is, if not ignored altogether, then sidelined.

Following Uesugi & Kishida, the quantification of surface texture with reference to  $R_t$  assessed over traverse lengths equal to  $D_{50}$  has become common within the soil mechanics literature. For sands with similar particle geometry but of different scales, a good correlation between surface roughness and peak interface resistance is often reported after normalising this roughness measure by  $D_{50}$  to obtain what has been termed the normalised roughness  $R_n$  (Uesugi & Kishida, 1986b). Paikowsky et al (1995), for instance, classified interfaces as either "smooth", "intermediate" or "rough", depending on the peak resistance it was able to offer after performing tests using glass beads in an apparatus devised specifically to investigate interface friction described in detail later. As illustrated in Figure 6.23(a), smooth interfaces exhibited a narrow range of friction angles and small volume changes with no indication of dilation. Rough interfaces exhibited large, density dependent specimen dilation and mobilised resistances equivalent to the intact sand's internal resistance. Intermediate interfaces were characterised by an increase in the frictional resistance with increasing surface roughness. Kishida & Uesugi (1987) found  $R_n$  to have similar correlating prowess when investigating interfaces featuring different gradings of the same sand. Paikowsky et al (1995) argue that the correlating ability of  $R_n$  relates to the observation that the contact plane between a rough surface and a sand particle will be more steeply inclined the smaller is the size of the particle.

Uesugi & Kishida (1986b) quantified the angularity of sand particles by using a "modified roundness" in which the particle's curvature in different locations was weighted into a single parameter which equalled unity for spherical particles and reduced with increasing angularity. Agreeing with Brummond & Leonard's (1973) observation, it was established that angular particles mobilised higher resistances. Multiplying the peak resistance by the modified roundness, as in figure Figure 6.23(b) provided a fair correlation when plotted against  $R_n$  for sands with particles ranging from very angular (Seto sand), through angular (Fujigawa sand) to sub-rounded (Toyoura sand). It was not attempted to explain this dependency of friction on particle angularity. However, it should be recalled that Maan & Broese Van Groenou (1977) found that during scratching experiments friction coefficients increased with the scratching asperity's sharpness due to an increased tendency for surface ploughing, illustrated



succinctly in Child's (1988) micro-graphs (Figure 6.9).

By recording the horizontal displacement of both the uppermost and lowermost aluminium plates of their SSA, Uesugi & Kishida (1986a) distinguished between the deformations of the sand mass from the slip between the sand and the surface. As illustrated in Figure 6.24(a), deformation primarily took place within the sand mass before peak resistance, thereafter being accounted for by slip at the sand-surface contact plane. Consequently, and as illustrated in Figure 6.24(b), the displacements to mobilise specific states were higher during direct shear tests than simple shear because the deformation of the sand mass was hidden by the rigid walls of the apparatus. No other differences between DSA and SSA test data were reported. A window later installed in the side of the apparatus allowed the tracking of the individual sand particles (Uesugi et al, 1988). On smooth surfaces, the sand mass approximated a rigid body and all shear displacement was accounted for by sliding on the sand steel contact plane. On a rough surface, however, the sand mass underwent a simple shear type deformation until peak resistance whereupon displacement between the sand mass and the surface began in earnest and particles adjacent to the surface slid, rolled and moved vertically as a thin shear zone was formed.

Uesugi & Kishida (1986a) also examined the effect of particle crushing during testing. Linear relationships dependent on normal stress were obtained between the weight of degraded particles, calculated by post-test sieving, and the shear displacement. The dependency on normal load was lost when the weight of crushed particles were plotted against what was termed the "plastic work of friction", equivalent to the cumulative product of  $S$  and the increment of  $v_x$ .

Uesugi et al (1989) went on to investigate the changes in interfacial resistance brought about by repeated loading, later mimicked but using a direct shear apparatus and carbonate sands by Al-Douri & Poulos (1991). Uesugi et al's (1989) tests remain the most comprehensive. After the initial shear displacement of 4mm, a cyclic shear amplitude of 8mm was applied with each reversal incrementing the number of cycles by one. The evolution of interface resistance with cycle number for interfaces with different  $R_n$  values are presented in Figure 6.25(a). When sand particles are small in comparison to the surface irregularities, i.e. the interface has a high  $R_n$ , peak resistance rapidly falls to what Uesugi et al (1989) called a "residual" value mimicking the terminology used by Yoshimi & Kishida (1981a & b), at which it stays irrespective of cycle number. Observation of sand particle motion through a window built into the side of the apparatus permitted the uniform deformation of the sand mass before peak resistance to be contrasted with the concentration of strains within a thin band of soil adjacent to the surface during later cycles. The development of this shear zone was used to explain the reduction in interface resistance. Figure 6.25(a) also shows the resistance of interfaces featuring the same sand, but having lower  $R_n$  values, to increase

with cycle number until a residual value, similar to that of the rougher interfaces, is mobilised. The increases in resistance were said to arise from particle crushing. Their explanation was that as the plastic work of friction increased the mass of smaller abraded particles, the  $R_n$  value of the interface increased, bringing with it increases in resistance. The relationship between Uesugi et al's (1989) residual interface resistances and  $R_n$  is contrasted with that of peak interface resistances in Figure 6.25(b) wherein the levelling effect of cyclic shearing is again evident.

### The 1990's

O'Rourke et al (1990) employed the by now standard DSA to investigate the friction between polymers and sand, primarily to discover the effect of surface hardness on interface response in relation to buried pipelines. An inverse linear relationship was established between hardness and peak resistance. Interfaces featuring the harder polymers such as HDPE exhibited neither peak resistance nor dilatancy whereas softer polymers were associated with density-dependent dilation and peak strengths. A visual examination of each polymer's topography after testing revealed the harder surfaces to be covered with striations, the number and depth of which increased with  $\sigma'_{yy}$ . Interface testing produced no change to the softer surface's topography. It was reasoned that the particle movement on hard counterfaces was "skidding", whereas on softer surfaces particles rolled, causing recoverable indentation.

Lehane (1992) sought to understand the mechanisms of pile shaft friction. His study featured saturated Labenne sand ( $D_{50} = 0.32\text{mm}$ ) and steel surfaces ( $R_a = 7 \pm 2.5\mu\text{m}$ ) loaded together to produce stresses of  $60 \pm 40\text{kPa}$ , conditions which corresponded to those imposed during instrumented pile field tests. The main features of his tests were that at small shear displacements, dense samples mobilised a peak resistance coinciding with a maximum dilatancy rate after which reductions in shear stress preceded a constant volume shearing condition, attained between 2 to 4mm of shear displacement. Looser samples tended to contract, exhibiting no clear peak resistance but mobilising the same constant volume shear resistance. In effect, the trends were similar to those often observed during conventional shear tests with  $D_r$  affecting peak but not constant volume resistances.

Jardine et al (1993) summarised and collated the interface tests performed at Imperial College by Lemos (1986), Everton (1991) and Lehane (1992). A critical state for interfaces was defined, which was said to be mobilised when grains became "unlocked" from the surface enabling large scale displacement to occur without changes in volume or stress. As summarised in Figure 6.26,  $\delta'_{crit}$  was reported to be independent of relative density, reduced with increasing  $D_{50}$ , and had an upper limit of  $\phi'_{crit}$ . In keeping with dilation characteristics, dense samples mobilised  $\delta'_{peak}$  values which exceeded  $\delta'_{crit}$  by a margin that increased

with  $D_r$ . Over the load range investigated, Everton (1991) found increases in  $\sigma'_{yy}$  bought with them decreases in both  $\delta'_{peak}$  and  $\delta'_{crit}$  and inconsistent changes in dilatancy trends, as illustrated in Figure 6.27. Other authors contradicting Uesugi & Kishida (1986a), by reporting similar stress-level effects, include Acar et al (1982), Lemos (1986), Boulon (1989) and Lehane (1992). Jardine et al (1993) conceded that further research on the dependence of  $\delta'$  on  $\sigma'_{yy}$  was required.

Paikowsky et al (1996) were concerned with the boundary effects occurring during conventional interface testing using the DSA. They pictured the stress distribution in a collection of photo-elastic disks when subjected to interface shear in a 2D direct shear apparatus. The pre-peak stress distribution is reproduced here in Figure 6.28 in which dark disks represent those which carry no load. It is clear that triangular unloading occurs at the upper-frame's front boundary. The stress was transmitted through the idealised granular material in arch shaped chains spanning between the rear boundary and the interface's surface. Paikowsky et al (1995) devised a novel apparatus called the Dual Interface Apparatus, illustrated in Figure 6.29, in an attempt to quantify behaviour over the central portion of a sample, away from the apparatus' end walls. The apparatus featured an upper and lower frame similar to those of a large DSA but divided by a horizontal plate called the "friction bar". Pulling the friction bar out from between the two frames when filled with sand simultaneously induced a sand-over-steel interface in the upper frame and steel-over-sand interface in the lower. Pressure sensor measurements on the front and rear vertical boundaries of the apparatus confirmed similar stress transfer mechanisms as during the idealised model tests (Paikowsky et al, 1996). However, instrumentation within the friction bar allowed the measurement of the shear stress over the friction bar's front, middle and rear portions<sup>2</sup>.

Data relating to the different regions of Paikowsky et al's (1995) apparatus during interface tests featuring Ottawa sand are reproduced in Figure 6.30 wherein interface displacement is seen to subject the rear of the sample to loading and the front to unloading. Thus dilation and contraction are exhibited at the rear and front respectively. The resistance of the apparatus' upper interface could not be separated from the lower and thus the behaviour illustrated in Figure 6.30 is an amalgamation of the distinct mechanisms of sand-over-steel and steel-over-sand interfaces, indicated by the dilatancy recorded below the friction bar being a fraction of that above.

---

<sup>2</sup> To correspond with the classification system here employed, Paikowsky et al's (1995) positional references have been reversed. Using their system, Paikowsky et al (1995) pulled their friction bar from the front of the apparatus. Here, for consistency, it is described as being pulled from the rear.

Dove and his co-workers (e.g. Dove et al, 1997, Dove & Frost, 1999, Frost & Han, 1999) have of late made a concerted effort to understand the mechanism of geomembrane interface friction employing the DSA. Although carrying on the tradition of focussing solely on peak resistances and not considering vertical displacements, their studies are notable in relating observed behaviour to tribological theory. Some interesting findings of these studies are highlighted.

A bi-linear relationship was recorded between  $\delta'_{peak}$  and  $\sigma'_{yy}$  for interfaces featuring smooth geomembranes on which dilatancy was not activated, as illustrated in Figure 6.31(a). At low stress levels, the reducing value of  $\delta'_{peak}$  with increasing  $\sigma'_{yy}$  arises from the primarily elastic contact mechanism and the area of contact between the particles and the geomembrane being related to  $N$  via a power law, as indicated by Hertz's analysis. The origin of interface resistance was said to be adhesion on the particle-geomembrane contact plane. At higher stress levels, hard sand particles were said to plough the softer geomembrane. An increase in stress level then brings greater particle-geomembrane indentation, increasing the apparent sharpness of the grains, and hence increases in  $\delta'_{peak}$  as suggested by Childs' (1988) micrographs (Figure 6.9). The transitional stress level between these different behaviours was dependent on the angularity of the particles; angular particles were said to have a greater ploughing ability, as indicated in Figure 6.31(b).

Dove & Frost (1999) and Frost & Han (1999) presented limited data for interfaces featuring steel surfaces that were said to trigger no dilatancy. Against such surfaces, smooth glass beads exhibited decreases in  $\delta'_{peak}$  with increasing stress level, just as for the softer geomembranes. It was concluded that ploughing is not a contributor to interface strength for hard surfaces since increased hardness constrains shear to a sliding mode well into high stress regions. Unfortunately, no data were presented concerning steel-sand interfaces.

## 6.11 Summary

The topography of macroscopically smooth surfaces is in actual fact extremely complex and a great many surface parameters are commonly used to quantify different topographical features. Here, four metallic surfaces and three granular surfaces of widely varying topography have been assessed using an array of the most commonly found roughness parameters and two newer fractal parameters. By considering the proportional increase of each roughness parameter as one progresses from the smoothest to the roughest surface, certain groups of parameters are found to bear a very similar relationship to one another. Perhaps most remarkable is that the smooth-rough crossover length  $C_r$  and the roughness complexity  $d_c$ , both derived from fractal analysis, resemble the conventional amplitude roughness parameters and

the surface slope parameters respectively. Unlike the conventional parameters, however, the fractal parameters have an inherent physical meaning and so must be the preferred choice of descriptor.

The common belief that friction is a well-understood and simple topic is misguided. Although scientific investigations have been undertaken for over 300 years, there remains no reliable method for estimating the friction coefficient that will be mobilised between surfaces other than through experimentation. Nevertheless, a much-lauded theory of friction attributed to Bowden and Tabor (1967) has identified the friction force to have two components, one due to ploughing and one due to adhesion. The ploughing component of friction only becomes significant when the difference in hardness between sliding surfaces is sufficiently large.

Relative to friction, wear has become the subject of scientific interest only recently. Abrasive wear occurs when a surface is made to interact with relatively hard particles under load, resulting in a changing surface topography and material removal. A number of interesting findings have been presented relating to two-body and three-body abrasive wear investigations:

- Increased ploughing is induced with sharper abrasive particles and increased hardness differential between the abrasive and the surface resulting in increases in both friction and wear coefficients.
- A size effect is apparent in which both friction and wear coefficients increase with the volume of surface material loaded. This may be due to increases in the number of operative dislocations in larger volumes of metal.
- Different movement patterns of abrasive particles affect the resulting surface topography differently. Sliding particles plough wear scars, whereas tumbling particles cause plastic-squeezing or pitting.

Abrasive wear systems commonly investigated have a great similarity to the interfaces found within the soil mechanics literature. It is surprising, therefore, that only the most recent interface friction investigations have started to assimilate the findings of tribology, and those that do primarily feature geosynthetics. Nevertheless, the soil mechanics literature presents the following noteworthy findings:

- Uesugi & Kishida's (1986a) normalised roughness coefficient  $R_n$ , which can successfully be used to correlate the peak resistances at which relative sliding between a granular mass and a steel surface commences.

- Uesugi et al (1989) found increases in cumulative interface displacement brought about by cyclic shear to increase the interface friction coefficient on smooth surfaces. This was thought to be due to the generation of crushed particle debris which find a given surface rougher than the original particles and thus mobilise a higher friction coefficient.
- Jardine et al (1993) and others defined a critical state for interfaces to exist when sand grains become unlocked from the adjacent surface and displacement can proceed without changes in volume or stress. This state was thus mobilised soon after peak.
- The differences in response of sand-on-steel interface tests to steel-on-sand interface tests explained by Subba Rao et al (1996a). The former configuration is preferred since, unlike the latter, it enables the mobilisation of a peak interfacial state.
- Polymers and geosynthetics have their topography influenced by interface friction in a similar manner to the harder surfaces considered in the tribology literature. When stress levels are sufficient to make ploughing dominant, increases in stress level bring with them increases in the angle of interface friction.

Aside from a general ignorance of tribology, the soil mechanics literature has a number of failings. There is a predisposition to investigate the resistance at the onset of sliding, sidelining or ignoring other test data such as dilatancy characteristics or the resistances mobilised at larger interface displacements. In addition, many contradictions are apparent within the literature probably due to the complexity of interface systems. These failings are redressed in the following chapter.

## 7. INTERFACE TESTING

The details and findings of an experimental investigation of interfaces using the WDSA developed in the Part 1 of this work and the surfaces described in Chapter 6 are now discussed.

### 7.1 Methodology

As noted in the previous chapter, the most comprehensive investigation of interface friction employed a simple shear type apparatus that enabled horizontal displacement component due to sample deformation to be distinguished from the slip between the sand grains and the surface (Uesugi & Kishida, 1986a). Clearly, when used to investigate interface behaviour, the DSA does not permit such separation of displacement components. However, because its kinematics correspond to the thin shear zone characteristic of interface failure, the DSA provides a more suitable foundation for interface investigation.

Paikowsky et al's (1995) concerns over the ability of the DSA to generate a uniform stress distribution across an interface's constituent surface are less relevant to the WDSA than his own Dual Interface Apparatus which makes no provision to limit the wall friction forces on the apparatus' internal walls. In effect, Paikowsky et al's (1995) apparatus is burdened by the same problems that mar many conventional DSA. At the rear of his apparatus, sample dilation produces the upward movement of grains relative to the upper-frame's internal wall, and wall friction therefore increases the normal stress on the interface's surface. Thus, if it is assumed that the normal force applied to the load pad is that acting on the rear interface portion, a substantial overestimate of  $\delta'$  results. The reverse is true at the front of his apparatus where contractancy in the upper frame results in a vertically upward wall friction force and an underestimate of  $\delta'$ . The free-floating nature of the symmetrical WDSA's upper ensemble limits the mobilisation of such troublesome wall friction forces and thus aids uniformity.

The behaviour of sand-steel interfaces was investigated using the WDSA in which the lower frame was replaced by an interfacial block with pre-described roughness. The dimensions of the resulting interface's constituent surface were made larger than the plan area of the WDSA to aid data interpretation by not necessitating an area correction. As noted in the previous chapter, this sand-over-steel interface configuration has been reported preferable since it can be used to obtain peak and large displacement interface states, whereas a steel-over-sand configuration merely provides the latter.

The majority of interface tests were performed employing the optimum configuration of the WDSA as identified in Chapter 4 in order to aid comparison with shearbox data. The apparatus' line of thrust was made coincident with the interface's constituent surface, an opening of  $5D_{50}$  was implemented between the upper ensemble and the surface, the symmetrical arrangement was employed without an upper dentated plate, and split rubber shielding was used to prevent sample extrusion. It could be argued that a more appropriate comparison with shearbox data would be provided if  $g$  was set at  $2.5D_{50}$  or if the surface was positioned  $2.5D_{50}$  below the line of thrust. However, the consequence of either of these on resulting data is minimal. It will be shown in Section 7.2 that interface test data is less sensitive to the WDSA's configuration than shear data.

Outside of the preparation and implementation of the interface blocks, the test procedure was identical to that given for direct shear tests in Chapter 4 and used in Chapter 5. The metallic surfaces were prepared and quantified, before and after testing, using the techniques highlighted in Chapter 6. The granular surfaces, whose topography changed little throughout the course of the testing program, were prepared only once.

As has been mentioned, the amount of time spent developing and optimising the WDSA necessitated the interface test program be curtailed. Three stages of testing were embarked upon.

- The first test series featured "ideal" interfaces consisting of the three sands investigated in Part 1 of this work and surfaces onto which were attached particles of the same constituent sand. VLB ideal interfaces were tested at a variety of stress levels and MGS ideal interfaces at a variety of density.
- The second test series comprised the main portion of the testing programme, each of which were taken to displacements of approximately 12mm. The primary control factor was taken to be the surface roughness and the majority of testing was carried out at low confining stresses (25kPa). The interfacial response of the three sands investigated in Part 1 of this work was investigated when deposited at densities close to their maximum. The influence of density was investigated using MGS deposits.
- The third test series featured predominantly dense VLB at different stress levels and on metallic surfaces of different roughness. Large cumulative interface displacements were invoked using "reverse" testing, where the WDSA's carriage travels back and forth between its limiting positions.

All in all, the testing program constituted 67 interface tests, a considerable database considering the



curtailed nature of the testing program. The findings of each test series are discussed in turn.

## 7.2 Ideal interface testing

It has been well documented within the soil mechanics literature that when a sand is displaced over a very rough surface, the internal resistance of the sand is mobilised (e.g. Kishida & Uesugi, 1987). Lemos (1986) and Everton (1991) concluded that the sand particles adjacent to very rough surfaces were effectively locked into the surface topography and could therefore neither roll nor slide. Such particles were consequently able to withstand a higher shear force than the particles in the overlying sand mass. Brumund & Leonards (1973) suggested interface failure would occur along the path of least resistance and thus, on rough surfaces, the internal resistance of the sand mass can be expected to be mobilised and a shear zone formed in the sand mass above the surface.

When an interface's constituent surface has a topography that corresponds to that of the constituent sand, created by attaching sand grains of the same type to an interface block, the interface is here termed "ideal". The roughness magnitude of ideal interface surfaces is high, irrespective of which particular roughness parameter is employed as quantifier (Chapter 6). It is expected that adjacent sand particles will become locked into ideal surface topography and the internal resistance of the sand mobilised. This was indeed found to be the case by Butterfield & Andrawes (1972) who are among the few to investigate the response of ideal interfaces. Here, ideal interface behaviour is compared to the shearbox equivalent.

Figure 7.1(a) and (b) contrasts ideal interface and shear behaviour featuring dense VLB confined under a variety of normal stresses. Characterisation of test data using cardinal parameters would reveal little difference between ideal interface and shearbox data since peak and large displacement resistances, along with dilatancy increments correspond closely. The good agreement gives confidence in the methods employed when interpreting shearbox data regarding the ever-reducing cross sectional area. Consequently, however, when the shear resistance is plotted with reference to work  $W$ , as in Figure 7.2, large displacement data is seen to follow a unique downward path described by the same line as that found for shear tests (Chapter 5). This anomalous behaviour is therefore not a result of the ever-reducing plan area of the WDSA.

When interpreting interface data it is the resistance offered parallel to the surface that is of interest. Therefore, the angle of interface friction  $\delta'$  is derived using:

$$\tan \delta' = (\tau_{v_r} / \sigma'_{yv})$$

7.1

Thus, ideal interfacial strengths correspond to  $(\phi'_{ds})_{peak}$ , the angle of internal friction mobilised on a zero extension plane, and are therefore approximately  $6^\circ$  less than inferred  $(\phi'_{ps})_{peak}$  values.

The presentation of test data in its entirety in Figure 7.1(a) reveals an increased rate of ideal interface response. Peak states are mobilised sooner, strain softening occurs more rapidly and  $v_y$  attains lower magnitudes. All this suggests ideal interfaces develop thinner shear zones than their direct shear counterparts. This is again suggested when investigating the influence of the size of opening  $g$  between an ideal interface's surface and the upper ensemble. As seen in Figure 7.3, the reinforcing effect that small openings had on WDSA data (Chapter 4) is not repeated for ideal interfaces.

The rotations undergone by the upper-ensemble when ideal interface testing are remarkably persistent. No substantial reductions were recorded when increasing the stress level (Figure 7.1b) or when increasing the lever arm  $f$  between the apparatus' line of thrust and the interface surface (Figure 7.4), both of which had great impact on the rotations recorded during shear tests (Chapter 4). (All subsequent test data was obtained with  $f$  set to zero.) This persistence is thought to relate to the cross-symmetry of direct shear tests being removed when interface testing.

During interface testing using the DSA, distinct regions of sample loading and unloading are apparent at the rear and front of the apparatus respectively, as indicated by Paikowsky et al's (1996) model interface test featuring photo-elastic disks, as illustrated in Figure 6.28. Within a direct shear test, similar regions exist but are underlain by the portion of the sample contained within the lower frame. Thus, the unloaded portion of soil at the front of the upper frame overlies a region of heavily loaded soil within the lower frame, akin to that within the rear of the upper frame. Conversely at the rear of the upper frame, the highly loaded soil would overlie another triangular unloaded portion. Thus, a cross-symmetry exists which acts to produce more uniform displacement of the WDSA's upper ensemble when compared to ideal interface test where no such cross-symmetry exists.

Ideal interface tests conducted using MGS at different densities are compared to equivalent shear tests in Figure 7.5 revealing similar trends to tests featuring VLB reported above. When tests were performed with SFS, however, the significant differences were observed between shear and ideal interface results unlike those of the other sands, as seen in Figure 7.6. The data relating to the SFS ideal interface test reproduce the trends that one would expect to find when shearing a fine sand. The peak state is followed by a rapid strain softening to a resistance which remains constant for the remainder of the test's duration,

indicating a thin shear zone which corresponds to the constituent sands small particle diameter. Vertical displacements of the upper ensemble are likewise small. In addition, a reasonable 1:1 trace is seen when stress ratio is plotted against dilation increment. In effect, and unlike WDSA data featuring SFS, ideal interface data provide no indication of progressive failure. It is thought that a greater degree of constraint is offered by the interface test's sample boundaries brought about by the decreased dimensions of the sand mass, which promotes the more uniform behaviour of fine sands.

The progressive failure of a WDSA sample featuring dense SFS ensures that  $(\phi'_{ds})_{peak}$  lies below the equivalent  $\delta'_{peak}$  value. Thus the interface appears stronger than the sand mass. This may explain Kulhawy & Peterson's (1979) finding that the  $\delta'_{peak}/(\phi'_{ds})_{peak}$  ratio for dense sand obtained using a shearbox of a size large enough to promote progressive failure (406 by 406mm) is typically greater than unity. The  $\delta'_{peak}$  value for the ideal SFS interface is found to be 43.2°. Alongside the  $\psi_{peak}$  value of 17.0° an estimate of  $\phi'_{ps}$  can be obtained for SFS using Davis' (1968) relationship modified for ideal interfaces:

$$\sin \phi'_{ps} = \frac{\tan(\delta'_{ii})_{peak}}{\cos(\psi_{ii})_{peak} + \sin(\psi_{ii})_{peak} \tan(\delta'_{ii})_{peak}} \quad 7.2$$

where the subscript *ii* is intended to indicate parameters obtained during ideal interface tests. For SFS, the estimate of  $\phi'_{ps}$  obtained in this manner equals 49.7°, 6.5° above  $(\delta'_{ii})_{peak}$ . It should be recalled that the difference between  $(\phi'_{ps})_{peak}$  and  $(\phi'_{ds})_{peak}$  recorded for VLB and MGS when direct shear testing was of similar magnitude at around 6°.

It can be concluded that ideal interface tests, or perhaps interface tests employing a standardised rough surface, can provide a means for verifying direct shear data or indeed as a substitute for the direct shear test altogether. Further support for this proposal comes from the finding that interface tests are less sensitive to WDSA configuration than shear tests, as previously seen when changing *g* and *f* values.

### 7.3 Unidirectional interface testing

The interfacial response of surfaces with very different initial topographies in combination with three sands, all deposited at densities close to their maximum, confined under around 25kPa is displayed in matrix form in Figure 7.7. The columns of the matrix represent the different sand types, decreasing in mean particle diameter as one progresses from left to right. The rows represent the different data sets obtained during testing:  $\tau_{y1}/\sigma'_{y1}$ ,  $v_y$ ,  $\psi$ , and  $\omega$ , each plotted with reference to  $v_x$ . Each element of the matrix compares the relevant data for the particular sand on surfaces of different roughness. The

particular surface roughness is indicated in the legend at the figure's end wherein roughness is seen to increase from left to right.

Considering first the interfacial resistance, the onset of displacement brings with it rapid increases in  $\tau_v/\sigma'_{yy}$  at a rate independent of surface topography. The overwhelming majority of tests exhibited peak behaviour, with the magnitude of the peak increasing with surface topography, followed by a period of strain softening, the magnitude of which again increased with surface topography. A near constant large displacement resistance was subsequently mobilised. Thus, the following parameters can be defined:

$$\tan \delta'_{peak} = \left( \tau_{yv} / \sigma'_{vv} \right)_{peak} \quad 7.3$$

$$\tan \delta'_{ld} = \left( \tau_{yx} / \sigma'_{yy} \right)_{ld} \quad 7.4$$

$(\tau_{yx}/\sigma'_{yy})_{ld}$  is derived by averaging the final ten resistance measurements and is thought to correspond with Jardine et al's (1993) "critical state" for interfaces, discussed in the previous chapter and indicated with subscript *crit*. The large displacement subscript is intended to indicate the conditions at the end of a single traverse of the shear carriage during shear displacements around 10-12mm, and hence be appropriate for comparison with the large displacement data of direct shear tests discussed in the first part of this thesis. In subsequent sections, "reverse" interface tests are performed during which the WDSA's carriage is displaced back and forth between its limiting positions bringing corresponding increases to the cumulative shear displacement. Thus, although larger (cumulative) displacements will be applied, "large displacement" data is that recorded at the end of a single traverse.

Returning to the interface test data of Figure 7.7, the shape of the  $\tau_{yx}/\sigma'_{yy}$  plot for rough surfaces bears a close resemblance to that relating to the direct shear testing of a dense sand. The shapes of  $\tau_{yx}/\sigma'_{yy}$  plots for smoother surfaces, however, are more similar to direct shear results of looser sands. This analogy can be extended when considering dilatancy data. Rows two and three of Figure 7.7 reveal that the degree to which the dilatancy potential of the sand is activated is dependent on surface topography. The roughest surfaces are associated with a dilation response that corresponds to equivalent shear tests. The smoother the surface topography becomes, the less dilatancy is exhibited and the lower the dilatancy rate becomes. The smoothest surfaces are associated with negligible volume changes. In addition, the peak dilatancy rates seem to correspond with the peaks in interface resistance. Thus, just as during direct shear tests, an interfacial angle of dilation can be defined:

$$\tan \psi_{peak} = \left( \frac{dv_y}{dv_x} \right)_{peak} \quad 7.5$$

The rotation of the upper ensemble, illustrated in row 4 of Figure 7.7, shows a similar dependence on surface topography as  $v_y$ , with rotations becoming larger with increasing roughness. Similar effects in Paikowsky et al's (1995) apparatus were said to result from the loading and unloading at a direct shear sample's rear and front respectively, bringing additional dilatancy at the rear.

### 7.3.1 Correlating peak state interface data with surface roughness

The clear dependence of interfacial behaviour on the constituent surface topography has impelled previous investigators to focus on this parameter when attempting to clarify behaviour. The correlating prowess of Uesugi & Kishida's (1986b) roughness parameter  $R_n$  when considering peak interface resistance has led to its wide, often unquestioned, acceptance. Here, it is attempted to dispel the mystery associated with its correlating ability.

As noted in the Chapter 6, Uesugi & Kishida's (1986a) roughness parameter is derived by averaging the  $R_t$  value (the maximum vertical distance between the highest peak and lowest valley) of numerous profile segments each of length equivalent to the  $D_{50}$  of the interface's constituent sand. The use of a roughness measurement based on extreme events such as  $R_t$  necessitates the averaging of many independent values preferably taken over a short length of profile in order to limit the influence of rare but extreme topographic features on the roughness measurement. If, for example, roughness of a surface with a single deep gorge across its centre was assessed using long profiles and  $R_n$ , then the resulting roughness measure would approximately equal the gorge's depth. The averaged  $R_t$  value of numerous short profiles taken at random positions across a surface and therefore not all spanning the gorge produces a more representative assessment of the general surface roughness. An automatically averaged roughness parameter such as the British Standard  $R_a$ , which by definition reduces the influence of extreme surface features, may thus provide a more practical roughness measure entailing a single measurement only.

Uesugi & Kishida (1986b) state that the limitation of profile lengths to  $D_{50}$  is necessitated if surface irregularities are present of wavelength greatly in excess of  $D_{50}$ . In fact, this is only true if the long irregularity wavelengths have amplitude significantly larger than the short wavelength irregularities. The design processes of the interfacial surfaces used here do not impart any such long wavelength irregularities to surface topography, and hence reduced traverses of length  $D_{50}$  would merely increase workloads. Therefore, and as has been highlighted (Chapter 6), traverse lengths of 5mm at five separate locations across the surface are used to gauge surface roughness. In addition, with consideration given to

the geometry of surface contact as depicted in Chapter 6, it is thought that the use of a surface roughness parameter whose magnitude is dependent on extreme events is not justifiable. Even on rough surfaces fine sand particles span a great many asperities implying the use of an averaged parameter would be more appropriate. In practice, however, the choice of amplitude parameter is inconsequential to data correlation since the proportional increase in roughness as one progresses from POL to the rougher surfaces is independent of the precise amplitude roughness parameter considered (Chapter 6). Because the British Standard (BS-1134) incorporates the  $R_a$  value as the standard parameter, it is that which is employed.

The variation of  $\tan(\delta'_{peak})$  and  $\psi_{peak}$  with  $\log R_a$  both before and after normalisation by  $D_{50}$  for the three different sands investigated is displayed in Figure 7.8(a) and (b) respectively. Horizontal lines at high roughness values show the peak resistance and dilatancy rate recorded for each of the sands in equivalent shear tests. The distinct linear relationships between  $\log(R_a)$  and peak resistance for each of the sands collapse into a single relationship when the roughness parameter is normalised by  $D_{50}$ . That no characterisation of particle geometry is necessary to achieve a unique correlation probably relates to small differences between the grain shapes of the sands. It is clear that the unifying effect on  $(\tau_{yx}/\sigma'_{yy})_{peak}$  brought about by normalising by  $D_{50}$  is not confined to Uesugi & Kishida's measure of roughness  $R_t$  but works with  $R_a$ . In addition, and never before noted, the normalisation brings comparable unification to  $\psi_{peak}$ . Comparable diagrams but considering the smooth-rough crossover  $C_r$  as derived from structured walk analysis comprise Figure 7.9 which illustrates further that numerous roughness parameters can be used successfully to correlate peak-state interface data.

It can be concluded that the peak interface response recorded here fits the framework suggested by Paikowsky et al (1995) who characterised interfaces as smooth, intermediate or rough, depending on the peak resistance they are able to offer. Smooth interfaces mobilise a narrow range of low peak resistances and no volume change, rough interfaces mobilise the shear strength of the intact sand, and these two are separated by the transitional intermediate interfaces. What sets the present study aside from Paikowsky et al's (1995) and numerous others that have presented similar findings, is that the classification system for interfaces based on peak strength is also found to be appropriate when considering the interface's peak dilatancy response.

When dilatancy is not activated, the primary movement pattern of particles relative to the surface is sliding and the system resembles a typical two-body abrasive wear scenario. Surface topographies rough enough to promote particle rolling as the preferred movement necessarily trigger dilatancy and thus create a system more like that commonly occurring in soil mechanics. Thus one might expect the findings of tribology to apply in the former case and those of soil mechanics to apply in the latter. Evidence for

this is provided by plotting  $(\tau_{yx}/\sigma'_{yy})_{peak}$  and  $\psi_{peak}$  with  $\Delta_a$ , the arithmetic mean of the absolute profile slope, the parameter reported most successful at correlating frictional behaviour between macroscopic surfaces (Chapter 6). Figure 7.10 shows that the reasonable correlation between peak resistance and  $\Delta_a$  existing for smooth interfaces breaks down at higher values of  $\Delta_a$  as the surface roughness becomes sufficient to activate substantial dilation. Further evidence for the applicability of the findings of tribology on smooth interfaces is found elsewhere, as detailed in the following sections.

### 7.3.2 The effect of particle size on peak interface response

When investigating the interface response of different gradings of the same sand, Uesugi & Kishida (1986b) found the effect of particle size on  $\delta'_{peak}$  to be entirely accounted for by the normalisation of their surface roughness parameter using  $D_{50}$ . Paikowsky et al (1995) found the same when investigating the interface behaviour of glass beads of various sizes. Here, it has been shown that the normalisation of  $R_a$  by  $D_{50}$  has correlated the behaviour of three sands having different response to direct shear. This is likely to result from differences in particle angularity between the sands being small. However, the direct comparison of the three sands is complicated by their different shear response. Here, peak interface data for the three sands are compared after normalising by the appropriate peak response in equivalent direct shear tests for VLB and MGS, and ideal interface tests for SFS, for which direct shear test data is unreliable.

Figure 7.11 presents the normalised peak interface response using VLB ( $D_{50}$  circa 0.8mm), MGS ( $D_{50}$  circa 0.4mm), and SFS ( $D_{50}$  circa 0.2mm). For the rougher interfaces in which dilatancy is activated, a decreasing peak stress ratio is apparent with increasing particle diameter. Uesugi & Kishida's (1986b) postulate was developed to explain this: fine sands find a given surface rougher than coarse sands, and on such surfaces will mobilise more of their internal shear strength. During interface tests featuring surfaces not rough enough to activate dilation, however, an increasing ratio with increasing  $D_{50}$  is observed. A viable explanation for this phenomenon relies on reference to the size effect encountered frequently in the tribology literature. Fine particles interact with a lower volume of material and thus encounter a material with an increased hardness. Less ploughing of the surface occurs and the friction coefficient is as a result lower.

Thus, depending on the roughness of the interface's constituent surface, it is possible to draw very different conclusions as to the effect of particle size on peak interface response. This observation helps explain how investigators can find no influence of  $D_{50}$  on  $\delta'_{peak}$  (Noorany, 1985) whereas others, using

identical apparatus, find substantial decreases in  $\delta'_{peak}$  with increasing  $D_{50}$  (Lehane, 1992).

### 7.3.3 The effect of density on interface response

The effect of reducing the density of an interface's constituent sand was investigated using MGS confined under 25kPa and can be seen in the now standard matrix format in Figure 7.12. The peak interface response using surfaces of different roughness is documented with respect to relative density  $D_r$  in Figure 7.13. In this figure the peak strength and dilatancy response recorded during equivalent shear tests is presented for comparison. Again it is apparent that the rougher the interface's constituent surface, the closer the peak response corresponds to that recorded when shearing an intact portion of the same sand deposited in the same initial state. This aside, the general effect of increasing sample density is to increase the peak strength and dilatancy response of the interface with increases in density having a larger impact on rougher surfaces.

The peak states are plotted against surface roughness, here quantified as  $R_a$ , in Figure 7.14. Since all data corresponds to MGS no normalisation by  $D_{50}$  has been attempted as the effect on all data would be equivalent. The horizontal lines at large magnitudes of roughness correspond to the values recorded during shear tests. The trends depicted are similar to those indicated by Jardine et al (1993) as illustrated in Figure 6.26(a). It is seen that the influence of density on peak resistance decreases as the interface's constituent surface becomes smoother.

A surface rough enough to activate interface dilation produces a density-dependent response since interface displacement is accounted for by deformation within the sand mass. On smoother surfaces, where sliding at the grain metal contact plane accounts for interface displacement, density might have an impact on interfacial resistance, but only if it determines the number of grains in contact with the surface. However, it is likely that the structural arrangement of the particles constituting the sand mass is affected by the presence of a solid surface just as their structural arrangement changes near the masses free surface. Subba Rao (1998) explained the differences between sand-over-steel and steel-over-sand interface tests by referring to a "surface film" of grains existing on the sand sample's free surface with a structure irrespective of the density to which the sand mass is prepared. For sand-over-steel tests, this may also be true of the layer of grains adjacent to an interface's constituent surface. Consequently, it is probable that a loose deposit has an equivalent number of grains in contact with the interface's surface as a dense deposit and thus, if the surface roughness is of insufficient magnitude to trigger dilation, sample density will play little role in determining peak interfacial resistance.



### 7.3.4 The effect of confining stress on interface response

Tests under increased confining stress primarily featured dense VLB. The behaviour recorded during tests using three surfaces roughened to different degrees are displayed in matrix form in Figure 7.15 in which the columns represent the different surfaces, be it POL, ALO or SIC, and the rows represent the different data formats. Interfaces with different constituent surface roughness show different dependency on stress level.

Considering the roughest SIC surface first, data for which comprise the third column of Figure 7.15, the recorded stress level effect is similar to that of direct shear tests. An increase in  $\sigma'_{yy}$  brings with it a reduction in the strength and dilatancy response of the interface. The smoothest surface, however, whose data comprise column one of the same figure, shows a much lower stress level dependency and  $\delta'_{peak}$  found to increase with  $\sigma'_{yy}$ , contrary to the trend for the rougher surfaces. This behaviour is summarised in Figure 7.16 where increasing  $\sigma'_{yy}$  induces reductions in  $\delta'_{peak}$  on rougher surfaces and increases in  $\delta'_{peak}$  on the smooth. The anomalous trend for these smooth surfaces, contrary to the stress level effects often reported in soil mechanics, can be explained with reference to the size effect. An increased contact pressure between sand particles and steel gives rise to greater indentation, the interaction of individual grains with a larger volume of softer material, increased ploughing, and thus an increased friction coefficient.

The intermediate surface roughness illustrated in the second column of Figure 7.15 marks the transition between behaviour exhibited on POL and SIC. Under low stress, dilatancy is activated and resistances exceed those recorded at higher stress levels. However, dilation becomes suppressed when the stress level is adequately raised. The preference for particles of sand to slide on a surface at increased confining stresses was demonstrated by Larsen-Basse & Premaratne (1983) and explained by Fang et al (1993) as discussed in Chapter 6. Once dilation has been suppressed by sufficient  $\sigma'_{yy}$ , clear reductions of  $\delta'_{peak}$  with increasing  $\sigma'_{yy}$  disappear.

Thus, like the effects of density and particle size on interface response, different trends are recorded depending on the topography of the interface's constituent surface. This may help explain why some authors report a negligible stress-level effect on  $\delta'_{peak}$  (Heerema, 1979, Tatsuoka & Haibara, 1985, Uesugi & Kishida, 1986a), whereas others report  $\delta'_{peak}$  to be strongly stress-level dependent (e.g. Everton, 1991).

### 7.3.5 Peak stress-dilatancy response of interfaces

Here, and for the first time, interface dilatancy has been quantified in a way that enables the stress-dilatancy response to be investigated. The reason for this never before being attempted is unclear, but may relate to the dilatancy data recorded in the optimised WDSA being better indicative of interface response than those provided by more conventional DSA.

Figure 7.17 (a), (b) and (c) plots  $\delta'_{peak}$  against  $\psi_{peak}$  for the three sets of tests already presented. The first of these sets contrasted the different response of SFS, MGS and VLB, all deposited at densities close to their maximum and confined under 25kPa, on surfaces of different roughness as illustrated in Figure 7.7. The second varied the density of MGS samples again confined under 25kPa against surfaces of various roughness depicted in Figure 7.12. The third examined the effects of  $\sigma'_{yy}$  on the response of interfaces featuring dense VLB and surfaces of different roughness and the resulting data was presented in Figure 7.15.

Considering the wide range of test parameters investigated, the reasonably unique correlation between peak strength and dilatancy as shown in Figure 7.17 is remarkable. The data for dilatant interfaces can be correlated reasonably well with Bolton's (1986) flow rule modified for interfaces which relates  $\delta'_{peak}$  to  $\psi'_{peak}$  and a constant  $C$ :

$$\delta'_{peak} = 0.8\psi'_{peak} + C \quad 7.6$$

A reasonable match to test data is found when  $C$  equals  $27^\circ$ . Equation 7.6 suggests that increases in peak strength with roughness are not primarily due to a steeper plane of relative movement between the particles and the surface, as has elsewhere been suggested. This explanation assumes particle sliding to be the operative mechanism whereas for most of the interfaces tested here, the increases in peak strength come from increases in dilatancy, indicating an increased preference for particle rolling.

The dependency of an interface's peak strength on its dilatancy characteristics can similarly be demonstrated using Taylor's (1948) energy correction in plots of  $(\tau_{yx}/\sigma'_{yy} - dv_y/dv_x)$  against  $v_x$  as done for the dense VLB-SIC interface tested at various confining stresses in Figure 7.18. Once the portion of the shear force used to supply the energy to dilation is accounted for, peak resistance behaviour vanishes, just as during shear tests.

Viewing interface behaviour in the manner of Figure 7.17 suggests that a two-tiered model provides a

more realistic representation of peak interface response than Paikowsky et al's (1995) three-tiered characterisation. In the two-tier model, interfaces are classified as either dilative or non-dilative depending on their peak response. On axes of  $\delta'_{peak}$  against  $\psi_{peak}$ , non-dilative interfaces lie close to the abscissa, somewhere between the origin and a transitional value of  $\delta'$ . Dilative interfaces mobilise  $\delta'_{peak}$  above this transitional value and correlate reasonably well with Equation 7.6.

Revisiting Paikowsky et al's (1995) three-tiered model in the light of the two-tiered model suggested by stress-dilatancy analysis reveals the dilatancy response to be masked in the former. Figure 7.19 redraws the trend-lines of the three-tiered model in Figure 7.8(b) for VLB but omits the data points themselves. Onto the first part of the diagram is drawn a horizontal line at a value of  $\tan 27$  or 0.510 corresponding to the stress ratio which divides the two-tiered model. The  $R_a/D_{50}$  value at which the three-tiered model intercepts this horizontal line is approximately 0.005. The same relative roughness value on the second part of the figure corresponds to a peak angle of dilation of around  $4^\circ$ .

Thus, and as indicated in Figure 7.19, an increase in  $\psi_{peak}$  from  $0^\circ$  to  $4^\circ$  could be interpreted as increasing the peak stress ratio from around 0.250 to 0.510. In relative terms, this accounts to a 16% increase in  $\psi_{peak}$  producing a 30% increase in interfacial resistance. This unequal weighting suggests that the strength increases that coincide with increasing roughness at low roughness values are not a dilatancy phenomena which is clear from the two-tiered model, but may be envisaged by a consideration of the three-tiered model alone. On these grounds it is suggested that the two-tiered stress-dilatancy model is a better representation of peak interface response.

### 7.3.6 A large-displacement critical state for interfaces?

The critical state for a granular material is defined as when deformation can proceed without changes in stress or volume. It is commonly thought that the shear resistance offered by a sand deforming at critical state is independent of stress level and initial density.

As reported in Chapter 6, Jardine et al (1993) carried out interface testing using a direct shearbox, various sands and surfaces with  $R_a$  roughness of between 5 and  $10\mu\text{m}$ , a relatively narrow range said to correspond to the topography of typical steel piles. They reported that the rate of change of data became small at around 3 or 4mm of relative displacement when the interface's constituent sand grains became "unlocked" from the surface topography allowing deformation to proceed without changes in volume. This condition was defined to be the critical state for interfaces and  $\delta'_{crit}$  was said to be the controlling angle of friction and its use recommended in (pile) design. The magnitude of  $\delta'_{crit}$ , as seen in Figure

6.26(b), was said to be upper bounded by  $\phi'_{crit}$ :

$$\delta'_{crit} \leq \phi'_{crit} \tag{7.7}$$

No reference is made to the derivation of  $\phi'_{crit}$  by Jardine et al (1993). However, the majority of data there presented are those of Everton (1991) wherein a test interpretation is employed which relies on the assumption that the maximum stress ratio is mobilised on the DSA's horizontal plane. Thus, it is Jardine et al's (1993) mistaken belief that the critical state angle of friction can be reliably estimated by taking the *arctangent* of the large displacement stress ratio mobilised within a DSA. In fact, however, and as discussed in Chapter 2 and reinforced with the excellent agreement of large displacement WDSA data with those of the Cambridge SSA in Chapter 5, the appropriate estimation of  $\phi'_{crit}$  is obtained by taking the *arcsine* of the same large-displacement stress ratio. Ultimately, Jardine et al (1993) confused  $\phi'_{ld}$  and  $\phi'_{crit}$ .

Perhaps the reason for this misinterpretation of DSA data relates to the especially high resistances mobilised in Everton's (1991) DSA. As seen in Figure 6.26(a), the large displacement stress ratio was measured as 0.7. An arctangent of this ratio gives an angle of 35.0°, equivalent to  $\phi'_{crit}$  presented by Stroud (1971), whereas an arcsine gives 44.4°, a rather unlikely estimate of  $\phi'_{crit}$ . The reason for such high stress ratios being recorded may relate to the incorrect estimation of  $\sigma'_{yy}$  acting on the central plane in Everton's (1991) archetypal DSA. Thus, Everton (1991) may have achieved a reasonable estimate of  $\phi'_{crit}$  via compensating errors.

This realisation has important consequences. With the nomenclature used here, the upper limit of  $\delta'_{ld}$  is not  $\phi'_{crit}$ , as Jardine et al (1993) conclude and indicated by Equation 7.7. Instead:

$$\tan \delta'_{ld} \leq \tan \phi'_{ld} \tag{7.8}$$

or, equivalently:

$$\tan \delta'_{ld} \leq \sin \phi'_{crit} \tag{7.9}$$

Thus, if  $\delta'_{ld}$  is indeed the operational angle of friction, a substantial overestimation of the maximum resistance will result if Jardine et al's (1993) upper limiting value is used.

The  $\delta'_{ld}$  values recorded in the WDSA for dense VLB confined under different stresses and MGS at different densities confined under 25kPa are presented in Figure 7.20(a) and (b) respectively. For comparison, estimates of  $\phi'_{crit}$  (the arcsine of the large-displacement stress ratio recorded during WDSA shear tests) are also therein presented. It is clear that even the very rough ideal interfaces mobilise large displacement angles of friction below  $\phi'_{crit}$ . In addition, the downward trend in  $\delta'_{ld}$  with increasing  $\sigma'_{yy}$  for each interface is equivalent to that recorded during shear tests, and density is found to have small influence on  $\delta'_{ld}$ .

The large displacement resistances of dense SFS, MGS and VLB confined under 25kPa are plotted against surface roughness quantified as  $R_a$  in Figure 7.21. Contrary to Lehane (1992) who investigated a limited roughness range around  $10\mu\text{m}$   $R_a$ ,  $\delta'_{ld}$  is found to be dependent on the surface topography, reducing as the surface becomes smoother. This finding sits well with Jardine et al's (1993) influence of  $D_{50}$  on  $\delta'_{crit}$ , as pictured in Figure 6.26(b).

From the above, it can be seen that large displacement interface data bears traits similar to those of shear tests, i.e. the resistances mobilised are found to be relatively stress-level and density independent. It is this finding that prompted Jardine et al's (1993) assertions concerning a critical state for interfaces. This definition is here questioned on two grounds:

- The resistance mobilised during large displacement interface testing is dependent on the relative geometry between the surface topography and the particle size, increases in  $\delta'_{ld}$  occurring with increasing roughness (Figure 7.20) or decreasing particle size (Jardine et al, 1993). The use of the term critical state is only appropriate if the paths followed by all tests arrive at a unique end state, a factor of which is a consistent large-displacement resistance. Clearly this is not so.
- For a state to be defined as critical, deformation must be able to proceed without changes in volume or stress. A closer examination of the large displacement data shown in Figure 7.7 and Figure 7.15 reveal neither of these conditions are satisfied for the majority of interface tests. Large displacement increases in shear resistance are sometimes apparent, most obviously on smooth surfaces and when using VLB, the coarsest of the sands investigated. In addition, upward movements of the upper frame are often exhibited up until the end of testing. Clearly, such behaviour contradicts the existence of a large-displacement critical state for interfaces.

## 7.4 Reverse interface testing

The effects of wear were investigated using "reverse" interface tests. The early stages of these tests are identical to those previously presented. After the apparatus' first traverse, however, when the WDSA's maximum limiting shear displacement was attained, a micro-switch was triggered, the direction of shear reversed and a second traverse commenced, driving the carriage back towards its starting position. The configuration of the WDSA does not permit any substantial overshoot of the carriage's starting position. Instead, the micro-switch is again triggered and the direction of shear reversed initiating a subsequent traverse. Reverse testing should not be confused with cyclic testing during which equivalent shear displacements are applied either side of the carriage's starting point, a test procedure unattainable for the WDSA due to the limitations of the WF-25300 from which it was constructed.

Care must be taken to avoid reading too much into the test data obtained during reverse shearing since when employing a substantial opening, as is done here, the amount of sample extrusion may become excessive.

All the data considered here are for dense VLB.

### 7.4.1 Signs of interfacial wear

A very fine powder was found distributed across the steel surface as interfaces were dismantled at the test's close. Judging by its colour, the dust primarily comprises abraded sand particles, although minute fragments of metal may be mixed within. Initially it was attempted to quantify the degree of particle crushing by dry sieving of abraded samples and comparing the resulting gradation curve with that for the virgin sand. However, the differences between gradation curves were generally small and lay within the natural variation of the virgin sand's gradation curve. It was thought that the loss of the dust in air currents and amongst the fibres of the brush used to remove it from the surface and sieves hampered the dry sieving procedure. Thus, after an initial weighing, a wet sieving procedure was used to remove all particles within the abraded sample finer than the  $D_{10}$  of the original sand and  $m_{10}$ , the mass of these fine particles, was found by drying and re-weighing.

Figure 7.22 shows  $m_{10}$  has a tendency to increase with the work  $W$  expended parallel the interface. The scatter in the data is large, however, perhaps due to the loss of fines, clogging of the sieve used during the procedure or the poor accuracy of the scales used to weigh the abraded sample, which hinders the usefulness of the crushing data. However, the mass of fine particles per unit sample volume accumulated during interface tests was smaller than that in shear tests, perhaps again providing more evidence

for a thinner shear zone generated adjacent to a solid surface.

Thorough scrubbing of an interface's constituent surface post-test is ineffectual at removing all traces of the tested sample. Swathes of orange of differing size and hue are distributed across the steel grey that must comprise collections of minute sand debris attached to the steel. The strong resistance of these coloured regions to removal indicates the existence of strong adhesive forces. Only through the re-preparation of the steel surface were the coloured regions removed.

In addition to the coloured regions, changes in surface topography were observed. There are no standard methods for assessing the change in surface topography due to frictional processes. However, the consequence of interface testing on surface topography can be appreciated using structured walk analysis. Changes in surface topography due to interface testing assessed in this way were seen to be dependent on that existing beforehand.

Figure 7.23 presents the results of structured walk analysis taken over a surface that was initially polished to achieve a mirror finish before and after tests at various confining stresses. The 25kPa test proceeded for a mere 12mm  $v_x$  whereas reverse shear of the 128kPa and 252kPa tests proceeded until cumulative  $v_x$  of close to 200mm was achieved. The profiles from which Figure 7.23(a) is derived were taken parallel to the direction of  $v_x$  whereas those of Figure 7.23(b) were taken perpendicular. On such initially smooth surfaces, interface testing brings with it increases in both  $d_c$  and  $C_r$ . In effect, the roughness of the surface increases. The resulting surface topography, being significantly rougher in the direction perpendicular to  $v_x$ , is anisotropic. Similar diagrams but for the initially rougher SIC surface are displayed in Figure 7.24 and which reveal very different characteristics. The effect of interface testing on the rougher topography is to decrease  $d_c$  but leave  $C_r$  unchanged. Fine surface detail is lost during testing. In addition, the worn surface topography is isotropic and much less dependent on  $\sigma'_{yy}$  than the smoother surface.

The changes in surface topography can be explained with reference to the motion of sand particles during testing. On surfaces smooth enough to not activate dilation, the predominant motion of particles relative to the surface is sliding. Such action ploughs wear scars into the softer metal surface, anisotropically roughening its topography. On the other hand, dilation is activated on rougher surfaces, indicating an increased preference for particle rolling as opposed to sliding. Thus, a succession of plastic deformation pits would be left as the surface is squeezed from under rolling particles and smoother, isotropic surface topography results.

Worn surface topography is far less affected by additional testing. The small effect on structured walks

taken after tests carried out under 252kPa on POL and SIC surfaces already previously subjected to testing at the same stress level can be seen in Figure 7.25 and Figure 7.26 respectively.

#### 7.4.2 Interfacial wear and test data

An example of reverse-shear interface data during which smoothing of the topography is recorded is presented in Figure 7.27. The interface in question consists of dense VLB and SIC under a confining stress of 128kPa. The left-hand side of the figure plots data against  $v_x$ , which represents the position of the WDSA's carriage. The reference axis on the right hand side of the figure is the cumulative interface displacement, termed  $V_x$  and derived as the accumulation of the absolute increase in  $v_x$ . The measured shear stress is presented against  $V_x$  along with its absolute value, shown as a dashed line. Figure 7.28 is the equivalent diagram but for an interface whose constituent surface topography becomes rougher during the course of testing. The interface in question features dense VLB and POL confined under 251kPa.

Considering first the stress data, it is apparent that between reversals in shear direction a dead spot exists over which displacement can occur with negligible resistance. This comprises the play between the load cell's web and casing and the slack inherent within the WDSA's loading system and is not thought to be a characteristic of the interface. In addition, the VLB-SIC interface data reveal the carriage to be able to move approximately 2mm back on itself before the micro-switch which triggers the direction reversal is activated. Data obtained in subsequent traverses of the VLB-POL interface, however, are not associated with the carriage attaining its maximum displacement. This is a product of a different test procedure brought about by a malfunctioning micro-switch.

During the testing of the SIC interface, Figure 7.27(a) shows reversals in direction of  $v_x$  to bring about a rapid unloading of the interface during which time the resistance falls to zero. Reloading in the opposite direction then brings the mobilisation of a resistance equivalent to that from which it fell. Further reversals have no impact on the resistance mobilised. Following Uesugi & Kishida (1989) this multi-reverse interfacial resistance found to be independent of  $V_x$  is denoted with subscript  $r$ . Turning attention to the dilatancy characteristics, each reverse of the direction of shear brings about initially contractant behaviour followed by expansion. After the first cycle, the effect of a load cycle is to produce a net compaction. The compaction associated with each loading reduces as the traverses add up producing an ever-reducing rate of contraction. Budhu (1979) has documented similar behaviour during reverse simple shear tests featuring LB 14-25.



The response of the VLB-POL interface depicted in Figure 7.28 is quite unlike that of Figure 7.27. Once the peak state associated with the first traverse has passed, the resistance increases with increasing  $V_x$  until a limiting value is asymptotically approached. The magnitude of this limiting resistance corresponds closely to that recorded on the rougher surface in Figure 7.27. It is proposed that instead of "residual", which has connotations of low shear strength recorded after extreme shearing of cohesive soils, the subscript should stand for "run-in", suggesting the occurrence of wear processes. Like the VLB-SIC interface, the general trend for  $v_y$  on the smoother surface is contraction at a reducing rate. Superimposed on this general trend, however, the changes in  $v_y$  associated with any particular loading cycle are seen to grow as the test progresses, the final traverses being associated with significant expansions and contractions. The gains in strength of the interface occur during the period when the increases in  $v_y$  associated with any particular traverse are small. It can be inferred that the preferred particle movement changes from sliding to rolling as the test progresses and that gains in interface resistance are bought about when sliding is the preferred particle movement.

To illustrate the evolution of the response of both interfaces, the data obtained during individual traverses of the apparatus are separated from one another and compared as if individual tests in Figure 7.29 for the VLB-SIC interface and Figure 7.30 for the VLB-POL. Whereas the initial traverses produce a very different response, the behaviour exhibited after the interface has been run-in is similar.

The responses of interfaces of different initial roughness are compared to the multi-reverse data previously considered in Figure 7.31. The presented stress data relate to the absolute value of the resistance with the large valleys associated with the reversal of displacement direction in-filled for clarity. The data of POL(w) relate to an interface test whose constituent initial surface roughness was that remaining after POL was tested under 252kPa, shown in Section 7.4.1 to be considerably rougher than POL. As can be seen, the rougher the initial surface, the less shear displacement is required to mobilise  $\delta'_r$  and the sooner dilatancy is recorded. Data relating to the final traverse of these interfaces are displayed alongside one another in Figure 7.32. Considering that the vertical displacements on the smoother interfaces are in the process of enlarging (Figure 7.30), the response of the four interfaces is similar enough to conclude that behaviour after running in is independent of the initial surface roughness of the constituent surface.

The effect of confining stress on the behaviour of both SIC and ALO interfaces is seen in Figure 7.33. Low confining stresses are associated with a degradation in resistance towards  $(\tau_{yx}/\sigma'_{yy})_r$  and large changes in  $v_y$  associated with every traverse from the outset. Increases in  $\sigma'_{yy}$  bring with them reductions in  $(\tau_{yx}/\sigma'_{yy})_{peak}$ , and the suppression of dilation. Once  $\sigma'_{yy}$  has increased sufficiently to reduce  $(\tau_{yx}/\sigma'_{yy})_{peak}$

to a magnitude corresponding to  $(\tau_{yx}/\sigma'_{yy})_r$ , the changes in  $v_y$  recorded during the initial traverses become small, indicating a transition of the preferred particle movement to sliding, and post-peak gains in interfacial strength are recorded. The magnitude to which  $\sigma'_{yy}$  needs be raised to bring about post-peak increases in interface resistance is dependent on the initial surface roughness. Whereas the rougher SIC surface experiences strengthening when the confining stress goes from 128 to 252kPa, the smoother ALO surface experiences post-peak strengthening as  $\sigma'_{yy}$  goes from 25 to 86kPa. Thus, the larger asperities of the rougher surface promote particle rolling and larger confining stresses are required on this surface if particles are to slide.

$\delta'_{peak}$  and  $\delta'_r$  values from each of the multi-reverse tests are plotted against  $\sigma'_{yy}$  in Figure 7.34(a) indicating the evolution of interface resistance. Figure 7.34(b) mimics the conventional shear stress versus normal stress diagram often used to analyse direct shear test results. A linear failure envelope orientated at  $26.7^\circ$  to the abscissa describes the run-in condition.

### 7.4.3 Discussion

Whereas the running in of VLB interfaces constituting smoother surfaces is already apparent in the large displacement data of Figure 7.7, the resistance data for both MGS and SFS appear stable, long and level plateaus extending from soon after peak to the end of a single traverse. The tribology literature indicates that wear rates during two and three body abrasive wear increase with abrasive particle size. Thus, one might expect a coarser VLB interface to run-in substantially faster. However, without reverse interface test data for a wider variety of sands, only tentative conclusions can be drawn regarding the run-in state and any conclusions qualified with reference to VLB only.

Here, it is tentatively proposed that the run-in value of wall friction is linked to a true critical state for interfaces. Like the "large displacement" state Jardine et al (1993) defined as representing an interfacial critical state, the magnitude of  $\delta'_r$  is independent of stress level. Unlike  $\delta'_{id}$ , however,  $\delta'_r$  is independent of initial surface roughness and constant with further increases in cumulative interface displacement. In addition, and because after repeated shear the interface is covered with wear debris, it is likely that  $\delta'_r$  will be independent of the initial particle size. Thus, from the limited data available, it appears that run-in response better corresponds to a unique end state necessary for the definition of critical state to be applicable.

Reconsidering Figure 7.34(b), which presents the run-in envelope for the metallic VLB interfaces in comparison with the large-displacement data recorded during shear tests, therein indicated by a dashed

line, reveals:

$$\tan \delta'_r < \sin \phi'_{crit} \quad 7.10$$

This inequality is also apparent in Uesugi et al's (1989) simple shear test data as pictured in Figure 6.25(b); the stress ratio recorded after cyclic simple shear tests had a tendency to upper bound that after cyclic interface tests. (It should also be noted that the values of  $\tan \delta'_r$  recorded in Uesugi et al's (1989) SSA are similar in magnitude to those recorded here.) To investigate further, an ideal interface test featuring dense VLB was performed under 252kPa to maximise wear rates. The resulting data is pictured in Figure 7.35. It is seen that despite reverse shearing,  $\delta'_r$  did not reduce to a value of similar magnitude to that recorded for metallic interfaces (indicated in Figure 7.35 by a horizontal dashed line) but instead remained at a value corresponding to  $\sin \phi'_{crit}$ . Thus, either a fundamental difference exists between sand-steel and sand-sand friction, or the measured run-in data, which seems to indicate a unique end state, is actually transitory and slow increases of interface resistance are to be expected. The Author is of the opinion that the first hypothesis is true, since the run-in plateau is remarkably level and arrived at both from above, when rough surfaces are investigated, and from below, when interface constituent surfaces are smooth. However, it would be rash to identify the run-in data as indicative of an interfacial critical state until parameters influencing  $\delta'_r$  are more fully investigated.

With the limited data presented here, the value of  $\delta'_r$  found to mark the transition between dilative and non-dilative in the two-tiered model of peak interface response (Section 7.3.5) correlates well with the value of  $\delta'_r$ . Reconsidering the two-tier model of interface friction, condensed in Equation 7.6, in the light of the correspondence between  $\delta'_r$  and the transitional value of  $\delta'_r$ , dilatant interface behaviour can be categorised using a relationship of the form:

$$\delta'_{peak} = \delta'_r + 0.8\psi_{peak} = \delta'_r + f(R, D_r, p') \quad 7.11$$

where  $R$  is a measure of normalised roughness,  $D_r$  is the relative density, and  $p'$  represents the stress level. In effect, the function of  $R$ ,  $D_r$  and  $p'$  would indicate the degree to which a particular interface climbs the two-tiered model's dilative wing. For non-dilatant interfaces a more appropriate relationship may take the form:

$$\delta'_{peak} = \delta'_r - g(R, p') \quad 7.12$$

The functions  $f$  and  $g$  can be characterised when a sufficient data base of interface behaviour exists. If found to hold true for a wide variety of interfaces, these equations potentially hold great power. The first half of Equation 7.11 could be used to estimate the magnitude of  $\delta'_r$  from a number of tests that adequately quantify the peak state of dilatant interfaces. Thus, reverse testing would not be necessitated and test duration reduced accordingly. Characterisation of the function  $f$  would then allow the peak resistance of any interface to be estimated providing the stress level, density and relative roughness were known. However, and leaving aside peak response, the importance of the run-in resistance should be recognised.

Although 200mm of displacement applied during direct shear or interface tests is considered substantial by laboratory standards, in the field such displacements are regularly exceeded. Pile driving, for example, imparts many meters of displacement to sand-steel interfaces before the pile becomes operational. Thus, it could be argued that  $\delta'_r$  is more relevant to the operative coefficient of interface friction in such environs than either  $\delta'_{peak}$  or  $\delta'_{ld}$  and should hence be employed in design. Equation 7.11 and 7.12 may provide an expedient tool for the experimenter to estimate this important angle.

## 7.5 Summary

Interface behaviour has been investigated using the WDSA with its lower frame replaced by a solid block of steel of equivalent dimensions and with uppermost surface of pre-determined roughness. Although the literature presents numerous examples of the DSA being used when investigating interface friction, this is the first time an apparatus modified to limit the archetype's disadvantages has been employed to this end. Experimentation has confirmed many of the findings presented within the literature using far more sophisticated pieces of equipment. The relative simplicity of the WDSA combined with kinematics that correspond to the failure characteristics of interfaces highlight the apparatus' suitability for interface friction research.

An investigation was undertaken into the behaviour of ideal interfaces, those where the constituent surface has a topography equivalent to a layer of the constituent sand. The behaviour of such interfaces have rarely been examined within the literature. For VLB and MGS, the cardinal stress ratios and dilation increments were seen to correspond exactly to those recorded during equivalent direct shear tests. For SFS, however, and unlike its response in direct shear, the ideal interface response differed from the direct shear response in that it showed no indication of progressive failure. It is reasoned that the high degree of kinematic constraint imparted to the granular portion of an ideal interface by the proximity of the boundary walls was sufficient to stop such undesirable behaviour. Two recommendations can

be made, the second becoming activated if the first is overlooked:

- The ideal interface test should replace the direct shear test as the standard method for estimating the shear strength of a granular material on the grounds that such tests are less sensitive to DSA configuration and less prone to progressive failure. Thus a modified version of Davis' (1968) relationship (Equation 7.2) can be confidently used to estimate the plane-strain strength parameter .
- Ideal interface tests should be used to verify questionable direct shear test results. Signs that direct shear data are erroneous include:

$$(\delta'_{ii})_{peak} > (\phi'_{ds})_{peak} \quad 7.13$$

$$(\psi_{ii})_{peak} > (\psi_{ds})_{peak} \quad 7.14$$

$$(\delta'_{ii})_{ld} < \phi'_{ld} \quad 7.15$$

Surface roughness is highly influential in determining interface behaviour. Peak interface strength can be described using a three-tiered model when plotted against surface roughness normalised by the mean particle diameter, as previously described by Paikowsky et al (1995). For the wide range of surface topographies investigated here, the similarity between the proportional increase of various roughness parameters as one progresses from one surface to the next implies that good correlation may be achieved using a variety of roughness parameters. Five different amplitude roughness parameters, three wavelength parameters and the smooth-rough crossover length derived from structured walk analysis all provide reasonable correlations with peak interface resistance. The latter is the preferred parameter not because it provides better correlating ability but because it is associated with a clear physical meaning: the scale above which the solid surface can be considered planar.

The strength-dilatancy response of interfaces has for the first time been investigated using quantitative dilatancy analysis. If dilatancy is activated, gains in interfacial peak strength bought about by increased constituent surface roughness, decreased confining stress and increased density go hand in hand with proportional increases in dilatancy. This finding suggests a two-tiered model, illustrated on axes of  $\delta'_{peak}$  and  $\psi_{peak}$ , provides a more realistic representation of peak interface response than Paikowsky et al's (1995) three-tiered model. Dilatancy is either activated, and peak strengths mobilised accordingly, or it is not, and peak strengths are low. Analysed in this manner, the peak interfacial stress-dilatancy response

featuring three different sands and a range of density and confining stress correlates reasonably well with a modified version of Bolton's (1986) flow rule (Equation 7.6) when the constant term is taken to be  $27^\circ$ .

Once the peak state has been overcome, further interface displacement results in the mobilisation of near constant resistances apparently independent of density and dependent on stress-level to a similar degree as  $\phi'_{crit}$  when estimated from WDSA shear tests. Unlike Lehane (1992), whose interface tests included only a small range of constituent surface roughness, here large-displacement resistances are found to be highly dependent on surface topography. In addition, large displacement data does not indicate a constant volume condition and on smooth surfaces with coarse sand, the interface resistance increases with displacement. Clearly the application of large displacement (circa 12mm) does not produce a unique end state and to call such a condition a critical state (Jardine et al, 1993) is thus unwarranted.

The evolution of interfacial resistance was investigated using reverse direct shear tests. The increase in resistance with  $v_x$  recorded for coarse sand on smooth surfaces at large displacement was followed by further increase with  $V_x$ , the cumulative interface displacement, at a reducing rate until an upper limiting value was attained. The magnitude of this upper limit was equivalent to the resistance mobilised far sooner during tests featuring initially rougher surfaces and on which dilation was triggered from the outset. Thus, multi-reverse shearing caused interface resistance to converge on a unique value confirming the findings of Uesugi et al (1989) and similarly termed  $\delta'_r$ , the subscript standing for run-in as opposed to Uesugi et al's (1989) residual, indicating the occurrence of wear processes.

Increases in resistance coincided with traverses of the apparatus that induced negligible dilation, i.e. when sliding at the soil-metal contacts predominantly accounted for the shear displacement. Thus, it is unlikely that they are brought about by an increasing number of smaller worn fragments of abraded sand particles finding the surface rougher than the original particles, as concluded by Uesugi et al (1989). Instead, sliding particles cause wear-scars to be ploughed into the steel by the relatively hard particles, anisotropically increasing the surface roughness, a process able to be visualised by the structured walk plots of fractal analysis. The rougher the surface, the more likely particles are to roll as opposed to slide and thus the dilatancy associated with each traverse increases with the traverse number. This process, combined with the accumulation of worn particle fragments along the surface, is thought to underlie the convergence of interfacial resistance to a unique run-in value.

The magnitude of  $\delta'_r$  for VLB on steel surfaces of various roughness confined under various loads was equivalent to the transitional value of  $\delta'$  within the two-tiered model of peak interface response. Thus, if found to be true for a wider variety of interfaces, an estimate of  $\delta'_r$  can be obtained by considering the

peak state stress and dilatancy data for a number of dilatant interfaces (Equation 7.11). It is suggested that  $\delta'_r$  represents a better estimation of the operative angle of interface friction occurring in the field.

## 8. CONCLUDING REMARKS

In line with the structure of the thesis, the concluding remarks are presented in two parts; the first relating to direct shear testing and the second to interface testing. Discussion is followed by the recommendations for further work.

### 8.1 Direct shear testing

Although the simplicity of the direct shear apparatus has proved popular, the literature abounds with its criticism. From the East, such criticism predominantly focuses on the inability to obtain a reliable estimate of the normal stress acting on the central plane due to the mobilisation of substantial friction forces on the internal walls of the box. To overcome this, the Japanese Geotechnical Society (JGS, 2000) has recently stipulated that a load cell be included on the apparatus' load receiving side, in which wall friction is minimised by the prevention of displacement between the sample's grains and the apparatus' internal walls. In the West, it is the nonuniformity of stress and strain within the apparatus that has been the focus of criticism, and in particular the occurrence of oblique ruptures propagating through the sample. The much-reported rotation of the apparatus' components during testing has been said to be indicative of nonuniformity and a number of rotation-limiting modifications have been implemented (e.g. Wernick, 1979, Jewell, 1989). Such apparatus retain the archetype's simplicity and are therefore attractive for practical reasons.

Appraisal of the standard practice of direct shear tests has revealed inconsistencies between the Standards and a general lack of care as to appropriate procedures and interpretations. Logical modifications to standard practice include:

- The inclusion of the self-weight of the upper components of the shearbox when estimating the normal stress acting on the central plane. Failure to account for this inherent load will result in underestimation of  $\sigma'_{yy}$  and consequential overestimation of the shear strength, and an apparent cohesion intercept.
- The assumption of an appropriate angle of interface friction (approximately  $12^\circ$ ) on the progressively revealed face of the lower frame. In this way large displacement data can indicate a constant shear resistance.



In addition, it is improbable that the sample deposition methods recommended by the Standards will produce uniform samples. It is recommended that they be replaced, at least for research purposes, by sample pluviation techniques. Requiring standard laboratory equipment, pluviation provides a quick and straightforward way of reconstituting reproducible and highly homogenous deposits at a variety of densities.

A direct shear device handicapped by the reported symptoms of non-uniformity and uncertainty relating to the correct load estimation has been analysed and redesigned providing substantial improvements in performance. The application of the shear load through a system of ball-races ensures the upper half of the Winged Direct Shear Apparatus (WDSA) is free-floating. Thus,  $\sigma'_{yy}$  can be reliably estimated from external forces. In addition, the articulation of the redesigned apparatus minimises any rotation-born secondary forces and moments whilst ensuring that the line of thrust coincides as closely as possible with the central plane at all stages of testing. However, and unlike the working DSA found in the literature, the redesigned apparatus bears a close resemblance to the archetype and may be implemented following relatively minor, cost-effective modifications.

An experimental investigation, predominantly at low stress levels, has been performed in order to optimise the WDSA's performance. The findings and recommendations resulting from this investigation are noted in the order they were presented in the thesis.

- Dentated plates are ineffectual at applying the shear load to the sample, but instead produce consistent underestimation of peak dilation rates. Their expulsion from standard practice is recommended.
- The benefits provided by following Jewell & Wroth (1987) and securing the load pad to the upper frame prior to the imposition of shear displacement are plentiful. The running of tests is more straightforward, with the displacement of only a single component requiring monitoring, intermittent interactions between the load pad and the upper frame occurring during unsymmetrical tests are banished, and the upper frame is less likely to interact directly with the lower during the course of a test. On these grounds it is recommended that the symmetrical configuration become the standard.
- Opposed to Jewell's (1989) findings, and for uncertain reasons, substantial rotations of the upper ensemble remain when symmetrical testing. An inherent cause of rotation identified here is the additional volume created at the front of the upper frame, adjacent to the opening between the frames, due to sample extrusion at the rear. This becomes less influential as the sample length  $L$

increases and thus has small relevance to Jewell's (1989) 250mm long apparatus. The additional volume can be limited with the use of shielding to reduce sample extrusion especially when the opening between the frames assumes large values. Shielding comprises strips of rubber membrane attached with silicone grease to the internal walls of the shearbox and extending down to span the opening between the frames. To prevent the requirement for a membrane correction, the shielding attached to the walls of the upper frame should be separate from that in the lower.

- The size of the opening between the upper and lower frame can bolster strengths when small and reduce strengths when large. Openings of magnitude  $5D_{50}$  were found optimum, allowing the unrestricted development of a rupture while not subjecting too great a sample volume to stress release. It is recommended that shielded openings of this magnitude be employed for standard testing. To prevent the disturbance of a sample's fabric, the opening should be established prior to sample deposition using a simple system of screws threaded vertically through the upper frame. To prevent the opening from closing prior to testing, the screws should be removed only once the upper-frame is secured to the load pad.
- Minimum sample dimensions ensure that a sample will not be subject to passive failure or dominated by boundary effects. From the limited data presented here, it is suggested that a direct shear sample should have length of at least 60mm if large displacement data is desired and height of at least a quarter of the length to prevent passive failure. It is recognised that progressive failure may be prevented by stipulating a maximum scale of the DSA in terms of a limiting  $L/D_{50}$  ratio. Disparate working ratios are revealed in the literature. For the WDSA, progressive failure seems to occur at  $L/D_{50}$  ratios of around 250.

Certain undesirable characteristics are exhibited in WDSA data. As mentioned above, the apparatus' upper ensemble rotates during shear, albeit to a small degree. The novel way in which the shear load is applied to the upper frame has allowed an investigation into the effect of this rotation on test data. By applying moments to the upper ensemble it has been shown that rotation does not necessarily influence either the measured shear force or average vertical displacement. It is concluded that rotations of the upper half of the apparatus do not necessarily provide a reliable indicator of the WDSA's performance.

More importantly, and as has been demonstrated in the Cambridge Simple Shear Apparatus, the behaviour of a sand sample within the WDSA depends on the degree of constraint offered by the sample boundaries. Small sand particles are less aware of the boundaries than larger particles making samples comprised of smaller particles more prone to progressive failure and oblique ruptures. The features in test

data indicative of such undesirable failure mechanisms include:

- a bi-linear relationship when stress ratio is plotted against dilation increment.
- prolonged dilatancy.
- low rates of strain softening resulting in a large-displacement stress ratio the arcsine of which provides an unrealistically high estimate of  $\phi'_{crit}$ .
- underestimation of  $\psi_{peak}$ .

Data from an equivalent ideal interface test can be used to provide an expedient check on the reliability of questionable direct shear test data since the increased kinematic constraint provided by the test's boundaries reduces the likelihood of undesirable failure mechanisms. Mismatch between the cardinal parameters extracted from direct shear and equivalent ideal interface tests indicates unreliability of the direct shear test data. On the grounds of reduced chance of progressive failure, there is an argument for the adoption of the ideal interface test in place of the direct shear test as a standard means for obtaining robust estimates of a sand's shear strength.

The most reliable aspect of direct shear test data irrespective of sample failure mechanism is the peak shear resistance, although it may be slightly underestimated if progressive failure occurs. Thus, if a universal interpretation of shearbox data is required which will not produce an overestimation of shear strength, it should be based on this measure alone. With a reliable measure of  $\phi'_{crit}$  obtained outside of the DSA, the flow-rule analysis suggested by Jewell (1989) will provide safe estimates of  $\phi'_{ps}$ . Without such external data, however, the data presented herein suggest  $\phi'_{ps}$  can be estimated by adding  $6^\circ$  to  $\phi'_{ds}$ , the arctangent of the peak stress ratio. Such a test interpretation is useful in that the test duration need only encapsulate peak behaviour. In addition, dilation data, which are especially sensitive to test configuration, are not required.

WDSA data from 19 tests featuring both medium and coarse sand deposited at various densities within the optimised WDSA confined at stress levels spanning the apparatus' limits were investigated in detail. In general, the trends apparent in test data agreed with conventional wisdom and published test data. The salient features of this investigation include:

- The reliability of DSA data can be verified by plotting stress ratio against dilation rate. A near 1:1

line intercepting the ordinate at  $\sin\phi'_{crit}$  implies a good correlation with Taylor's (1948), Rowe's (1962) and Bolton's (1986) flow rules indicating high data quality. In addition, agreement between estimates of  $\phi'_{ps}$  obtained using Davis' (1968) relationship, which involves measures of  $\phi'_{ds}$  and  $\psi_{peak}$ , and Rowe's (1969) relationship, involving  $\phi'_{ds}$  and  $\phi'_{crit}$  (estimated from large displacement shearbox data), similarly verifies the reliability of test data

- $\phi'_{crit}$  cannot be reliably estimated from the stress ratio at the point of maximum sample contraction. For dense samples, the rates of change of data during the early stages of testing are too high to produce an accurate estimate.
- When data are considered between their peak and large displacement values, unique strain softening trends are recorded independent of stress level.
- Large displacement stress data show a slight stress level dependency that although being unified by changing the reference axis from shear displacement to work, may be a product of the apparatus configuration (perhaps shielding deformations). It is clear that such behaviour is not a consequence of the ever-reducing plan area of the central plane, since similar stress level dependency is recorded during ideal interface tests.

The overriding conclusion from Part 1 of the thesis is that the WDSA is able to provide reliable estimates of a sand's shear strength parameters, in which a number of simple checks can give confidence. Even when hampered by progressive failure, appropriate test interpretations can still produce reasonable estimates of the shear strength. Thus, when appropriately modified, the DSA has a place in modern soil mechanics.

## 8.2 Interface testing

The science of sand-steel interface friction is multi-disciplinary, a fact that the soil mechanics literature has, until recently, neglected. Similar systems are commonly found within the tribology literature, where the principal interest is the interaction between surfaces in relative motion, encompassing the subjects of friction and wear. Most analogous are abrasive wear scenarios, where hard abrasive particles interact under load with softer metal surfaces. Mechanisms of interaction can then involve the indentation and ploughing of the surface. Consequently changes to the surface topography occur; particle sliding causes wear scars to be ploughed in to the soft surface whereas particle rolling produces indentation pits. In addition, a size effect is apparent in that friction and wear coefficients increase with the volume of

material stressed by the surface process.

The geometric complexity of even macroscopically smooth surfaces has led to the definition of numerous measures of roughness which are commonly used to quantify different aspects of texture. Here a number of conventional parameters have been compared to newer fractal parameters derived from structured walk analysis for seven surfaces of very different texture. From the smoothest surface to the roughest, the proportional increase in the smooth-rough crossover value, which defines the scale below which a surface should be considered rough, corresponds to that of the conventional amplitude roughness parameters. The absolute maximum slope of the fractal plot, which is a measure of the intricacy or complexity of the surface features, corresponds to surface slope parameters. The clear physical meaning inherent in the fractal parameters sets them aside from conventional roughness parameters.

The agreement of the various amplitude parameters when expressed in relative terms means that the peak resistance provided by the interface can be successfully correlated using measures other than that proposed by Uesugi & Kishida (1986a) and whose use has since become common. In fact, and for practical reasons, the use of a roughness parameter based on average deviations of a surface profile, such as the British Standard  $R_a$ , is recommended rather than one based on extreme events. Profilometry workloads are then substantially reduced.

The response of interfaces consisting of sand overlying a solid surface were investigated using the optimised WDSA. Although commonly used to investigate interface friction, a DSA modified to limit the defects of the archetype has never before been used to this end. The upshot has been the quantification of interface dilation, which have led to a radically different characterisation of interface behaviour. Three interfacial states has been investigated: peak, large displacement (corresponding to the end of a single traverse of the WDSA's carriage and indicated by subscript  $ld$ ), and run-in (indicated by subscript  $r$ ). The concluding remarks relating to each will be discussed in turn.

The peak response of an interface is determined by the preferred movement pattern of its constituent particles. For sliding at the sand-steel contact points to predominate, the surface needs to be smooth enough and subjected to a high enough confining stress. The hardness ratio between quartz and steel is sufficient to activate abrasive wear processes and sliding particles plough scars into the steel surface. Peak resistances are then low and behavioural traits correspond with those reported within the tribology literature where abrasive wear mechanisms have been investigated, characteristics of which include an increasing peak resistance with stress level and the anisotropic roughening of surface topography. There are no standard methods of analysis to investigate changes in topography due to surface processes, but

the structured walk plots of fractal analysis provide an effective visualisation.

If the relative roughness between a surface and a particulate mass is of sufficient magnitude and the stress level is sufficiently low, dilatancy is activated indicating the occurrence of rolling as the preferred particle movement. Higher peak strengths are then mobilised accordingly, and Bolton's (1986) flow rule, when appropriately modified for interfaces, can be used to correlate data. Thus, opposed to the three-tier model of peak interface response offered by Paikowsky et al (1995) which masks the fundamental difference in dilatancy response, a two-tiered characterisation is proposed between dilatant and non-dilatant interfaces. For the three sands investigated with wide ranging particle sizes, deposited at a range of densities and confined under various stresses, it is found that the transitional angle of friction between dilatant and non-dilatant interfaces is 27°.

Beyond peak, further shear displacement brings about the mobilisation of a near-constant resistance at large displacement that has been mistakenly identified within the literature as representative of a critical state (Jardine et al, 1993). This classification is inappropriate because:

- Interface resistances are not necessarily constant
- A constant volume condition is rarely achieved
- The resistance is dependent on the relative roughness between the sand and the surface

The evolution of interface response was investigated using reverse testing in which the WDSA's carriage travelled back and forth between its maximum limiting displacements. Non-dilatative interfaces experienced substantial increases in resistance at a reducing rate until an upper limiting value was approached. The increases in resistance coincide with traverses of the apparatus which did not trigger dilatancy and are thus associated with particle sliding and consequential ploughing of the surface. For the limited data available, the limiting resistance  $\delta'_r$  correlated precisely with the transitional value of  $\delta'$  within the two-tiered model of interface response.

From the limited data presented herein, it appears that for coarse Leighton Buzzard sand and mild steel interfaces, the following inequality holds:

$$\tan \delta'_r < \sin \phi'_{crit} \quad 8.1$$

This is also apparent in the cyclic interface test data presented by Uesugi et al (1989). A reverse shear test featuring an ideal VLB interface under high stress to maximise wear rates revealed  $\tan\delta'_r$  to equal  $\sin\phi'_{crit}$ . Thus it is hypothesised that a fundamental difference exists between the ideal and metallic interfaces and it is concluded that the run-in state probably represents the true critical state for interfaces.

From this, it can tentatively be concluded that the following flow rule provides an appropriate characterisation of dilatant interfaces:

$$\delta'_{peak} = \delta'_r + 0.8\psi \quad 8.2$$

Thus a limited number of interface tests which adequately characterise the peak response of dilatant interfaces can provide a measure of  $\delta'_r$  without the need for time-consuming reverse interface tests. It is likely that  $\delta'_r$  is the operational angle of interface friction for many applications.

### 8.3 Recommendations for further work

The suggestions for further work can be split into two categories. The first relates to significant omissions from this work due to time restrictions caused by the prolonged consideration of the DSA. The second relates to the broader areas of research now required.

Further work needed to satisfy the omissions of the present study primarily require a large database of shearbox and interface data to be obtained for a variety of sands tested under different conditions within the WDSA. From this database it should be possible to:

- Investigate the wider applicability of the simple interpretation of direct shear data suggested by this work which involves merely adding a constant to the peak direct shear angle of friction. Such an interpretation is useful, as it does not rely on other types of direct shear data that are liable to be inaccurately measured.
- Ascertain the ratio of grain size to sample dimension necessary to induce a failure mechanism comprising a single rupture across the WDSA's central plane. Clear guidance can then be given as to the appropriate size of shearbox for any given soil.
- Explore more fully Bolton's (1986) flow rule as modified for interfaces. It should be possible, given a large enough database, to empirically derive a function involving quantifiable interface parameters

of roughness, sample density, and stress level that allows the peak interfacial dilatancy response, and thereby the peak resistance, to be estimated.

- Determine whether  $\delta'_r$  is indeed a unique state parameter and establish its determining characteristics.

Some broader areas of research can also be highlighted:

- It is a frustrating outcome of this work that the reasons for the rotations of the upper components of the DSA remain hidden. Consideration of the sample's force and moment equilibrium does not, as reported in the literature, provide insight into the reasons for rotation. Since this line of reasoning treats the soil as a continuum, modelling the soil as a collection of discrete elements with associated localisation phenomena may reveal the reasons for rotation. Additionally, such models may help confirm or modify the WDSA configuration herein determined optimum.
- Within the field, sand-steel interaction will commonly occur in the presence of water. The effect of moisture on interface resistance is not clear from the literature. Potyondy (1961) found water to have a lubricating effect on interface behaviour, reducing friction coefficients by around 5°. Rowe (1962) found the reverse, an increasing interfacial resistance on saturation. Skinner (1969) also disputed Potyondy's (1961) findings by showing the interfacial resistance to approximately double when a mass of glass ballotini sliding on a glass block became saturated. More recently it has been suggested that interface resistance is independent of the presence of water (Lehane, 1992). Further research on the dependence of interface response on the presence of water is required as it clearly has important implications, for example for the design of piles.

Steel surfaces found in the field are somewhat dissimilar to those highly idealised, laboratory prepared examples considered here. As rolled, they are covered with millscale and may, in addition to roughness, suffer from longer wavelength "waviness" components in their surface topography. Steel corrodes in the presence of air and water becoming coated in a highly porous and compressible ferric oxide rust. With the fundamental understanding of "idealised" interfaces presented here, it is now appropriate to widen the scope of investigation to address more directly the response of such "real" interfaces.



## References

- Acar, Y.B., Durgunoglu, H.T. & Tumay, M.T. (1982): Interface properties of sand. *J. Geotech. Engng* 108, ASCE, No. 4, pp 648-654
- Al-Douri, R.H. & Poulos, H.G. (1991): Static and cyclic direct shear tests on carbonate sands. *Geotech. Test. Jnl* 15, GTJODJ, No. 2, pp 138-157
- Allersma, H.G.B. (1999): Optical analysis of stress and strain in a number of shear devices. 2<sup>nd</sup> Int Conf Pre-failure deformation characteristics of geomaterials, Vol. 1, pp 501-508
- Amontons, G. (1699): De la resistance causée dans les machines. *Mémoires de l'Académie Royale*, Vol. 12, pp 257-282
- Archard, J.F. (1953): Contact and rubbing of flat surfaces. *J. Appl. Phys.*, Vol. 24, pp 981-988
- Arnell, R.D., Davis, P.B., Halling, J. & Whomes, T.L. (1991): *Tribology, Principles and design applications*. Macmillan: London
- Arthur, J. R. F. & Dunstan, T. (1988): Discussion on the 6<sup>th</sup> Geotechnique symposium in print. *Geotechnique* 38, No. 4, pp 651-652
- Arthur, J. R. F., Dunstan, T., Al-Ani, Q. A. J. L. & Assadi, A. (1977): Plastic deformation and failure in granular media. *Geotechnique* 27, No. 1, pp 53-74
- Arthur, J. R. F. & Menzies, B. K. (1972): Inherent anisotropy in a sand. *Geotechnique* 22, No 1, pp 115-128
- Askeland, D. G. (1996): *The Science and Engineering of Materials*, Chapman & Hall, 1996
- Assadi, A. (1975): Rupture Layers in granular materials. PhD thesis, University of London
- ASTM, (1995a): Annual book of ASTM standards, Soil and Rock (I), Vol. 04.08, American Society for Testing and Materials, ASTM, Philadelphia, PA, pp 981
- ASTM, (1995b): Annual book of ASTM standards, Soil and Rock (II), Vol. 04.09, American Society for Testing and Materials, ASTM, Philadelphia, PA, pp 625
- Athanasopoulos, G. A. (1993): Effect of particle size on the mechanical behaviour of sand-geotextile composites. *Geotextiles and Geomembranes*, Vol. 12, pp 255-273
- Bardet, J. P. (1997): *Experimental soil mechanics*. Prentice-Hall, New Jersey
- Bica, A. V. D. & Clayton, C. R. I. (1998): An experimental study of the behaviour of embedded lengths of cantilever walls. *Geotechnique* 48, No. 6, pp 731-745

- Bishop, A. W. (1950): Discussion on the measurement of the shear strength of soils in relation to practice. *Geotechnique* 2, No. 2, pp113-116
- Bolton, M.D. (1986): The strength and dilatancy of sands. *Geotechnique* 36, No. 1, pp 65-78
- Bolton, M.D. (1987): Discussion on the strength and dilatancy of sands. *Geotechnique* 37, No. 2, pp 225-226
- Bosscher, P.J. & Ortiz, C. (1987): Frictional properties between sand and various construction materials. *J. Geotech. Engng* 113, ASCE, No. 9, pp 1035-1039
- Boulon, M. (1989): Basic features of soil-structure interface behaviour. *Computers and Geotechnics* 7, pp 115-131
- Bowden, F.P. & Tabor, D. (1967): *Friction and Lubrication*. London: Methuen & Co. LTD.
- British Standards Institution, (1972): BS-1134: Parts 1 & 2: Method for the assessment of surface texture. BSI, Milton Keynes, UK
- British Standards Institution, (1990): BS 1377: Part 7: 4: Determination of shear strength by direct shear. BSI, Milton Keynes, UK
- Brown, C. A. & Savary, G. (1991): Describing ground surface texture using contact profilometry and fractal analysis. *Wear*, Vol. 141, pp 211-226
- Brumund, W.F. & Leonards, G.A. (1973): Experimental study of static and dynamic friction between sand and typical construction materials. *Journal of Testing and Evaluation* 1, JTVEVA, No. 2, pp 162-165
- Brumund, W.F. & Leonards, G.A. (1987): Discussion. *Soils Fnds* 27, No. 2, pp 66-68.
- Budhu, M. (1979): Simple shear deformation of sands. PhD Thesis, University of Cambridge
- Butterfield, R. & Andrawes, K.Z. (1972): On the angles of friction between sand and plane surfaces. *Jrnl. of Terramechanics* 8, No. 4, pp 15-23
- Childs, T. H. C. (1988): The mapping of metallic sliding wear. *Proc. Instn. Mech. Engrs.*, Vol 202, No. C6, pp 379-395
- Cole, E.R. (1967): The behaviour of soil in the simple shear apparatus. PhD Thesis, University of Cambridge
- Cornforth, D. H. (1964): Some experiments on the influence of strain conditions on the strength of sand. *Geotechnique* 14, No. 1, pp 143-167
- Cornforth, D. H. (1973): Prediction of drained strength of sands from relative density measurements. In

- Evaluation of relative density and its role in geotechnical projects involving cohesionless soils. ASTM STP 523, pp 281-303
- Coyle, H.M. and Sulaiman, I.H. (1967): Skin friction for steel piles in sand. *Jrnl Soil Mech. & Fnds Div.* 92, ASCE, No. 2, pp 261-278
- Crewe, A.J., Lings, M.L., Taylor, C.A., Yeung, A.K. & Andeighetto (1995): Development of a large flexible shear stack for testing dry sand and simple direct foundations on a shaking table. *European Seismic Design*, ed. A.S. Elnashai, Balkema: Rotterdam, pp 163-168
- Dagnall, H. (1980): *Exploring surface texture*, Rank Taylor Hobson Limited: Leicester
- Davis, E. H. (1968): Theories of plasticity and the failure of soil masses. *Soil Mechanics, selected topics* (ed. I. K. Lee). London: Buterworth
- De Gennaro, V. & Lerat, P. (1997): Soil structure behaviour under cyclic loading. Pre-failure Defm. *Characteristics of Geomaterials*, ed. Lancellotta & Lo Presti, Balkema: Rotterdam, pp 183-189
- Dove, J. E. & Frost, J. D. (1999): Peak friction behaviour of smooth geomembrane-particle interfaces. *Jrnl. Geotech. and Geoenv. Eng.*, ASCE, Vol. 125, No. 7, pp 544-555
- Dove, J. E., Frost, J. D., Han, J., & Bachus, R. C. (1997): The influence of geomembrane surface roughness on interface strength. *Proc. Geosynthetics 97*, Vol. 1, pp 863-876
- Dyer, M.R. (1985): Observation of the stress distribution in crushed glass with applications to soil reinforcement. DPhil thesis, University of Oxford
- Evans, M.D. & Fennick, T.J. (1995): Geosynthetic/soil interface friction angles using a rotation shear device. *Geotech. Test. Jrnl* 18, GTJODJ, No. 2, pp 271-275
- Everton, S.J. (1991): Experimental Study of Interface frictional shearing resistance between non-cohesive soils and construction materials. MSc thesis, Imperial College, University of London
- Evgin, E. & Fakharian, K. (1996): Effect of stress paths on the behaviour of sand steel interfaces. *Can. Geotech. J.* 33, pp 853-865
- Fang, L., Kong, X. L., Su, J. Y. & Zhou, Q. D. (1993): Movement patterns of abrasive particles in three body abrasion. *Wear*, Vol. 163-164, pp 782-789
- Frost, J. D. & Han, J. (1999): Behaviour of interfaces between fibre-reinforced polymers and sands. *Jrnl. Geotech. and Geoenv. Eng.*, ASCE, Vol. 125, No. 8, pp 633-640
- Gane, N. & Skinner, J. (1973): The friction and scratch deformation of metals on a micro scale, *Wear*, Vol. 24, 207-217
- Garner, M. J. & Dietz, M. S. (1995): The use of the direct shear box for evaluating the friction between

sand and a steel surface. BEng dissertation, University of Bristol

Gere, J. M. & Timoshenko, S.P. (1987): Mechanics of materials. PWS Engineering, Boston

Glossop, R. & Skempton, A. W. (1945): Particle size in silts and sands. Proc. Inst. Civ. Eng. Paper No. 5492

Goddard, J. & Wilman, H. (1962): A theory of friction and wear during the abrasion of metals, Wear, 5, 114-135

Golder, H. Q. (1942): An apparatus for measuring the shear strength of soils. Engineering, 153, pp 501-503

Gudehus, G. & Tejchman, J. (1988): Discussion. Soils Fnds 28, No. 3, pp 178-182.

Hartley, S. (1982): Shear bands in sand. Undergraduate project, Cambridge University

Head, K. H. (1982): Manual of soil laboratory testing- Volume 2: Permeability, shear strength and compressibility tests. Pentech Press, London

Heerema, E.P. (1979): Relations between wall friction, displacement velocity and horizontal stress in clay and in sand for pile driveability analysis. Grnd Enng 12, No. 9, pp 55-61 & 65

Hertz, H. (1882): Study on the contact of elastic solids. Jrnl. Reine Angew. Math., Vol. 29, pp 156-171; SLA translations SLA-57-1164

Houlsby, G.T. (1991): How the dilatancy of soils affects their behaviour. Proc. 10<sup>th</sup> ECSMFE 4, Florence, pp 1189-1202

Hryciw, R. D. & Irsyam, M. (1993): Behaviour of sand particles around rigid ribbed inclusions during shear. Soils Fnds 33, No. 3, pp 1-13

Huang, S. L., Oelfke, S. M. & Speck, R. C. (1992): Applicability of fractal characterisation and modelling to rock joint profiles. Int. J. Rock Mech. Min. Sci. & Geomech. Abstr., Vol. 29, No. 2, pp 89-98

Hutchings, I. M. (1992): Tribology: Friction and wear of engineering materials. Edward Arnold, London

Hvorslev, J. (1939): Torsion shear tests and their place in the determination of the shearing resistance of soils. Proc. ASCE, Vol. 39, pp 999-1022

Japanese Geotechnical Society, (2000): JGS 0561-2000: Method for consolidated constant pressure direct box shear test on soils, JGS, Tokyo, Japan

Jardine, R. J., Lehane, B. M. & Everton, S. J. (1993): Friction coefficients for piles in sands and silts. Soc. Underwater Tech. 28: Offshore site investigation and foundation behaviour, pp 661-677.

- Jewell, R.A. & Wroth, C.P. (1987): Direct shear tests on reinforced sand. *Geotechnique* 37, No. 1, pp 53-68
- Jewell, R.A. (1989): Direct shear tests on sand. *Geotechnique* 39, No. 2, pp 309-322
- Johnson, K.L. (1985): *Contact mechanics*. Cambridge University Press: UK
- Khrushchov, M. M. (1974): Principles of abrasive wear. *Wear*, Vol. 28, pp 69-88
- Kim, D. E. & Suh, N. P. (1991): On microscopic mechanisms of friction and wear. *Wear*, Vol. 149, pp 199-208
- Kishida, H. & Uesugi, M. (1987): Tests of the interface between sand and steel in the simple shear apparatus. *Geotechnique* 37, No. 1, pp 45-52
- Koura, M. M. & Omar, M. A. (1981): The effect of surface parameters on friction. *Wear*, Vol. 73, pp 235-246
- Kulhawy, F.H. & Peterson, M.S. (1979): Behaviour of sand concrete interfaces. Proc. 6<sup>th</sup> Pan-Am Conf. SMFE 2, pp 225-236
- Kuwano, R. (1999): The stiffness and yielding anisotropy of sand. PhD Thesis, Imperial College, London
- Lambe, T.W. & Whitman, R.V. (1969): *Soil Mechanics*. New York: J. Wiley and Sons.
- Larsen-Basse, J. & Premaratne, B. (1983): Ed. Ludema, K. C., Proc. Int. Conf. Of Wear of Materials, ASME: New York, pp 161-166
- Lehane, B.M. (1992): Experimental investigations of pile behaviour using instrumented field piles. PhD Thesis, Imperial College, University of London
- Lemos, L. (1986): The effect of rate on residual strength of soil. PhD Thesis, Imperial College, University of London
- Lo Presti, D.C.F., Berardi, R., Pedroni, S. & Crippa V. (1993): A new travelling sand Pluviator to reconstitute specimens of well-graded silty sands. *Geotech. Test. Jnl* 16, GTJODJ, No. 1, pp 18-26
- Maan, N. & Broese Van Groenou, A. (1977): Low speed scratch experiments on steel. *Wear* 42, 365-390
- Malkin, S. & Joseph, N (1975): Minimum energy in abrasive processes. *Wear*, Vol. 32, 15-23
- Mandelbrot, B. B. (1977): *The fractal geometry of nature*. Freeman, San Francisco
- Matthews, M.C. (1988): The engineering application of direct and simple shear testing. *Grnd Engng* 21, No. 2, pp 13-21

- Maeda, K. & Miura, K. (1999): Confining stress dependency of mechanical properties of sands. *Soils Fnds* 39, No. 1, pp 53-67
- Mikasa, M. (1960): New direct shear apparatus. *Proc. 15<sup>th</sup> Ann. Conv. JSCE, Tokyo*, pp 45-48 (in Japanese)
- Misra, A. & Finnie, I. (1981): On the size effect in abrasive and erosive wear. *Wear*, Vol. 65, pp 359-373
- Misra, A & Finnie, I. (1983): An experimental study of three-body abrasive wear. *Wear*, Vol. 85, 57-68
- Miura, S. & Toki, S. (1982): A sample preparation method and its effects on static and cyclic deformation-strength properties of sand. *Soils Fnds* 22, No. 1, pp 61-77
- Miura, K., Maeda, K. & Toki, S. (1997): Method of measurement for the angle of repose of sands. *Soils Fnds* 37, No. 2, pp 89-96
- Moore, M. A. (1974): A review of two-body abrasive wear. *Wear*, Vol. 27, pp 1-17
- Morgenstern, N. R. & Tchalenko, J. S. (1967): Microscopic structures in Kaolin subjected to direct shear. *Geotechnique* 17, No. 4, pp 309-328
- Mott, B. W. (1957): *Micro-indentation hardness testing*. Butterworths, London
- Mulilis, P. H., Seed, H. B., Chan, C. K., Mitchell, J. K. & Arulanandan, K. (1977): Effects of sample preparation on sand liquefaction. *Jrnl Geotech. Engng* 03, No. 2, pp 91-109
- Nedderman, R. M. & Laohakul (1980) The thickness of the shear zone in flowing granular materials. *Powder Technol.*, Vol 21, pp17
- Nakamaru, S., Pradhan, T. B. S. & Fujitani, M. (1985): Strength and deformation properties of various sands in direct shear test. *Proc. Symp. Direct shear box testing of soils, JSSMFE*, pp 111-118 (in Japanese)
- Negussey, D., Wijewickreme, W.K.D. & Vaid, Y.P. (1988): Geomembrane interface friction. *Can. Geotech. Jrnl.*, Vol. 26, pp 165-169
- O'Rourke, T.D., Druschal, S.J. & Netravali, A.N. (1990): Shear strength characteristics of sand-polymer interfaces. *J. Geotech. Engng* 116, ASCE, No. 3, pp 451-469
- Paikowsky, S.G., Player, C. M. & Connors, P.J. (1995): A dual interface apparatus for testing unrestricted friction of a soil along solid surfaces. *Geotech. Test. Jrnl* 18, GTJODJ, No. 2, pp 168-193
- Paikowsky, S.G., Player, C. M. & Connors, P.J. (1996): Closure. *Geotech. Test. Jrnl* 19, GTJODJ, No. 4, pp 447-451

- Palmeira, E. M. (1988): Discussion on the Sixth Geotechnique Symposium in Print: the engineering application of direct and simple shear testing. *Geotechnique* 38, No 1, pp 146-148
- Palmeira, E. M. & Milligan G. W. E. (1989a): Scale effects in direct shear tests on sand. Proc. 12<sup>th</sup> ICSMFE (Rio), Vol. 1, Ses. 8, No. 17, pp 739-742
- Palmeira, E. M. & Milligan G. W. E. (1989b): Scale and other factors affecting the results of pull-out tests of grids buried in sand. *Geotechnique* 39, No. 3, pp 511-524
- Potts, D. M., Dounias, G. T. & Vaughan, P. R. (1987): Finite element analysis of the direct shear box test. *Geotechnique* 37, No. 1, pp 11-23
- Potyondy, J.G. (1961): Skin friction between various soils and construction materials. *Geotechnique* 11, No. 4, pp 339-353
- Qiu, J. Y., Tatsuoka, F. & Uchimura, T. (2000): Constant pressure and constant volume direct shear tests on reinforced sand. *Soils Fnds* 40, No. 4, pp 1-17
- Richardson, R. C. D. (1968): The wear of metals by relatively soft abrasives. *Wear*, Vol. 11, pp 242-275
- Roscoe, K. H. (1953): An apparatus for the application of simple shear to soil samples. Proc. 3<sup>rd</sup> ICSMFE, Vol. 2, pp 186-191
- Roscoe, K. H. (1970): The influence of strains in soil mechanics. *Geotechnique* 20, No. 2, pp 129-170
- Rowe, P.W. (1962): The stress dilatancy relation for static equilibrium of an assembly of particles in contact. Proc. Roy. Soc. A269, pp 500-527
- Rowe, P.W. (1969): The relation between the shear strength of sands in triaxial compression, plane strain and direct shear. *Geotechnique* 19, No. 1, pp 75-86
- Rowe, P. W., Barden, L & Lee, I. K. (1964): Energy components during the triaxial cell and direct shear tests. *Geotechnique* 14, No. 3, pp 247-261
- Saada, A. S. & Townsend, F. C. (1981): State of the art: Laboratory strength testing of soils. Laboratory shear strength of soil, ASTM STP 740, eds. R.N. Yong & F.C. Townsend, pp 7-77
- Scarpelli, G. (1981) Shear bands in sand. M. Phil. Thesis, Cambridge University
- Scarpelli, G. & Wood, D. M. (1982): Experimental observations of shear band patterns in direct shear tests. Proc. IUTAM Symp. Deformation and Failure of Granular Materials (eds P.A. Vermeer & H. J. Luger), Balkema, Rotterdam, pp 473-484
- Shaw, M. C. (1971): The fundamental basis of the hardness test. In: The science of hardness testing and its research applications, Ed. Westbrook, J.H. & Conrad, H., American Society for Metals: Ohio,

Section 1, Chapter 1, pp 1-11

- Shibuya, S., Mitachi, T. & Tamate, S. (1997): Interpretation of direct shear box testing of sands as quasi-simple shear. *Geotechnique* 47, No. 4, pp 769-790
- Sin, H. Saka, N. & Suh, N. P. (1979): Abrasive wear mechanisms and the grit size affect, *Wear*, 55 (1979), 163-190
- Skempton, A. W. (1949): Alexandre Collin: A note on his pioneer work in soil mechanics. *Geotechnique*, 1, 4, 216-221
- Skinner, A.E. (1969): A note on the influence of interparticle friction on the shearing strength of a random assembly of spherical particles. *Geotechnique* 19, No. 1, pp 150-157
- Stroud, M.A. (1971): The behaviour of sand at low stress levels in the simple shear apparatus. PhD Thesis, University of Cambridge
- Subba Rao, K.S., Allam, M.M. & Robinson, R.G. (1996a): A note on the choice of interfacial friction angle. *Geotech. Engng* 119, *Proc. Inst. Civ. Eng.*, No. 2, pp 123-128
- Subba Rao, K.S., Allam, M.M. & Robinson, R.G. (1996b): Discussion. *Geotech. Test. Jnl* 19, GTJODJ, No. 4, pp 446
- Subba Rao, K.S., Allam, M.M. & Robinson, R.G. (1998): Interfacial friction between sands and solid surfaces. *Geotech. Engng* 131, *Proc. Inst. Civ. Eng.*, pp 123-128
- Summers-Smith, D. (1969): An introduction to tribology in industry. Machinery Publishing Co., London
- Takada, N. (1993): Mikasa's direct shear apparatus, test procedure and results. *Geotech. Test. Jnl.*, GTJODJ, Vol. 16, No. 3, pp314-322
- Tatsuoka, F. & Haibara, O. (1985): Shear resistance between sand and smooth or lubricated surfaces. *Soils Fnds* 25, No. 1, pp 89-98.
- Tabor, D. (1987): Friction and wear-developments over the last fifty years. *Proc. Inst. Mech. Eng.*, C245, pp 157-172
- Tabucanon, J.T., Airey, D.W. & Poulos, H.G. (1995): Pile skin friction in sands from constant normal stiffness tests. *Geotech. Test. Jnl* 18, GTJODJ, No. 3, pp 350-364
- Taylor, D. W. (1948): *Fundamentals of soil mechanics*. Wiley, New York
- Tika-Vassilikos, T. (1991): Clay-on-steel ring shear tests and their implications for displacement piles. *Geotech. Test. Jnl* 14, GTJODJ, No. 4, pp 457-463



- Thomas, T. R. (1982): *Rough surfaces*. Longman: New York.
- Uesugi, M. & Kishida, H. (1986a): Influential factors of friction between steel and dry sands. *Soils Fnds* 26, No. 2, pp 33-46.
- Uesugi, M. & Kishida, H. (1986b): Frictional resistance at yield between dry sand and mild steel. *Soils Fnds* 26, No. 4, pp 139-149.
- Uesugi, M., Kishida, H. & Tsubakihara, Y. (1988): Behaviour of sand particles in sand-steel friction. *Soils Fnds* 28, No. 1, pp 107-118.
- Uesugi, M., Kishida, H. & Tsubakihara, Y. (1989): Friction between sand and steel under repeated loading. *Soils Fnds* 29, No. 3, pp 127-137.
- Uesugi, M., Kishida, H. & Uchikawa, Y. (1990): Friction between dry sand and concrete under monotonic and repeated loading. *Soils Fnds* 30, No. 1, pp 115-128.
- Underwood, E. E. & Banerji, K. (1986): Fractals in fractography. *Materials science and engineering*, Vol. 80, pp 1-14
- Vaid, Y. P. & Negusse, D. (1984): Relative density of pluviated sand deposits. *Soils Fnds* 24, No. 2, pp 104-105
- Vaid, Y. P. & Negusse, D. (1988): Preparation of reconstituted sand specimens. In *Advanced triaxial testing of soil and rock*, ASTM STP 977, ed Donaghe, R. T., pp 405-417
- Vaid, Y. P., Sivathayalan, S. & Stedman, D. (1999): Influence of specimen reconstituting method on the undrained response of a sand. *Geotech. Test. Jnl.*, Vol. 23, No. 3, pp 187-195
- Vallejo, L. E. (1995): Fractal analysis of granular materials. *Geotechnique*, Vol. 45, No. 1, pp 159-163
- Vallejo, L. E. & Zhou, Y. (1995): Fractal approach to measuring roughness of geomembranes. *Jnl Geotech. Eng.*, Vol. 121, No. 5, pp 442-446
- Wernick, E. (1977): Stresses and strains on the surface of anchors. *Proc. 9th ICSMFE (Tokyo)*, Spec. Sess. No. 4, pp 113-119
- Wernick, E. (1979): A true direct shear apparatus to measure soil parameters of shear bands. *Proc. 7th ECSMFE (Brighton)*, Vol. 2, pp 175-182
- Williams, J.A. & Hyncica, A.M. (1992): Abrasive wear in lubricated contacts. *J. Phys. D: Appl. Phys.* 25A, pp 81-90
- Wood, D. M. & Budhu, M. (1980): The behaviour of leighton buzzard sand in cyclic simple shear tests. *Proc. Int. Symp. On Soils under cyclic and transient loading*, Swansea (eds G. N. Pande & O. C.

Zienkiewicz), Balkema, Rotterdam, No 1, pp 9-21

Wroth, C. P. (1958): The behaviour of soils and other granular media when subjected to shear. PhD Thesis, University of Cambridge

Yasin, S. J. M., Umetsu, K., Tatsuoka, F., Arthur, J.R.F, & Dunstan, T. (1999): Plane strain strength and deformation of sands affected by batch variations and different apparatus types. Geotechnical Testing Journal, GTJODJ, Vol. 22, No. 1, pp 80-100.

Yoshimi, Y. & Kishida, T. (1981a): Friction between sand and a metal surface. Proc. 10<sup>th</sup> ICSMFE 1, pp 831-834

Yoshimi, Y. and Kishida, T. (1981b): A ring torsion device for evaluating friction between soil and metal surfaces. Geotech. Test. Jnl 4, GTJODJ, No. 4, pp 145-152.

## Figures

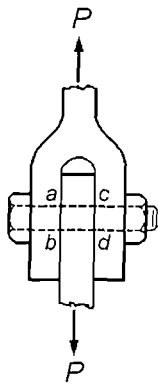


**Figure 2.1:** Bolt subjected to direct shear (Gere & Timoshenko, 1989)

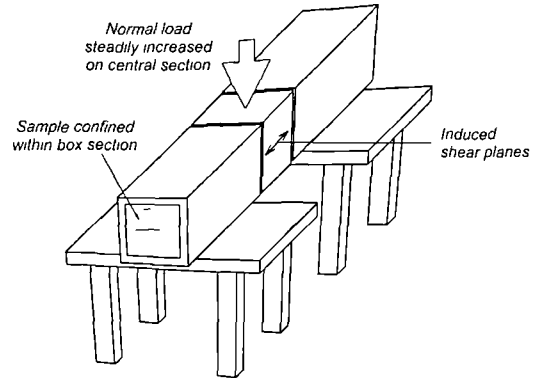


**Figure 2.2:** Schematic diagram showing Collin's direct shear apparatus

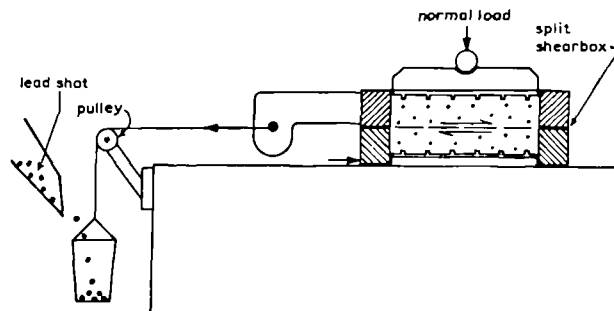


**Figure 2.3:** Principle of early type of controlled stress shearbox (from Head, 1982)

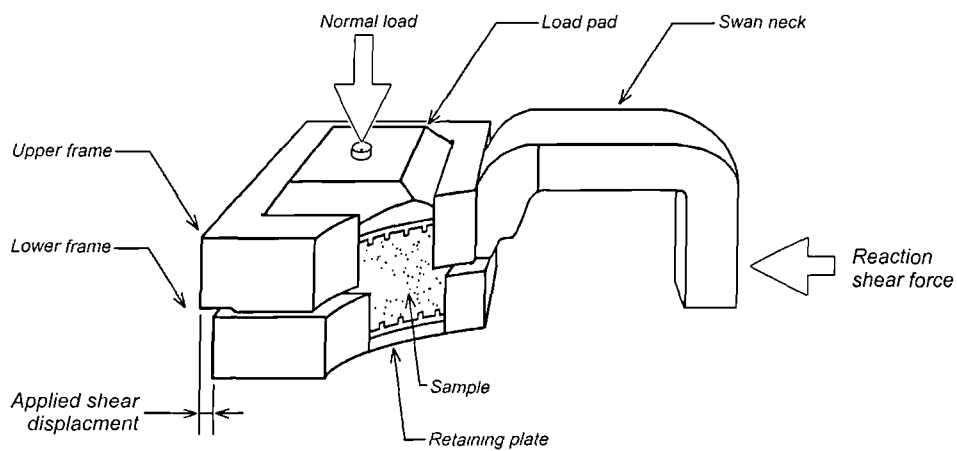


**Figure 2.4:** The direct shearbox while testing

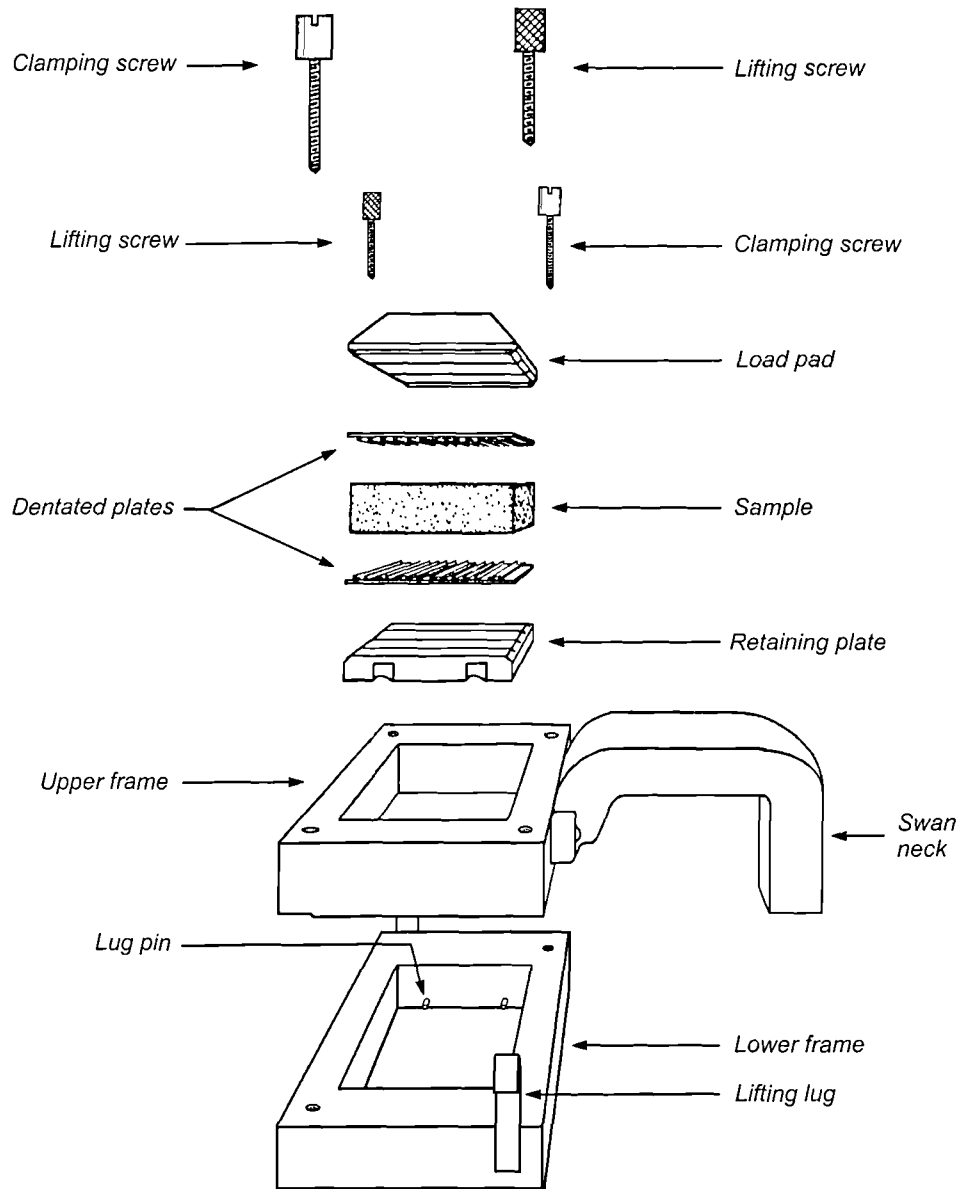


Figure 2.5: The Direct Shearbox (modified from Head, 1982)

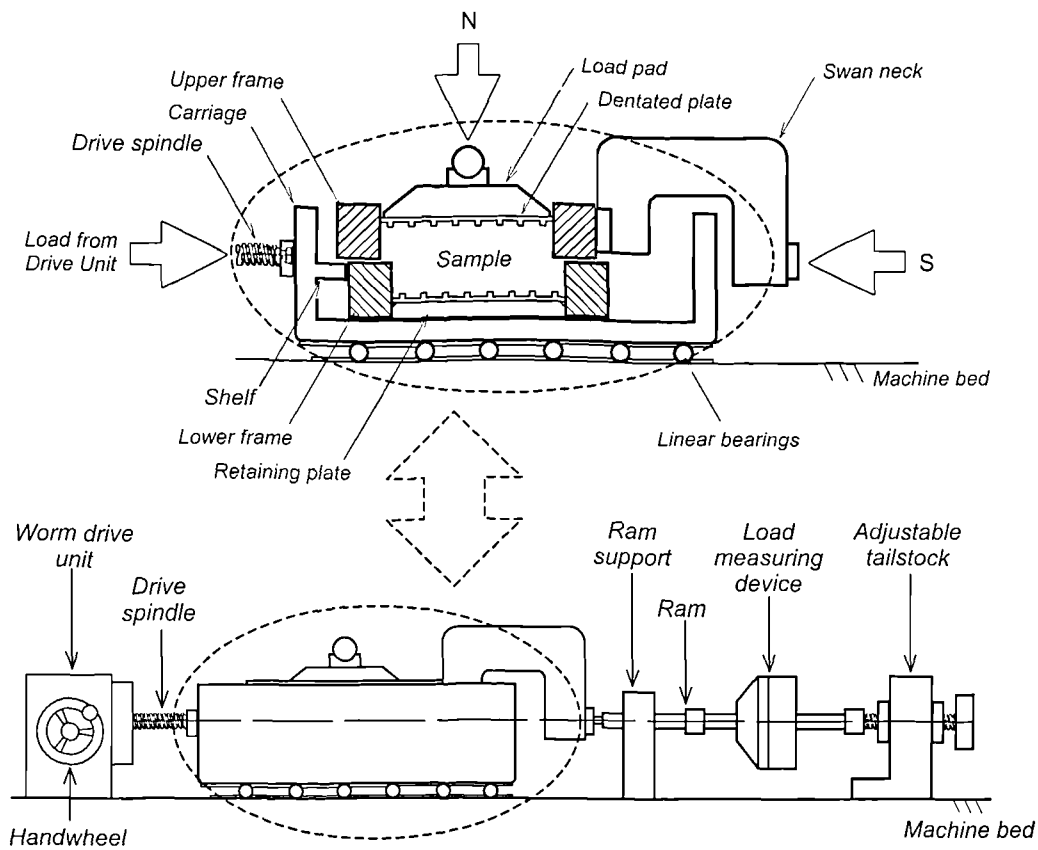


Figure 2.6: Long section of the DSA illustrating its general configuration

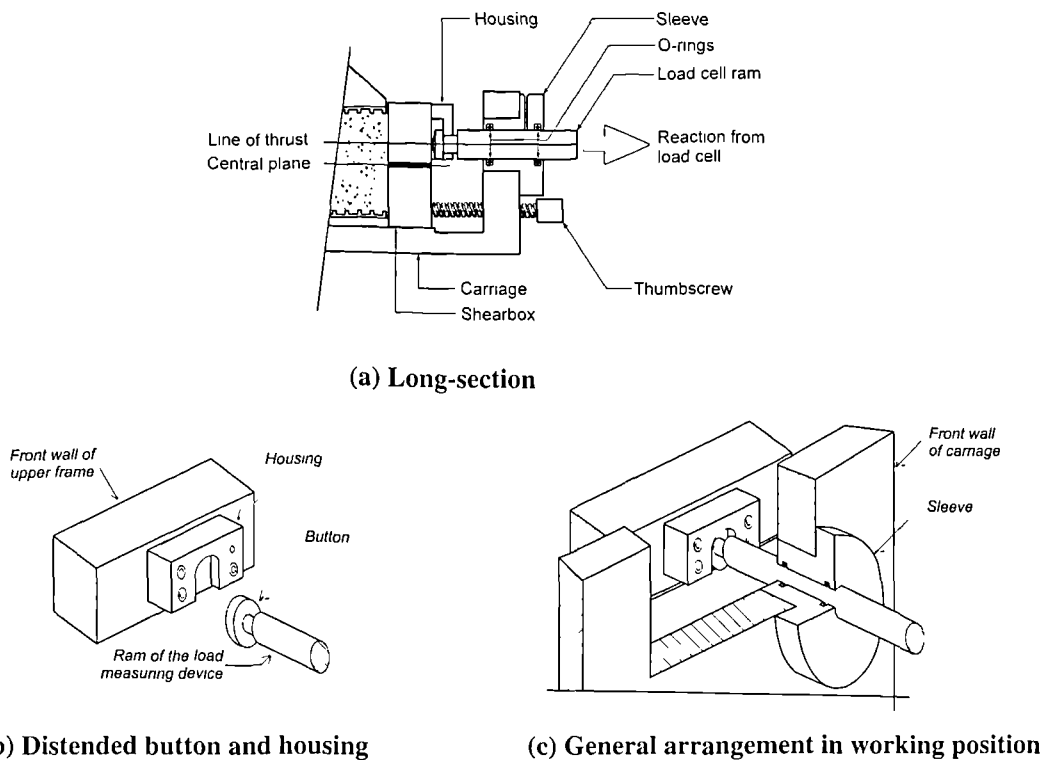
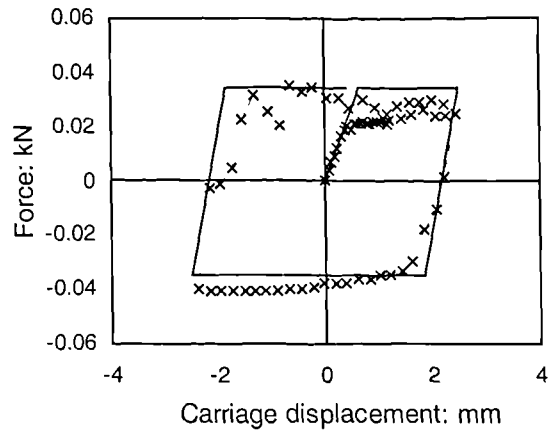
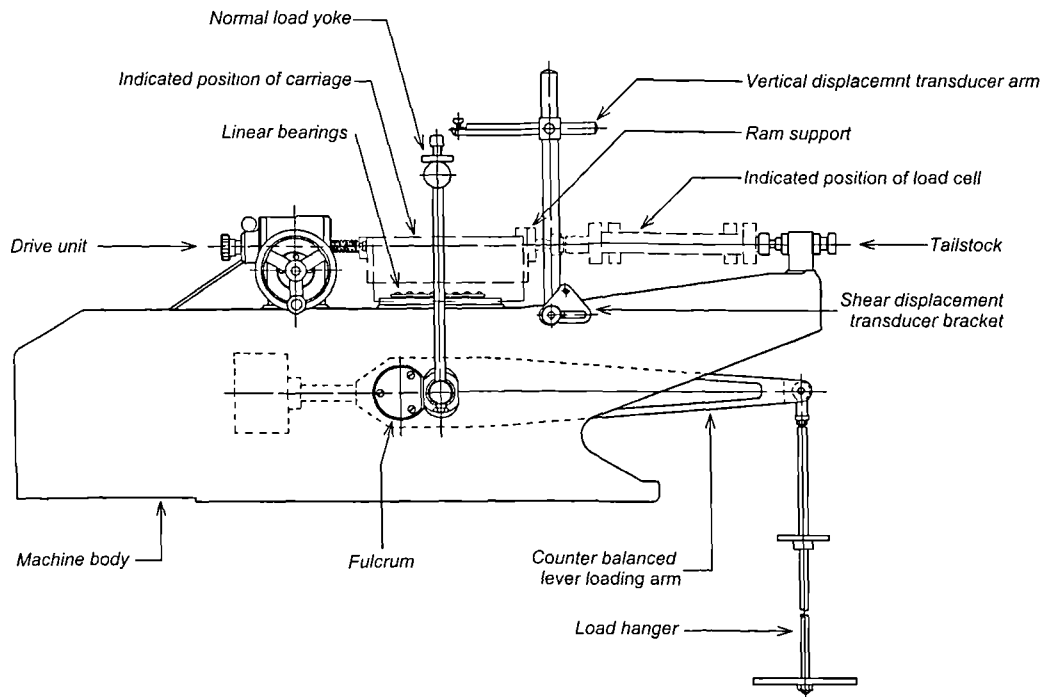


Figure 2.7: The WF-25300's arrangement for transmitting the shear force to the upper frame



**Figure 2.8: The frictional force inherent in the WF-25300's arm and sleeve arrangement**



**Figure 2.9: Long section of the WF-25300 (adapted from Wykeham Farrance's WF-25300 literature)**

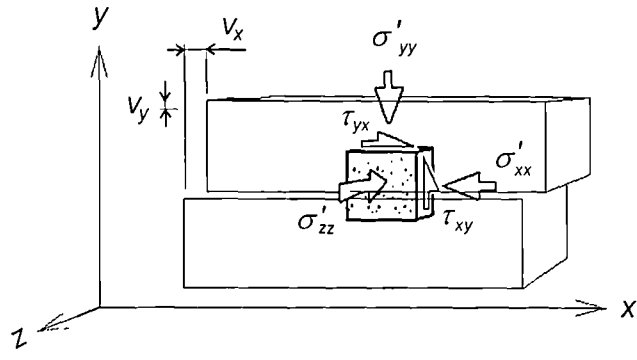


Figure 2.10: Stresses acting on an element taken from the central region of a direct shear sample whilst testing

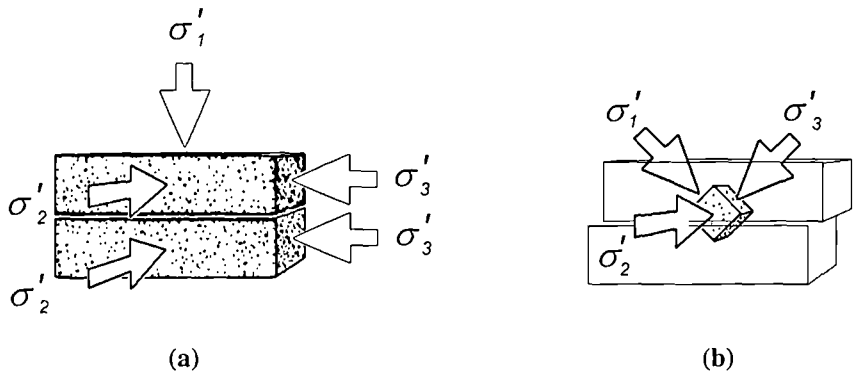


Figure 2.11: Principal stresses acting during direct shear testing (a) after consolidation and (b) after an increment of shear displacement

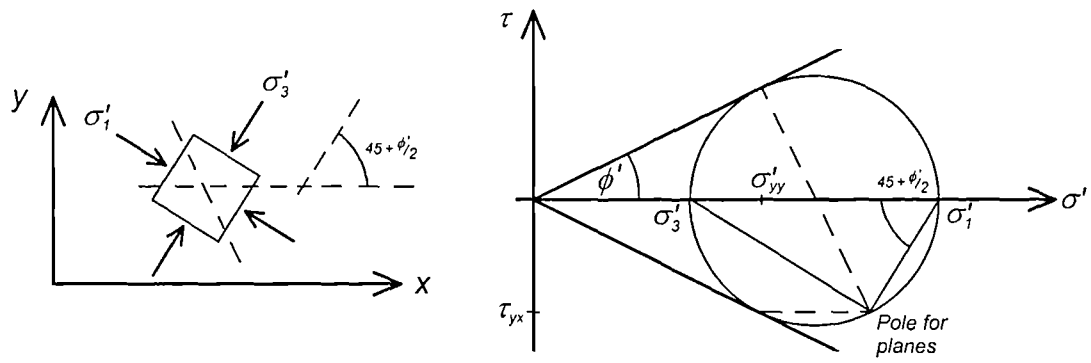


Figure 2.12: Mohr's circle of stress assuming the central plane aligns with planes of maximum stress ratio

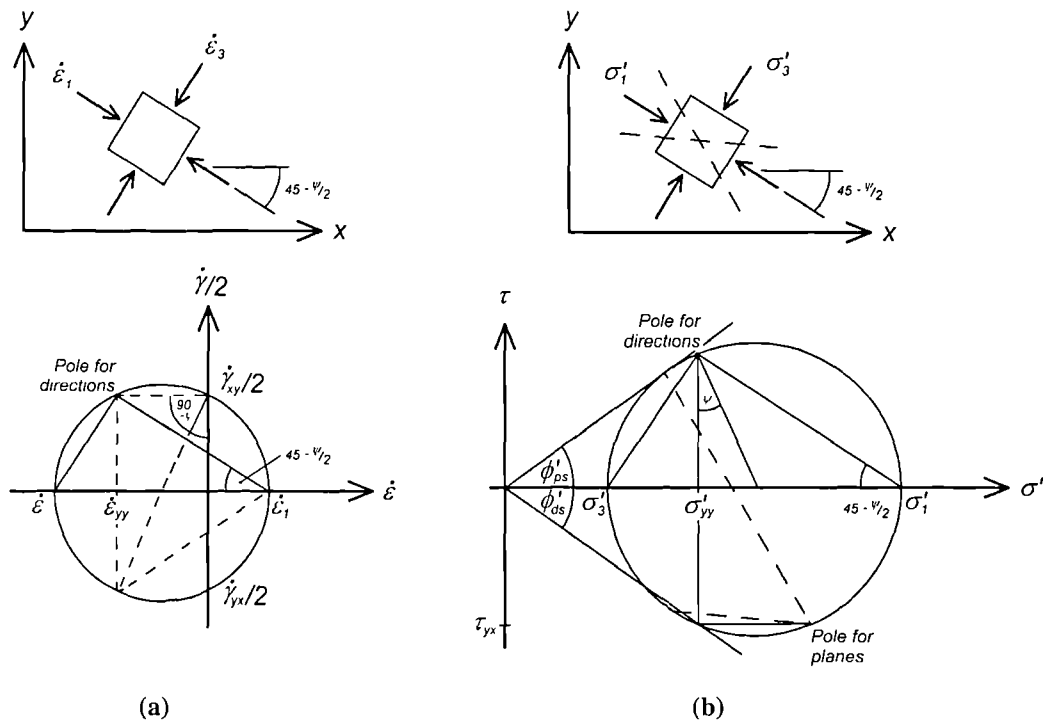


Figure 2.13: Mohr's circles of (a) strain and (b) stress for an element of soil taken from a zero-extension, horizontal rupture band of the DSA

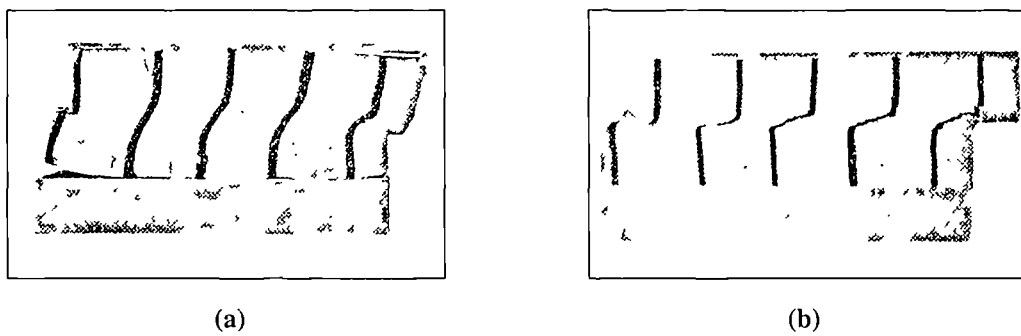


Figure 2.14: Deformations of a plasticine sample subjected (a) 12.4kPa and (b) 494.4kPa confining stress in the DSA (after Roscoe, 1953)



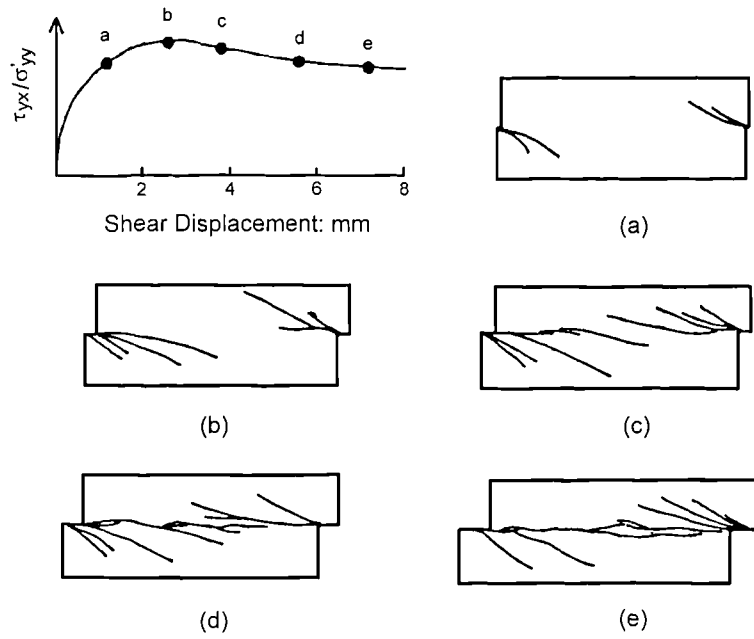


Figure 2.15: Sequence of ruptures forming within a kaolin DSA sample (after Morgenstern & Tchalenko, 1967)

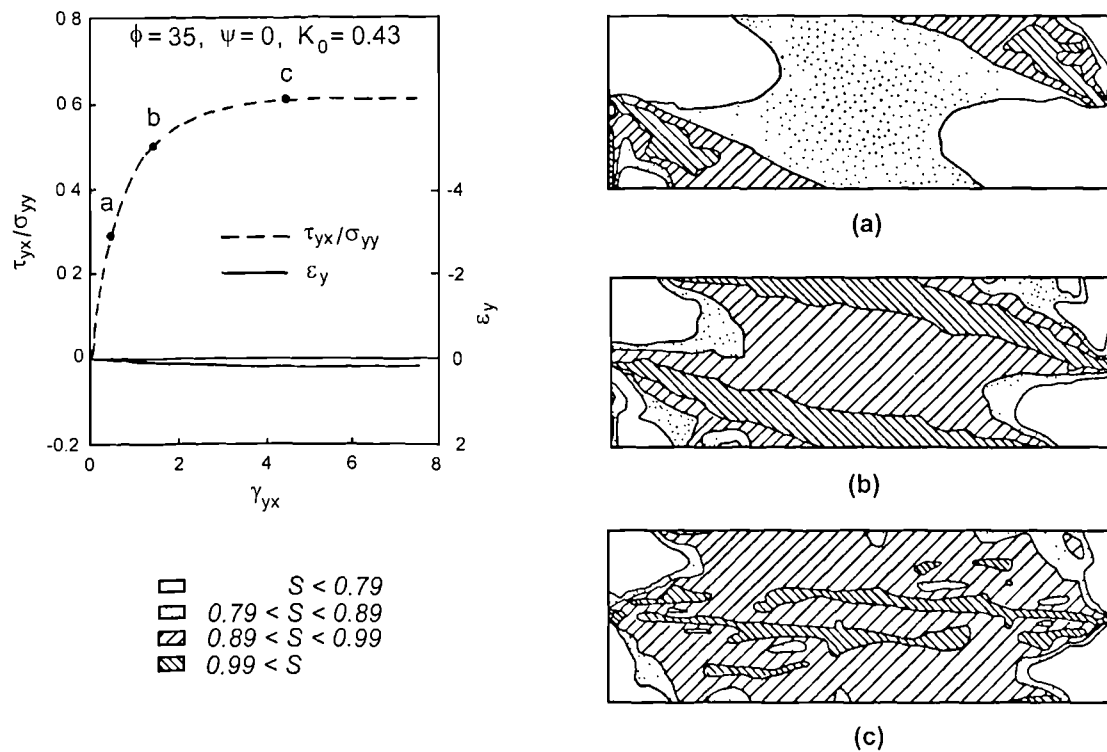


Figure 2.16: Contours of stress level  $S$  within the DSA obtained as the finite element simulation progresses (after Potts et al, 1987)

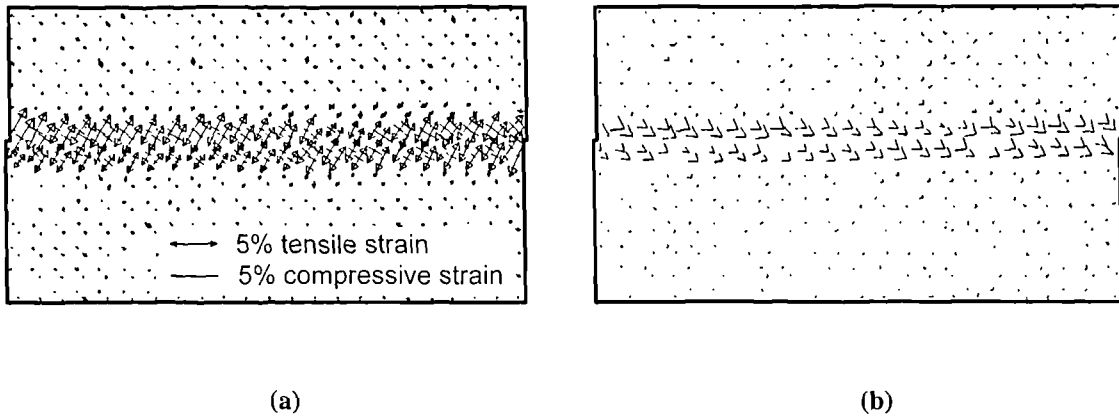


Figure 2.17: Measured incremental strains at peak shearing resistance within the DSA: (a) principle strains; (b) directions of zero incremental linear strain (after Jewell & Wroth, 1987)

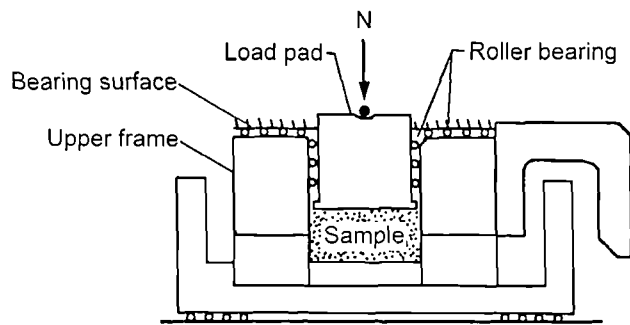


Figure 2.18: Long section of Wernick's (1977) direct shearbox

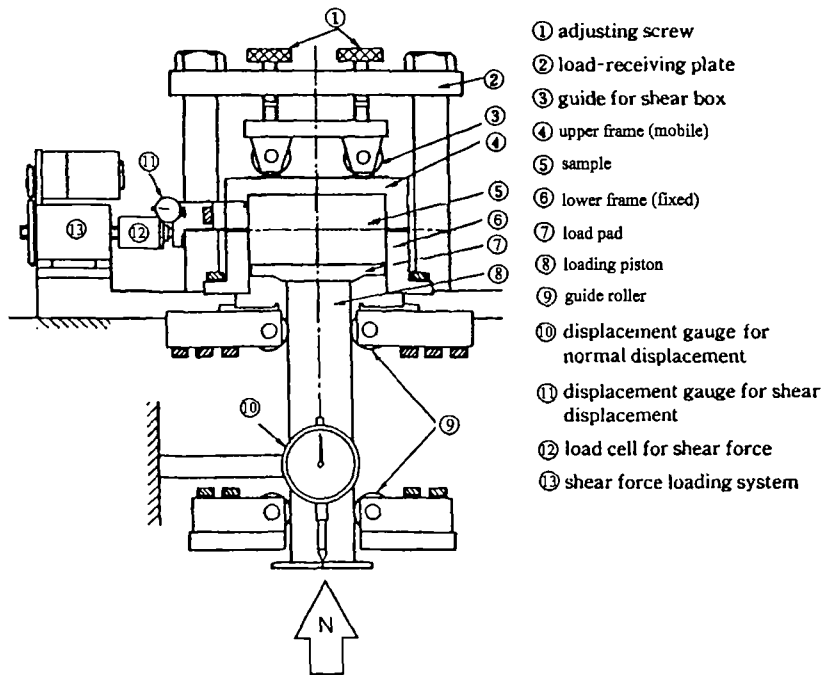


Figure 2.19: Long section of Mikasa's direct shear apparatus (modified from JGS 0561-2000)

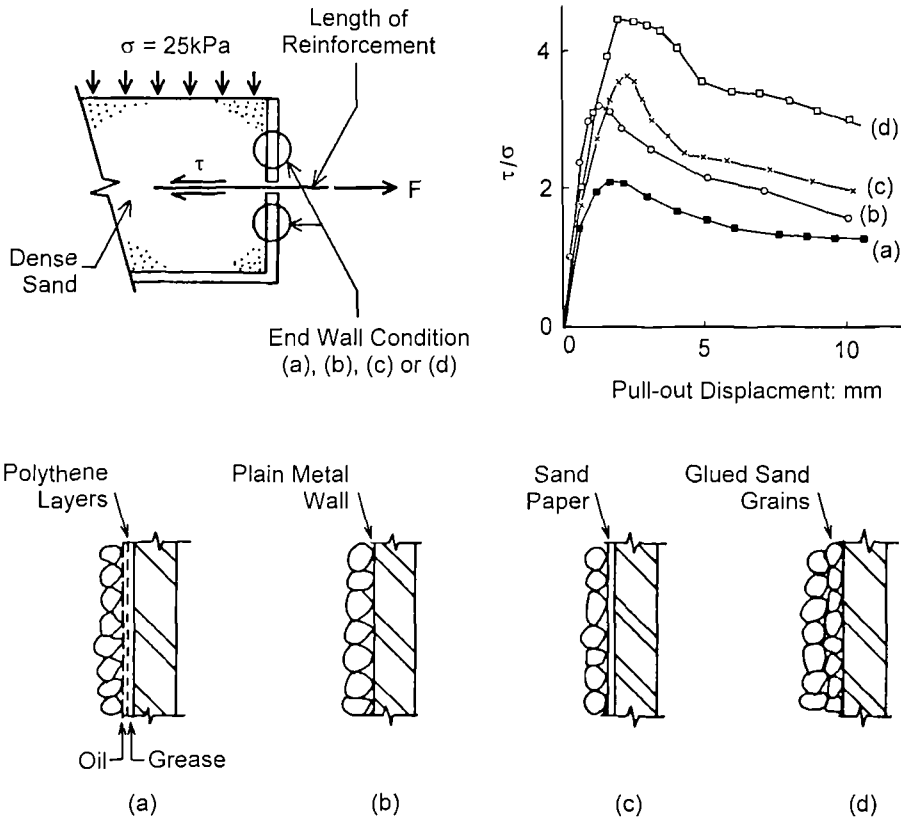


Figure 2.20: The influence of front wall roughness on the pull-out resistance of a length of reinforcement (after Palmeira & Milligan, 1989b)

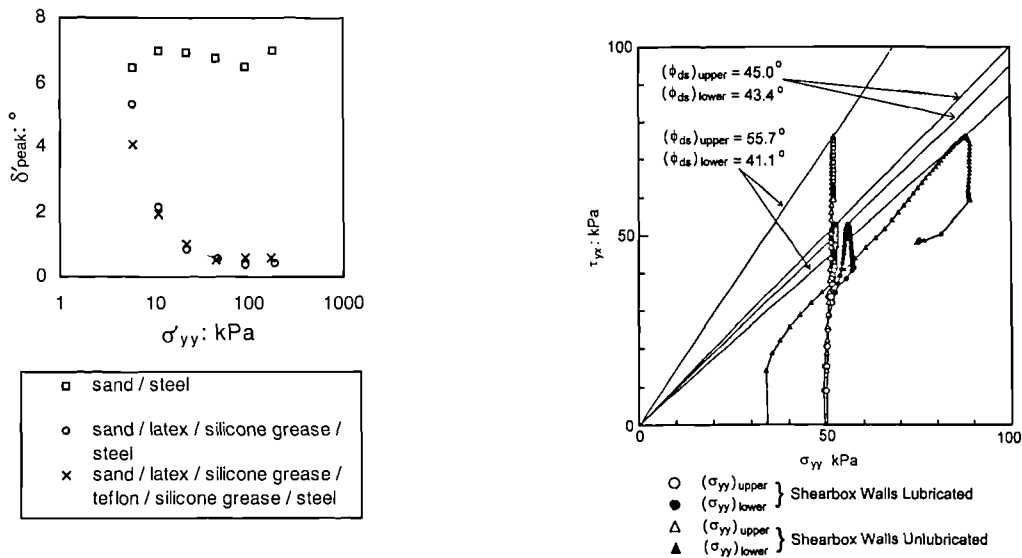


Figure 2.21: The effect of increasing  $\sigma'_{yy}$  on the friction angle between sand and a solid surface with different degrees of lubrication (after Tatsuoka & Haibara, 1985)

Figure 2.22: Stress paths for direct shear tests with lubricated and unlubricated internal walls illustrating the influence of wall friction (after Shibuya et al, 1997)

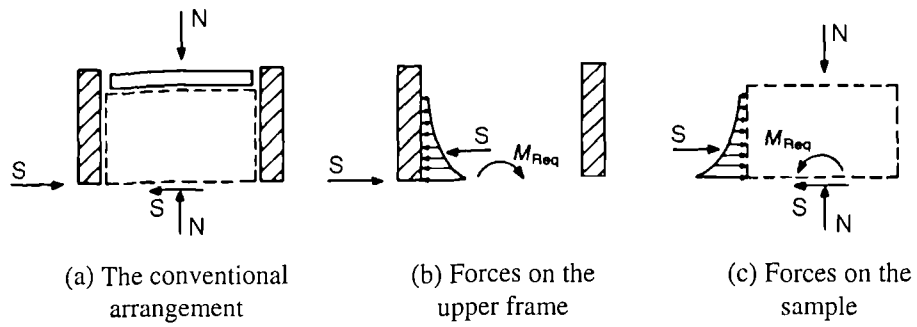


Figure 2.23: Force diagrams illustrating the couples applied when employing the conventional arrangement (Jewell, 1989)

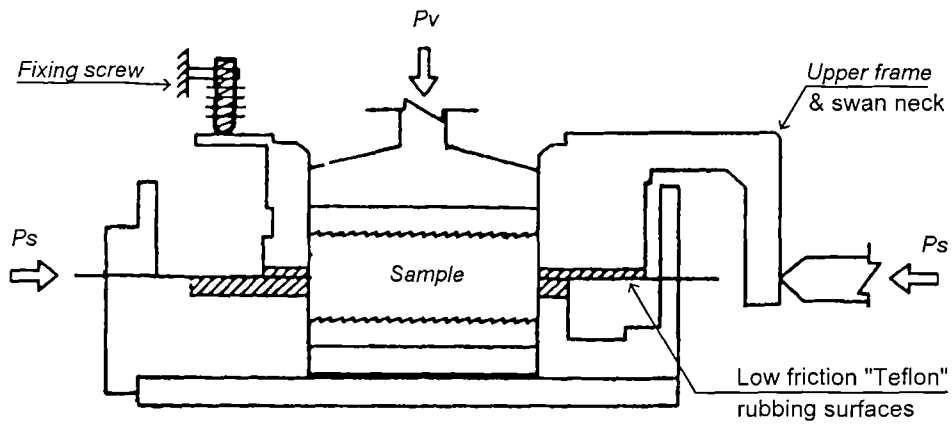


Figure 2.24: The Japanese Standard Direct Shearbox with Fixing Screw (adapted from Matsuoka & Liu, 1998)

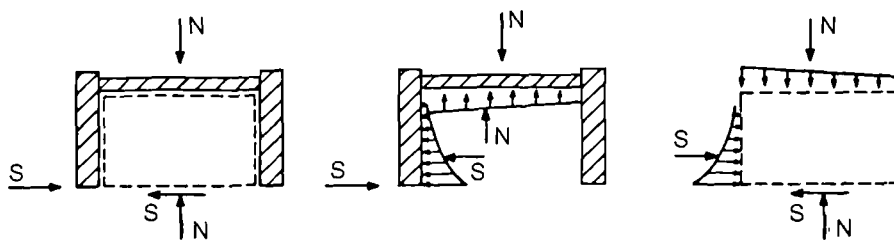


Figure 2.25: Force diagrams illustrating the force distribution during symmetrical direct shear tests (Jewell, 1989)

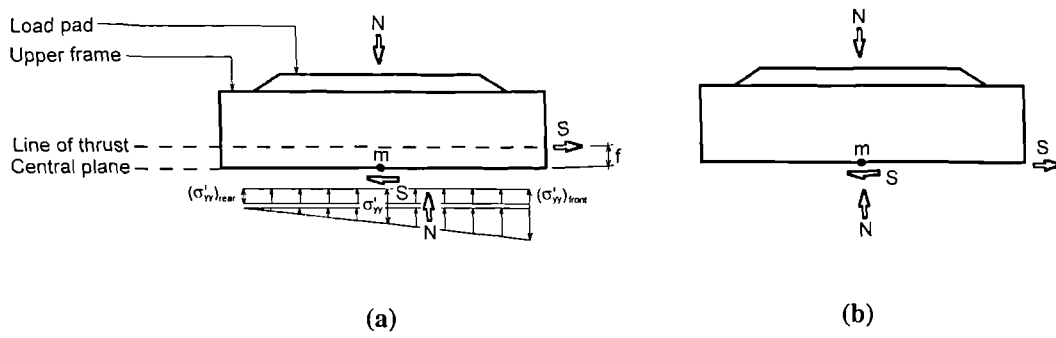


Figure 3.1: Force and moment consideration of the shearbox's upper half when the line of thrust is (a) distant from and (b) coincides with the central plane

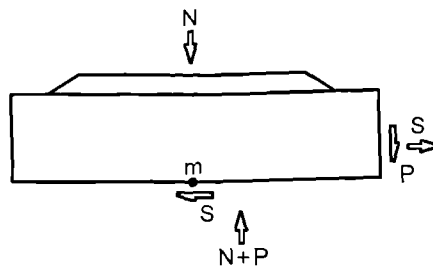


Figure 3.2: Equilibrium of the WF-25300's upper half considering the loading applied by the button and housing arrangement

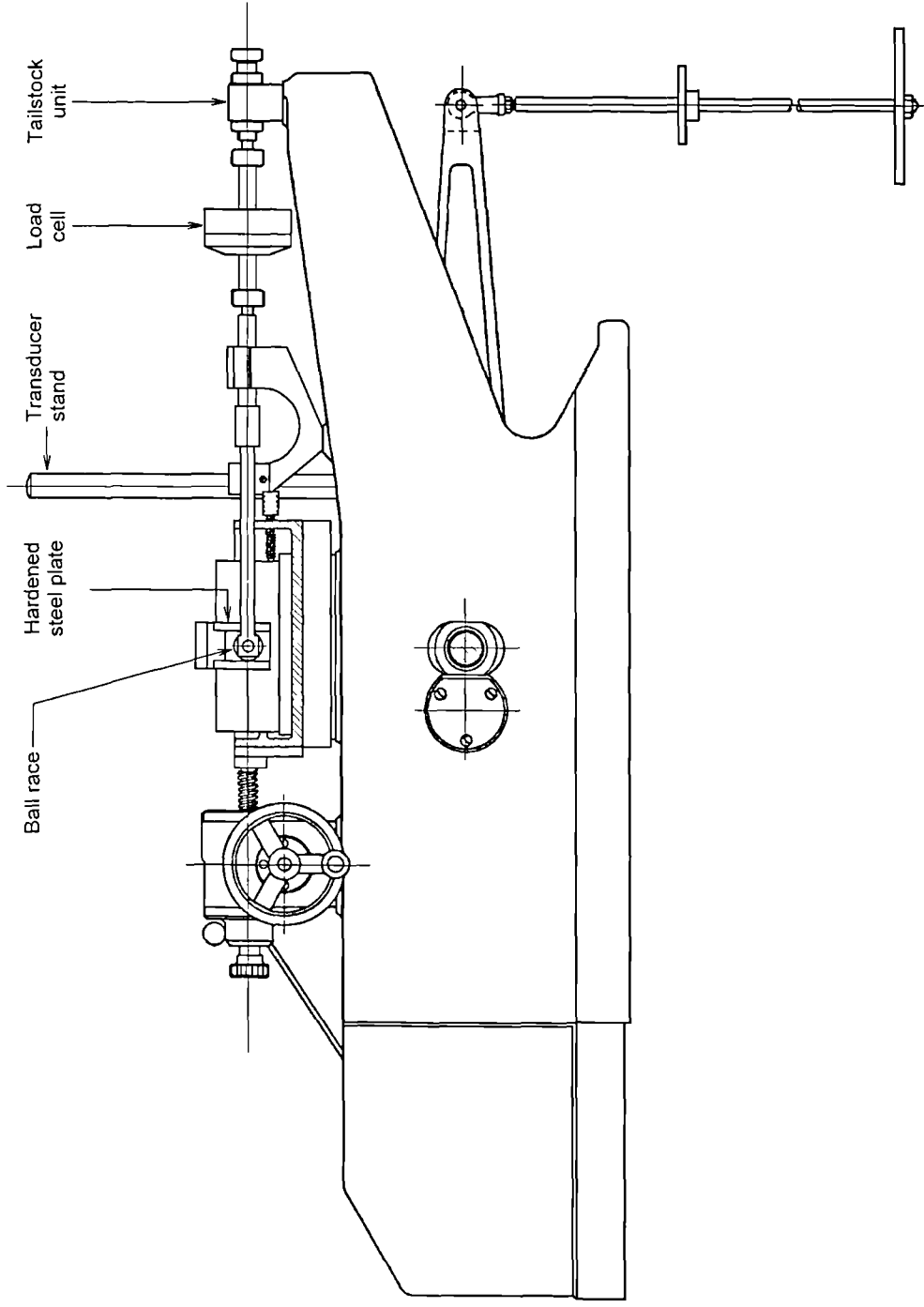


Figure 3.3: Long section of the WDSA prior to testing (excluding the normal loading yoke and transducer clamps)

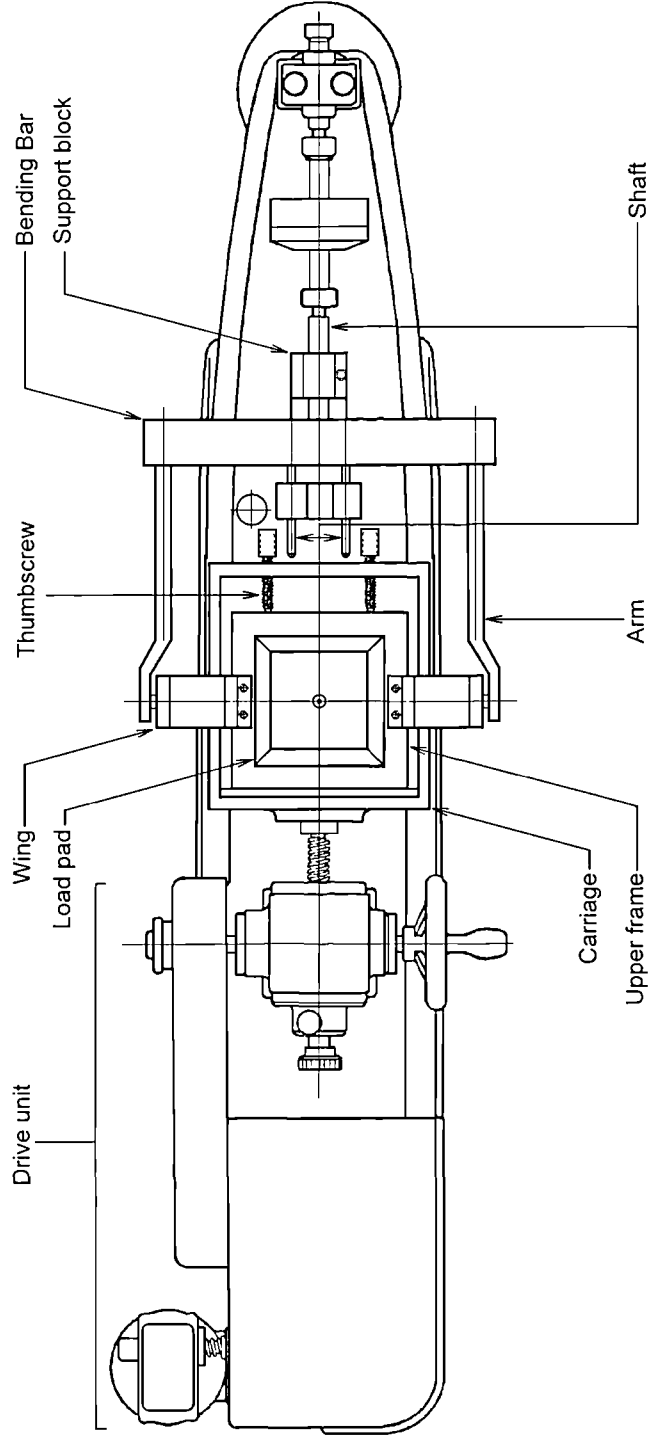


Figure 3.4: plan of the WDSA prior to testing (excluding the normal loading yoke and transducer clamps)

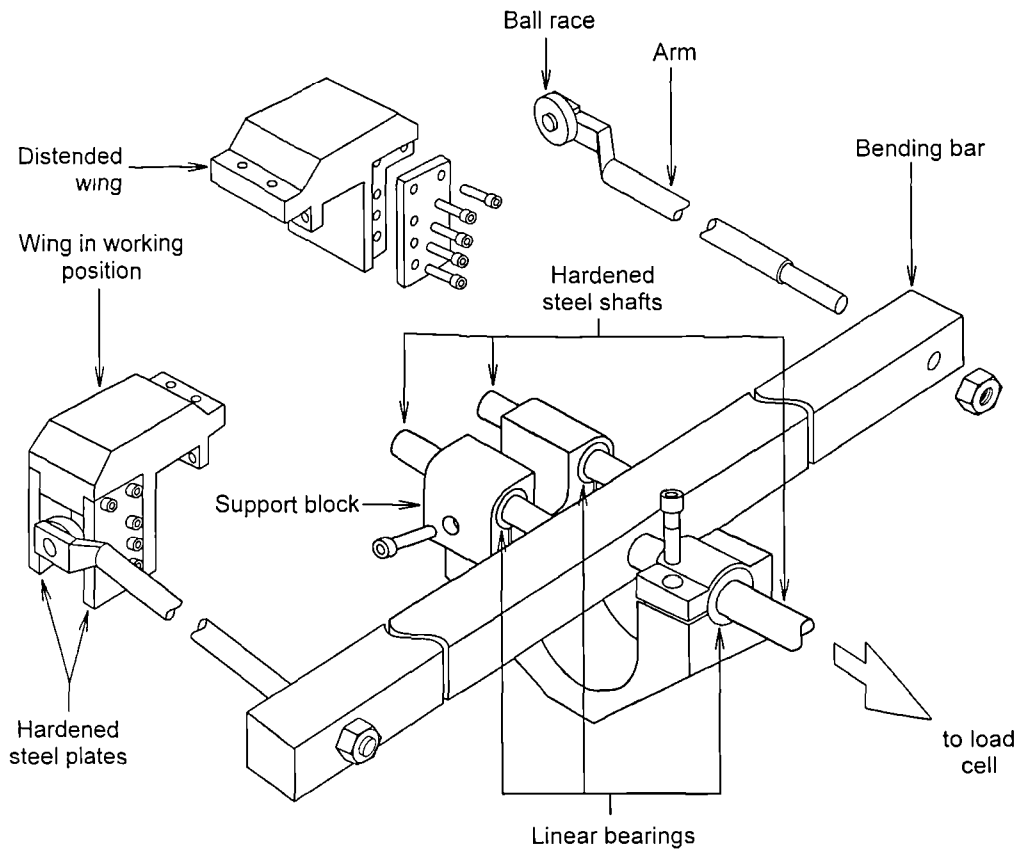


Figure 3.5: Essential modifications that comprise the WDSA

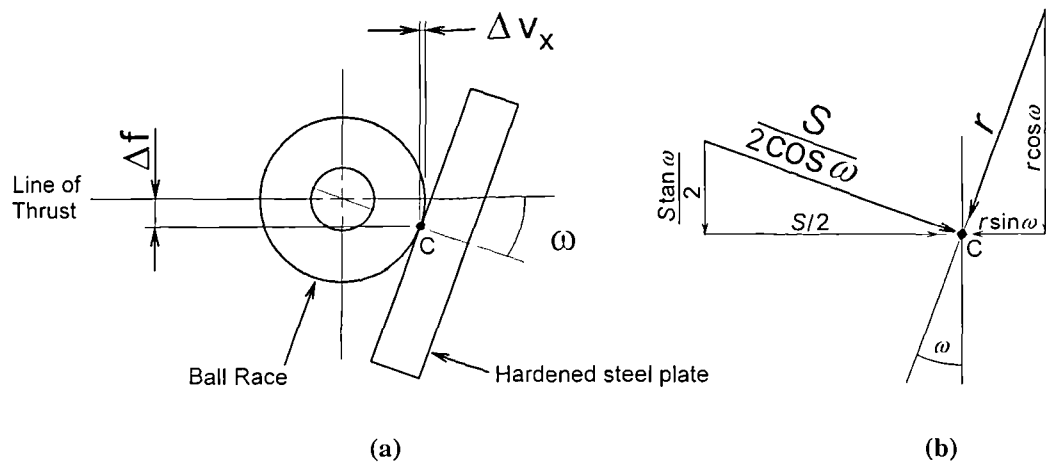
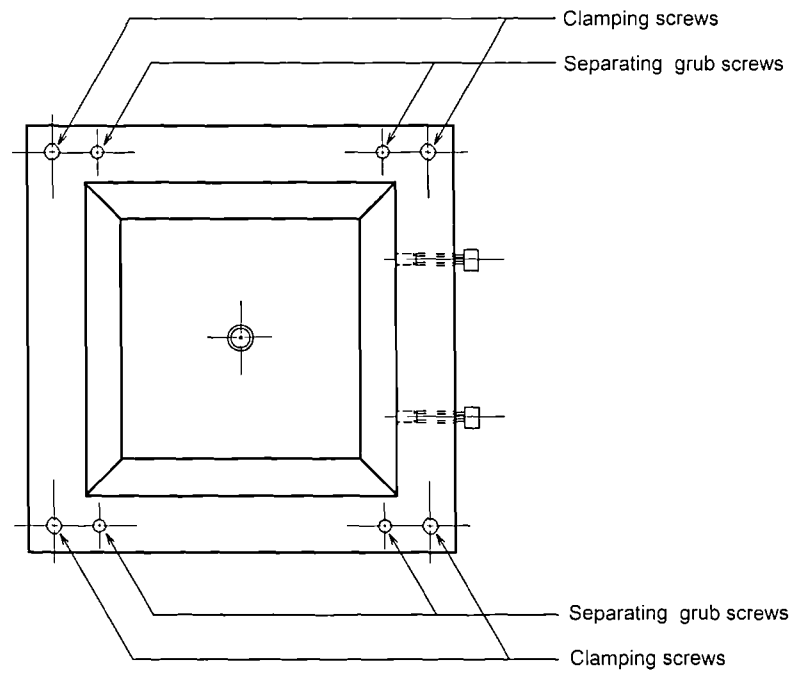
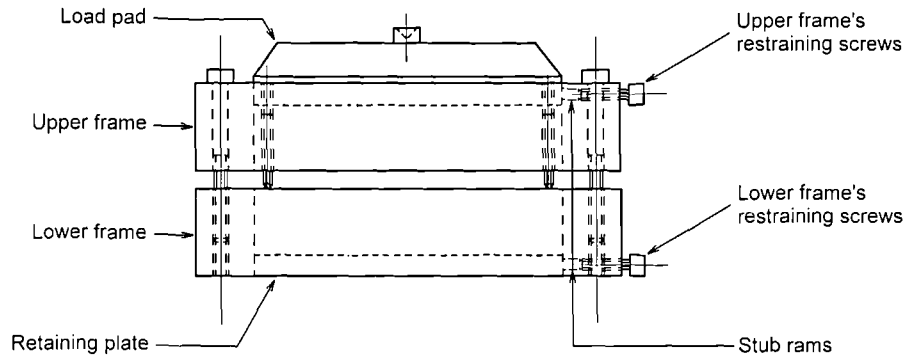
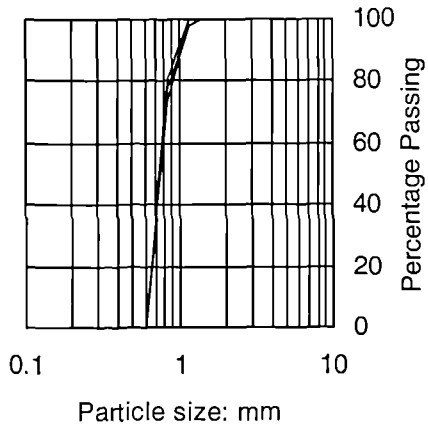


Figure 3.6: (a) Schematic diagram of a ball race bearing on a wing's hardened steel plate after substantial upper ensemble rotation  $\omega$  and (b) the forces acting on the plate

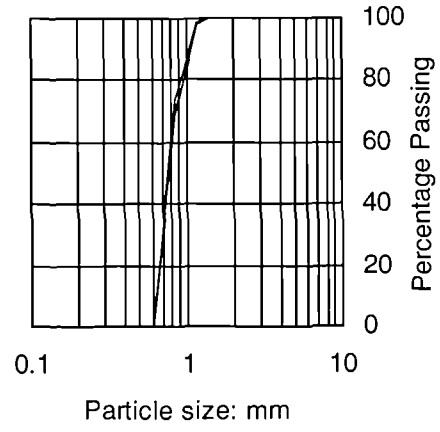




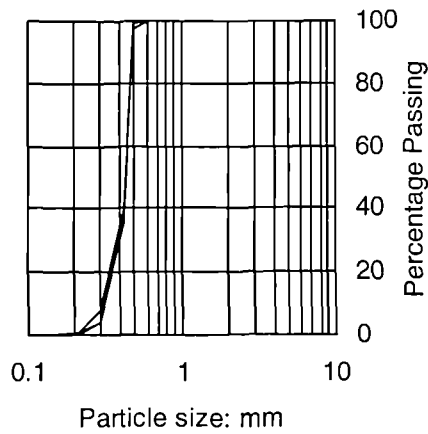
**Figure 3.7: The Winged Apparatus' Shearbox**



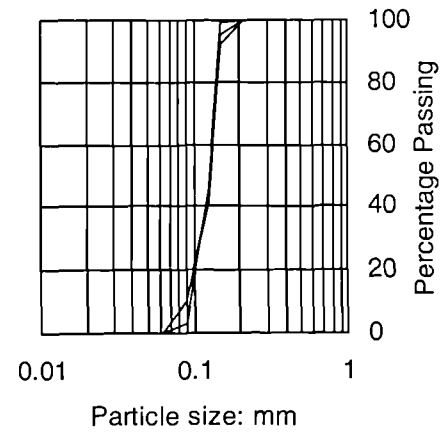
(a)



(b)



(c)



(d)

**Figure 3.8: Particle size distribution charts for the test materials: (a) ALB, (b) VLB, (c) MGS and (d) SFS**

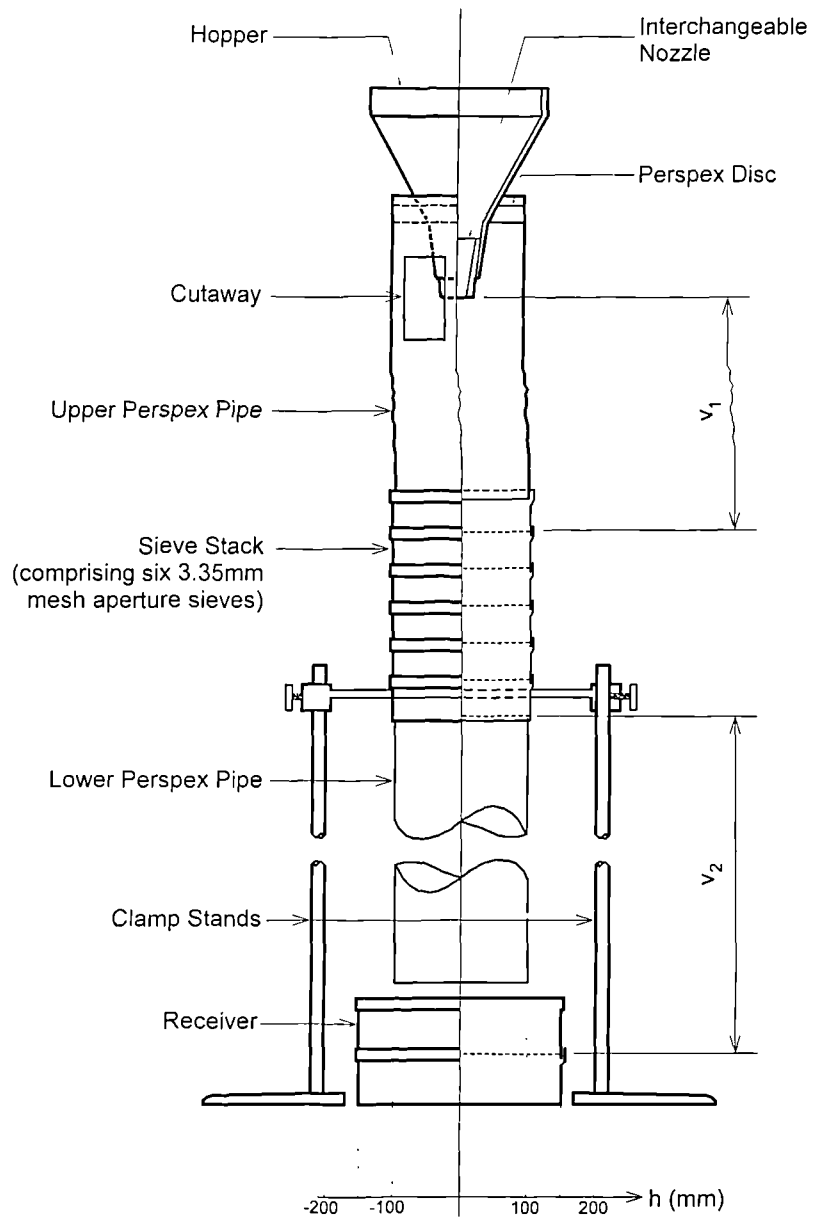


Figure 3.9: The configuration of the MSP

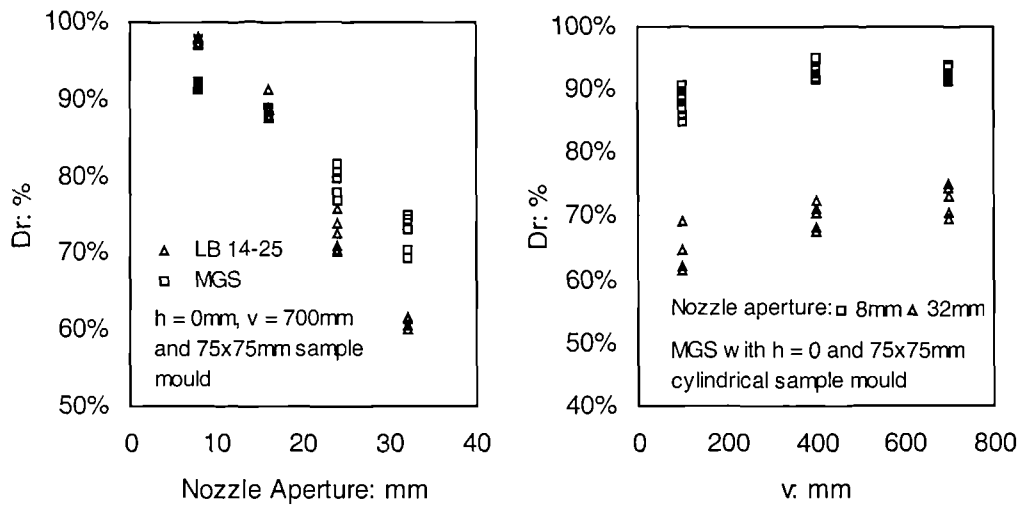


Figure 3.10: The effect the Pluviator's control parameters have on average  $D_r$

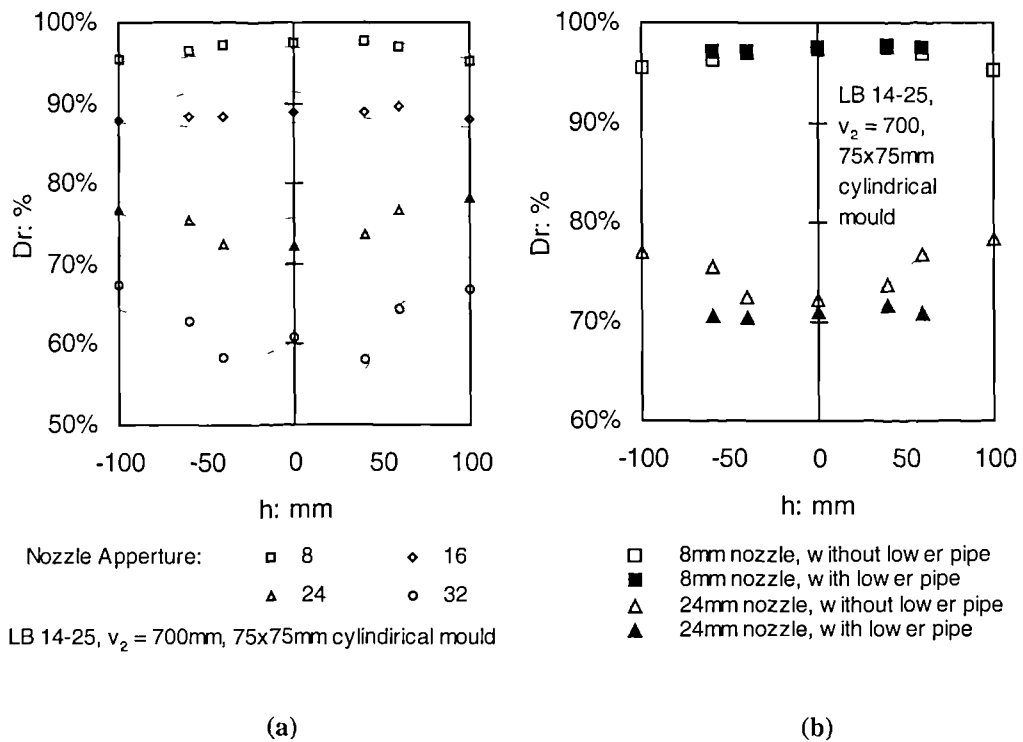


Figure 3.11: The effect of the lower pipe on the Pluviator's horizontal density distribution

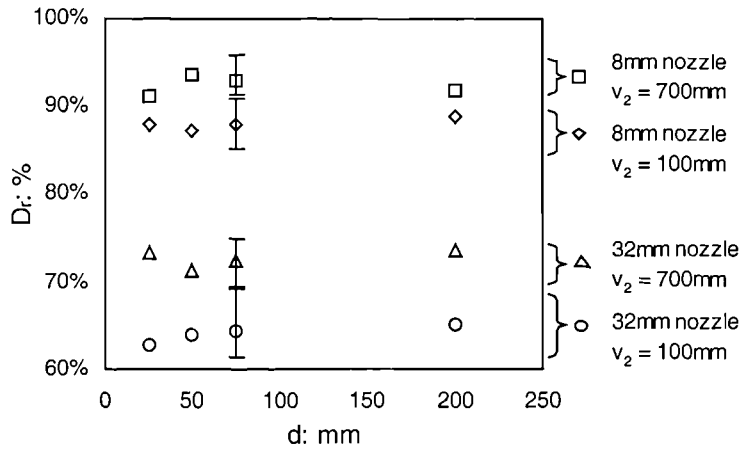


Figure 3.12: Pluvial deposition using different nozzles and different heights of drop into moulds of varying depth d

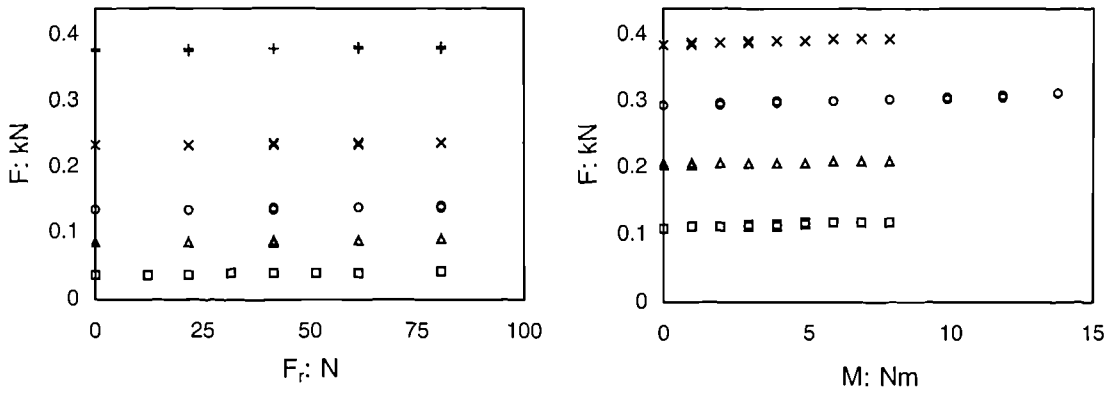


Figure 3.13: (a) Shear force and (b) moment sensitivity of the load cell

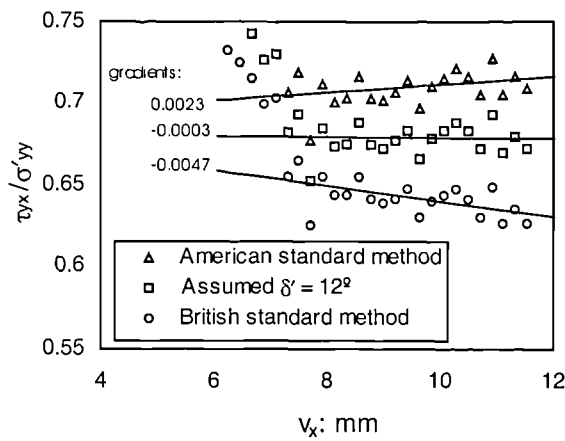


Figure 3.14: The effect of area-correction assumptions on large displacement test data

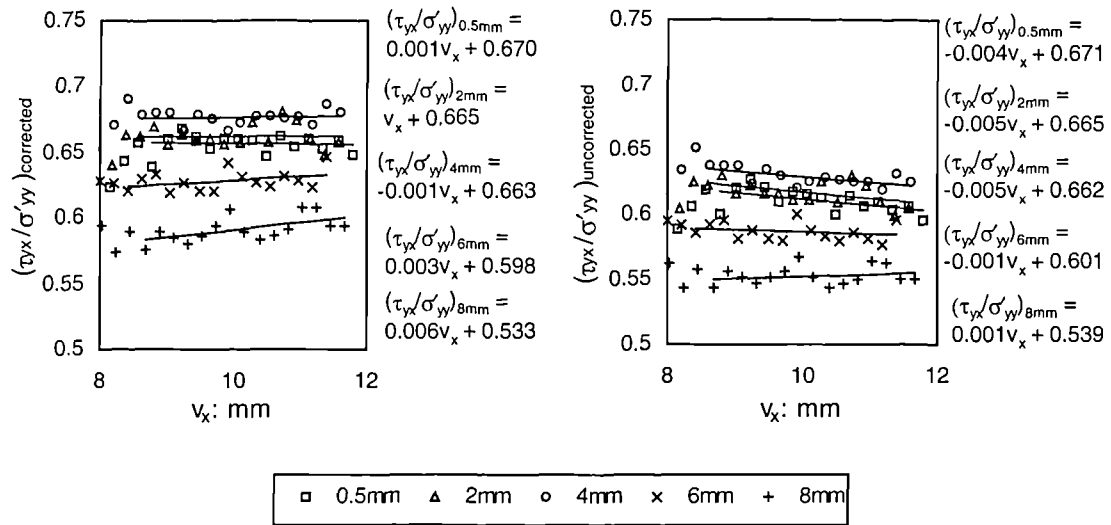


Figure 3.15: Large-displacement stress data obtained with different  $g$  values (a) after employing a correction to account for the transition in shear area and (b) with no such correction

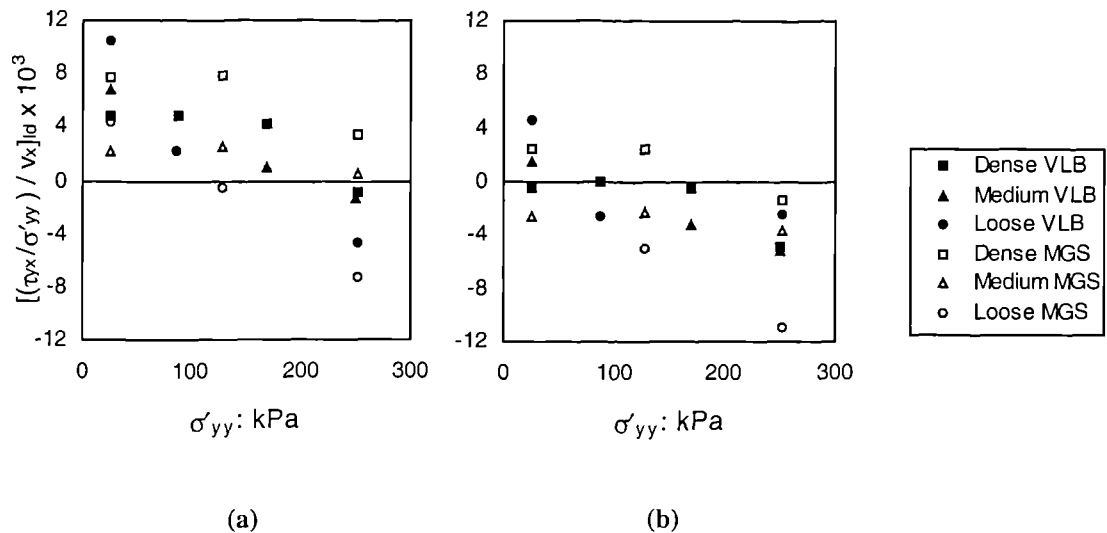


Figure 3.16: The gradient of the large-displacement stress ratio plot for tests with  $g$  circa  $5D_{50}$  for two sands deposited at various densities and confined under different stresses (a) after employing the area correction and (b) with no area correction

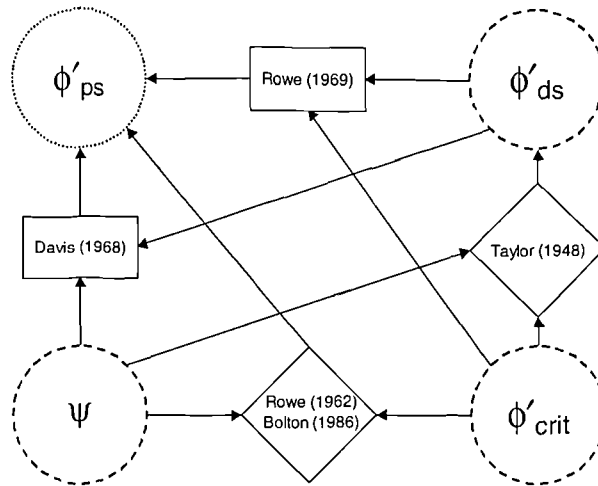


Figure 3.17: The linking of parameters (circles), both measured (dashed) and derived (dotted), using flow rules (diamonds) and other relationships (rectangles)

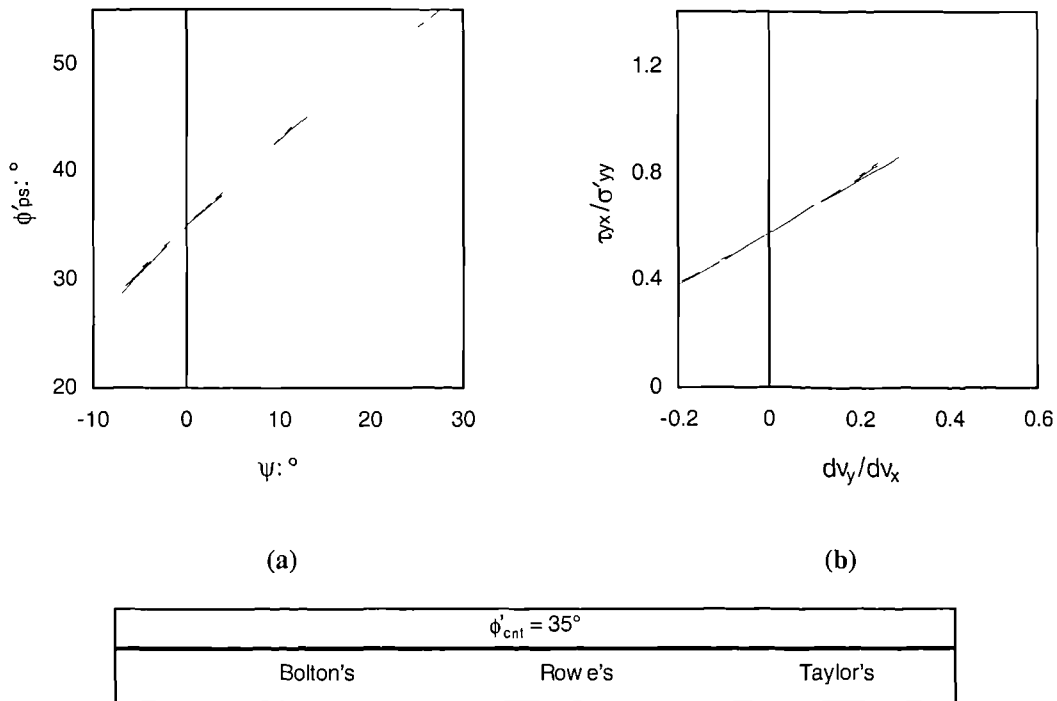


Figure 3.18: Comparison of Taylor's (1948), Rowe's (1962) and Bolton's (1986) flow rules on axes relating to (a) plane strain and (b) direct shear

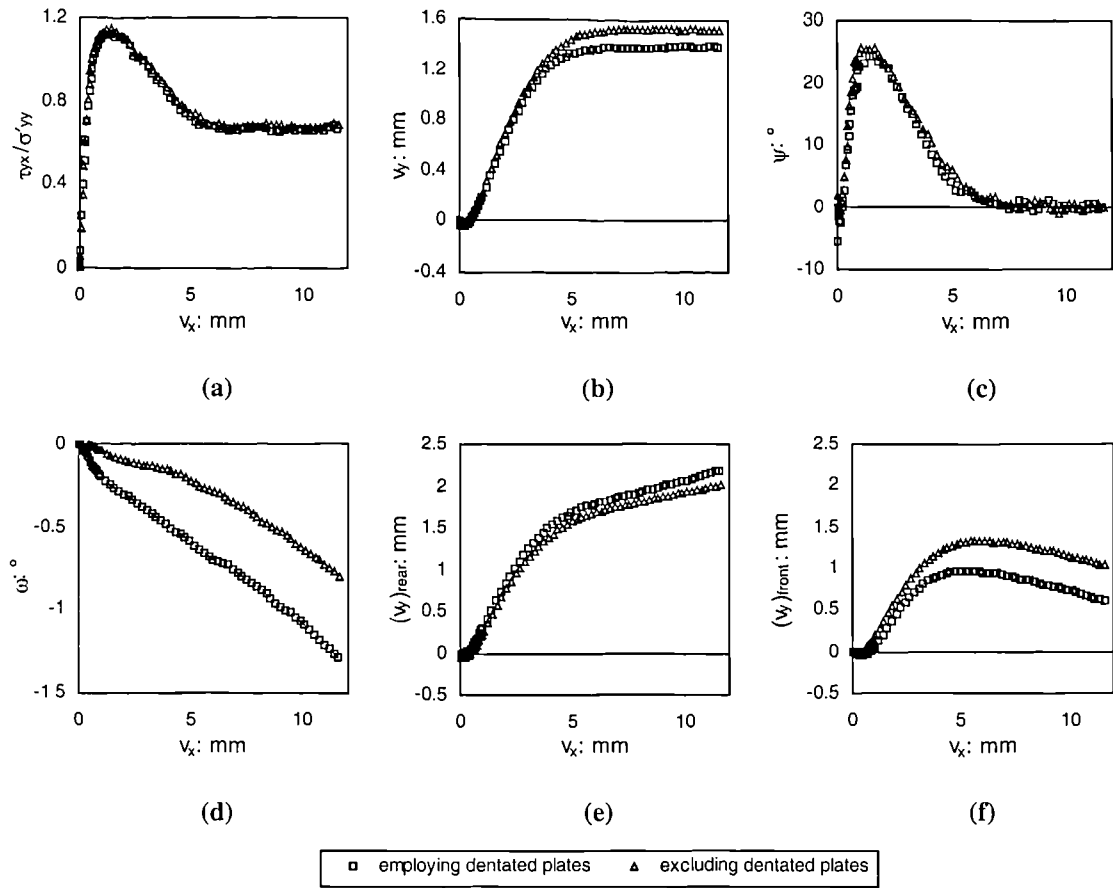


Figure 4.1: The influence of dentated plates on WDSA test data (VLB,  $D_r = 95\%$ ,  $\sigma'_{yy} = 25$  kPa,  $f = 0$ mm,  $g = 5D_{50}$ )

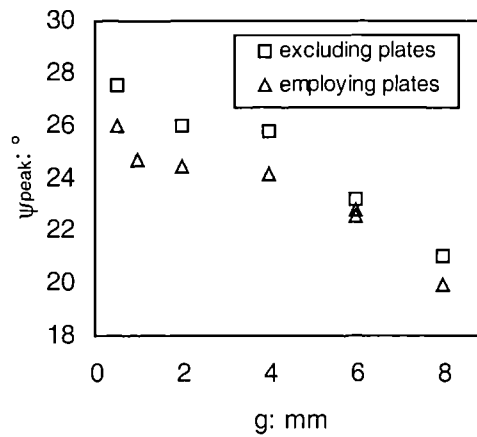


Figure 4.2: Reductions of  $\psi_{peak}$  brought about by including dentated plates during WDSA tests with various initial openings between frames (VLB,  $D_r = 95\%$ ,  $\sigma'_{yy} = 25$  kPa,  $f = 0$ mm)



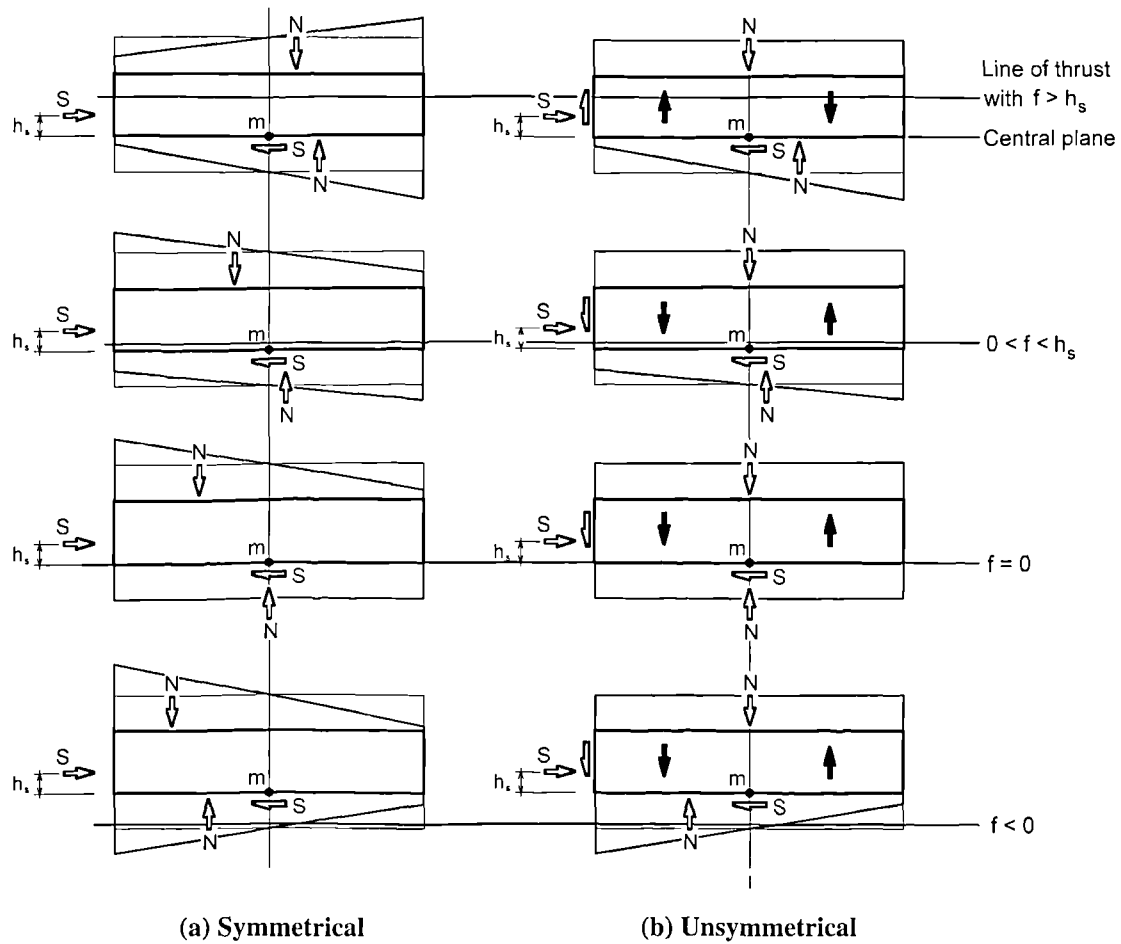
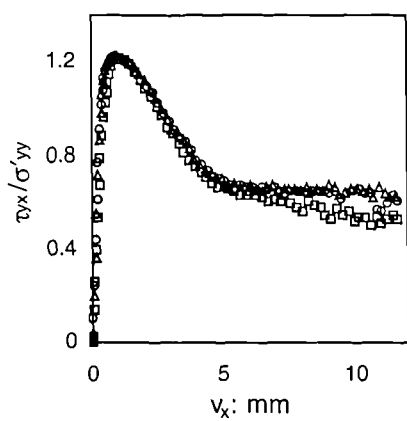
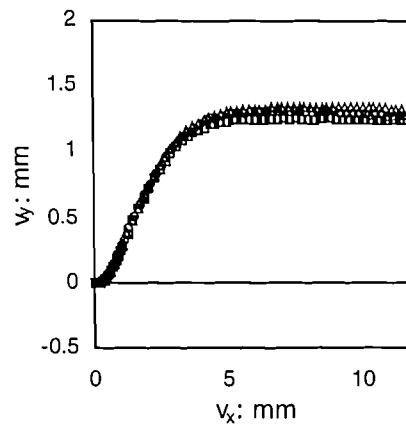


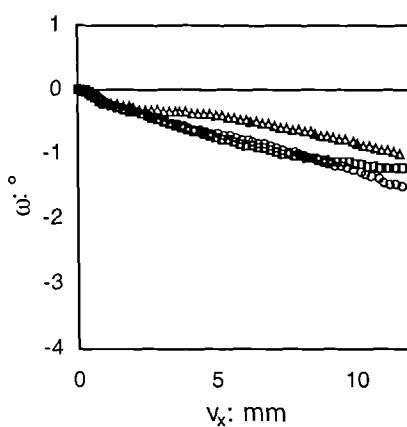
Figure 4.3: The force and moment equilibrium of the upper half of a WDSA sample with different separations between the central plane and the line of thrust for (a) the symmetrical arrangement and (b) the unsymmetrical arrangement



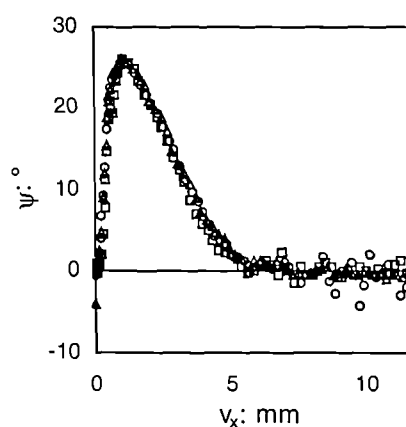
(a)



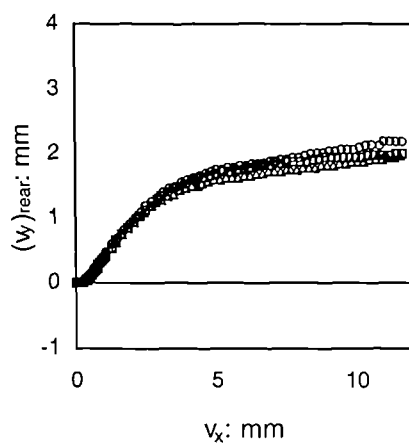
(b)



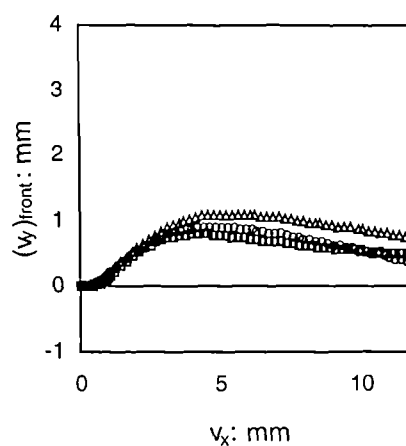
(c)



(d)



(e)



(f)

Figure 4.4: Data for three identical symmetrical WDSA tests featuring dense VLB confined under 25kPa ( $g = 0.5\text{mm}$ ,  $f = 10\text{mm}$ , no shielding)

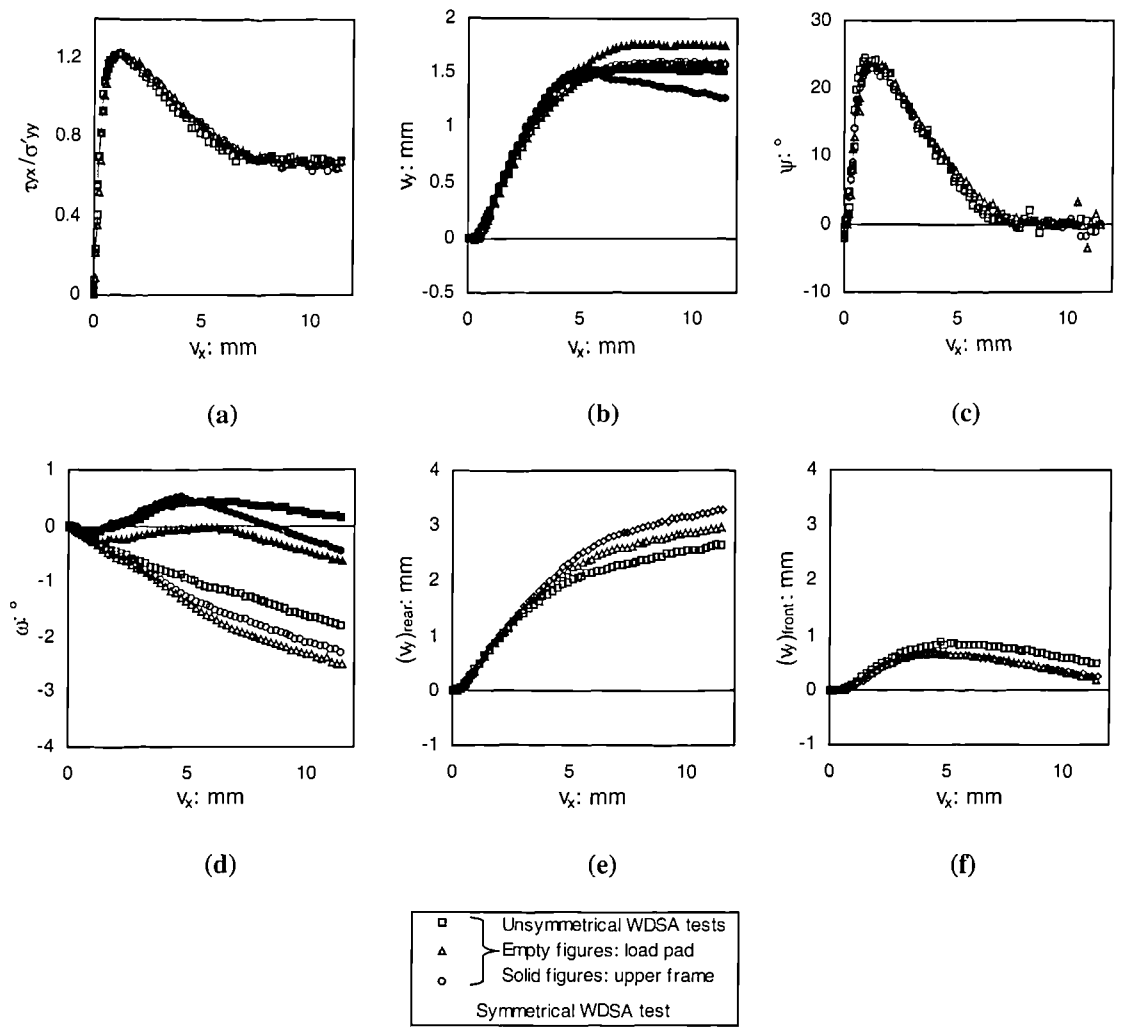


Figure 4.5: Data for three identical unsymmetrical WDSA tests featuring dense VLB confined under 25kPa ( $g = 0.5\text{mm}$ ,  $f = 10\text{mm}$ , no shielding) compared to the representative symmetrical WDSA test

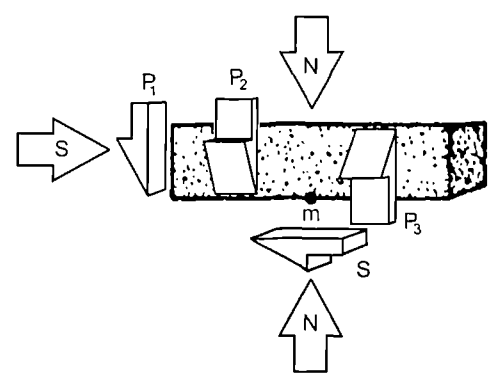


Figure 4.6: The shear stresses imposed on the sample's boundaries by the clockwise rotation of the load pad within the upper frame

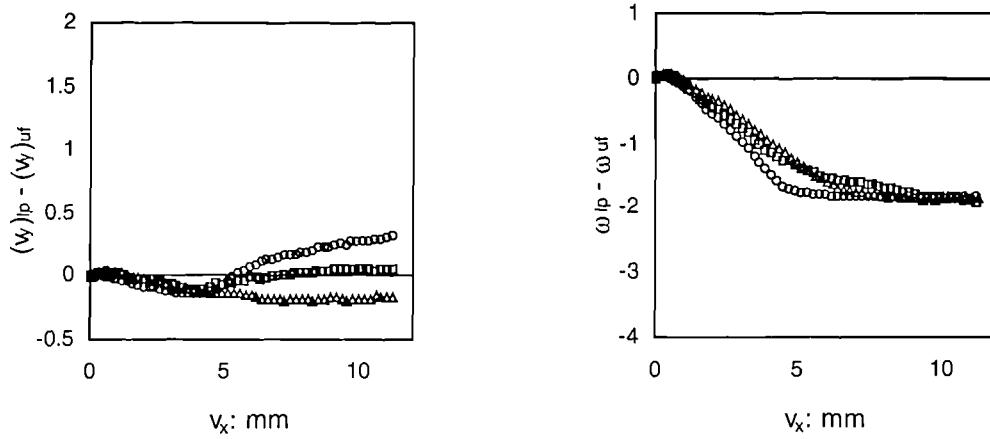


Figure 4.7: The relative displacements of the unsymmetrical WDSA's load pad within the upper frame for three tests featuring dense VLB confined under 25kPa ( $g = 0.5\text{mm}$ ,  $f = 10\text{mm}$ , no shielding)

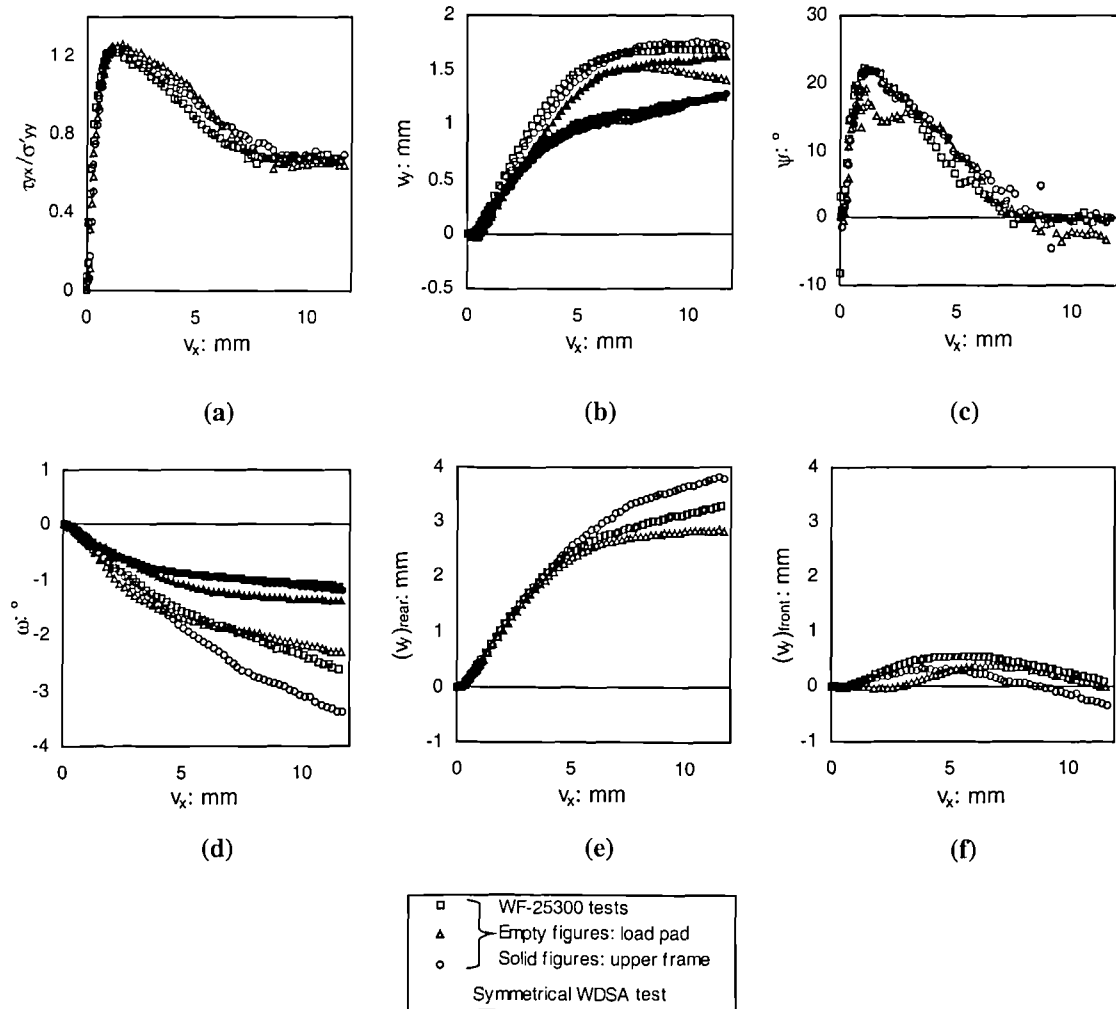


Figure 4.8: Data for three WF-25300 tests featuring dense VLB confined under 25kPa ( $g = 0.5\text{mm}$ ,  $f = 10\text{mm}$ , no shielding) compared to the representative symmetrical WDSA test

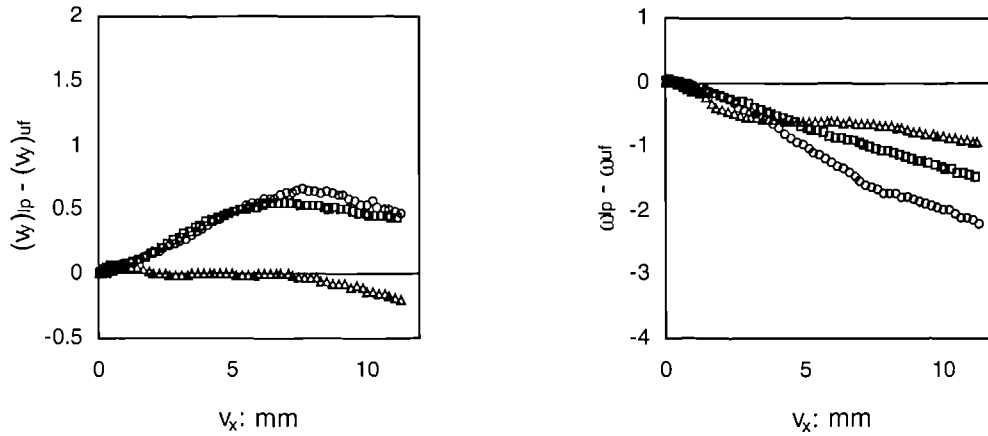


Figure 4.9: The relative displacements of the WF-25300's load pad within the upper frame for three tests featuring dense VLB confined under 25kPa ( $g = 0.5\text{mm}$ ,  $f = 10\text{mm}$ , no shielding)

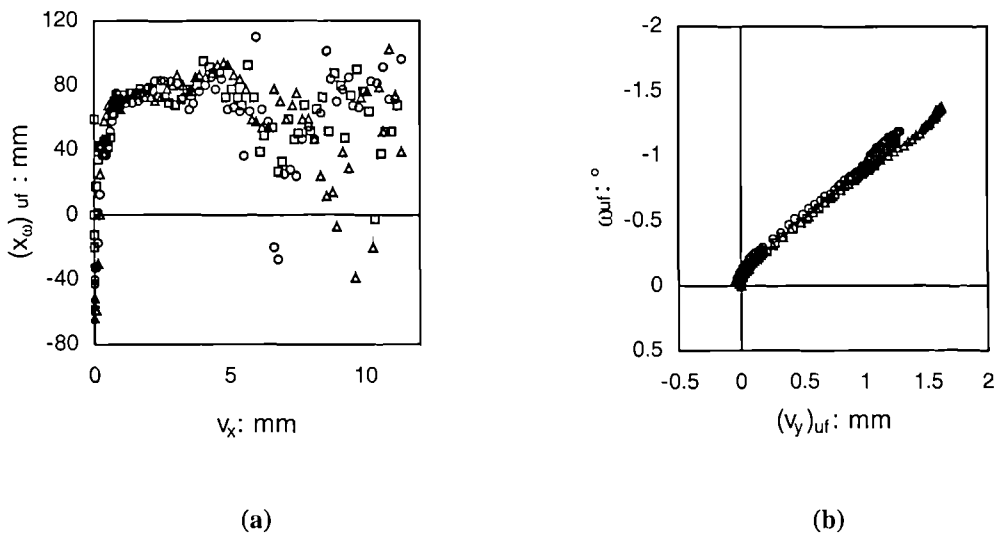


Figure 4.10: (a) The x ordinate, relative to the sample centre, about which the upper frame rotates during testing and (b) the relationship between vertical displacement and rotation of the upper frame when using the WF-25300 and dense VLB confined under 25kPa ( $g = 0.5\text{mm}$ ,  $f = 10\text{mm}$ , no shielding)

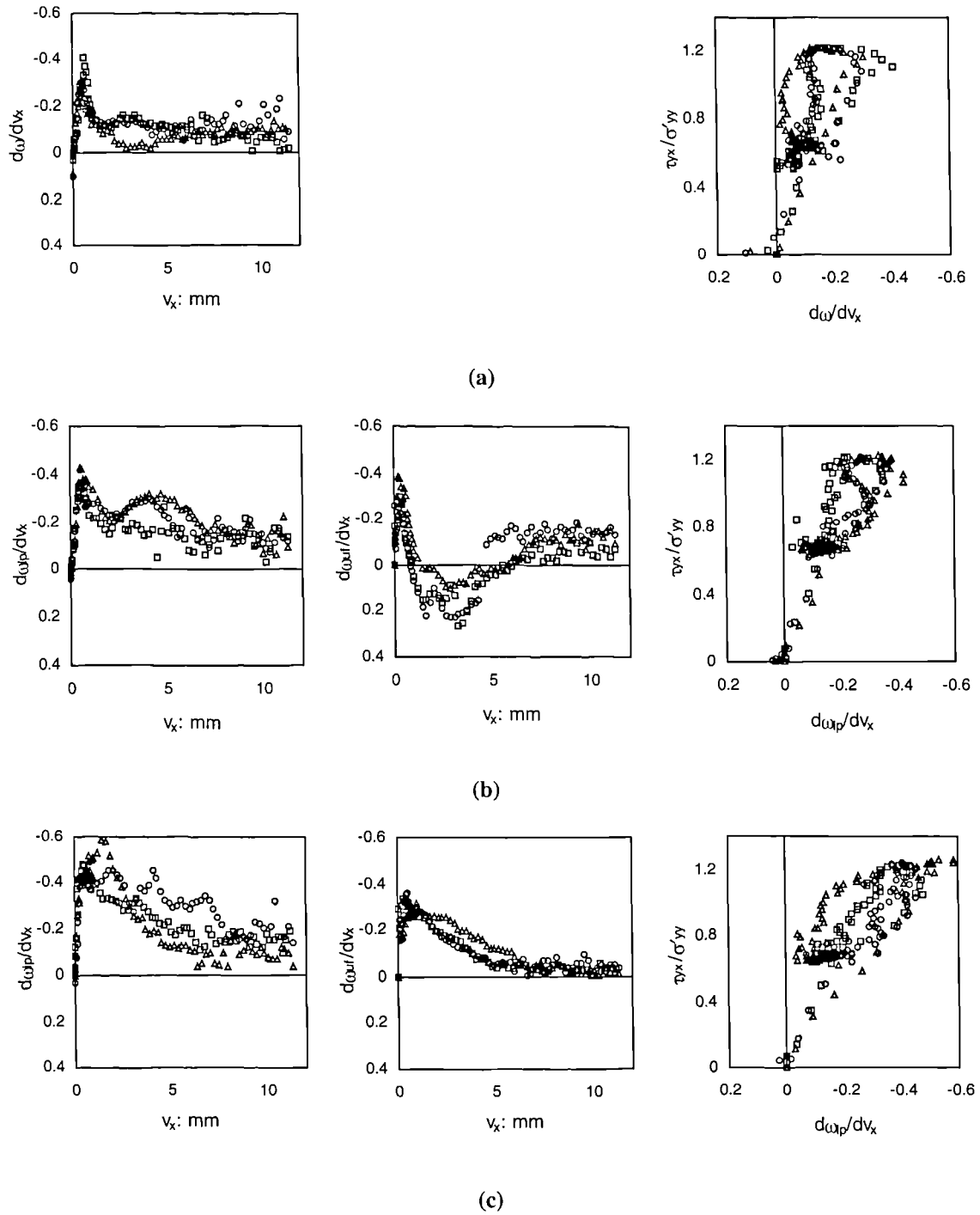


Figure 4.11: The incremental rotations of (a) the symmetrical WDSA's upper ensemble, (b) the unsymmetrical WDSA's load pad and upper frame and (c) the WF-25300's load pad and upper frame (dense VLB,  $\sigma'_{yy} = 25\text{kPa}$ ,  $g = 0.5$ , no shielding,  $f = 10\text{mm}$ )

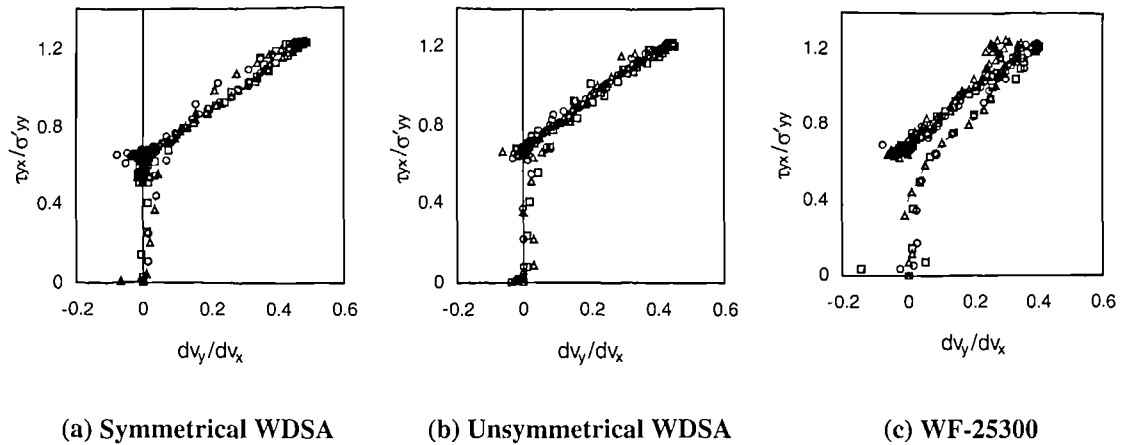


Figure 4.12: The stress dilatancy relation recorded using different apparatus (dense VLB,  $\sigma'_{yy} = 25\text{kPa}$ ,  $g = 0.5$ , no shielding,  $f = 10\text{mm}$ )

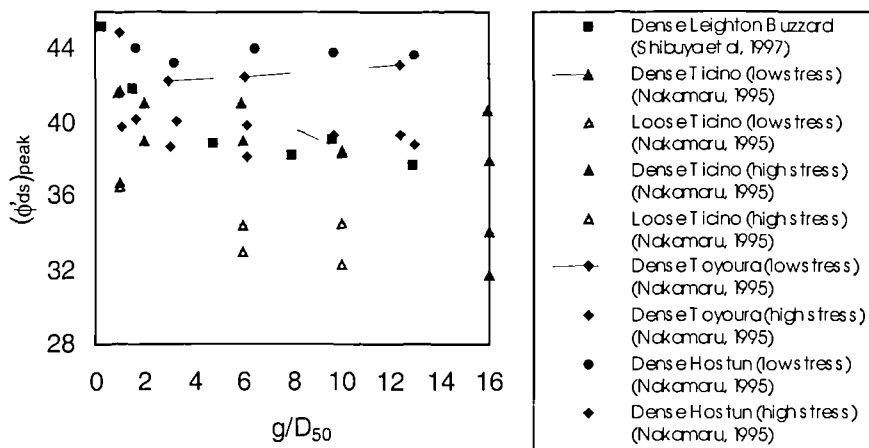


Figure 4.13: The effect of  $g$  on test data featuring a number of sands with various densities and at various stress levels within the JGS's standard DSA

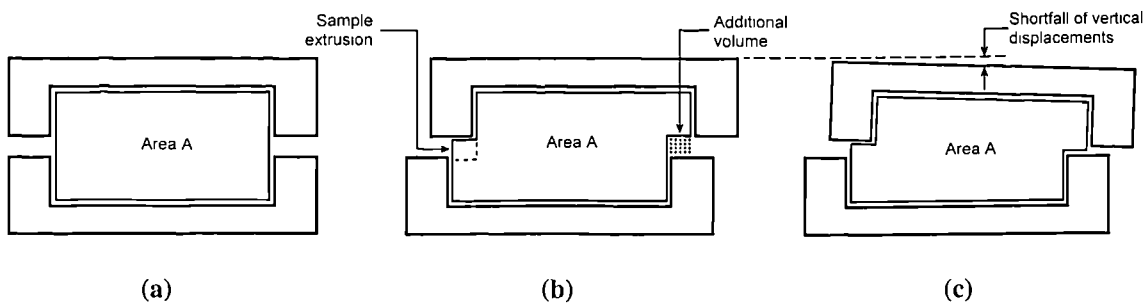


Figure 4.14: The generation and effect of the additional volume created during the shear of a non-dilatative sample

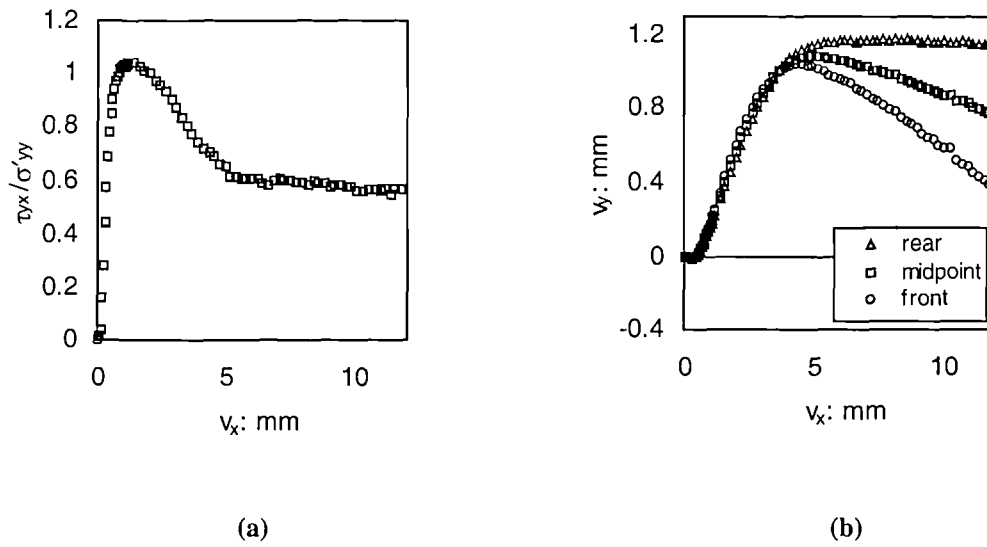


Figure 4.15: Unshielded WDSA data (VLB,  $\sigma'_{yy} = 25\text{kPa}$ , 90%  $D_r$ ,  $f = 0\text{mm}$ ,  $g = 5D_{50}$ )

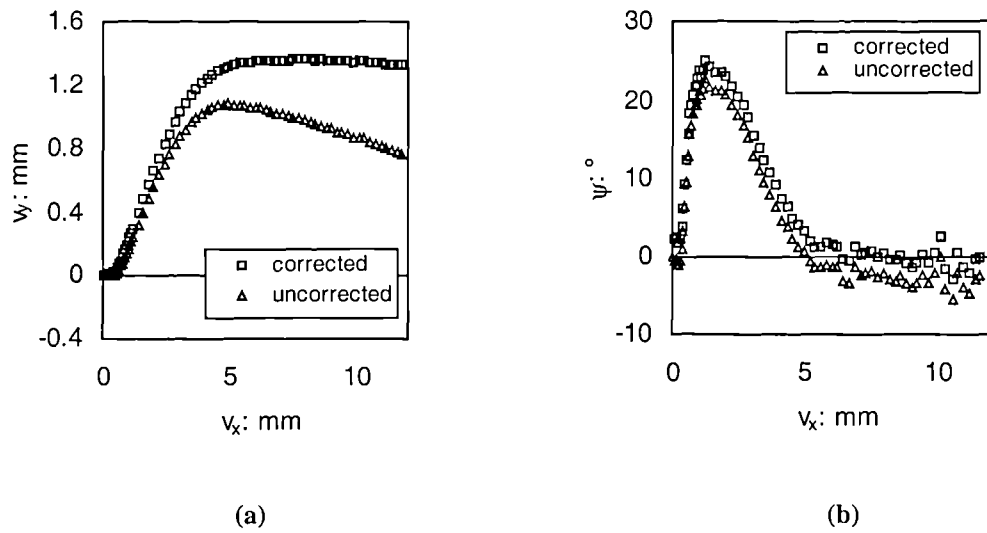


Figure 4.16: Unshielded WDSA displacement data corrected to account for the additional volume created during shear (VLB,  $\sigma'_{yy} = 25\text{kPa}$ , 90%  $D_r$ ,  $f = 0\text{mm}$ ,  $g = 5D_{50}$ )



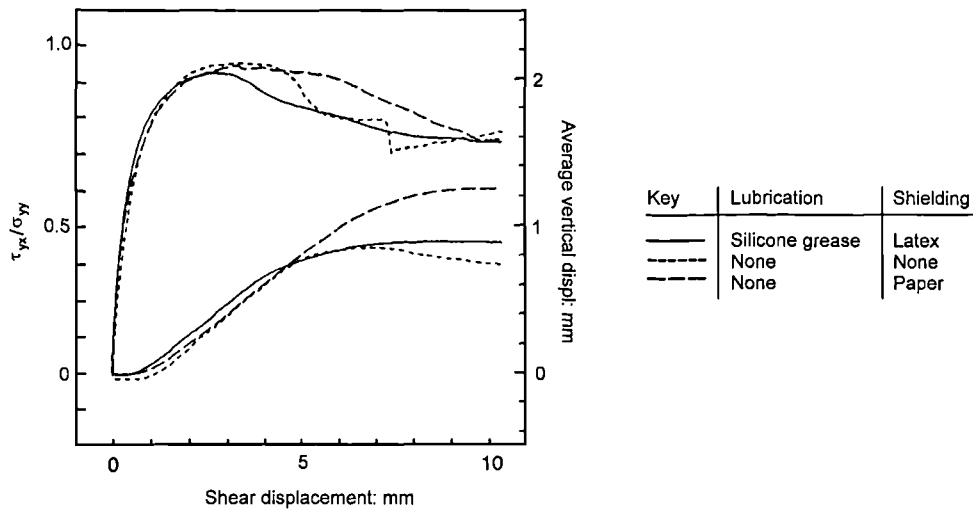


Figure 4.17: The effect of shielding configuration on the direct shear test data of dense Toyoura sand ( $\sigma'_{yy} = 49\text{kPa}$ ,  $D_{50} = 0.16$ ,  $g = 3\text{mm}$ ) (after Shibuya et al, 1997)

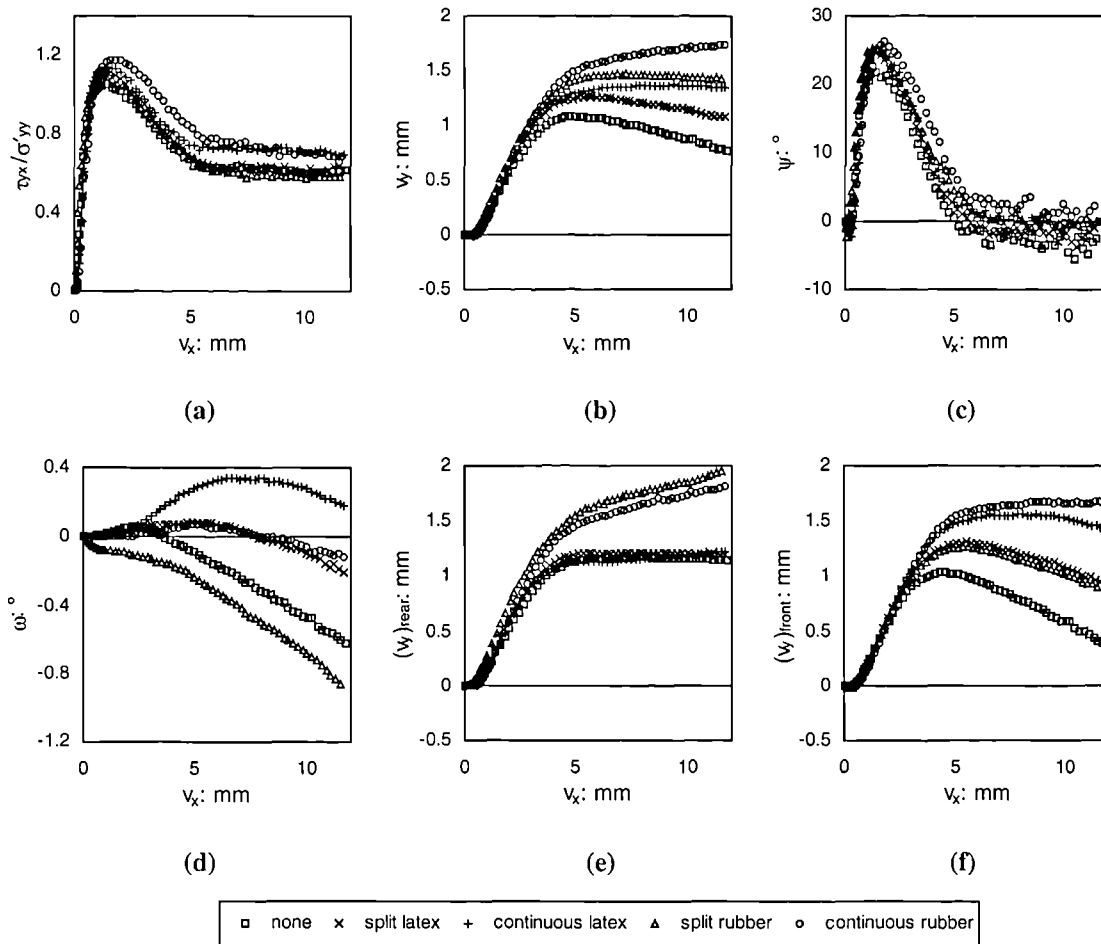


Figure 4.18: Effect of shielding on test data on test data (VLB,  $\sigma'_{yy} = 25\text{kPa}$ , 90%  $D_r$ ,  $f = 0\text{mm}$ ,  $g = 5D_{50}$ )

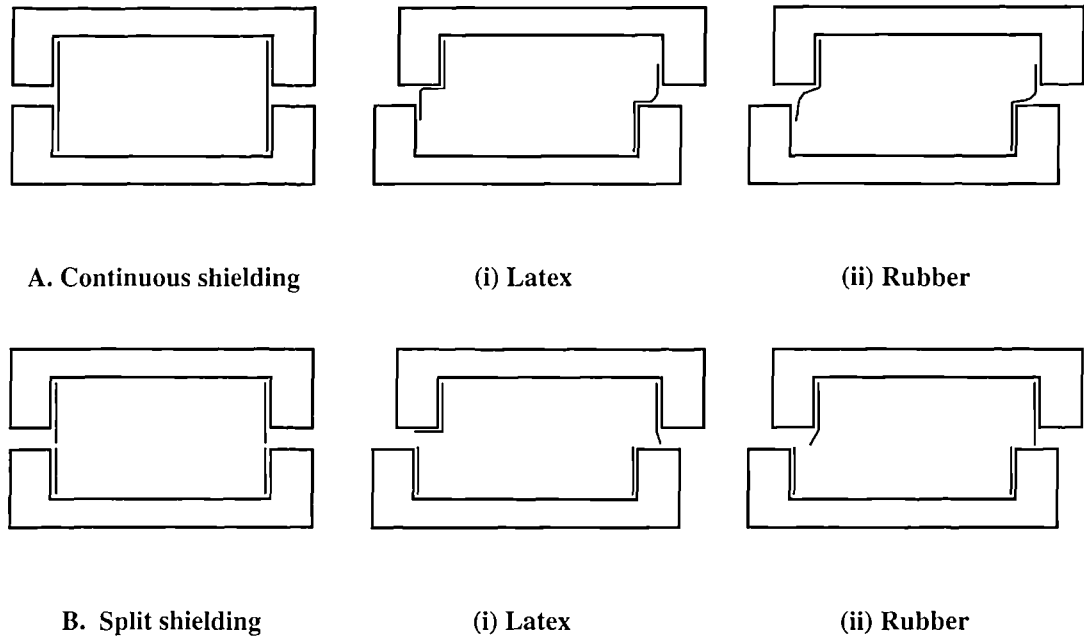


Figure 4.19: Deformations of (a) continuous and (b) split shielding after considerable  $\nu_x$

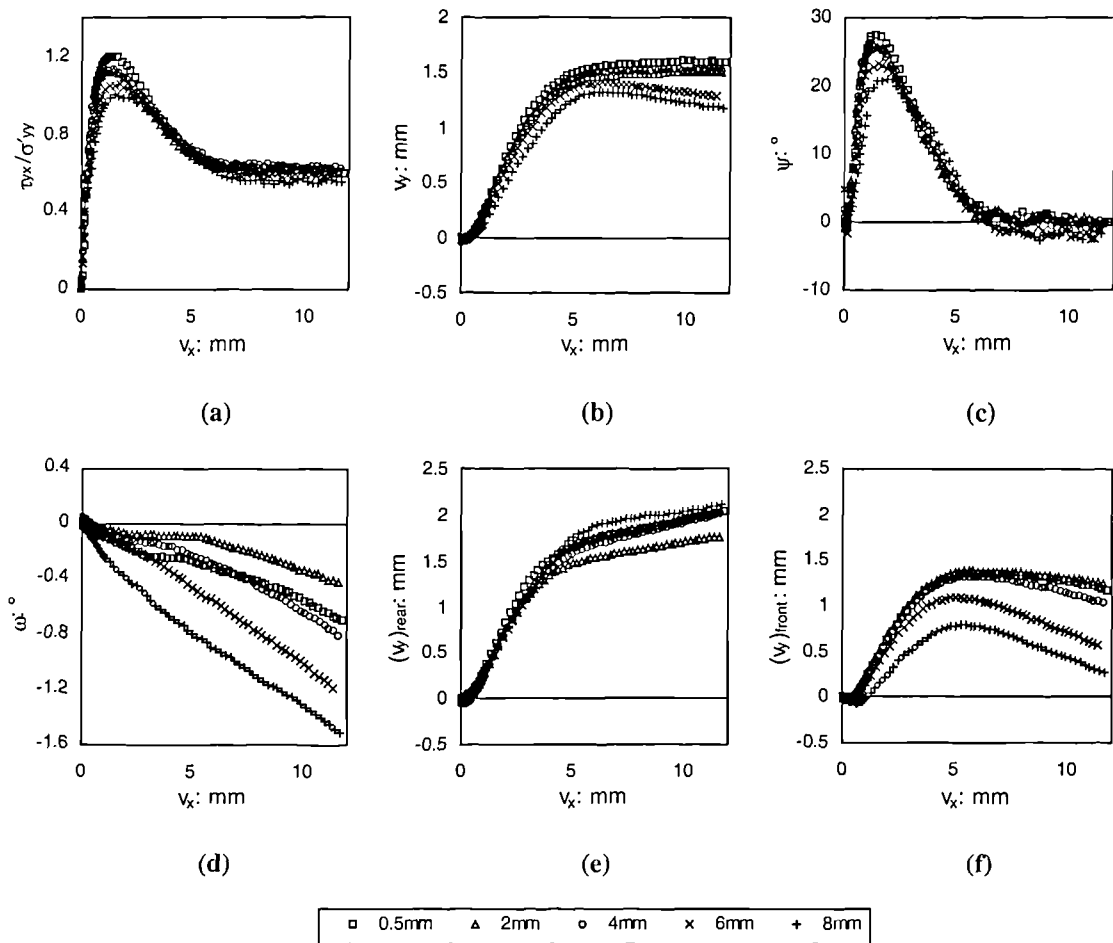


Figure 4.20: The effect of increasing  $g$  on WDSA test data (VLB, 95%  $D_r$ ,  $\sigma'_{yy} = 25\text{kPa}$ ,  $f = 0\text{mm}$ )

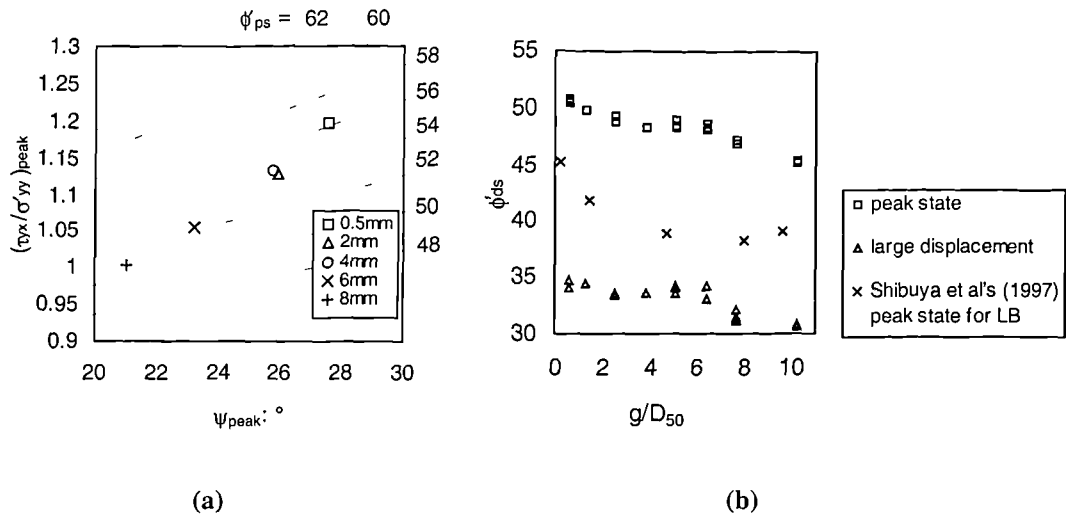


Figure 4.21: The effect of increasing  $g$  on (a) peak stress dilatancy response and (b) direct shear angles of friction (VLB, 95%  $D_r$ ,  $\sigma'_{yy} = 25\text{kPa}$ ,  $f = 0\text{mm}$ )

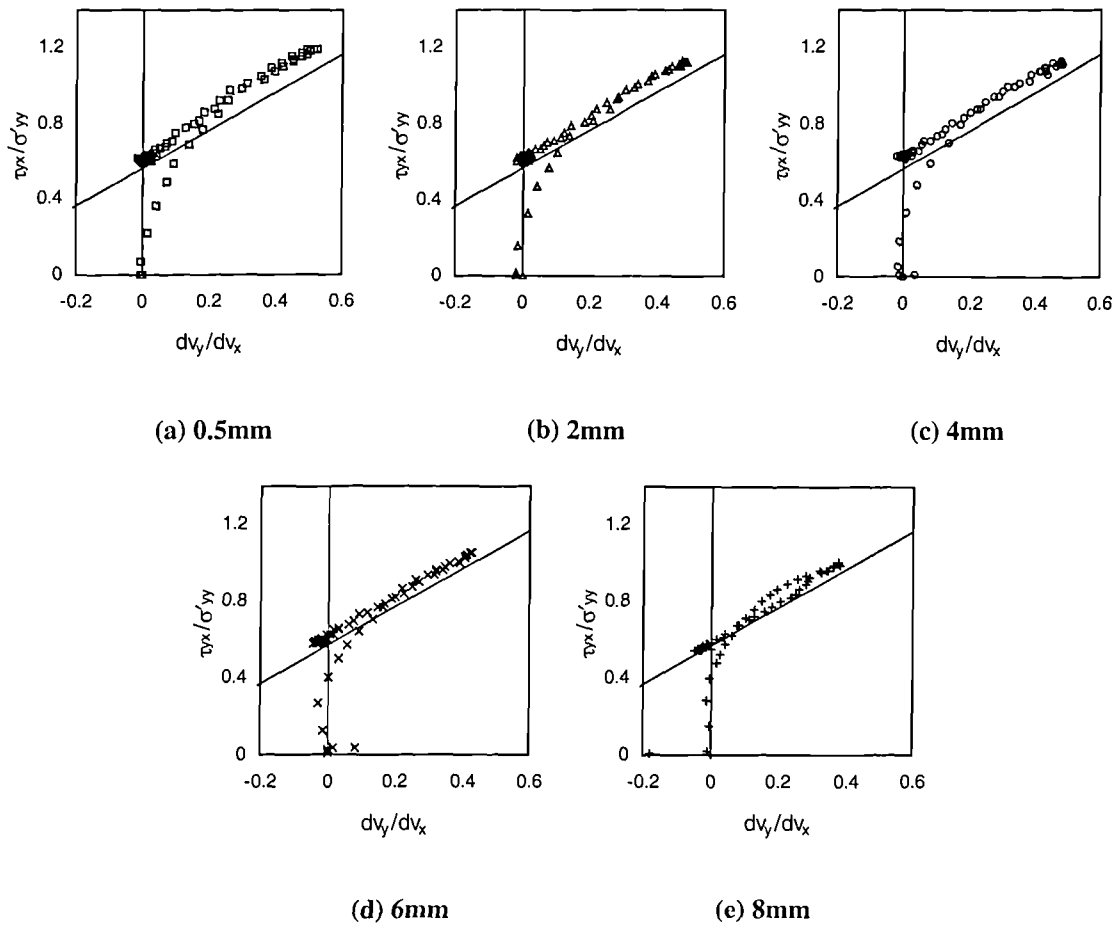


Figure 4.22: The stress-dilatancy response of dense VLB confined under 25kPa in the symmetrical WDSA with  $g$  values as indicated (VLB, 95%  $D_r$ ,  $\sigma'_{yy} = 25\text{kPa}$ ,  $f = 0\text{mm}$ )

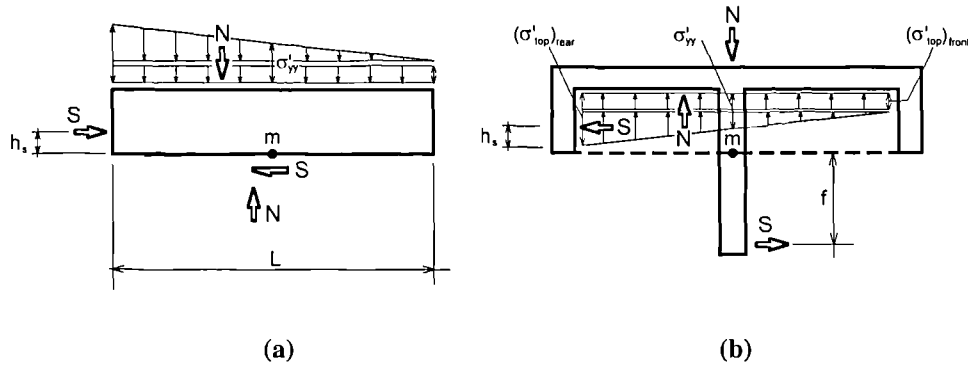


Figure 4.23: The system of forces acting on (a) the portion of the sample contained within the upper ensemble and (b) the upper ensemble

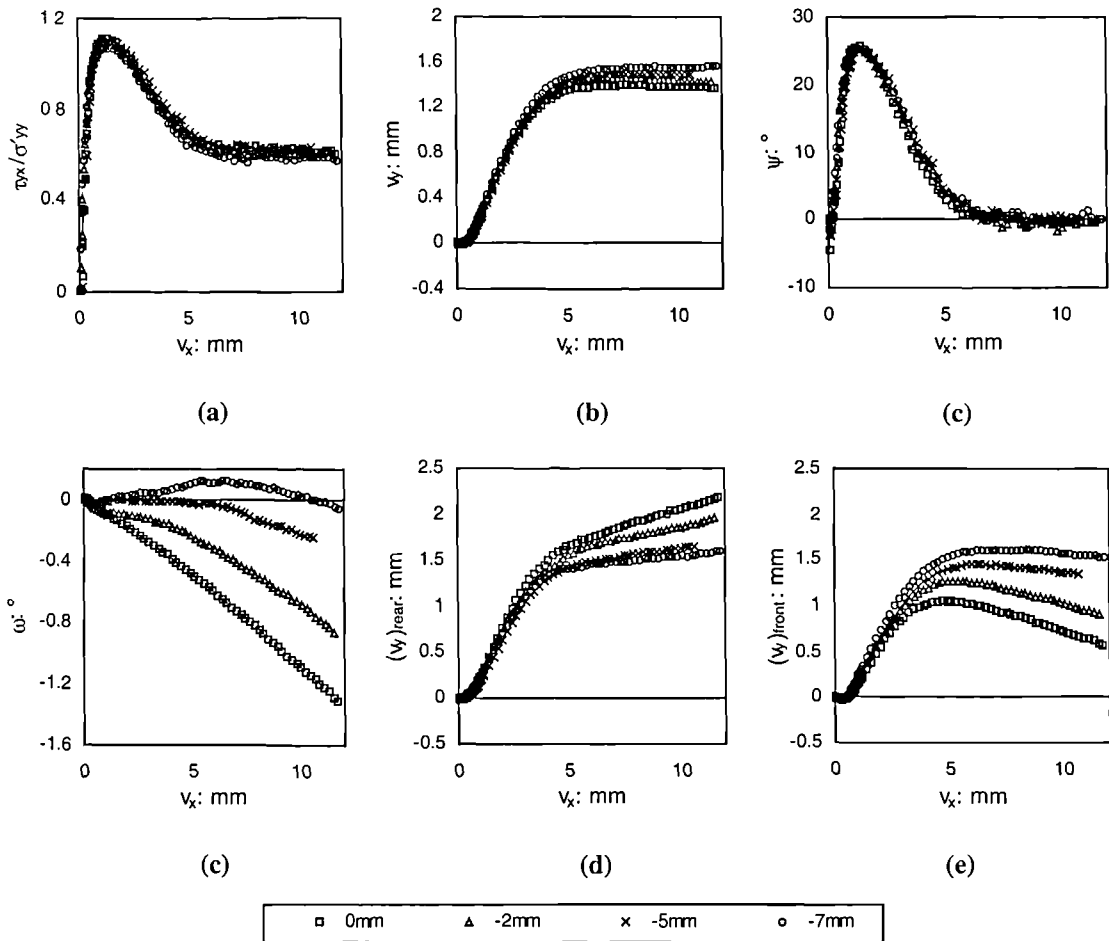


Figure 4.24: The effect on test data of limiting the rotation undergone by the upper ensemble by increasing the anticlockwise moment applied to the sample

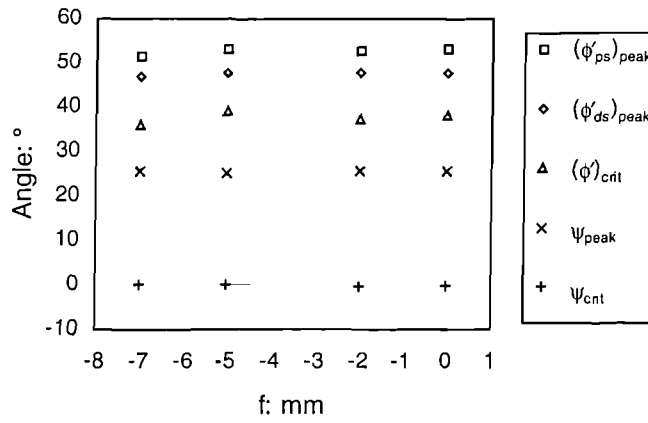
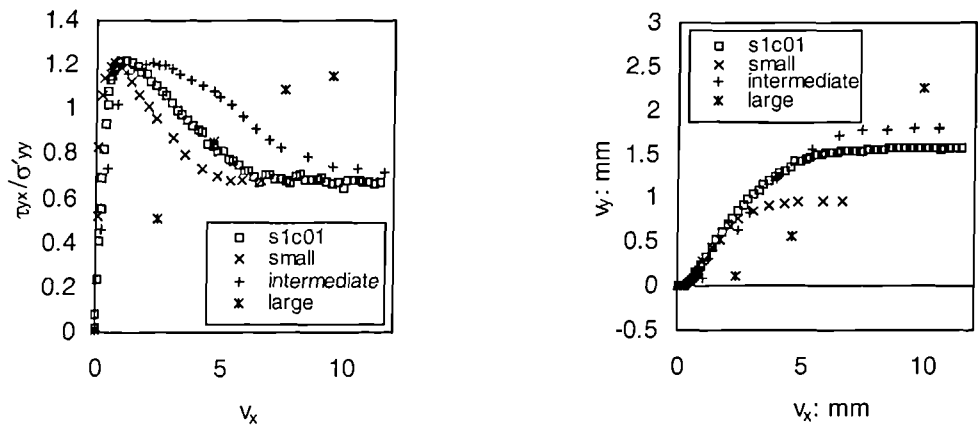
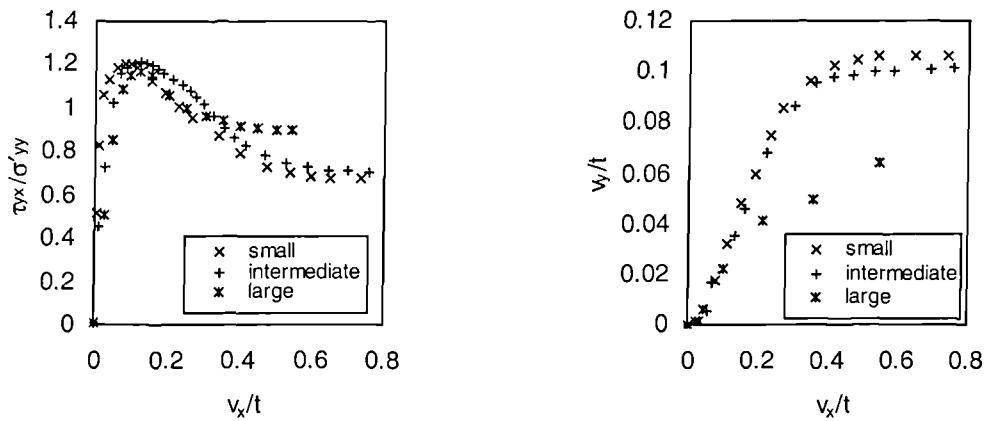


Figure 4.25: The effect on cardinal parameters of increasing the separation between the line of thrust and the central plane



(a)



(b)

Figure 4.26: Palmeira & Milligan's (1989) DSA data obtained in shearboxes of different sizes: (a) and (b) compared to WDSA test data, (c) and (d) normalised by shear zone thickness

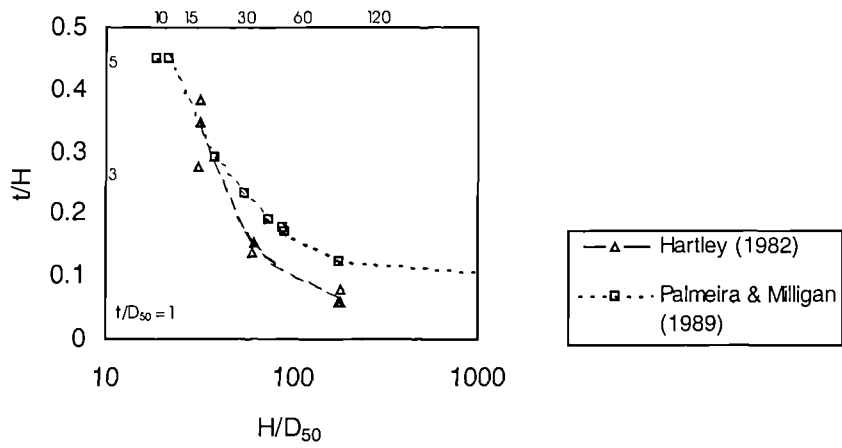


Figure 4.27: The relationship between  $t/H$  and  $H/D_{50}$  found by different authors for the same sand in shearboxes of different sizes

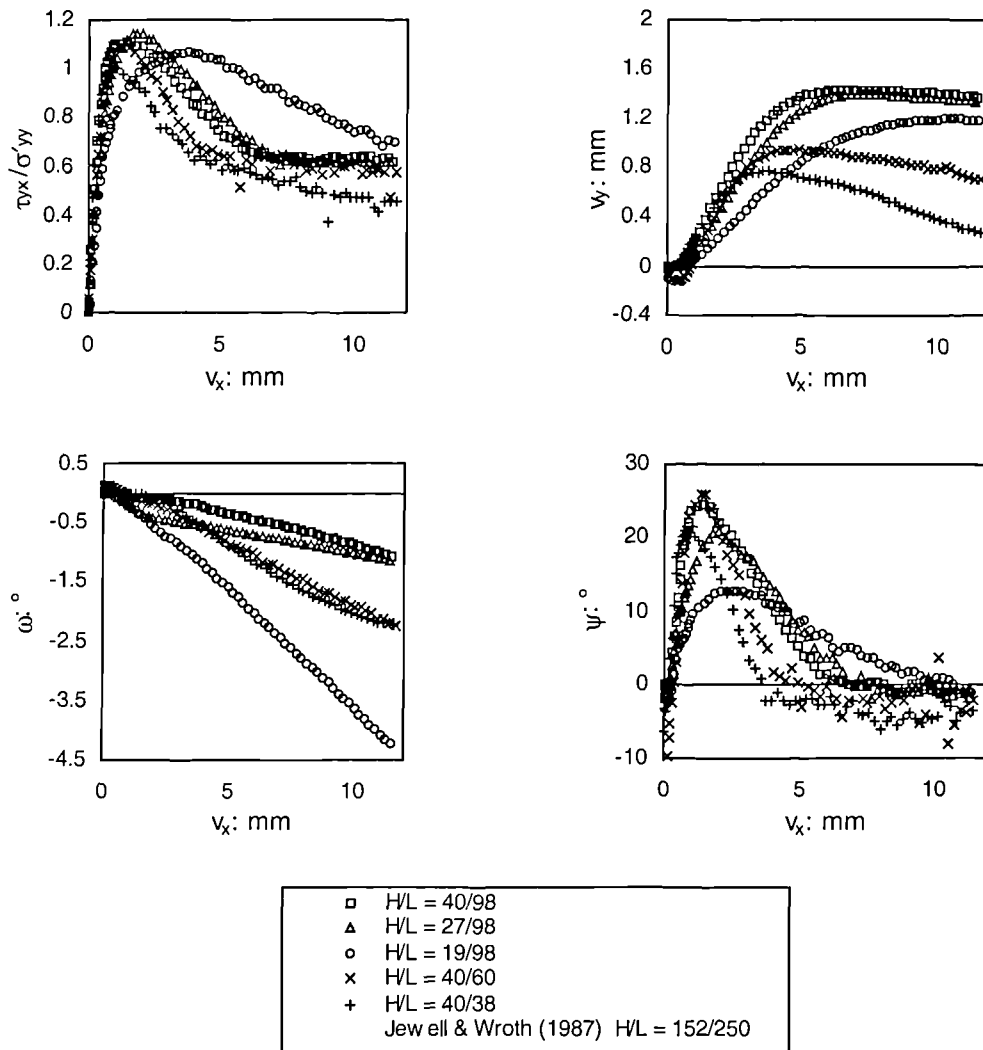


Figure 4.28: The effect of sample dimensions on dense VLB data ( $\sigma'_{yy} = 25\text{kPa}$ ,  $g = 5D_{50}$ ,  $f = 0\text{mm}$ )

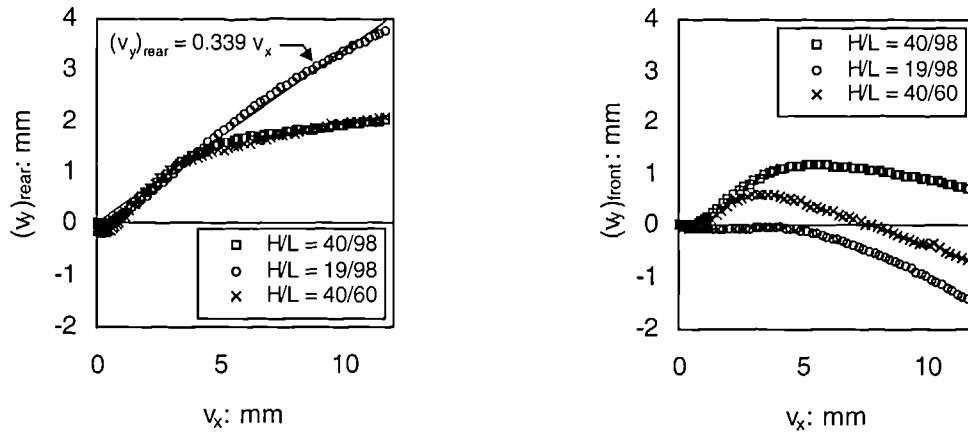


Figure 4.29: Vertical displacements recorded at the front and rear of dense VLB samples of different dimension ( $\sigma'_{yy} = 25\text{kPa}$ ,  $g = 5D_{50}$ ,  $f = 0\text{mm}$ )

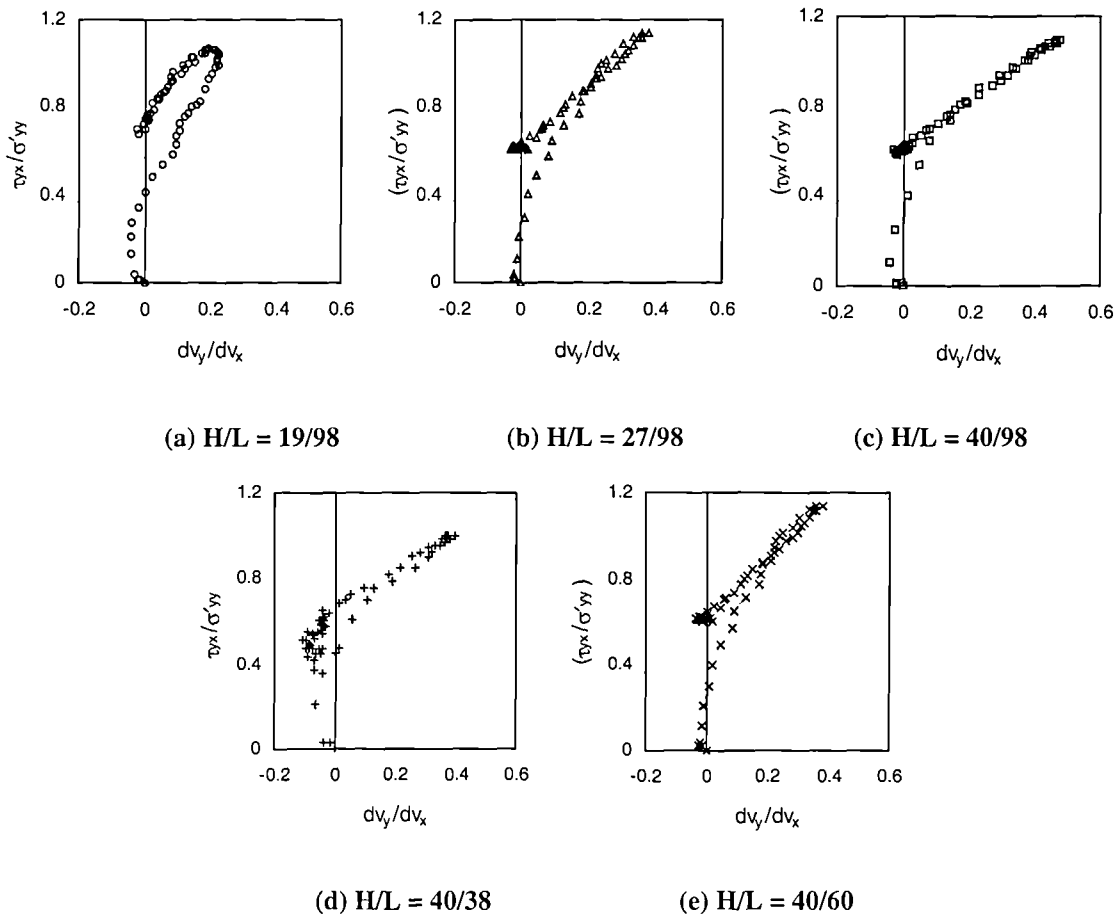


Figure 4.30: The effect of sample dimensions on the stress-dilatancy relationship of VLB ( $\sigma'_{yy} = 25\text{kPa}$ ,  $g = 5D_{50}$ ,  $f = 0\text{mm}$ )

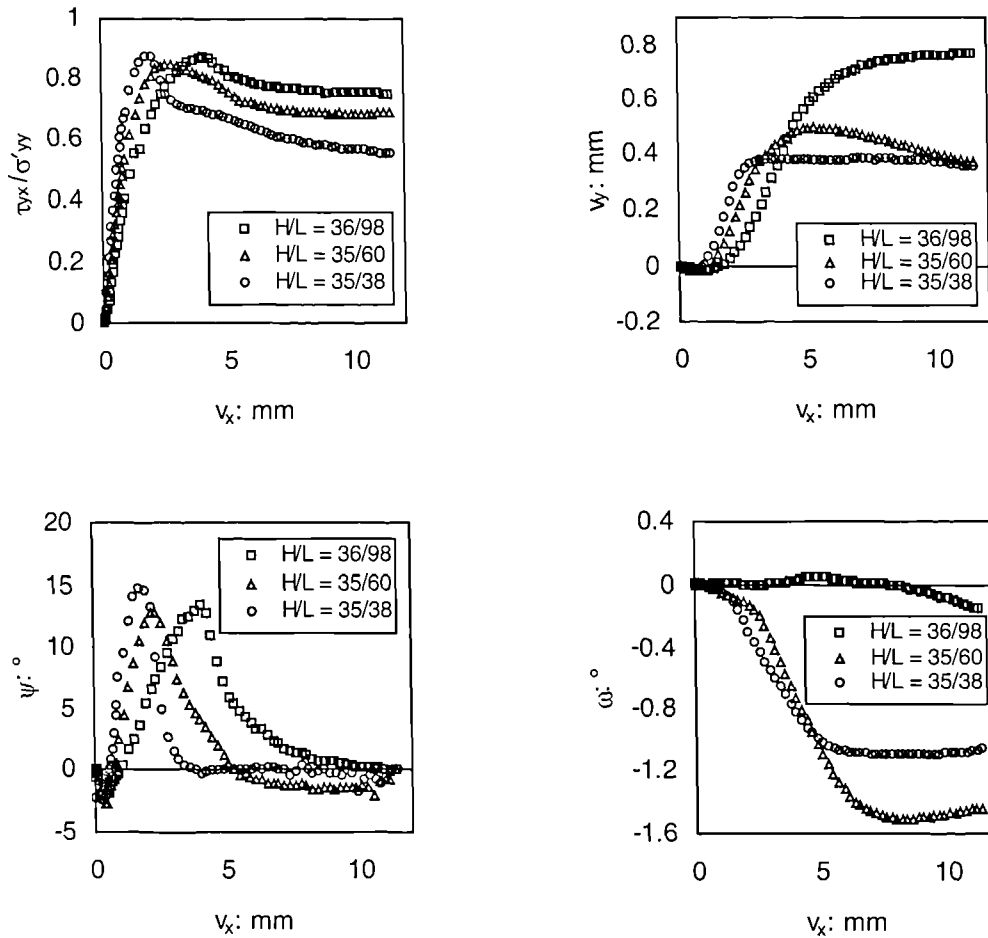


Figure 4.31: The effect of reducing the length  $L$  of a dense SFS sample ( $\sigma'_{yy} = 252\text{kPa}$ ,  $g = 5D_{50}$ ,  $f = 0\text{mm}$ )

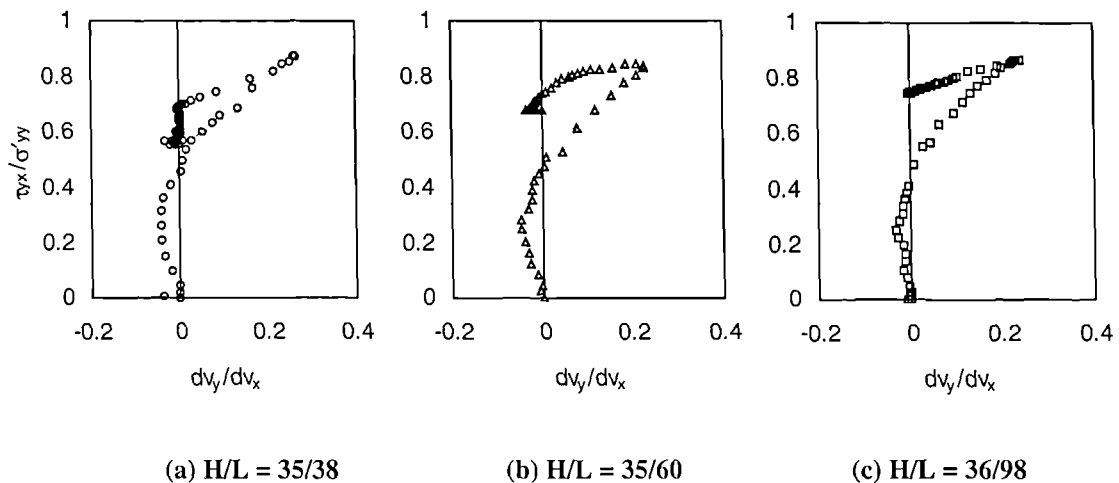
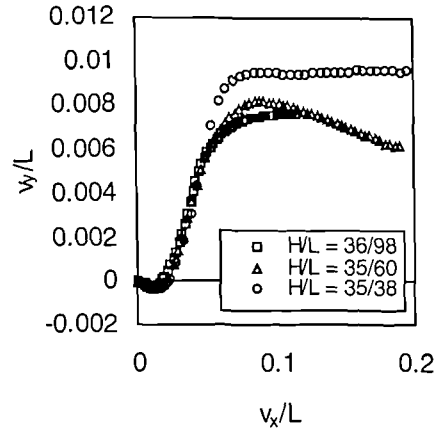
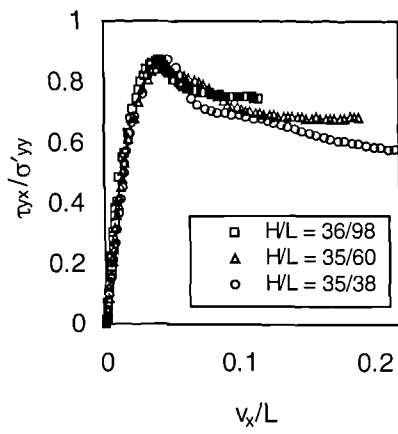
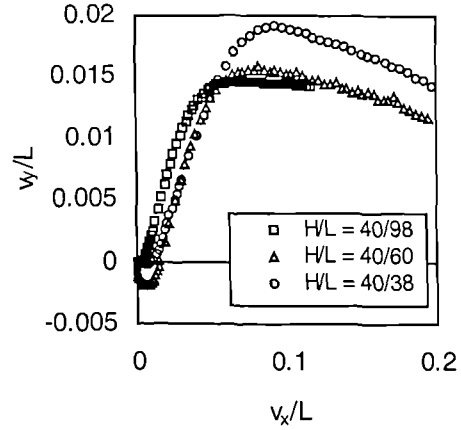
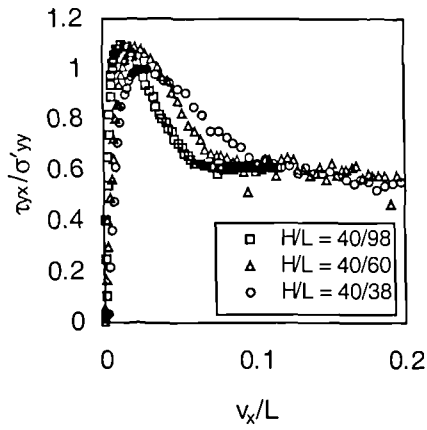


Figure 4.32: The relationship between stress ratio and dilation rate for dense SFS samples of different length  $L$  ( $\sigma'_{yy} = 252\text{kPa}$ ,  $g = 5D_{50}$ ,  $f = 0\text{mm}$ )

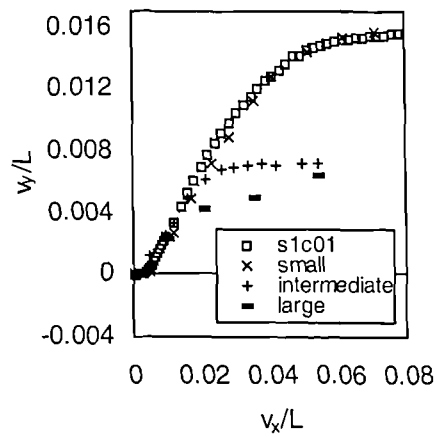
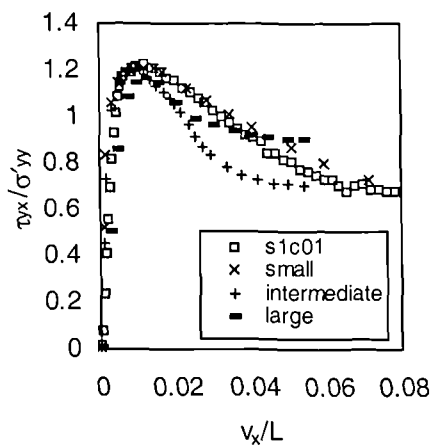




(a) SFS



(b) VLB



(c) Palmeira & Milligan's (1989) LB

Figure 4.33: The effect of normalising dense (a) SFS and (b) VLB data with by specimen length  $L$

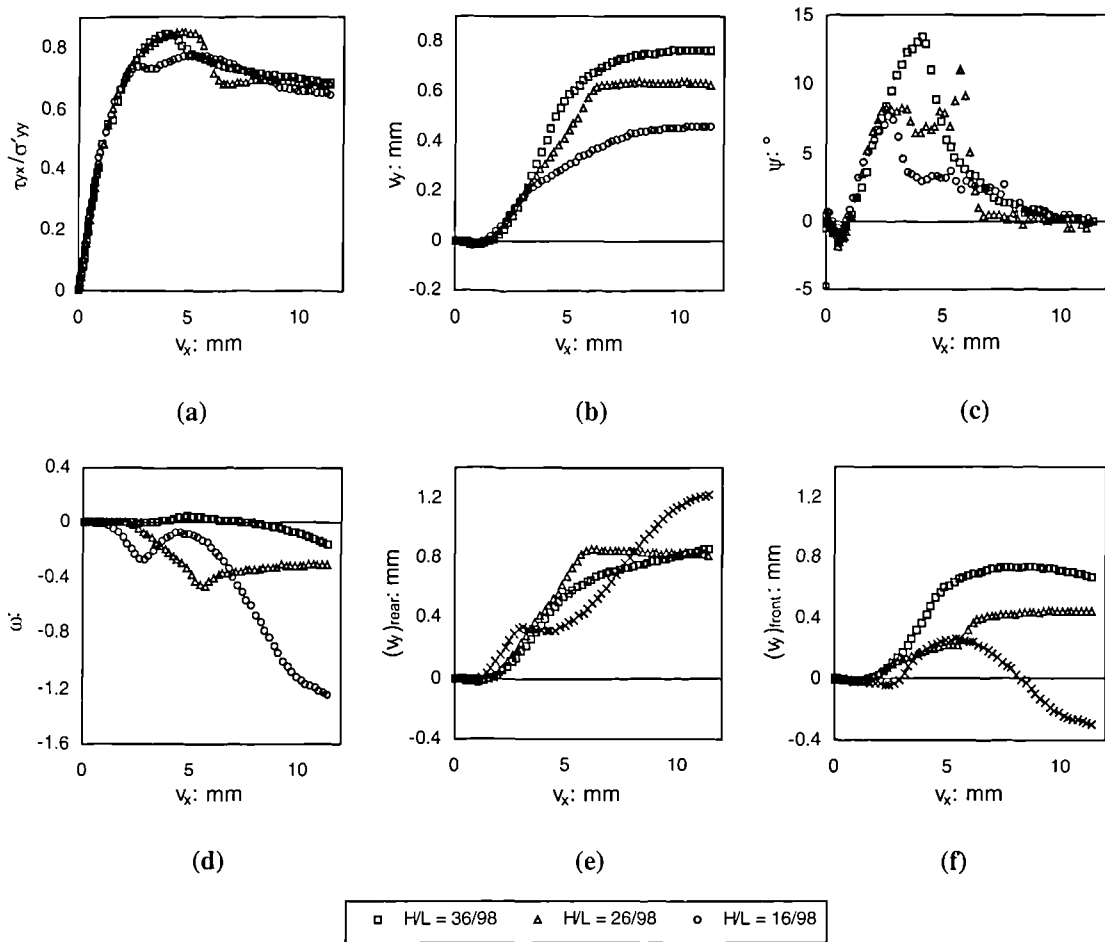


Figure 4.34: The effect of reducing the height  $H$  of a dense SFS sample ( $\sigma'_{yy} = 252\text{kPa}$ ,  $g = 5D_{50}$ ,  $f = 0\text{mm}$ )

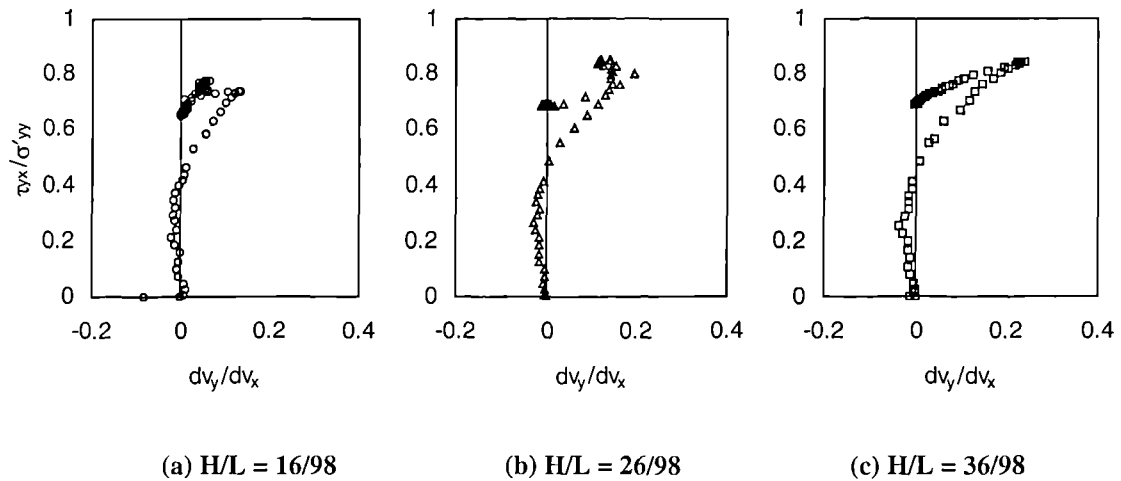


Figure 4.35: The relationship between stress ratio and dilation rate for dense SFS samples of different heights  $H$  ( $\sigma'_{yy} = 252\text{kPa}$ ,  $g = 5D_{50}$ ,  $f = 0\text{mm}$ )

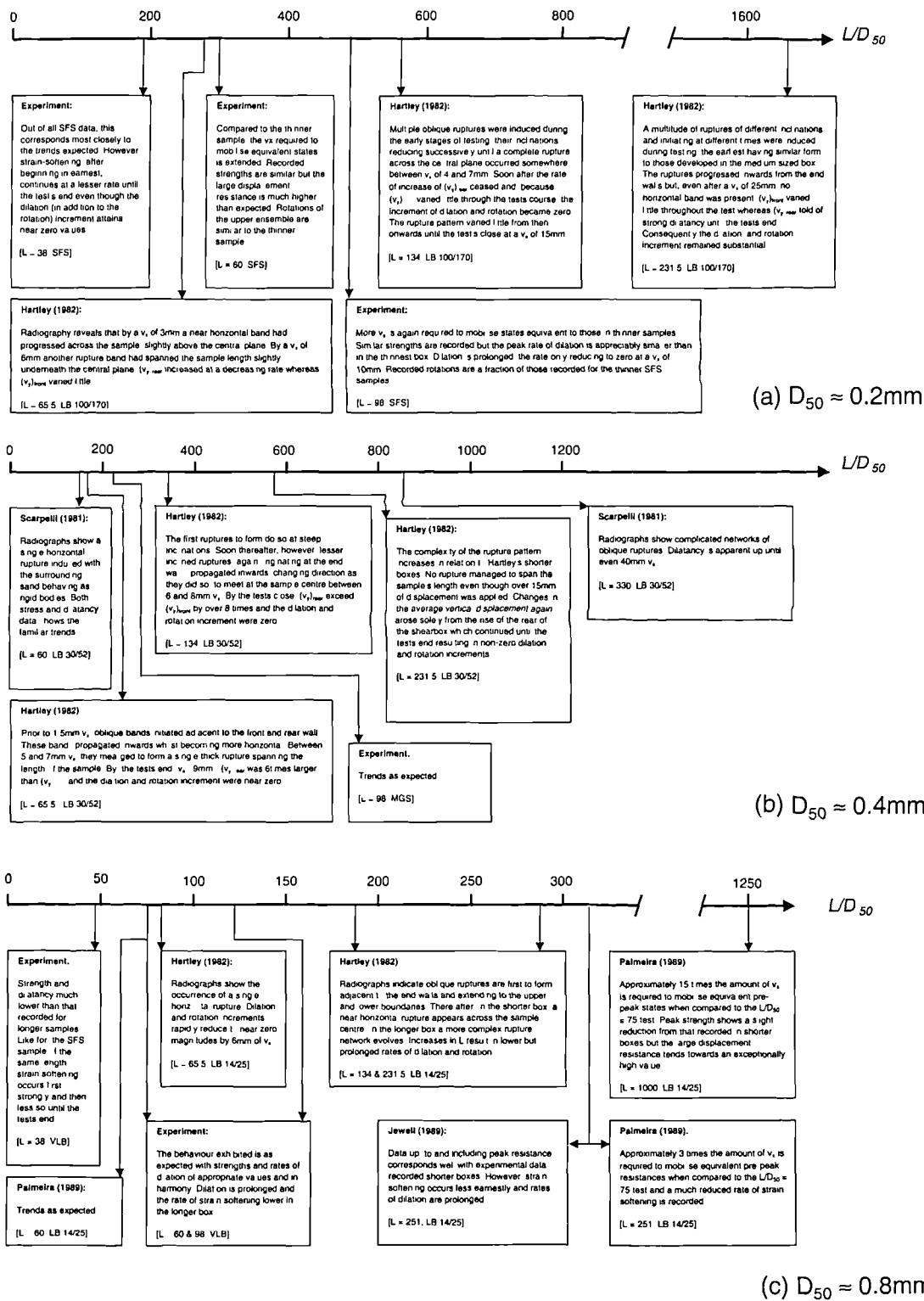


Figure 4.36: The effects found in the literature and during experimentation of increasing the length  $L$  of sands with different gradings

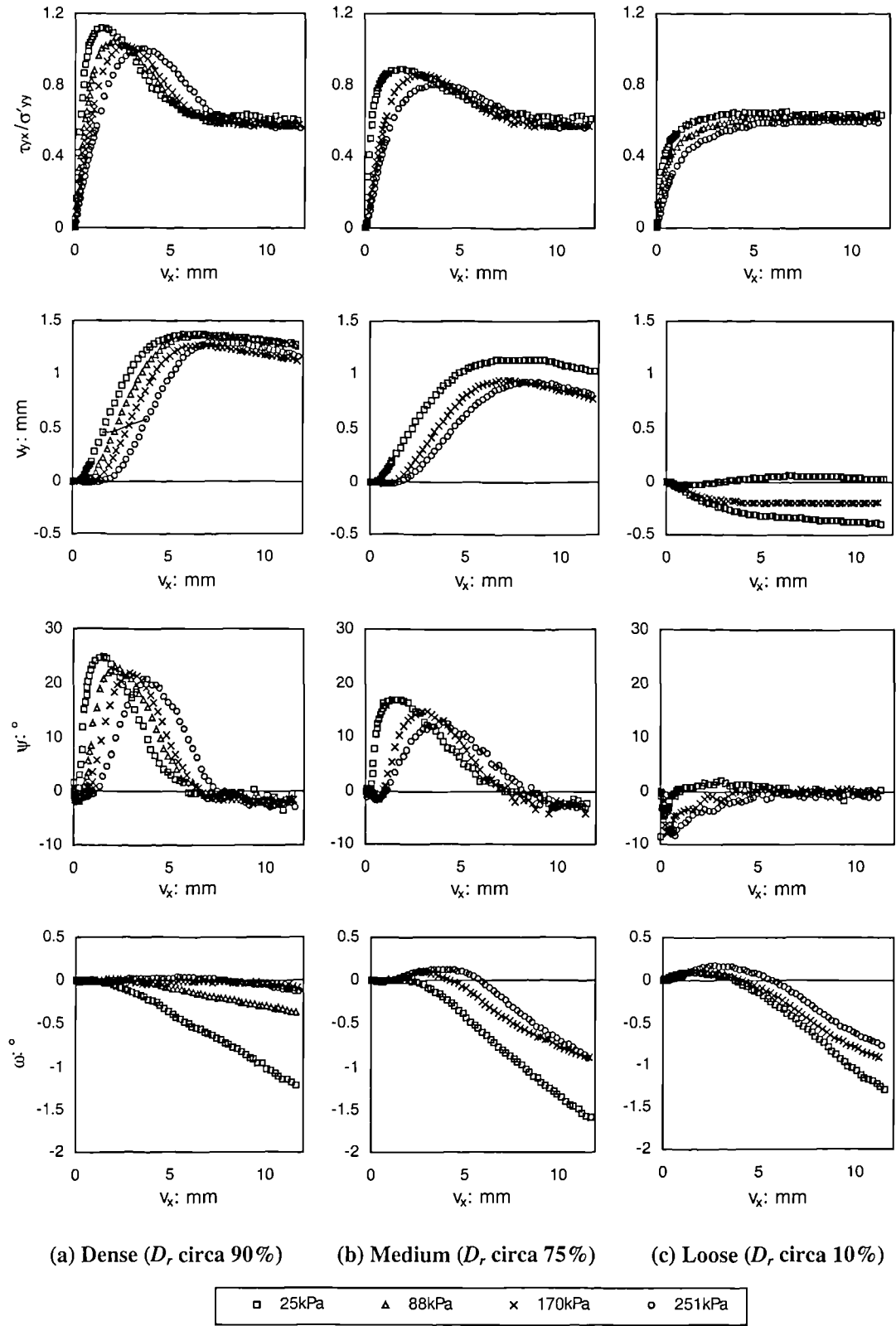
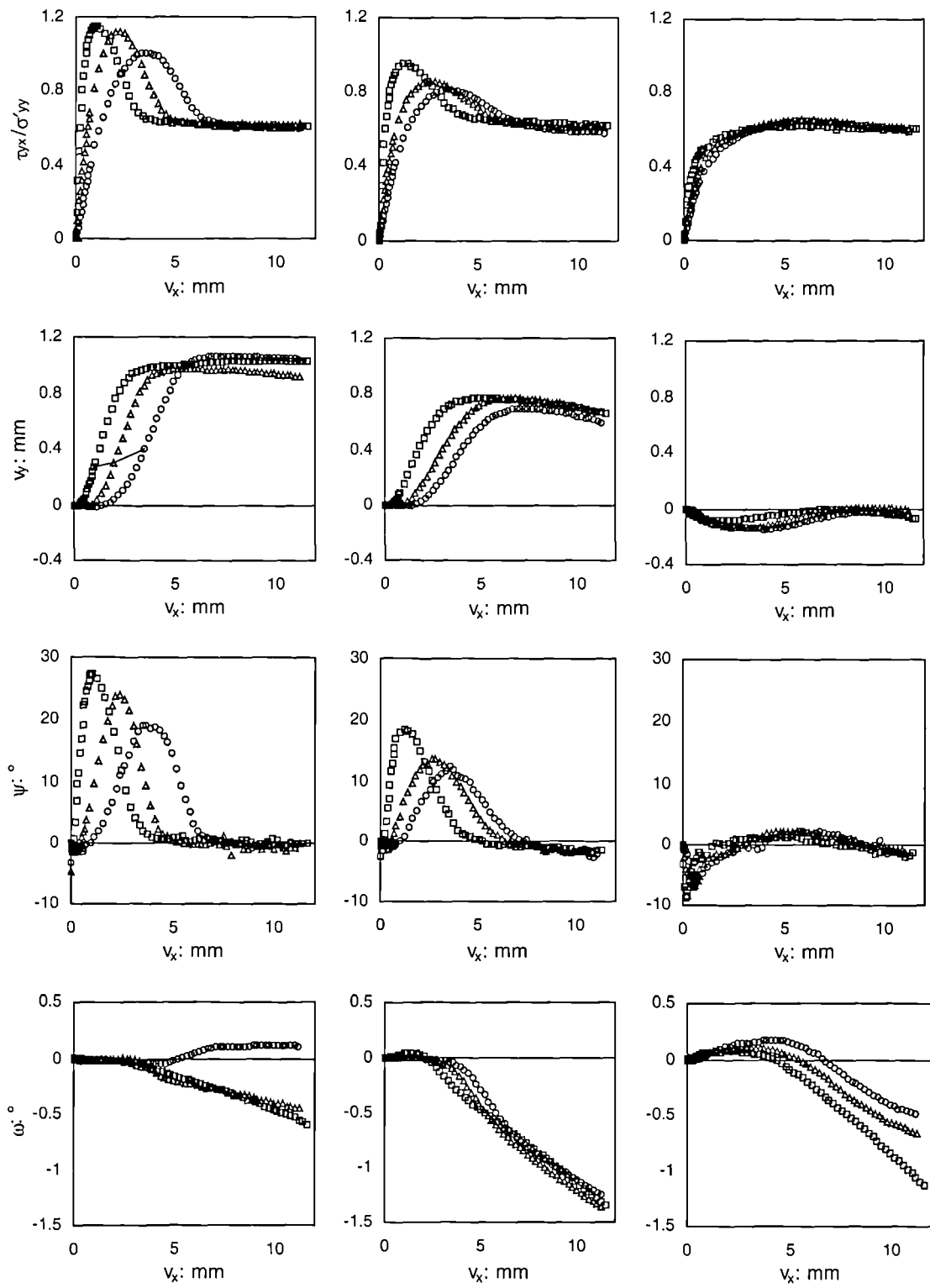


Figure 5.1: VLB test data



(a) Dense ( $D_r$ , circa 90%)

(b) Medium ( $D_r$ , circa 75%)

(c) Loose ( $D_r$ , circa 10%)

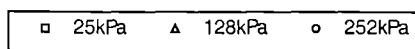


Figure 5.2: MGS test data

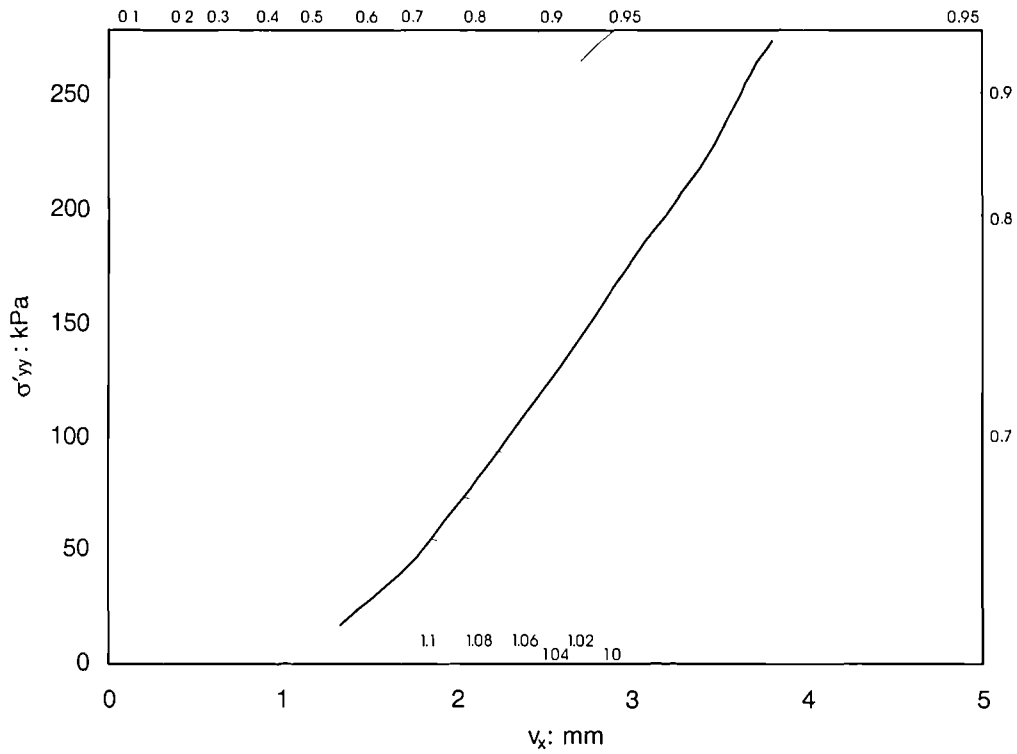


Figure 5.3: Contours of stress ratio  $\tau_{yx}/\sigma'_{yy}$  in  $(\sigma'_{yy}, \nu_x)$  space for dense VLB ( $D_r$  circa 90%) in the WDSA

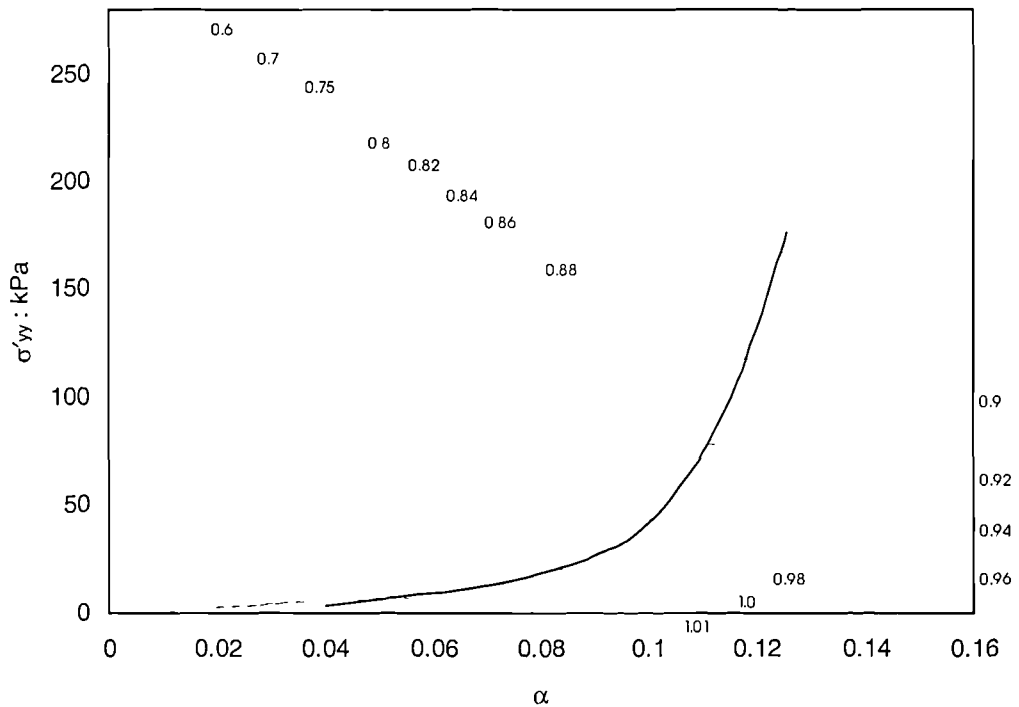
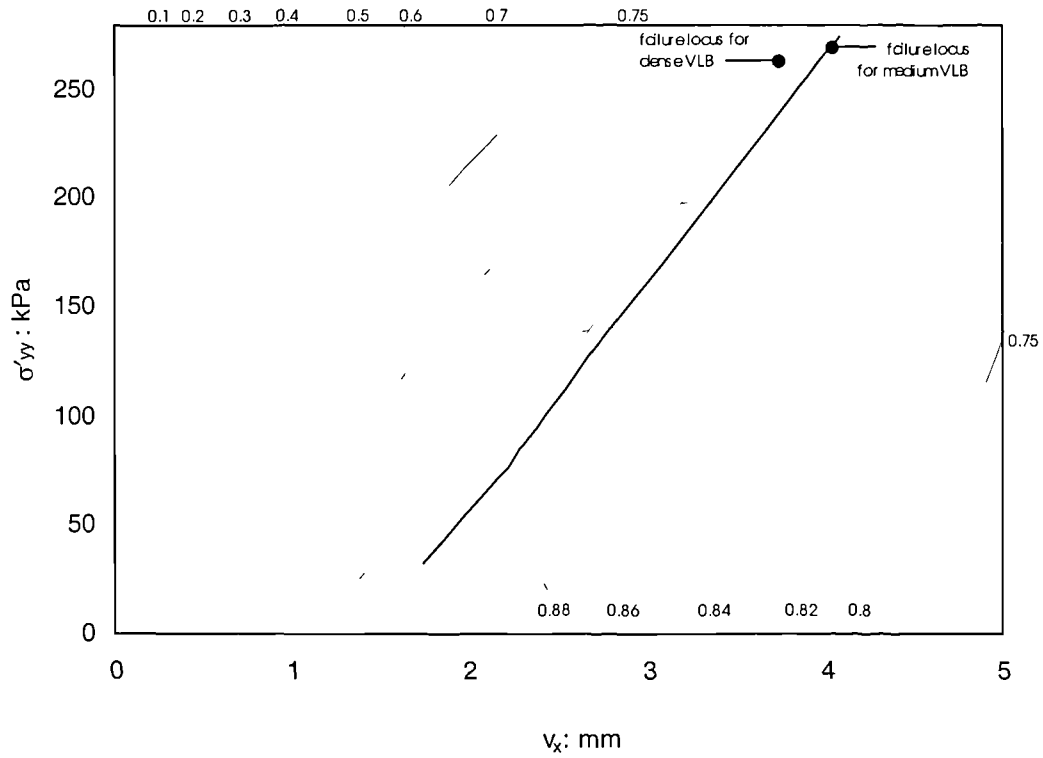
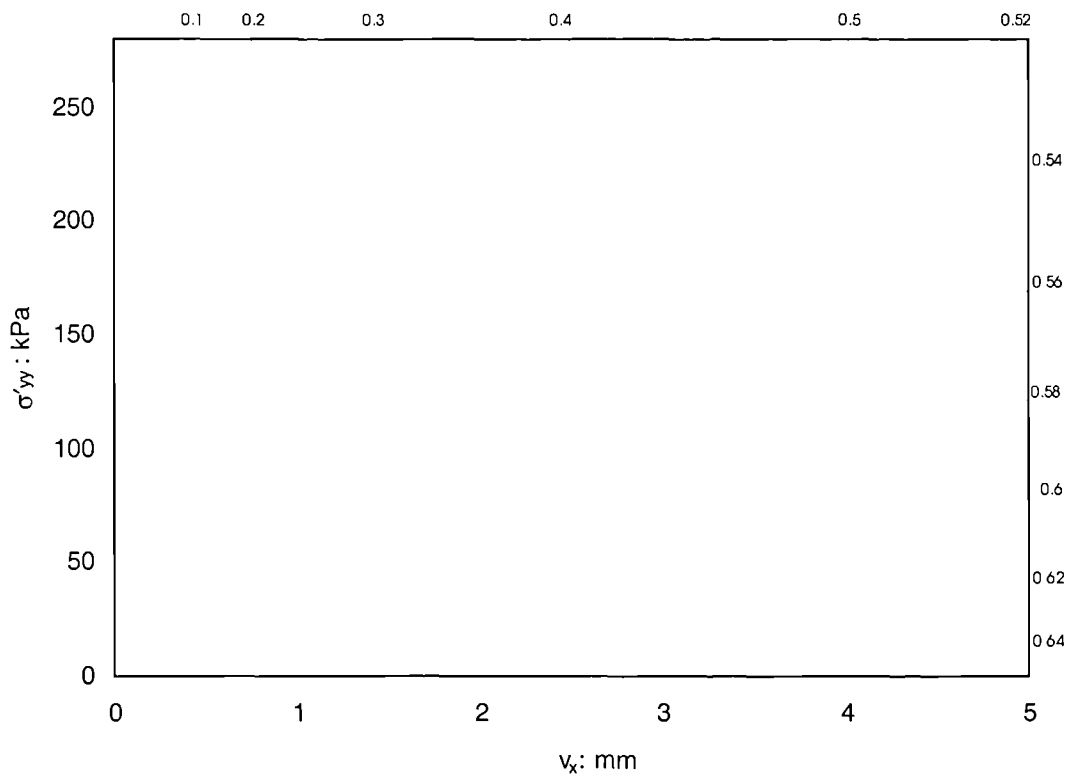


Figure 5.4: Contours of stress ratio  $\tau_{yx}/\sigma'_{yy}$  in  $(\sigma'_{yy}, \alpha)$  space for dense VLB in Stroud's (1971) SSA



(a) Medium VLB ( $D_r$  circa 75%)



(b) Loose VLB ( $D_r$  circa 10%)

Figure 5.5: Contours of stress ratio  $\tau_{yx}/\sigma'_{yy}$  in  $(\sigma'_{yy}, v_x)$  space for (a) medium VLB and (b) loose VLB in the WDSA

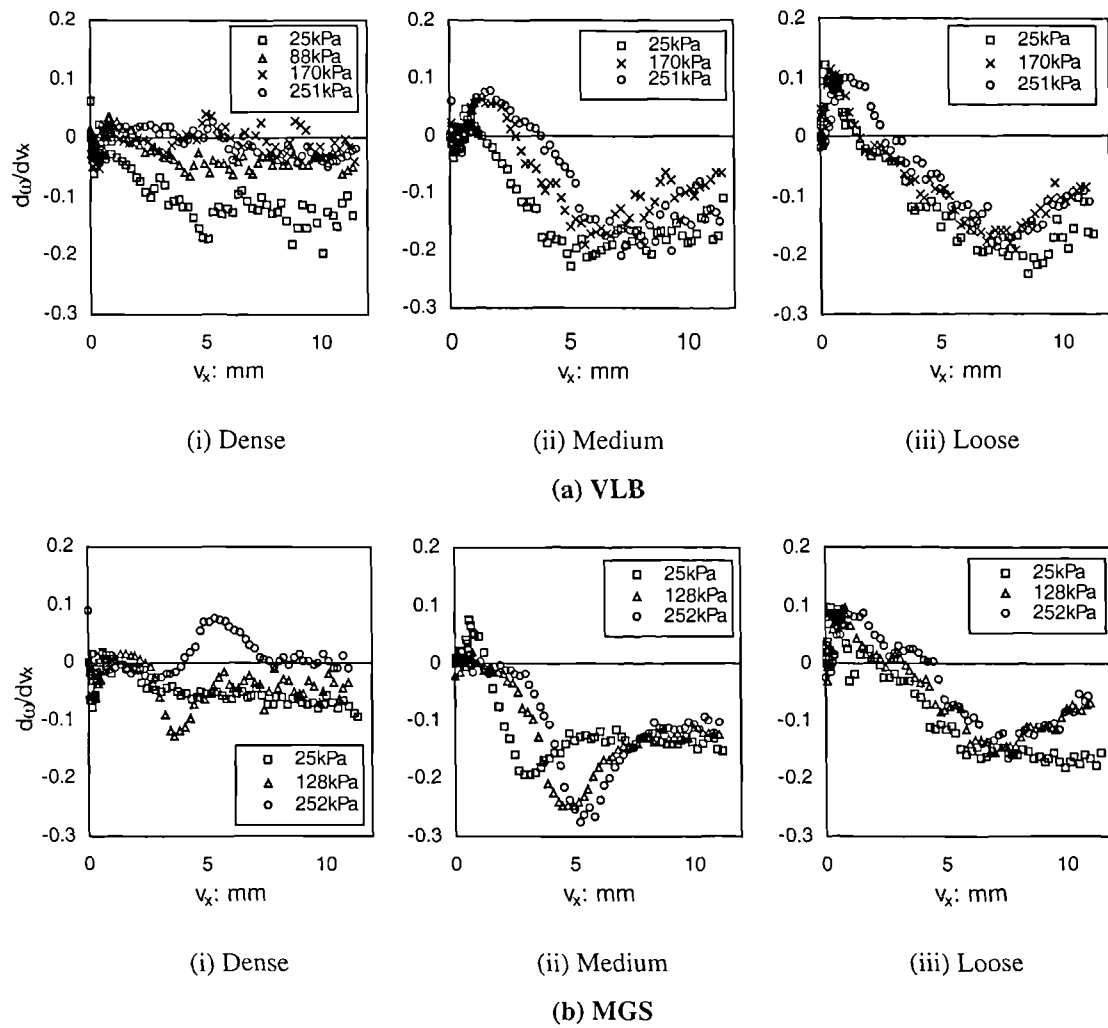


Figure 5.6: The rate at which the upper ensemble rotates during WDSA testing using (a) VLB and (b) MGS deposited at various densities and at different stress levels

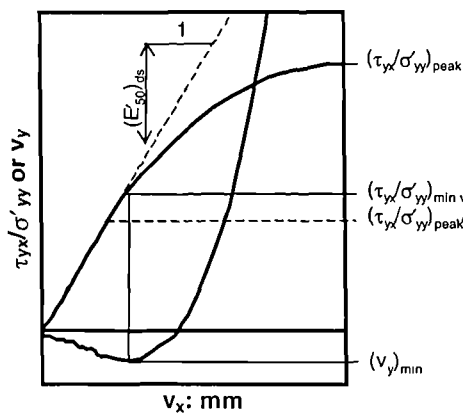


Figure 5.7: The definition of pre-peak stress and deformation parameters

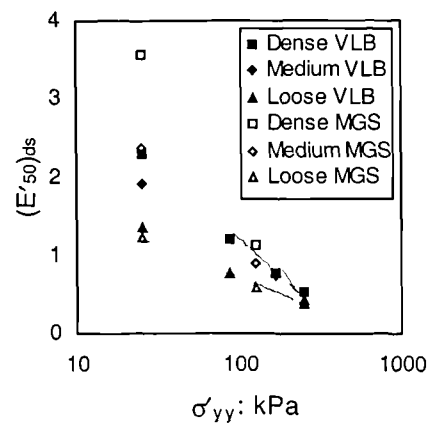


Figure 5.8: The variation of  $(E'_{50})_{ds}$  with  $D_r$  and  $\sigma'_{yy}$  for VLB and MGS



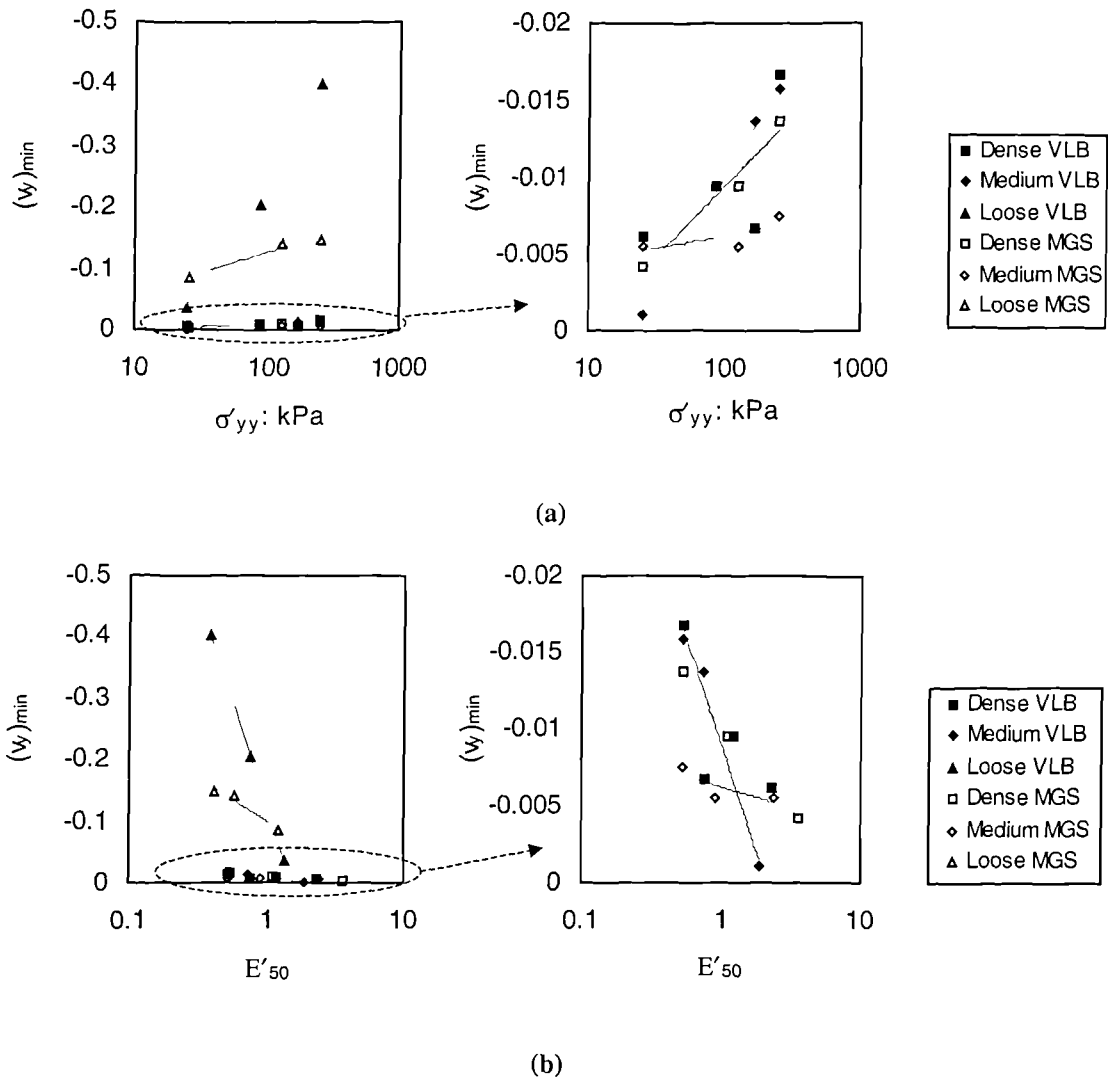


Figure 5.9: The variation of  $(y_y)_{min}$  with (a) stress level and (b) stiffness for VLB and MGS

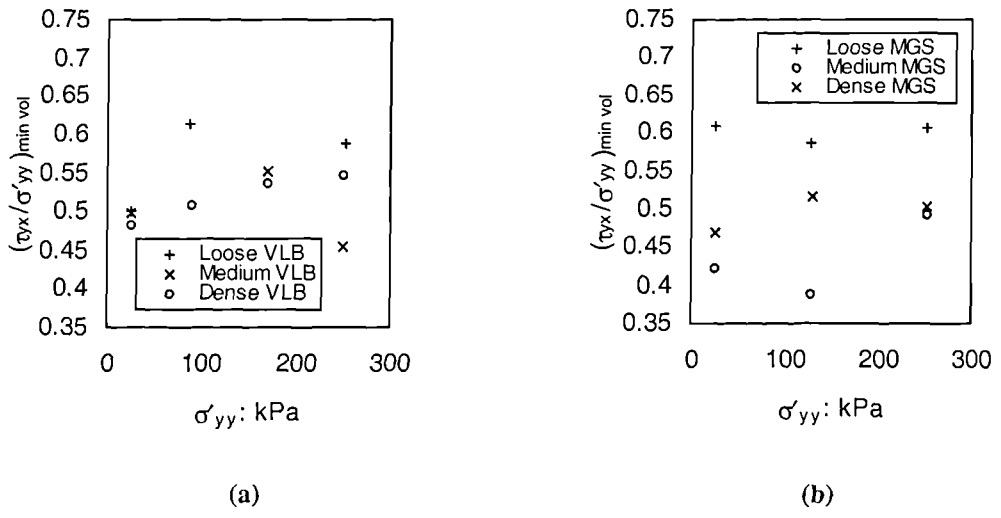


Figure 5.10:  $(\tau_{yx}/\sigma'_{yy})_{min vol}$  at maximum contraction (a) VLB and (b) MGS at various  $D_r$  and  $\sigma'_{yy}$

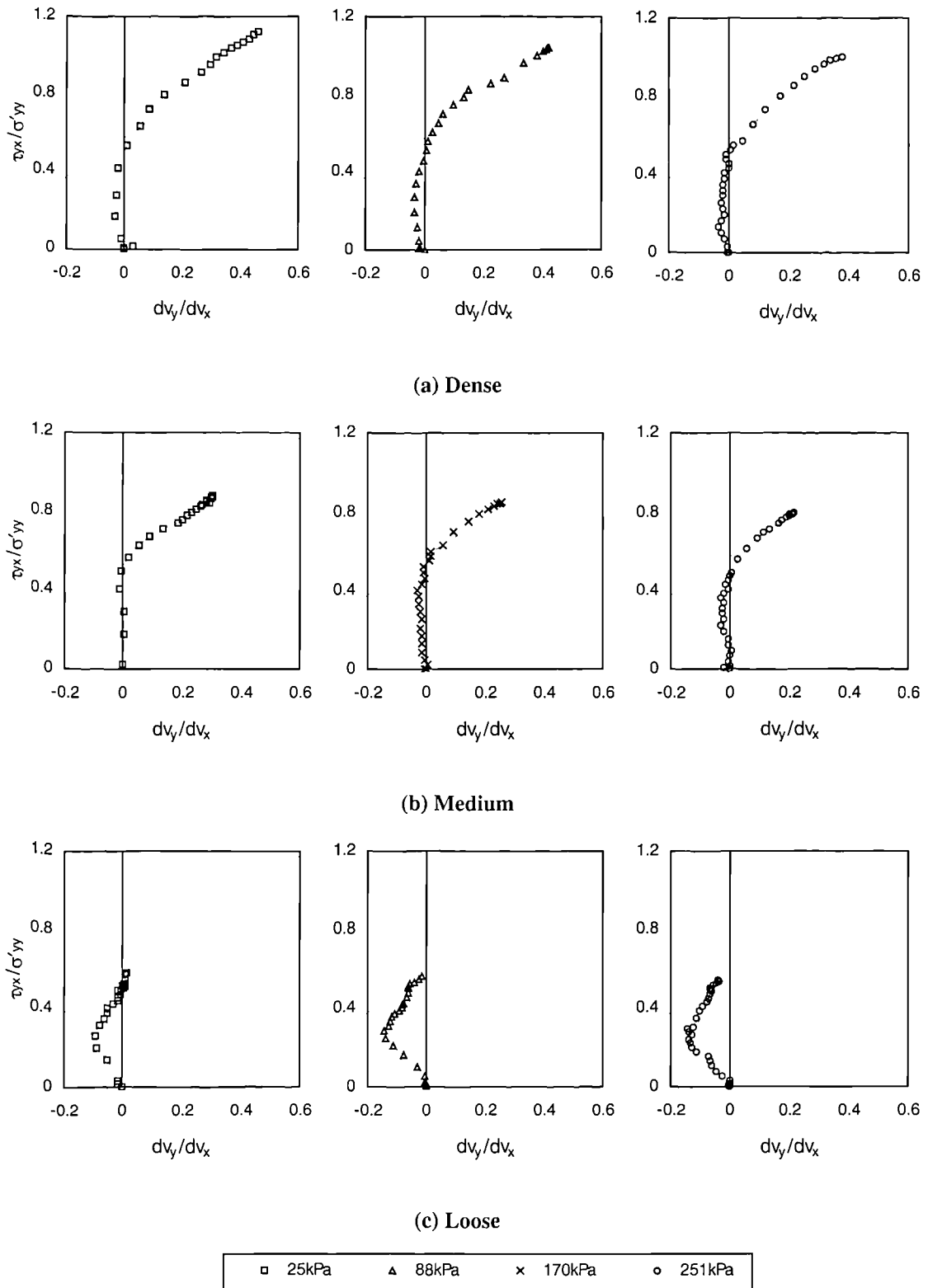
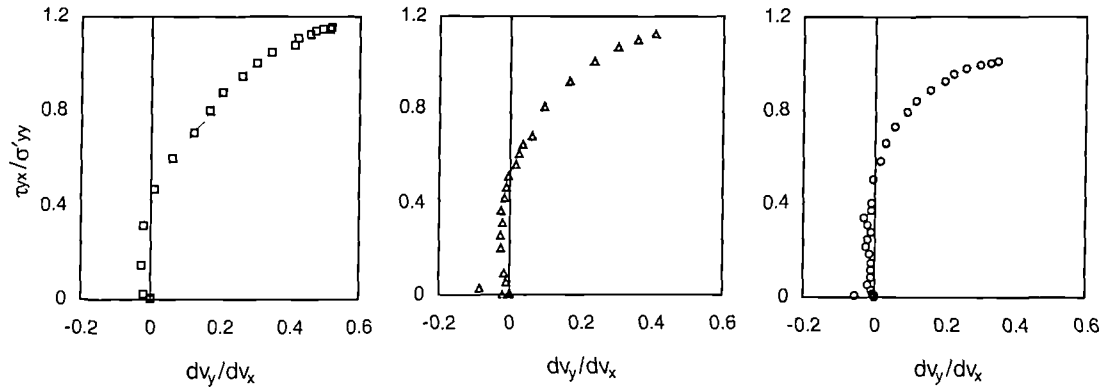
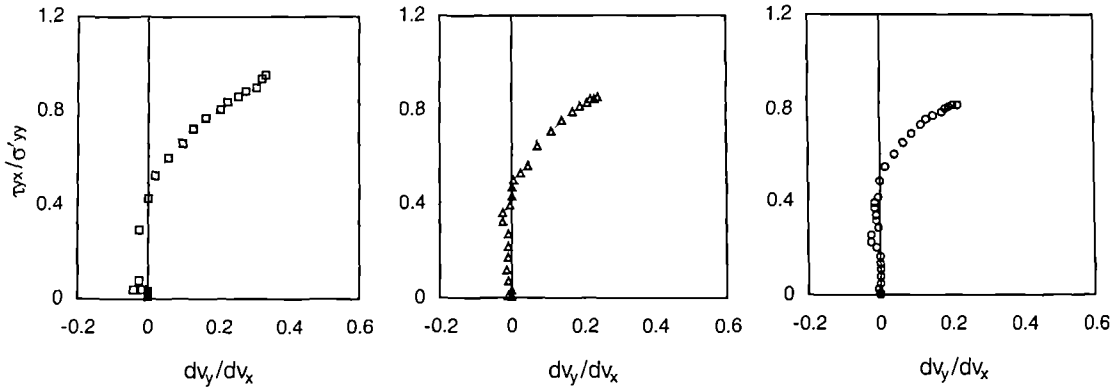


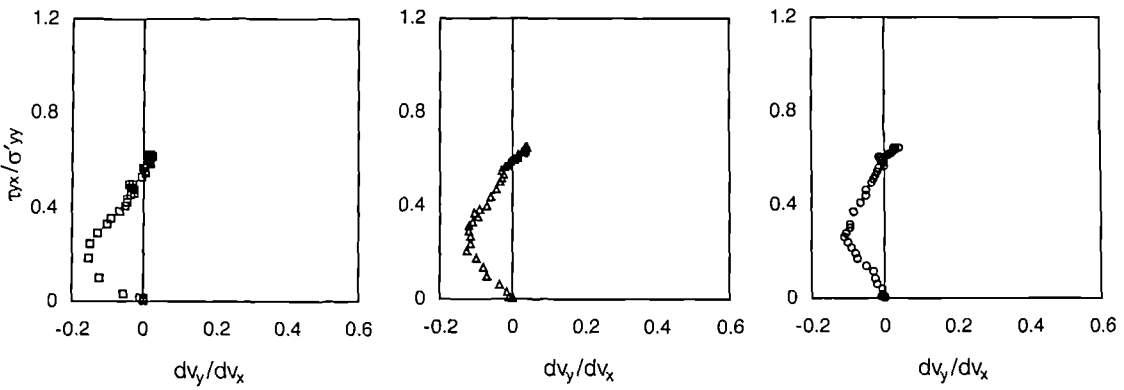
Figure 5.11: Pre-peak relationships between  $\tau_{yx}/\sigma'_{yy}$  and  $dv_y/dv_x$  for (a) dense, (b) medium and (c) loose VLB at various stress levels



(a) Dense



(b) Medium



(c) Loose

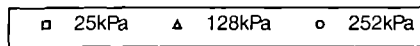


Figure 5.12: Pre-peak relationships between  $\tau_{yx}/\sigma'_{yy}$  and  $dv_y/dv_x$  for (a, b & c) dense, (d, e & f) medium and (g, h & i) loose MGS at various stress levels

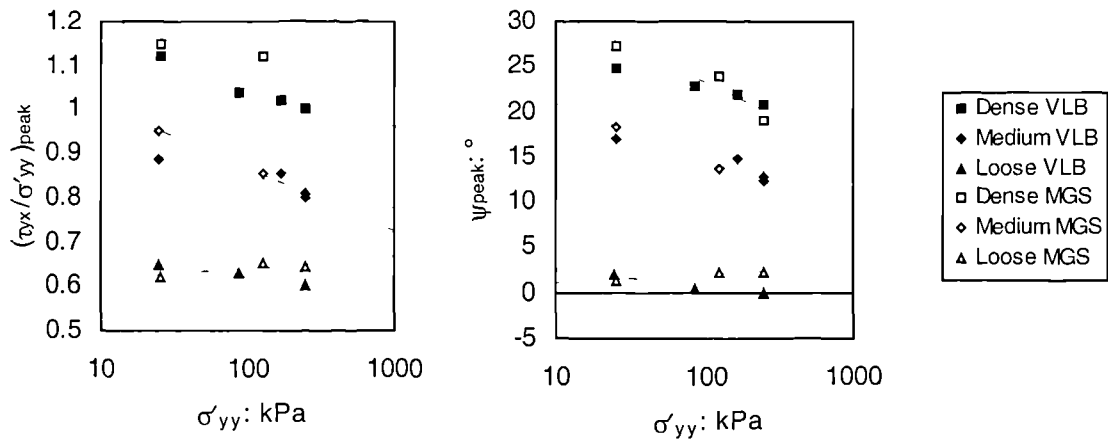


Figure 5.13: The variation of peak state data with stress level and initial sample density

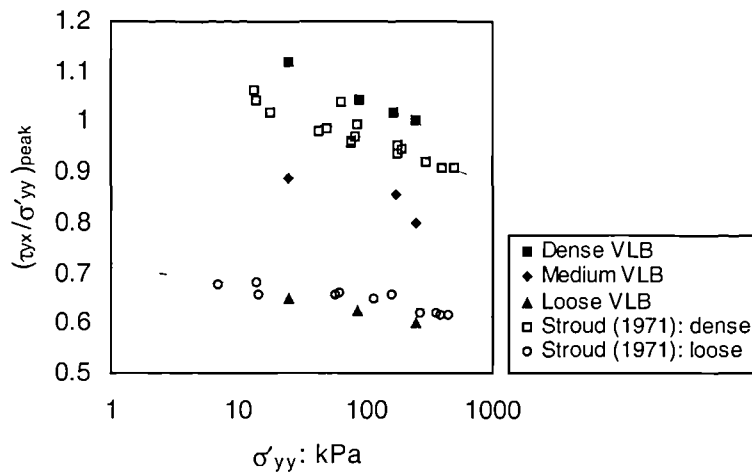


Figure 5.14: Contrasting the peak state stress ratio recorded in Stroud's (1971) SSA with WDSA data for VLB

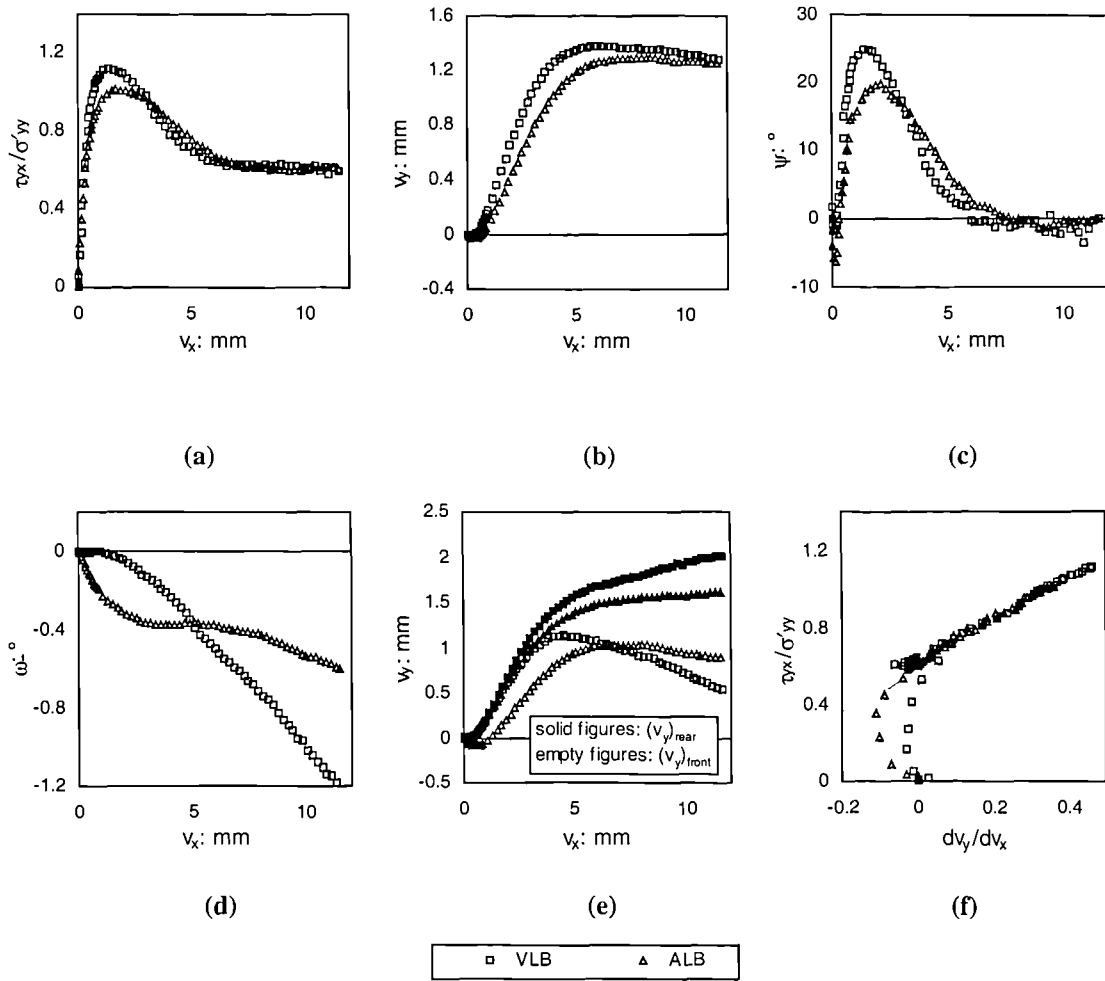


Figure 5.15: Different batches of LB tested under identical conditions in the WDSA ( $\sigma'_{yy} = 25\text{kPa}$ , 90%  $D_r$ ,  $g = 5\text{mm}$ )

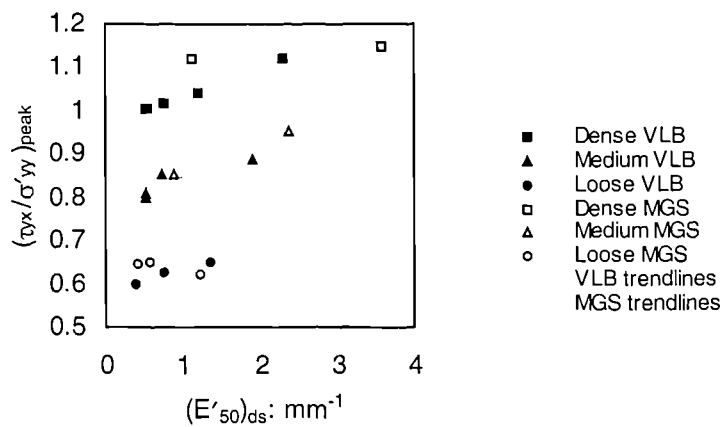


Figure 5.16: The relationship between sample strength and sample stiffness as measured in the WDSA

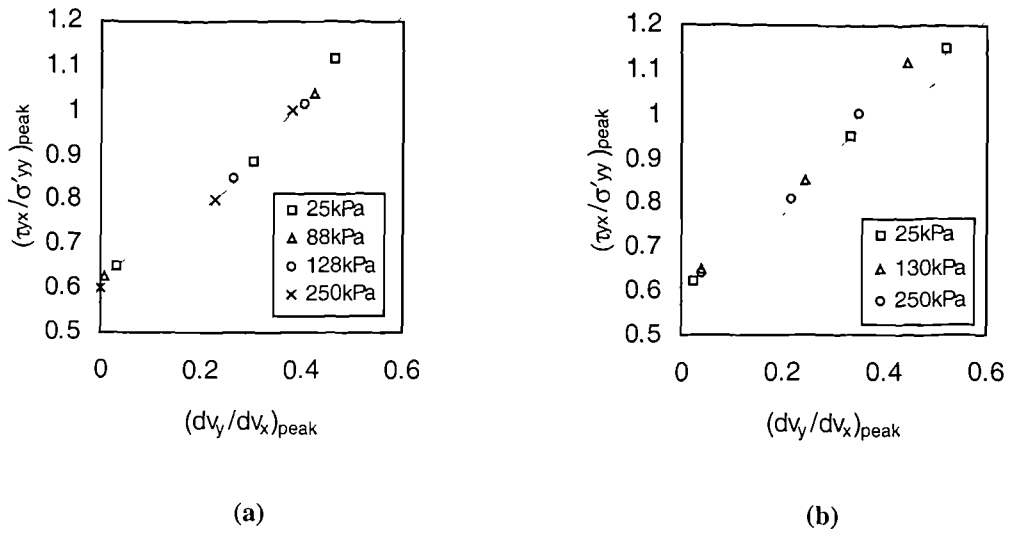


Figure 5.17: Peak stress ratio and rate of dilation values for (a) VLB and (b) MGS compared with Taylor's (1948) energy correction with  $\phi'_{crit} = 35^\circ$  and  $38^\circ$

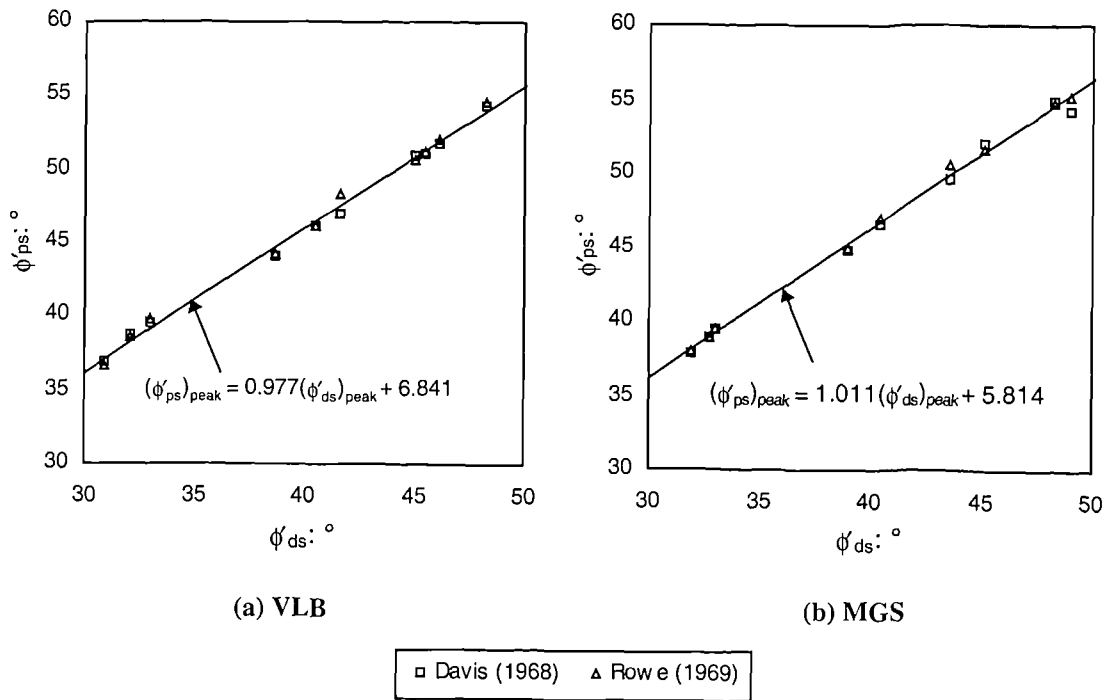


Figure 5.18: Different estimates of  $\phi'_{ps}$  for (a) VLB and (b) MGS tested under wide ranging conditions

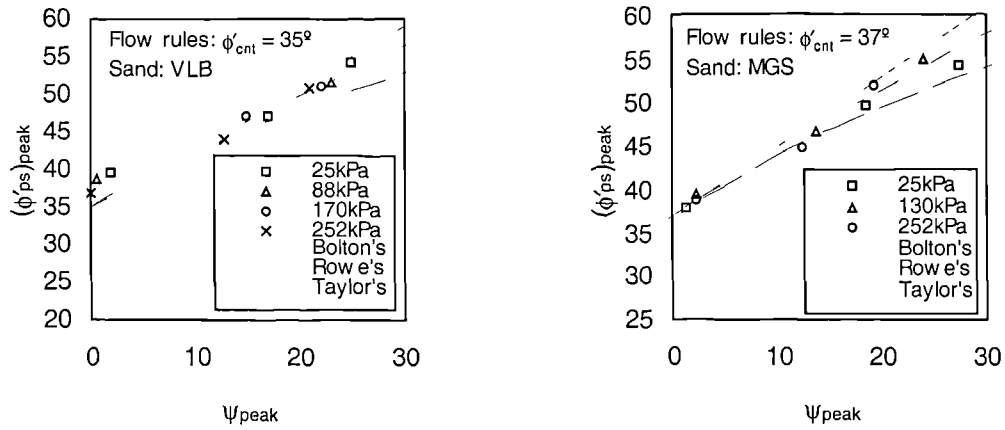


Figure 5.19: Comparison of peak, plane-strain experimental data with three flow rules

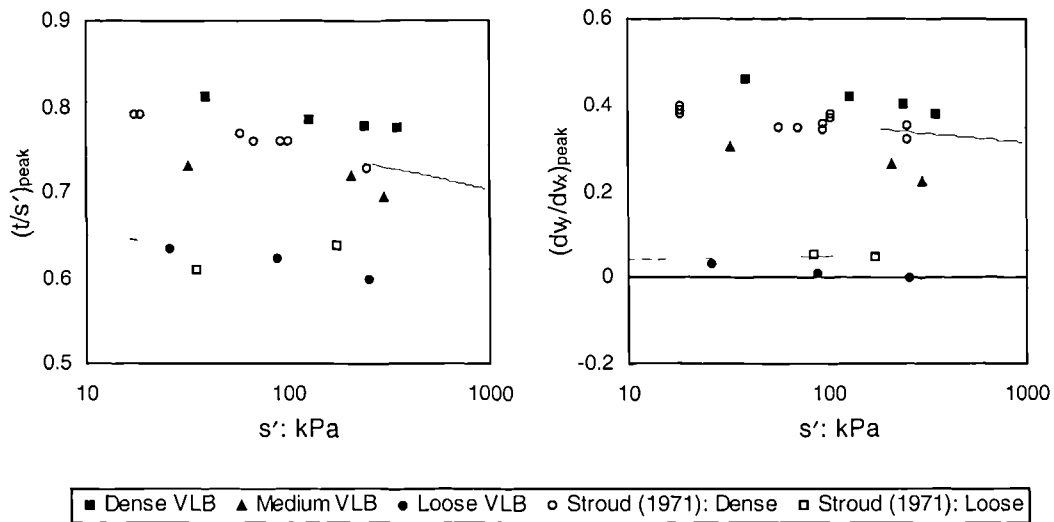


Figure 5.20: The reduction of  $(t/s')_{peak}$  and  $\Psi_{peak}$  with increasing stress level  $s'$

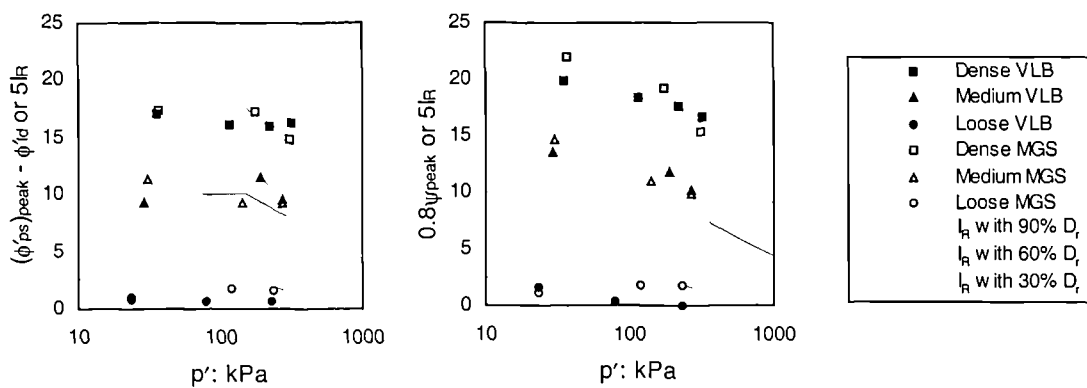


Figure 5.21: Comparison of peak state data with Bolton's (1986, 1987) relative dilatancy index

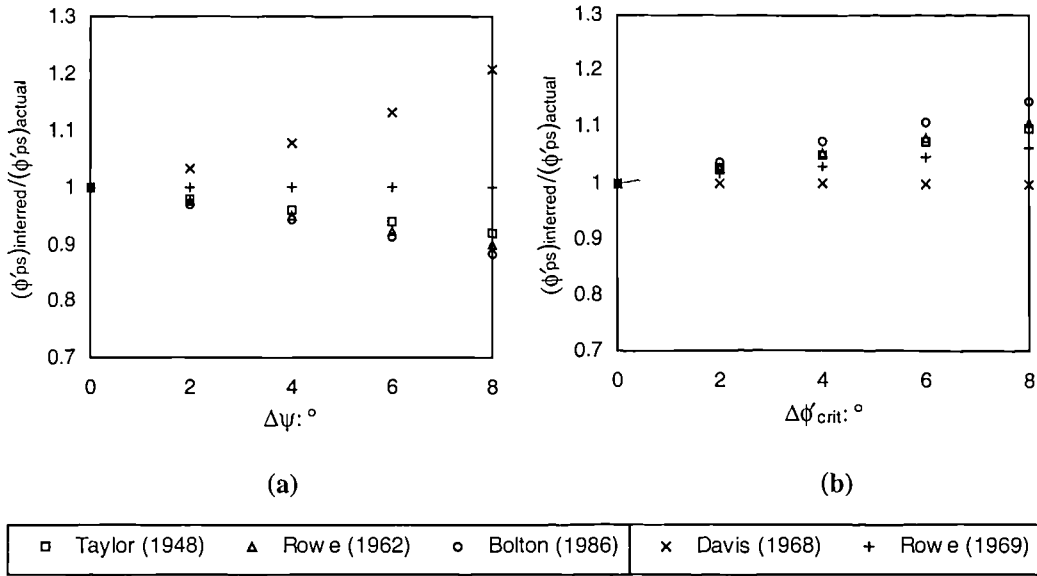


Figure 5.22: The deviations of  $\phi'_{ps}$  for a sample with  $(\phi'_{ds})_{peak} = 45^\circ$ ,  $\psi_{peak} = 25^\circ$  and  $\phi'_{crit} = 35^\circ$  derived using various relationships when (a)  $\psi_{peak}$  is underestimated by  $\Delta\psi$  and (b)  $\phi'_{crit}$  is overestimated by  $\Delta\phi'_{crit}$

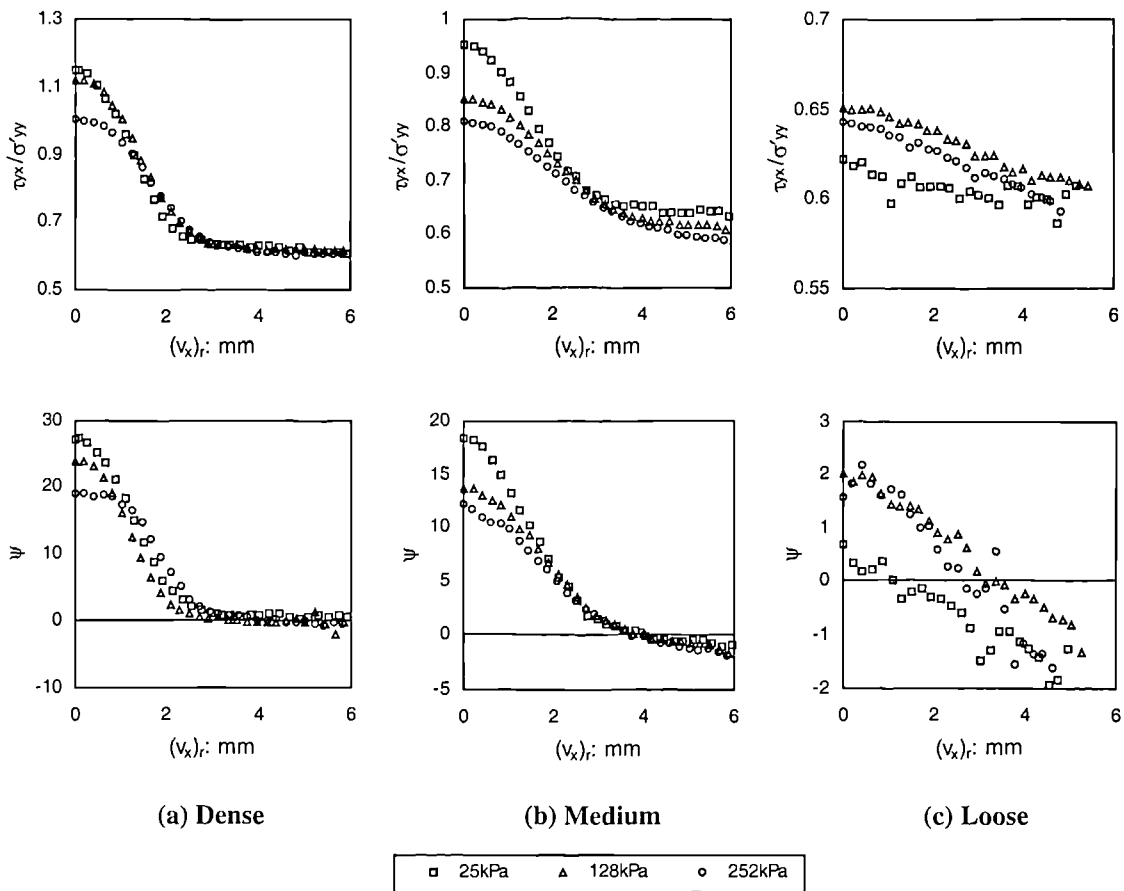


Figure 5.23: The reduction in  $\tau_{yx}/\sigma'_{yy}$  and  $\psi$  from peak for (a) dense, (b) medium and (c) loose MGS



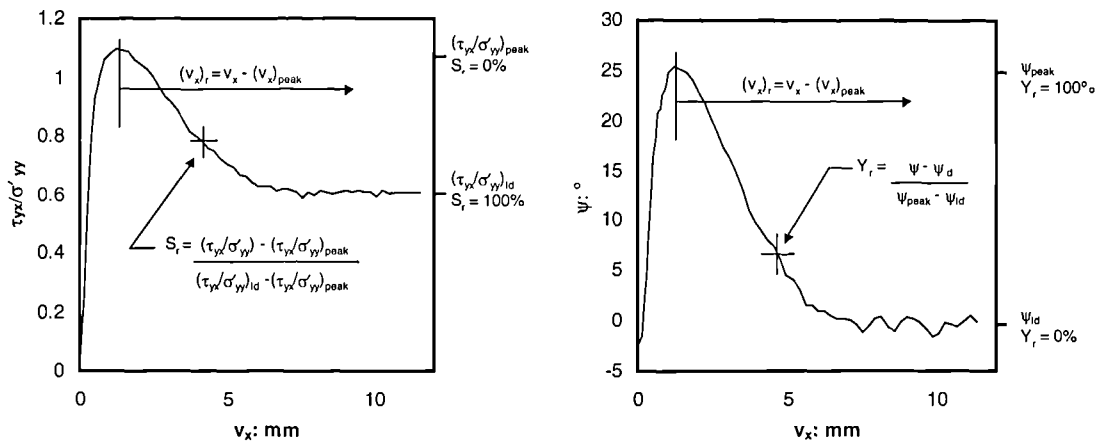


Figure 5.24: The definition of strain softening parameters  $S_r$  and  $Y_r$

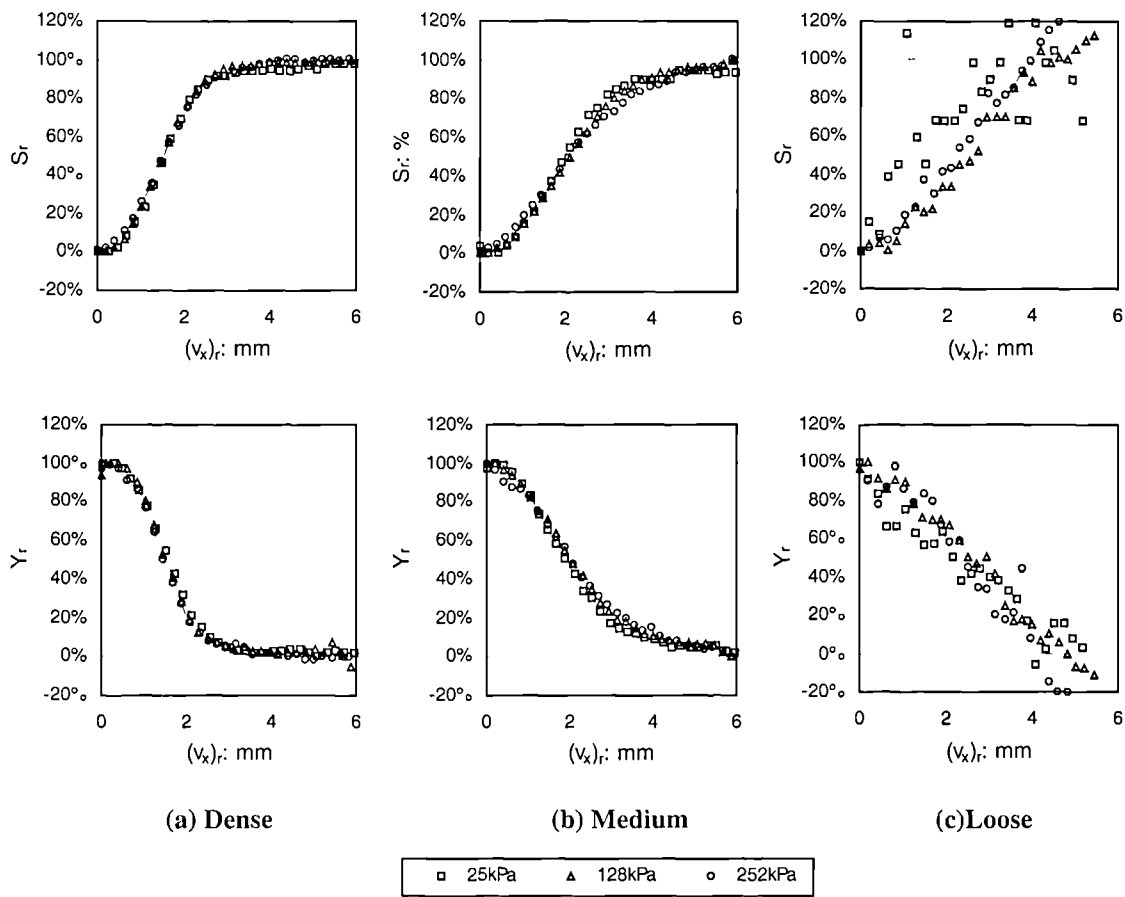
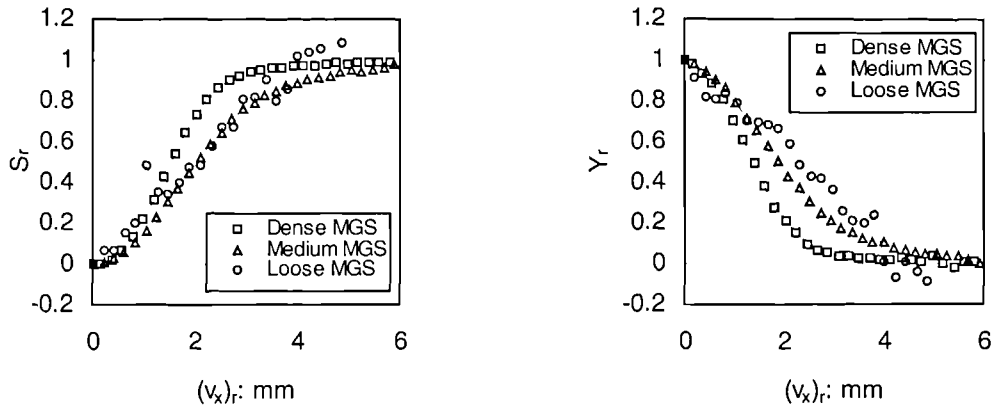
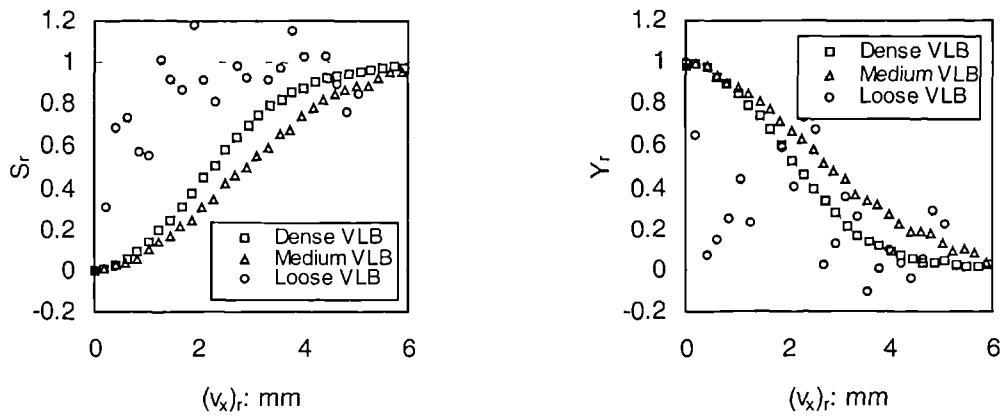


Figure 5.25: The variation of strain softening parameters  $S_r$  and  $Y_r$  with the displacement from peak shear resistance for (a) dense, (b) medium, and (c) loose MGS

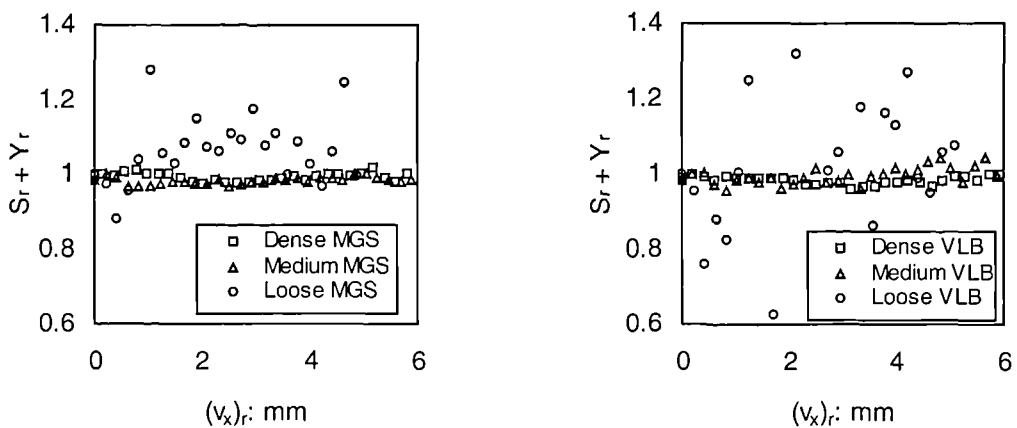


(a) MGS



(b) VLB

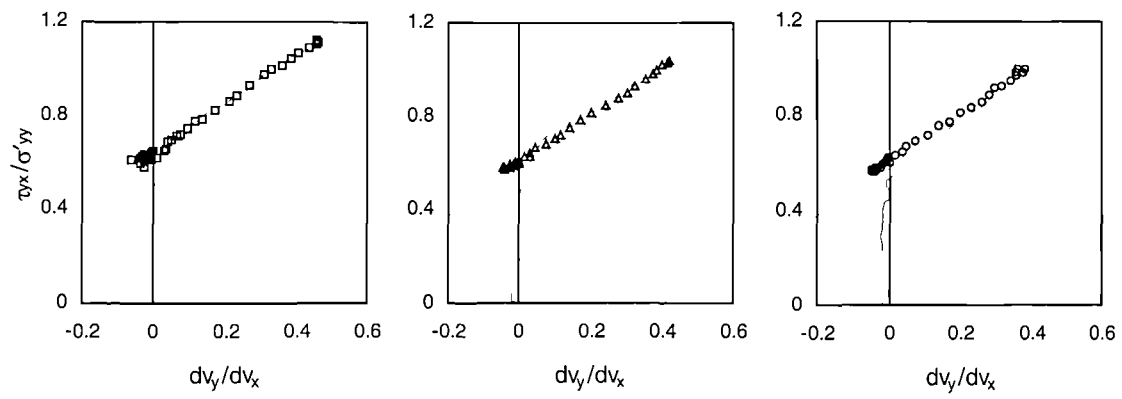
Figure 5.26: Averaged strain softening data for (a) MGS and (b) VLB



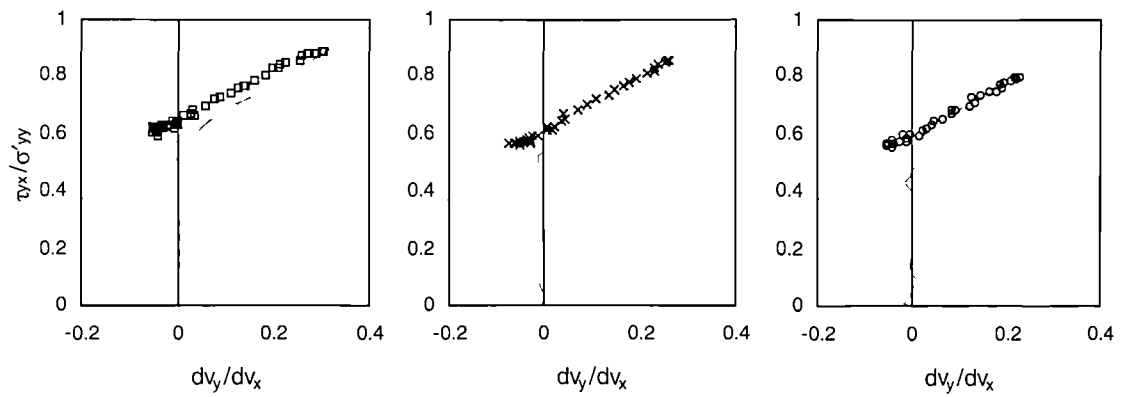
(a) MGS

(b) VLB

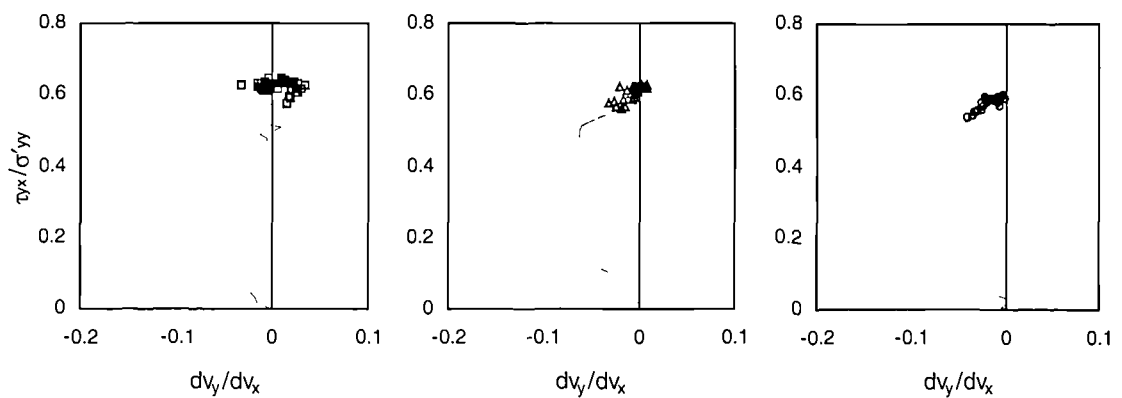
Figure 5.27: The equal transition between softening parameters  $S_r$  and  $Y_r$  for (a) MGS and (b) VLB



(a) Dense



(b) Medium



(c) Loose

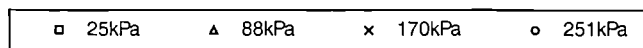
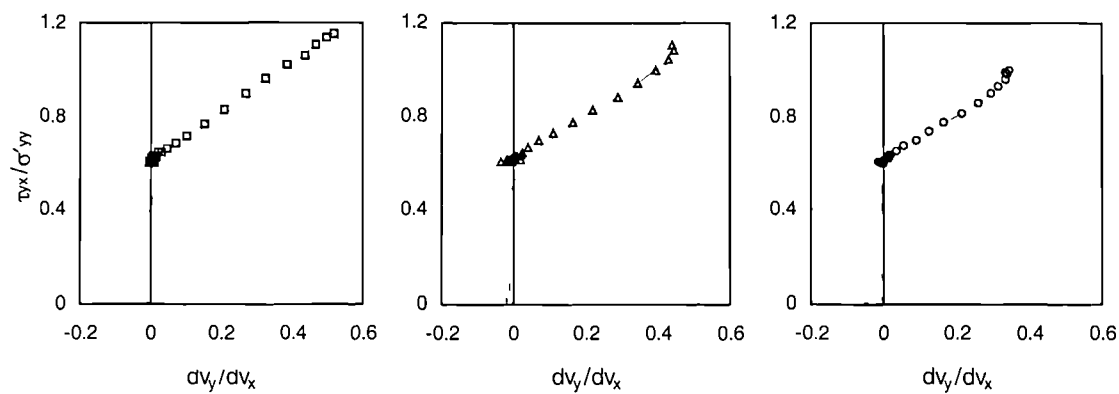
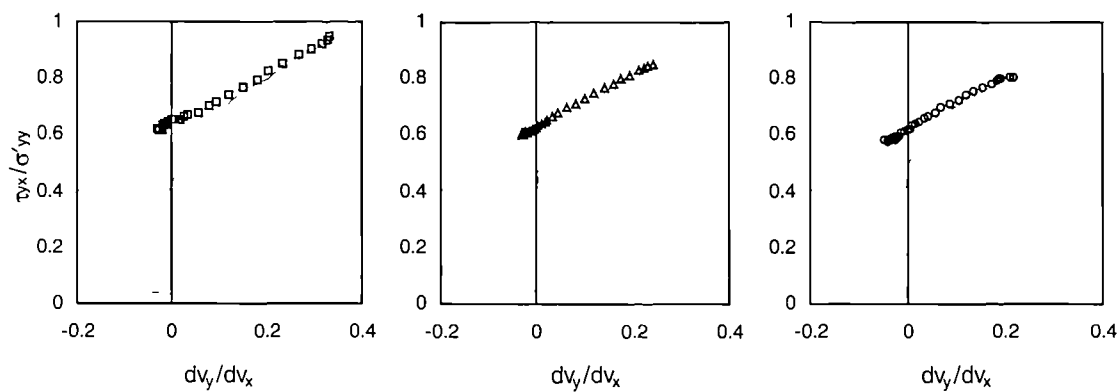


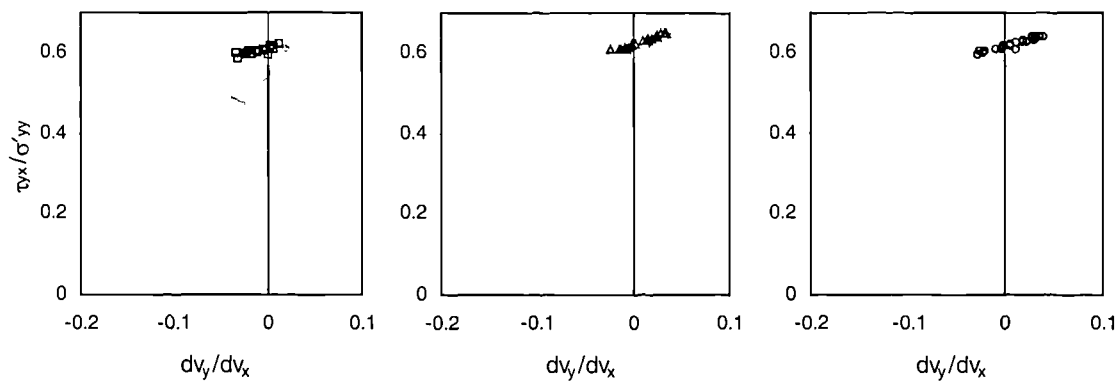
Figure 5.28: The relationship between  $\tau_{yx}/\sigma'_{yy}$  and  $dv_y/dv_x$  during the strain softening of VLB samples



(a) Dense



(b) Medium



(c) Loose

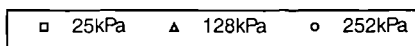


Figure 5.29: The relationship between  $\tau_{yx}/\sigma'_{yy}$  and  $dv_y/dv_x$  during the strain softening of MGS samples

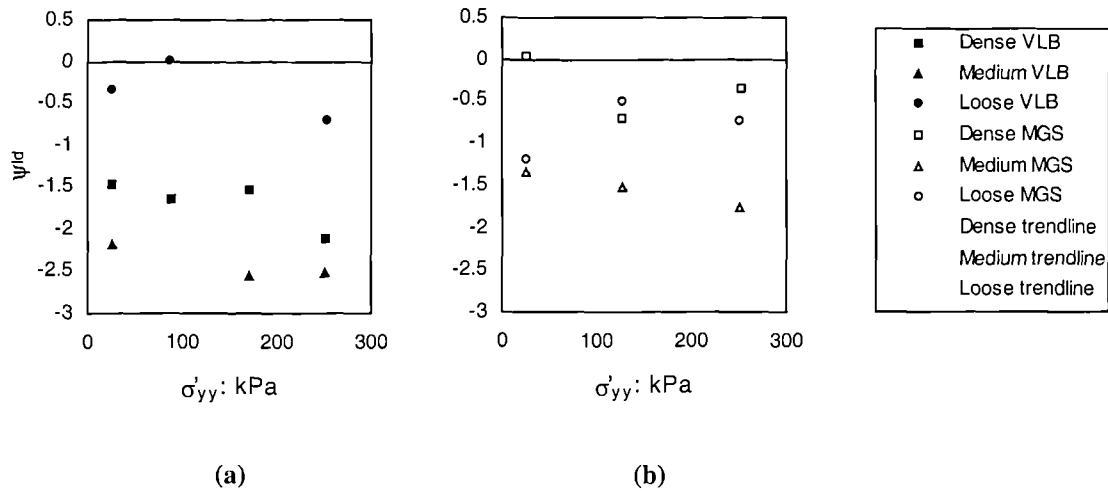


Figure 5.30: Negative values of  $\psi_{id}$  for (a) VLB and (b) MGS

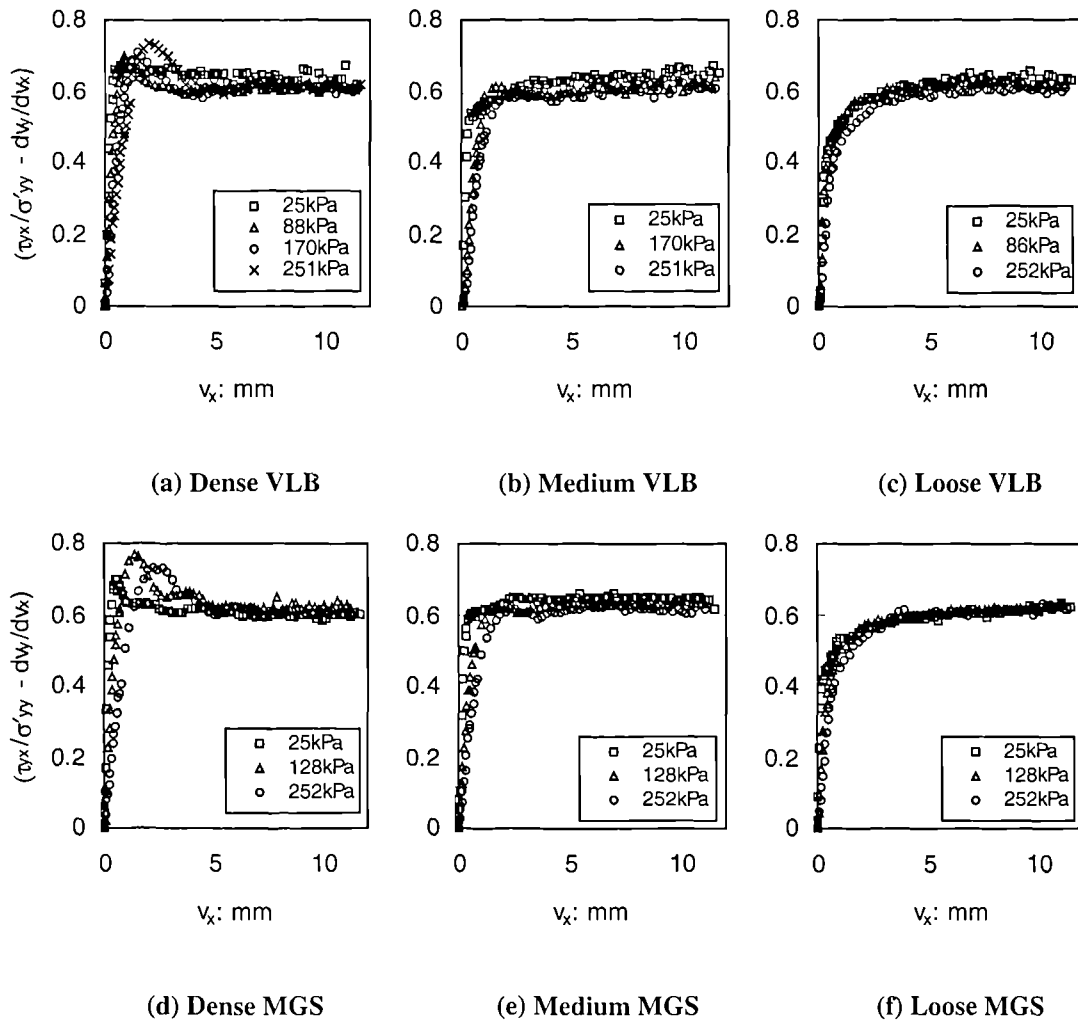


Figure 5.31: Taylor's (1948) energy correction applied to WDSA data

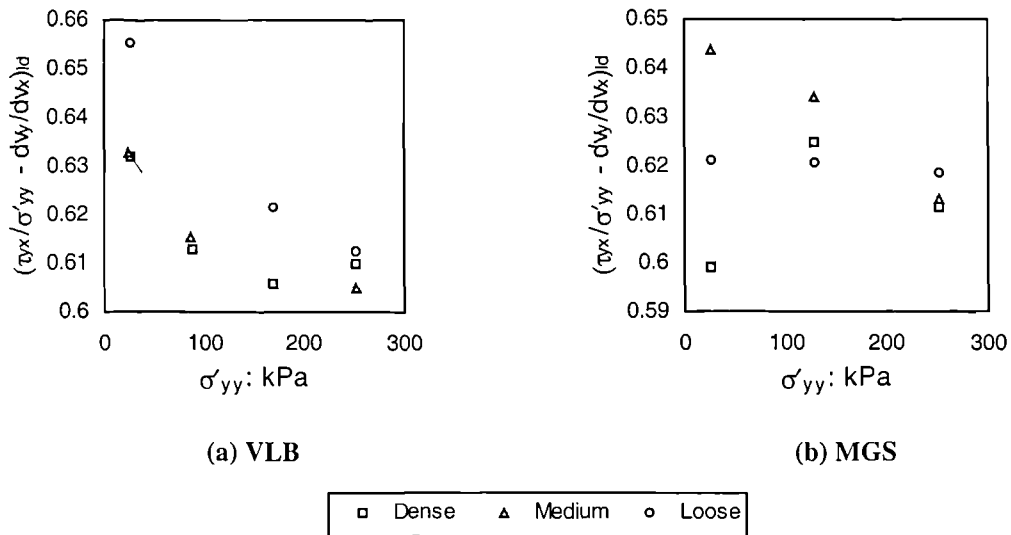


Figure 5.32: The value of  $\sin \phi'_{crit}$  ( $= \tan \phi'_{ds} - \tan \psi$ ) obtained using Taylor's (1948) flow rule for different sands deposited at different densities and at different stress levels

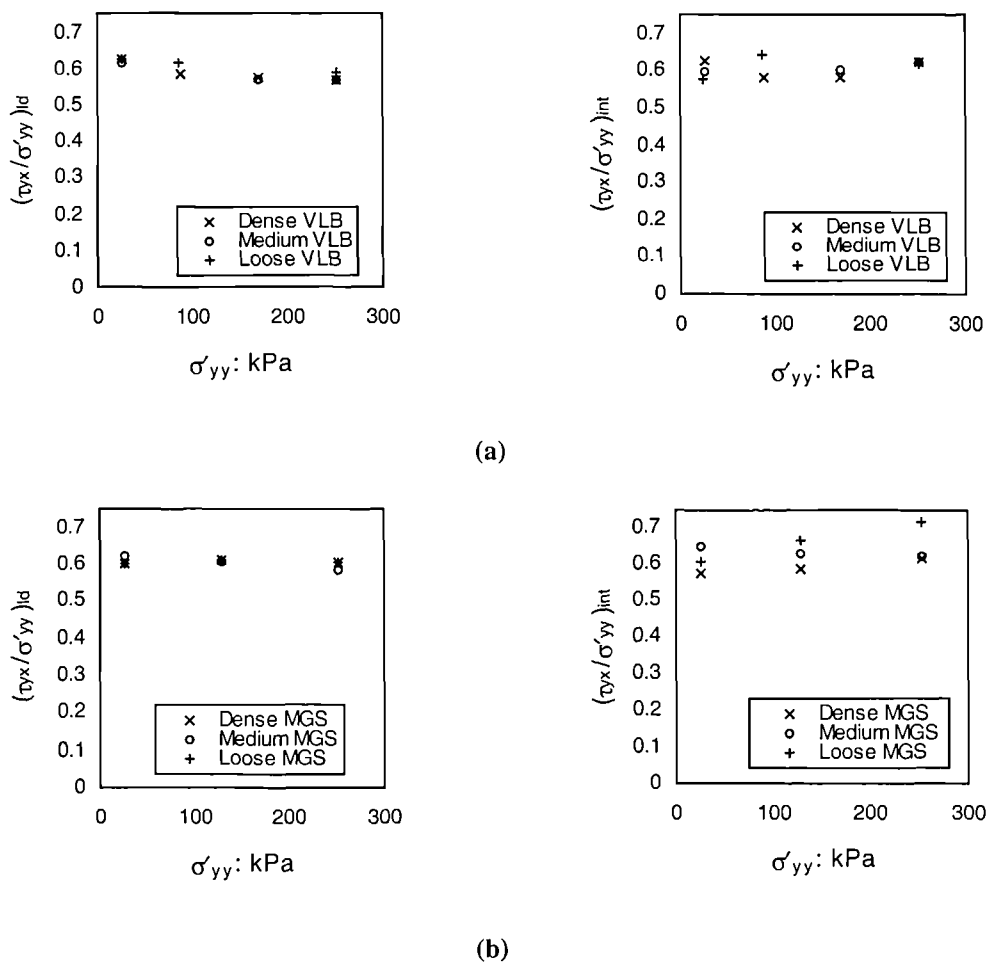


Figure 5.33: Comparison between  $(\tau_{yx}/\sigma'_{yy})_{ld}$  and  $(\tau_{yx}/\sigma'_{yy})_{int}$  to illustrate the small gradients of the large displacement stress data

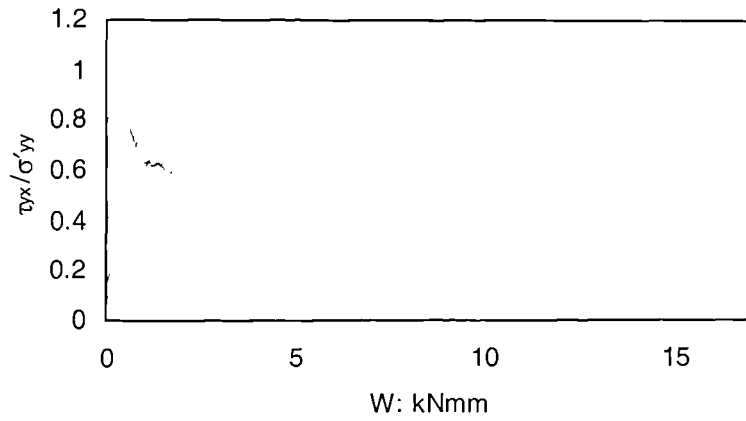


Figure 5.34: The relationship between  $\tau_{yx}/\sigma'_{yy}$  and  $W$  for all VLB tests

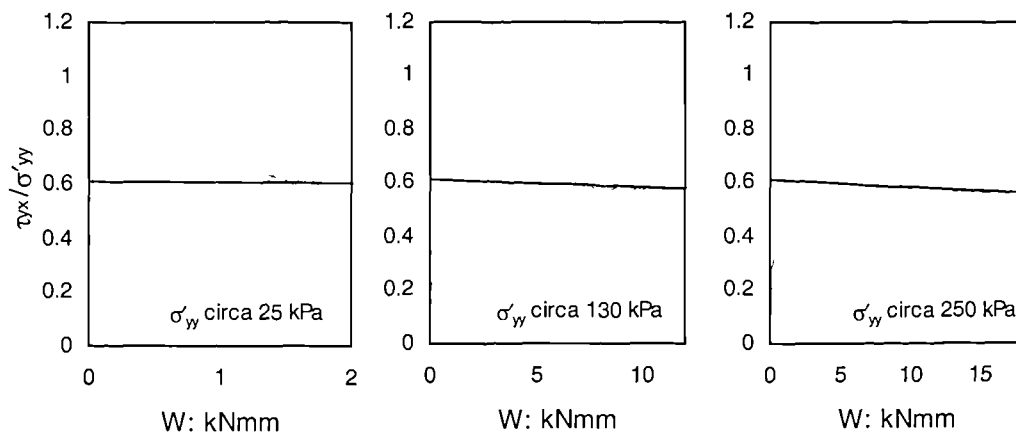


Figure 5.35: The relationship between  $\tau_{yx}/\sigma'_{yy}$  and  $W$  for VLB tests at different stress levels

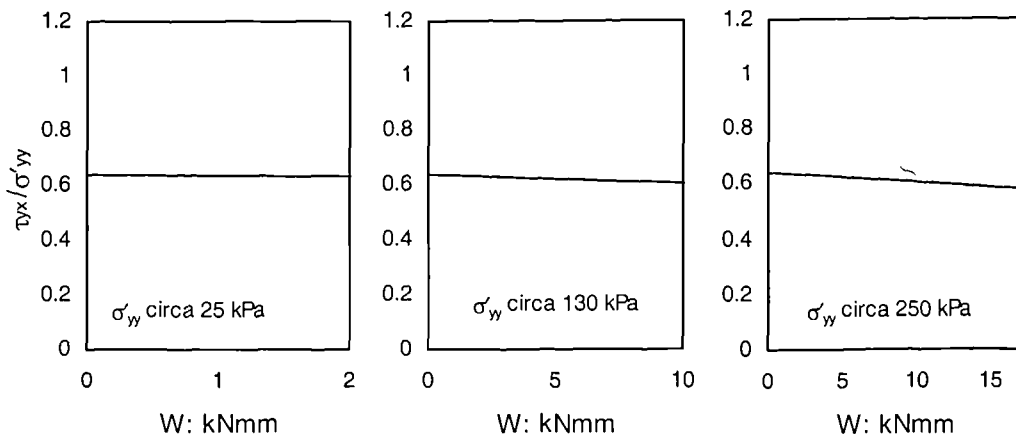


Figure 5.36: The relationship between  $\tau_{yx}/\sigma'_{yy}$  and  $W$  for MGS tests at different stress levels

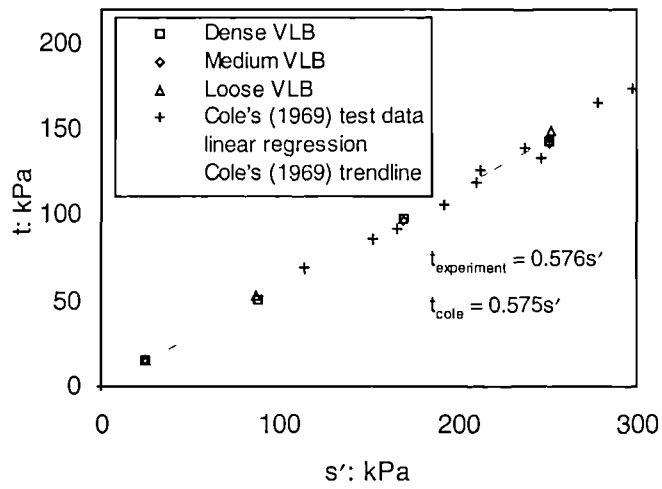


Figure 5.37: Large displacement shear resistance compared to that reported for Leighton Buzzard 14-25 by Cole (1967)

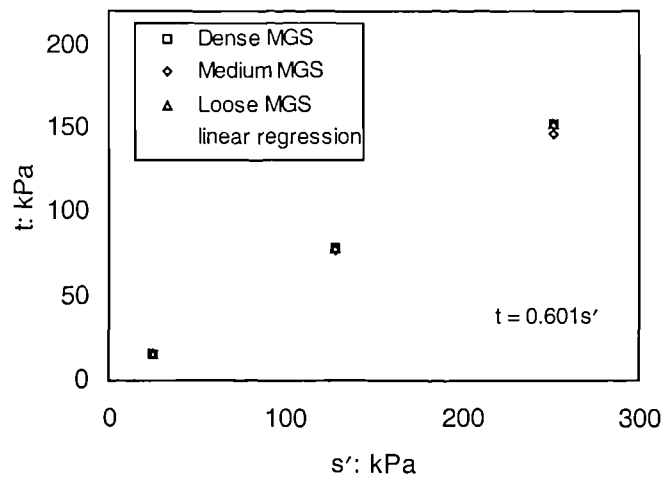


Figure 5.38: Large displacement shear resistance of MGS at various initial densities and stress levels



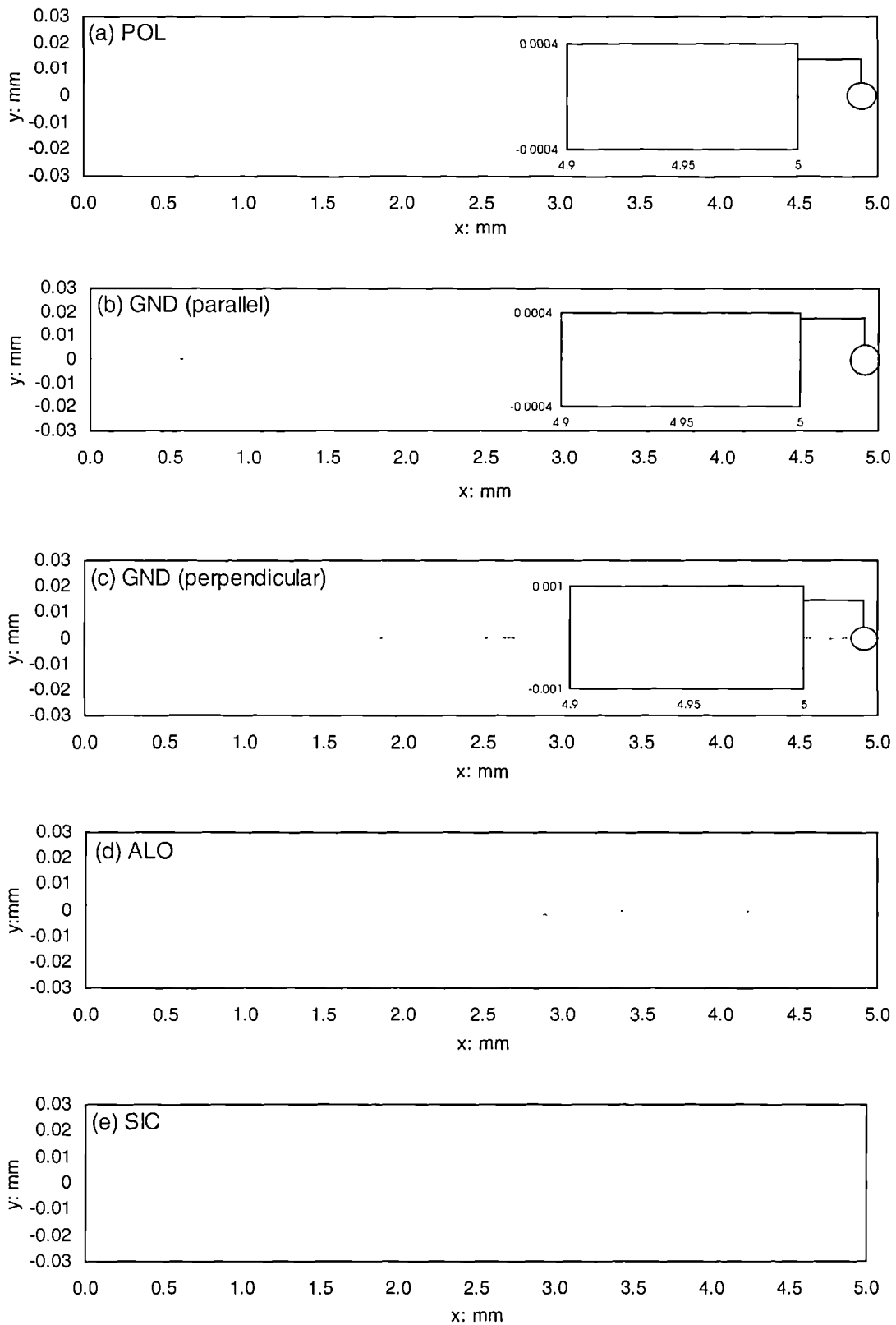


Figure 6.1: Profiles of the steel surfaces used during interface testing

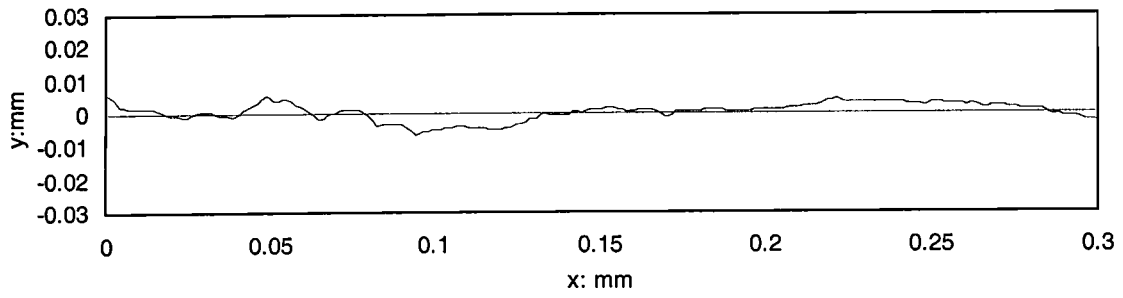


Figure 6.2: ALO surface profile with equivalent vertical and horizontal scales

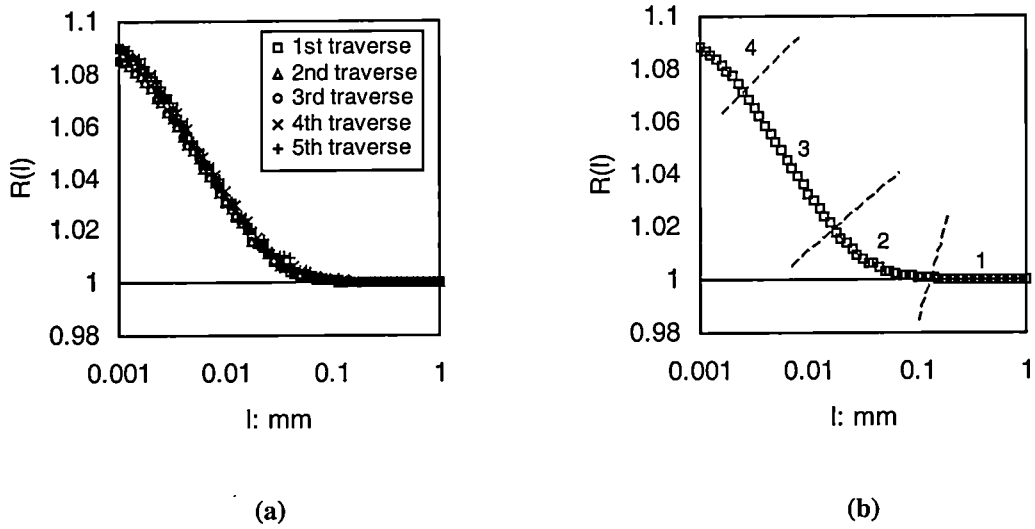


Figure 6.3: Fractal analysis of the ALO surface

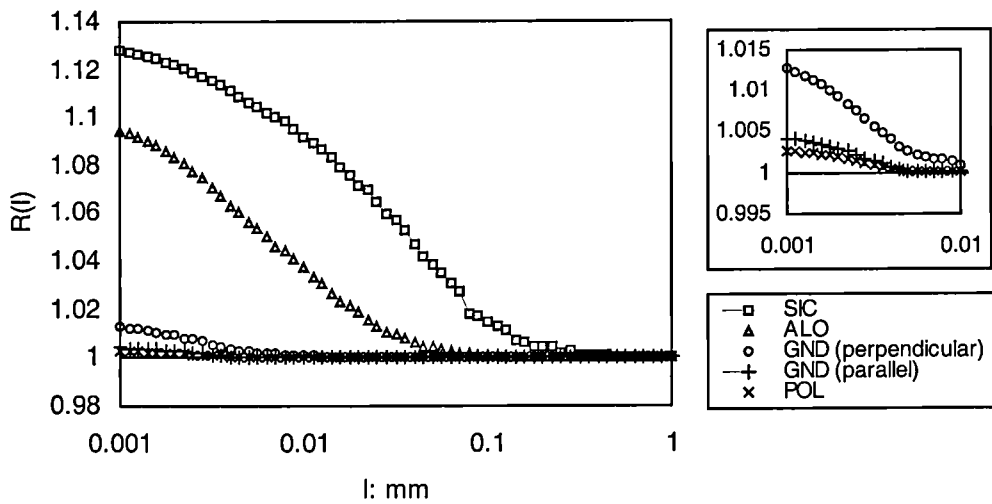


Figure 6.4: Comparison of average fractal plots of the metal surfaces

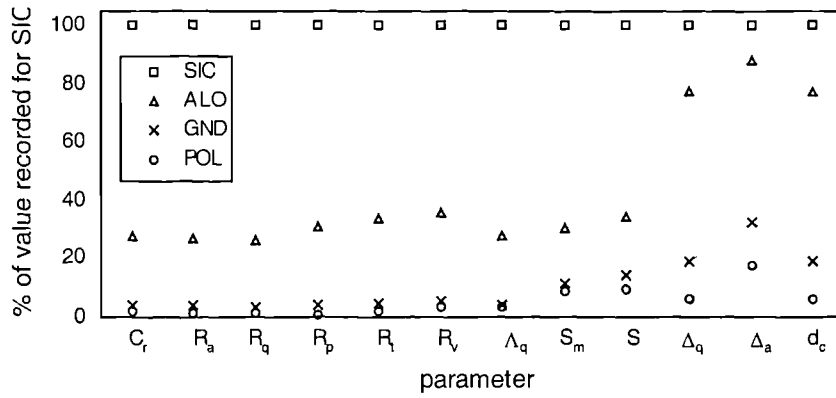


Figure 6.5: Comparison of the magnitudes of various roughness parameters in relation to that recorded for the roughest metal surface

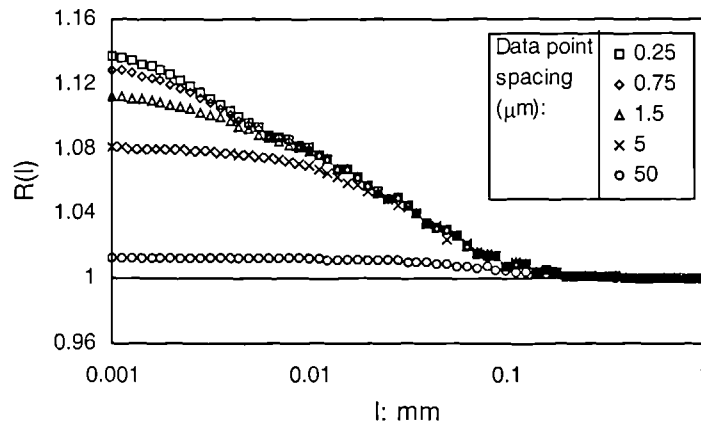


Figure 6.6: The effect of decreasing the data point spacing on the structured walk plot

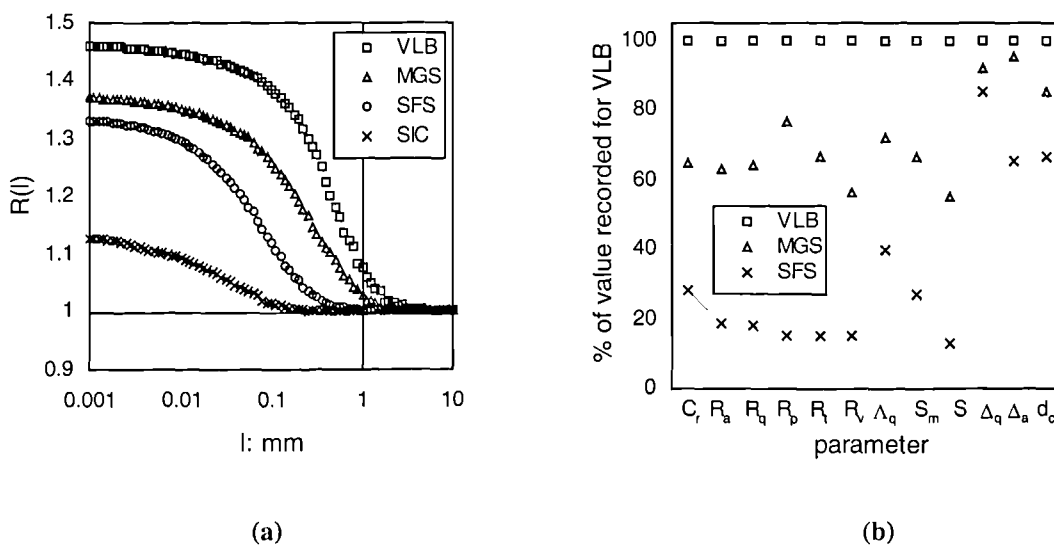


Figure 6.7: Comparison of (a) the fractal plots and (b) roughness parameters of granular surfaces

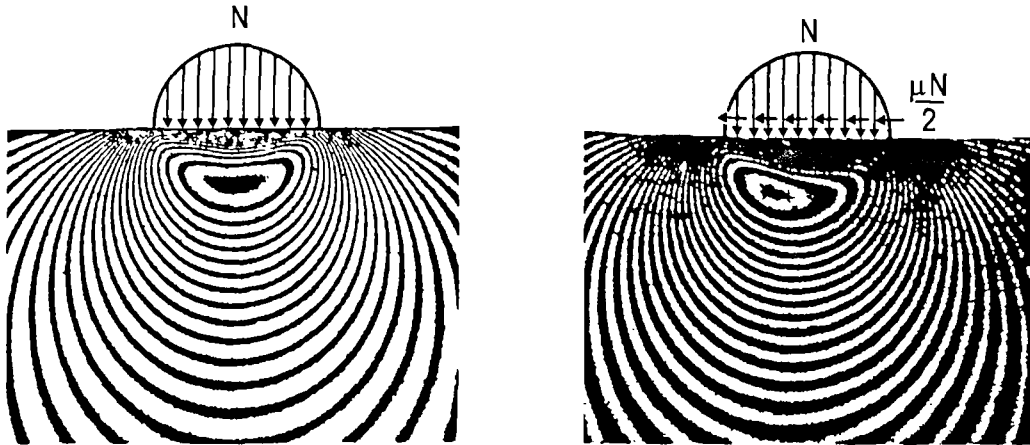


Figure 6.8: Isocromatics beneath the contact between a cylinder and a plane due to (a) normal load and (b) normal and tangential load (after Arnell et al, 1991)

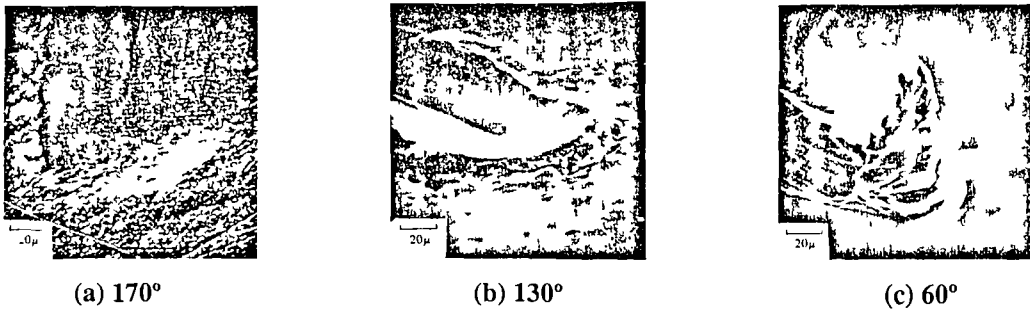


Figure 6.9: Pictures of wear scars left by conical asperities of different internal apex angle (Childs, 1988)

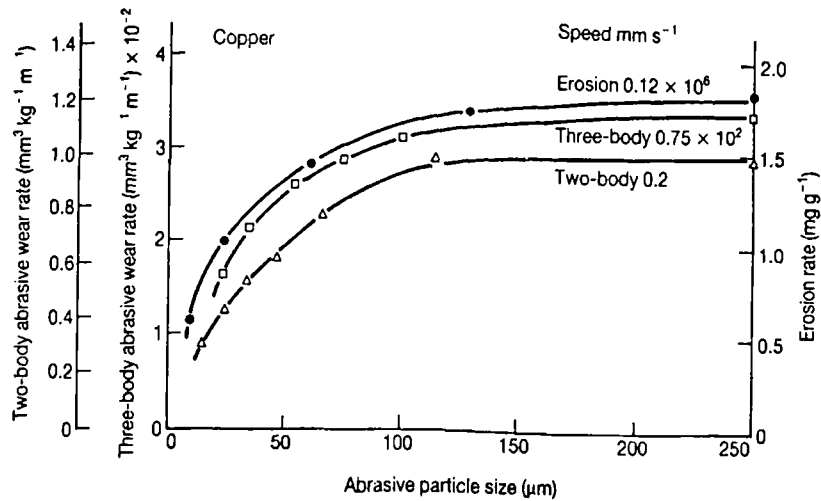


Figure 6.10: The effect of abrasive particle size during the two-body, three-body and erosion wear of copper (Misra & Finnie, 1981)

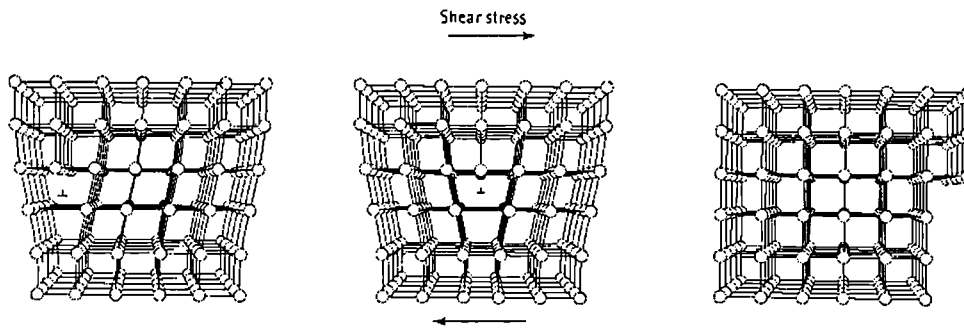


Figure 6.11: Applying a shear stress to a crystal lattice containing a dislocation (modified from Askeland, 1996)

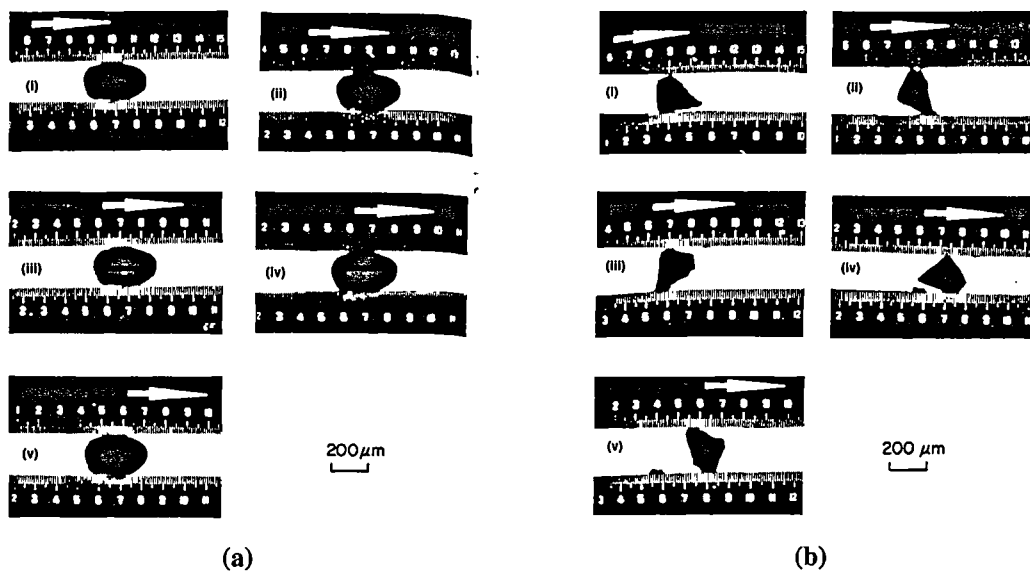


Figure 6.12: Silhouettes of (a) a sliding particle and (b) a rolling particle (Fang et al, 1993)

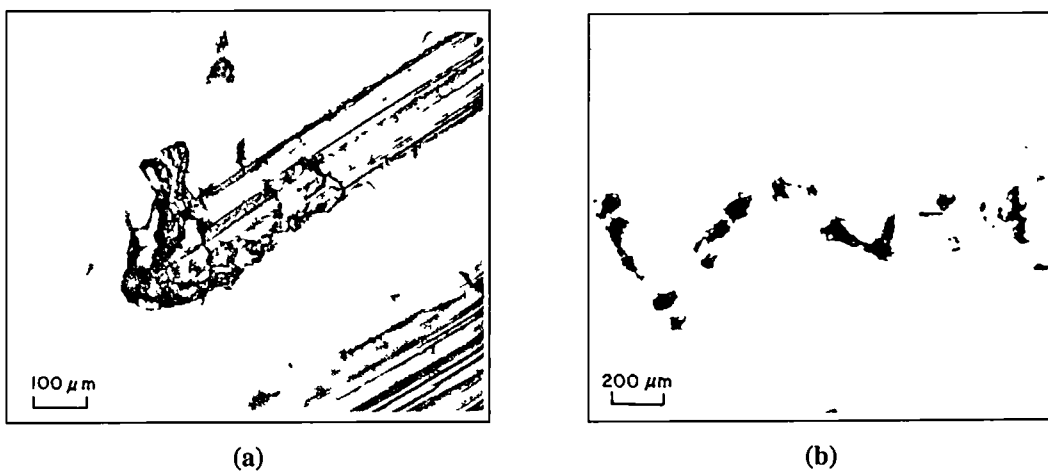


Figure 6.13: Tracks left by (a) a sliding particle and (b) a rolling particle (Fang et al, 1993)

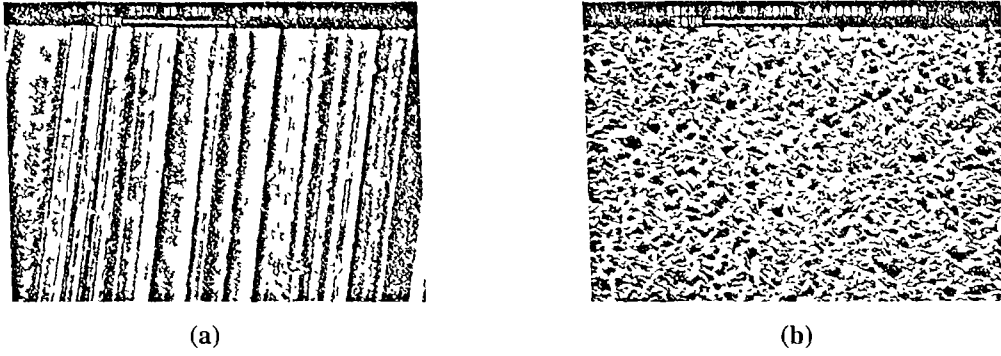


Figure 6.14: Micrographs of a phosphor-bronze surface after abrasive wear featuring primarily (a) sliding and (b) tumbling particles (Williams & Hyncica, 1992)

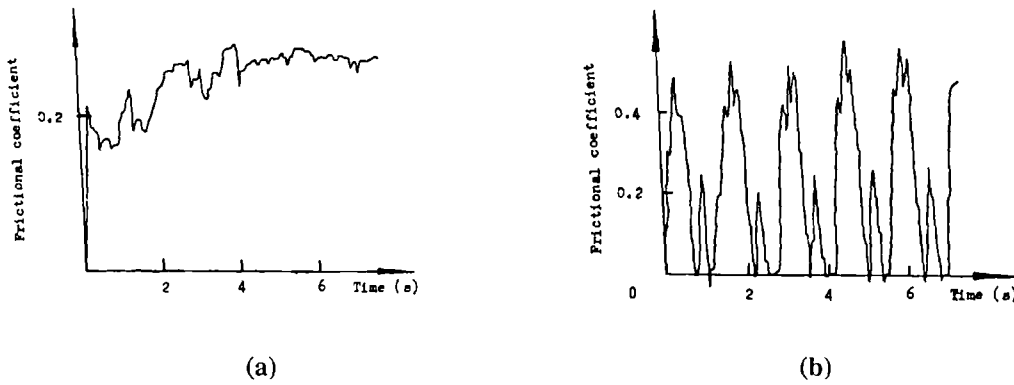


Figure 6.15: Friction coefficients of (a) a sliding particle and (b) a rolling particle (from Fang et al, 1993)

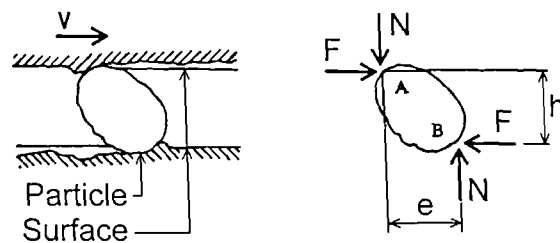


Figure 6.16: The force equilibrium of Fang et al's (1993) abrasive particle

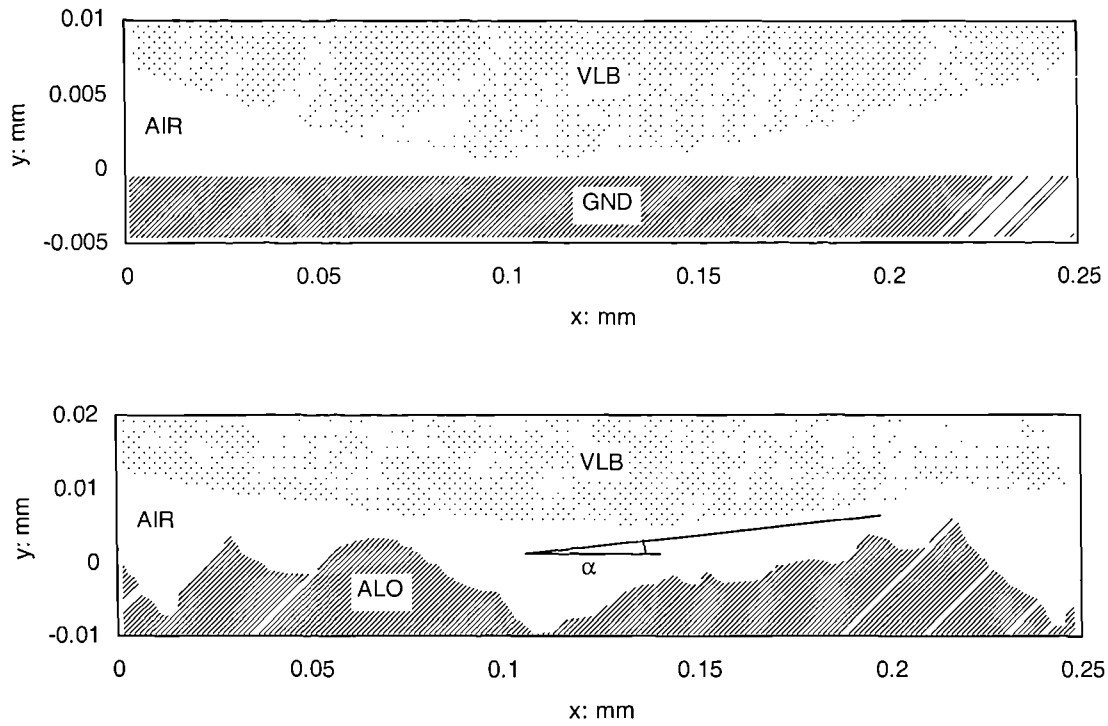


Figure 6.17: Contact between a single VLB particle and two surfaces of different roughness

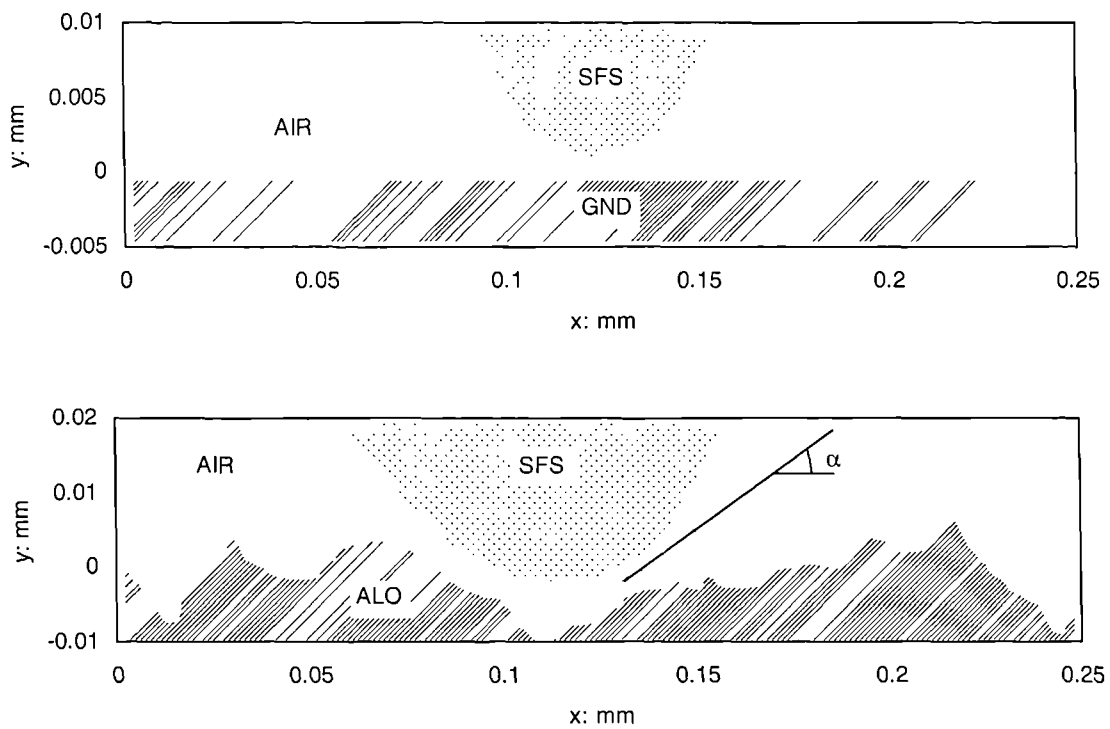
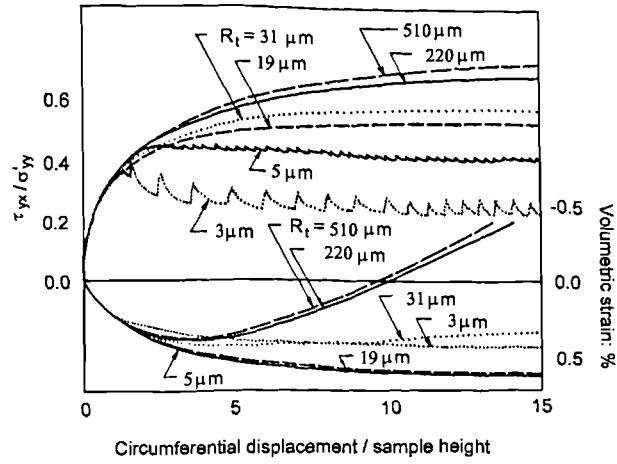
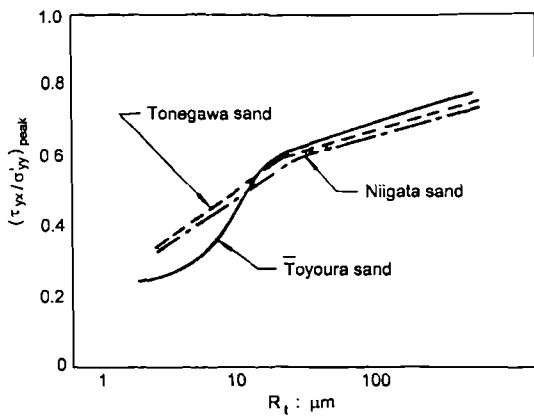


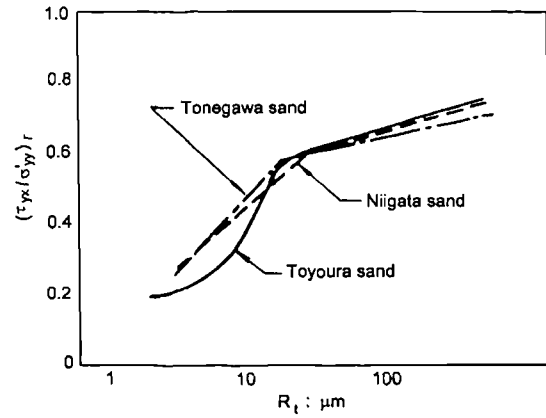
Figure 6.18: Contact between a single SFS particle and two surfaces of different roughness



(a) Behaviour of Tonogawa sand on surfaces of different roughness



(b)  $(\tau_{yx}/\sigma'_{yy})_{peak}$  of various sands



(c)  $(\tau_{yx}/\sigma'_{yy})_{cv}$  of various sand

Figure 6.19: Yoshimi & Kishida's (1981b) ring shear interface data for Tonogawa ( $D_{50} = 0.27$ ), Niigata ( $D_{50} = 0.27$ ), and Toyoura ( $D_{50} = 0.27$ ) sand confined under 105kPa

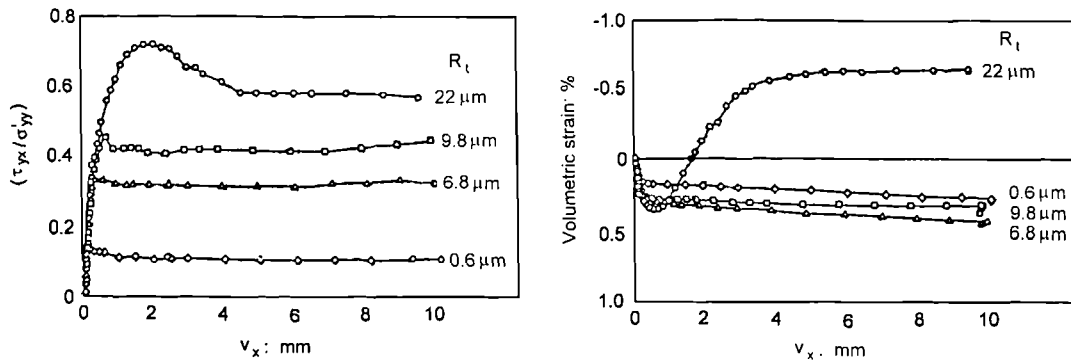


Figure 6.20: Uesugi & Kishida's (1986a) simple shear data featuring Toyoura sand under 78.4kPa on surfaces of different roughness



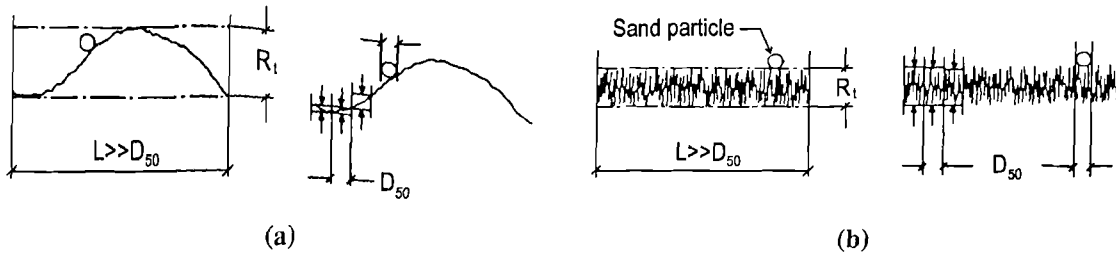


Figure 6.21: Functional filtering of surface texture on surface (a) with and (b) without large wavelength irregularities (after Kishida & Uesugi, 1987)

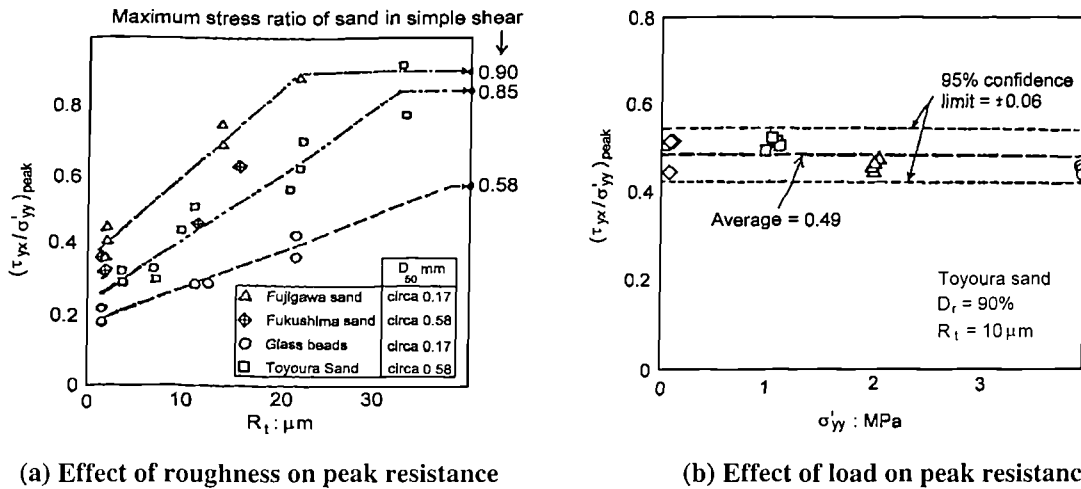


Figure 6.22: Effect of (a) surface roughness and (b) confining stress on peak interfacial resistance after Uesugi & Kishida (1986a)

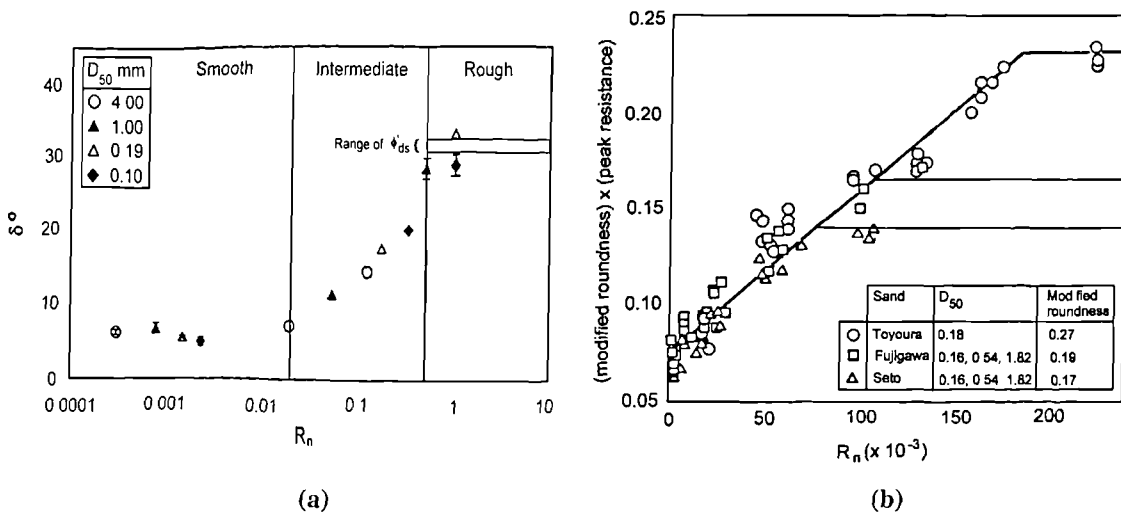


Figure 6.23: (a) The classification of interfaces using Uesugi & Kishida's (1986b) normalised roughness (after Paikowsky, 1995) (b) Correlation of peak resistance considering particle shape (after Uesugi & Kishida, 1986b)

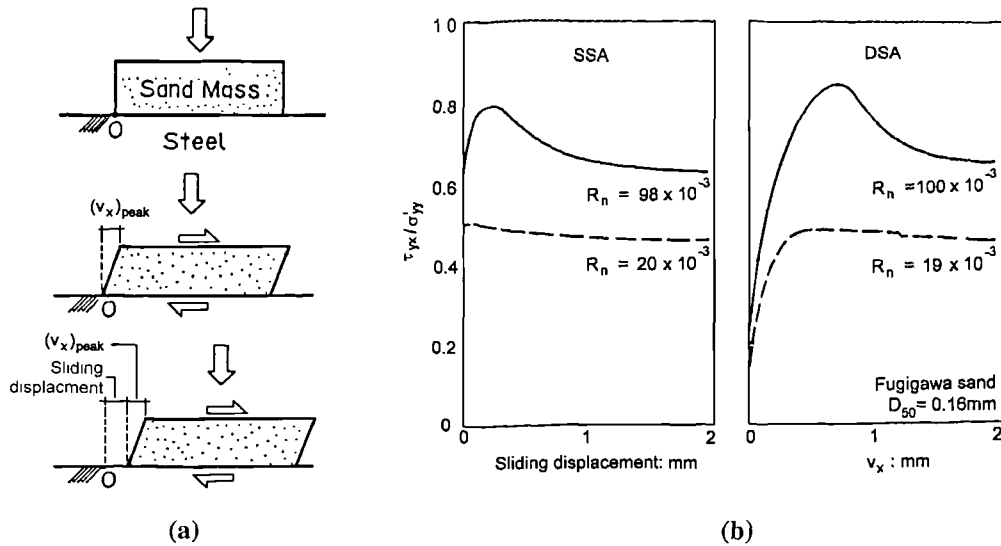


Figure 6.24: (a) Schematic diagram of the transition of deformation during SSA interface tests (modified from Uesugi & Kishida, 1986a) and (b) contrast between SSA and DSA interface data (from Kishida & Uesugi, 1987)

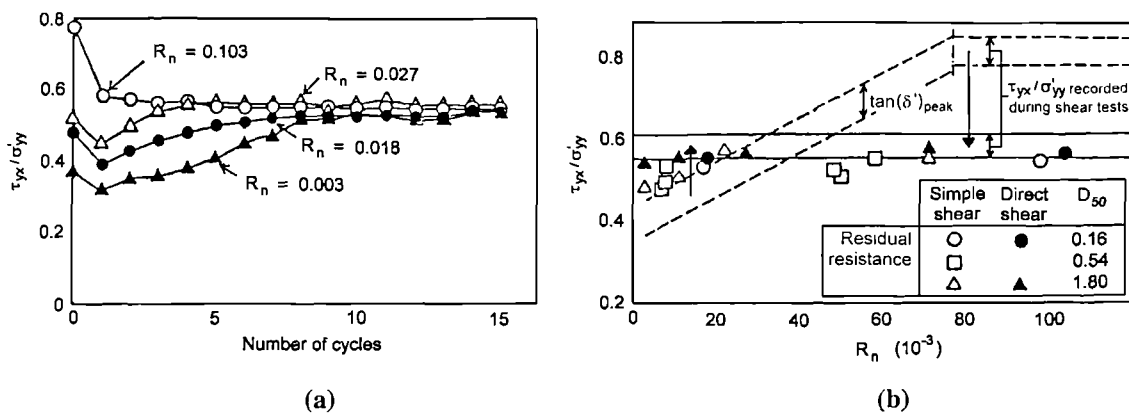


Figure 6.25: Uesugi et al's (1989) (a) influence of cycle number on interface resistance and (b) resistance after repeated loading for dense Seto sand under 98kPa

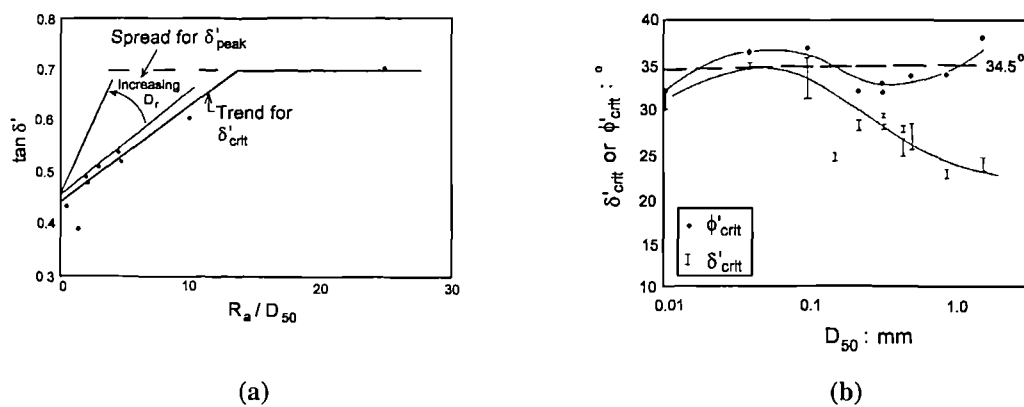


Figure 6.26: Jardine et al's (1993) (a) summary of  $\delta'$  values on interfaces featuring various sands confined under 100kPa on surfaces with  $R_t \approx 10\mu\text{m}$  and (b) effect of particle size on  $\delta'_{crit}$

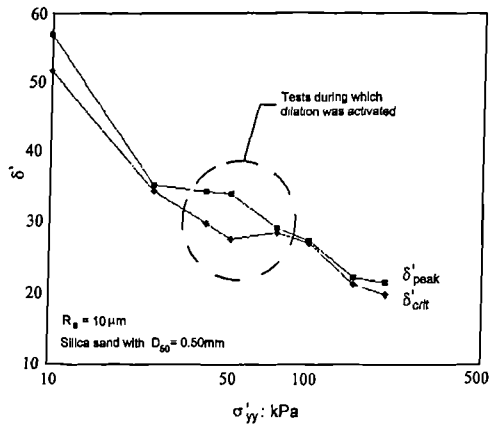


Figure 6.27: Everton's (1991) normal stress effect on peak and critical interface resistance

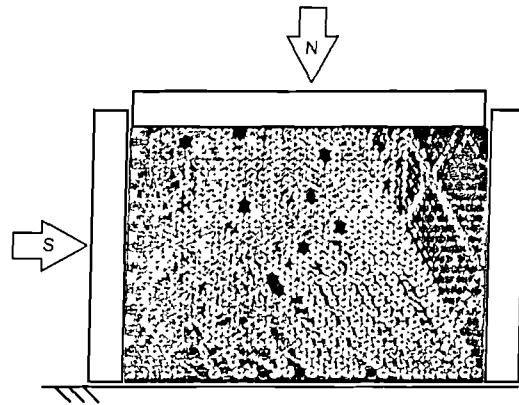


Figure 6.28: The pre-peak stress distribution within a collection of photo-elastic disks subjected to direct shear against a rough surface (Paikowsky et al, 1996)

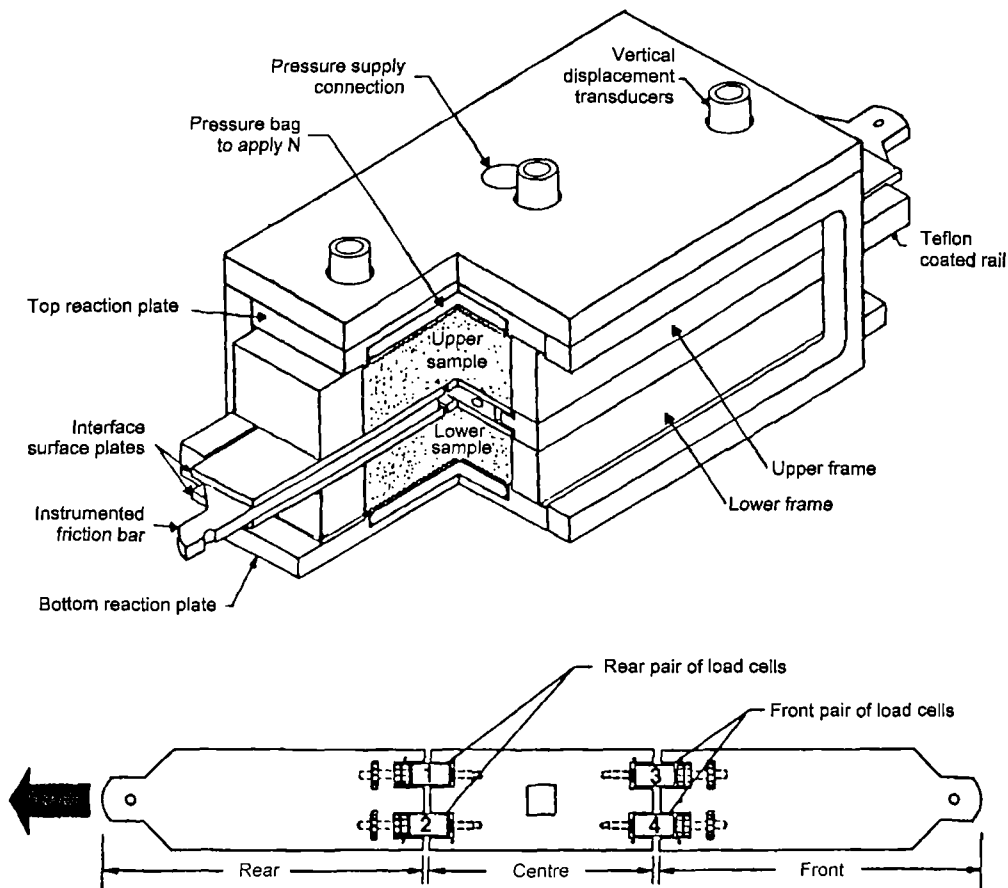


Figure 6.29: Paikowsky et al's (1995) apparatus: isometric view and detail of the instrumented friction bar

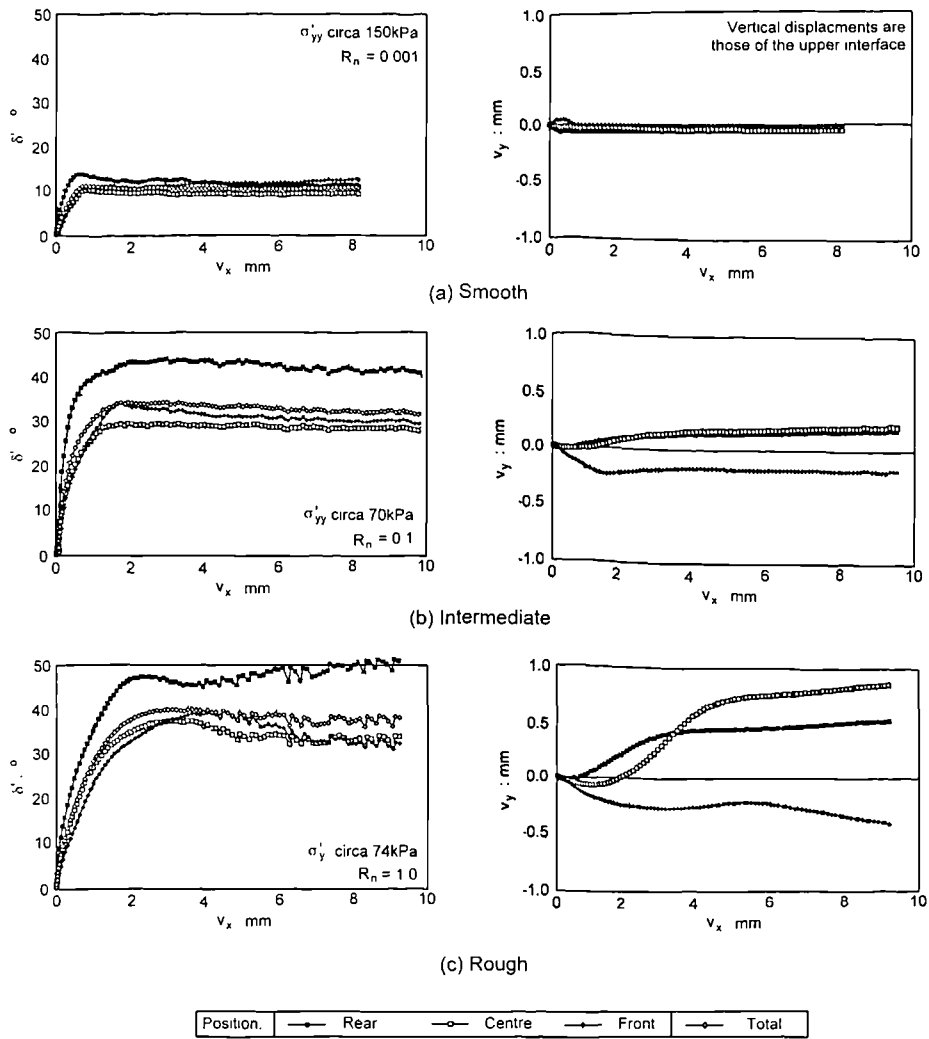


Figure 6.30: Distribution of friction angles and vertical displacements along interfaces featuring dense Ottawa sand and various surfaces (after Paikowsky, 1995)

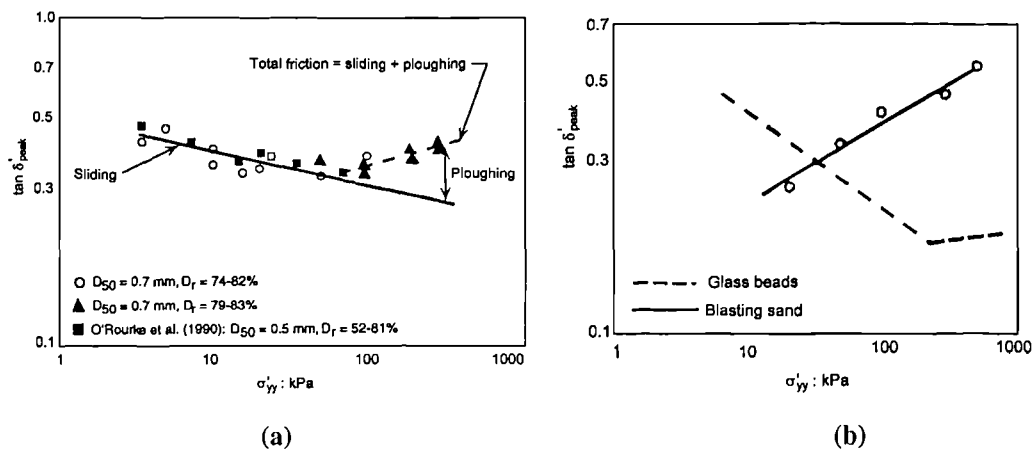


Figure 6.31: Peak interfacial resistance of interfaces comprising a smooth HDPE Geomembrane and (a) Ottawa sand and (b) glass beads and an angular blasting sand (after Dove & Frost, 1999)

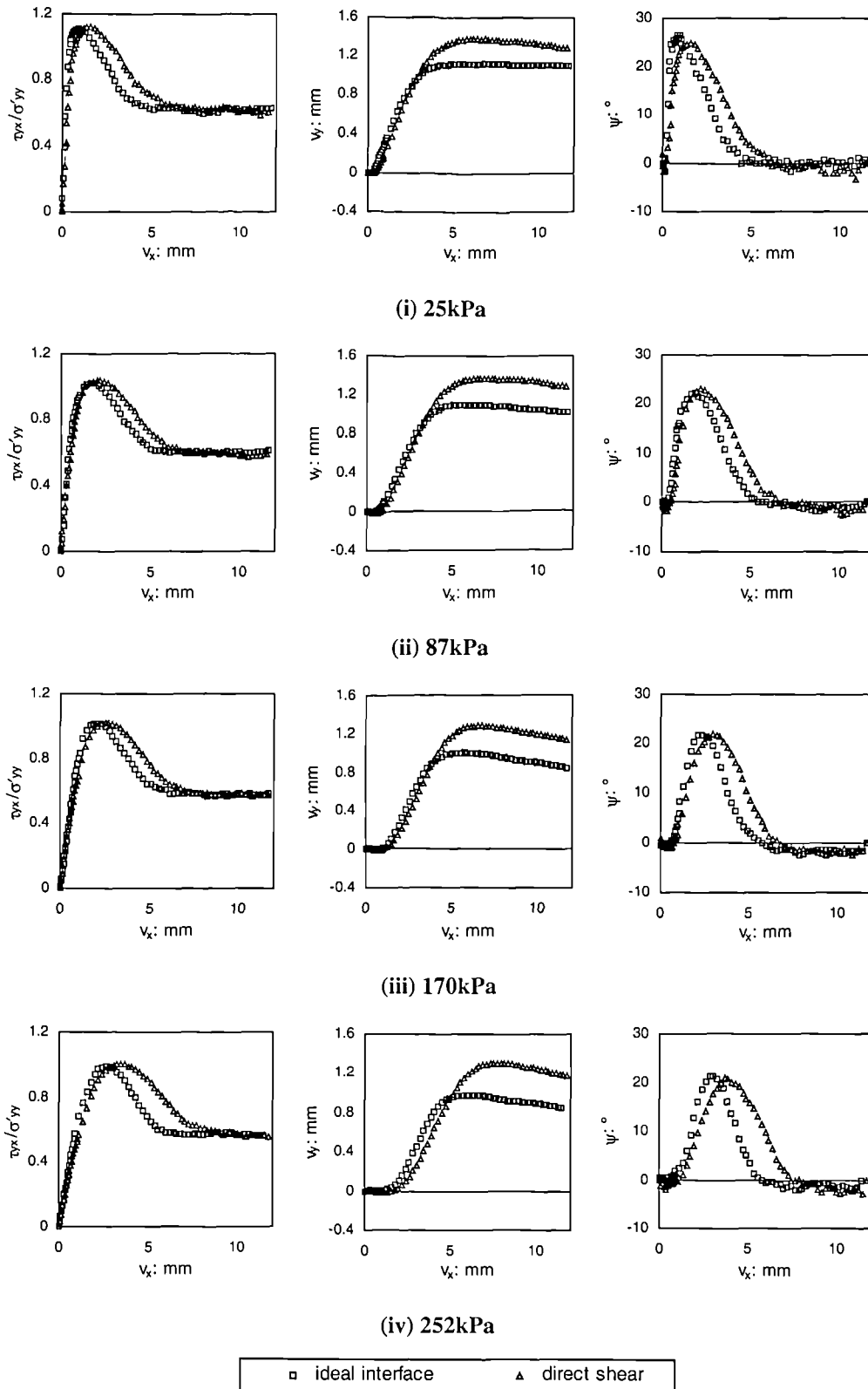


Figure 7.1(a): Equivalent ideal interface and shear tests for dense VLB at various stress levels

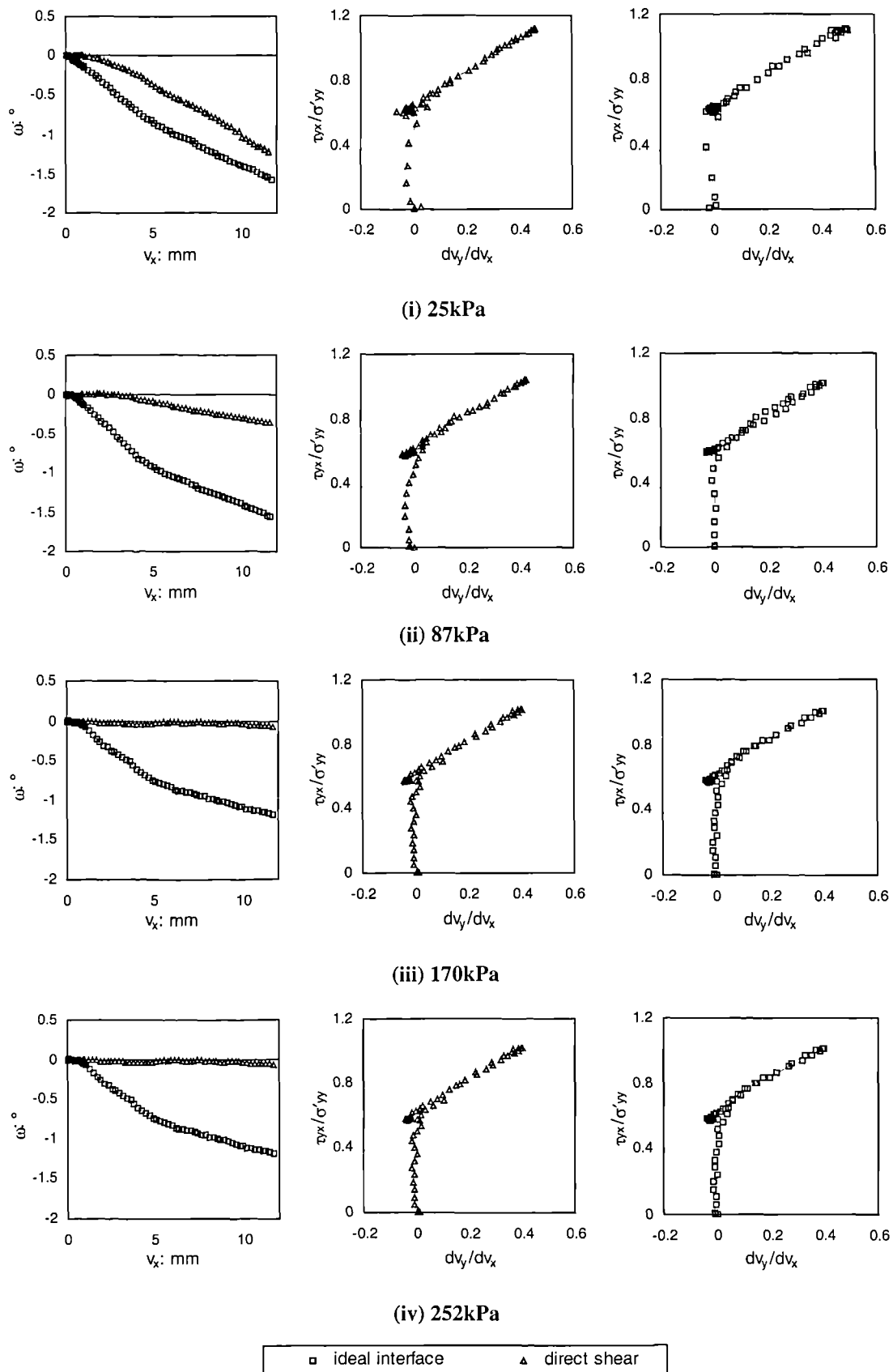


Figure 7.1 (b): Equivalent ideal interface and shear tests for dense VLB at various stress levels

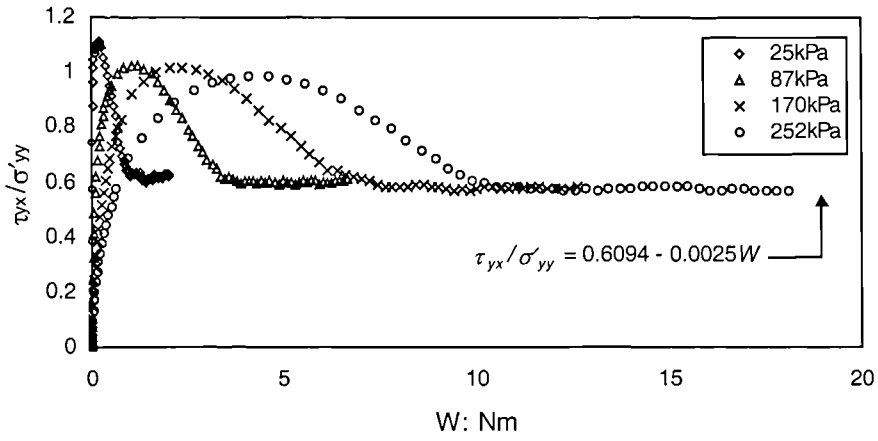


Figure 7.2: Ideal interface resistance of dense VLB confined under different stresses when work is used as the reference axis

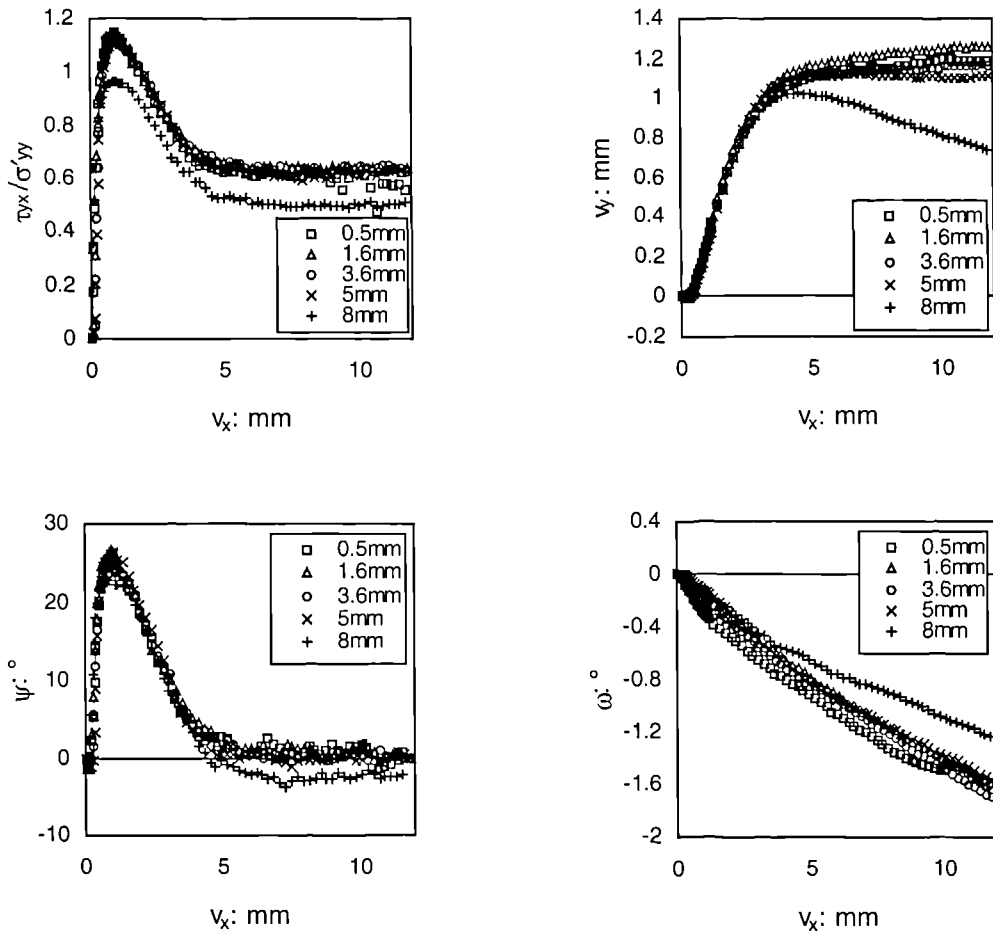


Figure 7.3: The effect of  $g$  while ideal interface testing using dense VLB under 25kPa

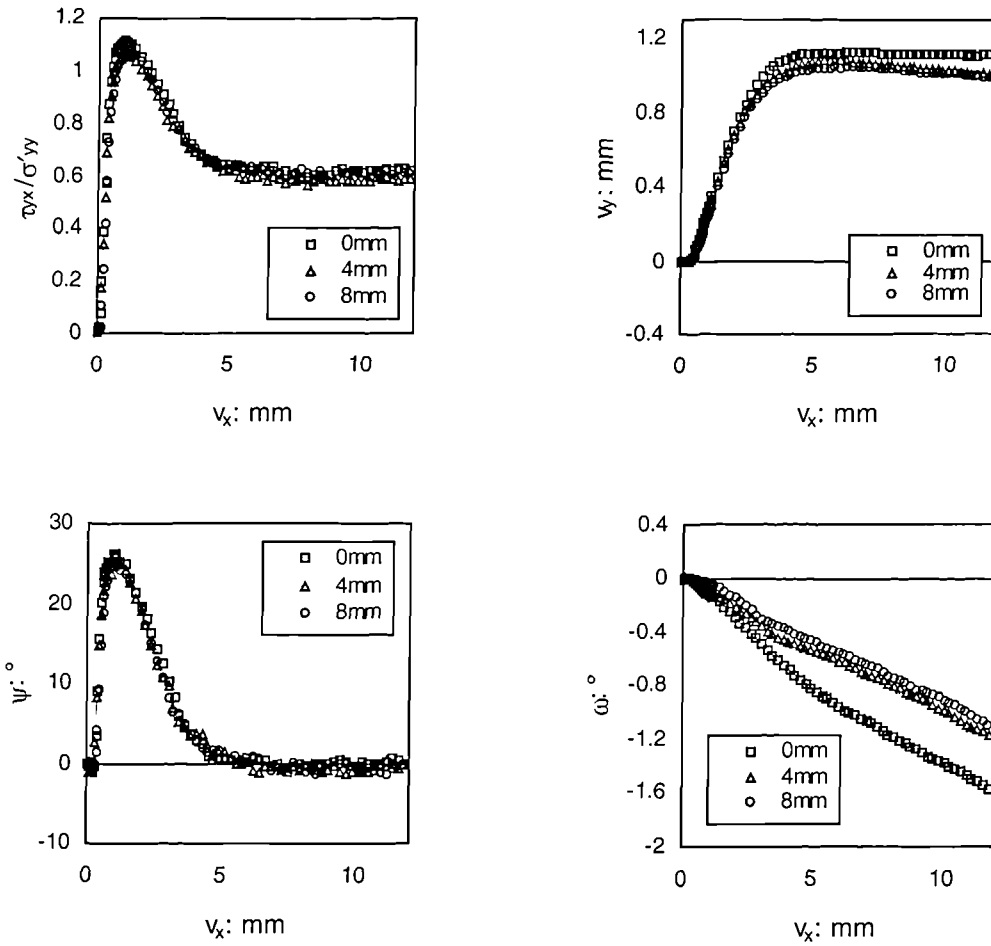
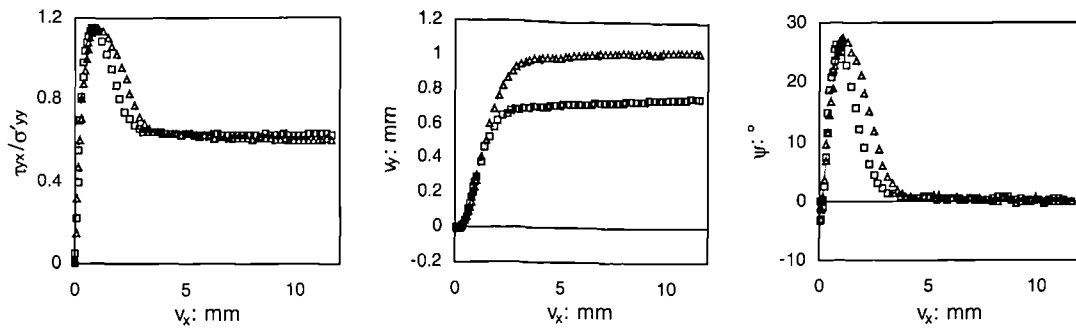
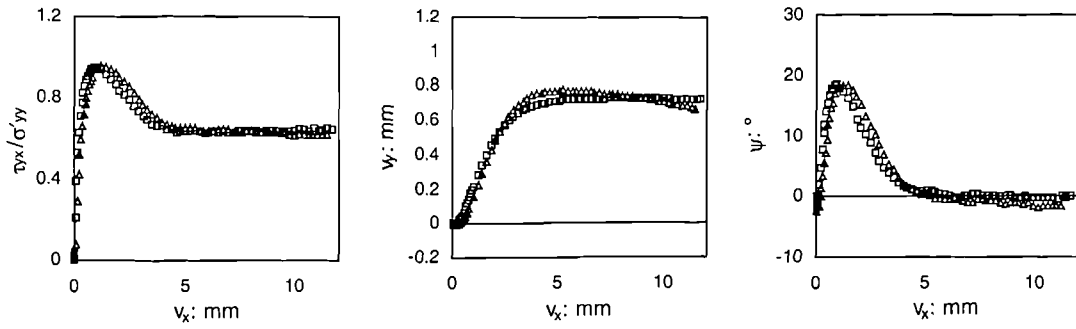


Figure 7.4: The effect of increasing  $f$  and hence the anticlockwise moment on ideal interface behaviour of dense VLB confined under 25kPa

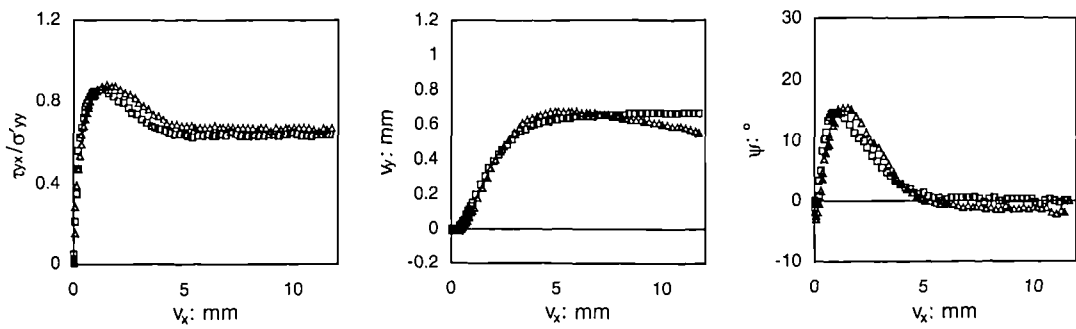




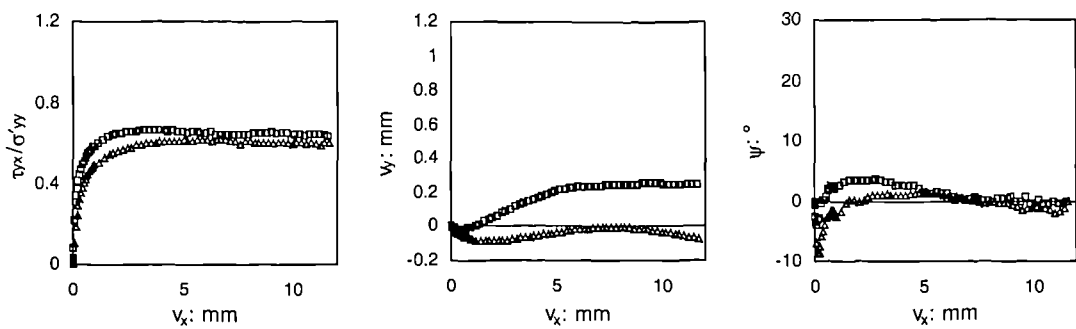
(i) Dense ( $D_r$ , circa 90%)



(ii) Medium dense ( $D_r$ , circa 76%)



(iii) Medium loose ( $D_r$ , circa 50%)



(iv) Loose ( $D_r = 19\%$  for direct shear,  $D_r = 27\%$  for ideal interface)

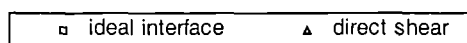
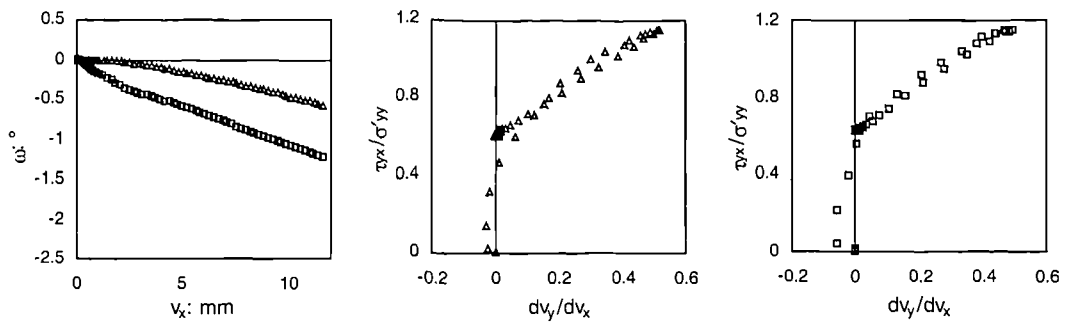
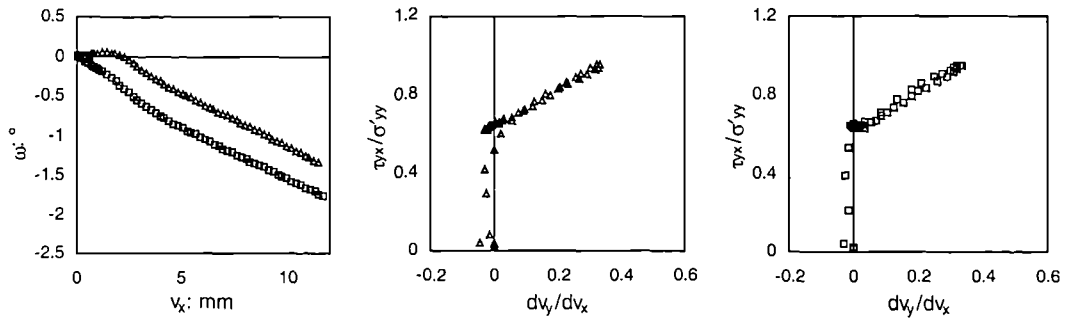


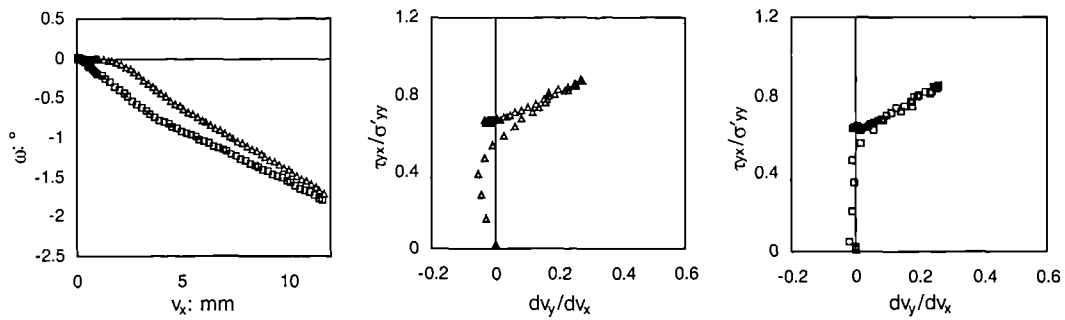
Figure 7.5(a): Comparison between ideal interface and equivalent shear tests for MGS at different density under 25kPa



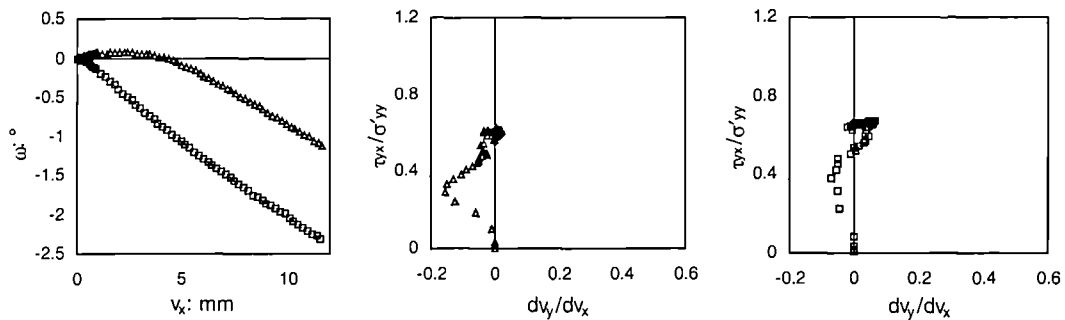
(i) Dense ( $D_r$ , circa 90%)



(ii) Medium dense ( $D_r$ , circa 76%)



(iii) Medium loose ( $D_r$ , circa 50%)



(iv) Loose ( $D_r = 19\%$  for direct shear,  $D_r = 27\%$  for ideal interface)

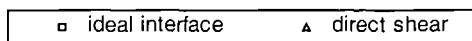


Figure 7.5(b): Comparison between ideal interface and equivalent shear tests for MGS at different density under 25kPa

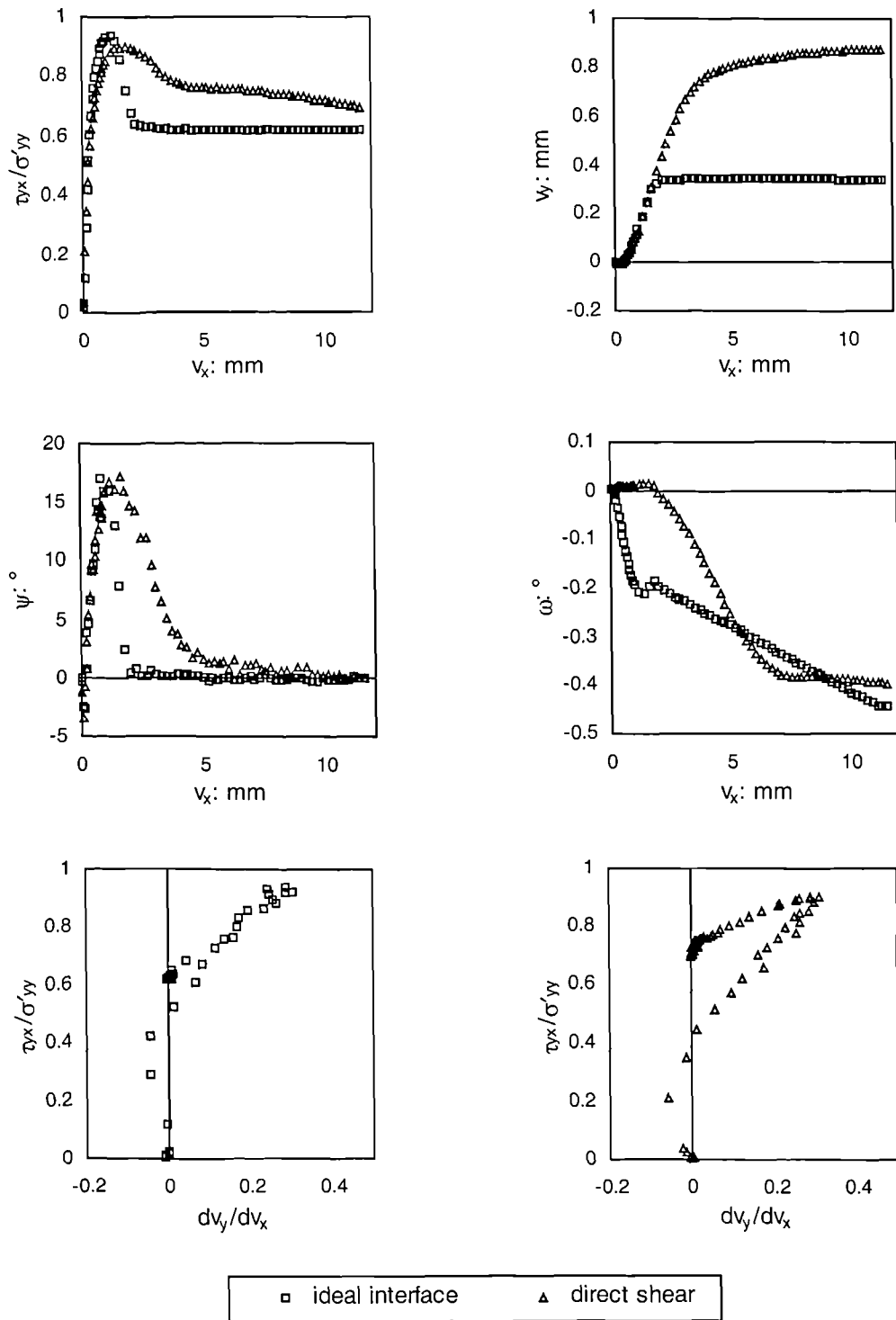
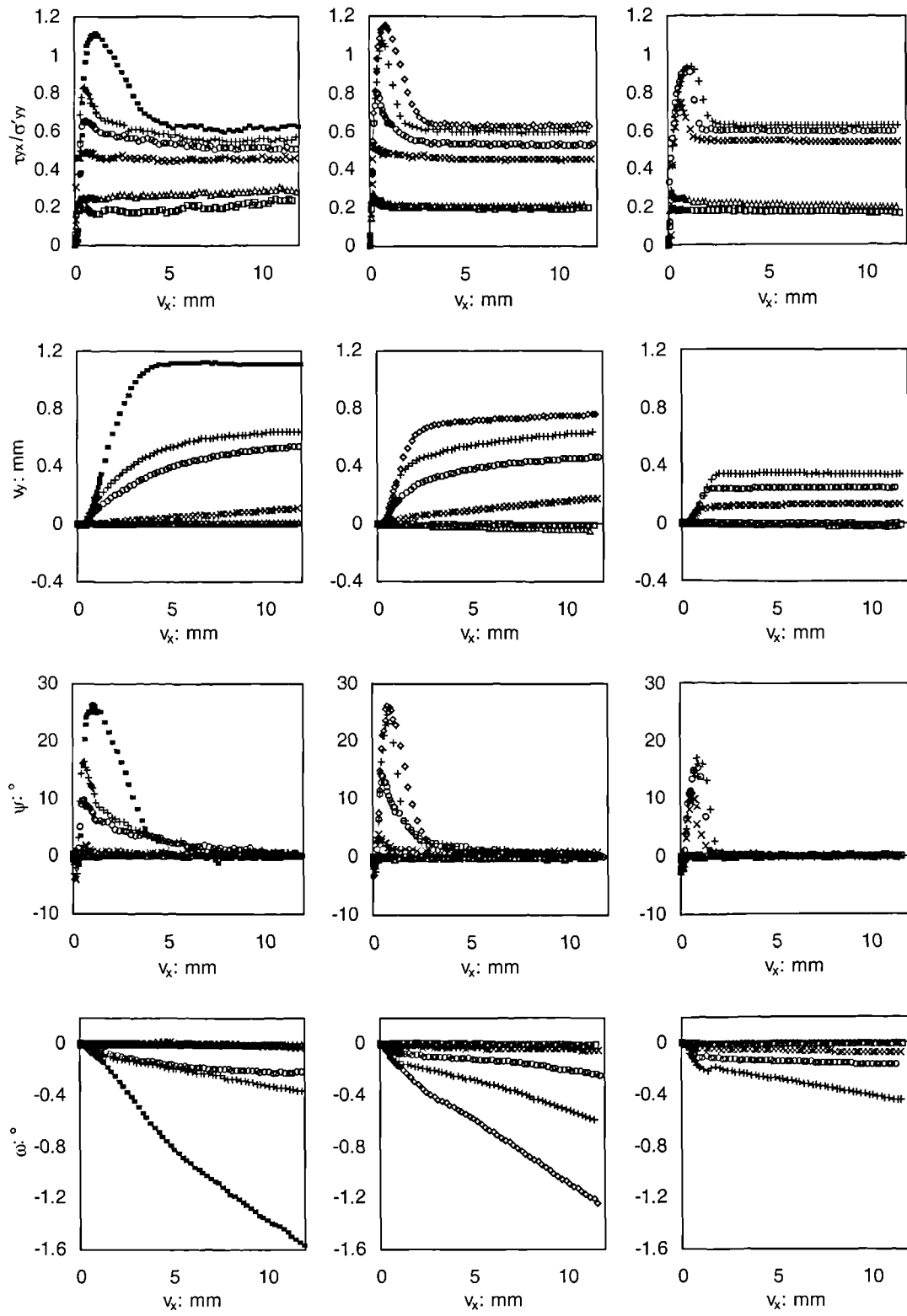


Figure 7.6: Comparison between ideal interface and shear tests using dense SFS and 25kPa confining stress



(a) Sand type: VLB

(b) Sand type: MGS

(c) Sand Type: SFS

Surface type: □ POL    △ GND    × ALO    ○ SIC    + SFS    ◇ MGS    -·- VLB

Figure 7.7: Interfacial behaviour of dense sands on surfaces of different roughness under 25kPa

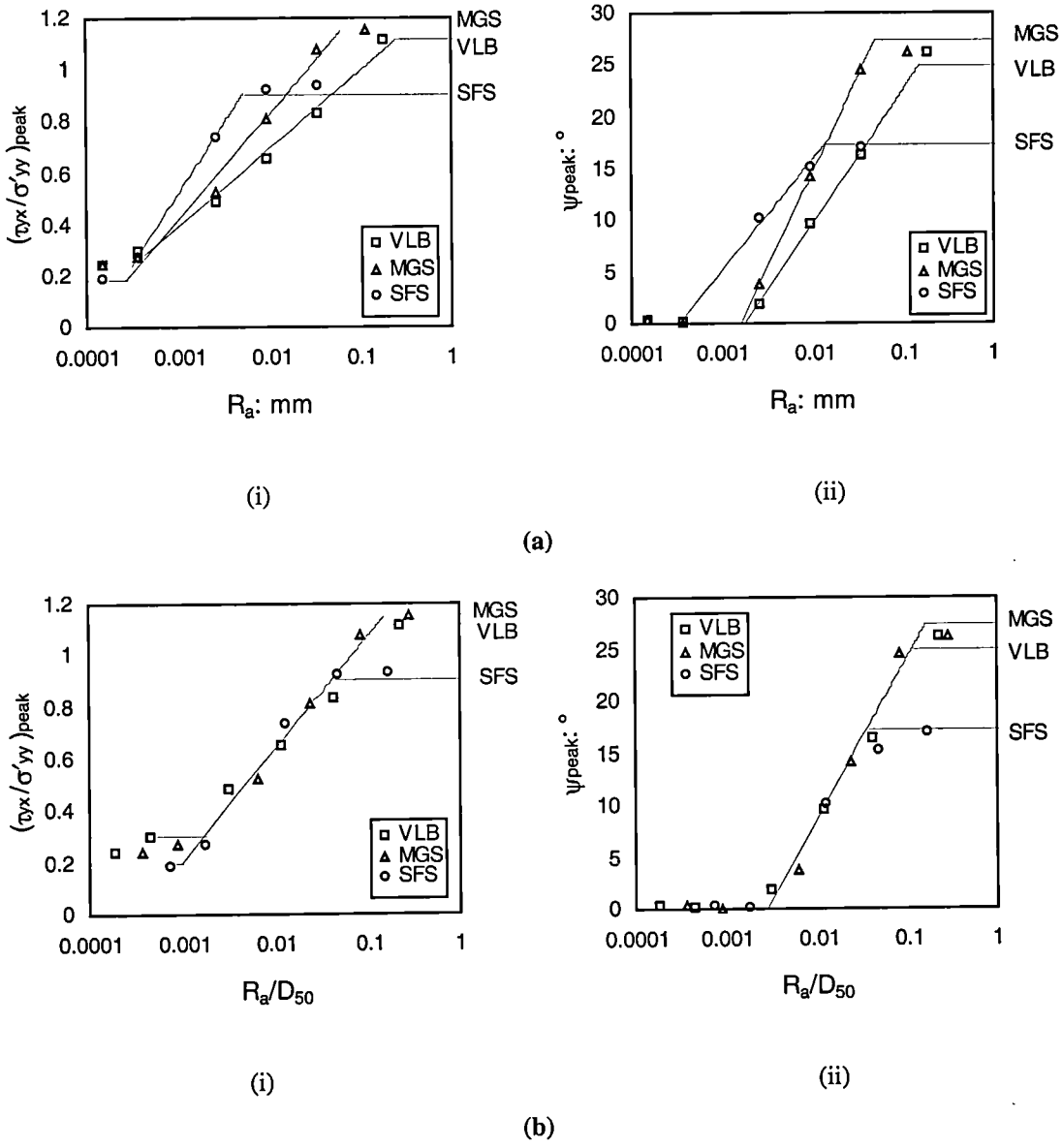
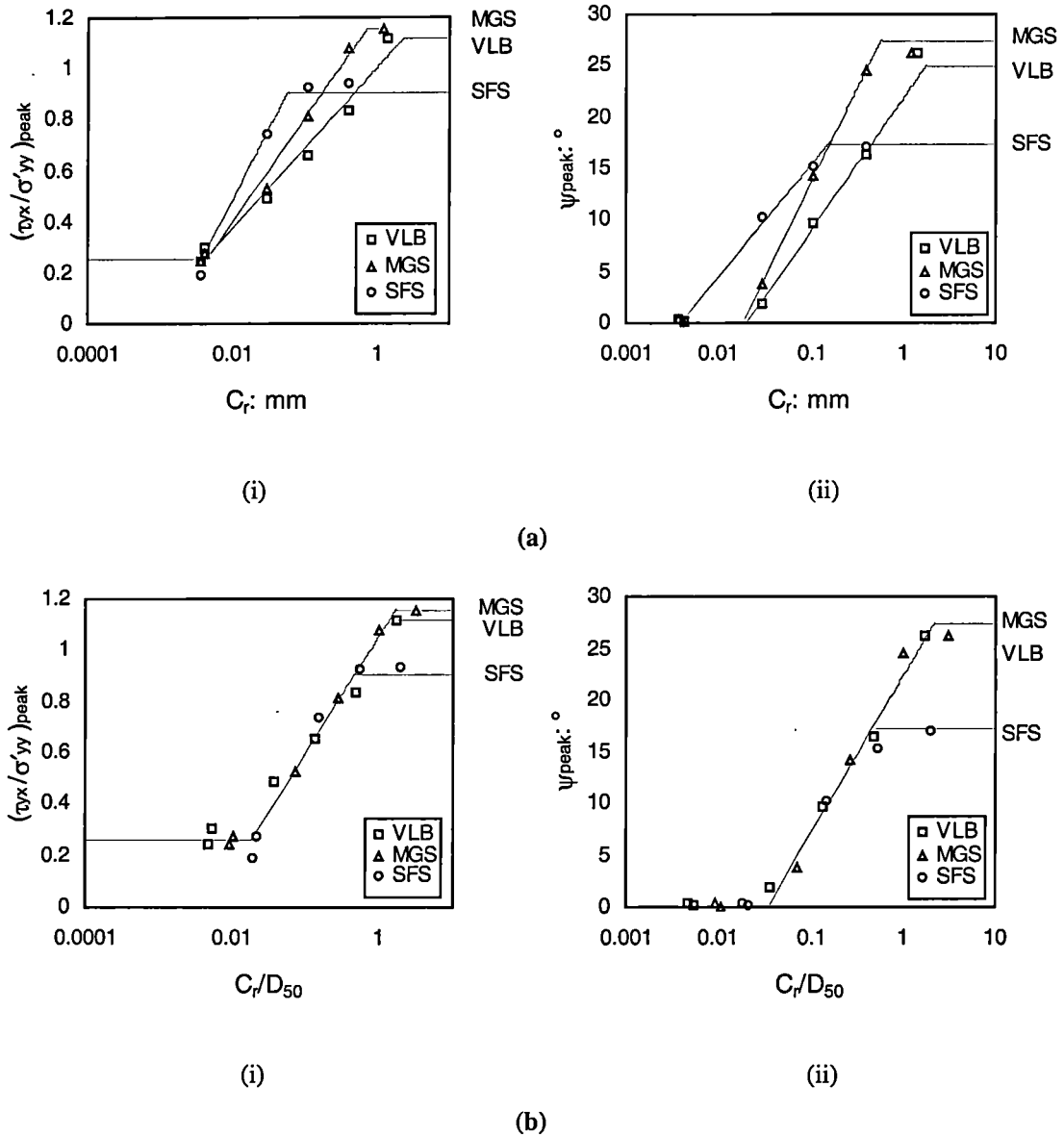


Figure 7.8: The variation of peak interface resistance dilatancy rate with (a)  $R_a$  and (b)  $R_a/D_{50}$  for different sands, deposited at densities close to their maximum and tested under confining stress of 25kPa



**Figure 7.9:** The variation of (i)  $\tan(\delta'_{peak})$  and (ii)  $\psi_{peak}$  with (a)  $C_r$ , the smooth-rough crossover length derived from structured walk analysis, and (b)  $C_r/D_{50}$  for different dense sands under 25kPa confining stress

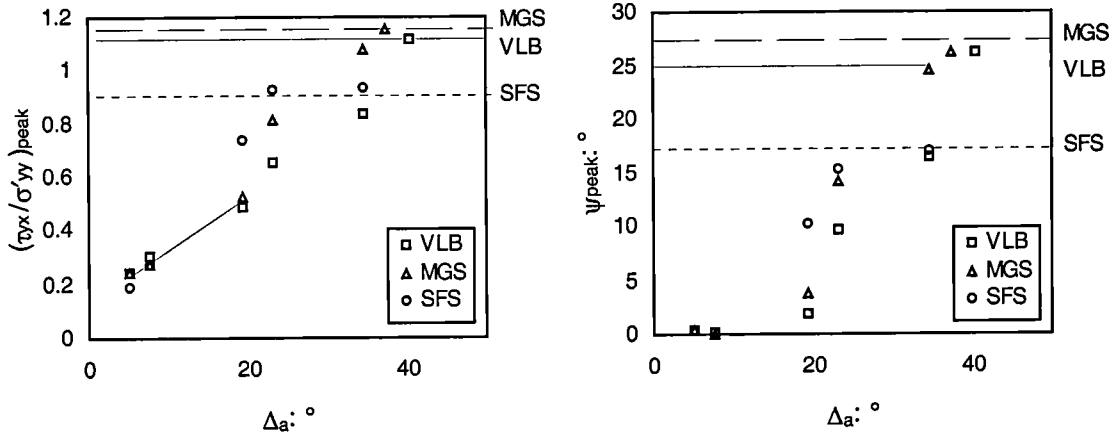


Figure 7.10: Peak-state interface data featuring various dense sands confined under 25kPa on surfaces of various roughness quantified using  $\Delta_a$

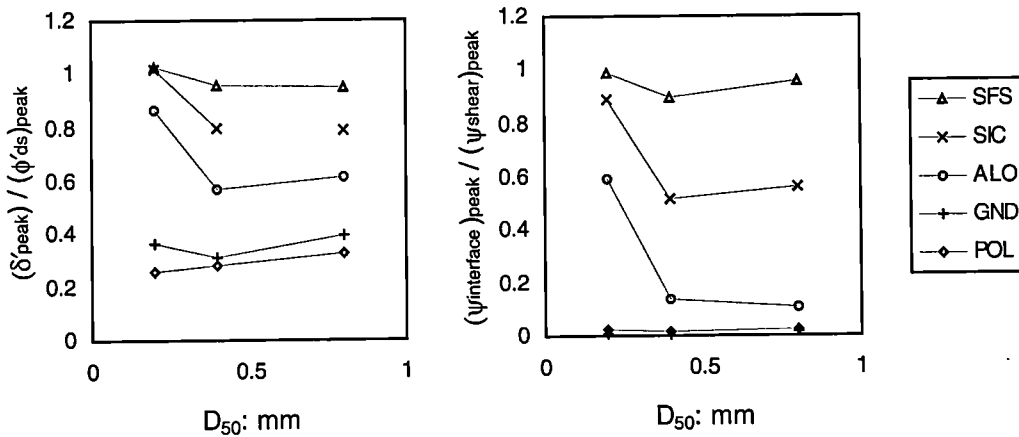


Figure 7.11: The peak response of interfaces featuring various sands and various surfaces plotted with reference to  $D_{50}$

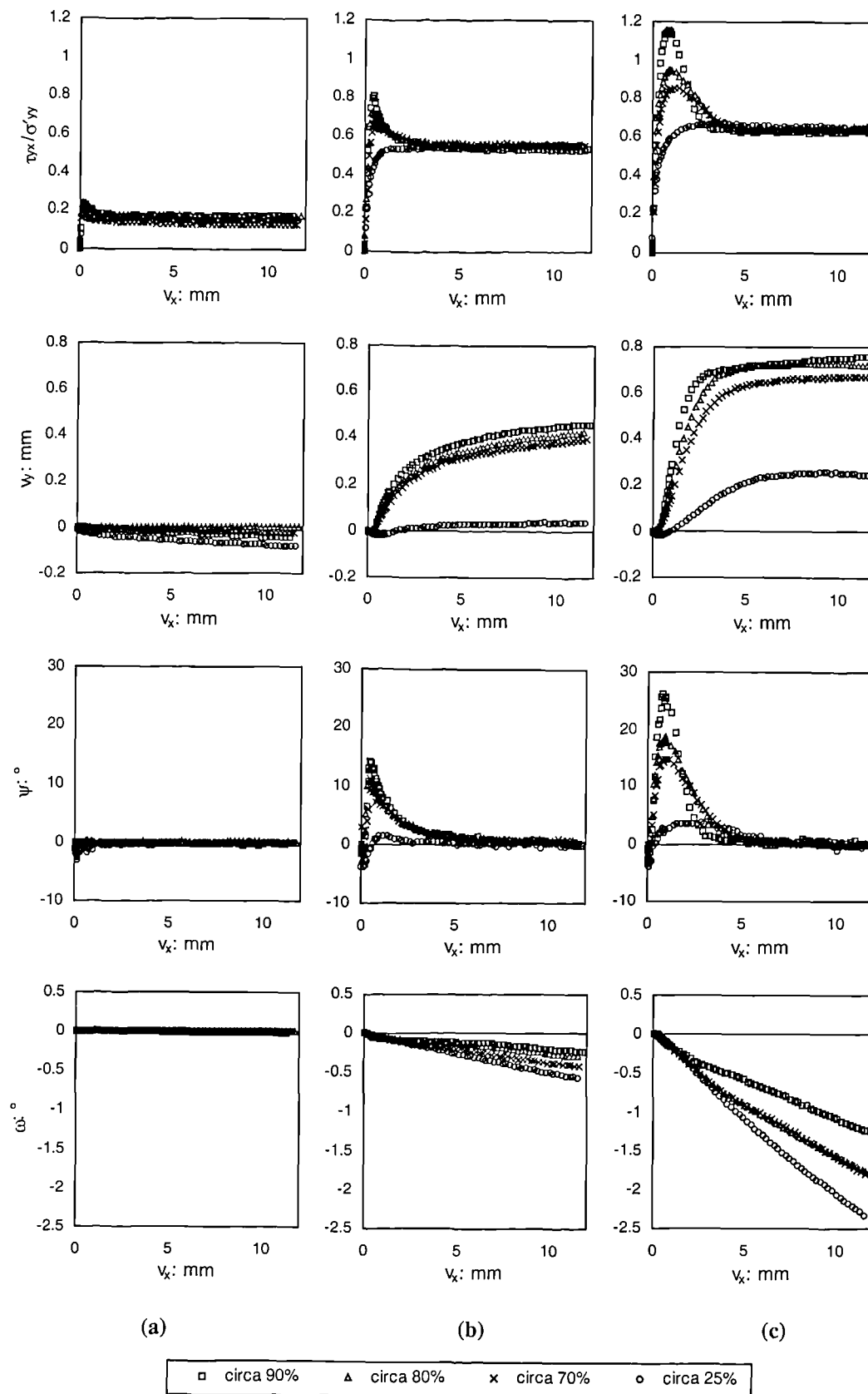


Figure 7.12: Response of interfaces featuring MGS deposited at different densities confined under 25kPa on surfaces with roughness (a) GND, (b) SIC, (c) MGS



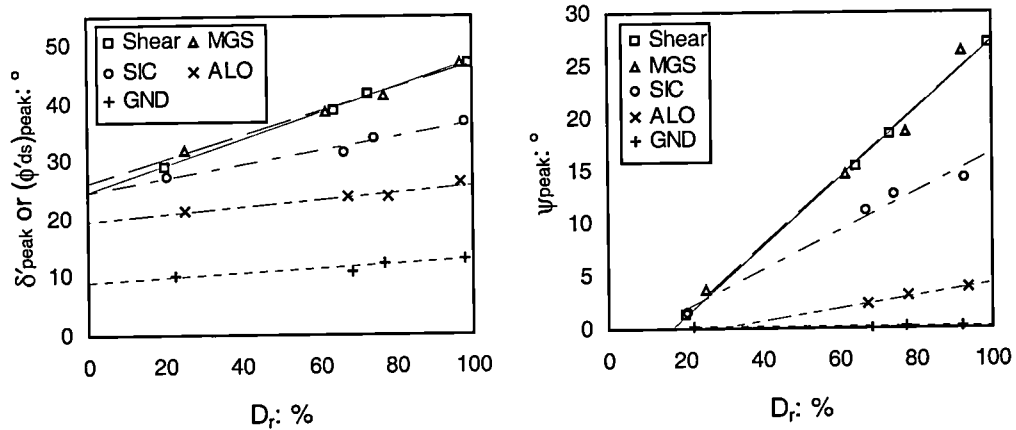


Figure 7.13: The effect of density on MGS's peak response during interface and direct shear testing when confined under 25kPa

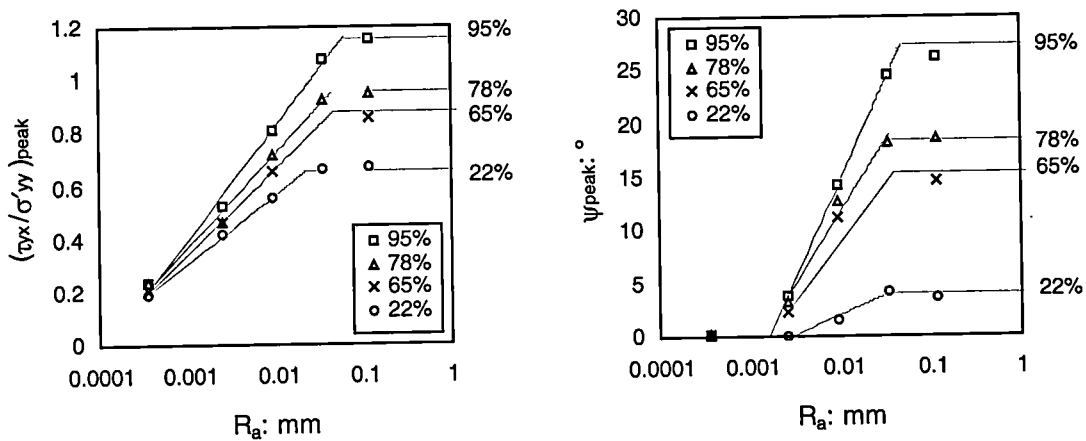


Figure 7.14: The influence of density on the interfacial resistance of MGS under 25kPa on surfaces of different roughness



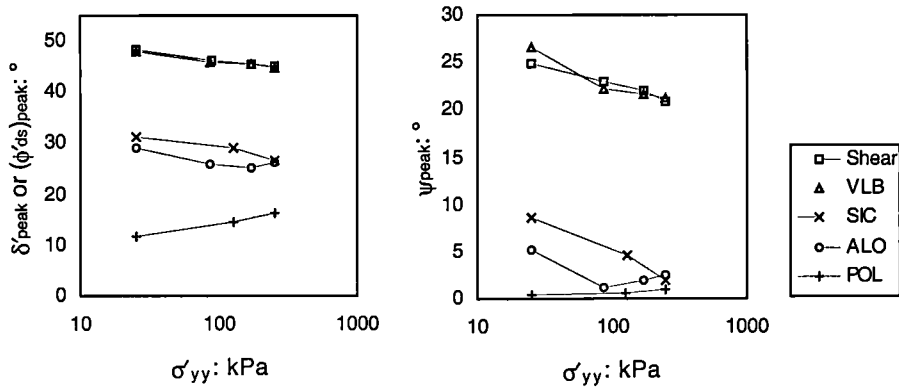


Figure 7.16: The effect of  $\sigma'_{yy}$  on the peak states of interfaces of different roughness as indicated

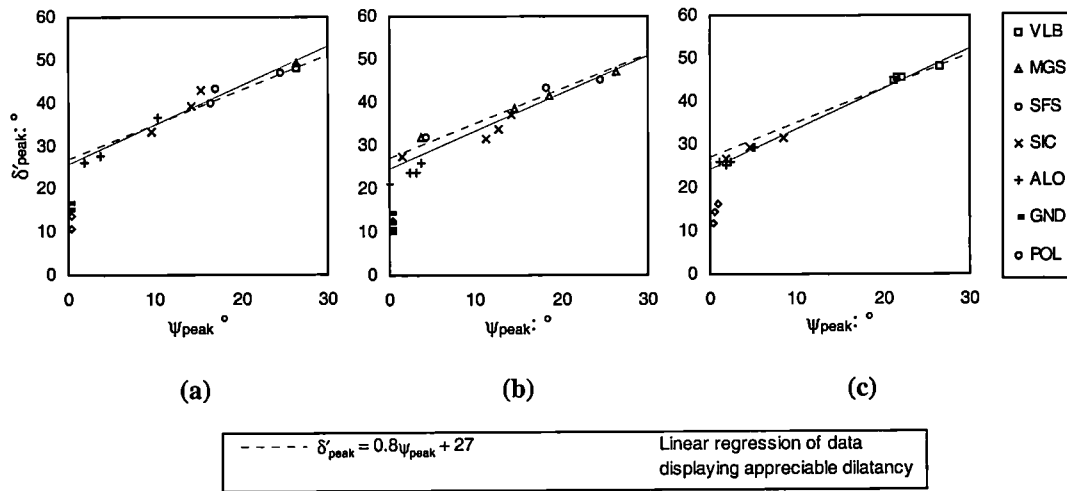


Figure 7.17: The strength-dilatancy relationship for interfaces featuring surfaces of various roughness, as indicated, and (a) three different dense sands confined under 25kPa, (b) MGS at different densities confined under 25kPa, (c) dense VLB confined under various  $\sigma'_{yy}$

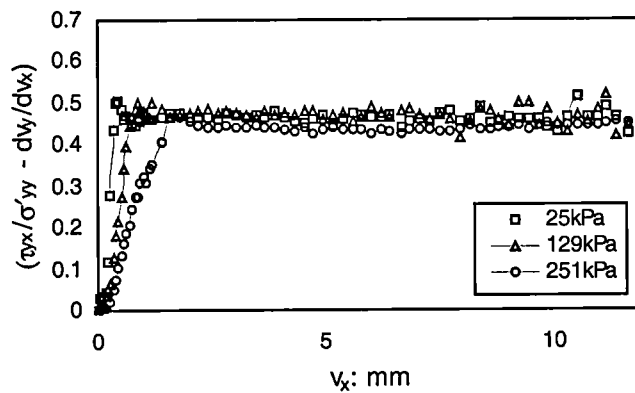


Figure 7.18: Taylor's (1948) flow rule applied to tests that experience dilation from the outset

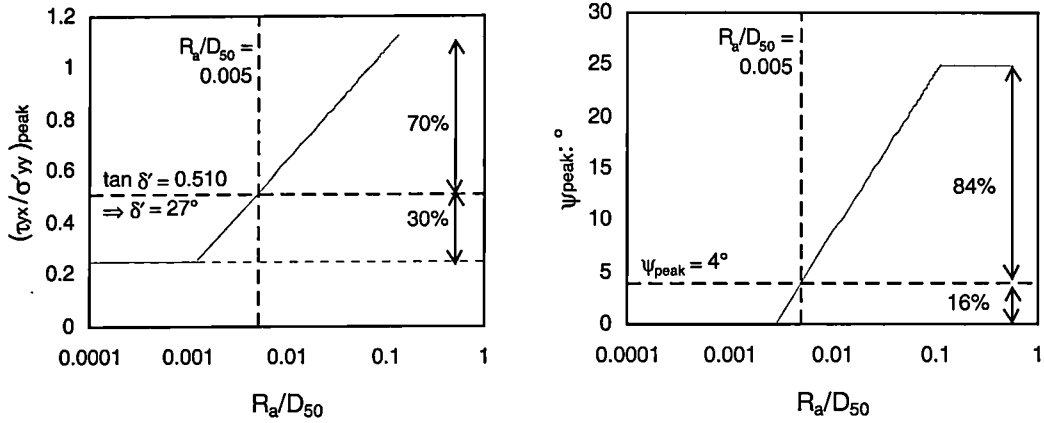


Figure 7.19: Consideration of Paikowsky et al's (1995) model of interface friction in the light of stress-dilatancy interface analysis

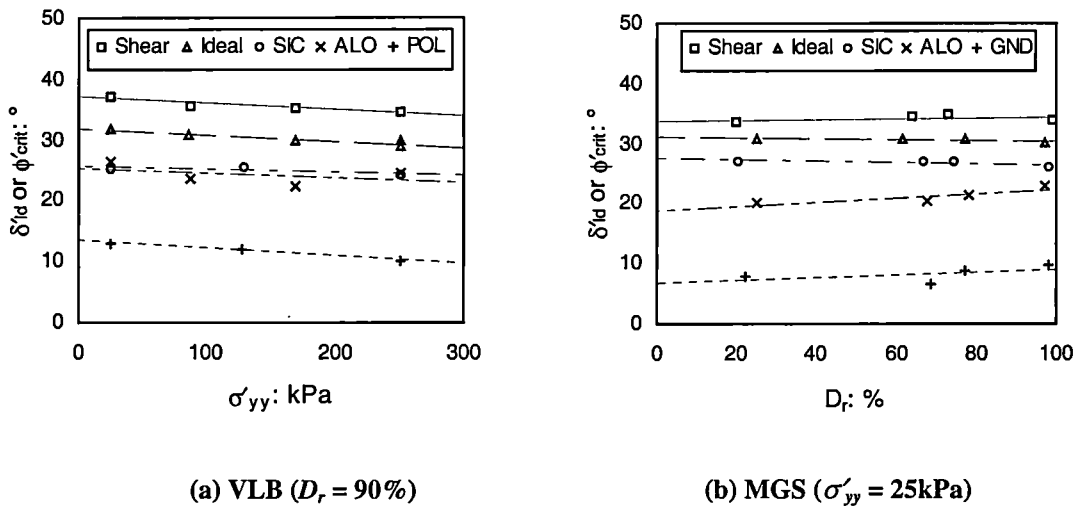


Figure 7.20: Large displacement resistance of VLB and MGS on surfaces of different roughness

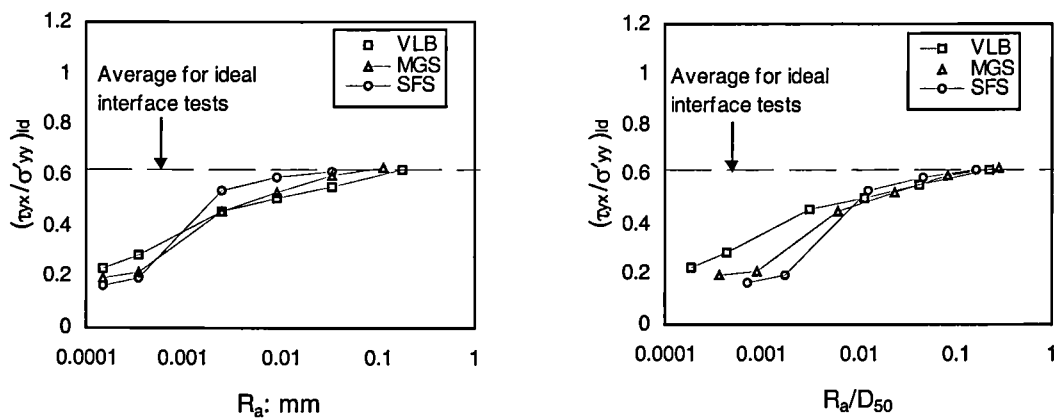


Figure 7.21: The influence of roughness on the  $(\tau_{xx}/\sigma'_{yy})_{ld}$  featuring various densely deposited sands

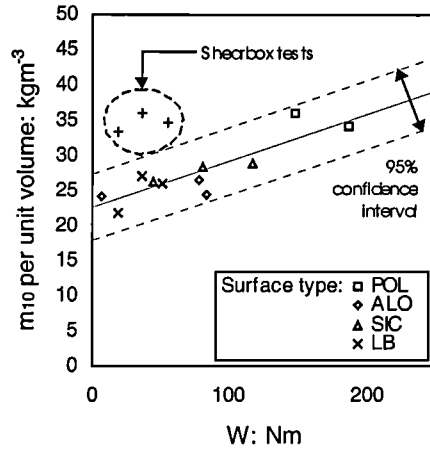


Figure 7.22: The increase in worn fragments brought about by interface testing on various surfaces

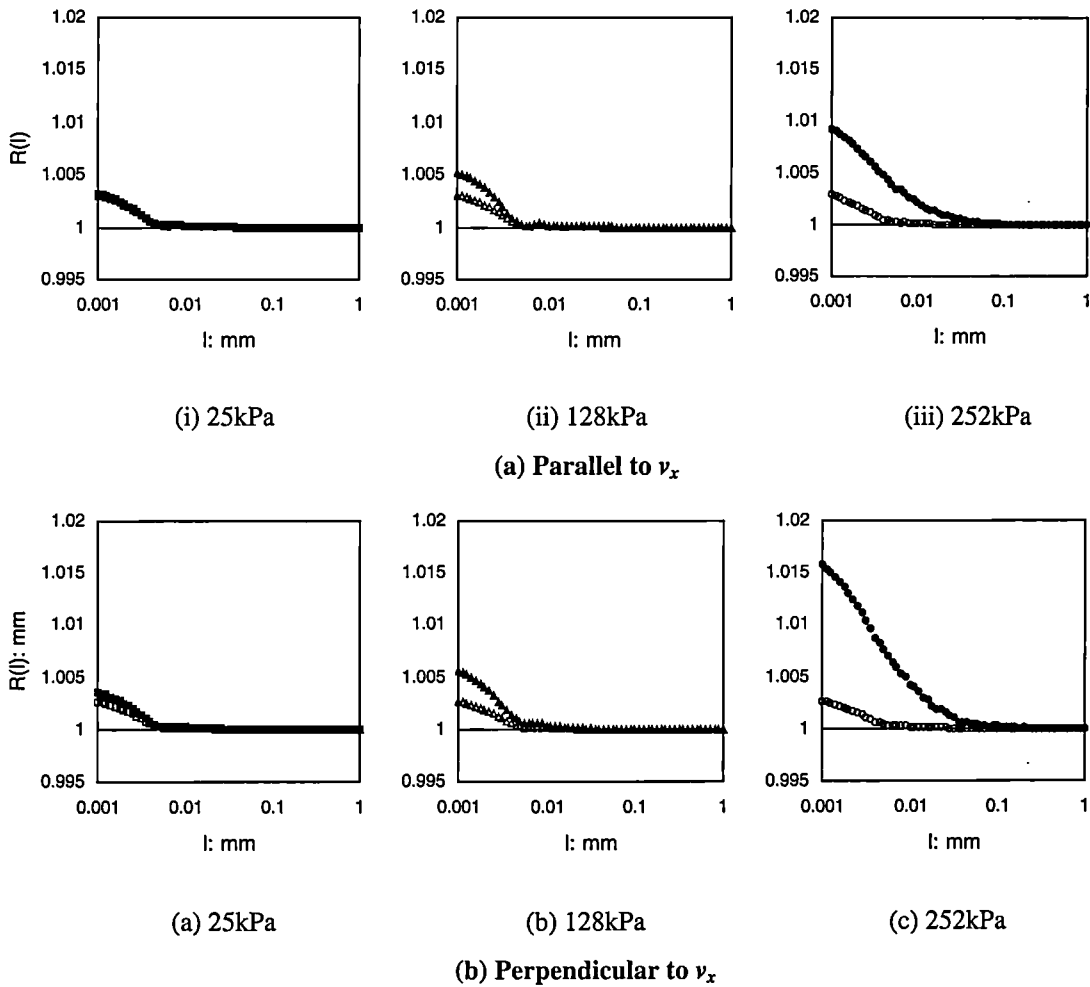


Figure 7.23: Results of structured walk analysis of an initially smooth surface (POL) taken (a) parallel and (b) perpendicular to  $v_x$  before (empty figures) and after (solid figures) interface tests at increasing  $\sigma'_{yy}$

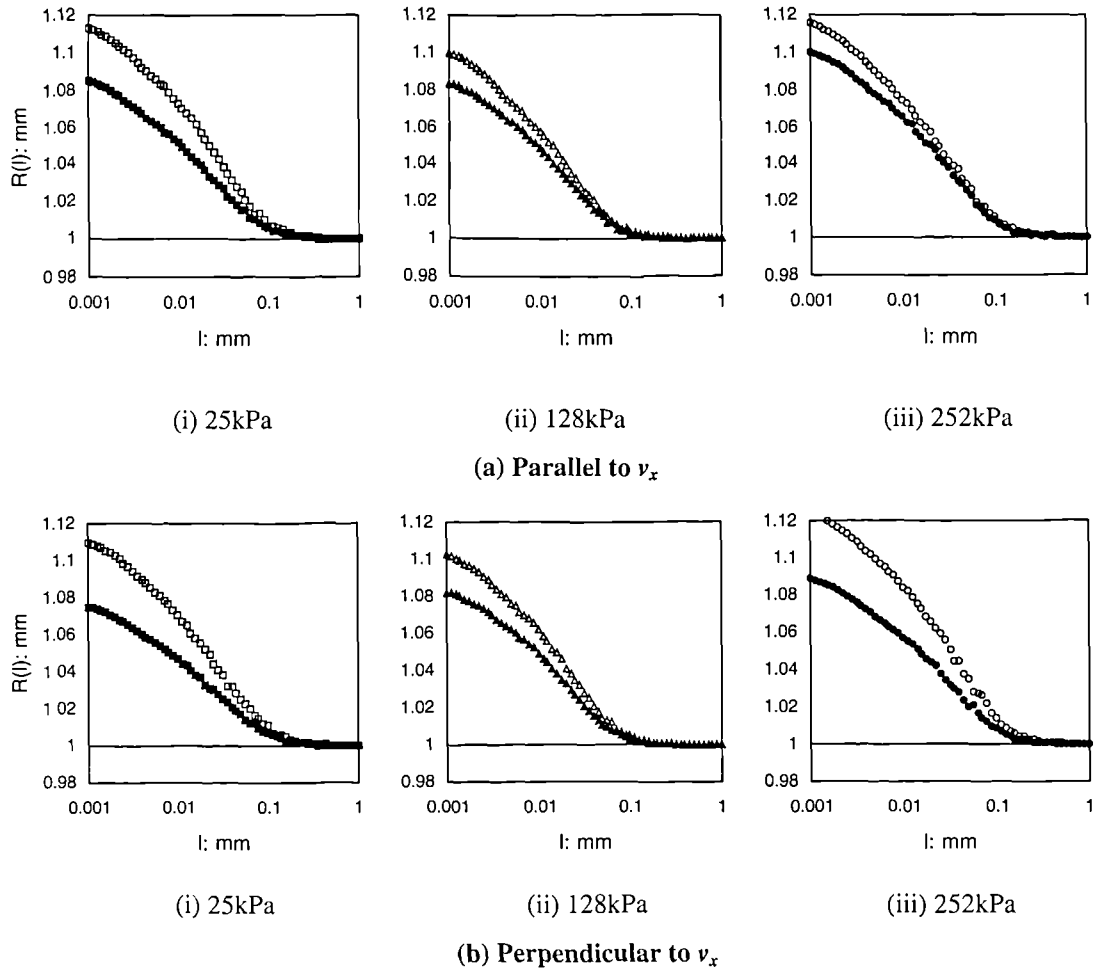


Figure 7.24: Structured walks taken (a) parallel and (b) perpendicular to  $v_x$  over an initially rough surface (SIC) before (empty figures) and after (solid figures) testing at the confining stresses indicated

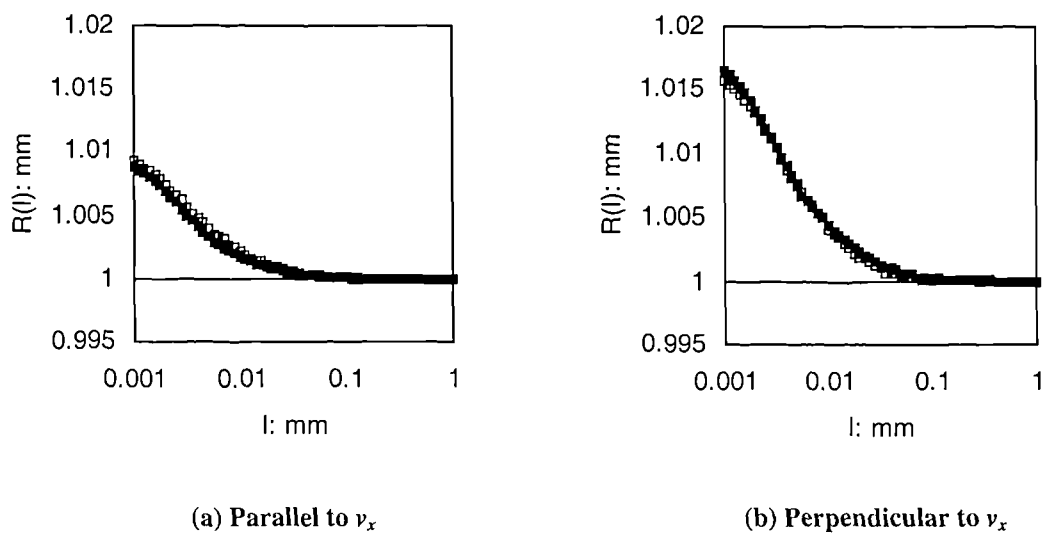


Figure 7.25: The effect of subjecting worn surfaces to further testing-POL

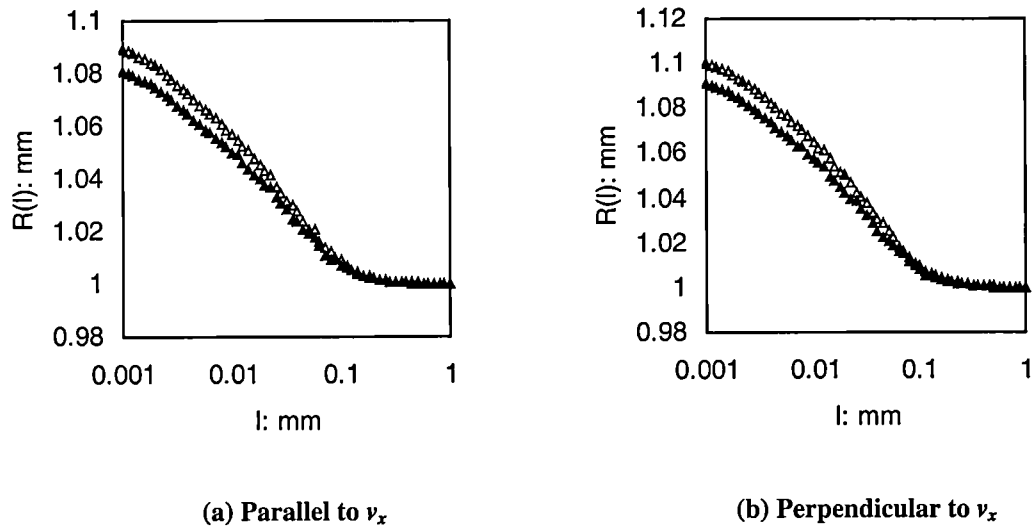


Figure 7.26: The effect of subjecting worn surfaces to further testing- SIC

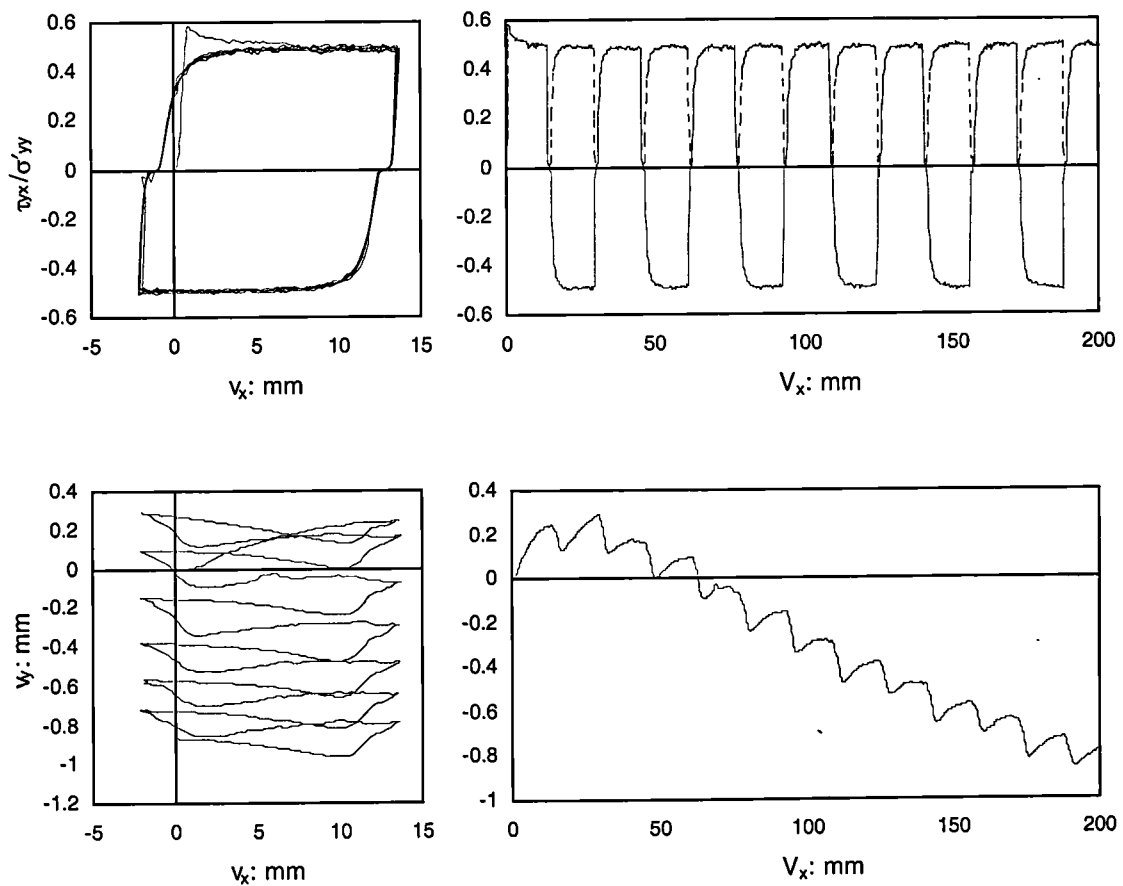
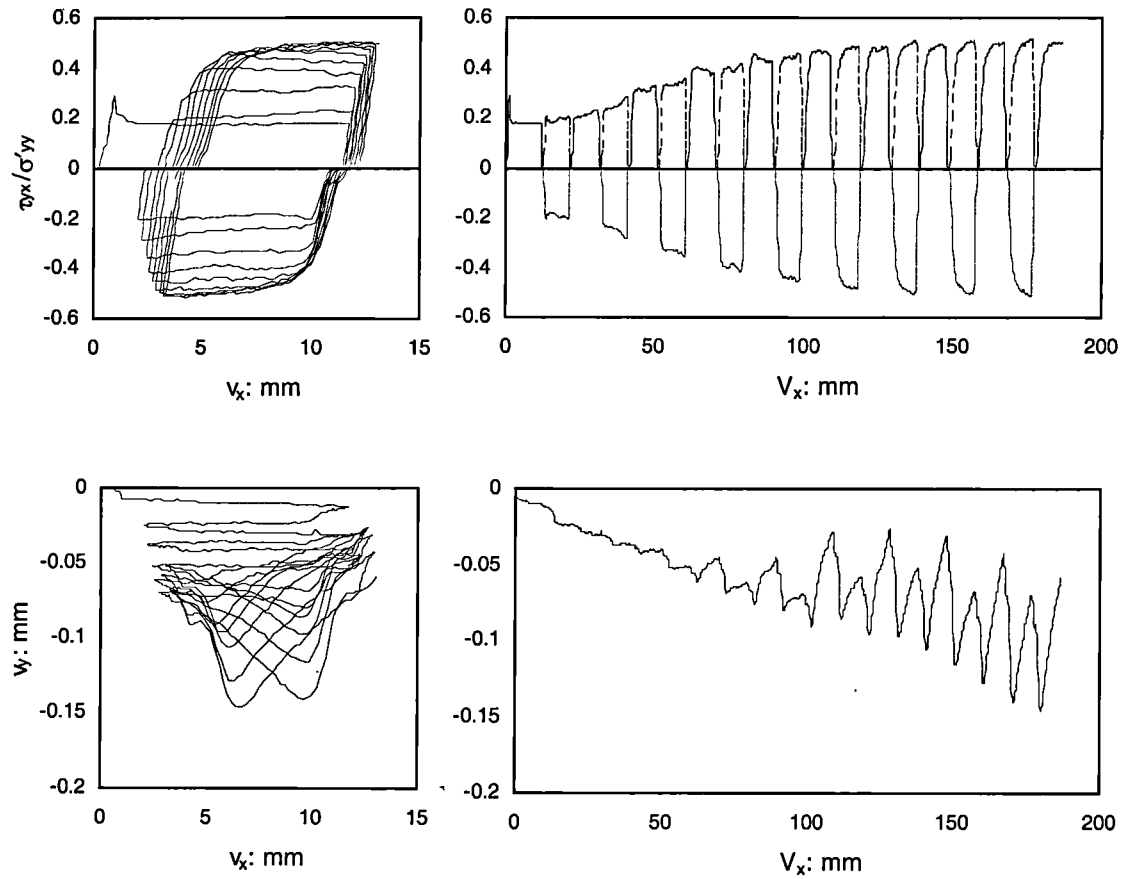


Figure 7.27: Repeated shear of a dense VLB-SIC interface under 128kPa confining stress



**Figure 7.28: Repeated shear of a dense VLB-POL interface under 252kPa confining stress**



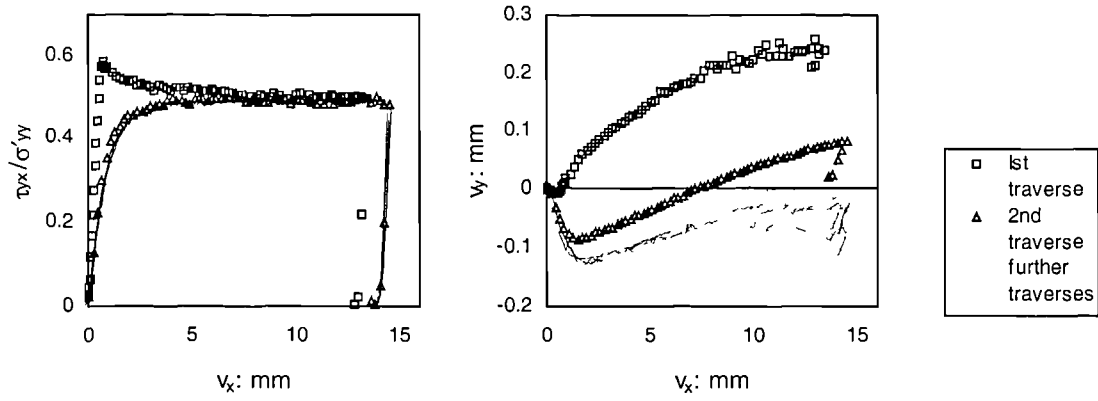


Figure 7.29: The evolution of response of a dense VLB-SIC interface ( $\sigma'_{yy} = 252\text{kPa}$ )

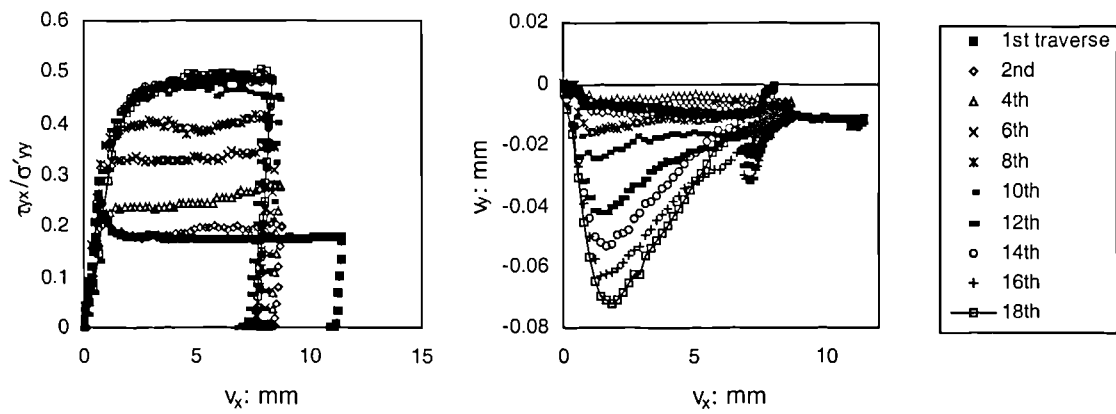


Figure 7.30: The evolution of response of a dense VLB-POL interface ( $\sigma'_{yy} = 252\text{kPa}$ )

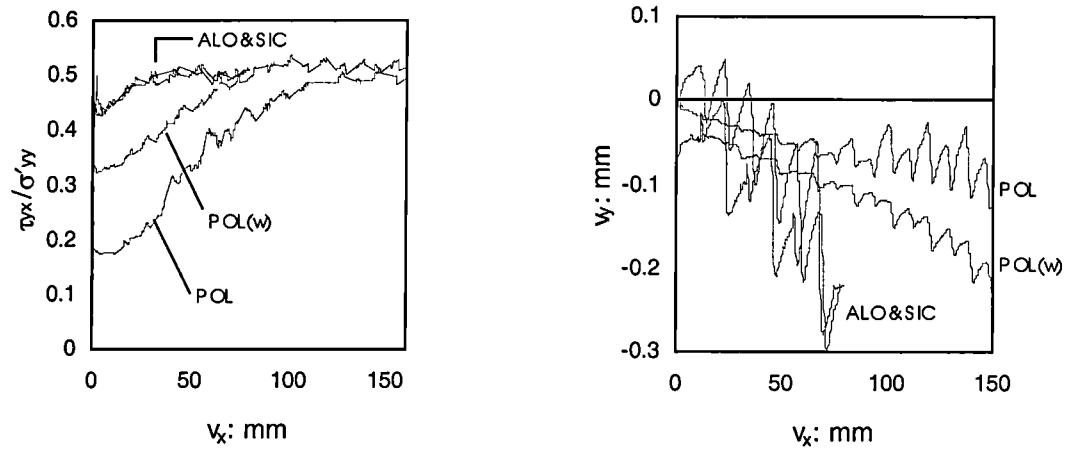


Figure 7.31: The effect of initial roughness on multi-reverse interface behaviour featuring dense VLB confined under 252kPa

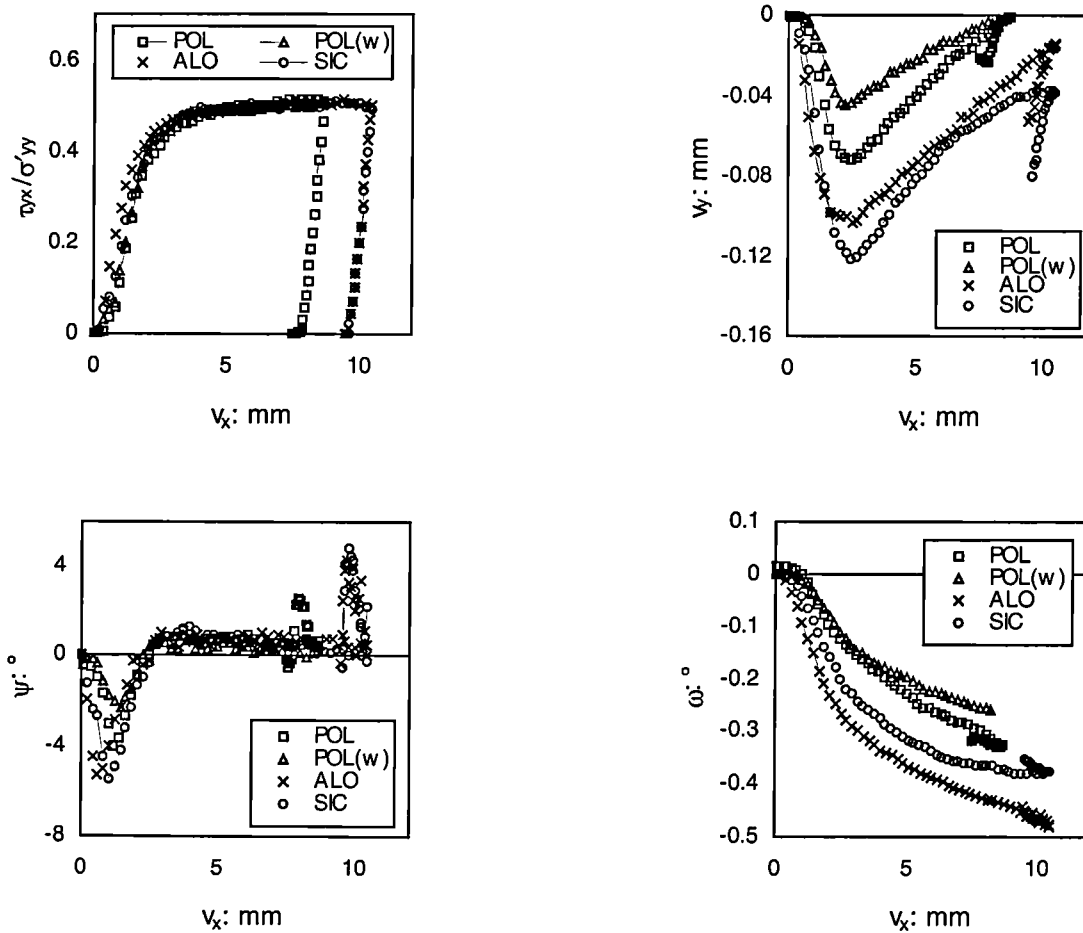


Figure 7.32: The final traverse of interfaces featuring dense VLB and surfaces of different initial roughness, each confined under 252kPa

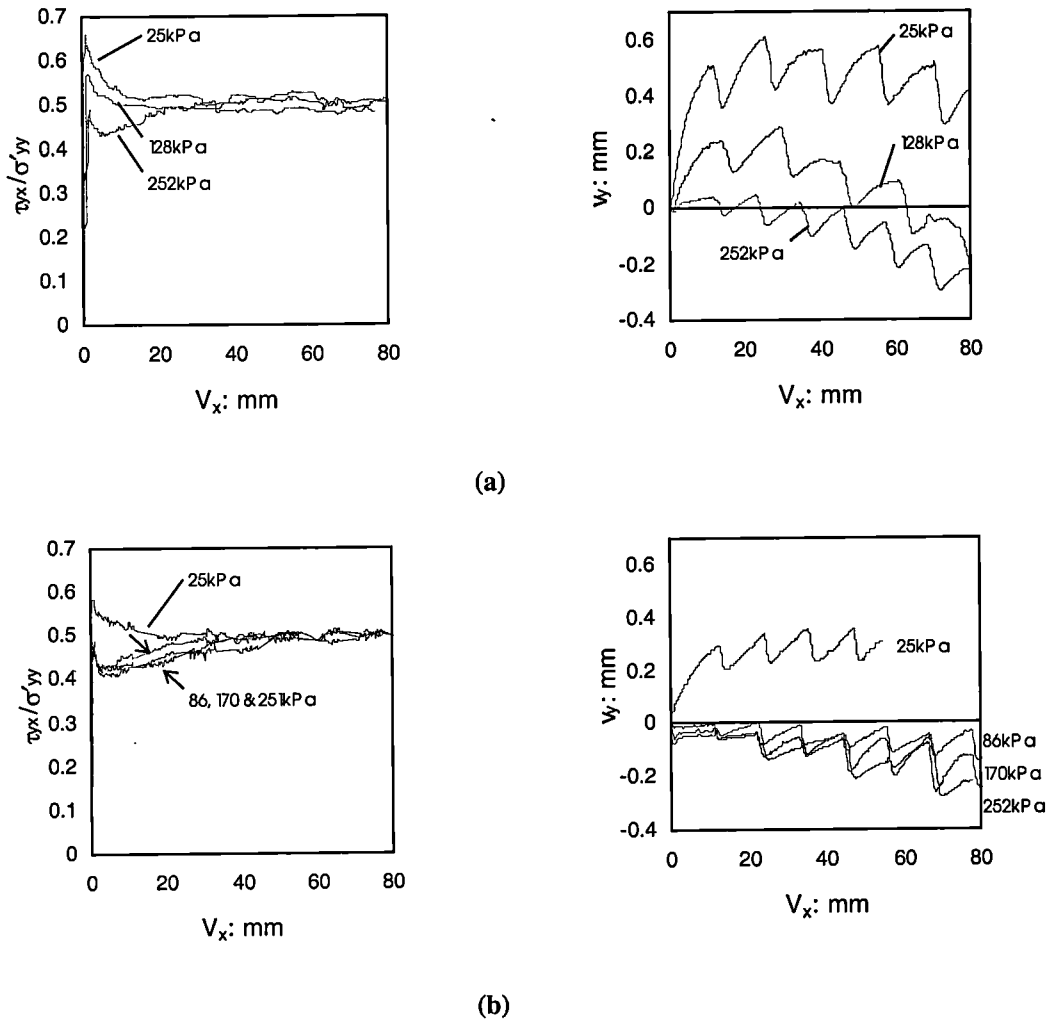


Figure 7.33: The effect of confining stress during the reverse shearing of an interface comprising dense VLB and (a) SIC and (b) ALO

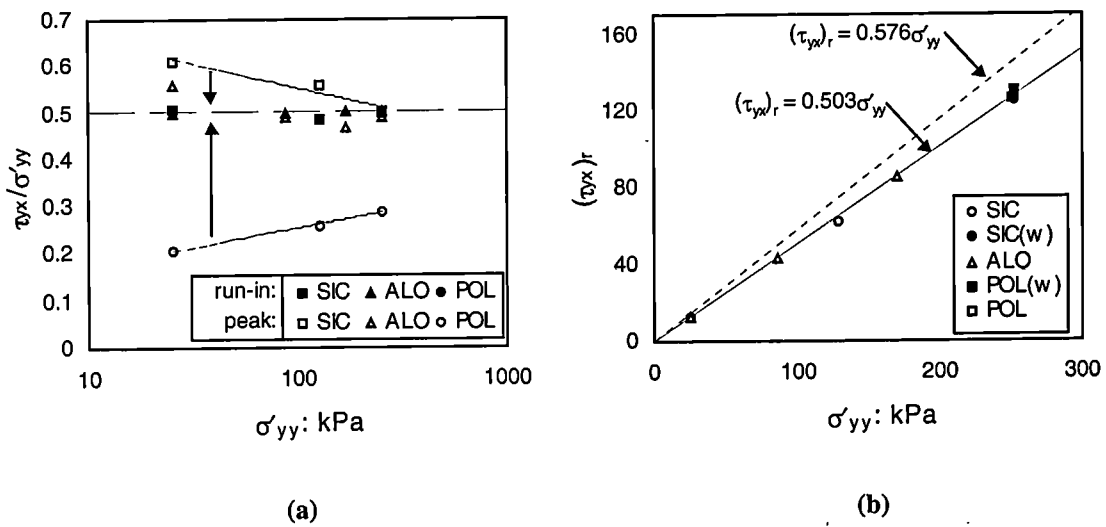


Figure 7.34: The relationship between  $\delta'_r$  and  $\sigma'_{yy}$  for dense VLB interfaces

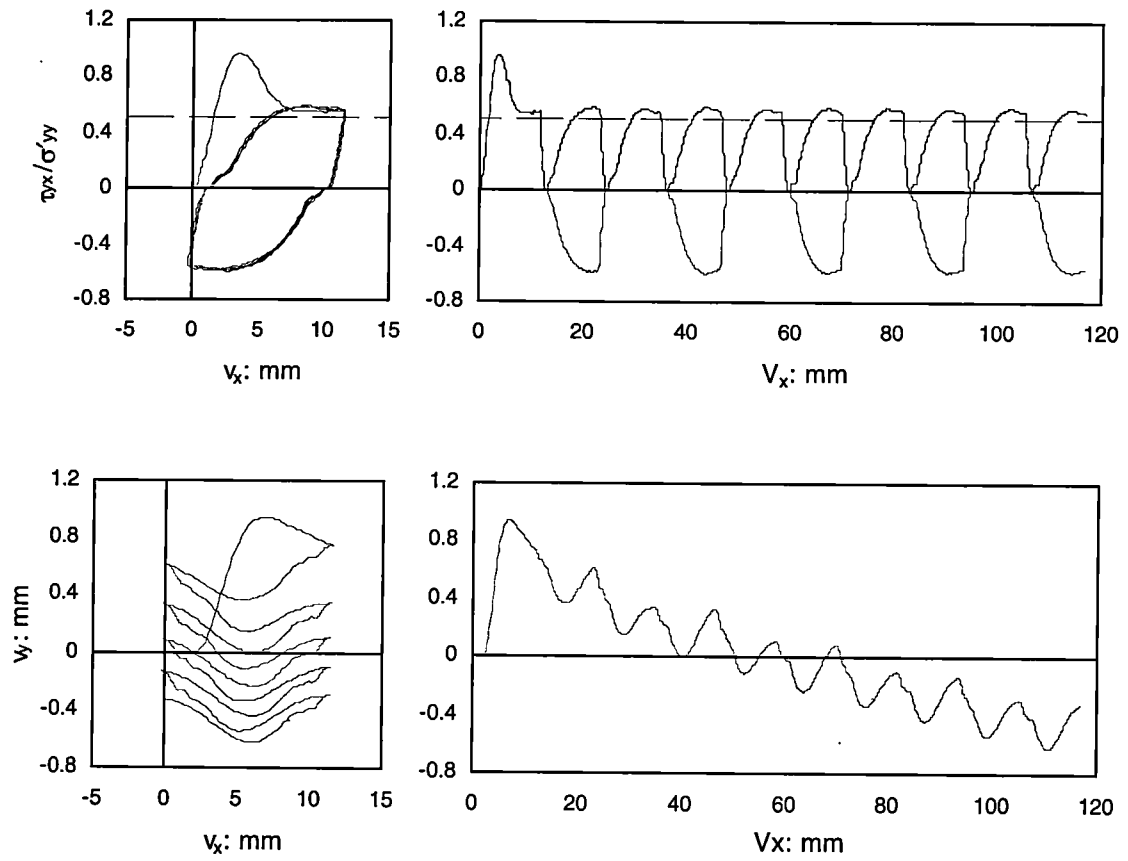


Figure 7.35: Reverse ideal interface test featuring dense VLB confined under 252kPa